Biodegradable and Self-Immolative Block Copolymers for Drug Delivery to Tumor Xenografts

विद्या वाचस्पति की
उपाधि की अपेक्षाओं की आंशिक पूर्ति में प्रस्तुत शोध प्रबंध

A thesis submitted in partial fulfillment of the requirements of the degree of Doctor of Philosophy

द्वारा / By
पठान शाहिदखान इलियासखान
Pathan Shahidkhan Iliyaskhan

पंजीकरण सं. / Registration No.:20193661

शोध प्रबंध पर्यवेक्षक / Thesis Supervisor:
प्रोफ. एम. जयकन्नन /Prof. M. Jayakannan

भारतीय विज्ञान शिक्षा एवं अनुसंधान संस्थान पुणे
INDIAN INSTITUTE OF SCIENCE EDUCATION AND RESEARCH PUNE
2025

Dedicated to

My family

INDIAN INSTITUTE OF SCIENCE EDUCATION AND RESEARCH (IISER), PUNE
(An Autonomous Institution, Ministry of Human Resource Development, Govt. of India)
Dr. Homi Bhabha Road, Pashan, Pune – 411 008

Declaration

Name of Student: **Shahidkhan Iliyaskhan Pathan**

Reg. No.: **20193661**

Thesis Supervisor(s): **Prof. M. Jayakannan**

Department: **Chemistry**

Date of joining program: **1st August 2019**

Date of Pre-Synopsis Seminar: **31st July 2024**

Title of Thesis: **Biodegradable and Self-immolative Block Copolymers for Drug Delivery to Tumor Xenografts.**

I declare that this written submission represents my idea in my own words and where others' ideas have been included; I have adequately cited and referenced the original sources. I declare that I have acknowledged collaborative work and discussions wherever such work has been included. I also declare that I have adhered to all principles of academic honesty and integrity and have not misrepresented or fabricated or falsified any idea/data/fact/source in my submission. I understand that violation of the above will be cause for disciplinary action by the Institute and can also evoke penal action from the sources which have thus not been properly cited or from whom proper permission has not been taken when needed.

The work reported in this thesis is the original work done by me under the guidance of Prof. M. Jayakannan.

Date: 15.01.2025

Shahidkhan I. Pathan

Reg. No.: 20193661

INDIAN INSTITUTE OF SCIENCE EDUCATION AND RESEARCH (IISER), PUNE
(An Autonomous Institution, Ministry of Human Resource Development, Govt. of India)
Dr. Homi Bhabha Road, Pashan, Pune – 411 008

CERTIFICATE

Certified that the work incorporated in the thesis entitled "***Biodegradable and Self-immolative Block Copolymers for Drug Delivery to Tumor Xenografts***", Submitted by **Mr. Pathan Shahidkhan Iliyaskhan**, was carried out by the candidate, under my supervision. The work presented here or any part of it has not been included in any other thesis submitted previously for the award of any degree or diploma from any other University or institution.

Date: 15/01/2025

Place: **Pune**

Prof. M. Jayakannan

(Research Supervisor) 15/01/2025

Acknowledgment

First and foremost, I would like to express my gratitude to my thesis supervisor Prof. M. Jayakannan for constant support, critical analysis, guidance and encouragement throughout this five year long journey. His passion, constant support and guidance led me to become a curious and critical thinker about the science and inspired me to take on challenges which I believe shaped me as aspiring science student or researcher. His teaching and passion for polymers and biomedical science inspired me to learn so many new things which I had never imagined. His hard work, discipline, curiosity, generosity, and boldness towards science and students motivated me to work every day. His teachings including courses, discussions, presentations, and scientific research methods helped me in exploring interdisciplinary science. His kindness, helping nature, support and appreciation made my Ph.D. journey easier. I could not have completed all my projects without his guidance and support. Thank you sir!

I sincerely thank to my RAC members Dr. J. Nithyanandhan (NCL Pune) and Dr. S. Britto for their critical and valuable suggestion during RAC evaluations which had shaped the project in best possible manner. I sincerely thank the IISER Pune and all the people of IISER Pune for facilities and support, without them this work would not have been possible. I express my gratitude to former and present director of IISER Pune, head of chemistry department, all the faculties, non-teaching and technical staff, academic staff and housekeeping staff maintaining the institute. I would like to thank the CSIR-UGC for funding me fellowship for five years and SERB project grant for funding my research project. I would like to thank central instrument facility, IISER Pune microscopy facility, and Perkin Elmer research center for instrumentation. I would also like to recognize the contribution of IISER Pune animal house facility and staff for their extending support in my research. I sincerely thank Dr. Asha (NCL Pune) for her support for scientific discussion and research facilities.

I would like to thank all my past and present lab members for their contribution and their direct or indirect help and support for my research and maintaining amazing lab environment. I thank Dr. Rahul Nisal for teaching me techniques of chemical reaction and for scientific discussion in Chai sessions. I sincerely thank Dr. Mehak for teaching me *in vitro* techniques and preliminary *in vivo* experimentation. I would like to thank Dr. Ruma and Dr. Dheeraj for their support and help. Thanks to all my previous lab members Dr. Sonashree, Dr. Khuddus, Devesh, Pranav, Kirthna, Aditi, Akash, Chandu, Rhujal, Ashutosh, Sanchi and

current lab members including Dr. Mishika, Utreshwar, Parshuram, Kajal, Akshay, Sunidhi, Bhushan, Sayali, Jewel and energetic Ridham for all their support.

I would like to thank all my batchmates and my IISER Pune friends and NCL Pune friends for their support and encouragement. I thank all my childhood friends, Moseen, kayyum, Munna and Akram.

Finally, I am particularly grateful to my parents, my sibling, my wife and family members for everything. Thank you Mom and Dad for constant support, love, motivation and important lessons about life.

Abstract

Effective cancer therapy is the one of the major challenges in human healthcare owing to poor efficacy and severity of side effects of conventional chemotherapy. Small molecules chemotherapeutic exhibits severe toxicities such as cardiotoxicity, nephrotoxicity neurotoxicity due to lack of targeting abilities and poor solubility. Moreover, therapeutics delivery to brain is the most challenging because of tightly packed nature blood brain barrier (BBB) which results in limited success in brain related disease treatments. To circumvent these limitations, polymeric nanocarrier mediated drug delivery strategies have been emerging and proven to improve efficacies, increase blood circulation time, accumulation at targeting side by passive targeting (EPR effect) and reduced toxicities. Unfortunately, most of the nanocarriers reported are mostly designed based on non-biodegradable polymers or inorganic nanoparticles and their fate is not clearly understood yet, which eventually can lead to longer accumulation and toxicity in body. Consequently, nanocarriers derived from biodegradable polymers urgently needs to be addressed in terms of their design, self-assembly, stabilities, efficacies and target specificity. To address this, biodegradable polymers based on aliphatic polyester backbone (PCL) has been designed using ring opening polymerization strategy. We investigated the importance of the architecture by designing 6-arm star-shaped copolymers and role of amphiphilicity by tuning shell of the star-shaped copolymer. These polymers were self-assembled in aqueous medium to form nanoparticles (NP) rages from 200 nm to 20nm. Their drug encapsulation, esterase enzyme-biodegradation in lysosome, *in-vitro* delivery capabilities and *in-vivo* tumor targeting and tumor suppression in xenograft mouse model were investigated in detail. In addition to that, performance of aggregated micelles was compared with unimolecular micellar NP. Succeeding, the surface charges of these star-shaped copolymers were fine tuned to achieve anionic, cationic and neutral nanoparticle to understand the critical role of surface charges and sizes in self-assembly and *in-vitro* and *in-vivo* brain specific delivery. Furthermore, the new generation of smart polymeric nanomaterials were engineered by combining enzymatic biodegradable PCL and self-immolative PAEs having zwitterionic properties and dual responsiveness. PAEs are excellent material of choice due to their auto-degradation into small units under physiological pH. However, their drug delivery applications are greatly limited because of instability of their drug formulations in, blood (pH 7.4). To mitigate these problems, we incorporated enzymatic biodegradable anionic PCL units along with self-immolative PAE in triblock architecture to design zwitterionic polymers. These zwitterions stabilized the unstable PAE units due to electrostatic interaction between anionic pendent of PCL and cationic units of PAE under physiological pH. These zwitterions exhibited excellent drug loading capabilities, and their lysosomal biodegradation, *in-vitro* and *in-vivo* drug delivery applications investigated. Efforts have been taken to further understand deeply about role of the topology and architecture of the star zwitterionic and star anionic polymers in encapsulation abilities for Doxorubicin (Dox) and delivery to solid tumors. These drugs loaded NP demonstrated longer blood circulation time and better tumor accumulation and tumor suppression in pancreatic cancer tumor mice model. Thus, currently designed polymers are superior in drug loading (~15 wt.%) and fully biodegradable, non-toxic with better efficacies for *in-vivo* tumor drug delivery.

Synopsis

Synopsis

Nanoparticle (NP) mediated drug delivery systems had emerged since 1970 and been proven promising in the treatment of cancer and other diseases by delivering drugs or genes. The major breakthrough in the polymeric nanocarriers transpired in 1975 in developing first model of ideal polymeric drug delivery and controlled-release macromolecular systems by notable researchers including Ringsdorf, Higuchi, Langer, Roseman, Peppas build the foundation for modern polymeric drug delivery. Subsequent discovery for passive targeting ability of nanocarriers known as enhanced permeability and retention (EPR) effect by Maeda in 1986 further substantiated the role of macromolecules in increasing tumor accumulation. Since then, the cancer treatment strategy involving conventional therapeutics have been substituted with nanoparticles or nanomedicine either by encapsulation or conjugation of drug to the macromolecules. These nanocarriers are being developed to circumvent the limitations of the conventional therapeutics based on small molecules involving poor solubility, stability, poor circulation half-life, less penetration and accumulation to solid tumors and non-specific targeting induced systemic toxicities. The nanoparticles offers advantage in increasing stability, improve pharmacokinetic profiles, better biodistribution, tumor targeting and penetration resulting in increased efficacy and reduced toxicity. The polymeric delivery system have been developing since then to further improve the efficiency and reduce the toxicities. To date, more than 50 polymeric NPs are in clinical trial and some of them have been approved by FDA US. However, there are many questions that still need to be answered for developing a sustainable, biodegradable and efficient polymeric nanocarriers in terms of their design, biophysiochemical properties, self-assembly and drug delivery aspects. For this purpose, nanoparticles based on combinations of fully biodegradable aliphatic polyester based on polycaprolactone (PCL and functional-PCL) along with next generational smart pH-responsive self-immolative poly(amino ester)s (PAE) appear to be well-comprehended choice owing to enzymatic biodegradation and biocompatibility.

This thesis work focused on the development of myriads of star shaped block copolymers structures based on the PCL and carboxylic acid functional-PCL monomers utilizing ring opening polymerization (ROP). These star shaped block copolymers were thoroughly investigated for Doxorubicin encapsulation and delivery to *in vitro* and *in vivo* tumor xenograft mouse models. Star shaped PCL systems were further tuned for producing different surface charges and sizes to understand the critical influence of charges and sizes in organ specific *in vivo* delivery aspect, particularly for brain. These understandings led

combination of PCL and self-immolative PAEs to develop the zwitterionic linear and star architecture for stabilization of nanoformulation and on-demand drug release at lysosomal compartment resulting complete degradation of polymer matrix by enzymatic biodegradation and self-immolation. These zwitterionic systems were investigated for drug delivery applications *in vitro* and *in vivo* tumor model. The thesis has been divided into the five chapters as follows:

1. **Chapter 1**: Chapter 1 is a compilation of thorough literature about nanoparticles based drug delivery system from their necessity to overcome the limitations of conventional therapeutics to their delivery applications *in vitro* and *in vivo*. Physicochemical properties of polymeric nanoparticles including shape, size, charge and their influence on delivery aspects across various external and internal biological barriers are discussed. The importance of architectures in renal clearance and resulting biodistribution and tumor accumulation has been illustrated. The requirement of unimolecular micelles to avoid the breakage under concentration gradient in order to enhance *in vivo* performance and recent development in this area have been highlighted. Recent developments in biodegradable polymers and self-immolative polymers with their pros and cons have been summarized and objective of thesis was illustrated.
2. **Chapter 2**: Fully biodegradable star amphiphilic polycaprolactone based block copolymers were designed using ring opening polymerization (ROP). Their aqueous self-assembly in the formation of aggregated or unimolecular micelles were systematically evaluated followed by encapsulation capabilities for doxorubicin. Enzymatic degradation and *in vitro* delivery aspects in different cancer cells line (breast and pancreatic) and vivo delivery aspects pancreatic tumor bearing mouse model (xenograft) were investigated.
3. **Chapter 3**: Star shaped star-shaped polycaprolactone core-shell block copolymers were tuned for different sizes and surface charges including anionic, cationic and neutral by appropriate functionality in the shell structure. Their self-assembly aspect and *in vitro* degradation and delivery aspects via confocal microscopy was evaluated. The role of size and surface charge for *in vivo* brain specific delivery ability across the blood-brain barrier was investigated in detail.
4. **Chapter 4**: Self-immolative Poly (amino esters) which are unstable at physiological pH hence not suitable for drug delivery. Efforts have been taken to stabilize the unstable PAEs at physiological pH (7.4) by combining with carboxylic acid functionalized PCL

by introducing electrostatic stabilization among PCL-carboxylate and PAE-amine resulting in zwitterionic polymers. The self-immolation of PAE and stability of zwitterionic-doxorubicin stability was investigated in depth for *in vitro* drug delivery, biodegradation and *in vivo* biodistribution using NIRF imaging.

5. **Chapter 5**: The star shaped zwitterionic block and random copolymers were engineered based on PCL, functional PCL and PAEs to investigate the role of architecture and topology in drug delivery aspects. The Doxorubicin loaded star zwitterionic formulations were evaluated delivery in pancreatic tumor bearing mouse model.

In chapter 2, Ring opening polymerization was utilized to develop 6-arm star block copolymers based on biodegradable polycaprolactone (PCL) platform produce the unimolecular or aggregated micelles amphiphilicity modulation. These polymers were self-assembled in aqueous medium to produce nanoparticles of sizes ranges from 200 nm (aggregated micelles or AgM) to 20 nm (unimolecular micelles UMM). Aggregated micellar nanoparticles (AgM) are prone to disassemble and disintegrate under physiological conditions *in vivo* and it became a bottle neck in therapeutic drug delivery in solid tumors. Here, we report a single polymer or unimolecular micelle nanoparticle (UMM) platform, which is enzymatically biodegradable, non-toxic and non-hemolytic, carry >14 % of clinical anticancer drug doxorubicin (DOX), very low IC_{50} *in vitro* analysis in breast cancer (MCF-7, MDA-MB-231, MDA-MBA-468) and Pancreatic cancer (MIA PaCa 2) compared to AgM. Confocal microscopy mediated cellular uptake in cancer and non-cancer cell line substantiated the higher cellular internalization ability of UMM over the AgM. Most strikingly UMM Np exhibited > 90 % reduction in MIA PaCa 2 (pancreatic cancer) tumor volume *in vivo* which are superior to AgM or free drug. For this purpose, a six-arm star polymer platform is chosen to structure engineer the core-shell nano-compartmentalization to optimize the correct macromolecular geometry of compact and tiny < 25 nm sized UMM. Fluorescent dye (or DOX) loaded UMM and AgM NP

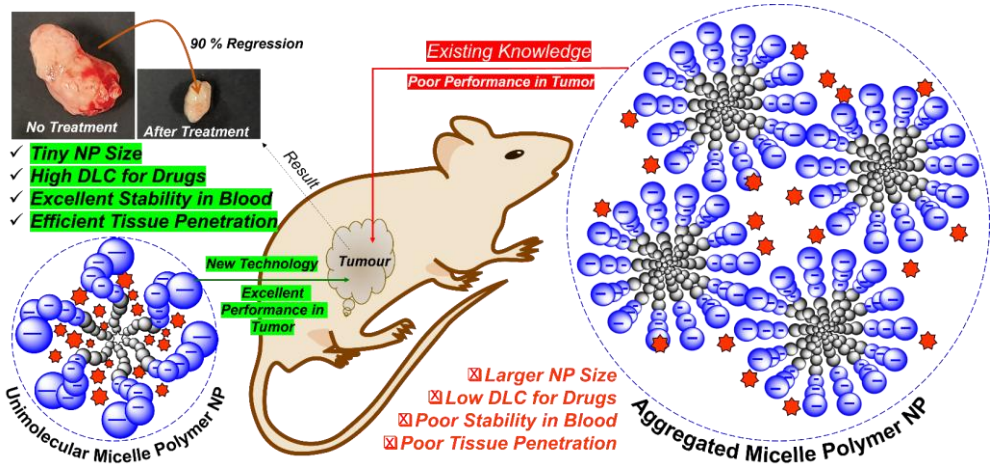

enabled *in vitro* differentiation of their endocytosis and intracellular lysosome biodegradation kinetics in living cancer cells by confocal microscopy. Deep tissue penetrable near infra-red IR-780 dye assisted with live animal biodistribution analysis established that the UMM platform is a superior nano-platform to deliver cargoes to solid tumors which account for the enhanced efficacy of tumor volume reduction *in vivo*.

In chapter 3, fully biodegradable star unimolecular approach based on polycaprolactone (PCL) and substituted PCL system core-shell nano-architectures is developed and thoroughly investigated *in vitro* and *in vivo* to understand the influence of size and surface charge on the BBB penetration. Therapeutic delivery to the brain remained most difficult owing to tightly packed protective blood-brain barrier (BBB). However, non-biodegradability and systemic toxicity of delivery system is of major concern. To address this, we report on engineering of polycaprolactone based star shaped block copolymers consisting of hydrophobic PCL core and hydrophilic shell. The precise shell modifications with appropriate functionality resulted in the anionic, cationic and neutral (non-ionic) surface charged nano-assemblies having ζ potentials in the range of -30, +35 and -5mV respectively. Star shaped anionic and cationic designed to self-assembled into aggregated (AgM) or unimolecular micellar (UMM) nanoparticles (NP) depending on the molecular weight and the surface modifications on the shell respectively. AgM-Ani and AgM-Cat exist as spherical shaped NPs of 70 and 200 nm. In contrast, UMM-Ani, UMM-Cat and UMM-Neu existed as spherical shaped NP of sizes ~20-30 nm. AgM and UMM polymers exhibited high DLC (>15%) for drug and dye and NPs were non-toxic, non-

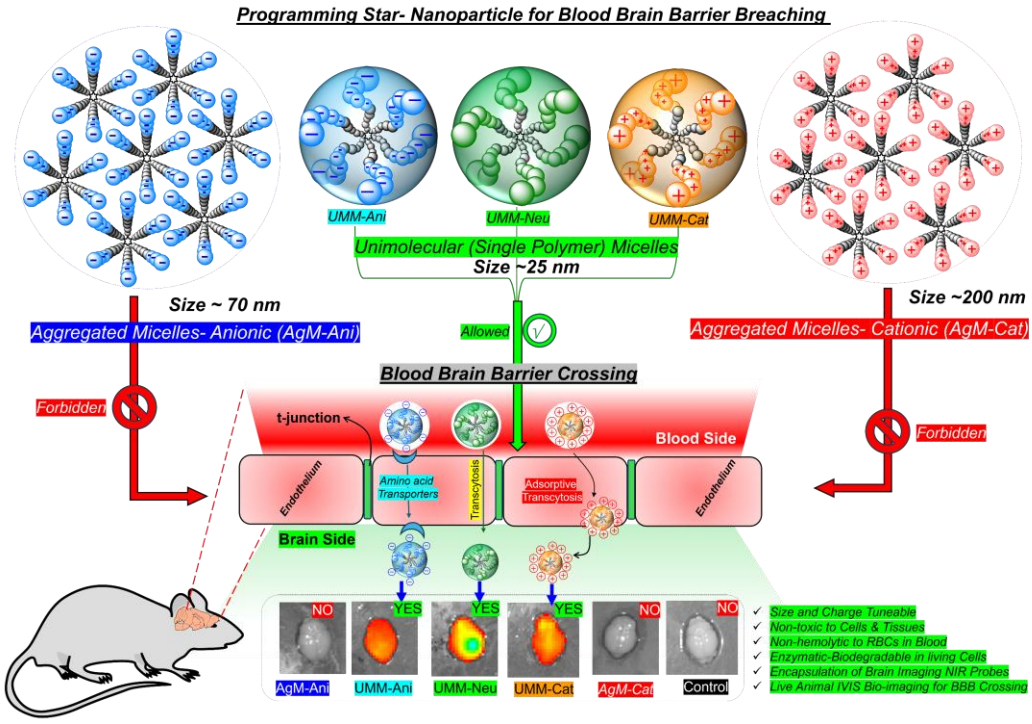

hemolytic and precisely designed to be enzyme-stimuli responsive biodegradable in lysosomal compartment to deliver the payload at the intracellular level. Confocal microscopy analysis revealed excellent cellular uptake in the WT-MEF, MCF-7, HeLa and neuroblastoma SH-SY5Y cell lines. The NIRF imaging using IR780 dye loaded NPs enabled *in vivo* biodistribution and organ specific distribution analysis. Biodistribution evaluations depicted prolonged blood circulation of UMM NP for than 72h in mice. Additional whole brain imaging and quantification revealed efficient crossing of BBB for UMM NPs of size <40 nm compared to AgM NP of sizes >50 nm substantiating the critical role of sizes in BBB breaching. The influence of surface charge among the UMM NP was not overly critical for crossing BBB compared to role of sizes implying different pathways of transcytosis functioning for each charged NPs. Star UMM demonstrates excellent stability, prolonging blood circulation and significant uptake in the brain proving promising candidatures as next generation nanocarriers for brain specific drug delivery application.

In chapter 4, In this study, a novel zwitterionic triblock copolymer strategy was introduced that was designed to stabilize the unstable PAEs by cleverly incorporating enzyme-biodegradable polycaprolactone (PCL) platform. The major bottleneck in employing polymer nano-vectors for biomedical application, particularly those based on self-immolative poly(amino ester) (PAE)s lies in their uncontrolled auto-degradation at physiological pH before they can reach the intended target. Here, an elegant triblock-copolymer strategy is designed to stabilize the unstable PAE chains via zwitterionic interactions under physiological pH (pH 7.4) and precisely program their enzyme-responsive biodegradation specifically within the intracellular compartments, ensuring targeted delivery of the cargoes. To achieve this goal, biodegradable polycaprolactone (PCL) platform is chosen, and structure-engineered several di- and triblock architectures to arrive the precise macromolecular geometry. Systematic efforts to

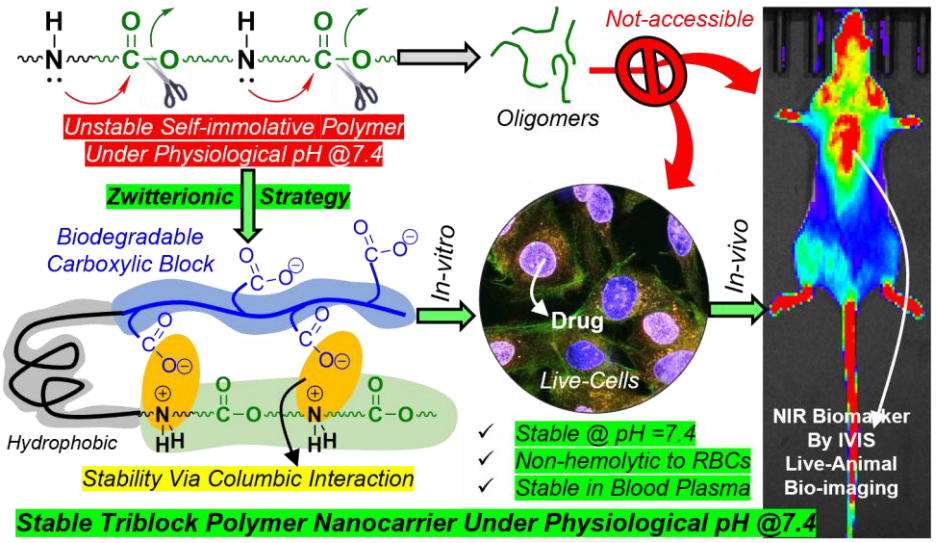

explore various cationic AB di-block, anionic AC di-block, zwitterionic BC di-block, and zwitterionic BAC or ACB tri-blocks to reach appropriate macromolecular architectures necessary for stabilizing the self-immolative PAEs. The hydrophobic-PCL core and hydrophilic anionic-PCL block at the periphery shielded PAEs against auto-degradation, thereby ensuring stability under physiological pH in PBS, FBS, cell culture-medium and blood-stream. The clinical anticancer drug doxorubicin and deep-tissue penetrable near-infrared IR-780 biomarker is encapsulated to study their biological actions by in vitro live-cancer cells and in vivo bioimaging in live-animals. These zwitterions are biocompatible, non-hemolytic, and real-time *in vitro* live-cell confocal studies have confirmed their internalization and enzymatic-biodegradation in the endo-lysosomal compartments to deliver the payload. *In vivo* bioimaging established their prolonged blood-circulation for over 72 h, and the biodistribution analysis revealed the accumulation of nanoparticles predominantly in the excretory organs.

In chapter 5, star-shaped zwitterionic block and random copolymers based on enzyme-biodegradable polycaprolactone (PCL) and self-immolative poly(βamino esters)s were synthesized via ring opening polymerization to investigate the impact of topology and architecture on self-assembly and drug delivery aspects. The combination enzymatic-biodegradability from anionic PCL units and self-immolation form cationic PAEs not only makes the structure zwitterionic in nature but also provide stability at physiological pH at extracellular conditions Aqueous self-assembly of diblock or triblock copolymers depict formation of tiny nanoparticles (NP) of sizes ~20-25nm with nearly neutral zeta potential at

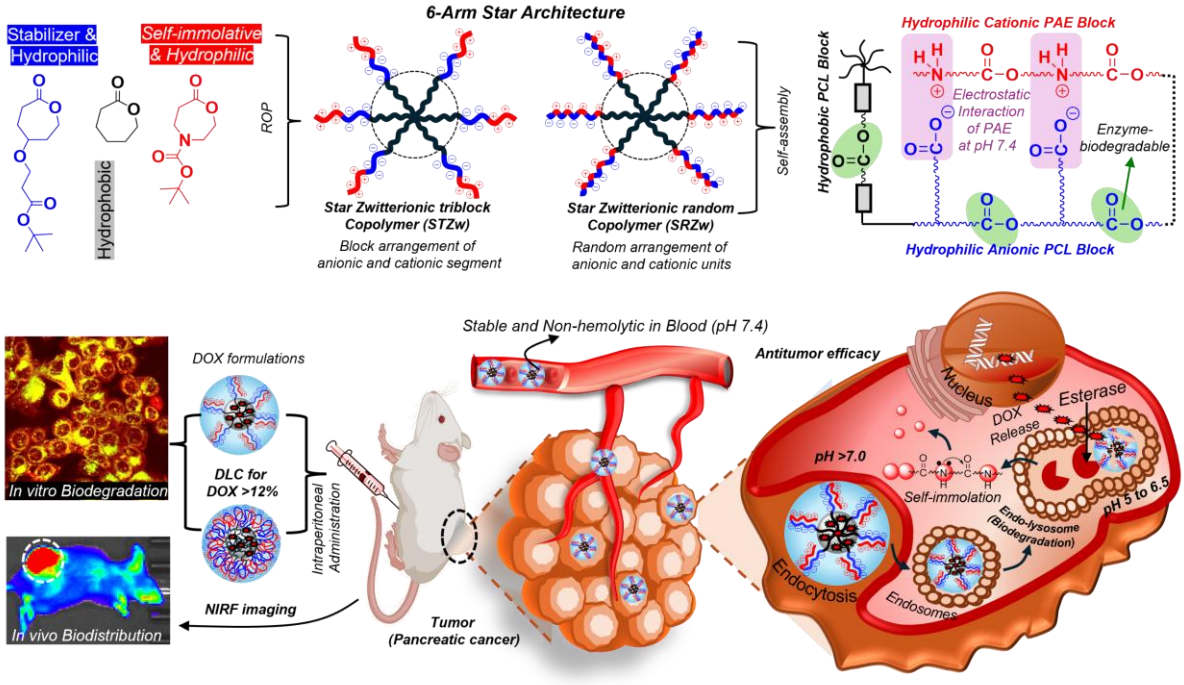

pH 7.4, while random copolymers produce larger NPs of 100 nm. The zwitterionic NP demonstrated high DLC for DOX >12% and great serum stability. pH-dependent studies showed stabilization of PAE against self-immolation at physiological pH 7.4, while on-demand enzymatic biodegradation in the intracellular (lysosomal) compartment facilitated release of DOX to the nucleus evident form confocal laser scanning microscopy (CLSM) imaging. Zwitterionic NPs were excellent biocompatible, non-hemolytic in nature. The NIRF imaging of IR780 loaded NP in MIA PaCa2 (human pancreatic cancer) tumor bearing xenograft mice model demonstrated longer blood circulation and retention in tumor for more than 72h. DOX loaded NP showed significant tumor suppression at lower dosage suggesting effective delivery via passive targeting (EPR) effect. This approach is not only restricted for delivery of one type of chemotherapeutic but also can be applied to other combinations of drugs and different type of cancer models.

To summarize, star-shaped unimolecular micelles (UMM) have been proved superior compared to star shaped aggregated micelles (AgM) for encapsulation abilities for Doxorubicin and other fluorescent dyes. *In vitro* and live-cell confocal imaging analysis proven enzymatic biodegradation and lower IC_{50} of DOX loaded UMM in multiple cancer cell lines. NIRF imaging based biodistribution suggested longer blood circulation and better accumulation of UMM in tumor surpassing AgM further proving efficient drug delivery reducing >90% pancreatic tumor volume. Furthermore, surface charge modified unimolecular micelles emphasized the critical importance of particle size and charge on the barrier crossing suggested unimolecular micellar nanoparticles of sizes >35nm could only cross the BBB and particles having sizes more than 50 nm were ineffective. In addition, impact of surface charge on brain delivery was evaluated by examining the BBB breaching capabilities of unimolecular micelles anionic, cationic and neural (non-ionic) having ζ potentials of -30mV, +30mV, and -5mV respectively. All three differently charged unimolecular micelle (UMM) NP depicted comparable uptake in the brain suggesting only sizes played important role. Further employment of carboxylic acid functionalized PCL in the stabilization of unstable self-immolative PAEs through electrostatic interactions resulting zwitterionic nanoparticles have been proven to stabilize the Doxorubicin formulation at extracellular conditions. This next generational zwitterionic nanoparticle exhibited lysosomal biodegradation and release of Dox to nucleus achieving efficient killing in breast and ovarian cancer cells and in vivo biodistribution confirmed stability of nanoparticles in longer blood circulation. Their star shape versions (zwitterionic) demonstrated higher accumulation in pancreatic tumor substantiated by

NIRF imaging and showed significant suppression in tumor growth by the treatment of DOX loaded zwitterionic nanoparticles. All these block copolymers demonstrated excellent biocompatibility, biosafety, non-hemolytic ability and promising results in the doxorubicin delivery for in vitro and in vivo mouse tumor model (xenograft). All the aforementioned critical observations have been summarized in “summery and Future Direction” in the last chapter in detail. The work of this thesis has opened up new opportunities for further exploration of new PCL and PAE based higher order architectures for preclinical investigations.

Table of Contents

Abstract……...…7
Synopsis……..……8
Chapter 1: Introduction……...…..20
1.1 Small molecules vs Nanomedicine……..21
1.2 Classes of Nanoparticles (NP)…….25
1.2.1 Lipid-based Nanoparticles……25
1.2.2 Inorganic Nanoparticles……...26
1.2.3 Polymeric Nanoparticles……...27
1.3 Factors Influencing Drug Delivery: Biological Barriers…….31
1.4 Impact of Physicochemical Properties of NP.……..34
1.4.1 Size……35
1.4.2 Surface Charge……...……...37
1.4.3 Shape and Architecture..……...38
1.5 Targeting Strategies for Nanoparticles……41
1.6 Evolution of Polymeric Drug delivery System (DDS)……42
1.7 Aggregated Micelles versus Unimolecular Micelles……...44
1.7.1 Dendrimer……45
1.7.2 Hyperbranched Polymer……...47
1.7.3 Brush-shaped Polymer……..50
1.7.4 Star Polymer……..51
1.8 Biodegradable polymer…….....55
1.9 Aim of the Thesis…….65
1.10 Reference……...68
Chapter 2: Probing the Efficacy of Aggregated and Unimolecular Micelles in Tumor Xenograft Model……84
2.1 Introduction…….….86
2.2 Experimental Section…….……..89
2.3 Results and Discussion……..……101
2.3.1 Synthesis and Characterization……...101
2.3.2 Thermal Properties…….….105
2.3.3 Self-Assembly……108
2.3.4 Encapsulation studies……..114
2.3.5 Enzyme-Responsive Drug Release……117
2.3.6 Endocytosis and Live-Cell Biodegradation……119
2.3.7 Cytotoxicity…….....125

2.3.8 Cellular Uptake studies……..…..127
2.3.9 Hemolysis assay……..….132
2.3.10 In Vivo Biodistribution assay……133
2.3.11 Antitumor Efficacy in Xenograft Model……..…….……136
2.4 Conclusion……139
2.5 References……...……..…140
Chapter 3: Impact of Size and Charge of Nanocarriers in Blood-Brain-Barrier Breaching …..145
3.1 Introduction……..…….…147
3.2 Experimental section……..152
3.3 Results and Discussion…….……163
3.3.1 Synthesis and characterization…….…….……..163
3.3.2 Self-assembly and drug encapsulation …….…….....166
3.3.3 Enzymatic biodegradation, endocytosis and lysotracker assay…….....172
3.3.4 Cytotoxicity…….....176
3.3.5 Cellular uptake studies.....177
3.3.6 Hemolysis assay.....179
3.3.7 *In vivo* Biodistribution and BBB Breaching.....181
3.3.8 Role of sizes in BBB breaching: Aggregated vs unimolecular micelles.....181
3.3.9 Role of surface charges in BBB breaching.....184
3.3.10 Role of sizes of cationic nanoparticles in BBB breaching.....188
3.3.11 Biodistributions analysis using ICG loaded UMM NP.....189
3.3.12 Mechanism of BBB crossing.....191
3.3.13 Integrity of blood-brain-barrier (BBB) using EB dye.....193
3.3.14 Integrity of blood-brain-barrier (BBB) using IR780.....194
3.4 Conclusion.....196
3.5 References.....197

Chapter 4: Zwitterionic Startegy to Stabilize Self-Immolative Polymer Nanoarchitecture under Physiological pH for Drug Delivery In Vitro and In Vivo.....201
4.1 Introduction.....203
4.2 Experimental section.....206
4.3 Results and Discussion.....221
4.3.1 Synthesis and Characterization.....221
4.3.2 Self-Assembly and Self-Immolation of Cat-AB.....228
4.3.3 Electrostatic Strategy to Stabilize Self-Immolation of Cat-AB.....231
4.3.4 Self-Assembly and Encapsulation studies of Zwitterionic Triblock polymers.....234
4.3.5 Extracellular Stability and Enzyme-Responsive Drug Release.....241

4.3.6 Endocytosis and Live-Cell Biodegradation....245
4.3.7 Cytotoxicity and Cellular Uptake Studies....249
4.3.8 Hemolysis and In Vivo Biodistribution Studies....255
4.4 Conclusion....257
4.5 References....258
Chapter 5: Star Shaped Zwitterionic Block and Copolymer for In Vitro and In Vivo Drug Delivery to Pancreatic Tumor....263
5.1 Introduction....265
5.2 Experimental Section....269
5.3 Results and Discussion....279
5.3.1 Synthesis and Characterization....279
5.3.2 Self-Assembly and Drug Encapsulation....285
5.3.3 Enzymatic-Responsive Biodegradation and Drug Release....290
5.3.4 Endocytosis....293
5.3.5 Real time Live-cell Enzymatic Biodegradation....294
5.3.6 Enzymatic Degradation Studies of Polymers....296
5.3.7 Cytotoxicity Studies....299
5.3.8 Cellular uptake studies....300
5.3.9 Hemolysis assay....302
5.3.10 In Vivo Biodistribution studies....303
5.3.11 Antitumor Efficacy in Xenograft mouse model....306
5.4 Conclusion....309
5.5 References....310
Summery and Future Direction....314
List of Publication....317
Appendix....325

Chapter 1

Introduction

1.1 Small molecules vs Nanomedicine

Cancer is the one of the leading causes of deaths worldwide responsible for more than 10 million deaths (Year 2022) has become major risk to humankind worldwide.[1] Cancer can be defined as a disease in which uncontrolled division (proliferation) of transformed cells leading to formation of tumor either malignant or benign which further spread (metastasis) to other part of the body from the origin.[2] In broader sense, cancer is group of more than 277 different types including carcinomas, sarcomas, leukemia, lymphoma and others. Different stages of cancers have been identified including several gene mutations involved in cancer pathogenesis.[3] Recent statistics suggests that almost one is six death is caused by cancer worldwide. The breast, lung, colon, pancreatic, prostate, stomach, bladder, brain, blood and lymphoma are some major types of cancer accountable for almost 50% incidences.[1] The pie chart in Figure 1.1a represent the distribution of new cases of cancer and deaths globally (185 countries) in both female and males. The Figure 1.1b depict the statistics of the major 10 types of cancers in both sexes account for more than 60% of new cases.

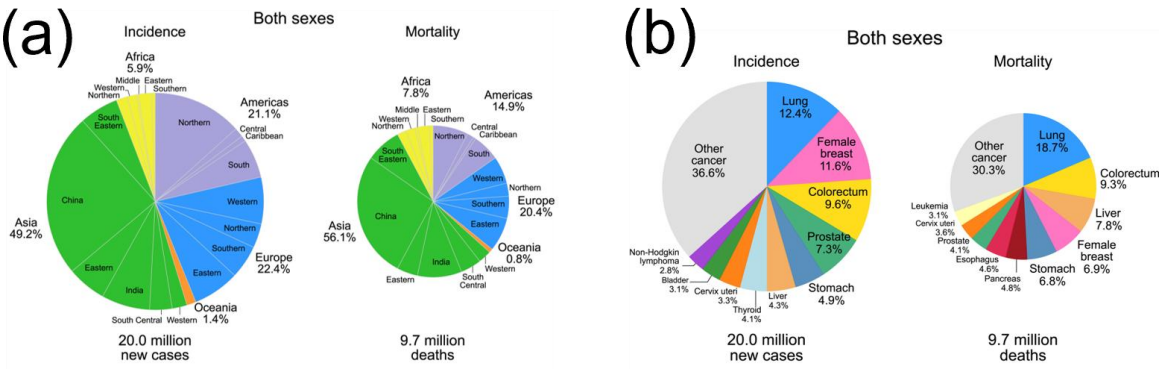

Figure 1.1. *(a) Distribution of new cases and deaths globally in both sexes represented by Pie chart. (b) Distribution of major types of cancer account for ~60% new cases and deaths globally in both sexes represented by Pie chart (Adapted form Bray, F. et al. CA. Cancer J Clin.* **2024**, *74,* 229-263*).*

Commonly used treatments against cancer depending on the stages and types can be broadly classified into i) Chemotherapy, ii) Radiation, iii) surgical removal of tumor, iv) immunotherapy, v) Hormone therapy.[4] One of the most effective treatments against the metastatic tumors is use of appropriate chemotherapeutics. Resistance of tumors to chemotherapy drugs, immunotherapy and radiation results in the failure of effective treatment and affects patients with different variety of cancer including solid tumors and blood cancers.

Unfortunately, cancer cells have evolved and simultaneously become able to develop resistance against chemotherapeutics known as multidrug resistance (MDR).[5] Resistance to the anticancer drugs can be broadly classified into two categories: i) Genetic and epigenetic alterations in the cancer cells affecting drug sensitivity, ii) The impaired drug delivery to tumors resulting in poor absorption of drug by tumor. Cellular multidrug resistance mechanism is depicted in Figure 1.2. MDR result from efflux pumps of the ATP-binding cassette (ABC) transporter family such as P-glycoprotein (Pgp). These pumps efflux drug molecules out the cells resulting in lower intracellular concentrations of drug.[6] Anticancer agents such as vinblastine, vincristine, doxorubicin, daunorubicin actinomycin-D and paclitaxel are the classical examples of drugs affected by multidrug resistance.[7] Moreover, the cells themselves can also activate mechanism to repair DNA damage induced by drugs. Defective apoptotic pathways can also cause resistance in cancers with mutant or non-functional p53 gene as a result of malignant transformation.[8]

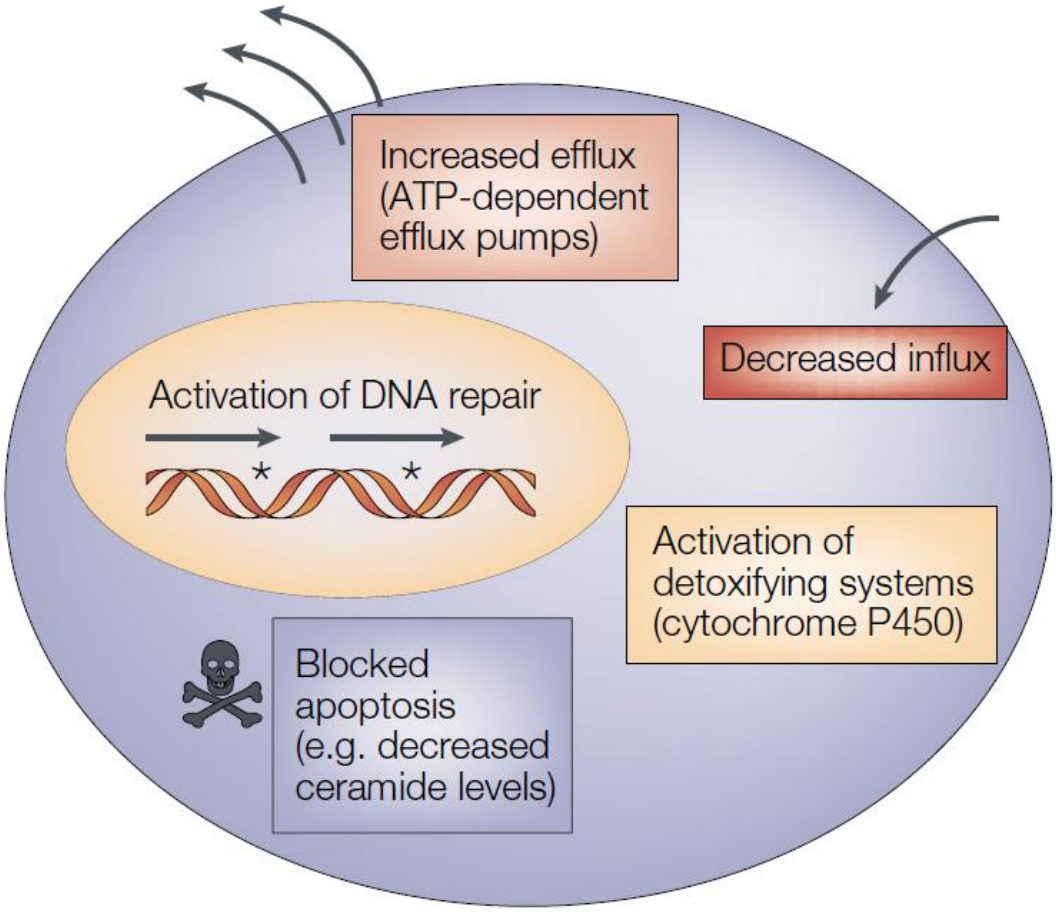

Figure 1.2. *Cellular mechanisms of Multidrug resistance (MDR) (Adapted form Gottesman, M. M. et al. Nat. Rev. Cancer* **2002**, *2,* 48-58*).*

The impair delivery of drug to the tumor can also results in the poor absorption of drugs in the tumor. This is mainly cause by the poor pharmacokinetic characteristics of small molecule based drugs including poor solubility, poor permeability and less bioavailability. [9] In addition to that small molecular drug often non-selective towards the tumor and can accumulate to the heathy tissue often lead to cardiotoxicity, nephrotoxicity, neurotoxicity and other systemic toxicities.[10] To overcome this limitations nanotechnology have been emerging to improve the strategies for effective drug delivery. Nanomedicines refers to structures having 1-200 nm in size used for making drug formulations and drug delivery. Nanomedicine can improve the drug solubility, enhance stability, improve pharmacokinetic profiles, prolong blood circulation, reduced opsonization and reticuloendothelial system (RES) uptake, enhance the tumor accumulation by active or passive targeting mechanisms and reduces side effects or toxicity.[11] The history of drug-delivery began in 1950, and timeline is briefly summarized in Figure 1.3.[12]

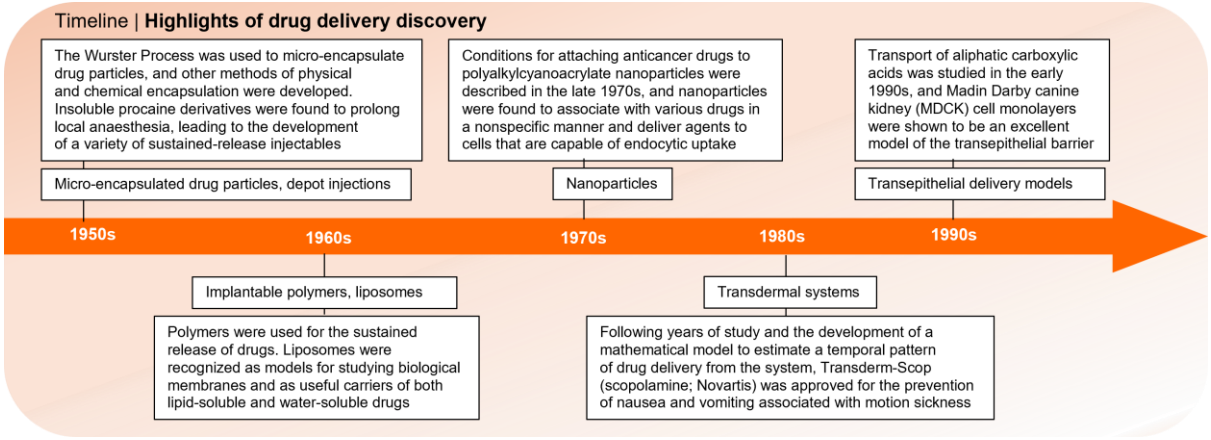

Figure 1.3. *Highlights of the drug delivery discovery (Adapted from Rosen, H. et al. Nat. Rev. Drug Discov.* **2005***, 4,* 381-385).

In the development of nanomedicine, a total of 13 nanomedicines have been approved by Food and Drug Administration (FDA) US till 2015 for different diseases. Recently nanotechnology research has been rocketed and total of 100 nanomedicines are being marketed by 2021 and 563 new nanomedicines products are in clinical trials.[9, 13] The statistics suggests that the 33% and 21% nanomedicines are in Phase I and Phase II clinical trials. Among them ~53% of nanomedicines are primarily for cancer treatment (see Figure 1.4). Moreover, lipid based nanoparticles (NP), antibody-drug conjugates and polymer-drug conjugates or polymeric NP account for ~68% of total nanomedicines which are in clinical trials suggesting promising in effective treatment and safety aspects. Doxil, Calyex, Myocet, Visudyne, DaunoXome,

Genexol-PM, Mircera, Cimzia, Krystexxa, Oncaspar, Apealea, Dexferrum, Abraxane, Ontak are examples some of the clinical approved nanomedicine for various diseases.

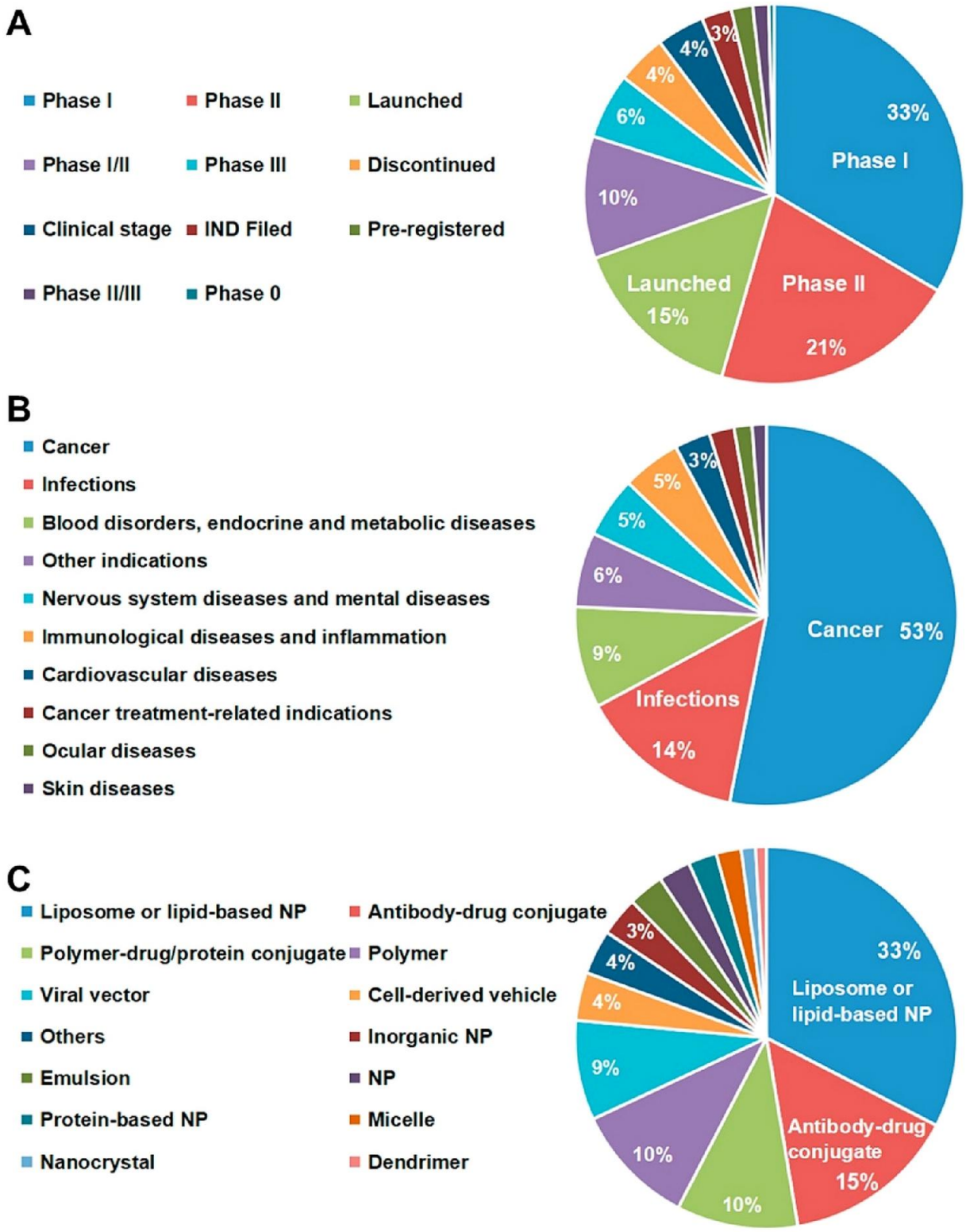

Figure 1.4. *Overview of Nanomedicines in clinical trials for various diseases (Adapted from Thapa, R. K. et al. J. Pharm. Investig.* **2023**, *53*, 19-33*).*

1.2 Classes of Nanoparticles (NP)

Nanoparticles have been proven to improve efficacy of the chemotherapeutic by enhancing the stability of drug resulting the protection of the drug inside nanoparticles. Therefore, improving pharmacokinetics and biodistribution and enhancing bioavailability of pharmacophores. These properties of nanoformulation are modulated either by encapsulation or chemical conjugation of drugs to the nanocarriers or nanoparticles. There are several types of nanoparticles that have been developed and can be broadly classified into three major categories, such as lipid-based, inorganic NP and Polymeric NP as shown in Figure 1.5.[14-15]

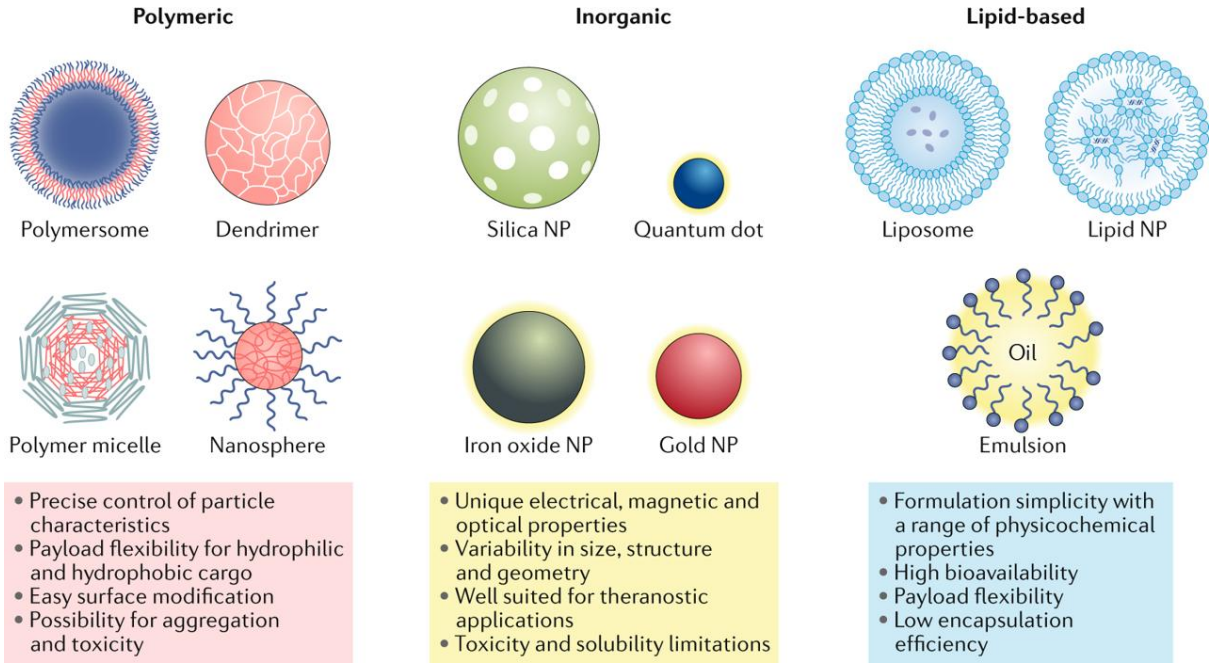

Figure 1.5. *Overview of types of nanoparticles (Adapted from Mitchell, M.J. et* al. *Nat Rev Drug Discov.* **2021**, *20*, 101–124).

1.1.1 Lipid-based Nanoparticles

Lipid-based NP are one of most commonly used nanoparticles in drug or gene delivery and in clinical trials. These are spherical shaped 50-500 nm in sizes nano assemblies composed of bilayer of lipids such phospholipids, cholesterol, cationic and ionizable lipids and PEG-lipids.[16] The lipid NP are often formulated with hydrophilic PEG to enhance blood circulation time and reduce opsonization. The Lipid based NP provides several advantages such as ease of fabrication, simplicity of formulation design, biocompatibility, and high drug carrying ability and also can encapsulate hydrophilic or hydrophobic drugs. [17] The most commonly used lipid based NP are liposomes, and solid-lipid nanoparticles. The Doxil, first FDA approved (1995)

PEGylated liposomal nano-formulation of anticancer drug Doxorubicin composed of phosphatidylcholine, cholesterol bilayer depicted enhance blood circulation of Doxorubicin by several time.[18] Recently DSPE-PEG-NH_2 based dual encapsulated mannosylated liposomal formulation of gefitinib and varinostat has been reported for dual-targeting and achieving EGFR downregulation offering potential method for EGFR-associated drug resistance nonsmall cell lung cancer therapy (see Figure 1.6).[19] Several examples of lipid based nanoformulation of mRNA, siRNA have been studied for gene delivery and shown promise for successful transfections. However, major drawbacks of lipid-based systems are uncontrolled or burst release, rapid clearance and insufficient cellular internalization leading to ineffective uptake.[20]

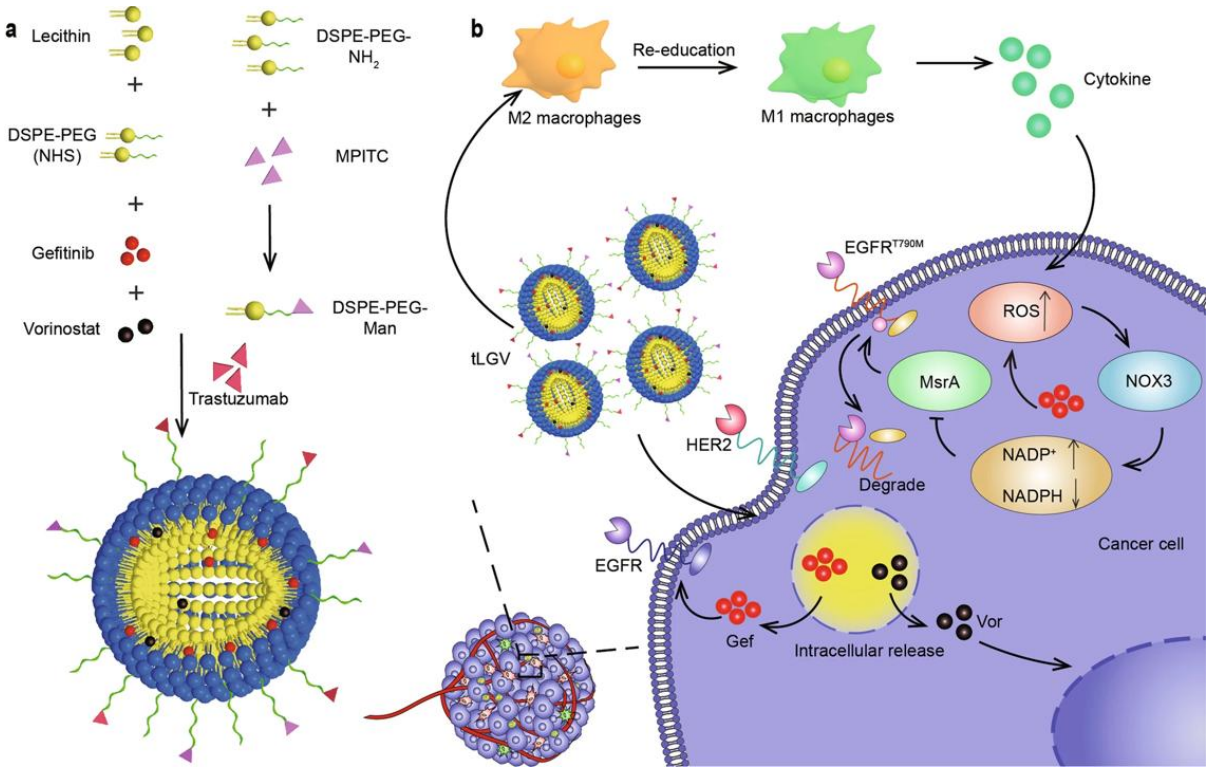

Figure 1.6. *Diagrammatic illustration of liposomal codelivery of Gefitinib and Vorinostat (Adapted from Gao, A. et* al. *Acta Pharmacol Sin* **2019**, *40*, 1129–1137).

1.1.1 Inorganic Nanoparticles

Nanoparticles composed of inorganic materials such as iron gold, silver, and silica have been developed for superior performance in translational medicines for various types of fields including iron-replacement therapy, antibacterial agents, antidots for heavy metal-poisoning, bone-graft substrates, antitumor therapy, etc.[21] The inorganic NPs can be precisely engineered

to have specific geometries, wide verities of sizes and structures. In addition, the inorganic NP possess unique physical, magnetic, electric, optical properties which can be utilized for developing diagnostic tools. Among inorganic NP, iron based NP such as dextran-iron formulations have been reported for iron-supplement in iron deficiency anemia treatment.[22] Magnetic resonance imaging (MRI) contrast agents based on Gd-nanoparticles such as Dextran-DTPA-Gd, chitosan-DTPA-Gd, Lipid-Gd, and PEG-PLL-DOTA-Gd have been reported for image-guided radiotherapy and diagnosis purposes.[23] Superparamagnetic iron oxide (SPIO) NPs also have been also widely used as MRI contrast agent in the diagnosis of liver tumor.[24] Among inorganic NPs, gold (Au) based NPs have been widely used owing to easily functionalization, delivery capabilities and ability to form different shapes such as nanorods, nanospheres nano-shells, nano-star, and nanocages.[25] Silica based nanoparticles based mesoporous silica nanoparticles (MSN) of 5-50 nm sizes have been studied for various applications including catalysis, remediation technologies, nanocarriers of drug delivery and many other biomedical applications. Other inorganic NP including calcium phosphates and quantum dots also have been developed for in vitro imaging applications. Unfortunately, major shortcomings in use of inorganic NP is poor solubility and toxicity concern owing to presence of heavy metal which limits their clinical applications. [26-27]

1.1.1 Polymeric Nanoparticles

Polymeric based NP are most widely studied and used class of nanomaterials for delivering drugs, genes, growth factors, proteins, kinase inhibitors, vaccines etc., and have been proven promising for biomedical applications including cancer medicine, gene therapy, and diagnostics.[28] Polymeric NP offers major advantages associated with drug delivery such as extreme versatility in synthesis and design, controllable architecture, shape, size, charge, tunable drug loading or conjugation capacities, biocompatibility, reduced toxicity and deliver more therapeutics to targeted tissues or tumor.[29] Polymeric NP are exceptional as key tool to enhance overall therapeutic efficacy by improving drug bioavailability, prolonging blood circulation half-time (pharmacokinetic profiles), biodistribution. In addition, biodegradability and tunable controlled released of drugs, less cytotoxicity make them highly attractive candidates for biomedical applications.[30] The polymeric NP can be designed based on either natural polymer such as carbohydrates including dextran, hyaluronic acid, chitosan, alginate, cellulose, gelatins, collagen, albumins, dextran, dextrose, or synthetic polymers such as polyester, polyether, polycarbonates, polyanhydrides, polyamide, polypeptide, polyurethanes, polyphosphates, polyacrylates, polyolefins etc., (see Figure 1.7).[31-32]

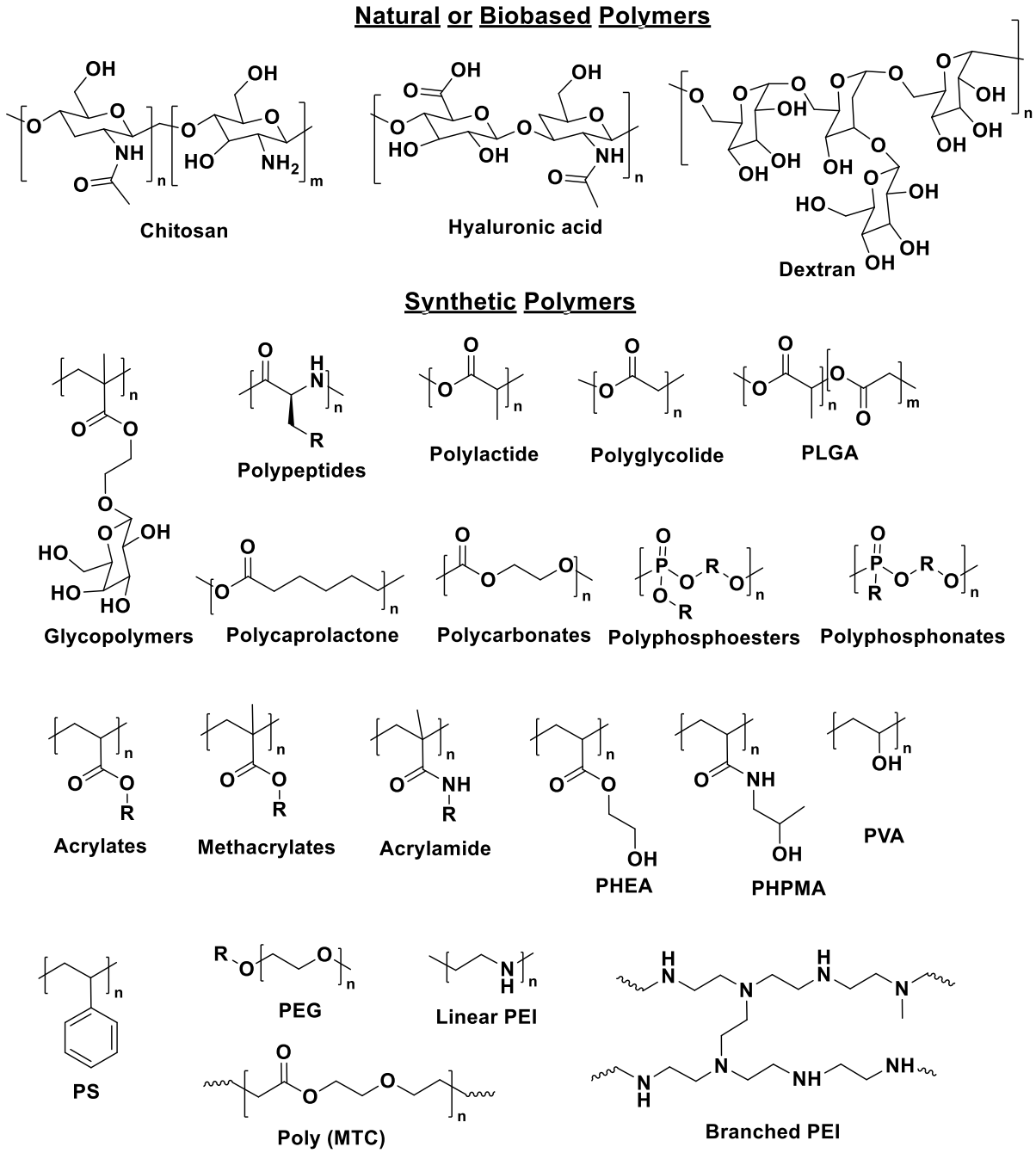

Figure 1.7. *General classes of natural and synthetic polymers used for fabrication of nanoparticles for drug delivery and other biomedical applications..*

In general, natural polymer are derived from natural resources or products offers biodegradable and non-toxic properties; however, they lack tunability, batch-batch to consistency and scope of functionalization.[33] On other hand,, synthetic polymers offer great advantages of precise control over structures and functionality, molecular weights, dispersity, and architectures. Synthetic polymers are produced from monomers using different polymerizations techniques including ring opening polymerization (ROP), condensation or

step-growth polymerization, atom transfer radical polymerization (ATRP), reversible addition-fragmentation chain transfer (RAFT), nitroxide mediated polymerization (NMP), anionic and cationic polymerization and polymerization induced self-assembly (PISA).[34-36] These polymerization techniques offers precise controlled over architectures such as linear block copolymers or random copolymers, comb, brush, star polymers, hyperbranched polymers. Polymers are constructed with hydrophobic and hydrophilic monomers called amphiphilic polymers.[37] Depending on the choice of polymer and drug properties, several methods have been developed for the fabrication of NP for encapsulation and chemical-conjugation of therapeutics into polymeric nanoparticles. These techniques can be broadly classified into bottom-up and top-down techniques. Bottom-up techniques such as emulsion polymerization, interfacial polymerization and precipitation polymerization, and controlled/living polymerization methods which employ monomer as initiator.[38] Although these techniques are precise for controlled size and shaped NP production, however major limitation lies in the type of restricted choice of materials mainly from non-biodegradable category. On other hand, top-down approaches for NP preparation are relatively better and offer myriads of materials choices including biodegradable and non-biodegradable polymer materials. These methods are mainly used for self-assembly of amphiphilic block copolymers including solvent evaporation/emulsification, nanoprecipitation/solvent displacement, salting-out, dialysis etc.[39-40] Self-assembly of block copolymers having hydrophobic and hydrophilic segment into different types of morphologies such as spherical micelles, cylindrical micelles, lamellae and vesicles (bilayers) etc., be predicted by a theoretical parameter known as packing parameter $p=v/al$ (see figure 1.8a).[41] Polymeric nanoparticles offers a large pool of structural varieties including micelles, nanosphere, dendrimers, vesicles (polymersome), nanosphere, nanogel, nanocomposites, and nanocapsules depending on the type of polymer, method of self-assembly (see Figure 1.8b). In addition, self-assembly can produce various types of micelles including normal micelles, reverse micelles, flower like micelles, unimolecular micelles, dendritic micelles, mixed micelles etc.; based on the composition of polymers such as block copolymers, random copolymers, graft polymers, star polymers, (see Figure 1.8c). The sizes of these different nanoarchitectures in general can be well controlled in the range of 1-1000 nm depending upon the choice of material and application (see Figure 1.8d).[42] Drugs or therapeutics (hydrophilic/hydrophobic) can be physically encapsulated into the hydrophobic cores of polymeric nanoparticles during self-assembly process via various interactions including hydrophobic interaction (see Figure 1.9) and up to ~20% drug loading can be achieved depending on the materials. Correspondingly, therapeutics can also be covalently

conjugated to polymers via stimuli-responsive chemical linkages achieving up to ~50% loading (see Figure 1.9).[43] However chemical conjugation involves tedious synthesis and is often limited by choice of materials, scalability, reproducibility.

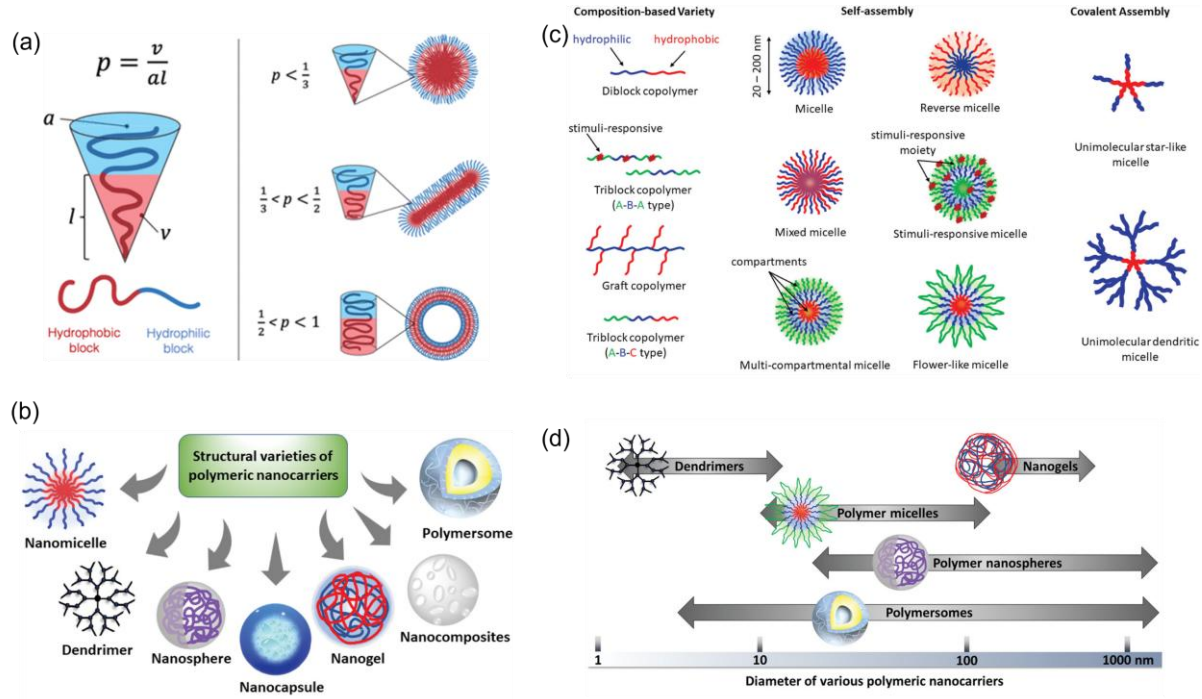

Figure 1.8. *Overview of polymeric NP. (a) Packing parameter predict morphology of nanoparticles such as spherical, cylindrical micelles, and vesicles (Adapted from Mai, Y. et al. Chem. Soc. Rev.* **2012**, *41,* 5969-5985*). (b) Types of polymeric NP based on structures. (c) Type of polymeric NP based on compositional variety and self-assembly. (d) Size ranges of polymeric NP (Adapted from De, R. et al. Adv. Sci.* **2022**, *9*, 2105373).

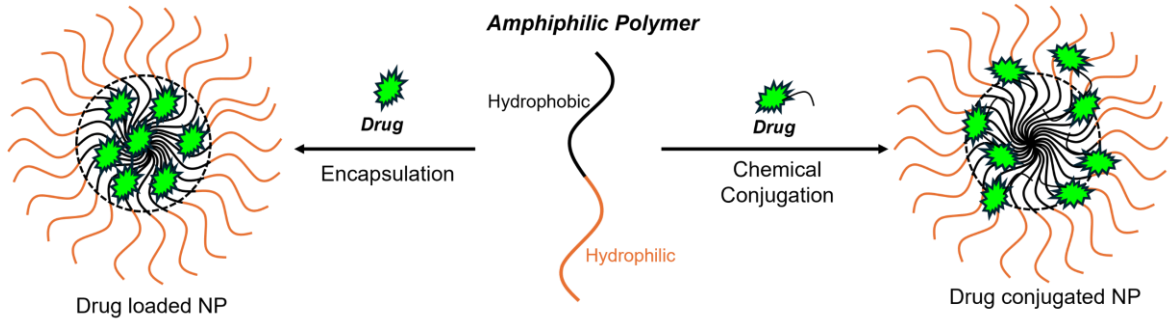

Figure 1.9. *Schematic representation of drug encapsulation and covalent conjugation to polymeric core-shell NP (micelle).*

1.3 Biological Barriers in Drug Delivery

Effective drug delivery using polymer NP required careful design and engineering of NP system to migrate a innumerable of biological barricade through both extracellular and intracellular environments. The barricades are specific to nature of drug and NP, route of delivery, and type of target endogenous disease.[44] The challenges for delivery of small molecules (low molecular weight) using polymeric NP involves stability, solubility and controlled release mechanisms. While delivery of larger molecules such as nucleic acid, and proteins requires enhanced stability and targeted delivery at specific target in cells. [45] Therefore understanding the interactions between NP and biological barriers is crucial for designing NP to alleviate specific treatment. In addition, physicochemical properties of NP, mechanism of targeting and type of stimuli for drug release also largely affect the outcome and efficiency of drug delivery system. During the delivery of nanoparticles many biological roadblocks comes into the picture including extracellular and intracellular. After the administration of nanoparticles, interaction with blood is the first step in the journey of NP. The blood is complex fluid composed of red blood cells (RBC), white blood cells (WBC), platelets (thrombocytes), proteins, salts, sugar, enzymes, amino acids and other substances which can interact with NP and cause instability by embolism and aggregation. Additionally, presence of immune cells in the blood and kidney filtration (renal filtration) are major players which can remove the NP from the circulatory system. However, long blood circulation time is crucial pre-requisite for successful extravasation of NP to the tumor tissues hence clear understanding of this barriers in order to develop the NP system is essential to avoid these obstacles.[46] The major biological barriers are depicted in Figure 1.10. Kidney performs important function of filtering plasma, metabolic wastes, and other foreign materials form the blood by glomerular filtration consisting of three barriers/filter layers such as glomerular endothelial fenestration, glomerular basement membrane (GBM), and podocyte filtration slit.[47] The pore size of these three barrier layers is about 6 nm therefore NP of sizes less than 6 nm and rod shaped, or cylindrical NPs are most likely to be cleared through the renal filtration. Moreover, the surface of capillary tubes is negatively charged hence cationic NP is most easily captured and filtered.[48-50] These obstacles of renal clearance are major challenges in delivery of NP to tumor since the renal filtration is self-protection mechanisms of the body. The important aspects is the presence of plasma proteins including serum albumin, laminin, fibronectin, immunoglobulin, apolipoprotein, and complement component etc., in the blood forms strong dynamic layers around NP after called protein-corona through hydrophobic and electrostatic interactions.[51] The plasma proteins change the surface properties of NP and weakens the tumor specificity, affect the drug release

profile and promote the degradation of NP.; thus the protein corona determines the fate of NP. Some of the plasma protein complementary factors known as opsonin are very much allied to clearance of NP from the blood by mononuclear phagocytic system (MPS) in selective manner. The MPS identify NP as foreign objects and captured due to presence of receptor on the macrophages that could specifically bind with opsonin. Then MPS secrets free radicals and enzymes to degrade the captured exogenous NP. In this event NPs composed of biodegradable polymers can clear out from body.; however, NPs constructed form non-biodegradable polymers tend to accumulate in MPS organs such as liver and spleen causing systemic toxicity.[52-53] Phagocytosis and opsonization of NP is mainly dependent on the physicochemical properties such as size, charge, shape and hydrophilicity. NPs having bigger size and positive surface charge (cationic) are more likely to be cleared form MPS system than smaller and negative charged or neutral NPs.[54] PEGylation (Polyethylene glycol) is one of the common strategy to avoid the opsonization and prevent MPS clearance.[55]

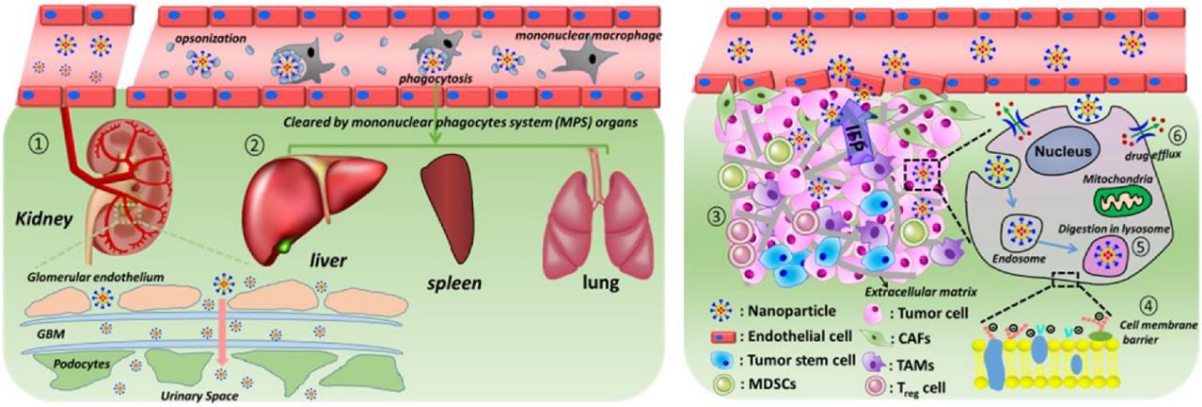

Figure 1.10. *Overview of biological barriers. 1)kidney clearance, 2) opsonization and MPS system clearance, 3) dense extracellular matrix and high tumor pressure, 4) cell membrane barriers, 5) endosome/lysosome, 6) MDR, 3) barriers from microenvironment of tumor (Adapted from Liu, J. et al, Nano Today* **2017***, 15,* 56-90*).*

For NP to reach the site of action, they must penetrate the depths of heterogenous tissues of tumor, encountering several barriers imposed by tumor microenvironment. Complexity of tumor is quite similar to that of organs, tumors are comprised of heterogenous dense tumor stroma including blood vessels, fibroblast, immune cells and extracellular matrix (ECM). The other characteristics of tumors including hypoxia, deficient blood supply, high intra-tumoral pressure, acidification, etc., posture enormous hurdle for tumor therapy resulting in poor efficacy and prognosis.[56] These complex hurdles should be kept in mind for designing the effective NP for tumor therapy. Therapeutic drugs mainly exert their effect either on nuclei or cytosol. Therefor to achieve efficient delivery NP system must traverse through cellular barriers

to enhance the intracellular concentration of drugs. The cellular barriers are cell membrane barrier, endosome/lysosomes, and multidrug resistance (MDR). The cell membrane barriers protect the cells and maintain physiological environment. However, NP systems must penetrate through cell membrane in order to release the drug at intracellular level. The penetration of NP (endocytosis) through cell membrane is highly dependent on several factors including shape, charge, and size. For examples smaller or larger NPs can be taken up by cells either via phagocytosis (cell eating) or pinocytosis (cell drinking). However small molecules are predominantly taken up by diffusion passive mechanism through selective permeable cell membrane owing to concentration gradient. Phagocytosis is particle-dependent, highly regulated (involving specific cell-receptor and signaling cascade) process conducted by specialized mammalian cells such as macrophages, monocytes and neutrophils majorly employed for clearance of pathogens or cell debris. The pinocytosis is also known as fluid-phase uptake pathway (uptake of fluid or solute) occurs in all mammalian cells by different mechanism such as macropinocytosis, clathrin-mediated endocytosis, caveolar-mediated endocytosis, clathrin/caveolar-independent endocytosis. These pathways are mechanically diverse and highly regulated. Internalization of NP can occur via several pathways including micropinocytosis, clathrin-mediated endocytosis, caveolar-mediated endocytosis, clathrin/caveolar-independent endocytosis (see Figure 1.11) utilizing lipid rafts to create special vesicles after engulfment.[57] Caveolin-mediated endocytosis is most common for the NP of sizes less than 60 nm and generally and negatively charged, sometimes rod shape is preferred. While other Clathrin-mediated pathways are the most common route taken by nearly various type NP, mainly relies on the receptor-mediated, electrostatic and hydrophobic interaction between cell membrane and NP.[58] During endocytosis process, the endosomes or vesicles mature through various steps involving compositional changes and pH and material which are pH responsive often depict release in the endosome upon the action of proton sponge effect (endosomal escape). The endosome upon complete maturation evolves into lysosome having lower pH, higher ionic strength and proteolytic enzyme which can affect the stability of nanoparticles and encapsulated cargo or drugs.[59] Cargo may still require to reach intracellular compartments after entering to cytosol. Reaching organelles might require crossing additional barrier such as intracellular membranes. This is because cells are very complex and highly compartmentalized.[60] In addition, drug resistance in the cellular level also contributes to the heterogeneity further create the challenge to NP delivery. The NP must be designed with optimal size, shape and surface properties that could easily penetrate through the cell membranes and deliver the drug to targeted organelles to achieve maximum efficiency.

Moreover, organ level barriers such as blood-brain barriers pose significant challenges and difficulties to NP mediated drug delivery. All together extracellular and intracellular barriers (biological) must be considered while designing NP for drug delivery.

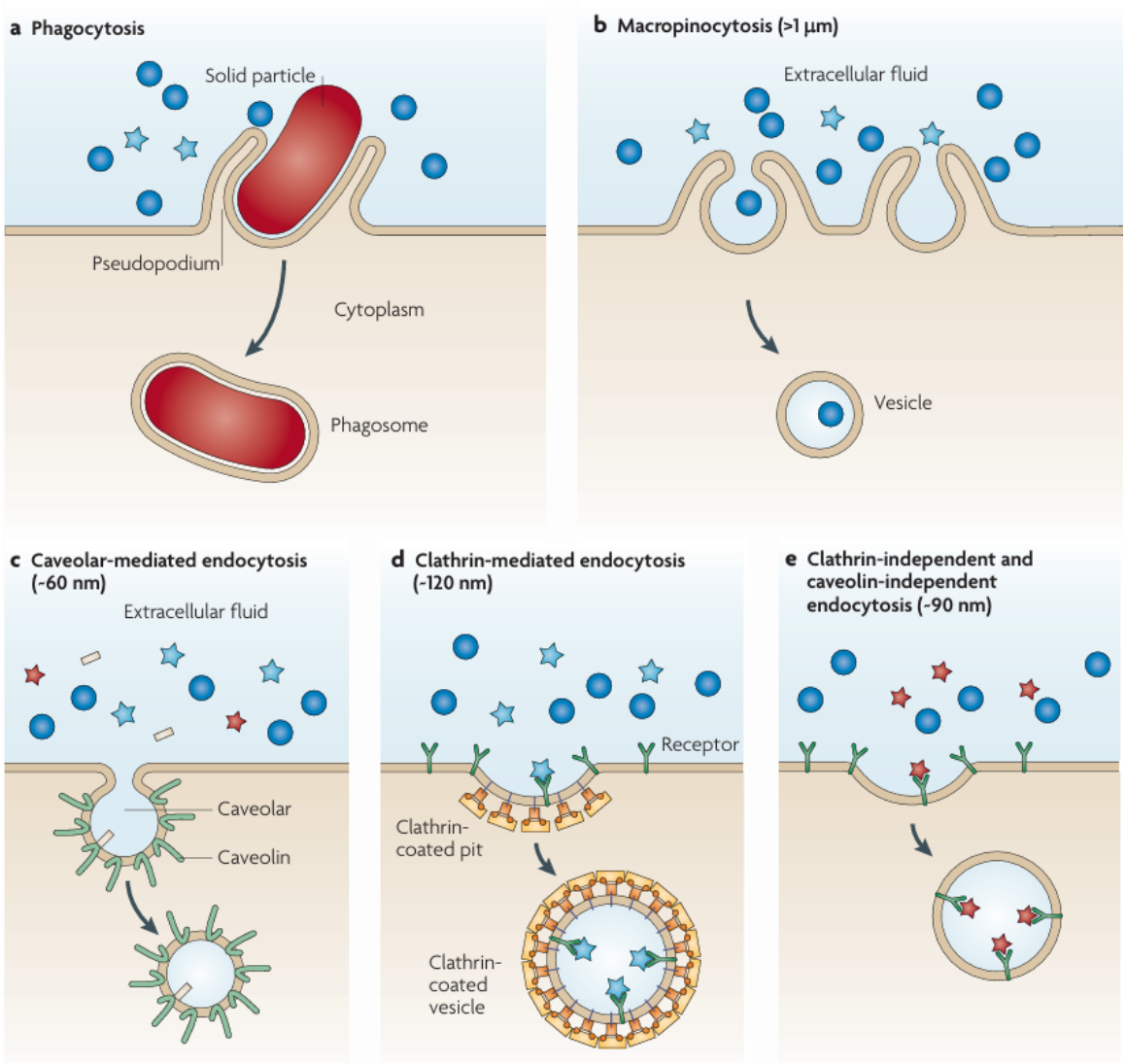

Figure 1.11. *Internalziation of nanoparticles facilitated by various pathways (Adapted from* Petros, R. A. et al, *Nat. Rev. Drug Discov.* **2010**, *9*, 615-627).

1.4 Impact of Physicochemical Properties of NP

The physicochemical properties of nanoparticles including size, shape and architectures, surface charge, and surface chemistry greatly impact the fate of NP in blood half-life-pharmacokinetic parameters, biodistribution, tumor penetration and cellular internalization (see Figure 1.12). The extracellular environmental factors such as components of blood including serum proteins, immune cells/macrophages, monocytes, phagocytes, dendritic cells

etc. The NP-Protein corona formation resulting in opsonization followed by reticuloendothelial system uptake (RES) and interaction of NP with macrophages (MPS) system result in the faster clearance of NP from the blood circulation system reducing half-life time significantly. These overall non-specific interactions greatly impact the pharmacokinetics, clearance and biodistribution of nanoparticles. Therefore, engineering the NP with precise comprehensions to avoid non-specific interaction and increase circulation time is necessary.[61-62]

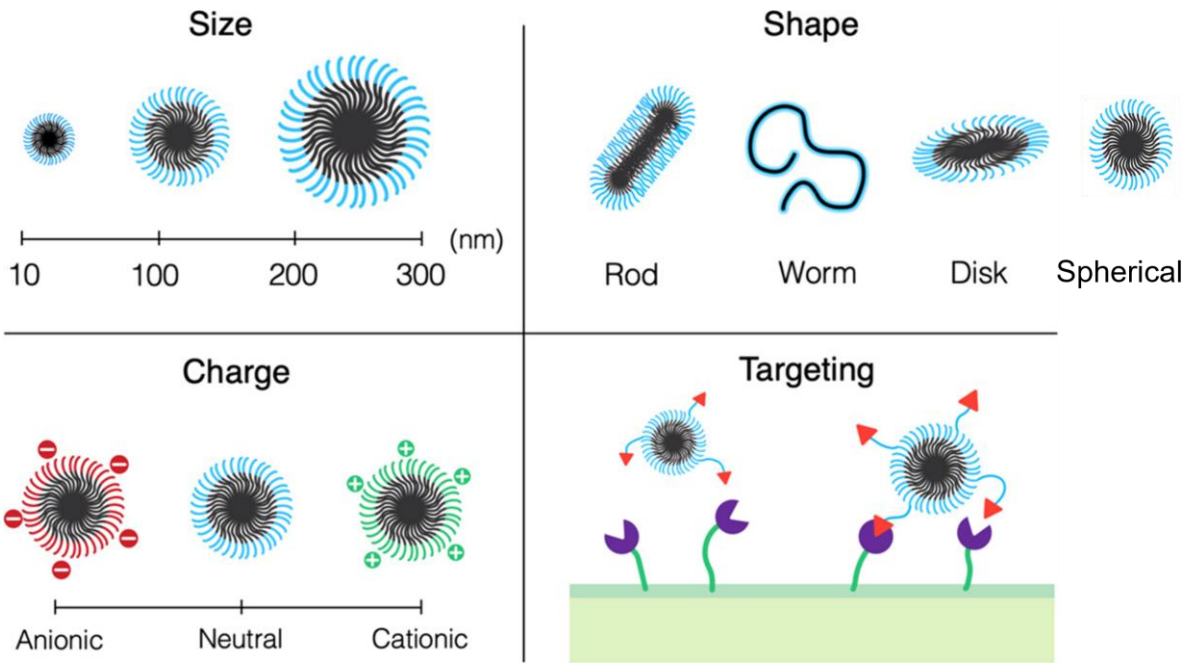

Figure 1.12. *Physicochemical properties of nanoparticles impact circulation time and biodistribution and cellular internalization (Adapted from* Beach, M. A. et al, *Chem. Rev.* **2024**, *124*, 5505-5616).

1.4.1 Size

Size of NP plays key role in the pharmacokinetic and biodistribution and recently reported literatures suggest NP of sizes 30-300nm can easily accumulate in tumors. Essential factors including renal clearance/ filtration, hepatic clearance, tumor extravasation and diffusion and cellular penetration/ endocytosis pathways govern the fate of nanoparticles. [63] In addition, drug loading capabilities, stability, and drug-release profiles are also affected by the size of nanoparticles. Nanoparticles of sizes less than 5-7 nm typically cleared form the circulation facilitated via glomerular filtration in kidneys. [64] Larger particles of more than 1 µm tend to be cleared from phagocytic system involving phagocytes, macrophages, neutrophils, dendritic cells.[65] In addition, larger NP can interact with opsonin, and they can undergo

opsonization and result in faster clearance. Also, larger NPs are prone to be cleared by MPS system mediated by Kupffer cells of liver and filtered via sinusoids in the spleen.[66] In general, the smaller NPs of 1-100 nm sizes show longer *in vivo* blood circulation time than larger NPs of sizes >1 μm.[67-68] Figure 1.13 depict the impact of sizes of nanoparticles in pharmacokinetics, biodistribution, and tumor targeting.

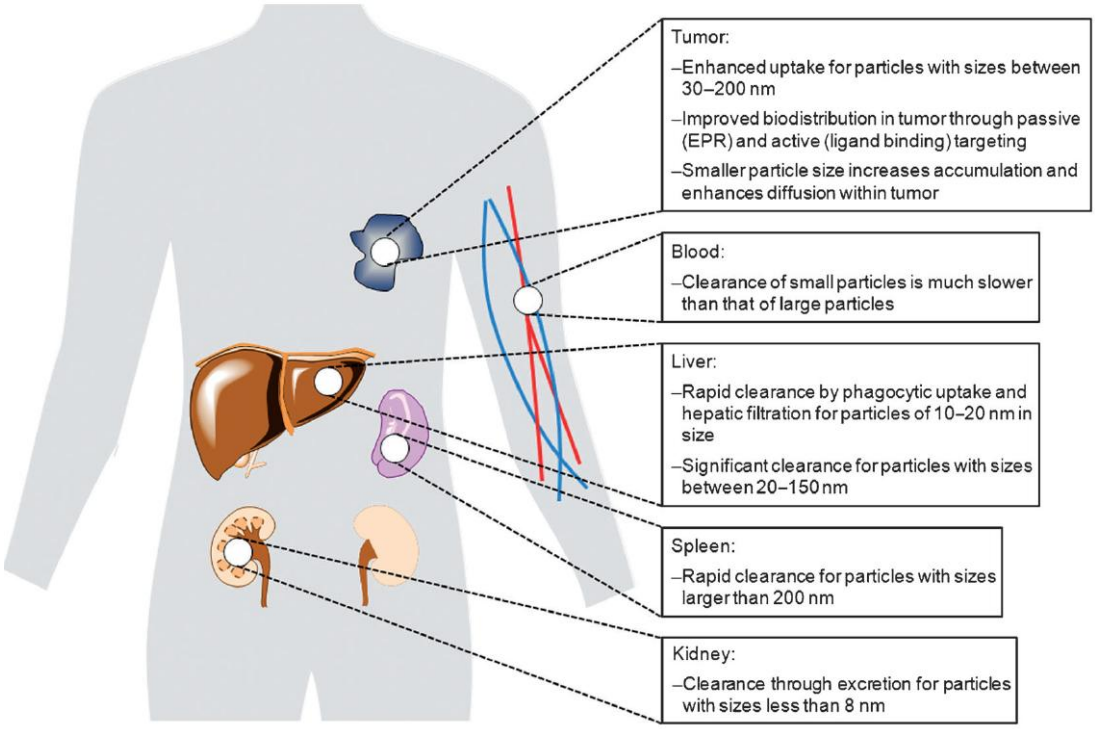

Figure 1.13. *Influence of nanoparticle size on biodistribution and clearance (adapted from Sun et al. Angew. Chem. Int. Ed.* **2014***, 53,* 12320 – 12364*).*

Upper size limits of NP for tumor extravasation have been observed ~400nm and generally NP of size >200nm can effectively accumulate in tumors.[69] However recent studies suggest that the NP of 10-20 nm can penetrate tumor maximum.[70] For example, Schadlich et al investigated influence of size of fluorescent labelled PLA-PEG polymeric NP in tumor xenograft of HT20 colon and A2780 ovarian carcinoma.[71] Using fluorescent imaging, they found that nanoparticle of sizes 111 and 141nm depicted higher accumulation in tumor compared to NP of sizes 166nm. In another study, Sykes, E.A. et al. synthesized PEG and Transferrin coated Au NP of 15, 30, 60 and 100 nm to investigate the role of size of NP influencing on active and passive tumor accumulation.[72] They found that the NPs which are active targeted accumulated 5-fold more than passive targeted of 60 nm in tumor. In addition, half-life of NPs having 30 nm and 60 nm sizes were longer compared to NP of sizes 100nm.

Cellular internalization is greatly influenced by the size of the NP and many reports in general suggested the maximum uptake of NP having sizes in the range of 40-50nm.[73]

1.4.2 Surface Charge

Surface charge of NP such as anionic, cationic and neutral depend on surface chemistry and environmental factors including ionic strength, pH etc., typically determined by zeta potential measurements.[74] The surface charge of NP is one major factor which contributes to nonspecific binding of NP to cells or protein ; thus, influence pharmacokinetics and membrane penetration and accumulation.[75] Non-specific interaction by protein with NP resulting in higher opsonization for cationic NP than anionic or neutral NP, as a result cationic NP are tend to be cleared faster from the blood circulation.[52] In addition NP possessing positive charge (> +30mV) are cleared rapidly by the cells of mononuclear phagocytic system (MPS) from the circulation. [76] For example in a study by Salvador-Morales et al., lipid-polymer NP were decorated with various functional groups such as carboxy, amino and PEGylated methoxy functional groups to design anionic, cationic and neutral NP (see Figure 1.14).[77] Among the different charges, cationic NP were found to be inducing highest levels of complement activation than the NP having anionic and neutral surfaces. In addition, NP decorated with neutral methoxy groups were found to be most immune-compatible. NP having higher zeta potentials > 30mv for cationic NP and < -30mV for anionic NP readily tend to be scavenged by MPS system. In another study, cationic (amine-functionalized) polystyrene microparticles showed higher phagocytosis than anionic (sulfate and carboxylate functionalized), and neutral (hydroxyl functionalized) polystyrene counterparts. [78] Moreover cationic nanoparticles are often associated with cytotoxicity and non-specific interaction with red blood cells resulting in rupture of RBC (hemolysis) and aggregation of platelet *in vivo*.[79-80] Another study pointed out the minimal macrophage uptake of NP having zeta potential <15 mV and resulted in longer circulation time and therefore increasing tumor accumulation. [81] NP with cationic surface charge may promote cellular binding with negatively charged cell membrane (phospholipids, and glycan) resulting in better membrane penetration and endocytosis. Similarly, anionic NPs also can show selective cellular uptake than neutral charged NPs. Studies have showed that the cationic NP shows energy dependent endocytosis involving dynamin and F-actin proteins, while anionic NPs internalized via dynamin-independent manner. In contrast, highly positive charged NP also can by-pass endocytosis and internalize in the cells by creating pores or holes in the cellular bilayer membrane. [82-83]

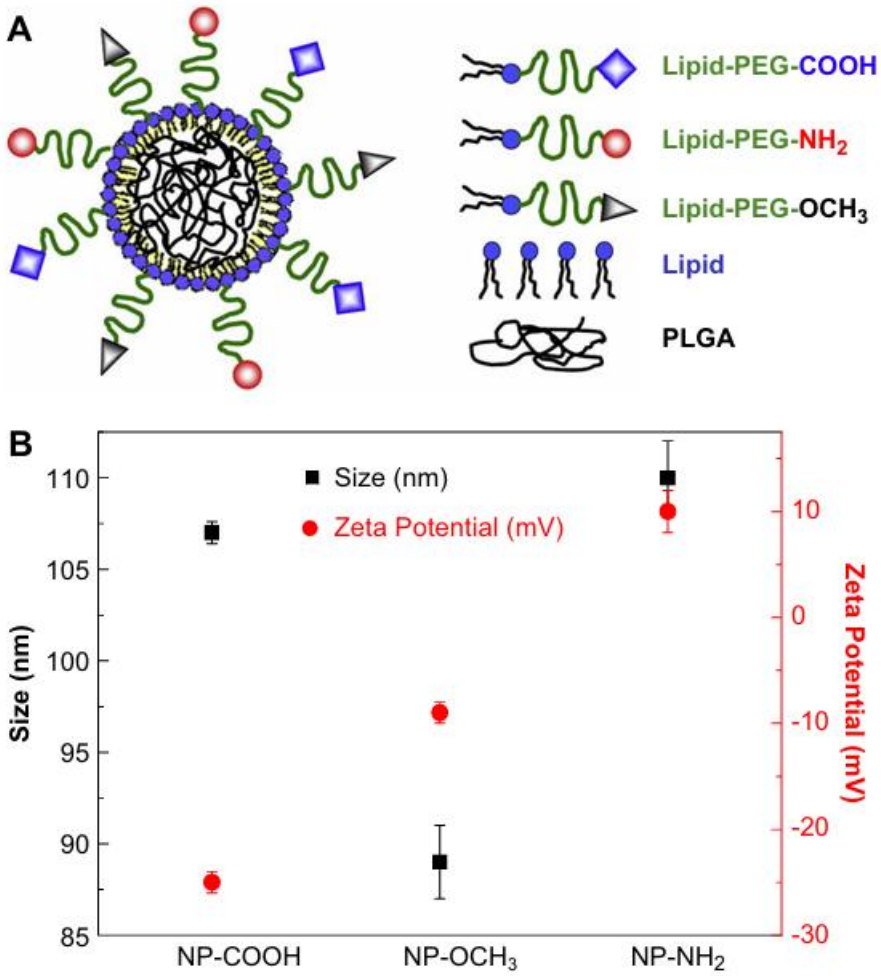

Figure 1.14. *Schematic illustration of hybrid lipid-polymer NP functionalized with different charges. (Adapted from Salvador-Morales, C. et al. Biomaterials.* **2009***, 30,* 2231-2240).

1.4.3 Shape and Architecture

Shape of NP is one of major key parameters having great influence on drug delivery performance in vitro and in vivo including interactions with blood components, renal filtration apparatus, MPS system etc. NP can be precisely designed with various shapes such as spherical, rod-like, cylindrical, disc shaped, ellipsoid, worm-like, fibrous network, filament-like etc.; by employing various techniques.[84] Rod shaped NP found to have longer blood circulation time, enhanced cellular internalization and increased specific binding.[85] In another study, Mitragotri and co-workers reported the synthesis of different shaped polystyrene NP of sphere, rod and disc morphology, suggested that rod-shaped NP had higher affinity towards endothelium of than spherical counterparts (see Figure 1.15).[86] In recent study by Wu et al. in which they synthesized a brush-shaped PCL-b-PEG polymer and encapsulated with doxorubicin and self-assembled into rod-shaped nanoparticles having 200nm and 80nm average length and diameter

respectively. These nanorods exhibited almost 2-fold higher cellular uptake efficiency compared to nascent drug suggesting enhanced cellular internalization by rod-shape NP (see Figure 1.16).[87] Liu et al, constructed pH-responsive nanodisks from organoalkoxysilane and dihexanoyl phosphatidylcholine encapsulated with doxorubicin.[88] The nanodisks depicted pH responsive drug-release, lower cytotoxicity and precise targeting to tumor and suppressed tumor growth.[89]

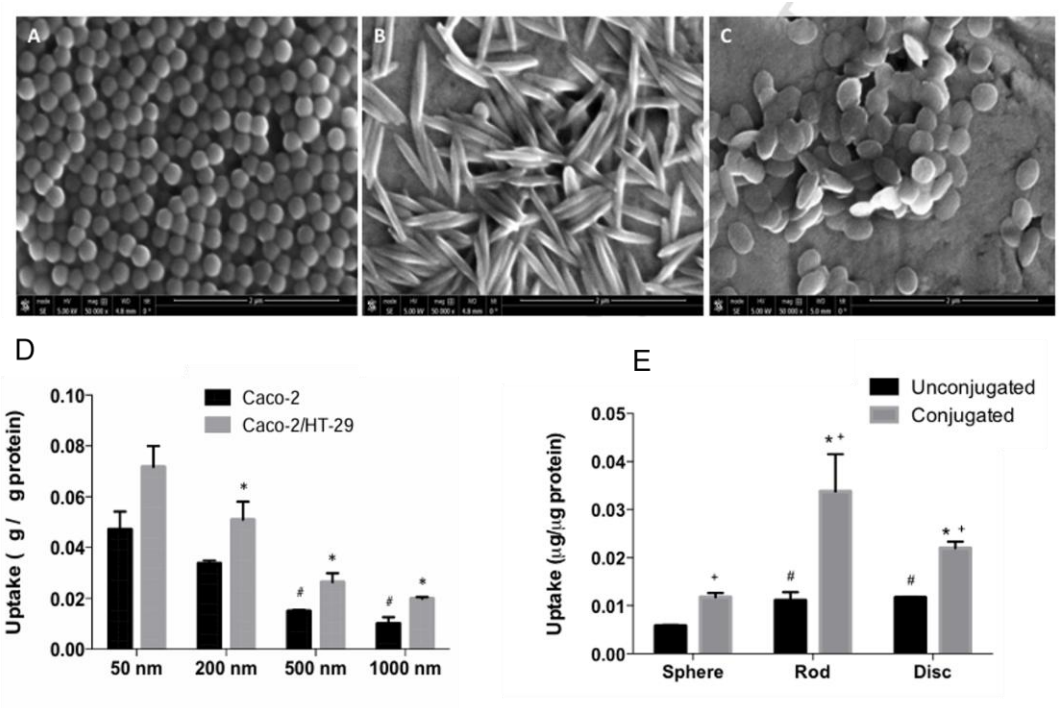

Figure 1.15. *FE-SEM images of Polystyrene NP (a) Sphere (b) Rod (C) Disc morphology. (d) size dependent uptake . (e) Shape dependent uptake (Adapted from* Banerjee, A. *et al. J. Control. Release* **2016**, *238*, 176– 185*).*

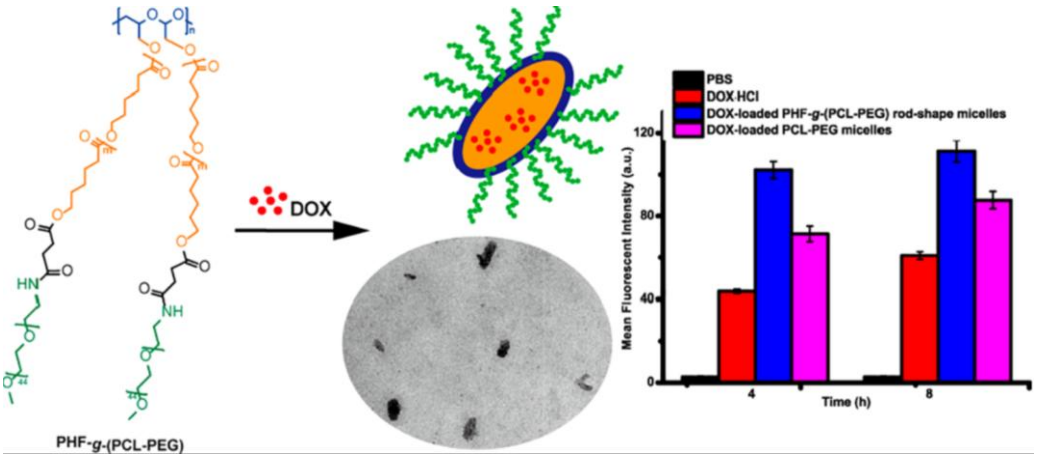

Figure 1.16. *Schematic representation of rod shaped PCL-PEG NP encapsulated with DOX (Adapted from* Wu, Y. *et al. Biomacromolecules* **2019**, *20*, 1167– 1177*).*

Worm-like micelles or nanoworm nanoparticles have high aspect ratio and demonstrated to improve accumulation within cells. Geng et al. investigated the comparative efficiency of worm-like micelles with spherical micelles and found that the worm-like exhibited better biodistribution than their spherical counterparts.[90] Ribbon-like fibrous nanometer scaffolds synthesized by Bortah et al. composed of acetylated dextran, loaded with resiquinod showed tunable drug release profile and strong biocompatibility. [91] Recent studies suggest that shape-shifting of NP upon stimuli can be utilized to overcome the limitations of shape. pH-responsive switching of NP shape can alter the electrostatic interaction, hydrophobicity/hydrophilicity and hydrogen bonding interactions which in turn can affect the uptake efficiency. For example, Han et al showed enhanced uptake of chimeric peptide in tumor upon response to acidic environment outside the cells.[92] This peptide produced spherical shaped NP under normal conditions; however, at acidic environments they spontaneously converted to rod-like NP driven by electrostatic interactions resulted in enhanced uptake in tumor. In another study, short filomicelles or filament like micelles showed similar blood circulation time with spherical micelles composed of pH responsive PEG-b-(CPTKMA-co-PEMA) system.[93] Role of particle shape on the internalization and attachment with macrophages was studied by Sharma et al, suggested that oblate ellipsoid shape depict higher phagocytosis than prolate ellipsoid or sphere.[94] Nonspecific interaction of MPS systems with nanoparticles can induce inflammation and toxic effects by triggering immune responses including secretion tumor necrosis factor (TNF), interleukins (ILs) and interferons. [95] Recent reports suggested higher phagocytic uptake and induced inflammation in macrophages for rod-shaped NP compared to spherical and star shaped NP. [96] Fréchet and coworkers reported the influence of macromolecular shape/ confirmation and flexibility of drug delivery vehicles on the pharmacokinetic, renal filtration and biodistribution, and tumor penetration ability (see Figure 1.17).[97] The polymers, in particular linear macromolecular moieties often self-assembled into loosely coiled structure which are flexible can easily deform and pass through pores. In contrast, rigid confirmation achieved by dendrimers, star like polymers, hyperbranched polymers do not undergo deformation and stay in rigid spherical form tend to avoid renal clearance by resisting entry into pores resulting in longer blood circulation time. Rod shaped elongated polymers nano assemblies can achieve easier tumor penetration and extravasation. The flexibility and stability branched architecture rely on the of branching density to achieve extravasation into tumor. Renal filtration can be substantially reduced by increasing branching density which results in longer circulation time.

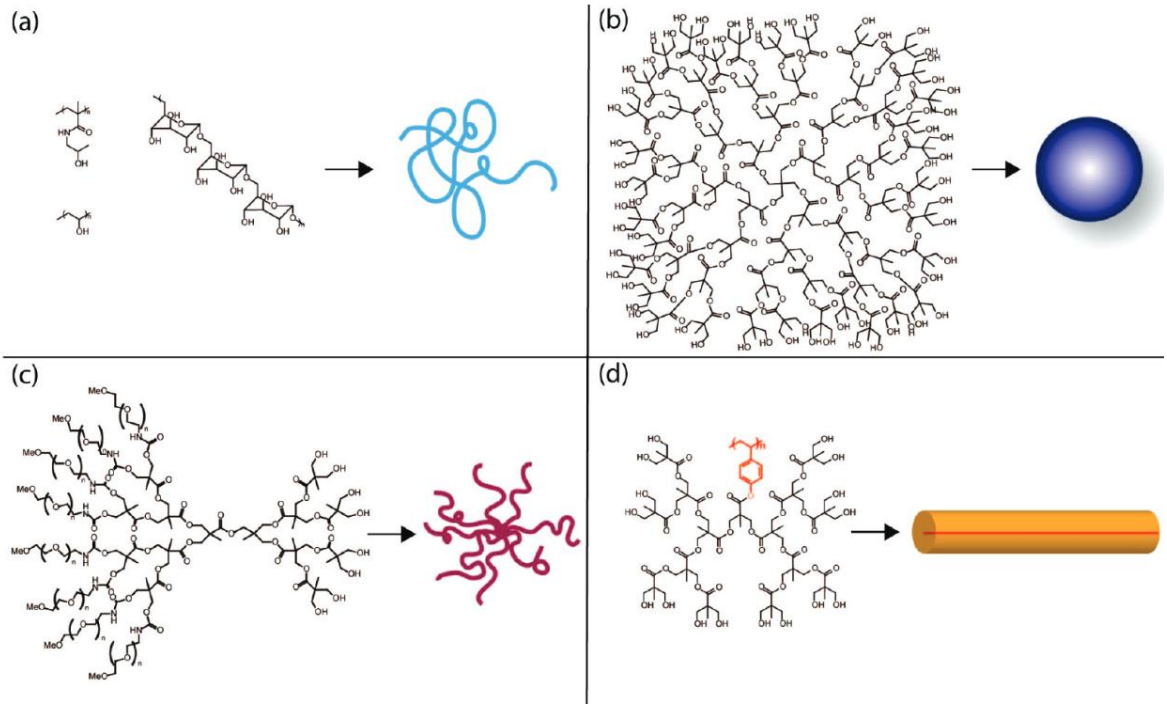

Figure 1.17. *Figure depicted various polymer architecture and confirmation adopted by them including loose coil-like, rigid sphere, branched star shaped and rigid rod (Adapted from Fox et al. Acc. Chem. Res.,* **2009***, 8,* 1141-1151*).*

1.5 Targeting Strategies for Nanoparticles

To improve the effectiveness of drug delivery system, nanoparticles must accumulate efficiently into tumor. Targeting tumor can be achieved by two strategies either passive or active targeting. Characteristic features of tumor biology exploited by the passive targeting to enhance the accumulation of nanoparticles in tumor by enhanced permeability and retention (EPR) effect. [98-99] Tumor are characterized by leaky vasculature and poor lymphatic drainage as well uneven cellular packing resulting in wider intercellular spaces. Free drug molecules, being small can easily diffuse in non-specific manner. In contrast the nanoparticles can extravasate into tumor facilitated by leaky blood vessels through EPR effect (see Figure 1.18).[100] Tumor cells grow rapidly and uncontrollably resulting in the increase of permeability of vasculature due to defective angiogenesis. Nanoparticles accumulate in tumor retained by dysfunctional lymphatic system and allows to internalized and release the drug in the cells. Studies using different sized liposomal nanoparticles and other system have shown that nanoparticles of sizes less than 200 nm are much more effective for tumor penetration and

accumulation exploiting EPR effect.[101] Other strategy of targeting involve the decoration of NP surface with ligands, targeting agents, antibodies, which are specific to receptor present on tumor surface termed as active targeting (see Figure 1.18).[102]

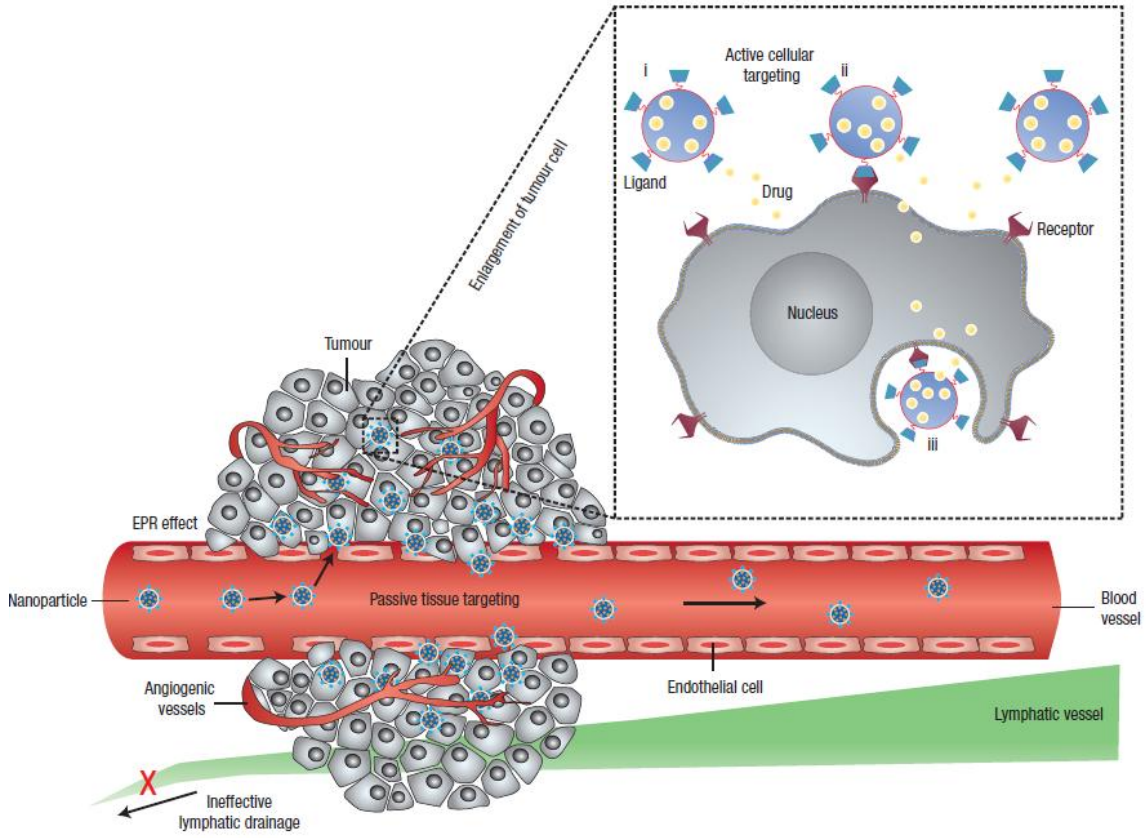

Figure 1.18. *Illustration of mechanism of polymeric nanoparticles uptake to tumor by active and passive targeting (Adapted from Peer et al. Nat. Nanotechnol.* **2007***, 2,* 751-760*).*

1.6 Evolution of Polymeric Drug delivery System (DDS)

The drug delivery system started to develop from 1960 to increase the efficacy of treatment and avoid side effects caused use non-specific interaction of small molecules. The new era of drug delivery emerged by evolution of polymeric drug delivery system from drug depot to injectable delivery system (nanoscale DDS) with the contribution of notable researchers Ringsdorf, Peppas, Higuchi, Langer, Folkman, Heller, Speiser and Roseman.[103-113] Discovery of EPR effect by Maeda et al., was a major breakthrough in passive targeting and the EPR effect paved pathway for modern drug delivery for cancer therapy and other biomedical applications. Micellar nanoparticles derived from PEGylated block copolymers composed of hydrophobic amino acid polymer and hydrophilic polyethylene glycol by Kataoka

co-workers and other was another milestone in the development of anticancer drug delivery vehicles.[114] PEGylated poly (aspartic acid) micellar NP was encapsulated with Doxorubicin by Matsumura named NK911 and various other polymeric nanoparticles including NK911, SP1049C, Genexol-PM etc.; were approved by FDA and able to successfully translated or in the process of translational into clinic for treatment of cancer and other diseases.[115-119] SP1049C is pluronic polymer encapsulated with doxorubicin found superior in ability to bypass the Pgp protein efflux pumps compared to free drug in the treatment of metastatic esophageal cancer. Genexol-PM is paclitaxel micellar formulation of PEG-b-PLA approved by South Korea and other countries for the treatment of various carcinomas including breast cancer. Polylactide acid-polyethylene glycol based micelles loaded with docetaxel (DTX) targeting prostate-specific membrane antigen (PSMA) for the treatment of prostate cancer developed by Farokhzad and co-workers led development of first targeted NP named BIND-014 and it is currently under clinical trial.[120] CALAA-01, a three component system based on cyclodextrin polymer (CDP), adamantine-PEG, and transferrin protein conjugated adamantine-PEG have been developed for encapsulation and pH triggered delivery of siRNA is another example of targeted NP for which is in the clinical trial.[121] Thus, polymeric drug delivery system have evolved from 1st generation of passive targeting to 2nd generation of system capable selective targeting tumors of leading towards and 3rd generation of delivery system are emerging as DDS system capable of targeting and stimuli-responsive drug release. Figure 1.19 depict the evolution of DDS over last 50 years.

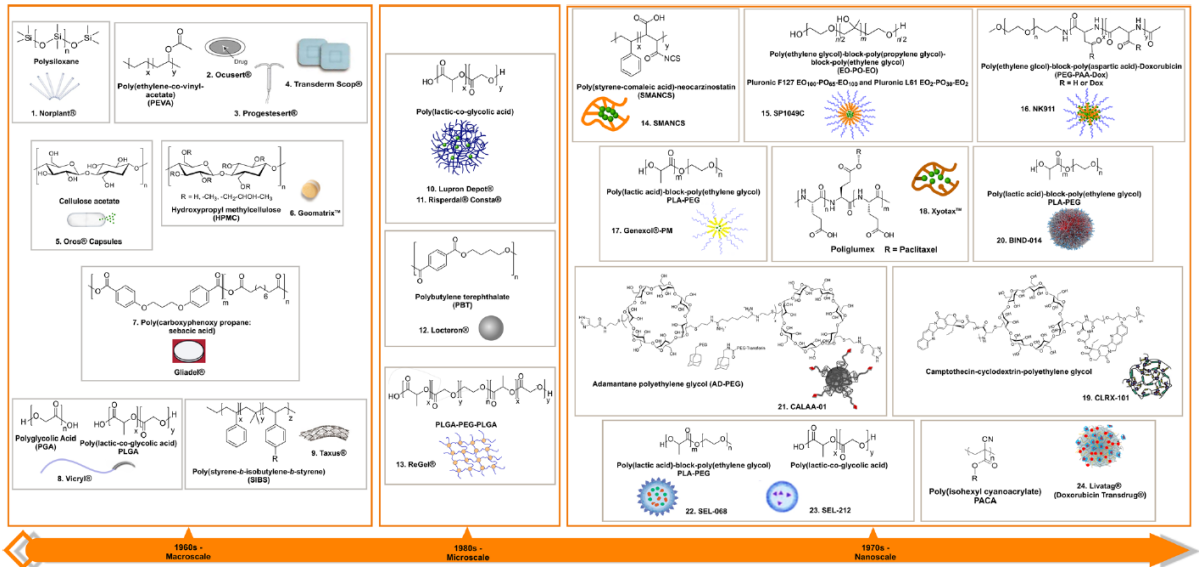

Figure 1.19. *Evolution of polymeric drug delivery system over last 50 years (Adapted form Kamaly et al. Chem. Rev.* **2016**, *116,* 2602-2663).

1.7 Aggregated Micelles versus Unimolecular Micelles

The *in vivo* performance of polymeric micelles is greatly related to stability of micelles in solution, drug encapsulation capabilities, release profiles, blood-circulation time, biodistribution and targeting. In general, amphiphilic polymers produce thermodynamically favorable micellar species above a certain concentration called critical micellar concentration (CMC). Micellization is thermodynamically driven process and below the CMC, the micelles dissociated into unimers or single polymeric chains.[122-123] These micelles further tend to aggregate to produce aggregated micellar NP rather than individual species. However, *in vivo* stability of aggregated micelles is often influenced by several factors including dilution, flow rate, pH , ionic strength etc.[124] These factors, in particular dilution, result in the dissociation of dis-assembly of aggregated or multimolecular micelles into individual polymer chains. Upon administration of aggregated micellar NP into *in vivo,* they encounter 1000-fold dilution in the blood and readily disintegrate into individual species leading to premature release of drug before reaching to target (see Figure 1.20).[125-128] A recent reports suggested poor micellar stability for the failure of NK911 micelle in clinical trial, highlighted burst release following the intravenous injection.[129] A study using PEG-polyester micellar nanoparticles also found that dissociation of >80% micelles within 1h of administration.[130]

To overcome the limitation of conventional aggregated micelles associated with stability against concentration, two strategies have been adopted. First the cross linking of core or shell strategy for example Leroux et al. cross linked the core of 8-arm poly(glycidyl methacrylate) (PGMA) polymer constructed using ATRP which resulted in formation of stable micelles.[131] Gong et al reported synthesis of ABA-type amphiphilic polymer and further cross linked them to form vesicle and utilized for drug delivery application. [132] Though cross linking strategy is effective in enhancing stability of micelles; however, the major imitation of this strategy is the poor drug release aspects and limited choice of material which can affect biodegradability.[133] The second strategy to stabilize the micelles is the utilization of micelles which do not undergo dissociation upon dilution, such structure introduced in 1991 by Newkome et al, called “unimolecular micelles.” The term “unimolecular micelles” refers to class of single polymer chain derived micelles constituted covalently bunded of core and shell. [134-136] They show extreme stability against the dilution and other environmental factors making them one of the preferred choices of materials for biomedical applications. [137-139] These unimolecular micelles can be constructed using various types of polymeric architectures including hyperbranched, dendrimer, brush and star polymers.

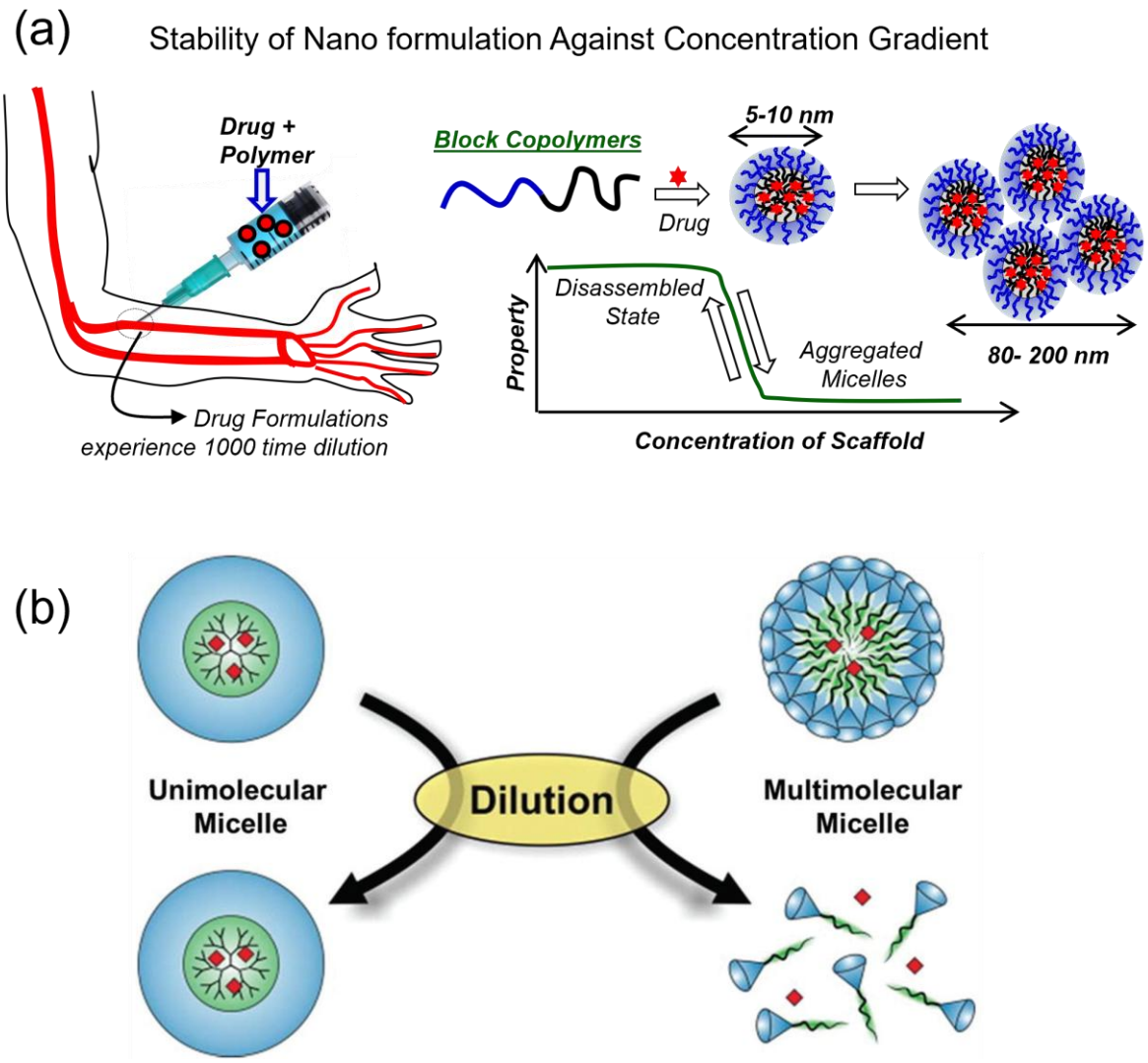

Figure 1.20**. (a) Stability of nanoformulation against concentration gradient. (b) influence of dilution on the stability of the aggregated micelles vs. the unimolecular micelles (Adapted from Lukowiak et al. Biotechnol. Adv.,* **2015, 33,* 1327–1341*).*

1.7.1 Dendrimer

Dendrimers are radial symmetric highly branched macromolecular architectures. Availability of large numbers of terminal groups allows dendrimers to achieve high functionalization and reactivity.; thus, these monodisperse, and globular structures can be utilized for the designing of unimolecular micelles. Dendrimers are versatile architecture owing to their nanometers size, dimensions and design scope and have been widely used in biomedical field as drug delivery carriers, biosensor , gene vector, and catalytic nanoreactors.[140-142] Amphiphilic dendrimers can be fabricated as unimolecular micelles due to their contrasting polarity and characteristic properties of dendritic architecture and small hydrodynamic volume.

Typically, dendrimers are synthesized convergent and divergent synthetic routes. First amphiphilic dendrimers was synthesized in 1993 by Fréchet and co-workers using convergent strategy. [143-144] This study reported 3,5-dihyroxybenzyl alcohol based polyether dendrimer having carboxyl terminal end groups capable of strong encapsulation ability for hydrophobic drugs which depicted linear relationship with the concentration of dendrimer. Another study by Meijer and co-worker reported synthesis of amphiphilic poly (propylene imine) at inner fifth generation.[145,146] The hydrophilic dye Rose Bengal was encapsulated into internal cavities of dendrimer and terminal group was sterically protected with bulky group t-butyl carbonyl protected phenyl alanine groups. The Upon acid hydrolysis mediated removal of 64 chain end t-butyl groups regenerated 'open shell' which programmed controlled release of Rose Bengal (see Figure 1.21).

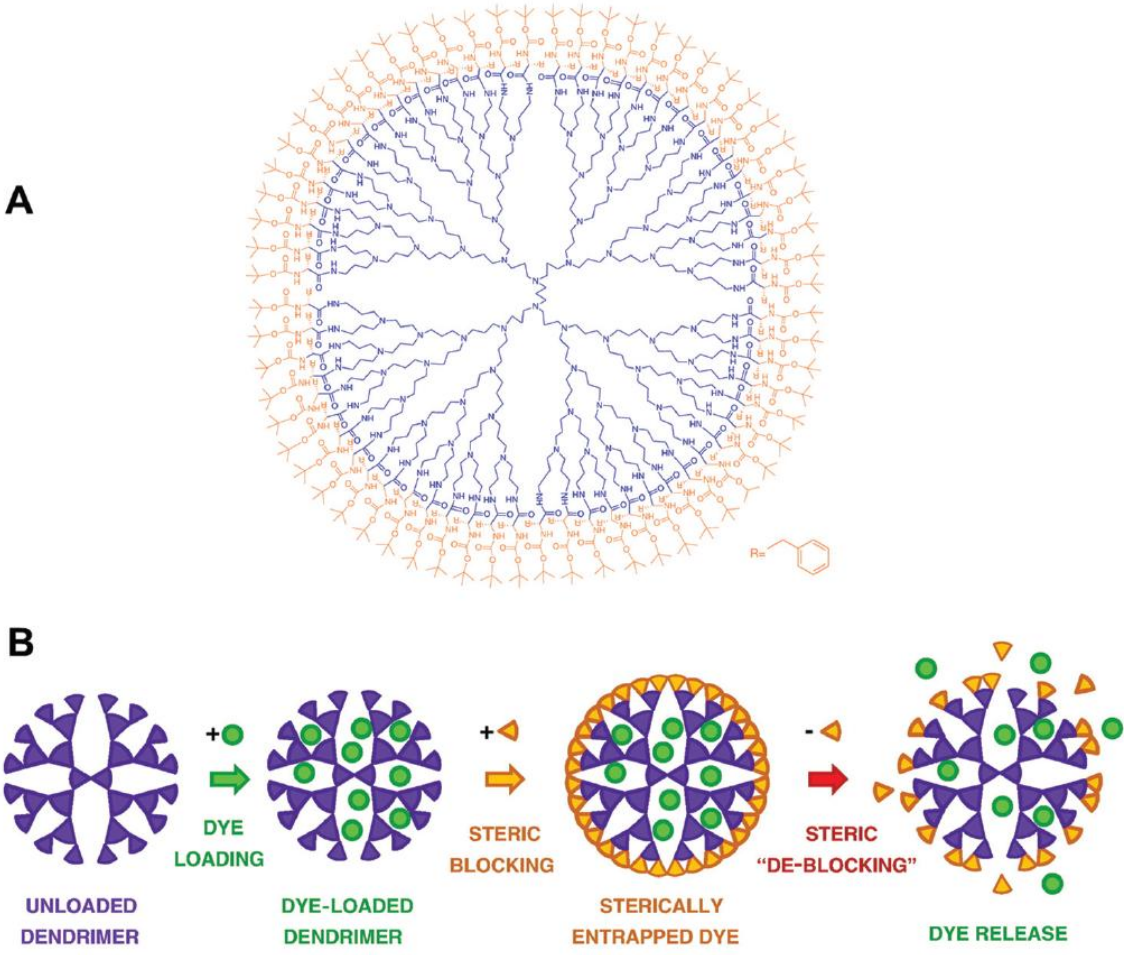

Figure 1.21. *Schematic representation of the dendritic box based on fifth generation poly(propylene imine and tBoc terminal. The dye released was programmed based on steric de-blocking (Adapted from Fan et al. Polym. Chem.* **2016**, *7,* 5898–5919*).*

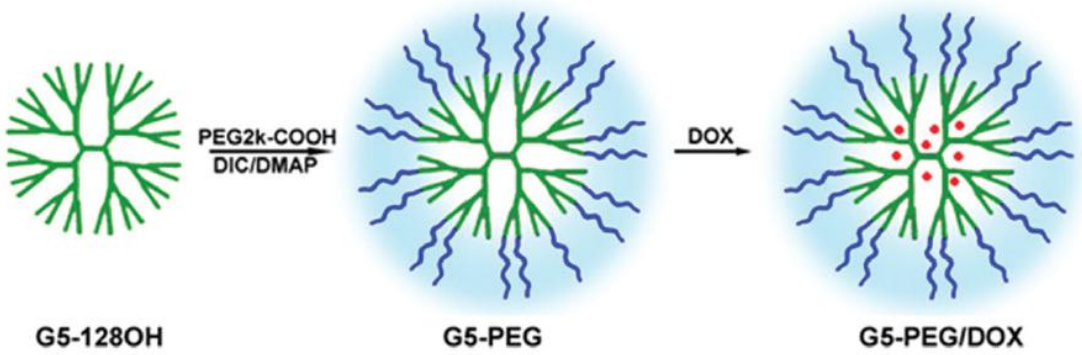

Figure 1.22. *Fifth generation PEGylated Polyester Dendrimer for doxorubicin encapsulation. (Adapted from Ma, X. et al. Macromolecules* **2013**, *46*, 37–42*).*

Recently PEGylation have been adopted as synthetic strategy to increase hydrophilicity of dendrimers for drug delivery applications.[147] Also recently dendrimers are synthesized based on biodegradable polymers such aliphatic polyester, which can degrade into smaller units and release the encapsulated cargo. For example, Ma et al reported fifth generational dendrimer synthesized from thiol/acrylate Michael addition reaction with esterification of AB_2-type monomers. This hydroxyl terminated dendrimer was PEGylated for hydrophilicity and encapsulation of doxorubicin (see Figure 1.22). Poly(amidoamine) (PAMAM) is another widely used class of dendrimers owing to their versatility in functionalization have been utilized for fabrication of unimolecular micelles. Hydroxyl functionalized fourth generation (G4) PAMAM dendrimer modified on terminal with PLA-PEG was reported to encapsulate 20 wt. % drug and self-assembled into unimolecular micelles. [148-151]

1.7.2 Hyperbranched Polymer

Hyperbranched polymers are relatively easier to synthesize using convenient one-pot synthetic approaches compared to dendrimer where tedious synthesis is required. Hyperbranched polymers are branched architectures typically synthesized using condensation, ring opening polymerization (ROP), vinyl polymerization techniques. The hyperbranched polymers have been widely used for fabrication of unimolecular micellar NP and have been used in biomedical applications due to their biocompatibility.[152-154] One of the most studied hyperbranched polymer, Boltorn (H30 and H40) synthesized from 2,2-bis (methoyl) propionic acid monomer.[155-156] PEGylation strategy is often adopted to render hydrophilicity and

encapsulation of hydrophobic drugs into the H40 based hyperbranched polymer, since H40 is hydrophobic. However, encapsulation of hydrophobic drug such as Paclitaxel (PTX) in the H40-PEG based NP was limited to ~0.3wt.% due to formation of smaller size of H40 (3nm) unimolecular micelles.[157] To circumvent the limitation of low encapsulation, recently new strategy of decoration of H40 on the top by polyesters such as polylactide (PLA) acid or polycaprolactone-polyethylene glycol (PCL-PEG) have been adopted (see Figure 1.23).[158-159] In this strategy terminal OH group of H40 can be used as initiator for ROP of lactide of caprolactone monomers and finally conjugation with PEG. This approach enable appropriate amphiphilicity as well as enhanced drug loading capacities in H40 based H40-Polyester unimolecular systems. For example , H40-PLA-PEG based unimolecular micelles depicted excellent drug loading content of 12wt% for doxorubicin and about 33wt% for 5-fluorouracil.[160-161]

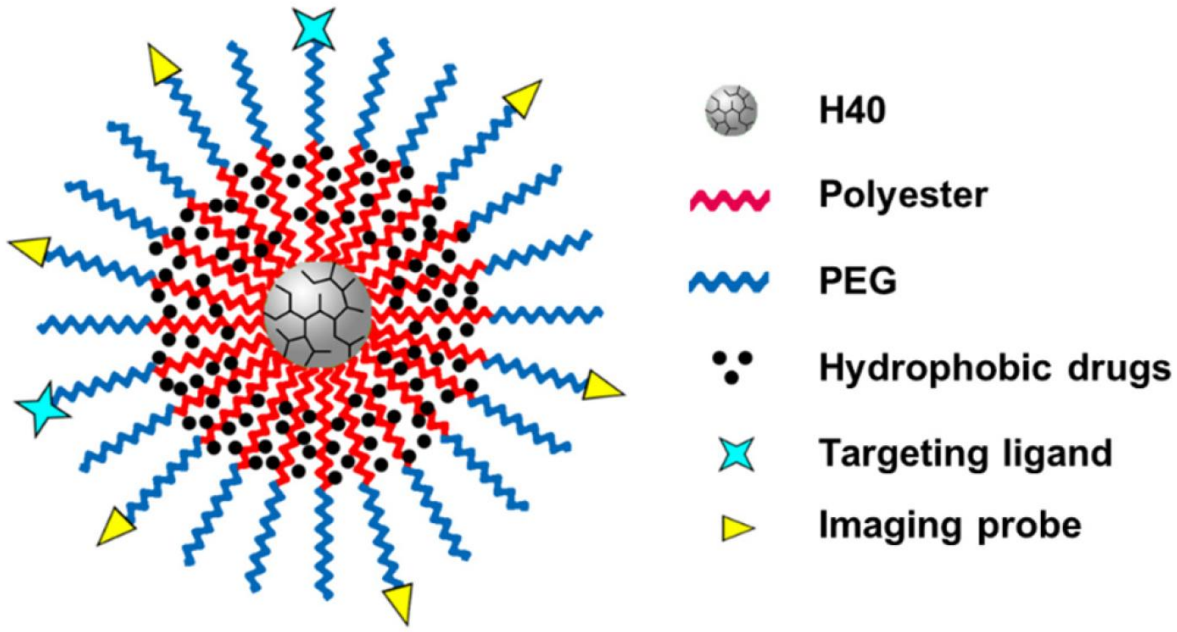

Figure 1.23. *Diagrammatic illustration of H40 based unimolecular utilizing polyester and PEG for encapsulation of hydrophobic drug (Adapted from Chen et al. Adv. Drug Deliv. Rev.* ***2018****, 130, 58–72).*

Luo et al reported the synthesis of H40 based unimolecular micelles having thermo-responsive inner core composed of poly (N, N-diethylacrylamide) and pH-sensitive cationic shell composed of poly (2-dimethylamino ethyl methacrylate) by using RAFT polymerization technique.[162] These H40 systems were self-assembled into unimolecular micelles and depicted dual responsive (pH and temperature) change in size which can be utilized for gene or drug

delivery applications. Another class of water soluble biocompatible hyperbranched polymers are derived from hyperbranched polyglycerol (HPG). HPG depict good biocompatibility, low viscosity and often conjugated with PCL-PEG system forming HPG-PCL-PEG which have been widely used as drug delivery vehicles.[163-164] In another study by Li et al, H40 based system H40-PCL-b-P(OEGMA-co-AzPMA) was synthesized by ROP of caprolactone with peripheral OH of H40 and ATRP of oligoethylene glycol monomethyl ether methacrylate (OEGMA) and 3-azidopropyl methylate (AzPMA) followed by clicking it with MRI contrast reagent along with targeting agent folic acid Gd-FA (see Figure 1.24). [165] Aqueous self-assembly produced stable unimolecular micelles with the excellent encapsulation of hydrophobic drug paclitaxel having 6.67wt%. The magnetic resonance (MR) imaging in Rat was utilized to track the accumulation of unimolecular micelles in tumors.

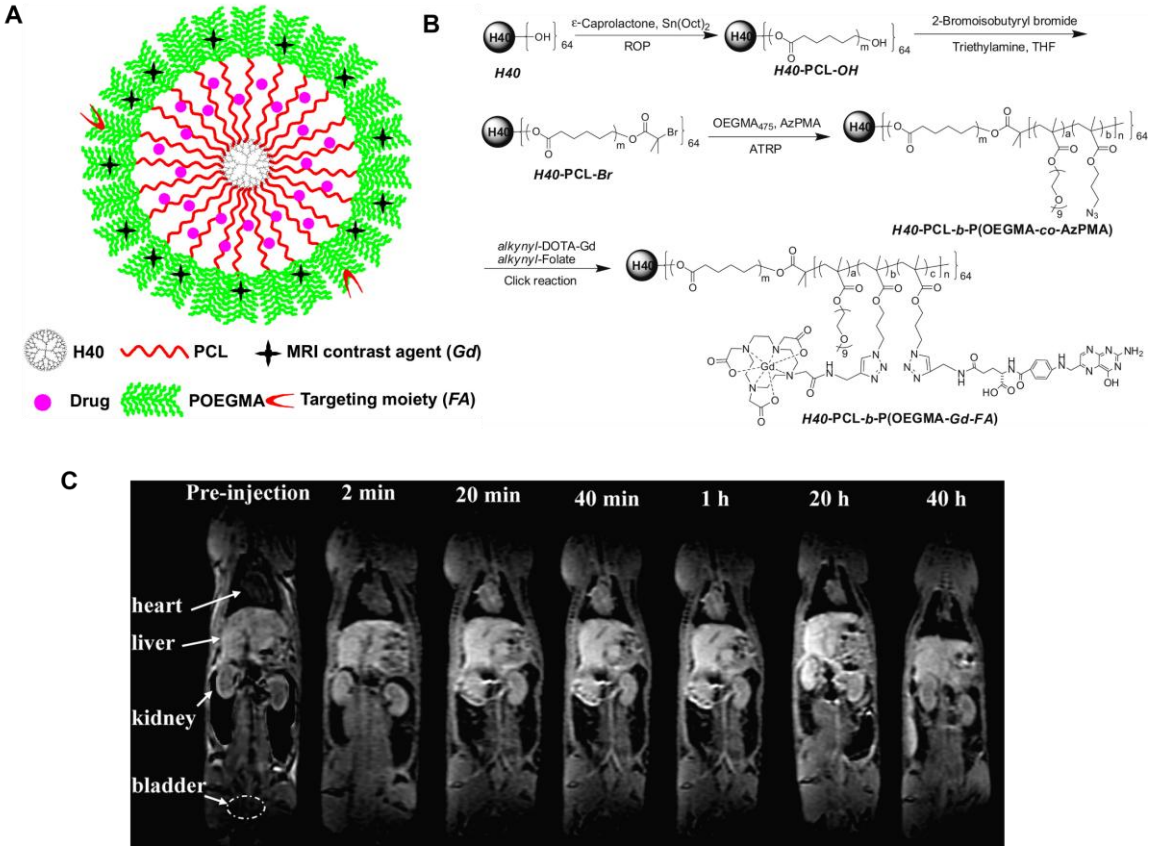

Figure 1.24. *H40 based unimolecular micelle for magnetic resonance imaging application. (Adapted from Li, X. et al. Biomaterials.* ***2011****, 32, 6595-6605).*

1.7.3 Brush-shaped Polymer

Brush-shaped polymer are another of class of synthetic higher order macromolecular architecture which can be utilized for fabrication of unimolecular micelles. Polymer brushes contain multiple side chain arms grafting/stanching from a main polymer backbone. [166] Brushes can be synthesized using three main strategies namely 'grafting through', 'grafting from', and 'grafting onto'.[167] Brush shape core-shell unimolecular micellar NP have gained attention in recent years. A worm-like micelle based high density grafting of polycaprolactone-polyethylene oxide (PCL-b-PEO) on the polymethacrylate backbone was synthesized using "grafting onto" approach. This brush polymer was self-assembled as worm-like structure before and after doxorubicin loading evident from the AFM images (see Figure 1.25).[168] Gong and co-worker reported amphiphilic block copolymer based brush shaped polymer composed of poly (2-hydroxyethyl methacrylate) with side chains of PLA-PEG using "grafting from" strategy to form stable unimolecular micelles for targeted drug delivery of doxorubicin to 4T1 tumor.[169] Recently our group reported brush polymer based on polyester urethane grafted with various chain length PEG.[170] The polyester urethane backbone was synthesized by condensation polymerization of amino acid monomer. The self-assembly of these brushes resulted in nanorod and nanosphere morphology and depicted excellent blood circulation time and deep tissue penetration in mice.

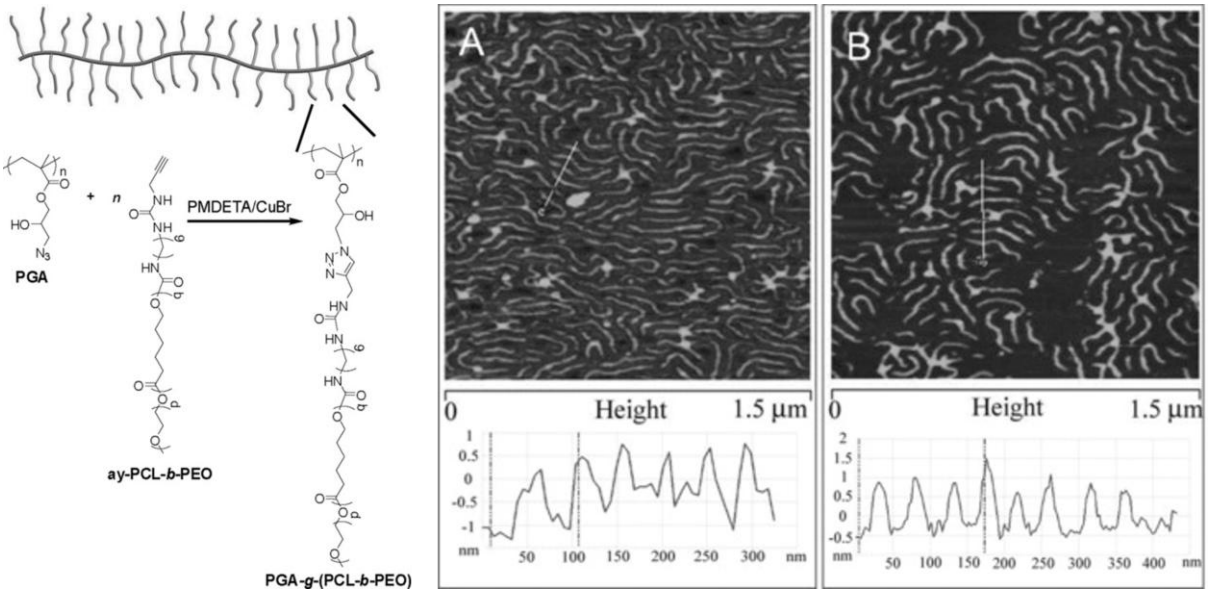

Figure 1.25. *Grafting onto approach for synthesis brush polymer and AFM images depicting worm-like morphology . (Adapted from Zhao, P. et al. Macromol. Rapid Commun.* ***2012****, 33, 1351-1355).*

1.7.4 Star Polymer

Star polymers are class of higher order macromolecular architecture having central core and originating arms from the core. Three approaches have been used for synthesis of star polymers including core-first, arm-first and coupling onto (see Figure1.26).[171] Based on the structure and composition star polymers can be classified into two major categories homoarm having similar composition on each arm and miktoarm having different chemical composition on each arm. Star polymers offers various advantages including structural tunability, functionalization scope, versatile and easier synthesis, precise core-shell fabrication, and large number of choices of materials making them suitable for biomedical applications.[172-173] Different polymerization strategies including ring opening polymerization, ATRP polymerization, RAFT polymerization, living anionic polymerization, and living cationic polymerization have been utilized to synthesized star polymers. [172] Wang et al reported the synthesis of series star-shaped cyclodextrin core based unimolecular micelles and encapsulated with paclitaxel to investigate *in vivo* behavior.[174] The *β*-cyclodextrin core was modified for exploiting ATRP polymerization strategy to synthesize *β*-CD-s- polyacrylic acid *(β*-CD-s-PAA) star polymer. In another example unimolecular micelles based on amphiphilic block star copolymer composed 21-arm β-cyclodextrin (β-CD) and poly(acrylic acid)-*b*-polystyrene (PAA-*b*-PS) was reported by Pang et al.[175] In this study, β-CD was modified with bromine-substituted functionality and subsequent ATRP with t-butyl acrylate and styrene monomer in sequential manner produced hydrophilic shell and hydrophobic core upon hydrolysis of t-butyl group. The unimolecular micelles were produced by aqueous self-assembly having sizes of ~19 nm and further suggested increasing size with molecular weights up to 65nm. Wang and co-worker reported pH-responsive β-CD based star-shaped amphiphilic block copolymer (β-CD-PLA-POEGMA) synthesized by ROP followed by ATRP.[176] This polymer was self-assembled into unimolecular micelles with 6-10wt% drug loading content for doxorubicin depending on the degree of polymerization of hydrophilic block. Doxorubicin encapsulated unimolecular micelles showed pH-responsive release in controlled manner and taken up by cell efficiently and showed enhanced tumor uptake and Doxorubicin delivery and excellent biocompatibility. Hyperbranched star copolymer based unimolecular novel micelle having reduction-responsive disulfide linkages and PEG shell has been reported by Pen et al., conjugated with camptothecin (CPT) drug.[177] This unimolecular micelle depicted diameters of 3.56-6.08 nm and triggered with pH 6.0 and 5.0 easily. In addition, DTT treatment degraded polymers from the 20300 to

2100 g/mol molecular weight oligomers. The redox-responsive anticancer CPT loaded unimolecular micelles demonstrated improved blood compatibility and targeting drug delivery.

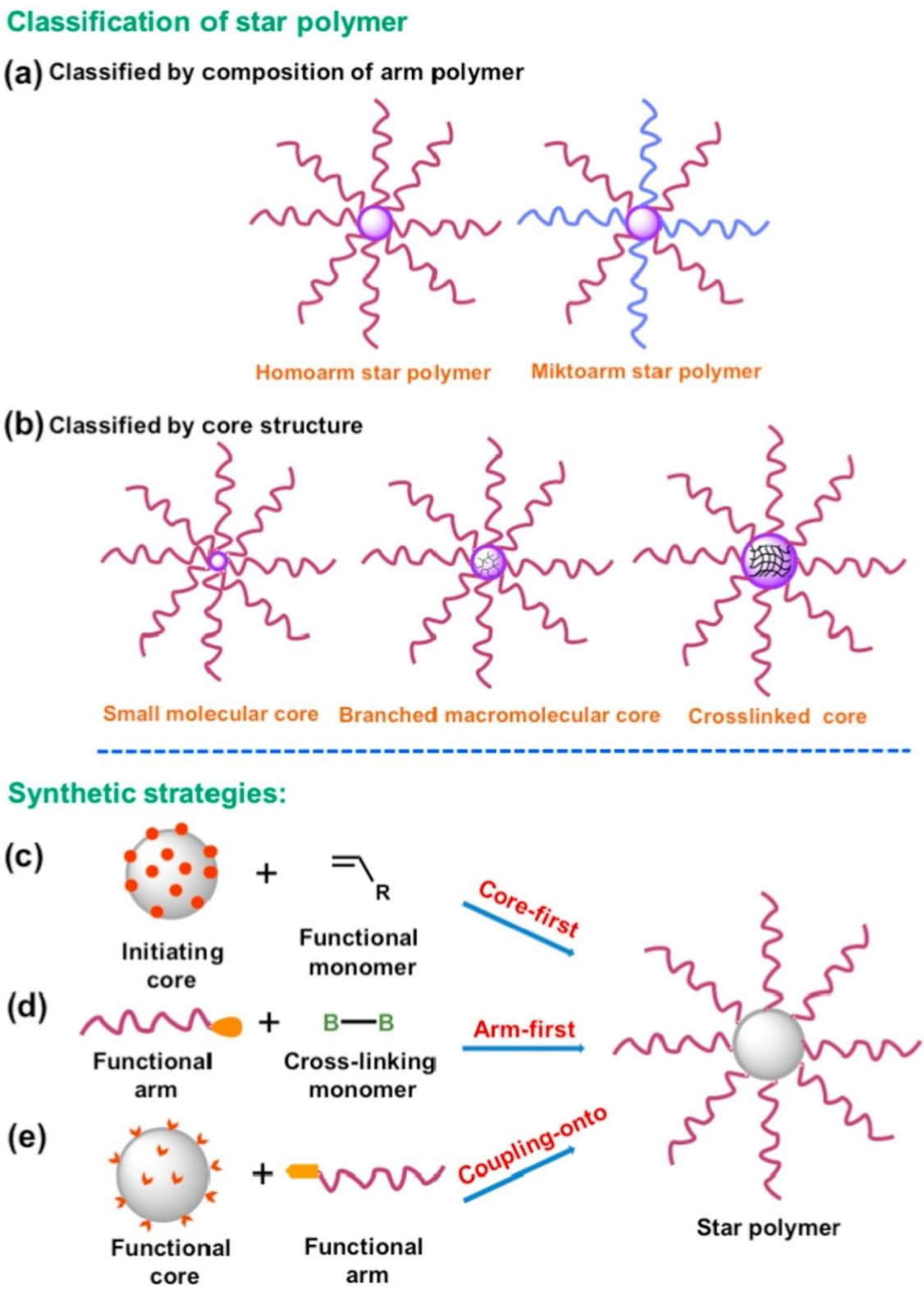

Figure 1.26. *Synthesis and type of star polymers. (Adapted from Jin, X. et al. Biomaterials* **2018**, *178*, 738-750*).*

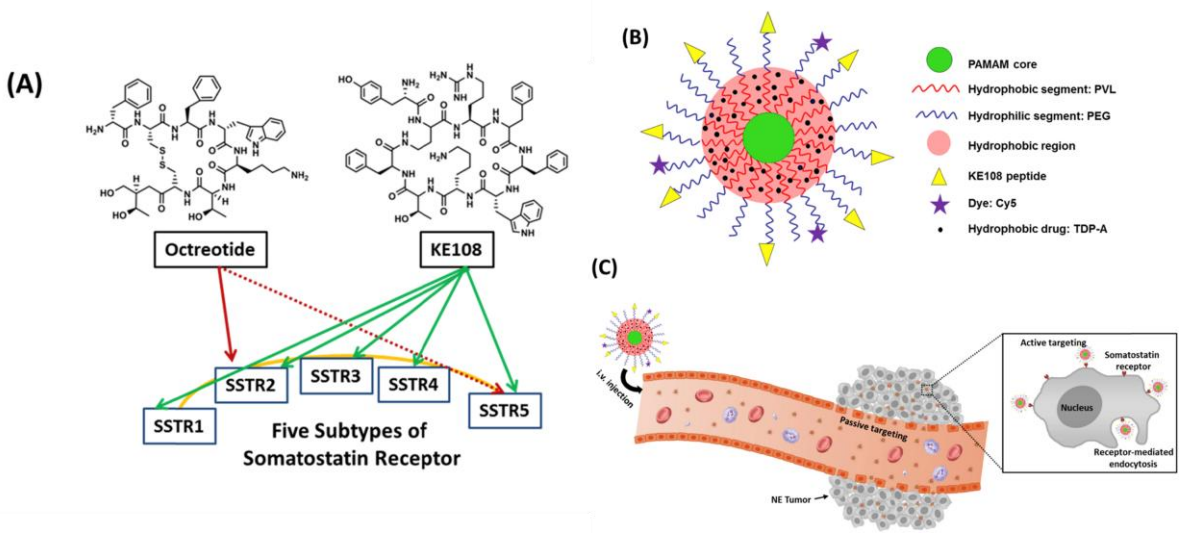

Figure 1.27. *Design of star shaped unimolecular micelle based on PAMAM core and PVL, PEG shell for targeted delivery oof HDAC inhibitor (Adapted from Chen, G. et al. Biomaterials* **2016**, *97*, 22-33*).*

Chen et al. reported the star shaped multifunctional multiarm unimolecular micelles for the delivery of HDAC inhibitors for neuroendocrine cancer therapy (see Figure 1.27). [178] In this study, unimolecular micelles were synthesized from amphiphilic block copolymer of poly (valerolactone) and polyethylene glycol on the poly(amidoamine) (PAMAM) dendritic core followed by conjugation with targeting agent KE108 peptide and Cy5 dye. These core-shell unimolecular micelles were encapsulated with hydrophobic drug thailandepsin-A (TDP-A), a HDAC inhibitor. TDP-A loaded targeted micelles demonstrated excellent anticancer efficacy and biocompatibility. Another example of unimolecular micelles for targeted chemotherapy and computed tomography (CT) imaging *in vivo* based on star shaped amphiphilic triblock copolymer and β-CD was reported by Lin et al, (see Figure 1.28). [179] In this investigation, 21-arm β-CD was used as used as macroinitiator for the ring opening of ε-caprolactone. This polymer was further functionalized at the end group for ATRP and subsequent ATRP polymerization using PAEMA and PPEGMA monomers produced star triblock copolymer β-CD-(PCL-PAEMA-PPEGMA). Theranostic nanomedicine was achieved doxorubicin loaded star block copolymers were further utilized for the fabrication of gold NP (Au NP) for chemotherapy and CT imaging as diagnostic tool. CT imaging using β-CD-(PCL-PAEMA-PPEGMA)/AuNPs/DOX unimolecular micelles demonstrated superior signal at tumor site compared to commercial contrast agent (omnipaque). In addition, excellent anticancer efficacy was achieved, and 87% suppression of tumor growth was observed compared to

control group suggesting better targeting ability and efficacy. A summary of unimolecular micellar nanocarriers utilized for Doxorubicin delivery *in vitro* and *in vivo* have been tabulated in Table 1.1. [180-194] Unfortunately, most of the unimolecular micelle's system are based on non-biodegradable polymers therefore they might impose severe side effects in long run. Also, their fate inside the body is still unknown therefore it is utmost important to develop unimolecular micelles based on biodegradable polymers.

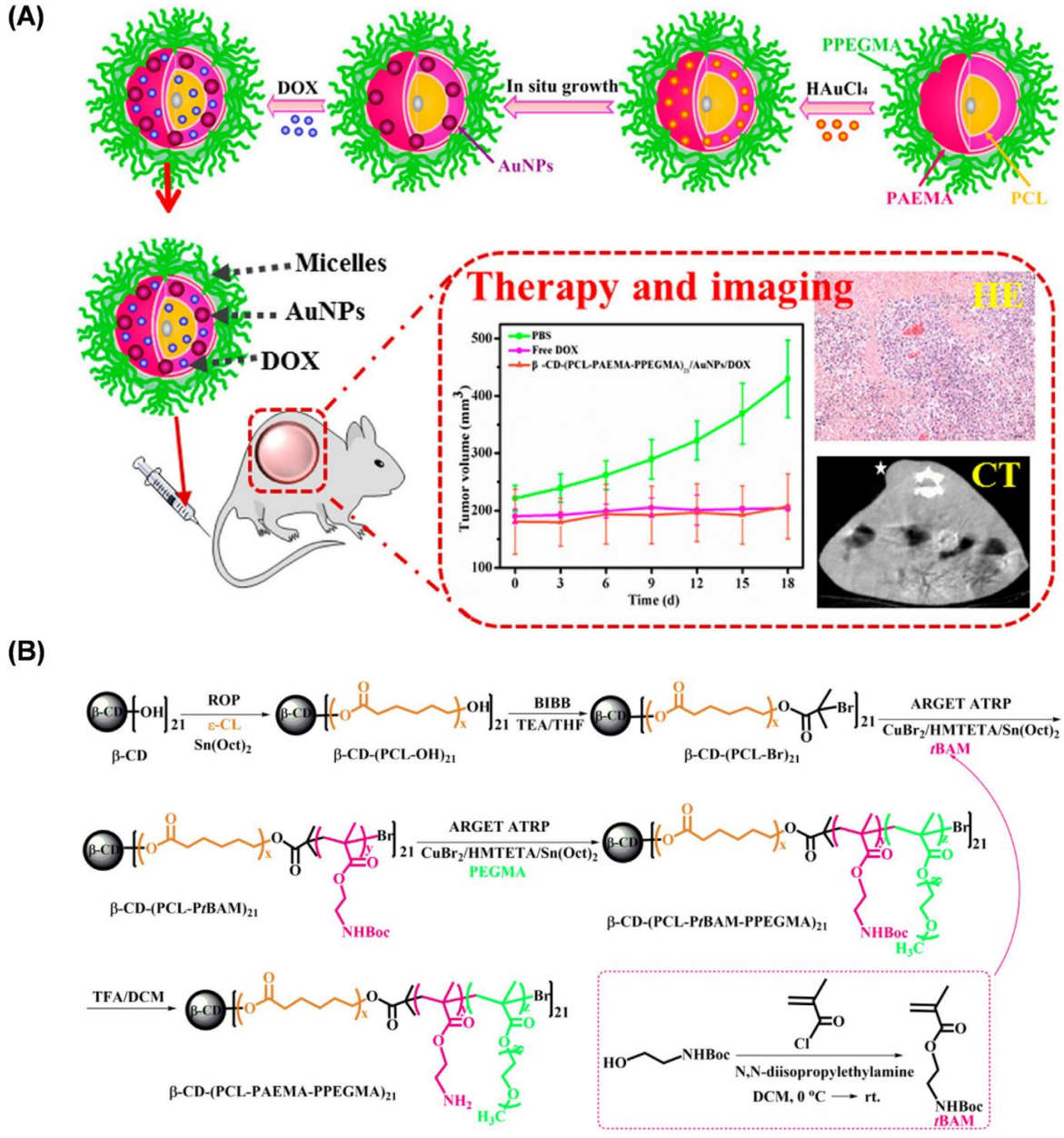

Figure 1.28. *Design of 21-arm β-CD based amphiphilic triblock copolymer for the anticancer delivery and CT imaging in vivo (Adapted from Lin et al. Biomacromolecules* **2017***, 18,* 3869–3880*).*

No.	Polymer System	Size (nm)	Cargo	DLC (wt.%)	Stimuli	Bio application	Refs
1	H40-PLA-PEG-Apt	20-37	Doxorubicin	10.4	pH (5.3)	CWR22Rv1 Tumor-Biodistribution-FL imaging	[180]
2	PMAM-PLA-*b*-PEG-TRC105	37	Doxorubicin	13.8	pH (5.3)	4T1 Tumor-PET imaging using 64Cu-labeled micelle	[181]
3	PHEMA-*g*-(PLLA-PEG)-TRC105	22-30	Doxorubicin	16.7	pH (5.3)	4T1 Tumor-PET imaging using 64Cu-labeled micelle	[169]
4	β-CD-(PLA-PDMAEMA-PEtOxMA)$_{21}$/AuNP	27-28	Doxorubicin	5.22 to 21.69	pH (5.0)	HepG2 Tumor-CT imaging and chemotherapy	[182]
5	β-CD-(PCL-PAEMA-PPEGMA)$_{21}$/AuNP	20-35	Doxorubicin	2.1 to 17.1	pH (5.0)	HepG2 Tumor-CT imaging and chemotherapy	[179]
6	PAMAM-*g*-PDMAE-MA-b-PSBMA	10-20	Doxorubicin	12.75± 1.75	pH and Temperature	CT26 Tumor-chemotherapy	[183]
7	PF$_{25}$-*g*-(PTyr-b-(POEGMA)$_2$	30	Doxorubicin	3.97 to 8.35	pH and Proteinase K	Bel-7402 Tumor-chemotherapy	[184]
8	P(OEGMA-*co*-DSMA-*co*-SBMA)-*b*-PTyr-*b*-P(OEGMA-*co*-DSDMA-*co*-SBMA)	51.55-139.3	Doxorubicin	14.9	GSH	Bel-7402 Tumor-chemotherapy	[185]
9	H40-PLA-*b*-MPEG/PEG-FA	10-20	Doxorubicin	11.6	pH (5.3)	In vitro delivery to 4T1 cells	[160]
10	POSS-(G$_3$-PLLA-b-PEO-COOH)$_8$	30	Doxorubicin	18.5± 2.3	pH 7.4-hydrolysis	Only In vitro release studies	[186]
11	H40-BPLP-PEG-cRGD	33±4	Doxorubicin	15.7	pH (5.3)	In vitro delivery to U87MG cells	[187]
12	CD-PCL-SS-PEG(PNIPAM)	110	Doxorubicin	9.1	GSH and Temperature	In vitro delivery to HepG2 cells	[188]
13	H40-star-PCL-a-PEG	20-23	Doxorubicin and Ketoprofen	20.3 and 13.7	pH	In vitro delivery to HeLa cells	[158]
14	β-CD-PDPA-POEGMA/ Cy5	17-21	Doxorubicin	31.1±2.1	pH 5.0	In vitro delivery to HeLa, MCF-7 and L929 cells	[189]
15	PAMAM-P(BEP-*co*-MP)-PBA	20	Doxorubicin	17.6	pH and Phosphodiesterase I	In vitro delivery to HepG2 cells	[190]
16	Ph-DPU-PEG	25-40	Doxorubicin	18.3	Ultrasound	In vitro delivery to HepG2 cells	[191]
17	DPU$_{Gly\text{-}SS}$-PEG	20-30	Doxorubicin	33.7	pH and GSH	In vitro delivery to HEpG2 and L02cells	[192]
18	Au-P(LA-DOX)-*b*-PEG-OH/FA	10-25	Doxorubicin conjugated	17	pH	In vitro delivery to 4T1 and NH-3T3 cells	[193]
19	DOX-DPU$_{TEA}$-PEG	39-55	Doxorubicin conjugated and Camptothecin loaded	13.8 and 29.6	pH	In vitro delivery to HepG2 cells	[194]

Table 1.1. *Summary of unimolecular micellar nanocarrier used for delivery of Doxorubicin.*

1.8 Biodegradable polymer

In the development of polymeric nanocarriers for drug delivery and biomedical applications, ample of examples are reported for non-degradable polymers, which are known to accumulate in the body (liver and spleen) causing systemic toxicities and induced immune responses.[10,68] This suggest the urgent necessity of such polymeric architectures which are capable of undergoing degradation inside or by the loving organism to avoid the non-specific side effects. Although the term biodegradable, bioabsorbable, bioeliminable, and bioerodible are used interchangeably for the system like polylactide or polylactic-co-polyglycolic acid; however, IUPAC defined the term “biodegradable” as the breakdown or degradation of

polymers by the cellular or in vivo biological actions.[195-196] The natural biodegradable materials such as plant fibers, wool fibers have been utilized 3000 years ago by ancient Egyptian, however from 1960 synthetic biodegradable polymers including the polyesters such as poly(glycolic acid) (PGA), poly(D,L-lactic acid) (PLA) and poly(lactic-*co*-glycolic acid) (PLGA) were developed and have been used in suture applications.[197] Owing to biocompatibility and degradability properties, biodegradable polymers have been emerged for drug delivery and other biomedical applications including tissue engineering. The biodegradable polymers can undergo degradation into non-toxic byproducts inside the body and can be completely eliminated from the system.[198] Biodegradable polymers can be naturally occurring polymers such as dextran, chitosan, hyaluronic acid, cellulose, alginate and synthetic polymers including poly (peptide), poly (esters), poly (ortho ester), poly(anhydrides), poly(phosphoesters), poly(ester amides), poly(alkyl cyanoacrylates), etc., as shown in the Figure 1.29.[196,199]

Naturally occurring biodegradable polymers derived from polysaccharides including chitosan, hyaluronic acid, dextran, cellulose, agarose, alginate, cyclodextrin, carrageenan and protein based polymers including albumin, gelatin, collagen have been widely explored in the biomedical applications.[200] Chitosan is most widely used lysosomal degradable polysaccharide with low degree of acetylation and take months for degradation and [201] Chitosan have been extensively used in oral drug delivery and other application of chitosan based materials includes wound healing and wound dressing due to antibacterial anti-inflammatory, and mucoadhesive properties.[202] Chitosan have been reported as gene delivery vector and also used as nanocarrier for pulmonary drug delivery. [203-204] However, chitosan is quite water insoluble, highly crystalline, takes several months to degrade in the biological system and sometime induce cytotoxicity hence application of chitosan is drug delivery is limited. Another important linear polysaccharide is Hyaluronic acid (HA) which is composed two distinct saccharide units including D-glucuronic acid having carboxylic acid and N-acetyl-D-glucosamine disaccharides having acetyl protected primary amine. [205] HA have been widely used tissue engineering and suture due to its biodegradable, biocompatible, non-immunogenic and non-toxic nature.[206] HA is negatively charged hydrophilic polymer at normal physiological pH (pKa 3-4) and used as water absorbable material due to expandable volume. The intrinsic targeting ability of HA for CD44 receptor has attracted HA for fabrication of drug delivery vehicles. [207-208]

Poly(esters):

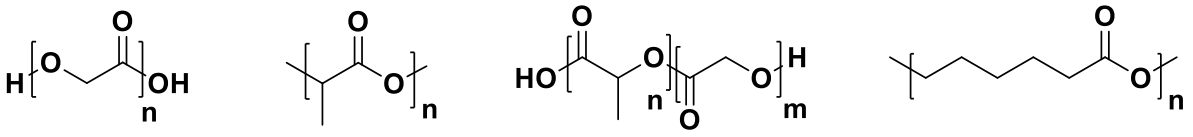

Poly(gycolic acid) PGA | Poly(lactic acid) PLA | Poly(lactic-co-glycolic acid) PLGA | Poly(caprolactone) PCL

Poly(ortho esters) (POE):

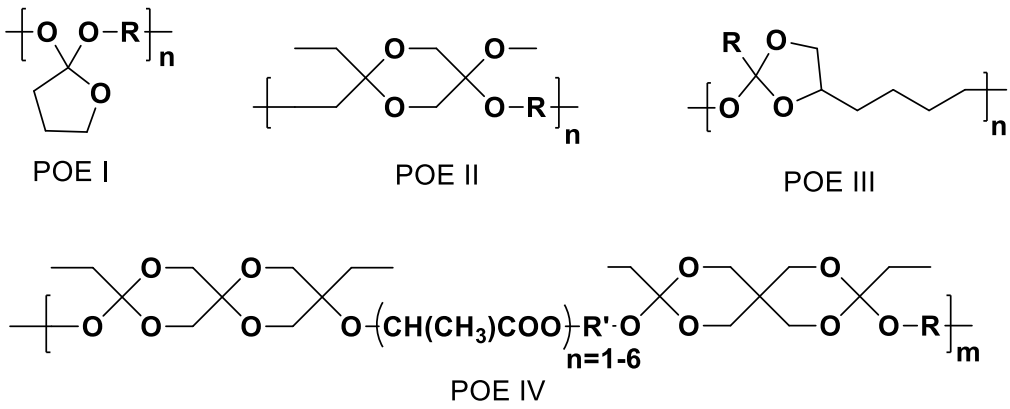

POE I | POE II | POE III | POE IV

Poly(anhydrides): **Poly(amides):** **Poly(ester amides):** **Poly(phosphoesters):**

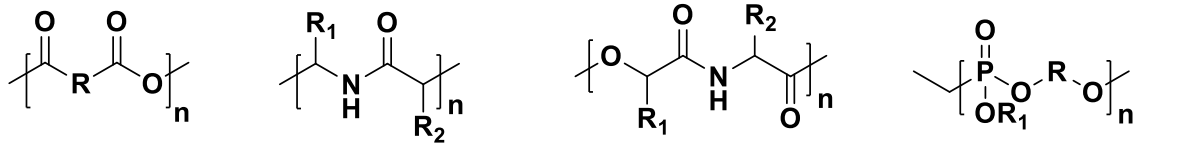

Poly(alkyl cynaoacrylates) (PACA): **Chitsoan:**

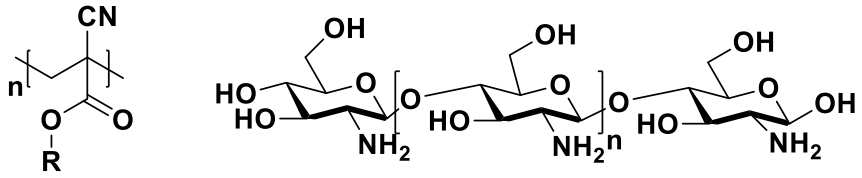

Hyaluronic acid (HA):

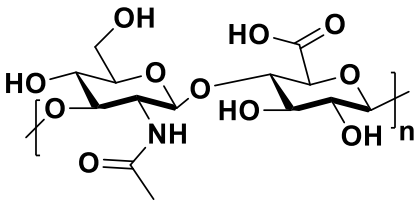

Figure 1.29. *Examples of biodegradable polymers (Adapted from Kamaly et al. Chem. Rev.* **2016***, 116,* 2602−2663*).*

Poly(ortho esters) (POE)s are synthetic polymers that have been developed since 1960 and widely used in the fabrication of suture materials.[209] POEs also have been explored for their use in drug and gene delivery vehicles mainly for delivering analgesics and nucleic acid.[210] Drug release mechanism in POEs mainly occur through diffusion and initiation of hydrolysis at outer matrix. However, their applications as drug delivery vehicles are greatly hampered due to highly hydrophobic backbone which hinder penetration of water molecules onto polymer matrix.[211-212] Nanoparticles formulation based on Poly(anhydrides) have been explored for intravenous or oral drug delivery applications. Degradation and drug release mechanism of Poly(anhydrides) are based on surface-erosion and solubility dependent.[213-215] Among poly (amides), polypeptide are the preferred choice for drug and gene delivery application owing to their non-immunogenicity and hydrolytic stability.[216] Poly(L-lysine) and poly(ɣ-glutamic acid) are most commonly explored polypeptide for biomedical application including gene delivery and drug delivery. [217-219] Cationic polypeptides typically preferred endosomal escape pathways; however, their use in *in vivo* application are limited due to unwanted systemic toxicity and sometime hemolytic behavior. [220] Poly(ester amides) are class of polymer composed of ester and amide linkages offering advantages of both components and have been widely explored biomedical applications. The hydrolysis of poly (ester amide) is slower process, but they degrade relatively faster by enzyme catalyzed reaction.[221] Poly(phosphoesters) often synthesized by ROP route, though condensation and addition polymerization can also be employed. Poly(phosphoesters) degrade into non-toxic byproducts therefore showed promising results in drug and gene delivery. In addition, resemblance of Poly(phosphoesters) with biopolymers facilitate their hydrolytic and enzymatic degradation into smaller units. [222-225]

An important class of synthetic polymers is aliphatic polyester having backbone composed of ester linkage facilitate hydrolytic as well as enzymatic degradation into non-toxic by products. Aliphatic polyesters have been widely explored in biomedical application including drug, gene delivery, tissue engineering , suture/ surgery, resorbable materials etc.; owing to their biocompatibility, non-toxicity, non-immunogenicity.[226-229] Among the aliphatic polyester, Poly(L-lactide) (PLA), poly(L-glycolide) (PGA), poly(L-lactide-*co*-glycolide)s (PLGA) and polycaprolactones (Poly(ε-caprolactone or PCL) systems are most frequently studied and utilized in biomedical applications and thermoplastic fabrication. Another commonly used polyester system for biomedical application is poly (caprolactone) (PCL). [180] Typically PCL is synthesized using ring opening polymerization of ε-caprolactone monomer

in various molecular weights and architectures. PCL is crystalline, hydrophobic material having very low glass transition temperature (-60 ºC) and exist as semirigid material at room temperature. PCL systems have been of great interest due to synthetic ease, versatility and combination of different properties mechanical stability, high miscibility with a range of other polymers, and biocompatibility. [230-232, 180] PCL show very slow degradation kinetics under physiological condition of around 2-3 years due to limited penetration of water molecules on the surface matrix owing to its high hydrophobicity and crystallinity.[233] Overview for comparative degradation of biodegradable systems is given in Figure 1.30. [234] The slower rate of degradation have been found to be one of the major hurdles for the drug delivery application of PLC based systems. Consequently, PCL based system have been explored much more in the field of tissue engineering as scaffold matrix material than as drug carriers.[186] to overcome the limitation of slower degradation kinetics, many groups including ours have been developing various functionalized polycaprolactone monomers including hydroxyl, carboxyl, ketone, azide, propargyl, cholesteryl, and so on (see Figure 1.31).[235-246] Our group have contributed to the field of functional polycaprolactone. The carboxylic-substituted caprolactone (entry M15 in Figure 1.31) was synthesized by Bapurao et al in 2013 which had opened up new avenue for drug delivery and antimicrobial applications and have been utilized widely for designing numerous block and random copolymers having several architectures. This carboxylic substituted monomer was used for pos-functionalization, drug conjugation and various other stimuli-responsive drug delivery applications. [247]

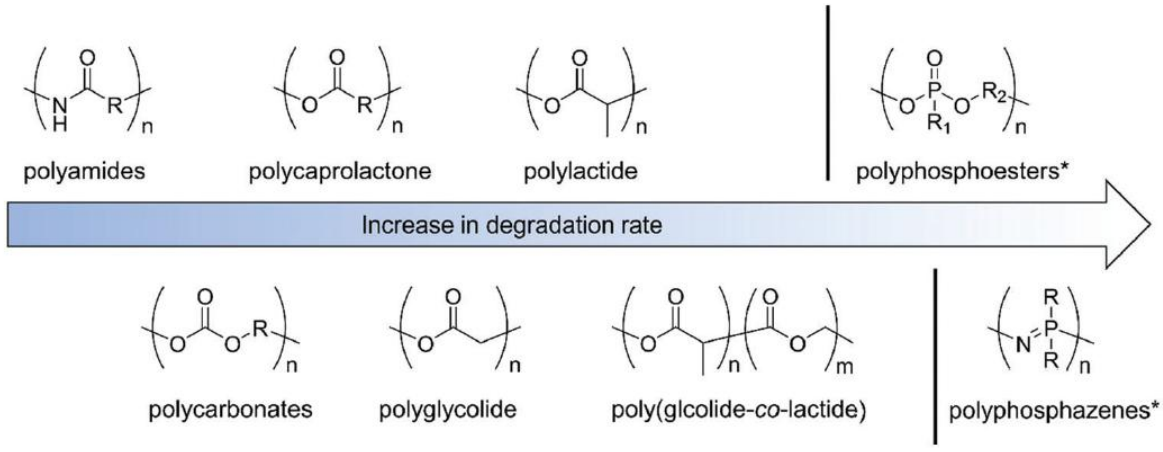

Figure 1.30. *Comparative degradation rates of biodegradable polymers (Adapted from Becker, G. et al. Chem. Soc. Rev.* **2018***, 47, 7739−7782).*

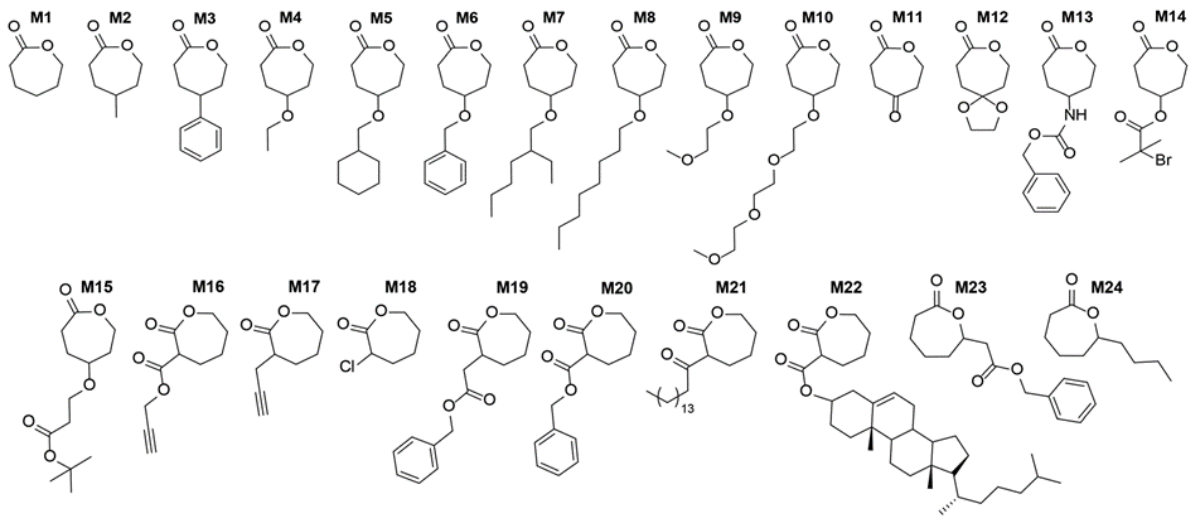

Figure 1.31. *Structures of different functionalized caprolactone monomers (Adapted from Rainbolt et al. Polym. Chem.* ***2015****, 6, 2369-2381).*

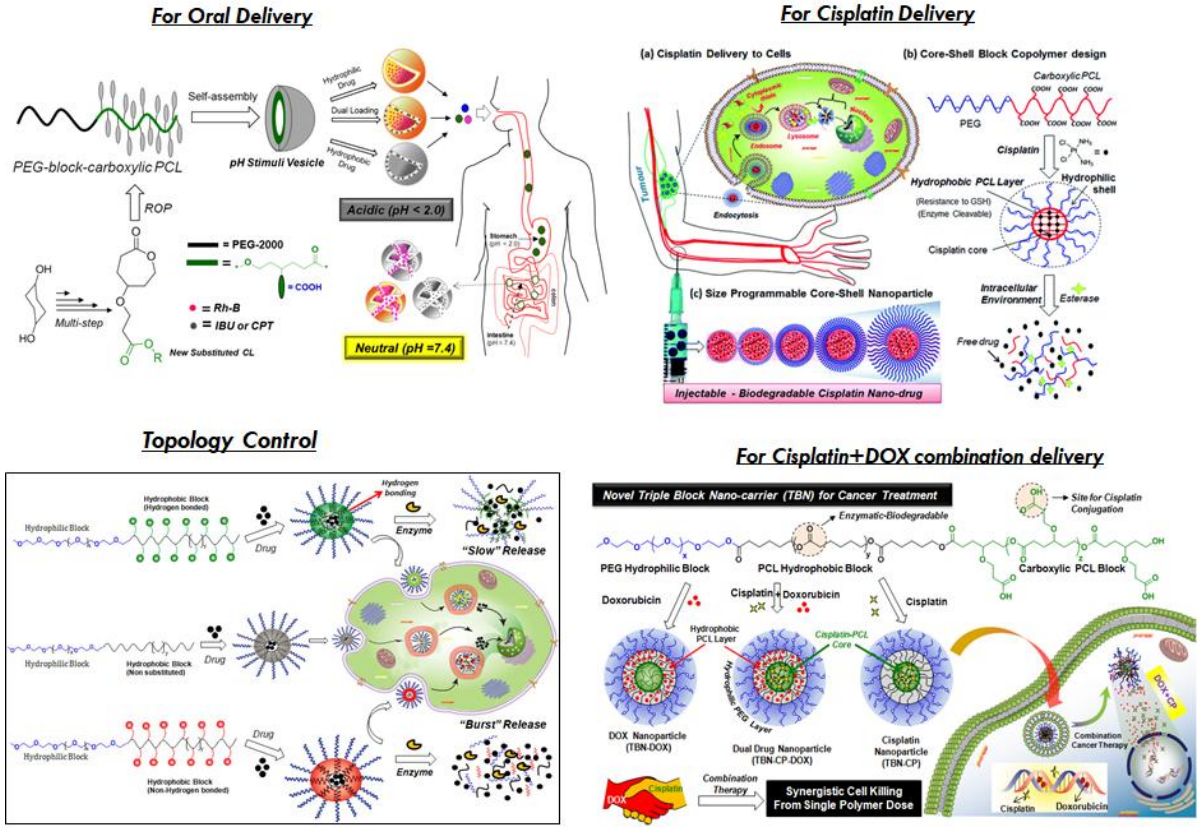

Figure 1.32. *Pictorial representation of work carried out using carboxylic-substituted monomer from our group in the field of drug delivery.*

Our group have made systemic efforts in recent years in the field of drug delivery and antimicrobial delivery to develop and design new PCL based macromolecules nano assemblies for efficient intracellular enzymatic biodegradation and release of drug to enhance efficacy of therapeutics. ROP of novel carboxylic substituted caprolactone monomer using PEG as initiator followed by deprotection of tButyl deprotection yielded carboxylic acid functionalized di and triblock copolymers. These polymers were self-assembled into pH -responsive nanovesicles and encapsulated with analgesic ibuprofen and anticancer drug Camptothecin (CPT) and demonstrated efficient oral drug delivery under gastrointestinal tract (GI) conditions.[247] Further effort were taken to chemically conjugate the Cisplatin (CP) drug to the carboxylic acid functional handles of di and triblock PLC polymers. These Pt-prodrug exhibited excellent stability under extracellular conditions and completely avoided GSH detoxification rendering efficient intracellular delivery of cisplatin to the breast cancer cells (see Figure 1.32).[248] In addition, synergistic therapy for the breast cancer was achieved by the combination of two antagonistic against doxorubicin and cisplatin using single carboxylic PCL based system.[249] These studies comprehended further deep insight about the delivery capability of PCL block copolymers for hydrophilic and hydrophobic drugs and intracellular degradation mechanistic aspects. Next generational, PCL block copolymers conjugated with fluorescent π-conjugated chromophores have been developed as nanoprobe for bioimaging application to understand cellular uptake.[250-251] Additionally FRET probes based on a π-conjugated chromophore (donor) were designed on PCL backbone and encapsulated with Nile red (acceptor) exploiting FRET phenomenon for understanding the mechanism of intracellular release assisted by bioimaging.[252] Recently polycaprolactone was post-functionalized with cationic moieties and have been explored for antimicrobial activity against *E. coli* bacteria (see Figure 1.33).[253]

To enhance the degradation and water solubility of non-functionalized PCL, PEGylation is often elected as strategy to make the whole structure amphiphilic. However, recent studies have found that PEG is not ideal choice for gaining hydrophilicity, though it is biocompatible, but it can still accumulate in the body because biodegradation mechanism of PEG are still unknown.[254-256] Therefore fully biodegradable system need to be developed and investigated in the *in vitro* and *in vivo*. Hence, the engineering of new class of polycaprolactone based macromolecules for drug delivery application is utmost necessary for long run. Therefor our group has focused on the development of fully PCL based systems. For examples, ROP of ε-caprolactone and carboxyl-substituted monomer was carried out to design fully PCL based

block and random copolymer. This PCL based block and random copolymers exhibited excellent drug loading capabilities of Doxorubicin and demonstrated efficient delivery, enzymatic biodegradation into cancer cells (see Figure 1.34).[257] Later effort was taken to understand the mechanisms of bacterial membrane breaching by polymer. For this purpose, our group has synthesized AIE-conjugated (donor) fully PCL based antimicrobial polymers and using FRET between acceptor crystal violet, mechanism of cell-membrane breaching and disruption was fully understood. [258]

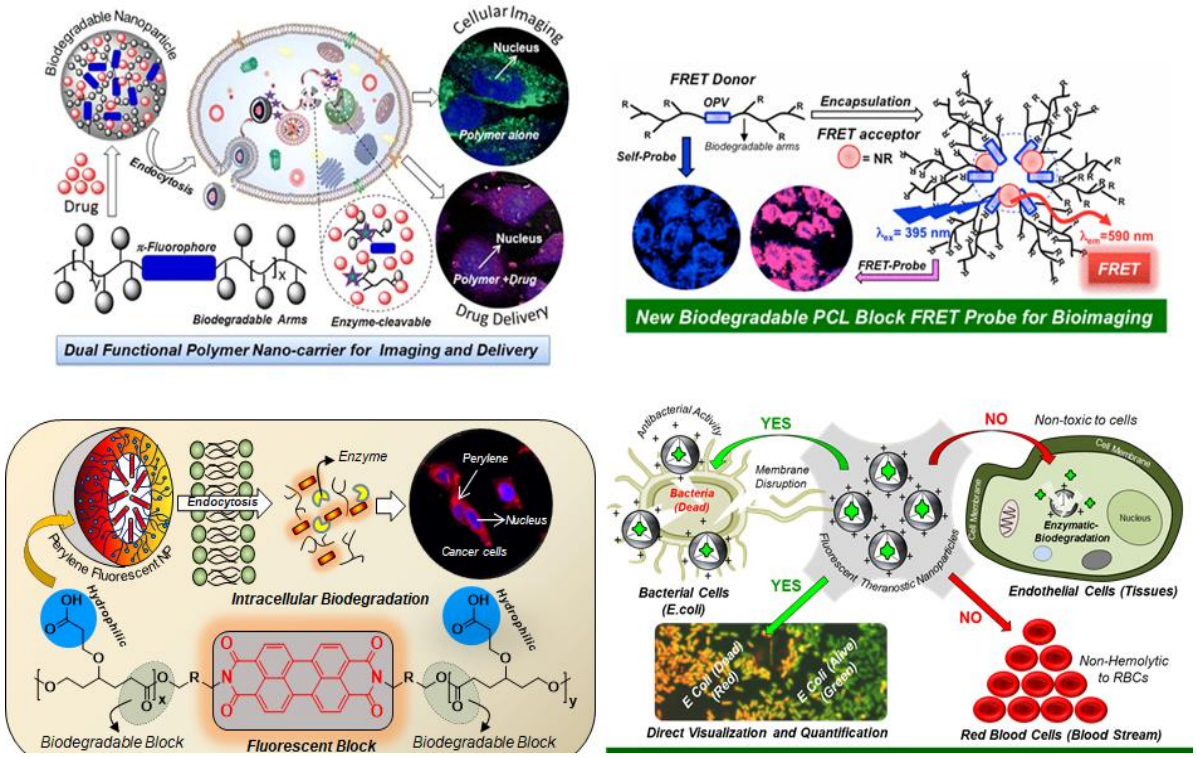

Figure 1.33. *Pictorial representation of work carried out using carboxylic-substituted monomer from our group in the field of bioimaging and antimicrobial activity.*

All these investigations led our group to comprehend depth about drug delivery using PCL based system *in vitro*. However, for successful delivery of drug *in vivo* is challenging task. These checkpoints need to be understood before designing the nanocarriers for *in vivo* drug delivery including stability of nanocarriers, design, toxicity, blood, circulation time, toxicity profiles, immunogenicity, targeting ability etc. It is well known fact in the literature that aggregated micelles often dissociate under dilution leading to premature release of drug form nanocarriers. In addition to that, enormous stress from the renal pump and cardiac pump also cause instability in the aggregated micellar nanocarriers. To overcome the first challenge of

nanocarriers stability under blood circulation, our group had made effort to synthesize one of the first unimolecular micellar nanocarrier fully based on PCL system.[259] Optimization of correct geometry through scanning of varying arm based star block copolymer lead the discovery of six-arm star block copolymer composed of fully PCL. These polymers were self-assembled into tiny unimolecular micelles of ~15 nm and depicted excellent drug loading capacity of 14wt% for doxorubicin. Preliminary in vitro investigation depicted extracellular stability of unimolecular micelles and demonstrated efficient drug delivery platform compared to aggregated analogues. Further effort have been made to investigate the blood-brain barrier breaching using the near infrared fluorescent dye labeled unimolecular micelles.[260] Successful delivery of unimolecular micelles across the blood brain was demonstrated by *in vivo* studies using appropriate mice model. Furthermore, in the star shape polymer was post-functionalized to understand selective breaching of prokaryotic and eukaryotic membrane (see Figure 1.35).[261]

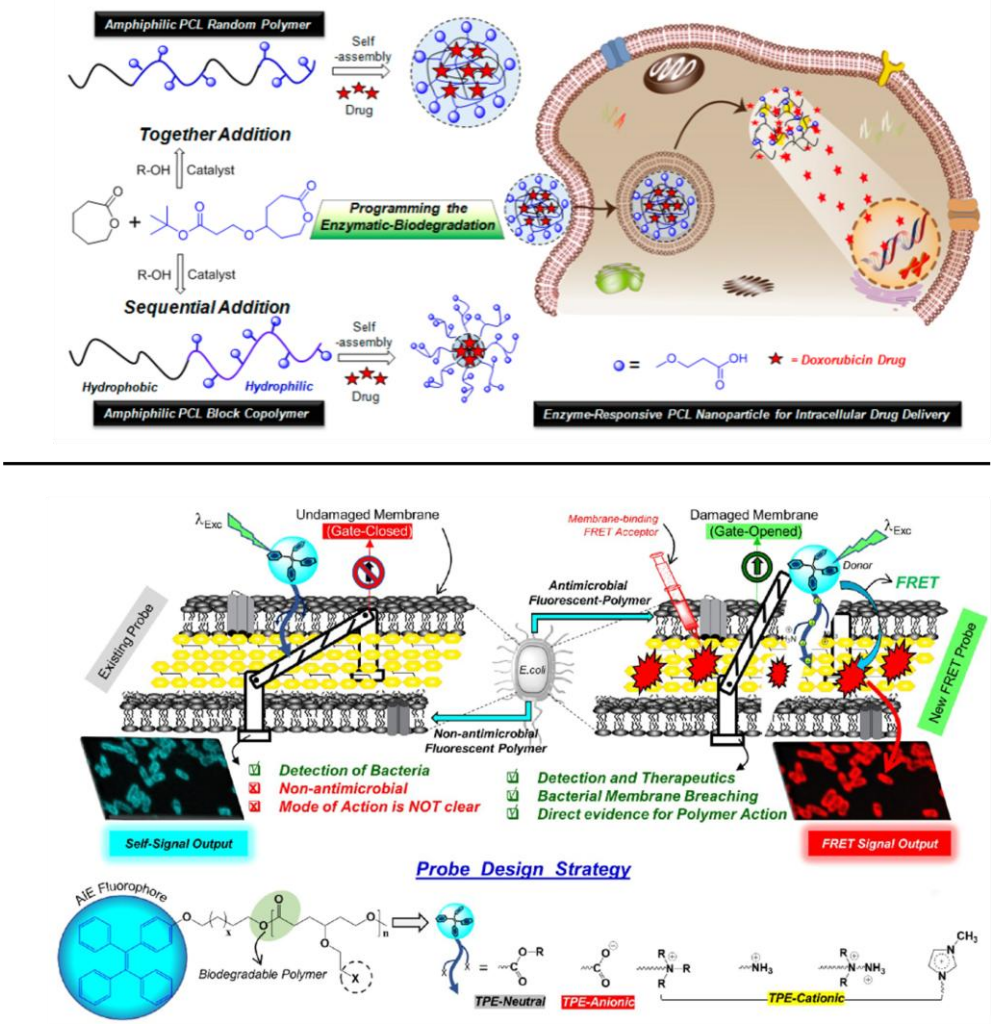

Figure 1.34. *Pictorial representation of work carried out using fully PCL based system for drug delivery and antimicrobial applications from our group.*

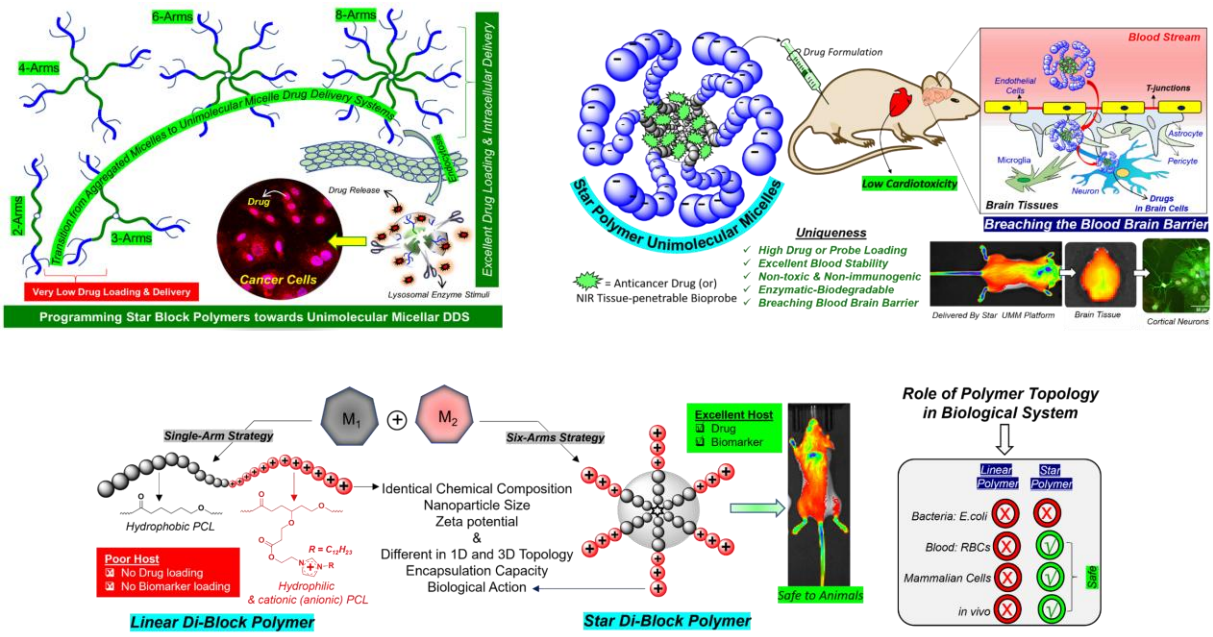

Figure 1.35. *Pictorial representation recent development of star shaped PCL based block copolymers from our group for brain specific drug delivery and antimicrobial applications.*

1.9 Aim of the Thesis

Aforementioned detailed literature review clearly depicted the effectiveness of nanoparticles in the drug delivery application. Unfortunately, drug delivery using of non-biodegradable system has major limitation systemic toxicity and prolong accumulation leading to induced immune responses. Moreover, release mechanisms and clearance of non-biodegradable polymeric system from the body are still questionable. To address this biodegradable of biocompatible system have been emerging. However biodegradable based systems including PCL need further detail investigation for their behavior towards *in vivo* drug delivery. We chose polycaprolactone (hydrophobic) and substituted polycaprolactone (hydrophilic) based on our lab expertise, to understand pharmacokinetics, biodistribution, and tumor targeting and antitumor therapy. Rationale of our study was to comprehend the role of unimolecular micelles in tumor delivery and blood brain barrier breaching with systematic *in vitro* and *in vivo* investigation. Next we utilized self-immolative polymer based on poly (amino ester) (PAE) system for drug delivery which was impossible before due to uncontrolled auto-degradation of PAEs at physiological pH. The self-immolative polymers are class of the polymers which undergo auto-degradation into small molecules or oligomers via cascade reactions upon application of specific stimuli. We developed zwitterionic polymers using electrostatic strategy to solve this limitation of PAE by combining it with carboxylic PCL system and demonstrated their application tumor drug delivery in xenograft model. Figure 1.36 represent the entire thesis work.

The thesis work has been further divided into four working chapters and brief comprehension have been explained below.

1. In **chapter 2**, a series of fully biodegradable star shaped (6-arm) block copolymers have been synthesized using ROP ε-caprolactone and carboxylic functional monomers. Amphiphilicity was varied to produced star shaped aggregated and unimolecular micellar NP. Detailed investigation of drug loading capabilities for doxorubicin and in vitro degradation along with comparative efficacy of aggregated and unimolecular micelles was carried out in multiple cancer cell lines. Further tumor penetration and accumulation ability was investigated using near infrared fluorescence (NIRF) imaging and tumor growth efficiency of DOX loaded unimolecular micelles was investigated in pancreatic cancer xenograft model.
2. **Chapter 3** highlights the engineering of star-shaped PCL based architectures utilizing ring opening polymerization and post-functionalization into anionic, cationic and

neutral surface charge in a sequential manner. Detailed self-assembly investigation demonstrated formation of aggregated and unimolecular micelles based on appropriate molecular weight and surface chemistry. We thoroughly investigated the influence of surface charge and size of nanocarrier in the blood-brain barrier using NIRF imaging in mice model.

3. In **chapter 4**, The new class of zwitterionic polymers to stabilize the unstable self-immolative PAE polymer at physiological pH 7.4 using carboxylic PCL. We introduced elegant electrostatic strategy for stabilization of PAE and on-demand degradation by enzymatic action followed by self-immolation render complete degradation of polymers at intracellular level. This linear zwitterion di and triblock polymer systems were investigated for *in vitro* and *in vivo* stability delivery capabilities. NIRF imaging demonstrated prolong blood circulation for more than 72h.
4. In **chapter 5**, the impact of architectures and topology on the drug loading capabilities of zwitterionic systems was investigated. For this purpose, star shaped triblock and random copolymers were synthesized and their doxorubicin delivery aspects were thoroughly investigated in pancreatic cancer xenograft mouse model. All the polymers were thoroughly investigated enzymatic biodegradation aspects using *in vitro* live cell model and cellular internalization was investigated using confocal microscopy techniques.

Finally, the entire work was summarized and objectives for the future research have been emphasized in the last section.

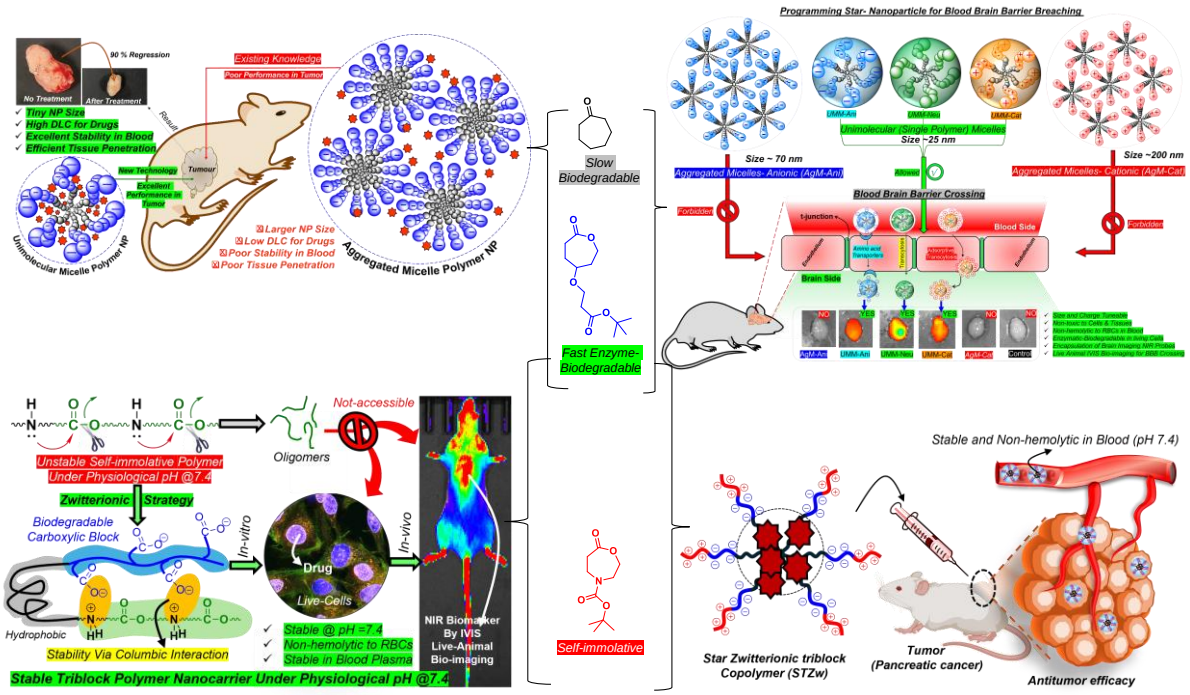

Figure 1.36. *Pictorial representation of the consolidated thesis work.*

1.10 References

1) Bray, F.; Laversanne, M.; Sung, H.; Ferlay, J.; M. E.; Siegel, R. L.; Soerjomatram, I. Jemal, A. Global Cancer Statistics 2022: GLOBOCAN Estimates of Incidence and Mortality Worldwide for 36 Cancer in 185 Countries. *CA. Cancer J Clin.* **2024***, 74,* 229-263.
2) Brown, J. S.; Amend. S. R.; Austin, R. H.; Gatenby, R. A.; Hammarlund, E. U.; Pienta, K. J. Updating the Definition of Cancer. *Mol. Cancer Res.* **2023**, *21*, 1142-1147.
3) Hassanpour, S. H.; Dehghani, M. Review of Cancer From Perspective of Molecular. *J. Cancer Res. Practice* **2017**, *4*, 127-129.
4) Falzone, L.; Salomone, S.; Libra, M. Evolution of Cancer Pharmacological Treatments at the Turn of the Third Millennium. *Front. Pharmacol.* **2018**, *9*, 1-26.
5) Persidis, A. Cancer Multidrug Resistance. *Nat. Biotechnol.* **1999**, *17*, 94-95.
6) Gottesman, M. M.; Fojo, T.; Bates, S. Multidrug Resistance in Cancer: Role of ATP-Dependent Transporter. *Nat. Rev. Cancer* **2002**, *2*, 48-58.
7) Ambudkar, S. V. et al. Biochemical, Cellular, and Pharmacological Aspects of the Multidrug Transporter. *Annu. Rev. Pharmacol. Toxicol.* 1999, **39**, 361–398.
8) Lowe, S. W.; Ruley, H. E.; Jacks, T.; Housman, D. E. p53-Dependent Apoptosis Modulates the Cytotoxicity of Anticancer Agents. *Cell* 1993, **74**, 957–967.
9) Thapa, R. K.; Kim, O. J. Nanomedicine-Based Commercial Formulations: Current Development and Future Aspects. *J. Pharm. Investig.* **2023**, *53*, 19-33.
10) Sun, T.; Zhang, Y. S.; Pang, B.; Hyun, D. C.; Yang, M.; Xia, Y. Engineered Nanoparticles for Drug Delivery in Cancer Therapy. *Angew. Chemie - Int. Ed.* **2014**, *53*, 12320–12364.
11) Meel, R. V. D.; Sulheim, E.; Shi, Y.; Keissling, F.; Mulder, W. J. M. Lammers, T. Smart Cancer Nanomedicine. *Nat. Nanotechnol.* **2014**, *14*, 1007-1017.
12) Rosen, H.; Abribat, T. The rise and rise of drug delivery. *Nat. Rev. Drug Discov*. **2005**,*4*, 381–385.
13) Anselmo, A. C.; Mitragotri, S. Nanoparticles in the Clinic: An Update. *Bioeng. Trans. Med.* **2019**, *4*, e10143.
14) Manzari, M.T.; Shamay, Y.; Kiguchi, H.; Rosen, N.; Scaltriti, M.; Heller, D. A. Targeted Drug Delivery Strategies for Precision Medicines. *Nat Rev Mater* **2021**, *6*, 351–370.
15) Mitchell, M.J.; Billingsley, M.M.; Haley, R.M.; Wechsler, M. E.; Peppas, N. A; Langer, R. Engineering Precision Nanoparticles for Drug Delivery. *Nat Rev Drug Discov* **2021**, *20*, 101–124.
16) Duan, Y.; Dhar, A.; Patel, C.; Khimani, M.; Neogi, S.; Sharma, P.; Siva Kumar, N.; Vekariya, R. K. A Brief Review on Solid Lipid Nanoparticles: Part and Parcel of Contemporary Drug Delivery Systems ***RSC Adv.*** **2020**, ***10***, 26777-26791.
17) Mehta, M.; Bui, T. A.; Yang, X.; Askoy, Y.; Goldys, E. M.; Deng, W. Lipid-Based Nanoparticles for Drug/Gene Delivery: An Overview of the Production Techniques and Difficulties Encountered in Their Industrial Development. *ACS Mater. Au* **2023**, *3*, 600−619.
18) Barenholz, Y. Doxil-The First FDA-Approved Nano-Drug: Lessons Learned. *J. Control. Release* **2012**, *160*, 117-134.

19) Gao, A.; Hu, Xl.; Saeed, M.; Chen, B-F.; Li, Y-P.; Yu, H-J. Overview of Recent Advances in Liposomal Nanoparticle-Based Cancer Immunotherapy. *Acta Pharmacol Sin* **2019**, *40*, 1129–1137.
20) Davis, M. E.; Chen, Z.; Shin, D. M. Nanoparticle Therapeutics: An Emerging Treatment Modality for Cancer. *Nat. Rev. Drug Discov.* **2008**, *7*, 771–782.
21) Huang, H.; Feng, Chen, W.; Shi, J. Inorganic Nanoparticles in Clinical Trials and Translations. Nano Today 2020, 35, 100972.
22) Havel, H. A. What are the Nanodrug? An Industry Perspective on Development of Drug Products Containing Nanomaterials. *AAPS J*. **2016**, *18*, 1351-1353.
23) Liu, Y.; Zhang, N. Gadolinium Loaded Nanoparticles in Theranostic Magnetic Resonance Imaging. *Biomaterials* **2012**, *33*, 5363-5375.
24) Zhang, M. Q.; Sun, C.; Lee, J. S. H. Magnetic Nanoparticles in MR Imaging and Drug Delivery. *Adv Powder technol.* **2006**, *17*, 1-28.
25) Yang, W.; Liang, H.; Ma, S.; Wang, D.; Huang, J. Gold Nanoparticle based Photothermal Therapy: Development and Application for Effective Cancer Treatment. *Sustain. Mater. Technol.* **2019**, *22*, e00109.
26) Wagner, A. M.; Knipe, J. M.; Orive, G.; Peppas, N. A. Quantum Dots in Biomedical Applications. *Acta Biomater.* **2019**, *94*, 44–63.
27) Zhang, Y.; Meng, S.; Ding, J.; Peng, Q.; Yu, Y. Transition Metal-Coordinated Graphitic Carbon Nitride Dots as a Sensitive and Facile Fluorescent Probe for β-Amyloid Peptide Detection. *Analyst* **2019**, *144*, 504–511.
28) Andrade, S.; Ramalho, M. J.; Loureiro, J. A. Polymeric Nanoparticles for Biomedical Applications. *Polymers* **2024**, *16*, 249.
29) Ulbrich, K.; Holá, K.; Šubr, V.; Bakandritsos, A.; Tuček, J.; Zbořil, R. Targeted Drug Delivery with Polymers and Magnetic Nanoparticles: Covalent and Noncovalent Approaches, Release Control, and Clinical Studies. *Chem. Rev.* **2016**, *116*, 5338– 543.
30) Begines, B.; Ortiz, T.; Aranda, M.; Martínez, G.; Merinero, M.; Arias, F.; Alcudia, A. Polymeric Nanoparticles for Drug Delivery: Recent Developments and Future Prospects. Nanomaterials 2020, 10, 1403.
31) Bjaradwaj, H.; Jangde, R. K. Current Updated Review on Preparation of Polymeric Nanoparticles for Drug Delivery and Biomedical Applications. *Next Nanotechnol.* **2023**, *2*, 100013.
32) Beach, M. A.; Nayanthara, U.; Gao, Y.; Zhang, C.; Xiong, Y.; Wang, Y.; Such, G. K. Polymeric Nanoparticles for Drug Delivery. *Chem. Rev.* **2024**, *124*, 5505-5616.
33) Tong, X.; Pan, W.; Su, T.; Zhang, M.; Dong, W.; Qi, X. Recent Advances in Natural Polymer-Based Drug Delivery Systems. *React. Funct. Polym.* **2020**, *148*, 104501.
34) Kricheldorf, H. R. Polypeptides and 100 Years of Chemistry of α-Amino Acid N-Carboxyanhydrides. *Angew. Chem., Int. Ed.* **2006**, *45*, 5752−5784.
35) Liu, C.; Hong, C.-Y.; Pan, C.-Y. Polymerization Techniques in Polymerization-Induced Self-Assembly (PISA). *Polym. Chem.* **2020**, *11*, 3673−3689.
36) Bagheri, A.; Fellows, C. M.; Boyer, C. Reversible Deactivation Radical Polymerization: From Polymer Network Synthesis to 3D Printing. *Adv. Sci.* **2021**, *8*, 2003701.

37) Sung, Y. K.; Kim, S. W. Recent Advances in Polymeric Drug Delivery Systems. *Biomater. Res.* **2020**, *24*, 12.

38) Rao, J. P.; Geckeler, K. E. Polymeric Nanoparticles: Preparation Techniques and Size-Control Parameters. *Prog. Polym. Sci.* **2011**, *36*, 887-913.

39) Grabnar, P. A.; Kristl, J. The manufacturing Techniques of Drug Loaded Polymeric Nanoparticles from Preformed Polymers. *J. Microencapsulation* **2011**, *28*, 323-335.

40) Chan, J. M.; Valencia, P. M.; Zhang, L.; Langer, R.; Farokhzad, O. C. Polymeric Nanoparticles for Drug Delivery.

41) Mai, Y.; Eisenberg, A. Self-Assembly of Block Copolymers. *Chem. Soc. Rev.* **2012***, 41,* 5969-5985.

42) De, R.; Mahata, M. K.; Kim, K-T. Structure-Based Varieties of Polymeric Nanocarriers and Influences of Their Physicochemical Properties on Drug Delivery Profiles. *Adv. Sci.* **2022**, *9*, 2105373.

43) Ekladious, I.; Colson, Y. L.; Grinstaff, M. W. Polymer-Drug Conjugate Therapeutics: Advances, Insights and Prospects. *Nat. Rev. Drug Discov.* **2019**, *18*, 273-294.

44) Vargason, A. M.; Anselmo, A. C.; Mitragotri, S. The Evolution of Commercial Drug Delivery Technologies. *Nat. Biomed. Eng* **2021**, *5*, 951– 967.

45) Mollé, L. M.; Smyth, C. H.; Yuen, D.; Johnston, A. P. Nanoparticles for Vaccine and Gene Therapy: Overcoming the Barriers to Nucleic Acid Delivery. *Wiley Interdiscip. Rev.: Nanomed. Nanobiotechnol.* **2022**, *14*, e1809.

46) Liu, J.; Li, M.; Luo, Z.; Dai, L.; Guo, X.; Cai, K. Design of Nanocarriers based on Complex Biological Barriers In Vivo for Tumor Therapy. *Nano Today* **2017**, *15*, 56-90.

47) Longmire, M.; Choyke, P. L.; Kobayashi, H. Clearance Properties of Nano-Sized Particles and Molecules as Imaging Agents: Considerations and Caveats. *Nanomedicine* **2008**, *3*, 703-717.

48) Davis, M. E.; Chen, Z.; Shin, D. M. Nanoparticle Therapeutics: An Emerging Modality for Cancer. *Nat. Rev. Drug. Discov.* **2008**, *7*, 771-782.

49) Liang, X.; Wang, H.; Zhu, Y.; Cogger, V. C.; Liu, X.; Xu, Z. P.; Grice, J. E.; Roberts, M. S. Short-and Long-Term Tracking of Anionic Ultrasmall Nanoparticles in Kidney. *ACS Nano* **2016**, *10*, 387-395.

50) Koboyashi, H.; Brenchbiel, M. W. Nano-Size MRI Contrast Agents with Dendrimer Cores. *Adv. Drug Deliv. Rev.* **2005**, *57*, 2271-2286.

51) Tenzer, S.; Docter, D.; Kuharev, J.; Musyanovych, A.; Fetz, V.; Hecht, R.; Schlenk , F.; Fischer, D.; Kiouptsi, K.; Reinhardt C. Rapid Formation of Plasma Protein Corona Critically Affects Nanoparticle Pathophysiology. *Nat. Nanotechnol*. **2013**, *8*, 772-781.

52) Owens III, D. E.; Peppas, N. A. Opsonization, Biodistribution, and Pharmacokinetics of Polymeric Nanoparticles. *Int. J. Pharm.* **2006**, *307*, 93-102.

53) Sahay, G. Alakhova, D.Y. Kabanov, A.V. Endocytosis of nanomedicines. *J. Control. Release* **2010**, *145*, 182-195.

54) Arvizo, R. R.; Miranda, O. R.; et al. Modulating Pharmacokinetics, Tumor Uptake and Biodistribution by Engineered Nanoparticles. *PLoS One* **2011**, *6*, e24374.

55) Harris, J. M.; Chess, R. B. Effect of Pegylation on Pharmaceuticals. *Nat. Rev. Drug Discov.* **2003**, *2*, 214-221.
56) Denison, T. A.; Bae, Y. H. Tumor Heterogeneity and its Implication for Drug Delivery. *J. Control. Release* **2012**, *164*, 187-191.
57) Petros, R. A.; DeSimone, J. M. Strategies in the Design of Nanoparticles for Therapeutic Applications. *Nat. Rev. Drug Discov.* **2010**, *9*, 615-627.
58) Foroozandah, P. Aziz, A. A. Insight into Cellular Uptake and Intracellular Trafficking of Nanoparticles. *Nanoscale Res. Lett.* **2018**, *13*, 339.
59) Behzadi, S. et al. Cellular Uptake of Nanoparticles: Journey of Inside of the cells. *Chem. Soc. Rev.* **2017**, *46*, 4218-4244.
60) Trimble, W. S.; Grinstein, S. Barriers to the Free Diffusion of Proteins and Lipid in the Plasma. *J. Cell Bio.* **2015**, *208*, 259-271.
61) Kolhar, P.; Anselmo, A. C.; Gupta, V.; Pant, K.; Prabhakarpandian, B.; Ruoslahti, E.; Mitragotri, S. Using Shape Effects to Target Antibody-Coated Nanoparticles to Lung and Brain Endothelium. *Proc. Natl. Acad. Sci. U. S. A.* **2013**, *110*, 10753–10758.
62) Ghezzi, M.; Pescina, S.; Paudela, C.; Santi, P.; Favero, E. D.; Cantu, L.; Nicoli, S. Polymeric Micelles in Drug Delivery: An Insight of the Techniques for their Characterization and Assessment in Biorelevant Conditions. *J. Control. Release* **2021**, *332*, 312-336.
63) Hoshyar, N.; Gray, S.; Han, H.; Bao, G. The Effect of Nanoparticles Size In Vivo Pharmacokinetics and Cellular Internalization. *Nanomedicine* **2016**, *11*, 673-692.
64) Choi, H. S.; Liu, W.; Misra, P.; Tanaka, E.; Zimmer, J. P.; Ipe, B. I.; Bawendi, M. G.; Frangioni, J. V.; Renal Clearnace of Quantum Dots. *Nat. Biotechnol.* **2007**, *25*, 1165-1170.
65) Zhao, F.; Zhao, Y.; Liu, Y.; Chang X.; and Chen, C. Cellular Uptake, Intracellular Trafficking, and Cytotoxicity of Nanomaterials. *Small* **2011**, *7*, 1322–1337.
66) Moghimi, S. M.; Hunterand, A.C.; Murray, J. C. Long-Circulating and Target-Specific Nanoparticles: Theory to Practice. *Pharmacol. Rev.* 2001, 53, 283–318.
67) Kamlay, N.; Xio, Z.; Valencia, P.; Raovic-Moreno, A. F.; Farokhzad, O. C. Targeted Polymeric Therapeutic Nanoaprticles: Design, Development and Clinical Translation. *Chem. Soc. Rev.* **2012**, *41*, 2971-3010.
68) Brigger, I.; Dubernet, C.; Couvner, P. Nanoparticles in Cancer Therapy. *Adv. Drug Deliv. Rev.* **2002**, *54*, 631-651.
69) Torchilin, V, P. Targeted Pharmaceutical Nanocarriers for cancer Therapy and imaging. *AAPS J.* **2007**, *9*, E128-E147.
70) Wong, C.; Stylianopoulus, J.; Cui, J.; Chauhan, V. P.; Fukumara, D. Multistage Nanoparticle Delivery System for Deep Penetration into Tumor Tissue. *Proc. Natl. Acad. Sci. U. S. A.* **2011**, *108*, 2426–2431.
71) Schadlich, A.; Caysa, H.; Mueller, T.; Tenambergen, F.; Rose, C.; Goferich, A.; Kuntsche, J.; Mader, K. Tumor Accumulation of NIR Fluorescent PEG–PLA Nanoparticles: Impact of Particle Size and Human Xenograft Tumor Model. *ACS Nano* **2011**, *5*, 8710-8720.

72) Sykes, E. A.; Chen, J.; Zheng, G.; Chan, W. C. W. Investigating the Impact of Nanoparticle Size on Active and Passive Tumor Targeting Efficiency. *ACS Nano* **2014**, *8*, 5696-5706.
73) Arap, W.; Haedicke, W.; Bernasconi, M.; Ruoslahti, E. Targeting the prostate for destruction through a vascular address. *Proc. Natl. Acad. Sci. U. S. A.* **1999**, *99*, 1527–1531.
74) Rabanel, J. M.; Aoun, V.; Elkin, I.; Mokhtar, M.; Hildgen, P. Drug-Loaded Nanocarriers: Passive Targeting and Crossing of Biological Barriers. *Curr. Med. Chem.* **2012**, *19*, 3070–3102.
75) Gessner, A.; Lieske, A.; Paulke, B.; Muller, R. Influence of Surface Charge Density on Protein Adsorption on Polymeric Nanoparticles: Analysis by Two-Dimensional Electrophoresis. *Eur. J. Pharm. Biopharm.* **2002**, *54*, 165–170.
76) Wang, J.; Byrne, J. D.; Napier, M. E.; Desimone, J. M. More Effective Nanomedicines through Particle Design. *Small* **2011**, 7, 1919-1931.
77) Salvador-Morales, C.; Zhang, L.; Langer, R.; Farokhzad, O. C. Immunocompatibility Properties of Lipi-Polymer Hybrid Nanoparticles with Heterogenous Surface Functional Groups. *Biomaterials.* **2009***, 30,* 2231-2240.
78) Alexis, F.; Pridgen, E.; Molnar, L. K.; Farokhzad, O. C. Factors Affecting the Clearance and Biodistribution of Polymeric Nanoparticles. *Mol. Pharm.* **2008**, *5*, 505–515.
79) Bexiga, M. G.; Varela, J. A.; Wang, F.; Fenaroli, F.; Salvati, A.; Lynch, I.; Simpson, J. C.; Dawson, K .A. Cationic Nanoaprticles Induces Caspase 3-, 7- and 9-mediated Cytotoxicity in Human Astrocytoma Cell Line. *Nanotoxicology* **2011**, *5*, 557-567.
80) Hwang, T-L.; Aljuffali, I .A.; Lin, C-F.; Chang, Y-T.; Fang, J-Y. Cationic Additives in Nanosystems Activate Cytotoxicity and Inflammatory Response of human Neutrophils; lipid Nanoaprticles verses polymeric Nanoparticles. *Int. J. Nanomed.* **2015**, *10*, 371-385.
81) He, C.; hu, Y.; Yin, L.; Tang, C.; Yin, C. Effect of Particle Size and Surface Charge on Cellular Uptake and Biodistribution of Polymeric Nanoparticles. *Biomaterials.* **2010***, 31,* 3657-3666.
82) Verma, A.; Stellacci, F. Effect of Surface Properties on Nanoparticle-Cell Interactions. *Small* **2009**, *6*, 12-21.
83) Dausen, J.; Msyanchi, A.; Dass, M.; Walther, P.; Schrezenmeier, H.; Landfester, K.; Mailander, V. Uptake Mechanism of Oppositely Charged Fluoroscent Nanoparticles in HeLa Cells. *Macromol. Biosci.* **2008**, *8*, 1135-1143.
84) Venkataraman, S.; Hedrick, J. L.; Ong, Z. Y.; Yang, C.; Rachel Ee, P. L.; Hammond, P. T.; Yang, Y. Y. *Adv. Drug Deliv. Rev*. **2011**, *63*, 1228-1246.
85) Zhu, X.; Vo, C.; Taylor, M.; Smith, B. R. Non-spherical micro-and nanoparticles in nanomedicine. *Mater. Horiz.* **2019**, *6*, 1094– 1121.
86) Banerjee, A.; Qi, J.; Gogoi, R.; Wong, J.; Mitragotri, S. Role of nanoparticle size, shape and surface chemistry in oral drug delivery. *J. Control. Release* **2016**, *238*, 176– 185.
87) Wu, Y.; Xiao, Y.; Huang, Y.; Xu, Y.; You, D.; Lu, W.; Yu, J. Rod-shaped micelles based on PHF-g-(PCL-PEG) with pH-triggered doxorubicin release and enhanced cellular uptake. *Biomacromolecules* **2019**, *20*, 1167– 1177.

88) Lin, L.; Wang, X.; Guo, Y.; Ren, K.; Li, X.; Jing, L.; Yue, X.; Zhang, Q.; Dai, Z. Hybrid bicelles as a pH-sensitive nanocarrier for hydrophobic drug delivery. *RSC Adv.* **2016**, *6*, 79811– 79821.
89) Yasuhara, K.; Miki, S.; Nakazono, H.; Ohta, A.; Kikuchi, J.-i. Synthesis of organic–inorganic hybrid bicelles–lipid bilayer nanodiscs encompassed by siloxane surfaces. *Chem. Commun.* **2011**, *47*, 4691– 4693.
90) Geng, Y.; Dalhaimer, P.; Cai, S.; Tsai, R.; Tewari, M.; Minko, T.; Discher, D. E. Shape effects of filaments versus spherical particles in flow and drug delivery. *Nat. Nanotechnol.* **2007**, *2*, 249– 255.
91) Borteh, H. M.; Gallovic, M. D.; Sharma, S.; Peine, K. J.; Miao, S.; Brackman, D. J.; Gregg, K.; Xu, Y.; Guo, X.; Guan, J. Electrospun acetalated dextran scaffolds for temporal release of therapeutics. *Langmuir* **2013**, *29*, 7957– 7965.
92) Han, K.; Zhang, J.; Zhang, W.; Wang, S.; Xu, L.; Zhang, C.; Zhang, X.; Han, H. Tumor-triggered geometrical shape switch of chimeric peptide for enhanced in vivo tumor internalization and photodynamic therapy. *ACS Nano* **2017**, *11*, 3178– 3188.
93) Ke, W.; Lu, M.; Japir, A.; Zhou, Q.; Xi, L.; Wang, Y.; Dutta, D.; Zhaou, M.; Pan, Y.; Ge, Z. Length effect of stimuli-responsive block copolymer prodrug filomicelles on drug delivery efficiency. J. Control. Release. 2020, 318, 67-77.
94) Sharma, G.; Valenta, D.; Altman, Y.; Harvey, S.; Xie, H.; Mitragitri, S.; Smith, J. W. Polymer Particle Shape Independently Influences Binding and Internalization by Macrophages. *J. Control. Release* **2010**, *147*, 408–412.
95) Roemeling, C.; Jiang, W.; Chan, C. K.; Weissman, I. L.; Kim, B. Y. S. Breaking Down the Barriers to Precision Cancer Nanomedicine. *Trends Biotechnol.* **2017**, *35*, 159–17.
96) Garapaty, A.; Champion, J. A. Shape of Ligand Immobilized Particles Dominates and Amplifies the Macrophage Cytokine Response to Ligands. *PLoS One* **2019**, *14*, e0217022.
97) Fox, M. E.; Szoka, F. C.; Fréchet, J. M. J. Soluble Polymer Carriers for the Treatment of Cancer: The Importance of Molecular Architecture. *Acc. Chem. Res.* **2009**, *42*, 1141–1151.
98) Ferrari, M. Cancer Nanotechnolgy: Opportunities and Challenges. Nat. Rev. Cancer. 2005, 5, 161-171.
99) Matsumura, Y.; Maeda, H. A New Concept For Macromolecular Therapeutics In Cancer Chemotherapy— Mechanism of Tumoritropic Accumulation Of Proteins and the Antitumor Agent Smancs. *Cancer Res.* **1986,** *46,* 6387–6392.
100) Peer, D.; Karp, J. M.; Hong, S.; Farokhzad, O. C.; Margalit, R.; Langer, R. Nanocarriers as an Emerging Platform for Cancer Therapy. *Nat. Nanotechnol.* **2007***, 2,* 751-760
101) Couvreur, P. Vauthier, C. Nanotechnology: Intelligent Design to Treat Complex Disease. *Pharm. Res*. **2006**, *23*, 1417-1450.
102) Allen, T. M. Ligand-Targeted Therapeutic in Anticancer Therapy. *Nat. Rev. Cancer* **2002**, *2*, 750-763.
103) R, L. Implantable Controlled Release Systems. *Pharmacol. Ther.* **1983**, *21*, 35–51.
104) NA, P.; EW, M. Development of Semicrystalline Poly(Vinyl Alcohol) Hydrogels for Biomedical Applications. *J. Biomed. Mater. Res.* **1977**, *11*, 423–434.
105) RS, L.; NA, P. Present and Future Applications of Biomaterials in Controlled Drug

Delivery Systems. *Biomaterials* **1981**, *2*, 201–214.
106) J, H. Controlled Release of Biologically Active Compounds from Bioerodible Polymers. *Biomaterials* **1980**, *1*, 51–57.
107) J, H.; KJ, H. Poly(Ortho Ester) Biodegradable Polymer Systems. *Methods Enzymol.* **1985**, *112*, 422–436.
108) Batz, H.-G.; Franzmann, G.; Ringsdorf, H. Model Reactions for Synthesis of Pharmacologically Active Polymers by Way of Monomeric and Polymeric Reactive Esters. *Angew. Chemie Int. Ed. English* **1972**, *11*, 1103–1104.
109) Ringsdorf, H. Structure and properties of pharmacologically active polymers. *J Polym Sci Polym Symp*; 1975, 135–153.
110) Khanna, S. C.; Jecklin, T.; Speiser, P. Bead Polymerization Technique for Sustained-Release Dosage Form. *J. Pharm. Sci.* **1970**, *59*, 614–618.
111) G, B.; PP, S. Polymerized Micelles and Their Use as Adjuvants in Immunology. *J. Pharm. Sci.* **1976**, *65*, 1763–1766.
112) Zaffaroni, A. Systems for Controlled Drug Delivery. *Med. Res. Rev.* **1981**, *1*, 373–386.
113) AS, H. The Origins and Evolution of "Controlled" Drug Delivery Systems. *J. Control. Release* **2008**, *132*, 153–163.
114) Otsuka, H.; Nagasaki, Y.; Kataoka, K. PEGylated Nanoaprticles for Biological and Pharmacrtical Applications. *Adv. Drug Deliv. Rev.* **2012**, *64*, 246-255.
115) Y, M.; T, H.; T, U.; K, M.; Y, Y.; Y, S.; K, S.; T, O.; H, U.; M, I.; N, W. Phase I Clinical Trial and Pharmacokinetic Evaluation of NK911, a Micelle-Encapsulated Doxorubicin. *Br. J. Cancer* **2004**, *91* , 1775–1781.
116) JW, V.; A, A.; C, N.; V, A.; G, P.; J, B.; S, C.; P, C.; EK, R.; M, R. A Phase 2 Study of SP1049C, Doxorubicin in P-Glycoprotein-Targeting Pluronics, in Patients with Advanced Adenocarcinoma of the Esophagus and Gastroesophageal Junction. *Invest. New Drugs* **2011**, *29*, 1029–1037.
117) S, D.; D, F.; V, A.; J, M.; D, K.; D, J.; M, B.; G, H.; M, R. Phase I Dose Escalation and Pharmacokinetic Study of Pluronic Polymer-Bound Doxorubicin (SP1049C) in Patients with Advanced Cancer. *Br. J. Cancer* **2004**, *90* , 2085–2091.
118) TY, K.; DW, K.; JY, C.; SG, S.; SC, K.; DS, H.; NK, K.; YJ, B. Phase I and Pharmacokinetic Study of Genexol-PM, a Cremophor-Free, Polymeric Micelle-Formulated Paclitaxel, in Patients with Advanced Malignancies. *Clin. Cancer Res.* **2004**, *10* , 3708–3716.
119) C, O.; W, B.; M, B.; G, S.; JF, N.; WE, H. Polymeric Micelles in Anticancer Therapy: Targeting, Imaging and Triggered Release. *Pharm. Res.* **2010**, *27*, 2569–2589.
120) Hrkach, J.; Hoff, D. H. Farokhzad, O. C.; Zale, S. et. Preclinical Development and Clinical Translation of a PSMA-Targeted Docetaxel Nanoparticle with a Differentiated Pharmacological Profile. *Sci. Transl. Med.* **2012**, *4*, 128ra39.
121) Me, D. The First Targeted Delivery of SiRNA in Humans via a Self-Assembling, Cyclodextrin Polymer-Based Nanoparticle: From Concept to Clinic. *Mol. Pharm.* **2009**, *6*, 659–668.
122) Fan, X.; Li, Z.; Loh, X. J. Recent Development of Unimolecular Micelles as Functional Materials and Applications. *Polym. Chem.* **2016**, *7*, 5898–5919.
123) Hwang, D.; Ramsay, J. D.; Kabanov, A. V. Polymeric Micelles for the Delivery of

Poorly Soluble Drugs: From Nanoformulation to the Clinical Approval. *Adv. Drug Deliv. Rev*. **2020**, *156*, 80-118.

124) Radoslav Savić; Tony Azzam; Adi Eisenberg, Maysinger, D. Assessment of the Integrity of Poly(Caprolactone)-b-Poly(Ethylene Oxide) Micelles under Biological Conditions: A Fluorogenic-Based Approach. *Langmuir* **2006**, *22*, 3570–3578.

125) Croy, S.; Kwon, G. Polymeric Micelles for Drug Delivery. *Curr. Pharm. Des.* **2006**, *12*, 466-4684.

126) Cabral, H.; Matsumoto, Y.; Mizuno, K.; Chen, Q.; Murakami, M.; Kimura, M.; Terada, Y.; Kano, M. R.; Miyazono, K.; Uesaka, M.; Nishiyama, N.; Kataoka, K., Accumulation of Sub-100 nm Polymeric Micelles in Poorly Permeable Tumours Depends on size. *Nat. Nanotechnol* **2011,** *6* (12), 815-823.

127) Luo, X.; Chen, M.; Zhang, Y.; Chen, Z.; Li, X. Pharmacokinetics and Antitumor Efficacy of Micelles Assembled from Multiarmed Amphiphilic Copolymers with Drug Conjugates in Comparison with Drug-Encapsulated Micelles. *Eur. J. Pharm. Biopharm.* **2016**, *98*, 9– 19.

128) Qi, M.; Zhou, Y., Multimicelle Aggregate Mechanism for Spherical Multimolecular Micelles: from Theories, Characteristics and Properties to Applications. *Mater. Chem. Front.* **2019,** *3* (10), 1994-2009.

129) Chen, G.; Wang, Y.; Xie, R.; Gong, S. A Review on Core–Shell Structured Unimolecular Nanoparticles for Biomedical Applications. *Adv. Drug Deliv. Rev.* **2018**, *130*, 58–72.

130) Sun, X.; Wang, X.; Zhang, H.; hu, S.; Liu, X.; tang, J.; Shen, Y. The blood clearance kinetics and pathway of polymeric micelles in cancer drug delivery. *ACS Nano* **2018**, *12*, 6179-6192.

131) Gao, H.; Jones, M.-C.; Chen, J.; Prud'homme, R. E.; Leroux, J.-C. Core Cross-Linked Reverse Micelles from Star-Shaped Polymers. *Chem. Mater.* **2008**, *20*, 3063–3067.

132) X, Y.; JJ, G.; IJ, R.; A, J.; SA, H.; DA, S.; S, G. Multifunctional SPIO/DOX-Loaded Wormlike Polymer Vesicles for Cancer Therapy and MR Imaging. *Biomaterials* **2010**, *31*, 9065–9073.

133) U, K.; P, P.; S, S.; V, K. Advances in Polymeric Micelles for Drug Delivery and Tumor Targeting. *Nanomedicine* **2010**, *6* (6), 714–729.

134) Liu, H.; Jiang, A.; Guo, J.; Uhrich, K. Unimolecular Micelles: Synthesis and Characterization of Amphiphilic polymer Systems. J. Polym. Sci.: Part A: Polym. Chem. 1999, 37, 703-711.

135) Liu, H.; Farrell, S.; Uhrich, K., Drug Release Characteristics of Unimolecular Polymeric Micelles. *J Control Release* **2000,** *68* (2), 167-174.

136) Newkome G. R.; Moorefield C. N.; Baker, G. R.; Saunders M. J.; Grossman, S. H. Unimolecular micelles. *Angew Chem Int Ed* **1991**, *30*, 1178–1180.

137) Xu, J.; Luo, S.; Shi, W.; Liu, S. Two-Stage Collapse of Unimolecular Micelles with Double Thermoresponsive Coronas. *Langmuir* **2006**, *22*, 989–997.

138) MC, L.; BN, T.; R, H. Dendritic Core-Shell Systems as Soft Drug Delivery Nanocarriers. *Biotechnol. Adv.* **2015**, *33*, 1327–1341.

139) Newkome, G. R.; Moorefield, C. N.; Baker, G. R.; Saunders, M. J.; Grossman, S. H. Unimolecular Micelles. *Angew. Chemie Int. Ed. English* **1991**, *30*, 1178–1180.

140) Boas, U.; Heegaard, R. M. H. Dendrimers in Drug Research. Chem. Soc. Rev. 2004, 33, 43-63.
141) Gillies E. R.; Frechet , J. M. J. Dendrimers and Dendritic Polymers in Drug Delivery. *Drug Discovery Today*, **2005**, *10* , 35-43.
142) Liu, M.; Kono, K.; Frechet , J. M. J. Water- Soluble Dendrimer-Poly(ethylene glycol) starlike Conjugate as Potential Drug carriers. *J. Polym. Sci., Polym. Chem.*, **1999**, *37* , 3492 -3503.
143) Hawker , C. J. Wooley, K. L. and Fréchet , J. M. J. Unimolecular micelles and globular amphiphiles: dendritic macromolecules as novel recyclable solubilization agents. *J. Chem. Soc., Perkin Trans. 1*, 1993, 1287-1297.
144) Longmire, M.; Choyke, P.; Koayashi, H. Clearance properties of nano-sized particles and molecules as imaging agents: considerations and caveats. *Nanomedicine* **2008**, *5*, 703-717.
145) Jansen , J.; De Brabander-Vanden Berg, E. M. M.; Meijer , E. W. Encapsulation of Guest molecules into a Dendritic Box. *Science*, **1994**, *266* , 1226-1229.
146) Fan, X.; Li, Z.; Loh, X. J. Recent Development of Unimolecular micelles as a Functional materials and Applications. *Polym. Chem.* **2016**, *7*, 5898–5919.
147) Veronse, F. M.; Pasut, G. PEGylation, Successful Approach to Drug Delivery. *Drug Discov. Today* **2005**, *10*, 1451-1458.
148) Ma, X.; Zhou, Z.; Jin, E.; Sun, Q.; Zhang, B.; tang, J.; Shen, Y. Facile Synthesis of Polyester Dendrimers as Drug Delivery Carriers. *Macromolecules* **2013**, *46*, 37–42.
149) Chen, G.; Shi, X.; Wang, B.; Xie, R.; Guo, L. W.; Gong, S.; Kent, K. C. Unimolecular Micelle-Based Hybrid System for Perivascular Drug Delivery Produces Long-Term Efficacy for Neointima Attenuation in Rats. *Biomacromolecules* **2017**, *18*, 2205–2213.
150) He, H.; Wang, Y.; Wen, H.; Jia, X. Dendrimer-Based Multilayer Nanocarrier for Potential Synergistic Paclitaxel–Doxorubicin Combination Drug Delivery. *RSC Adv.* **2013**, *4* , 3643–3652.
151) Brinkman, A. M.; Chen, G.; Wang, Y.; Hedman, C. J.; Sherer, N. M.; Havighurst, T. C.; Gong, S.; Xu, W. Aminoflavone-Loaded EGFR-Targeted Unimolecular Micelle Nanoparticles Exhibit Anti-Cancer Effects in Triple Negative Breast Cancer. *Biomaterials* **2016**, *101*, 20–31.
152) Feast, W. J.; Stainton, N. M. Synthesis, Structure and Properties of Some Hyperbranched Polyesters. *J. Mater. Chem.* **1995**, *5*, 405–411.
153) Bakhshi, H.; Agarwal, S. Hyperbranched Polyesters as Biodegradable and Antibacterial Additives. *J. Mater. Chem. B* **2017**, *5*, 6827–6834.
154) Kim, Y. Hyperbranched Polymers 10 Years After. *J. Polym. Sci., Part A: Polym. Chem.*, **1998**, *36* , 1685-1698.
155) Borgaonkar, P.; Sharma, S.; Chen, M; Shhmidt, D. F. A Flexible Approach to the Preparation of Polymer Scaffolds for Tissue Engineering. *Macromol. Biosci.* **2007**, *7*, 201–207.
156) Zager, E.; Zigon, M. Characterization of a Commercial Hyperbranched Aliphatic Polyester based on 2,2-bis (methoyl) propionic acid. *Macromolecules* **2002**, *35*, 9913-9925.
157) Kontoyianni, C.; Sideratou, Z.; Theodossiou, T.; Tziveleka, L.-A.; Tsiourvas, D.;

Paleos, C. M. A Novel Micellar PEGylated Hyperbranched Polyester as a Prospective Drug Delivery System for Paclitaxel. *Macromol. Biosci.* **2008**, *8*, 871–88.

158) Zhang, S.; Xu, J.; Chen, H.; Song, Z.; Wu, Y.; Dai, X.; Kong, J. Acid-Cleavable Unimolecular Micelles from Amphiphilic Star Copolymers for Triggered Release of Anticancer Drugs. *Macromol. Biosci.* **2017**, *17*, 1–10.

159) Nabid, M. R.; Bide, Y. H40-PCL-PEG Unimolecular Micelles Both as Anchoring Sites for Palladium Nanoparticles and Micellar Catalyst for Heck Reaction in Water. *Appl. Catal. A Gen.* **2014**, *469*, 183–190.

160) Prabaharan, M.; Grailer, J. J.; Pilla, S.; Steeber, Gong, S. Folate-Conjugated Amphiphilic Hyperbranched Block Copolymers Based on Boltorn® H40, poly (L-lactide) and poly (ethylene glycol) for Tumor-Targeted Drug Delivery. *Biomaterials* **2009**, *30*, 3009-3019.

161) Prabaharan, M.; Grailer, J. J.; Pilla, S.; Steeber, Gong, S. Amphiphilic Multi-Arm Block Copolymer Based on Hyperbranched Polyester (Poly-L-Lactide) and Poly (ethylene glycol) as a Drug Delivery Carrier. *Macromol. Biosci.* **2009**, *8*, 871-881.

162) Luo, S.; Han, M.; Cao, Y.; Ling, C.; Zhang, Y. Temperature and pH-responsive Unimolecular micelles with a Hydrophobic Hyperbranched core. *Colloid Polym. Sci.* **2011**, *289*, 1243-1251.

163) Abbina, S.; Vappala, S.; Kumar, P.; Siren, E. M. J.; La, C. C.; Abbasi, U.; Brooks, D. E.; Kizhakkedathu, J. N. Hyperbranched Polyglycerols: Recent Advances in Synthesis, Biocompatibility and Biomedical Applications. *J. Mater. Chem. B* **2017**, *5* (47), 9249–9277.

164) Du, F.; Honzke, S.; Newman, F.; Kelitz, J.; Chan, W.; Ma, N.; Hedrich, S.; Haag, R. Development of Biodegradable Hyperbranched Core-Multishell Nanocarriers for Efficient Topical Drug Delivery. *J. Control. Release* **2016**, *242*, 42–49.

165) Li, X.; Qian, Y.; Liu, T.; Hu, X.; Zhang, G.; You, Y.; Liu, S. Amphiphilic multiarm star block copolymer-based multifunctional unimolecular micelles for cancer targeted drug delivery and MR imaging. *Biomaterials.* **2011**, *32*, 6595-6605.

166) Jianhui Xia; Xuan Zhang, and; Matyjaszewski*, K. Synthesis of Star-Shaped Polystyrene by Atom Transfer Radical Polymerization Using an "Arm First" Approach. *Macromolecules* **1999**, *32*, 4482–4484.

167) Gao, H.; Matyjaszewski, K. Synthesis of Molecular Brushes by "Grafting onto" Method: Combination of ATRP and Click Reactions. *J. Am. Chem. Soc.* **2007**, *129*, 6633-6639.

168) Zhao, P.; liu, L.; Geng, X.; Wang, C.; Shuai, X.; Chen, Y. Molecular Nanoworm with PCL Core and PEO Shell as a Non-Spherical Carrier for Drug Delivery. *Macromol. Rapid Commun.* **2012**, *33*, 1351–1355.

169) Guo, J.; Hong, H.; Chen, G.; Shi, S.; Nayak, T. R.; Theuer, C. P.; Barnhart, T. E.; Cai, W.; Gong, S. Theranostic Unimolecular Micelles Based on Brush-Shaped Amphiphilic Block Copolymers for Tumor-Targeted Drug Delivery and Positron Emission Tomography Imaging. *ACS Appl. Mater. Interfaces* **2014**, *6* (24), 21769–21779.

170) Gavgane, U, A.; Jayakannan, M. Size- and Shape-controlled Biodegradable Polymer Brushes Based on L-Amino Acid for Intracellular Drug Delivery and Deep-Tissue Penetration. *Biomacromolecules* **2024**, *25*, 3756-3774.

171) Jin, X.; Sun, P.; Tong, G.; Zhu, X. Star Polymer-based unimolecualr micelles and their applications in Bio-imaging and Diagnosis. *Biomaterials* **2018**, *178*, 738-750.
172) Ren, J. M.; McKenzie, T. G.; Fu, Q.; Wong, E. H. H.; Xu, J.; An, Z.; Shanmugam, S.; Davis, T. P.; Boyer, C.; Qiao, G. G. Star Polymers. *Chem. Rev.* **2016**, *116* (12), 6743–6836.
173) Kaupp, M.; Hiltebrandt, K.; Trouillet, V.; Mueller, P.; Quick, A. S.; Wegener, M.; Barner-Kowollik, C. Wavelength Selective Polymer Network Formation of End-Functional Star Polymers. *Chem. Commun.* **2016**, *52*, 1975–1978.
174) Wang, J-J.; Qian, C.; Yao, J-Y.; Bi, X-L. Paclitaxel-loaded cyclodextrin-cored unimolecualr micelles and their in vivo behavior. *React. Funct. Polym.* **2020**, *150*, 104542.
175) Pang, X.; Zhao, L.; Akinc, M.; Kim, J. K.; Lin, Z. Novel Amphiphilic Multi-Arm, Star-like Block Copolymers as Unimolecular Micelles. *Macromolecules* **2011**, *44* (10), 3746–3752.
176) Xu, Z.; Liu, S.; Liu, H.; Yang, C.; Kang, Y.; Wang, M. Unimolecular Micelles of Amphiphilic Cyclodextrin-Core Star-like Block Copolymers for Anticancer Drug Delivery. *Chem. Commun.* **2015**, *51*, 15768–15771.
177) Qiu, L.; Liu, Q.; Hong, C-Y.; Pan, C-Y. unimoelcular mcielles of camptotehcin-bonded hyperbranched star copolymers via β-thiopropionate linkage: synthesis and drug delivery. *J. Mater. Chem. B.* **2016**, *4*, 141-151.
178) Chen, G.; Jaskula-Sztul, R.; Harrison, A.; Dammalpati, A.; Xu, W.; Cheng, Y.; Chen, H.; Gong, S. KE108-conjugated unimolecular micelles loaded with novel HDAC inhibitor thilandepsin-A targeted neuroendocrine cance therapy. *Biomaterials* **2016**, *97*, 22-33.
179) Lin, W.; Zhang, X.; Qian, L.; Yao, N.; Pan, Y.; Zhang, L. Doxorubicin-Loaded for Tumor-Targeted Chemotherapy and Computed Tomography Imaging. *Biomacromolecules* **2017**, *18*, 3869–3880.
180) Xu, W.; Siddiqui, I. A.; Nihal, M.; Pilla, S.; Rosenthal, K.; Mukhtar, H.; Gong, S. Aptamer-Conjugated and Doxorubicin-Loaded Unimolecular Micelles for Targeted Therapy of Prostate Cancer. *Biomaterials* **2013**, *34*, 5244-5253.
181) Guo, J.; Hong, H.; Chen, G.; Shi, S.; Zheng, Q.; Zhang, Y.; Theuer, C. P.; Barnhart, T. E.; Cai, W.; Gong, S. Image-Guided and Tumor-Targeted Drug Delivery with Radiolabeled Unimolecular Micelles. *Biomaterials* **2013**, *34*, 8323-8332.
182) Lin, W.; Yao, N.; Qian, L.; Zhang, X.; Chen, Q.; Wang, J.; Zhang, L. pH-Responsive Unimolecular Micelle-Gold Nanoparticles-Drug Nanohybrid System for Cancer Theranostic. *Acta Biomater*. **2017**, *58*, 455-465.
183) Lin, W.; Zhang, X.; Qian, L.; Yao, N.; Pan, Y.; Zhang, L. Doxorubicin-Loaded Unimolecular Micelle-Stabilized Gold Nanoparticles as a Theranostic Nanoplatform for Tumor-Targeted Chemotherapy and Computed Tomography Imaging. *Biomacromolecules* **2017**, *18*, 3869-3880.
184) Liu, F.; Wang, D.; Zhang, M.; Ma, L.; Yu, C-Y.; Wei, H. Synthesis of enzyme-Responsive Theranostic Amphiphilic Conjugated Bottlebrush Copolymers for Enhanced Anticancer Drug Delivery. *Acta Biomater.* **2022**, *144*, 15-31.

185) Liu, F.; Wang, J.; Qin, Y.; Huang, B.; Liu, C.; Zhang, H.; Yu, C-Y.; Wei, H.; One-Pot Synthesis of Enzyme and GSH Dual-Responsive Zwitterionic Copolymers with Cross-Linked Shells for Enhanced Anticancer Drug Delivery. *ACS Appl. Polym. Mater.* **2025**, *7*, 2061-2072.
186) Fan, X.; Hu, Z.; Wang, G. Synthesis and Unimolecular Micelles of Amphiphilic Copolymer with Dendritic Poly(L-Lactide) Core and Poly (Ethylene oxide) Shell for Drug Delivery. *RSC Adv.* **2015**, *5*, 100816.
187) Chen, G.; Wang, L.; Cordie, T.; Vokoun, C.; Eliceiri, K. W.; Gong, S. Multi-Functional Self-Fluorescent Unimolecular Micelles for Tumor-Targeted Drug Delivery and Bioimaging. *Biomaterials* **2015**, *47*, 41-50.
188) Fan, X.; Wang, X.; Cao, M.; Wang, C.; Hu, Z.; Wu, Y-L.; Li, Z.; Loh, X. J. "Y"-Shape Armed Amphiphilic Star-like Copolymers: Design, Synthesis and Dual-Responsive Unimolecular Micelle Formation for Controlled Drug Delivery. *Polym. Chem*. **2017**, *8*, 5611-5620.
189) Shi, X.; Ma, X.; Hou, M.; Gao, Y-E.; Bai, S.; Xio, B.; Xue, P.; Kang, Y.; Xu, Z.; Li, C. M. pH-Responsive Unimolecular Micelles Based on Amphiphilic Star-Like Copolymers with High Drug Loading for Effective Drug and Cellular Imaging. *J. Mater. Chem. B.* **2017**, *5*, 6847-6859.
190) Zhang, L.; Shi, D.; Gao, Y.; Zhou, T.; Chen, M. Phenylboronic Acid-functionalized Unimolecular Micelles Based on a Star Polyphosphoester Random Copolymer for Tumor-Targeted Drug Delivery. *Polym Chem.* **2020**, *11*, 2252-2261.
191) Chen, W.; Liu, P. Facile Synthesis of PEGylated Dendritic Polyurethanes as Unimolecular Micelles for Ultrasound-Triggered Localized Drug Delivery. *Polym. Chem.* **2022**, ***13***, 80-84.
192) Chan, W.; Liu, P. Design of GSH-Triggered Disintegrable Dendritic Polyurethane as Bioreducible Unimolecular Micelles for Tumor-Specific Chemotherapeutic Drug Delivery. *Eur. Polym. J.* **2023**, *200*, 112521.
193) Prabaharan, M.; Grailer, J. J.; Pilla, S.; Steeber, D. A.; Gong, S. Gold Nanoparticles with a Monolayer of Doxorubicin-Conjugated Amphiphilic Block Copolymer for Tumor-Targeted Drug Delivery. *Biomaterials* **2009**, *30*, 6065-6075.
194) Chen, W.; Liu, P. Dendritic Polymer Prodrug-Based Unimolecular Micelles for pH-Responsive Co-Delivery of Doxorubicin and Camptothecin with Synergistic Controlled Drug Release Effect. *Colloids Surf. B Biointerfaces* **2024**, *238*, 113906.
195) Kamaly, N.; Yameen, B.; Wu, J.; Farokhzad, O. C. Degradable Controlled-Release Polymers and Polymeric Nanoparticles: Mechanisms of Controlling Drug Release. *Chem. Rev.* **2016**, *116*, 2602-2663.
196) Vert, M.; Doi, Y.; Hellwich, K.-H.; Hess, M.; Hodge, P.; Kubisa, P.; Rinaudo, M.; Schué, F. Terminology for biorelated polymers and applications (IUPAC Recommendations 2012) *Pure Appl. Chem*. **2012**, *84*, 377– 410.
197) Kulkarni, R. K.; Moore, E. G.; Hegyeli, A. F.; Leonard, F. Biodegradable poly(lactic acid) polymers. *J. Biomed. Mater. Res.* **1971**, *5*, 169–181.
198) Fredenberg, S.; Wahlgren, M.; Reslow, M.; Axelsson, A. The mechanisms of drug release in poly(lactic-co-glycolic acid)-based drug delivery systems--a review. *Int. J. Pharm.* **2011**, *415*, 34– 52.

199) Marin, E.; Briceno, M. I.; Caballero-George, C. Critical evaluation of biodegradable polymers used in nanodrugs. *Int. J. Nanomed.* **2013**, *8*, 3071– 3090.
200) Ren, D.; Yi, H.; Wang, W.; Ma, X. The enzymatic degradation and swelling properties of chitosan matrices with different degrees of N-acetylation. *Carbohydr. Res.* **2005**, *340*, 2403– 2410.
201) Ulery, B. D.; Nair, L. S.; Laurencin, C. T. Biomedical Applications of Biodegradable Polymers. *J. Polym. Sci., Part B: Polym. Phys*. **2011**, *49*, 832– 864.
202) Ribeiro, M. P.; Espiga, A.; Silva, D.; Baptista, P.; Henriques, J.; Ferreira, C.; Silva, J. C.; Borges, J. P.; Pires, E.; Chaves, P.; Correia, I. J. Development of a new chitosan hydrogel for wound dressing. *Wound Repair Regen.* **2009**, *17*, 817– 824.
203) R, M.; J, W.; C, F.; F, C.; L, D. M.; CA, V.; M, C.; C, C.; M, F. Polyethylenimine and Chitosan Carriers for the Delivery of RNA Interference Effectors. *Expert Opin. Drug Deliv.* **2013**, *10* , 1653–1668.
204) L, C.; L, I. Chitosan in Nasal Delivery Systems for Therapeutic Drugs. *J. Control. Release* **2014**, *190*, 189–200.
205) Sudha, P. N.; Rose, M. H. Beneficial effects of hyaluronic acid. *Adv. Food Nutr. Res.* **2014**, *72*, 137-176.
206) Oh, E. J.; Park, K.; Kim, K. S.; Kim, J.; Yang, J. A.; Kong, J. H.; Lee, M. Y.; Hoffman, A. S.; Hahn, S. K. Target specific and long-acting delivery of protein, peptide, and nucleotide therapeutics using hyaluronic acid derivatives. *J. Controlled Release* **2010**, *141*, 2-12.
207) Laurent, T. C.; Fraser, J. R. Hyaluronan. *FASEB J*. **1992**, *6*, 2397– 2404.
208) Ghosh, S. C.; Neslihan Alpay, S.; Klostergaard, J. CD44: a validated target for improved delivery of cancer therapeutics. *Expert Opin. Ther. Targets* **2012**, *16*, 635– 650.
209) Heller, J.; Barr, J. Poly (Ortho esters)- from concept to reality. *Biomacroolecules* **2004**, *5*, 1625-1632.
210) M, Q.; X, L.; Y, Y.; S, Z. Electrospun Fibers of Acid-Labile Biodegradable Polymers Containing Ortho Ester Groups for Controlled Release of Paracetamol. *Eur. J. Pharm. Biopharm.* **2008**, *70*, 445–452.
211) Heller, J.; Sparer, R.; Zentner, G.; Chasin, M.; Langer, R. Biodegradable Polymers as Drug Delivery Systems; Marcel Dekker: New York, 1990.
212) J, H.; J, B.; SY, N.; HR, S.; K, S.-A.; S, E.; A, R.-W.; R, G. Poly(Ortho Esters) - Their Development and Some Recent Applications. *Eur. J. Pharm. Biopharm.* **2000**, *50* , 121–128.
213) Petersen, L. K.; Huntimer, L.; Walz, K.; Ramer-Tait, A.; Wannemuehler, M. J.; Narasimhan, B. Combinatorial Evaluation of in Vivo Distribution of Polyanhydride Particle-Based Platforms for Vaccine Delivery. *Int. J. Nanomedicine* **2013**, *8*, 2213.
214) LK, P.; CK, S.; B, N. High-Throughput Analysis of Protein Stability in Polyanhydride Nanoparticles. *Acta Biomater.* **2010**, *6*, 3873–3881.
215) BA, P.; JA, B.; R, L. Formulation and Surface Modification of Poly(Ester-Anhydride) Micro- and Nanospheres. *Biomaterials* **2005**, *26* ,117–124.
216) JM, A.; DF, G.; RL, M.; A, H.; R, W. The Potential for Poly-Alpha-Amino Acids as Biomaterials. *J. Biomed. Mater. Res.* **1974**, *8* (3), 197–207.

217) KE, U.; SM, C.; RS, L.; KM, S. Polymeric Systems for Controlled Drug Release. *Chem. Rev.* **1999**, *99* (11), 3181–3198.
218) Marck, K. W.; Wildevuur, C. R. H.; Sederel, W. L.; Bantjes, A.; Feijen, J. Biodegradability and Tissue Reaction of Random Copolymers of L-Leucine, L-Aspartic Acid, and L-Aspartic Acid Esters. *J. Biomed. Mater. Res.* **1977**, *11*, 405–422.
219) Martin, E. C.; May, P. D.; McMahon, W. A. Amino Acid Polymers for Biomedical Applications. I. Permeability Properties of L-Leucine DL-Methionine Copolymers. *J. Biomed. Mater. Res.* **1971**, *5*, 53–62.
220) D, L.; E, J.; A, Z. Drug Delivery of Oligonucleotides by Peptides. *Eur. J. Pharm. Biopharm.* **2004**, *58*, 237–25.
221) Guo, K.; Chu, C. C.; Chkhaidze, E.; Katsarava, R. Synthesis and Characterization of Novel Biodegradable Unsaturated Poly(Ester Amide)S. *J. Polym. Sci. Part A Polym. Chem.* **2005**, *43*, 1463–1477.
222) YH, L.; GS, H.; YH, R.; S, P.; JE, R.; M, E.; KL, W. Development of a Vinyl Ether-Functionalized Polyphosphoester as a Template for Multiple Postpolymerization Conjugation Chemistries and Study of Core Degradable Polymeric Nanoparticles. *Macromolecules* **2014**, *47* , 4634–4644.
223) Mao, H. Q.; Leong, K. W. Design of Polyphosphoester-DNA Nanoparticles for Non-Viral Gene Delivery. *Adv. Genet.* **2005**, *53*, 275–306.
224) Z, Z.; J, W.; HQ, M.; KW, L. Polyphosphoesters in Drug and Gene Delivery. *Adv. Drug Deliv. Rev.* **2003**, *55*, 483–499.
225) YC, W.; LY, T.; TM, S.; CH, L.; MH, X.; J, W. Self-Assembled Micelles of Biodegradable Triblock Copolymers Based on Poly(Ethyl Ethylene Phosphate) and Poly(-Caprolactone) as Drug Carriers. *Biomacromolecules* **2008**, *9*, 388–395.
226) Trollsås, M.; Lee, V. Y.; Mecerreyes, D.; Löwenhielm, P.; Möller, M.; Miller, R. D.; Hedrick, J. L. Hydrophilic Aliphatic Polyesters: Design, Synthesis, and Ring-Opening Polymerization of Functional Cyclic Esters. *Macromolecules* **2000**, *33*, 4619–4627.
227) Woodruff, M. A.; Hutmacher, D. W. The Return of a Forgotten Polymer - Polycaprolactone in the 21st Century. *Prog. Polym. Sci.* **2010**, *35*, 1217–1256.
228) Tang, M.; Purcell, M.; Steele, J. A. M.; Lee, K. Y.; McCullen, S.; Shakesheff, K. M.; Bismarck, A.; Stevens, M. M.; Howdle, S. M.; Williams, C. K. Porous Copolymers of ε-Caprolactone as Scaffolds for Tissue Engineering. *Macromolecules* **2013**, *46* , 8136–8143.
229) Woodruff, M. A.; Hutmacher, D. W. The Return of a Forgotten Polymer-Polycaprolactone in the 21st Century. *Prog. Polym. Sci.* **2010**, *35*, 1217–1256.
230) Tang, M.; Purcell, M.; Steele, J. A. M.; Lee, K. Y.; McCullen, S.; Shakesheff, K. M.; Bismarck, A.; Stevens, M. M.; Howdle, S. M.; Williams, C. K. Porous Copolymers of ε-Caprolactone as Scaffolds for Tissue Engineering. *Macromolecules* **2013**, *46*, 8136–8143.
231) Labet, M.; Thielemans, W. Synthesis of Polycaprolactone: A Review. *Chem. Soc. Rev.* **2009**, *38*, 3484–3504.
232) Samrot, A. V.; Sean, T. C.; Kumar, S. et al. Prodction, characterization and application of nanocarriers made of polysaccharides, proteins, bio-polyesters and other biopolymers: A review. *Int. J. Bio. Macromol.* **2020**, *165*, 3088-3105.

233) Middleton, J. C.; Tipton, A. J. Synthetic Biodegradable Polymers as Orthopedic Devices. *Biomaterials* **2000**, *21*, 2335–2346.
234) Becker, G.; Wurm, F. R. Functional Biodegradble Polymers via ring-opening polymerization of monomers without protective groups. *Chem. Soc. Rev.* **2018**, *47*, 7739-7782.
235) Tian, D.; Halleux, O.; Dubois, P.; Jerome, R.; Sobry, R.; Van den Bossche, G. Poly(2-Oxepane-1,5-Dione): A Highly Crystalline Modified Poly(ε-Caprolactone) of a High Melting Temperature. *Macromolecules* **1998**, *31*, 924–927.
236) Xiong, X. B.; Uludağ, H.; Lavasanifar, A. Biodegradable Amphiphilic Poly(Ethylene Oxide)-Block-Polyesters with Grafted Polyamines as Supramolecular Nanocarriers for Efficient SiRNA Delivery. *Biomaterials* **2009**, *30*, 242–253.
237) Yan, J.; Zhang, Y.; Xiao, Y.; Zhang, Y.; Lang, M. Novel Poly(ε-Caprolactone)s Bearing Amino Groups: Synthesis, Characterization and Biotinylation. *React. Funct. Polym.* **2010**, *70*, 400–407.
238) Yao, K.; Wang, J.; Zhang, W.; Lee, J. S.; Wang, C.; Chu, F.; He, X.; Tang, C. Degradable Rosin-Ester À Caprolactone Graft Copolymers. **2011**, 2171–2177.
239) Zhang, Y.; Li, J.; Du, Z.; Lang, M. Synthesis and PH-Responsive Assembly of Methoxy Poly(Ethylene Glycol)-b-Poly(ε-Caprolactone) with Pendant Carboxyl Groups. *J. Polym. Sci. Part A Polym. Chem.* **2014**, *52*, 188–199.
240) Cheng, Y.; Hao, J.; Lee, L. A.; Biewer, M. C.; Wang, Q.; Stefan, M. C. Thermally Controlled Release of Anticancer Drug from Self-Assembled γ-Substituted Amphiphilic Poly(ε-Caprolactone) Micellar Nanoparticles. *Biomacromolecules* **2012**, *13*, 2163–2173.
241) Rainbolt, E. A.; Washington, K. E.; Biewer, M. C.; Stefan, M. C. Towards Smart Polymeric Drug Carriers: Self-Assembling γ-Substituted Polycaprolactones with Highly Tunable Thermoresponsive Behavior. *J. Mater. Chem. B* **2013**, *1*, 6532–6537.
242) Rainbolt, E. A.; Washington, K. E.; Biewer, M. C.; Stefan, M. C. Recent Developments in Micellar Drug Carriers Featuring Substituted Poly(ε-Caprolactone)S. *Polym. Chem.* **2015**, *6* , 2369–2381.
243) Mahmud, A.; Patel, S.; Molavi, O.; Choi, P.; Samuel, J.; Lavasanifar, A. Self-Associating Poly(Ethylene Oxide)-b-Poly(α-Cholesteryl Carboxylate-ε-Caprolactone) Block Copolymer for the Solubilization of Stat-3 Inhibitor Cucurbitacin I. *Biomacromolecules* **2009**, *10* , 471–478.
244) Rainbolt, E. A.; Miller, J. B.; Washington, K. E.; Senevirathne, S. A.; Biewer, M. C.; Siegwart, D. J.; Stefan, M. C. Fine-Tuning Thermoresponsive Functional Poly(ε-Caprolactone)s to Enhance Micelle Stability and Drug Loading. *J. Mater. Chem. B* **2015**, *3* , 1779–1787.
245) Fan, J.; Zeng, F.; Wu, S.; Wang, X. Polymer Micelle with PH-Triggered Hydrophobic–Hydrophilic Transition and De-Cross-Linking Process in the Core and Its Application for Targeted Anticancer Drug Delivery. *Biomacromolecules* **2012**, *13* , 4126–4137.
246) Chen, T.; Cai, T.; Jin, Q.; Ji, J. Design and Fabrication of Fucntional Polycaprolactones *ePolymers* **2015**, *15*, 3-13.
247) Surnar, B.; Jayakannan, M. Stimuli-responsive Poly (Caprolactone) Vesicles for Dual Drug Delivery under the Gastrointestinal Tract. *Biomacromolecules* **2013**, *14*, 4377–

4387.
248) Surnar, B.; Sharma, K.; Jayakannan, M. Core-Shell Polymer Nanoparticles for Prevention of GSH Drug Detoxification and Cisplatin Delivery to Breast Cancer Cells. *Nanoscale* **2015**, *7* , 17964–17979.
249) Surnar, B.; Jayakannan, M. Triple Block Nanocarrier Platform for Synergistic Cancer Therapy of Antagonistic Drugs. *Biomacromolecules* **2016**, *17*, 4075–4085.
250) Kulkarni, B.; Surnar, B.; Jayakannan, M. Dual Functional Nanocarrier for Cellular Imaging and Drug Delivery in Cancer Cells Based on π-Conjugated Core and Biodegradable Polymer Arms. *Biomacromolecules* **2016**, *17*, 1004–1016.
251) Kulkarni, B.; Malhotra, M.; Jayakannan, M. Perylene-Tagged Polycaprolactone Block Copolymers and Their Enzyme-Biodegradable Fluorescent Nanoassemblies for Intracellular Bio-Imaging in Cancer Cells. *ACS Appl. Polym. Mater.* **2019**, *1*, 3375–3388.
252) Kulkarni, B.; Jayakannan, M. Fluorescent-Tagged Biodegradable Polycaprolactone Block Copolymer FRET Probe for Intracellular Bioimaging in Cancer Cells. *ACS Biomater. Sci. Eng.* **2017**, *3*, 2185–2197.
253) Ghosh, R.; Malhotra, M.; Madhuri Sathe, R. R.; Jayakannan, M. Biodegradable Polymer Theranostic Fluorescent Nanoprobe for Direct Visualization and Quantitative Determination of Antimicrobial Activity. *Biomacromolecules* **2020**, *21*, 2896–2912.
254) Parrott, M. C.; DeSimone, J. M. Relieving PEGylation. *Nat. Chem.* **2012**, *4*, 13.
255) Tyrrell, Z. L.; Shen, Y.; Radosz, M. Fabrication of Micellar Nanoparticles for Drug Delivery through the Self-Assembly of Block Copolymers. *Prog. Polym. Sci.* **2010**, *35*, 1128–1143.
256) Barz, M.; Luxenhofer, R.; Zentel, R.; Vicent, M. J. Overcoming the PEG-Addiction: Well-Defined Alternatives to PEG, from Structure-Property Relationships to Better Defined Therapeutics. *Polym. Chem.* **2011**, *2*, 1900–1918.
257) Malhotra, M.; Surnar, B.; Jayakannan, M. Polymer Topology Driven Enzymatic Biodegradation in Polycaprolactone Block and Random Copolymer Architectures for Drug Delivery to Cancer Cells. *Macromolecules* **2016**, *49*, 8098-8112
258) Ghosh, R.; Jayakannan, M. Theranostic FRET Gate to Visualize and Quantify Bacterial Membrane Breaching. *Biomacromolecules* **2023**, *24*, 739-755.
259) Pranav, U.; Malhotra, M.; Pathan, S.; Jayakannan, M. Structural Engineering of Star Block Biodegradable Polymer Unimolecular Micelles for Drug Delivery in Cancer Cells. *ACS Biomater. Sci. Eng.* **2023***, 9,* 743-759.
260) Malhotra, M.; Pardasani, M.; Pathan, S.; Srikanth, P.; Shaw, K.; Abraham, N. M.; Jayakannan, M. Star-Polymer Unimolecular Micelle Nanoparticles to deliver a Payload Across the Blood-Brain Barrier. *Nanoscale* **2024**, *16*, 21582-21593.
261) Ghosh, R.; Pathan, S.; Jayakannan, M. Structural Engineering of Cationic Block Copolymer Architectures for Selcetive Breaching of Prokarytoic and Eukaryotic Biological Species. *ACS Appl. Bio Mater.* **2024**, *7*, 7062-7075.

Chapter 2

Probing the Efficacy of Aggregated and Unimolecular Micelles in Tumor Xenograft Models

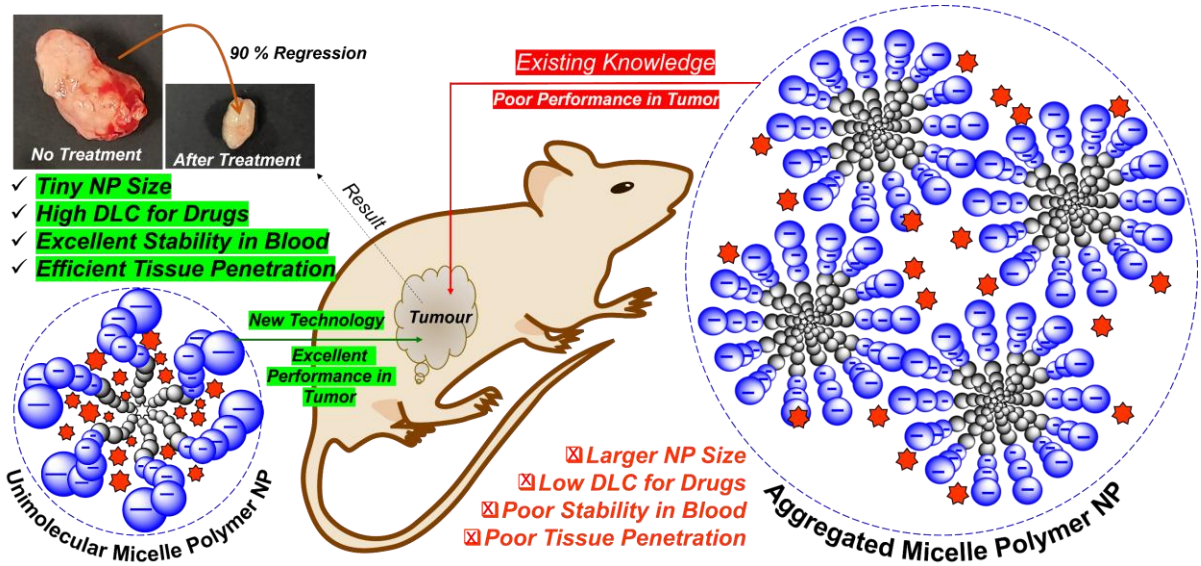

Abstract

Aggregated micellar nanoparticles (AgM NP) are prone to disassemble and disintegrate under physiological conditions in vivo and it became a bottle neck in therapeutic drug delivery in solid tumors. Here, we report a single polymer or unimolecular micelle nanoparticle (UMM NP) platform, which is enzymatically biodegradable, non-toxic and non-hemolytic, carry >14 % of clinical anticancer drug doxorubicin (DOX), very low IC_{50} in vitro, and most strikingly exhibit > 90 % reducing in pancreatic MIA PaCa 2 tumor volume in vivo which are superior to AgM or free drug. For this purpose, a six-arm star polymer platform is chosen to structure engineer the core-shell nano-compartmentalization to optimize the correct macromolecular geometry of compact and tiny < 25 nm sized UMM. Interestingly, formation of aggregated or unimolecular micelles was controlled by amphiphilicity modulation of star block copolymer. For that purpose, a series of block copolymers was engineered to achieve wide range of sizes ranging from 200nm in aggregated micelles to 20nm in unimolecular micelles. Fluorescent dye (or DOX) loaded UMM and AgM NP enabled in vitro differentiation of their endocytosis and intracellular lysosome biodegradation kinetics in living cancer cells by confocal microscopy. Deep tissue penetrable near infra-red IR-780 dye assisted with live animal biodistribution analysis established that the UMM platform is a superior nano-platform to deliver cargoes to solid tumors which account for the enhanced efficacy of tumor volume reduction in vivo.

2.1 Introduction

Synthetic nanoparticles are emerging as inseparable components in biomedical field to deliver payloads of anticancer, anti-inflammatory, antimicrobial drugs or genes under physiological conditions.[1-4] A surge in amphiphilic nanoparticles based on small molecules and polymers as therapeutic vehicles has been favorite in biomaterials field;[5-6] however, recent accounts pointed out that only <1 % of these candidates exhibited promising action under in vivo.[7-8] Several factors like imperfect design, unstable nano-formulations, premature cargo release under blood circulation, filtration by renal apparatuses, and most importantly non-biodegradation under physiological conditions appeared to be major bottlenecks in animal models for IP or IV drug administration.[9-13] Self-assembled nanoparticles (also vesicles) are typically constituted by multi-molecular micelles via hydrophilic-hydrophobic interactions in aqueous medium; thus, they are prone to undergo disassembly well-below their critical micellar concentration (CMC, or critical association constant) in vivo.[14-16] Further, these micellar nanoparticles predominantly exist as aggregated micelles rather than individual species in the solution. [17-19] This implies that nanoparticles of size much greater than twice the end-to-end distance of their molecular dimensions or kinetic chain length (in the case of polymers) should be categorized into aggerated micelle nanoparticles (AgM NP). AgM NP are prone to undergo disassembly upon exposure to concentration gradient in blood stream (by 100 to 1000 times dilution) during the in vivo.[20-21] This could be one of the main factors attributed to the premature release of loaded cargoes and this cannot be ruled out while designing the nanoparticles (or vesicles) for in vivo drug administration in mice models.[22-24] Fréchet and coworkers studied many polymer architectures such as rod-like, macrocycle, and branched macromolecules via membrane-pore model and they arrived at the conclusion that branched polymers possessed relatively high resistance against the renal filtration for prolonged circulation under blood stream.[25-26] This hypothesis has been tested for a few macrocyclic, hyperbranched polymers, bottlebrush and dendrimers by in vivo biodistribution analysis.[27-32] Alternatively, one can predict that the destabilization by concentration gradient could be evaded or minimized by designing well-defined branched macromolecular architectures that could undergo single polymer chain nanoparticles or unimolecular micelle nanoparticles (UMM NP) which do not obey CMC.[33-34] In this case, the increase or decrease in concentration would simply vary the number of carriers in solutions at a given concentration, as in the case of natural proteins in aqueous medium. Thus, UMM NP, in principle, would be devoid of the destabilization against concentration gradient for prolonged circulation under blood circulation in vivo. UMM NP based on block copolymers, star polymers, dendrimers, hyperbranched

polymers and polymer brushes were reported for material and biomedical applications.[35-42] Among them, hyperbranched H40 based UMM NP has proven to be successful for the administration of therapeutic drugs in vivo.[43-45] UMM NP based on H40-hyperbranched systems, and block copolymer systems depicted remarkable drug loading content of 5-15% for Doxorubicin and have been extensively studied for drug delivery.[46-51] Unfortunately, majority of these structures were built on non-biodegradable backbones, and therefore, their degradation kinetics or clearance under physiological conditions is still anonymous. This emphasized that next generation UMM NP needs to be designed biodegradable and the same time capable of loading substantial amounts of therapeutic drugs for enhanced efficacies in vivo. Fundamentally, it is also important to design both AgM NP and UMM NP constituted by identical chemical subunits (also biodegradable) so that their difference in efficacies could be probed in vivo which is yet to be understood in the literature. This fundamental problem at chemistry-biology interface and biomaterial science is addressed here by structure-engineering lysosomal-enzyme biodegradable star polycaprolactone (PCL) platform, self-assembly them into AgM NP and UMM NP, and demonstrate their drug delivering ability in mice xenograft tumor models as shown in Figure 2.1. The star polymers were build using two aliphatic polycaprolactone segments having relatively slow-biodegradable hydrophobic core and hydrophilic anionic-charged fast-biodegradable shell. The selection of these units is done based on one-decade expertise in the area of PCL system in anticancer, antimicrobial research, and blood-brain barrier research in biomedical field.[52-60] Substantial efforts have been taken by us to trace the role of linear versus branched architecture, block versus random copolymers, number of arms in star polymers, etc., to choose the 6-arm star-platform in the present investigation. The 6-arm star-architecture has fixed hydrophobic PCL core and variable chain length anionic-cum-hydrophilic carboxylic PCL shell that exhibits self-assembly transformation from AgM to UMM NP as shown in Figure 2.1a. The star-UMM self-assembled into core-shell nano compartmentalized particles of < 25 nm in size and exhibited excellent encapsulation capabilities for clinical anticancer drug doxorubicin (DOX) for more than 14 % drug loading content variety of intracellular fluorescent dyes such as HPTS and Sulforhodamine-B for studies in vitro living-cell and deep-tissue penetrable water soluble near-infra red fluorescent dye ICG and water insoluble dye IR-780 to study the biodistribution aspects in live-animals (see Figure 2.1b). The star-UMM exhibited excellent drug action in multiple cancer cell lines such as pancreatic (MIA PaCa-2), breast (MCF-7), triple negative breast cancers (MDA-MB-468 and MDA-MB-231), etc., at substantially low IC50 values. The efficacy of the UMM NP is further validated in Mia PaCa-2 xenograft solid tumor models in

mice revealed 90 % reduction in tumor volume compared to free drug or delivered from AgM NP platform (see Figure 2.1c). In a nutshell, the present investigation opens new avenue for unimolecular micelle as an efficient platform in drug delivery applications and also provides the direct account on the superiority of the UMNP over AgM NP in biomedical applications.

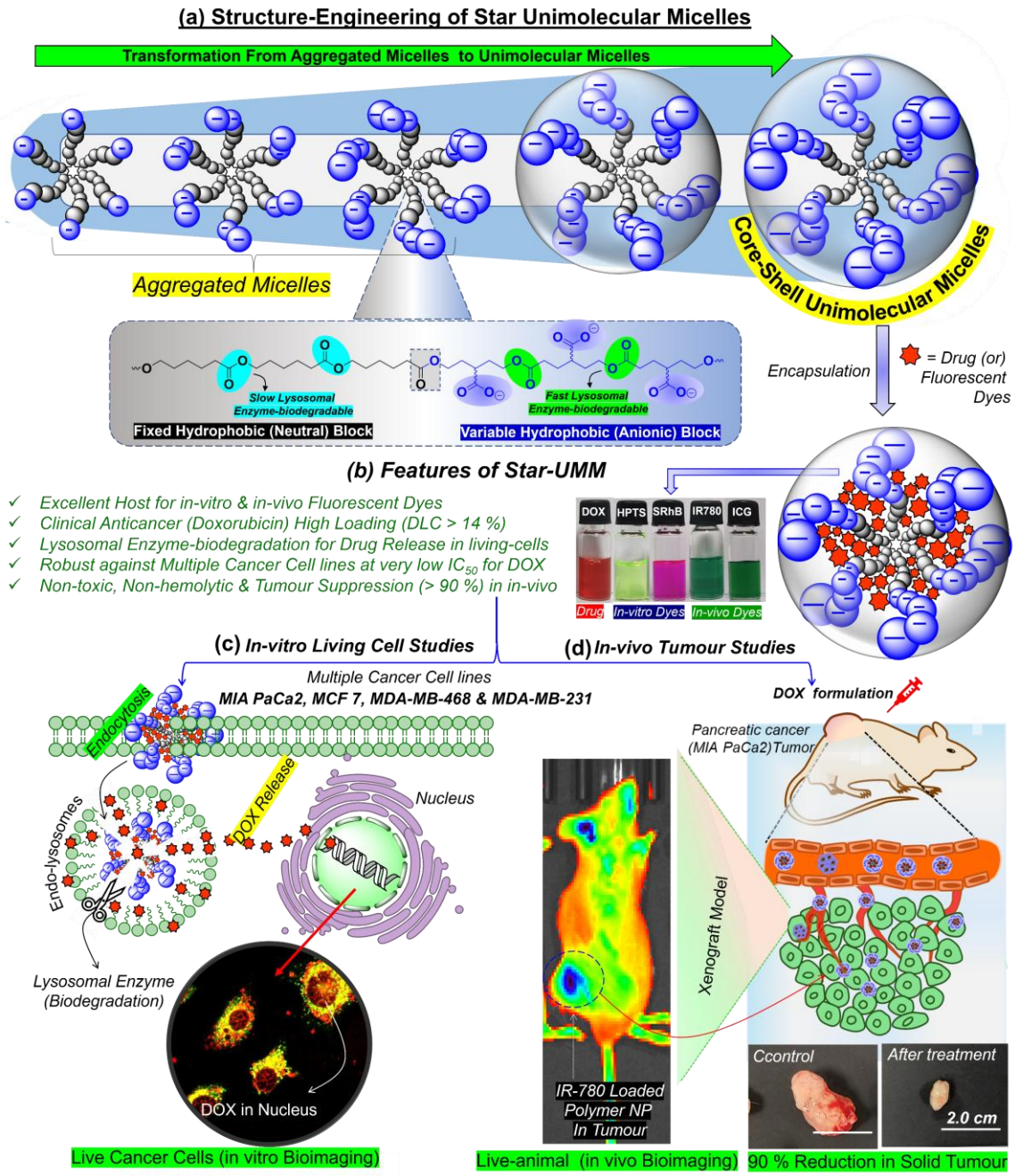

Figure 2.1. *(a) Sutural-engineering of unimolecular micelles in star block copolymers by modulating amphiphilicity and self-assembly aspects. (b) Encapsulation capability of unimolecular micelles. (c) In-vitro evaluation of aggregated and unimolecular micelles for biodegradation in living cells. (d) Tumor xenograft models for the live-animal bioimaging and their ability to suppress the solid tumor growth in mice models.*

2.2 Experimental Section

2.2.1 Materials

1,4-cyclohexanediol, PCC, mCPBA, ε-CL, tin (II) 2-ethylhexanoate, Doxorubicin hydrochloride, near infra-red NIR IR780 iodide, HPTS, thiazolyl blue tetrazolium bromide (MTT), Esterase from Horse liver (HLE), esterase from porcine live, and other chemicals were purchased from Sigma Aldrich. Other chemicals and were purchased locally and purified or used as it was. Tetrahydrofuran (THF), Dichloromethane (DCM), chloroform ($CHCl_3$), dimethyl sulfoxide (DMSO), and other solvents were purchased from Finar solvents and Aldrich. Biological reagents and media were obtained from ThermoFisher Scientific. Cell culture reagents, DMEM media, GIBCO's fetal bovine serum, penicillin-streptomycin antibiotic, Lysotracker DND-26, DAPI and Spectra/Por semi-permeable membrane (MWCO 1KD and 3.5KD) dialysis tubing materials were purchased from ThermoFisher Scientific.

2.2.2 Methods

The Bruker 400 MHz NMR spectrometer was used for analysis of NMRs. Agilent PlGel 20μm Mixed-A with Viscotek VE 3580 RI detector was employed for size exclusion chromatography (SEC) in $CHCl_3$ as eluent and polystyrene as standard. PerkinElmer thermal analyzer STA 6000 used to carry out thermogravimetric analysis (TGA) and TA Q20 Differential Scanning Calorimeter (DSC) used for thermal analysis utilizing N_2 atmosphere with 10°C/min heating/cooling rate. Dynamic light scattering (DLS) measurements were done using Zetasizer ZS-90 with 633 nm laser light and 90^0 angles scattering. HR_TEM images were captured using Joel JEM2200FS 200 KeV systems. Samples were drop-caste on copper grid (formvar) for TEM analysis. Bruker D8 advanced powder X-ray diffractometer was used for analysis of crystallinity of polymers. Shimadzu UV-1900i spectrometer was used for absorbance and transmission measurements. Water contact angle measurements were performed using GBX Model (DIGIDROP instrument) at 25 °C. A Perkin-Elmer Ensight microplate reader was used to record absorbance. CLSM images were captured using Zeiss Anisotropy 710 microscope and processed using ImageJ software. Live animal whole body imaging and biodistribution analysis were done using the Perkin-Elmer IVIS spectrum, Live Imager. Origin 9.0

2.2.3 Synthetic procedures

Synthesis of *tert*-butyl 3((4-hydroxycyclohexyl) oxy) propanoate (Compound 1): This compound was synthesized by following earlier report.[52] Cyclohexane-1,4-diol (35.0 g, 300.00 mmol) in 400 mL dry THF and catalytic amount (1.12g, 10.00 mmol) of potassium *tert*-butoxide were refluxed for 30 minutes under N_2 atmosphere. The content brought to ambient temperature, *tert*-butyl acrylate in 100 mL dry THF was added dropwise, and the reaction was refluxed for 36 h. After completion of the reaction, the mixture was filtered off and filtrate was concentrated. DCM (200 mL) was added to concentrated solution to precipitate unreacted cyclohexane-1,4-diol and filtered off using Buckner filtration setup. Filtrate in DCM was concentrated and purified by column chromatography using 10% v/v Ethyl acetate/pet ether system. Yield = 22.5 g (38%) Colorless oil. ^{1}H NMR (400 MHz, $CDCl_3$) δ ppm: 3.73-3.62 (m, 3H), 3.38 (sept, *J*=6.2 Hz, 0.56H), 3.30-3.23(m, 0.44H), 2.45 (td, *J*=6.5 Hz, 4.9 Hz, 2H), 2.03-1.90, (m, 2H), 1.84-1.76 (m, 2H), 1.72-1.57(m, 2H), 1.44 (s, 9H), 1.31(t, *J*=9.5Hz, 2H). ^{13}C NMR (100 MHz, $CDCl_3$) δ ppm: 171.38, 171.26, 80.56, 76.98, 74.30, 69.74, 68.60, 64.15, 63.74, 36.90, 32.73, 30.55, 29.35, 28.23, 27.63. ATR-FTIR (cm^{-1}): 2937, 2867, 1728, 1454, 1393, 1368, 1251, 1159, 1102, 1058, 846, 765. HRMS (ESI): [M+Na] calcd for $C_{13}H_{24}O_4$, 267.1573; found, 267.1565.

Synthesis of *tert*-butyl 3((4-oxycyclohexyl) oxy) propanoate (Compound 2): Compound 1 (22 g, 90.90 mmol) was charged into 1000 mL round bottom flask and dispersed in 450 mL anhydrous THF. To this, molecular sieves (4Å) were added followed by Potassium chlorochromate (PCC, 39.0 g, 181.00 mmol). The reaction mixture was stirred for 6 hours at room temperature under inert N_2 atmosphere. Reaction progress monitored by TLC using 30% v/v Ethyl acetate/pet ether system as eluent. After completion of reaction, content was filtered on Whatman filter paper and dried over anhydrous Na_2SO_4 and concentrated. Crude product purified using column chromatography using 20% v/v EAPE system as eluent. Yield = 18.8 g (86%) Colorless oil. ^{1}H NMR (400 MHz, $CDCl_3$) δ ppm: 3.78-3.67 (m, 3H), 2.60-2.53 (m, 2H), 2.50 (t, *J*=6.2 Hz, 2H), 2.26-2.19 (m, 2H), 2.13-2.06 (m, 2H), 1.93-1.84 (m, 2H), 1.89 (s, 9H). ^{13}C NMR (100 MHz, $CDCl_3$) δ ppm: 211.66, 171.19, 80.76, 72.93, 64.19, 37.19, 3673, 30.58, 28.22. ATR-FTIR (cm^{-1}): 2977, 1722, 1393, 1367, 1248, 1157, 1109, 1041, 846, 757. HRMS (ESI): [M+Na] calcd for $C_{13}H_{22}O_4$, 265.1416; found, 266.0693.

Synthesis of *tert*-butyl 3((7-oxooxepan-4-yl) oxy) propanoate (Monomer M2): $NaHCO_3$(10.41 g, 125 mmol) and mCPBA (3-cholorperbenzoic acid, 14.24 g, 82.70 mmol)

were added into compound 3 (10 g, 41.32 mmol) in dry DCM (300 mL). The reaction was continued as described for monomer M1 and purification was done by column chromatography using 10% v/v Ethyl acetate/pet ether system as eluent. Yield = 8.4 g (78 %) Colorless oil. ^{1}H NMR (400 MHz, $CDCl_3$) δ ppm: 4.47 (dd, *J*=12.7 Hz, 10.3 Hz, 10.3 Hz, 1H), 4.02 (qd, *J*=6.1 Hz, 1H), 3.70-3.61 (m, 3H), 2.96 (td, 14.1 Hz, 2H), 2.46 (t, *J*= 6.1 Hz, 2H), 2.40, (m, 1H), 2.08-1.76 (m, 4H), 1.44 (s, 9H). ^{13}C NMR (100 MHz, $CDCl_3$) δ ppm: 176.29, 171.10, 80.83, 74.04, 64.05, 63.43, 36.58, 33.96, 28.22, 27.89, 27.41. ATR-FTIR (cm^{-1}): 2979, 1752, 1478, 1443, 1392, 1367, 1289, 1234, 1154, 1100, 1060, 846, 756. [M+Na] calcd for $C_{13}H_{22}O_5$, 281.1364; found, 281.1364.

Synthesis of SMI (Star-PCL60 Macroinitiator): The polymerization was carried out in custom-made melt reactor to overcome the viscosity-build-up during ring opening polymerization (ROP). [ref] ε-Caprolactone monomer (1.0 g, 8.76 mmol), was taken into custom-made melt reactor with Di-pentaerythritol (37.1 mg, 0.14 mmol). The catalyst $Sn(Oct)_2$ (30 mg, 0.08 mmol) was then added, and tube was vacuum sealed by applying vacuum of 10^{-2} mbar for 45 min at 25 ºC . Then polymerization (ROP) was carried out for 8 hours at 110 ºC and polymer was cooled to ambient temperature. The content was then dissolved in 2mL tetrahydrofuran (THF) and precipitated in cold methanol (70mL). After precipitation the polymer was filtered and dried in vacuo. Yield = 0.91 g (90%). ^{1}H NMR (400 MHz, $CDCl_3$) δ ppm: 4.05 (t, *J* = 6.7 Hz, 120H), 3.64 (t, *J* = 6.5 Hz, 12H), 3.37 (m, 4H), 2.30 (t, *J* = 7.5 Hz, 122H), 1.64 (m, 240H), 1.37 (m, 121H). ^{13}C NMR (100 MHz, $CDCl_3$) δ ppm: 173.70, 64.28, 62.89, 34.25, 32.46, 28.47, 25.66, 24.81. ATR-FTIR (cm^{-1}): 3041, 2864, 1724, 1462, 1419, 1365, 1294, 1161, 1104, 1045, 926, 749.

Synthesis of SB-12tBu (Star-PCL60-*b*-*t*BuPCL-12): M2 monomer (300 mg, 1.20 mmol), SMI macroinitiator (690 mg, 0.10 mmol), $Sn(Oct)_2$ (20 mg, 0.05 mmol). Polymerization was done for 2 hours at 130 ºC and precipitated in cold mixture of hexane in diethyl ether (60mL). Yield = 0.85 g (85%). ^{1}H NMR (400 MHz, $CDCl_3$) δ ppm: 4.15-4.11 (m, 24H), 4.05 (t, 122H), 3.66-3.62 (m, 34H), 3.46-3.43 (m, 16H), 2.43 (t, 25H), 2.36 (t, 25H), 2.33 (t, 122H), 1.88-1.76 (m, 70H), 1.68-1.60 (m, 260H), 1.44 (s, 120H), 1.41-1.33(m, 122H). ^{13}C NMR (100 MHz, $CDCl_3$) δ ppm: 173.66, 173.60, 170.96, 80.67, 75.59, 64.88, 64.24, 61.21, 36.55, 34.20,29.42, 28.16, 25.61, 24.66. ATR-FTIR (cm^{-1}): 2938, 1728, 1365, 1156, 1100.

Synthesis of SB-24tBu (PCL60-*b*-*t*BuPCL-24): M2 monomer (400 mg, 1.55 mmol), SMI macroinitiator (470 mg, 0.06 mmol), $Sn(Oct)_2$ (13 mg, 0.04 mmol). Polymerization was done

for 4 hours at 130 ºC and precipitated in cold mixture of hexane in diethyl ether (60mL). Yield = 0.77 g (88%). ^{1}H NMR (400 MHz, $CDCl_3$) δ ppm: 4.15-4.11 (m, 47H), 4.05 (t, 122H), 3.66-3.62 (m, 60H), 3.46-3.43 (m, 28H), 2.43 (t, 48H), 2.36 (t, 49H), 2.33 (t, 122H), 1.88-1.76 (m, 110H), 1.68-1.60 (m, 260H), 1.44 (s, 220H), 1.41-1.33(m, 123H). ^{13}C NMR (100 MHz, $CDCl_3$) δ ppm: 173.70, 173.60, 170.99, 80.72, 75.62, 64.91, 64.28, 61.36, 36.59, 34.24, 33.03, 29.77, 29.03, 28.47, 28.20, 25.65, 24.69. ATR-FTIR (cm^{-1}): 2932, 1730, 1366, 1158, 1102.

Synthesis of SB-36tBu (Star-PCL60-*t*BuPCL-36): M2 monomer (535 mg, 2.00 mmol), SMI macroinitiator (420 mg, 0.06 mmol), $Sn(Oct)_2$ (12 mg, 0.03 mmol). Polymerization was done for 6 hours at 130 ºC and precipitated in cold mixture of hexane in diethyl ether (60mL). Yield = 0.77 g (88%). ^{1}H NMR (400 MHz, $CDCl_3$) δ ppm: 4.15-4.11 (m, 66H), 4.05 (t, 122H), 3.66-3.62 (m, 78H), 3.46-3.43 (m, 39H), 2.43 (t, 64H), 2.36 (t, 60H), 2.33 (t, 122H), 1.88-1.76 (m, 184H), 1.68-1.60 (m, 306H), 1.44 (s, 258H), 1.41-1.33(m, 122H). ^{13}C NMR (100 MHz, $CDCl_3$) δ ppm: 173.69, 173.60, 170.99, 80.70, 75.59, 68.10, 64.28, 61.37, 36.60, 34.25, 33.04, 29.82, 29.04, 28.48, 28.22, 25.74, 24.71. ATR-FTIR (cm^{-1}): 2933, 1730, 1366, 1158, 1102.

Synthesis of SB-48tBu (Star-PCL60-*b*-*t*BuPCL-48): M2 monomer (600 mg, 2.30 mmol), SMI macroinitiator (354 mg, 0.05 mmol), $Sn(Oct)_2$ (10 mg, 0.02 mmol). Polymerization was done for 8 hours at 130 ºC and precipitated in cold mixture of hexane in diethyl ether (60mL). Yield = 0.79 g (82%). ^{1}H NMR (400 MHz, $CDCl_3$) δ ppm: 4.15-4.11 (m, 86H), 4.05 (t, 122H), 3.66-3.62 (m, 110H), 3.46-3.43 (m, 52H), 2.43 (t, 92H), 2.36 (t, 92H), 2.33 (t, 130H), 1.88-1.76 (m, 238H), 1.68-1.60 (m, 319H), 1.44 (s, 405H), 1.41-1.33(m, 124H). ^{13}C NMR (100 MHz, $CDCl_3$) δ ppm: 173.72, 173.63, 171.02, 80.74, 75.65, 64.94, 64.30, 61.37, 46.86, 36.61, 34.25, 33.04, 29.05, 28.49, 28.22, 25.74, 24.71. ATR-FTIR (cm^{-1}): 2933, 1729, 1366, 1157, 1102, 847.

Synthesis of SB-60tBu (Star-PCL60-*b*- *t*BuPCL-60): M2 monomer (700 mg, 2.71 mmol), SMI macroinitiator (325 mg, 0.04 mmol), $Sn(Oct)_2$ (55 mg, 0.13 mmol). Polymerization was done for 12 hours at 130 ºC and polymer precipitated in a cold mixture of hexane in diethyl ether (70mL). Yield = 0.84 g (82%). ^{1}H NMR (400 MHz, $CDCl_3$) δ ppm: 4.15-4.11 (m, 124H), 4.05 (t, J = 6.7 Hz, 120H), 3.65 (m, 133H), 3.44 (bs, 68H), 2.44 (t, J = 6.3 Hz, 128H), 2.40 – 2.33 (t, 121H), 2.30 (t, J = 7.6 Hz, 121H), 1.80-1.72 (m, 312H), 1.64 (m, 292H), 1.44 (s, 591H), 1.40-1.34 (m, 122H). ^{13}C NMR (100 MHz, $CDCl_3$) δ ppm: 173.70, 173.6, 171.0, 80.0, 75.60, 64.95, 64.30, 61.30, 46.8, 36.6, 34.2, 33.0, 29.0, 28.50, 28.25, 25.75, 24.70. ATR-FTIR (cm^{-1}): 2931, 1728, 1366, 1157, 1103, 847.

General procedure for deprotection: Typically, all linear and star block copolymers were deprotected using mild acid trifluoracetic acid (TFA) in dichloromethane (DCM) in cold condition. Polymer was taken in round bottom flask and dissolved into DCM and cooled to 0^0C. TFA was added along walls of flask slowly and reaction content was stirred 40 minutes at cold condition then TFA and DCM were evaporated using rotary evaporator and polymer was precipitated in in cold mixture of hexane in diethyl ether (30mL) twice. Solvent decanted and polymer dried in vacuo.

Synthesis of SB-12 (Star-PCL60-*b*-CPCL-12): Star-PCL60-*b*-*t*BuPCL-12 (225 mg), TFA (2.25 mL), DCM (4 mL). After deprotection polymer was precipitated in cold mixture of hexane in diethyl ether (30mL). Yield = 150 mg. ^{1}H NMR (400 MHz, DMSO-d_6) δ ppm: 4.05-4.01 (m, 24H), 3.97 (t, 122H), 3.57-3.54 (m, 34H), 3.39-3.35 (m, 16H), 2.39 (t, 25H), 2.31 (t, 25H), 2.26 (t, 122H), 1.73-1.63 (m, 70H), 1.56-1.48 (m, 260H), 1.32-1.25(m, 122H). ^{13}C NMR (100 MHz, DMSO-d_6) δ ppm: 172.77, 171.18, 63.49, 60.53, 33.52, 33.37, 32.15, 27.81, 25.05, 24.90, 24.43, 24.09. ATR-FTIR (cm^{-1}): 2927, 1734, 1460, 1275, 1460, 1275, 1260, 1164, 1102, 764, 754, 615.

Synthesis of SB-24 (Star-PCL60-*b*-CPCL-24): Star-PCL60-*b*- *t*BuPCL-24 (260 mg), TFA (2.6 mL), DCM (5 mL). After deprotection polymer was precipitated in cold mixture of hexane in diethyl ether (30mL). Yield = 150 mg. ^{1}H NMR (400 MHz, DMSO-d_6) δ ppm: 4.05-4.01 (m, 47H), 3.97 (t, 122H), 3.57-3.54 (m, 60H), 3.39-3.35 (m, 28H), 2.39 (t, 48H), 2.31 (t, 49H), 2.26 (t, 122H), 1.73-1.63 (m, 110H), 1.56-1.48 (m, 260H), 1.32-1.25(m, 122H).^{13}C NMR (100 MHz, DMSO-d_6) δ ppm: 172.77, 172.65, 74.88, 64.22, 63.50, 60.77, 34.91, 33.51, 32.38, 32.16, 29.07, 28.62, 27.80, 24.86, 24.89, 24.09. ATR-FTIR (cm^{-1}): 2946, 1731, 1358, 1275, 1260, 1166, 1103, 764, 749.

Synthesis of SB-36 (Star-PCL60-*b*-CPCL-36): Star-PCL60-*b*-*t*BuPCL-36 (300 mg), TFA (3.0 mL), DCM (6 mL). After deprotection polymer was precipitated in cold mixture of hexane in diethyl ether (30mL). Yield = 240 mg. ^{1}H NMR (400 MHz, DMSO-d_6) δ ppm: 4.05-4.01 (m, 66H), 3.97 (t, 123H), 3.57-3.54 (m, 78H), 3.39-3.35 (m, 39H), 2.39 (t, 64H), 2.31 (t, 60H), 2.26 (t, 122H), 1.73-1.63 (m, 184H), 1.56-1.48 (m, 307H), 1.32-1.25(m, 122H). ^{13}C NMR (100 MHz, DMSO-d_6) δ ppm: 172.88, 172.75, 172.65, 74.89, 64.24, 63.52, 60.77, 34.93, 33.54, 33.39, 32.39, 32.17, 29.37, 27.82, 25.07, 24.99, 24.91, 24.37, 24.10. ATR-FTIR (cm^{-1}): 2928, 1731, 1713, 1461, 1359, 1275, 1260, 1167, 1104, 764, 749.

Synthesis of SB-48 (Star-PCL60-*b*-CPCL-48): Star-PCL60-*b*- *t*BuPCL-48 (300 mg), TFA (3.0 mL), DCM (6 mL). After deprotection polymer was precipitated in cold mixture of hexane in diethyl ether (30mL). Yield = 270 mg. ^{1}H NMR (400 MHz, DMSO-d_6) δ ppm: 4.05-4.01 (m, 86H), 3.97 (t, 123H), 3.57-3.54 (m, 110H), 3.39-3.35 (m, 52H), 2.39 (t, 92H), 2.31 (t, 94H), 2.26 (t, 124H), 1.73-1.63 (m, 238H), 1.56-1.48 (m, 319H), 1.32-1.25(m, 122H). ^{13}C NMR (100 MHz, DMSO-d_6) δ ppm: 172.88, 172.75, 172.68, 74.87, 64.23, 60.76, 34.91, 33.36, 32.39, 29.28, 28.62, 27.81, 24.89, 24.05. ATR-FTIR (cm^{-1}): 2956, 2921, 1730, 1712, 1460, 1274, 750.

Synthesis of SB-60 (Star-PCL60-*b*-CPCL-60): Star-PCL60-*b*- *t*BuPCL-60 (300 mg), TFA (3.0 mL), DCM (6 mL). After deprotection polymer was precipitated in cold mixture of hexane in diethyl ether (30mL). Yield = 250 mg. ^{1}H NMR (400 MHz, DMSO-d_6) δ ppm: 4.05 (m, 124H), 3.98 (t, 121H), 3.56 (m, 123H), 3.46 – 3.31 (m, 76H), 2.39 (t, 120H), 2.32 (m, 121H), 2.27 (m, 120H), 1.71 (m, 240H), 1.54 (h, 238H), 1.30 (m, 120H). ^{13}C NMR (100 MHz, DMSO-d_6) δ ppm: 172.8, 172.7, 172.7, 74.9, 64.2, 60.7, 34.9, 33.4, 32.4, 29.4, 28.6, 27.8, 24.8, 24.0. ATR-FTIR (cm^{-1}): 2952, 1729, 1712, 1356, 1259, 1166, 1102, 750.

2.2.4 Self-assembly, nanoparticle characterization

All the deprotected polymers SB-x were self-assembled using the dialysis method. Typically, 5 mg polymer was dissolved in 0.6 mL of DMSO and slowly added to 4.2 mL deionized water with constant stirring for 4h. Then content was transferred to semipermeable membrane (Spectra/Por CE cellulose ester membrane, MWCO 3.5KD) and dialyzed against fresh water for 24h while replenishing with fresh water each hour to remove DMSO. Finally, the content was filtered stored at 4 ºC until further analysis. The sizes of self-assembled nanoparticles were measured using DLS at the concentration of 0.1 mg/mL. The sizes and zeta potential measurements of nanoparticles were done in water or pH 7.4, Britton-Robinson 10 mM buffer. All measurements were carried out at least three independent times and obtained results are expressed as a means with standard deviation.

2.2.5 CMC determination

Critical micellar concentration (CMC) was determined using pyrene as an environment sensitive probe. Precoated vials with a fixed concentration of pyrene (0.6 μmol, 3.6×10^{-7} g/mL) were added with various concentrations ranging from 1.0×10^{-6} mg/mL to 0.5 mg/mL of self-assembled SB-x polymers to prepare the solution and these solutions were sonicated for 3h followed by overnight equilibration. These solutions were subjected to fluorescence

measurements using 337 nm excitation wavelength and emission was collected from 350 nm to 500 nm. The ratio of PL intensities of vibronic levels corresponding to I_1 (372 nm) and I_3 (382 nm) was plotted against concentration to calculate the CMC.

2.2.6 Water contact angle measurements

Water contact angle (WCA) was measured using GBX Model (DIGIDROP instrument) at 25 °C. Polymers were dissolved in minimum amount of dichloromethane and a thin film was cast by solution casting on glass slides and air dried. Then a drop of distilled water was plunged using a 1mL syringe on thin film and images were captured using DIGIDROP instrument and images were analyzed for water contact angle in ImageJ software.

2.2.7 Encapsulation and stability studies

Doxorubicin (DOX) was used as model drug for encapsulation studies for SB-x polymers. Typically, 5 mg polymer and pre neutralized Doxorubicin (0.5 or 1.0 or 2 mg) were dissolved in 0.8 mL HPLC grade DMSO and slowly mixed with 4.2 mL deionized water with moderate stirring at room temperature and subsequently dialyzed against deionized water for 48hours using 3.5KD dialysis membrane. Water in the container was replenished each hour with fresh water to remove DMSO and unencapsulated drug molecules. At the end DOX encapsulated nanoparticles solutions were filtered using 0.45 μ PES syringe filters. DOX concentrations were calculated by measuring absorbance and using Lambert-Beer law which were used for determination of drug loading content (DLC). A similar strategy was used to encapsulate the other drug or dyes such as HPTS, Sulforhodamin-b (SRhB), Cardio green (ICG) and IR780 iodide. The drug loading content (DLC) and drug loading efficiency (DLE) were calculated as described in our previous report using equation 1 and 2.[55,59]

$$\text{Drug loading content (DLC \%)} = (\text{Total weight of drug encapsulated in Nanoparticles} / \text{Weight of Nanoparticle taken}) \times 100 \quad \ldots.(1)$$

$$\text{Drug loading efficiency (\%)} = (\text{Total weight of drug encapsulated inside Nanoparticles} / \text{Total Weight of drug taken in feed}) \times 100 \quad \ldots.(2)$$

The stability of AgM+DOX and UMM+DOX nanoparticles were tested on fetal bovine serum (FBS). For that Purpose, nanoparticles (1mg/mL) were incubated in 10% fetal bovine serum (FBS) containing PBS (pH 7.4, 1x) at 37°C. Size of the nanoparticles were DLS measured by periodically for more than 7 days. The experiment was done in triplicate and plotted in the form of average size versus incubation time.

2.2.8 *In vitro* enzymatic release studies

The *in vitro* release kinetic studies of doxorubicin loaded nanoparticles were investigated for enzymatic biodegradation using horse liver esterase (HLU, 3 U) enzyme. 1 mL of DOX loaded nanoparticle and 3 mg of esterase enzyme were taken together in dialysis tube (MWCO 1KD) and immersed 3mL of PBS, pH 7.4 in reservoir incubated at 37 °C. For the control, the DOX loaded nanoparticles were incubated in PBS, pH 7.4 without any enzyme. 2mL of solutions from reservoir was taken out and subjected for absorbance measurements at regular intervals. At each measurement 2.0 mL was taken to measure the absorbance, the solution is transfer back to the reservoir again. Therefore, eventually, there is no loss of the solution. The amount of DOX release was estimated as previously described method [59] by using equation 3, and cumulative drug release plotted against time.

$$\text{Cumulative release (\%)} = (C_t \times V_{PBS} / C_0) \times 100 \quad \ldots.(3)$$

where C_t = total amount of DOX released at time interval 't', V_{PBS} = volume of PBS taken in reservoir and C_0 = initial amount of DOX present in nanoparticles taken for release.

2.2.9 Enzymatic degradation studies

The enzymatic biodegradation of star block copolymer was studied by turbidity measurements, DLS, NMR and MALDI-TOF techniques. the porcine liver esterase enzyme (28U/mg) was utilized. Typically, 5mg of SB-60 (UMM) polymer was dissolved in 5 mL of PBS, pH 7.4 (1mg/mL) and incubated at 37 ºC with moderate stirring. The esterase enzyme (5mg) was added to it. The % transmittance (measure of turbidity) and DLS size were measured at every 2h till 48h. For the control, the UMM was dissolved in PBS (1mg/mL) without enzyme. The % transmittance at 600 nm was utilized as measure of turbidity and plotted against time. Similarly, in another experiment, UMM (10mg) and esterase (10mg) were incubated in PBS, pH 7.4 at 37 ºC, and aliquots were removed at regular intervals and content was lyophilized for further analysis by 1H NMR/ MALDI-TOF.

2.2.10 Cell culture methods

Wild type mouse embryonic fibroblast (WT-MEF), Breast cancer (MCF-7), triple negative breast cancer (MDA-MB-231, MDA-MB468), and pancreatic cancer (MIA PaCa2) cells were cultured using Dulbecco modified eagle medium (DMEM) supplemented with 10% fetal bovine serum (FBS) and 1% penicillin-streptomycin (PenStrep). The cells were cultured in an incubator with a humidified 5% CO_2 atmosphere at 37 ºC.

2.2.11 Cell viability assay (MTT assay)

The cytotoxicity of nascent nanoparticles, DOX loaded nanoparticles were determined using (3-(4,5-dimethylthiazol-2-yl)-2,5-diphenyltetrazolium bromide), tetrazolium dye (MTT) assay. Cells with density of 1000 per well seeded in 96-well plate seeded in 100 µL media and adhered for 16h prior to compound addition. Then the media was replaced with 300 µL media containing nascent nanoparticles, free DOX and DOX loaded nanoparticles subsequently incubated for 72h at similar condition. A column was added only with fresh media as a control. After that the media was aspirated and replaced by MTT solution (100 µL, 0.5mg/mL in media) and further incubated for 4h. Finally, the MTT solution was aspirated and DMSO (100 µL) was added to each well to dissolve the purple formazan crystals and plates were subjected to absorbance measurements at 570 nm and cell viability was estimated.

2.2.12 Cellular uptake via confocal microscopy imaging (CLSM)

Cellular uptake studies were performed by using confocal laser microscopy (CLSM). WT-MEF, MCF-7, MDA-MB-231, MDA-MB-468, and MIA PaCa2 cells with density of 1×10^5 cells per well seeded onto glass cover slip in 6-well plates in 2mL media. After 16h of incubation the media was replaced with fresh media containing free DOX, and DOX loaded nanoparticle (concentration of DOX 2.5 µg/mL) and incubated for desired time and the cells were fixed with 3.5% PFA solution followed by co-staining with DAPI or phalloidin. Then cover slips were fixed on glass slides and visualized using Zeiss anisotropy confocal microscope with the lasers of λ=405 nm (blue channel for DAPI/ CPT/CUR), λ=488 nm (green channel for DOX). CLSM images processed in ImageJ software and CTCF (corrected total cell fluorescence) were calculated. Similar protocol was used for HPTS and SRhB loaded UMM nanoparticles. Lasers of λ=405 nm (for HPTS), λ=488 nm (phalloidin), λ=561 nm (red channel for SRhB) and λ=633 nm (red channel for SYTO nuclei dye).

2.2.13 Temperature dependent Cellular uptake studies through CLSM

Temperature dependent cellular uptake was studied for endocytosis. For this purpose, 1×10^5 cells of MCF-7 cells line were seeded onto glass cover slip per well in 2 mL medium in 6-well plate and incubated for 16 h prior to treatment. Media was replaced with media containing AgM+DOX and UMM+DOX (DOX concentration 2.5 µg/mL) and incubated at 37 °C and 4 ^{o}C for 3h. After incubation the cells were fixed and imaged as described earlier and processed using ImageJ software.

2.2.14 Time dependent Cellular uptake studies through CLSM

MCF-7 cells (1×10^5) were seeded onto each glass cover slip in 6-well plate and incubated for 16 h. Media was replaced with fresh media containing UMM+DOX (DOX concentration 2.5µg/mL) and incubated for 30 min to 8 h and later the cells were fixed and co-stained with DAPI and visualized using CLSM. CLSM images were further processed in ImageJ software.

2.2.15 Live cell imaging using CLSM

Live cell lysotracker imaging was carried out using CLSM to understand enzymatic biodegradation in endo-lysosomal compartment of cells. 50,000 MCF-7 cells were seeded in multi-well confocal chamber and incubated for 16h. After ensuring adherence of cells the media was aspirated and AgM+DOX or UMM+DOX nanoparticles (DOX 2.5µg/mL) in 1 mL fresh media were added and incubated for 30 min. After that the media was aspirated and 1 mL of fresh media containing lysotracker green DND-26 (100 nM) was added and incubated for another 30 minutes. Then the lysotracker was removed and cells were washed with PBS (1x) and cells were visualized using Zeiss Anisotropy microscope for desired timepoints. Lysotracker green and DOX were visualized using λ=488 nm and λ=561 nm laser. The CLSM images were processed using ImageJ software. Similar protocols were followed for live-cell imaging in MIA PaCa 2 cells.

2.2.16 Animal handling, and Experimentation

All the animal experiments were carried out at National Facility for Gene Function in Health and Diseases (NFGFHD, IISER Pune, India) under the guidelines of Institutional Animal Ethics Committee India (IAEC). Healthy Balb-C (6-8-week-old) and NOD-SCID (6-8-week-old) mice were used for the experiments.

2.2.17 Hemolysis assay

The hemolysis assay was performed to understand the compatibility of nanoparticles with red blood cells (RBC). A healthy Balb-C mouse (6–8-week-old) was anesthetized using isoflurane and 0.5mL blood was withdrawn from retro-orbital plexus in 5% EDTA pre-coated centrifuge tube. The blood was then centrifuged at 5000 rpm for 10 minutes, supernatant plasma was removed carefully, and RBC pellet was washed with PBS buffer. The RBC was diluted with PBS buffer (5% v/v) and used for further assay. The RBC solution (100 µL per well) was added in 96-well and added with the nanoparticle's solutions (in PBS 100 µL, 1 mg/mL). Triton-X (1% v/v) was used as positive control (100% hemolytic activity), and PBS was as negative control (no hemolysis) for the assays. Plates were incubated at 37 ºC for 1h and the content

was centrifuged at 5000 rpm. 100 µL from each well was then transferred to another plate and subjected to absorbance measurement using λ =576 nm wavelength in microplate reader. Percentage hemolysis was calculated based on our earlier reports by using equation 4.[56]

$$\text{Hemolysis (\%)} = [(\text{O.D. at 576nm in polymer solution} - \text{O.D. at 576nm PBS buffer}) / (\text{O.D. at 576nm in Triton X} - \text{O.D. at 576nm PBS buffer})] \times 100 \quad \ldots.(4)$$

2.2.18 *In vivo* biodistribution via IVIS imaging

In-Vivo Imaging System (IVIS spectrum Perkin-Elmer) was utilized for the near infrared fluorescence whole body live animal imaging biodistribution studies equipped with excitation source of 745 nm and emission filter of 800 nm. NOD-SCID mice with subcutaneous tumors (~80-100 mm^3) were intraperitoneally injected with IR780 loaded nanoparticles (*n=3*). IR-780 iodide is an advantageous near infrared fluorescent dye used for biodistribution studies due to minimum background and deep tissue penetration ability of IR wavelength. Typically, the animals were injected with AgM+IR780 and UMM+IR780 (0.7mg/kg of IR780) in 100 µL PBS, and for control group animals were injected with free IR780 (5% DMSO in 100 µL PBS) of similar dose. Live animal imaging was carried out for 4, 24, 48, 72 and 96 h using Isoflurane I.P. anesthesia and finally the animals were sacrificed for organ collection. The animals were anesthetized, pericardially perfused with PBS buffer followed by collection of major organs and tumors. Harvested organs were washed with PBS and imaged with IVIS. All the IVIS images were then processed using IVIS spectrum Living Image 4.7 software (PerkinElmer).

2.2.19 Pancreatic cancer Xenograft Tumor model and Anticancer Efficacy

6-8-week-old healthy NOD-SCID animals were obtained from NFGFHD, IISER Pune, India. 2×10^6 MIA PaCa2 cells (human Pancreatic Carcinoma) in 100 µL PBS buffer were subcutaneously injected into the right flanks of the animals. Treatment study started once tumor reached ~70 mm^3 volume. All the animals were divided into 4 groups (*n=4*), group one served as control group was injected intraperitoneally with 100 µL volume of PBS, pH 7.4 buffer (1x) every fourth day. The second group was intraperitoneally injected with Doxorubicin.HCl (2mg/kg) in 100 µL PBS every fourth day. The third and fourth groups were intraperitoneally injected with AgM+DOX and UMM+DOX (2mg/kg) in 100 µL PBS every fourth/fifth day respectively. Each group received a total of 5 injections throughout the study. The body weights and tumor volume were measured with digital caliper using the formula [0.5 × (length × $width^2$)]. After termination the animals were euthanized using CO_2 and tumors were harvested, weighed and fixed with 4% neutral formalin (NBF) for further studies.

2.2.20 Statistical analysis

All the statistical analysis was performed using GraphPad prism 8.0 software. Results are expressed as mean ± SD ($n \geq 3$). For multiple comparison t-tests, one-way ANOVA test and two-way ANOVA tests were used to perform statistical analysis. $*p < 0.05$ was considered statistically significant.

2.3 Results and Discussion

2.3.1 Synthesis and Characterization

The rationale of the current study was to understand the role of amphiphilicity in the transition from aggregated micelles to unimolecular micelles by structural designing the 6-arm star shaped core-shell block co-polymers. The core and shell are constructed with fixed length of hydrophobic PCL units and variable length of γ-substituted carboxylic PCL units as shown in Figure 2.2a. Monomer M2 was synthesized using our previously reported[52] multistep protocol from 1.4-cyclohexane-diol as shown in Scheme 2.1. The 6-arm star-hydrophobic PCL core was synthesized by ring opening polymerization (ROP) of commercial ε-caprolactone monomer (ε-CL, M1) using dipentaerythritol as a 6-arm alcohol initiator (M/I=60) in the presence of $Sn(Oct)_2$ catalyst (see Scheme 2.2). By ^{1}H-NMR analysis the degree of polymerization (DP) was estimated to be 60 which suggests the statistically distribution of 10 units in each arm (see ^{1}HNMR of PCL macroinitiator in Appendix). This star-PCL was employed as macroinitiator for the subsequent ROP of *t*BuPCL monomer **M2** (*t*-butyl carboxylic ester γ-substituted ε-caprolactone) by varying the M/I ratio from 12, 24, 36, 48 and 60 (statistically 2, 4, 6, 8 and 10 per arm) as shown in Scheme 2.2. The ^{1}H-NMR spectrum of star polymer synthesized for M/I=60 is shown in Figure 2.2b, and peaks are assigned alphabetically with respect to its structure. The degree of polymerization (DP) was estimated by comparing the integration of peak ***a*** corresponding to -C**H**$_2$-O-C=O- of ester backbone in the PCL segments to the peak ***a'*** corresponding to -C**H**$_2$-O-C=O- or peak ***d*** corresponding to -C**H**$_2$-C=O- of *t*BuPCL units. By this method, the DP in the resultant 6-arm star di-block copolymers were estimated to have statistically 2, 4, 6, 8 and 10 *t*BuPCL repeating units per arm (see their NMR details in Appendix) and exhibited very good control in the ROP process.

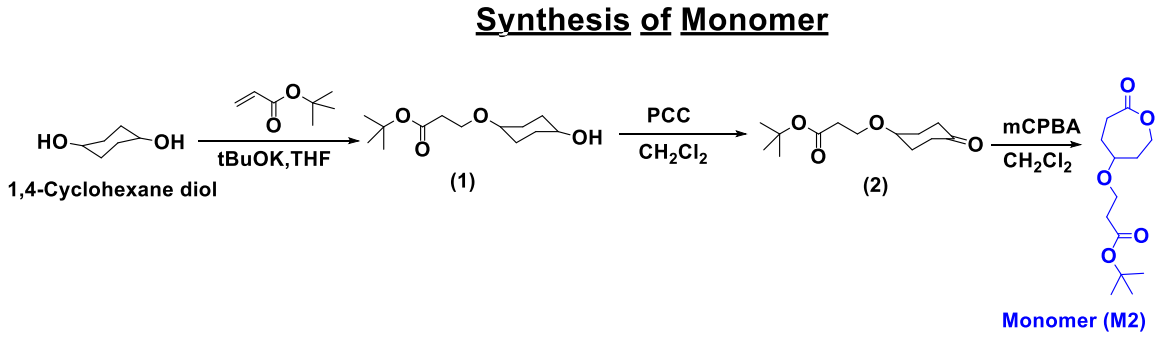

Scheme 2.1. *Multistep synthesis of monomers M2 from 1.4-cyclohexan-diol. Diol was mono-functionalized with t-Butyl acrylate (Michael addition) followed by PCC oxidation and Baeyer-Villiger Oxidation to get Monomer M2.*

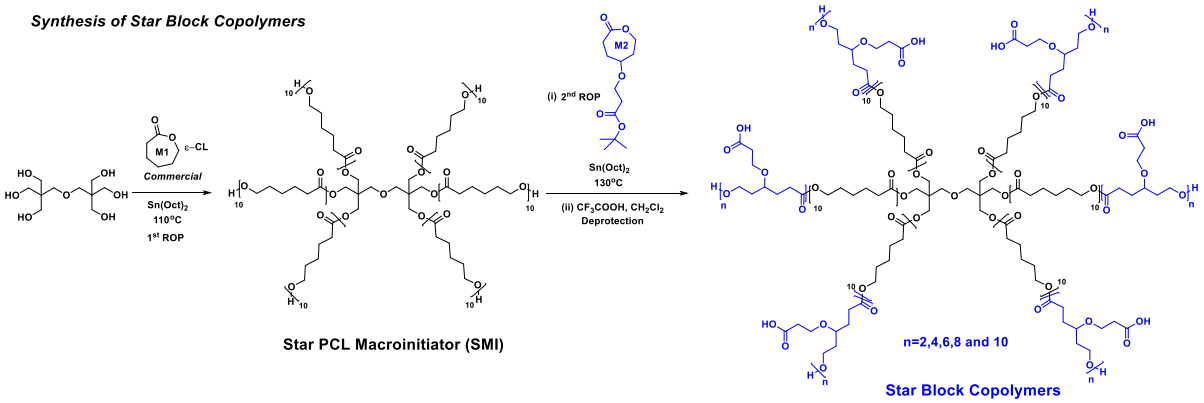

Scheme 2.2. *Synthesis of star PCL macroinitiator and star block copolymers by varying the M/I ratio of 2nd ROP using Sn(Oct)2 catalyst. The tButyl ester were deprotected using trifluoracetic acid to yield star block copolymers having carboxylic acid pendent groups.*

The molecular weights and distribution of the star block copolymers were analyzed using the size exclusion chromatography (SEC) equipped with RI detector in $CHCl_3$ eluent and the polystyrene was used as standard for calibration at 25 ºC. SEC traces of *t*Butyl-protected diblock copolymers and SMI (star PCL macroinitiator) are shown in Figure 2.3a. All the polymers exhibited monomodal distributions with narrow polydispersity index (Đ) ranging from 1.2 to 1.6 and well-defined molecular weights (M_w, M_n) and details are tabulated in Figure 2.3b. The SEC based number average molecular weights (M_n) were in good agreement with the obtained M_n from 1H-NMR analysis. As expected, the diblock copolymers with a greater number of *t*BuPCL units eluted earlier compared to lesser units as well as SMI, suggesting the control over ROP. The *t*Butyl ester group was subjected to acid catalyzed deprotection to yield carboxylic-PCL amphiphilic block copolymers referred as SB-x where x represents the total number of carboxylic acid PCL (CPCL) units in all 6-arms together (x=12, 24, 36, 48, and 60 for SB-12, SB-24, SB-36, SB-48 and SB-60). The t-butyl ester de-protection was confirmed by disappearance of the peak at 1.45ppm corresponding to t-Butyl groups in ^{1}H-NMR. The stack plot of 1H-NMR for deprotected polymers is shown in Figure 2.4. ^{1}H-NMR of deprotected polymers revealed that DP was not affected by acid-catalyzed deprotection, and structure had remained intact. The integration values as well as the nature of peaks were preserved and suggested acid catalyzed deprotection did not cause any polyester backbone cleavage.

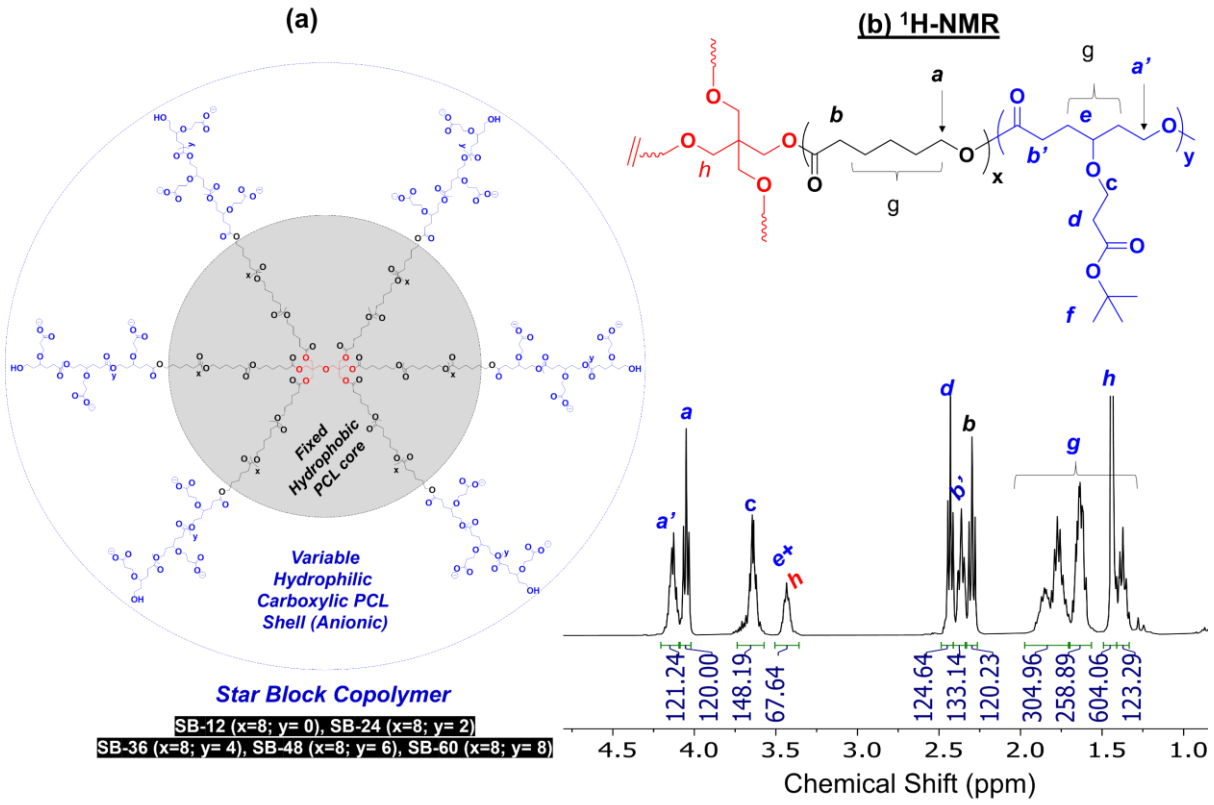

Figure 2.2. *(a) Structure of star block copolymers synthesized by varying the M/I ratio of 2nd ROP. (b) [1]H-NMR spectra of tButyl ester protected SB-60 block copolymer (SB-60tBu) and peaks are assigned alphabetically.*

(a) SEC elution traces

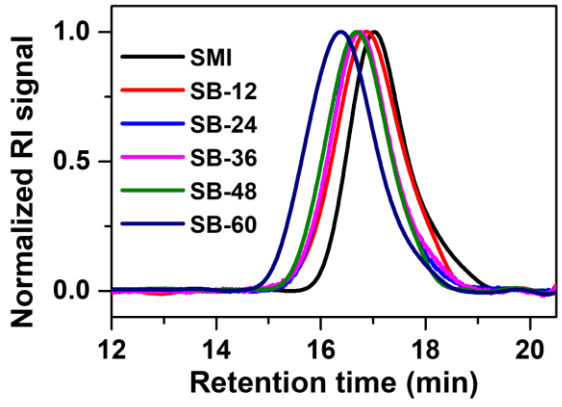

(b) Molecular weights details

Sample	M_n ¹H-NMR (g/mol)[a]	M_n SEC (g/mol)[b]	M_w SEC (g/mol)[b]	Đ[b]
SMI	7200	9200	11300	1.2
SB-12	10300	9300	15000	1.6
SB-24	13400	11900	19000	1.6
SB-36	16500	14000	18100	1.3
SB-48	19500	15200	22300	1.4
SB-60	22700	20000	30900	1.5

a) The total number of PCL and carboxylic PCL repeating units are estimated by ¹H NMR analysis. Molecular weights are estimated by multiplying the repeat unit mass. b) Molecular weights are estimated for the t-butyl carboxylic ester derivatives by SEC in $CHCl_3$ using polystyrene standard for calibration.

Figure 2.3. *(a) SEC plots of tButyl derivative of star block copolymers in $CHCl_3$ at 25 ºC using RI detector and polystyrene as standard. (b) Tabulated details of molecular weight (M_n) based on [1]H-NMR analysis and SEC based molecular weights and polydispersity index in $CHCl_3$.*

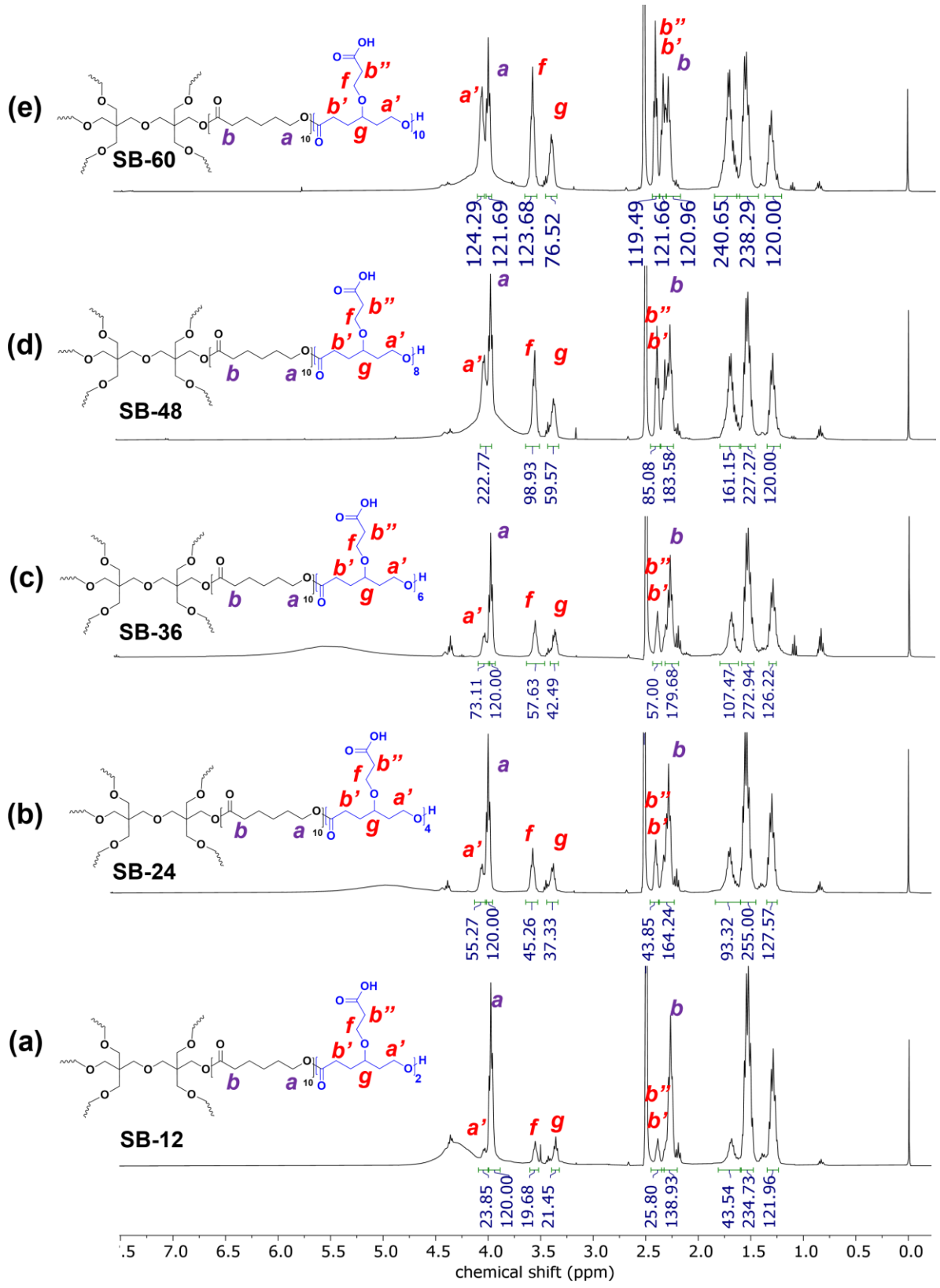

Figure 2.4: *^{1}HNMR plots of SB-12, SB-24, SB-36, SB-48, SB-60 in DMSO-d_6. All-important peaks are assigned alphabetically in respective spectra.*

2.3.2 Thermal Properties

Thermogravimetric analysis of the polymers depicted thermal stability up to 320-350 ºC from the TGA plots as shown in Figure 2.5b. The SMI macroinitiator showed degradation onset temperature at 320 ºC, whereas the *t*Butyl ester block copolymers (see Figure 2.5a for structures) exhibited onset of decomposition at ca. 250 ºC with one-step degradation for the *t*Butyl ester group in the block copolymer as shown in Figure 2.5b. Moreover the % degradation of the step increased due to increased number of repeating units of ^{t}Butyl ester block from SB-12*t*Bu to SB-60*t*Bu suggesting successful incorporation of second block with varying degree of polymerization. However, the overall thermal degradation of block copolymers was found to be similar to SMI. Differential scanning calorimetry (DSC) thermograms in Figure 2.5c-d depicted the semicrystalline nature of the star-PCL MI in the heating and cooling cycles whereas the *t*Butyl ester diblock copolymers exhibited semicrystalline to amorphous transition while increasing the content of *t*BuPCL units. The semi-crystalline nature of the diblock copolymer remained up to 36 *t*BuPCL units (6 *t*BuPCL units per arm) and further increase in the *t*BuPCL units made them to be predominantly amorphous and exhibited only glass transition temperature in range -45 to -49 ºC (see table in Figure 2.5f). The melting transition (T_m) for S-PCL MI was observed at 43 ºC, which further reduced to 21 ºC in the SB-36*t*Bu block copolymer. Thus, the enthalpy of melting (ΔH_m) and crystallization (ΔH_c) were found to be lower in block copolymers compared to SMI depending on the degree of *t*BuPCL incorporation. This trend was further supported by a drastic reduction in the % crystallinity from 34% in SMI to 5.7% in SB-36*t*Bu as shown in tables in Figure 2.5f. The % crystallinity of the PCL was estimated using the expression % Xc= $[\Delta H_m /139.6] \times 100$.[59] The reduction in % crystallinity of the star diblock copolymer with respect to increase in the increase in the increase in the increase in the *t*BuPCL content is attributed to poorly packed nature of *t*BuPCL segments having the ^{t}Butyl ester pendent units as side chain compared to SMI (PCL) where ordered chain packing is found. Furthermore, semicrystalline nature of SMI and block copolymer were investigated by the powder XRD (pXRD) analysis supported the similar trend as of DSC and pXRD diffraction patterns are shown in Figure 2.5e. The SMI exhibited two sharp peaks at 2Θ = 21.9 and 24.3º, a typical pattern of PCL with d-spacing values 4.05 and 3.66 Å respectively. This pattern retained in the SB-12*t*Bu, SB-24*t*Bu and SB-36*t*Bu depicting semi-crystalline nature. In contrast, broad peaks with no quantifiable reflections were obtained for SB-48*t*Bu and SB-60*t*Bu suggesting amorphous nature of these diblock copolymers where *t*BuPCL units are more than 36 are incorporated as shown in Figure 2.5e.

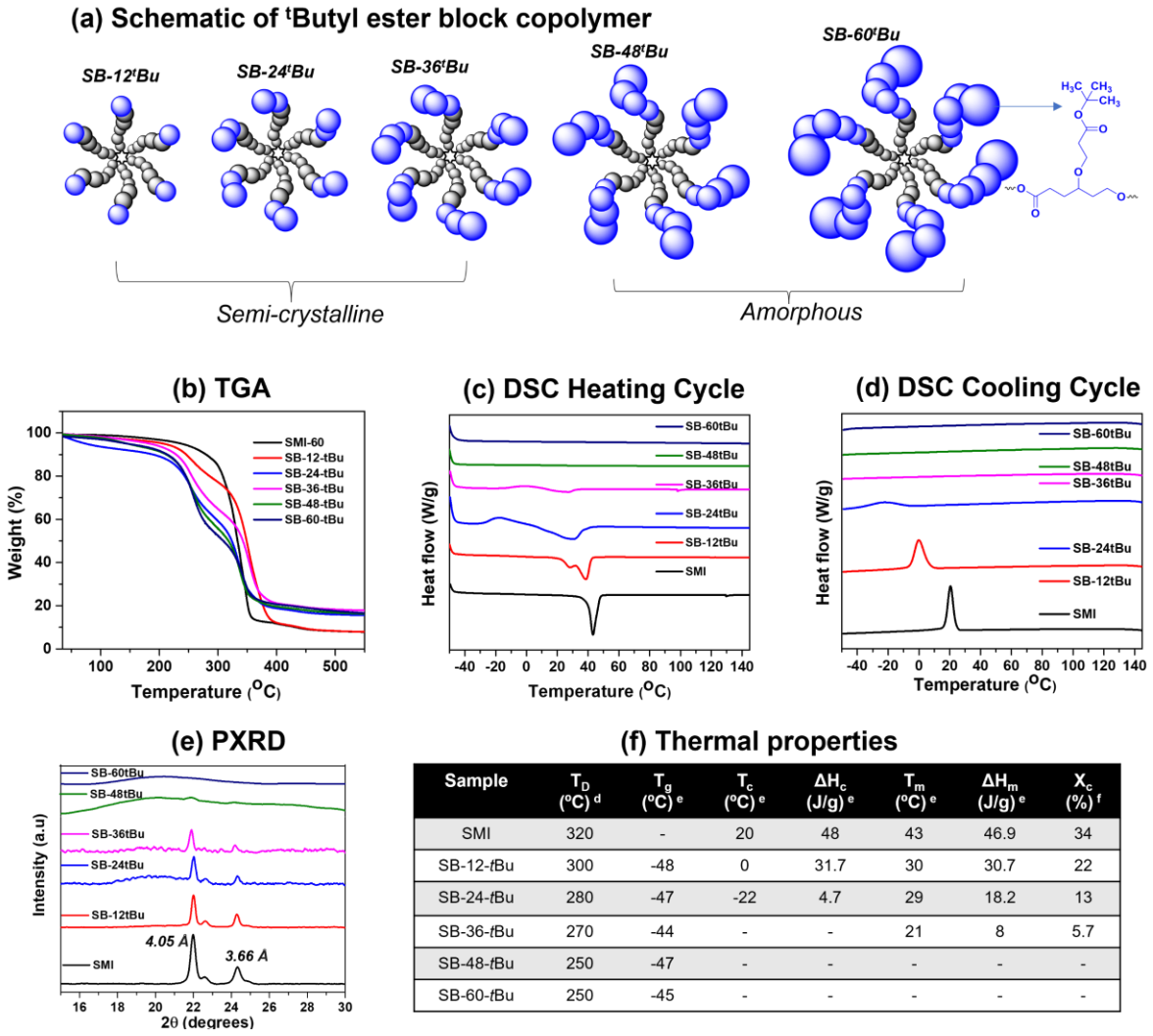

Sample	T_D (°C) [d]	T_g (°C) [e]	T_c (°C) [e]	ΔH_c (J/g) [e]	T_m (°C) [e]	ΔH_m (J/g) [e]	X_c (%) [f]
SMI	320	-	20	48	43	46.9	34
SB-12-*t*Bu	300	-48	0	31.7	30	30.7	22
SB-24-*t*Bu	280	-47	-22	4.7	29	18.2	13
SB-36-*t*Bu	270	-44	-	-	21	8	5.7
SB-48-*t*Bu	250	-47	-	-	-	-	-
SB-60-*t*Bu	250	-45	-	-	-	-	-

Figure 2.5: *(a) Schematic of tButyl ester protected star block copolymer. (b) TGA plot, (c) & (d) DSC thermograms of star block copolymers. (e) pXRD patterns of tButyl star block copolymers. (f) Tabulated details of thermal properties and % crystallinity vs % of star diblock copolymer (tButyl protected versions).*

TGA analysis of the deprotected block polymers with the pendent carboxylic acid units depicted thermal stability up to 250 ºC as shown in TGA plot in Figure 2.6a. DSC and PXRD analyses of revealed semi-crystalline nature of deprotected polymers as shown in Figure 2.6b-2.5d. Furthermore, polymers were transitioned completely amorphous upon increasing the carboxylic unit's content as shown in Figure 2.6e (see tabulated details). The first derivative of weight loss (%) from TGA data are shown in Appendix S2.3 to understand the degradation onset temperature for all the polymers. The deprotected carboxylic substituted star di-block polymers were found to be semi-crystalline while having a smaller number of carboxylic units; however, turned into be predominantly amorphous at higher analogues (see Figure 2.6e). These

studies revealed the star-polymers showed significant difference in the chain packing with respect to the number of *t*BuPCL or carboxylix-PCL units at each arm. At lower number of *t*BuPCL (or carboxylix-PCL) units in the periphery, the fixed central PCL core drove the chain packing, and the star-polymers SB-12, SB-24 and SB-36 become semi-crystalline. The substitution of large number of *t*BuPCL (or carboxylic-PCL) units in the periphery induce a steric hindrance (also branching in each arm) and the star-polymers SB-48 and SB-60 sluggish to chain packing and become amorphous. The percent crystallinity contributed by the central PCL core to the star di-block become less prominent when we increase the carboxylic PCL more than 6 repeating units per arm. This is attributed to loosely packed side pendant of carboxylic PCL units. The star PCL-b-*t*BuPCL polymers are water insoluble and highly hydrophobic in nature; thus, they can be typically useful for material science applications and limited scope in biomedical field.

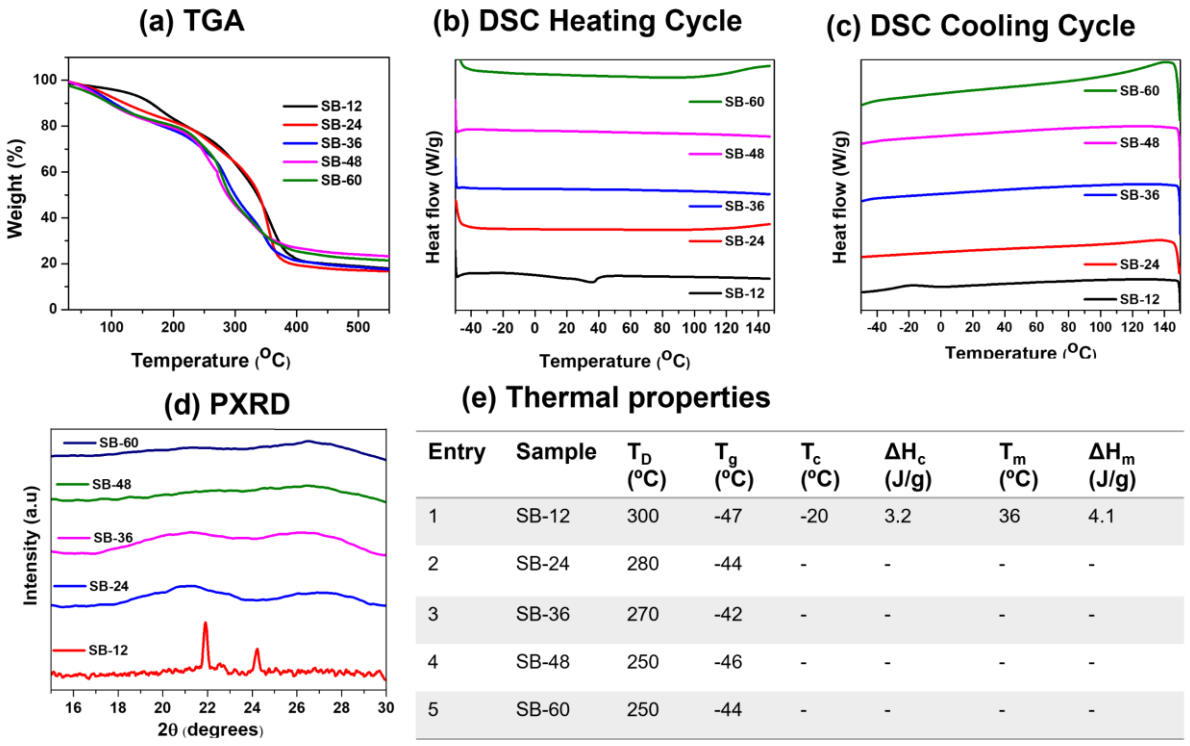

Entry	Sample	T_D (°C)	T_g (°C)	T_c (°C)	ΔH_c (J/g)	T_m (°C)	ΔH_m (J/g)
1	SB-12	300	-47	-20	3.2	36	4.1
2	SB-24	280	-44	-	-	-	-
3	SB-36	270	-42	-	-	-	-
4	SB-48	250	-46	-	-	-	-
5	SB-60	250	-44	-	-	-	-

Figure 2.6: *(a) TGA plot, (b) & (c) DSC thermograms, (d) pXRD patterns of deprotected star block copolymers having carboxylic acid pendant groups (SB-12, SB-24, SB-36, SB-48, SB-60). (e) Tabulated details of thermal properties and % crystallinity for star block copolymers.*

2.3.3 Self-Assembly

The star polymer having hydrophobic PCL core and anionic carboxylic acid functionality at the periphery have in-built amphiphilicity for phase segregation in water to produce stable self-assembled nano-scaffolds. In order to understand the role of amphiphilicity in the self-assembly process, the polymers SB-12 to SB-60 were subjected to water contact angle (WCA) by casting polymer thin film onto glass slides (WCA images are in Figure 2.7a-2.7b values in the Table 2.1 and). As anticipated, the WCA of *t*Butyl ester star-diblock copolymers were obtained as 106 to 73º suggesting their highly hydrophobic nature (see Figure 2.7a). In contrast the star-carboxylic di-block copolymers exhibited WCA from 81º (SB-12) to 46º (SB-60) at the higher number of CPCL segments suggesting the transition from hydrophobic to more amphiphilic in nature (see Figure 2.7b and 2.7c). Furthermore, the ratios of molecular weights of hydrophobic and hydrophilic segments ($M_{hydrophobic}/M_{hydrophilic}$) in the SB-x copolymer were estimated (Figure 2.7d) to correlate with the resultant amphiphilicity. This transition depicted by WCA could be correlated with $M_{hydrophobic}/M_{hydrophilic}$ ratio and the polymers seem to be attained amphiphilicity for the values less than unity.

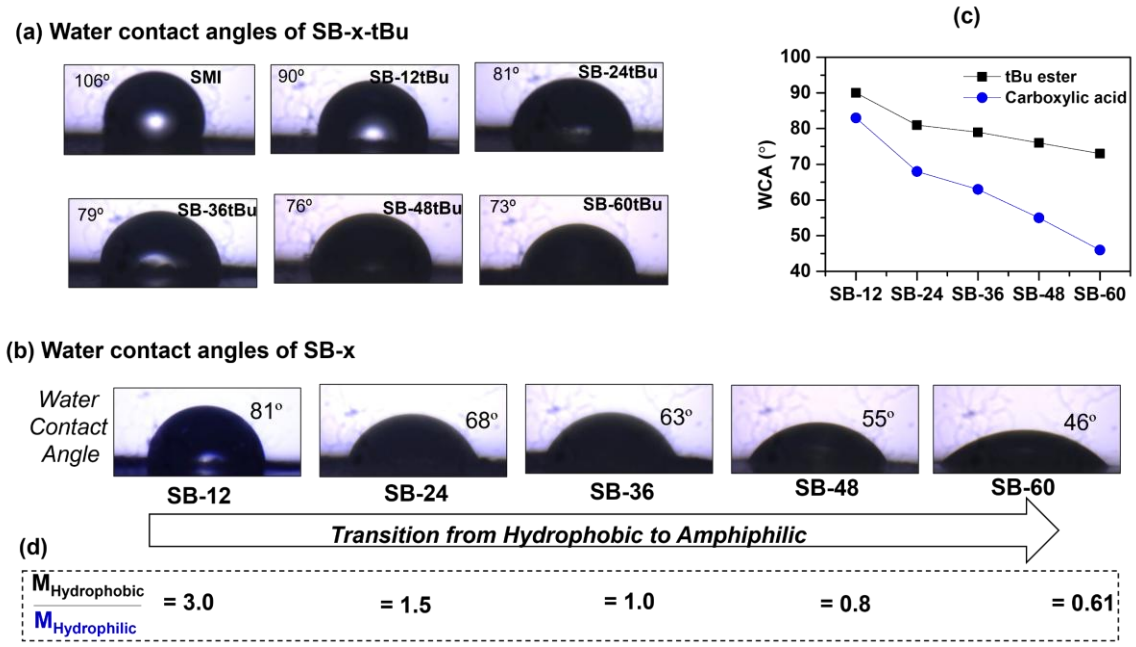

Figure 2.7: *(a) Water contact angles of tButyl ester protected star block copolymers (SB-12tBu, SB-2412tBu, SB-3612tBu, SB-4812tBu, SB-6012tBu). (b) Water contact angles of star block copolymers having carboxylic acid pendent groups showing transition from hydrophobic to amphiphilic entities. (c) Plot of water contact angles of tButyl ester protected and deprotected (acid pendants) star block copolymers. (d) Ratios of molecular weights of hydrophobic to hydrophilic segment in each star block copolymers.*

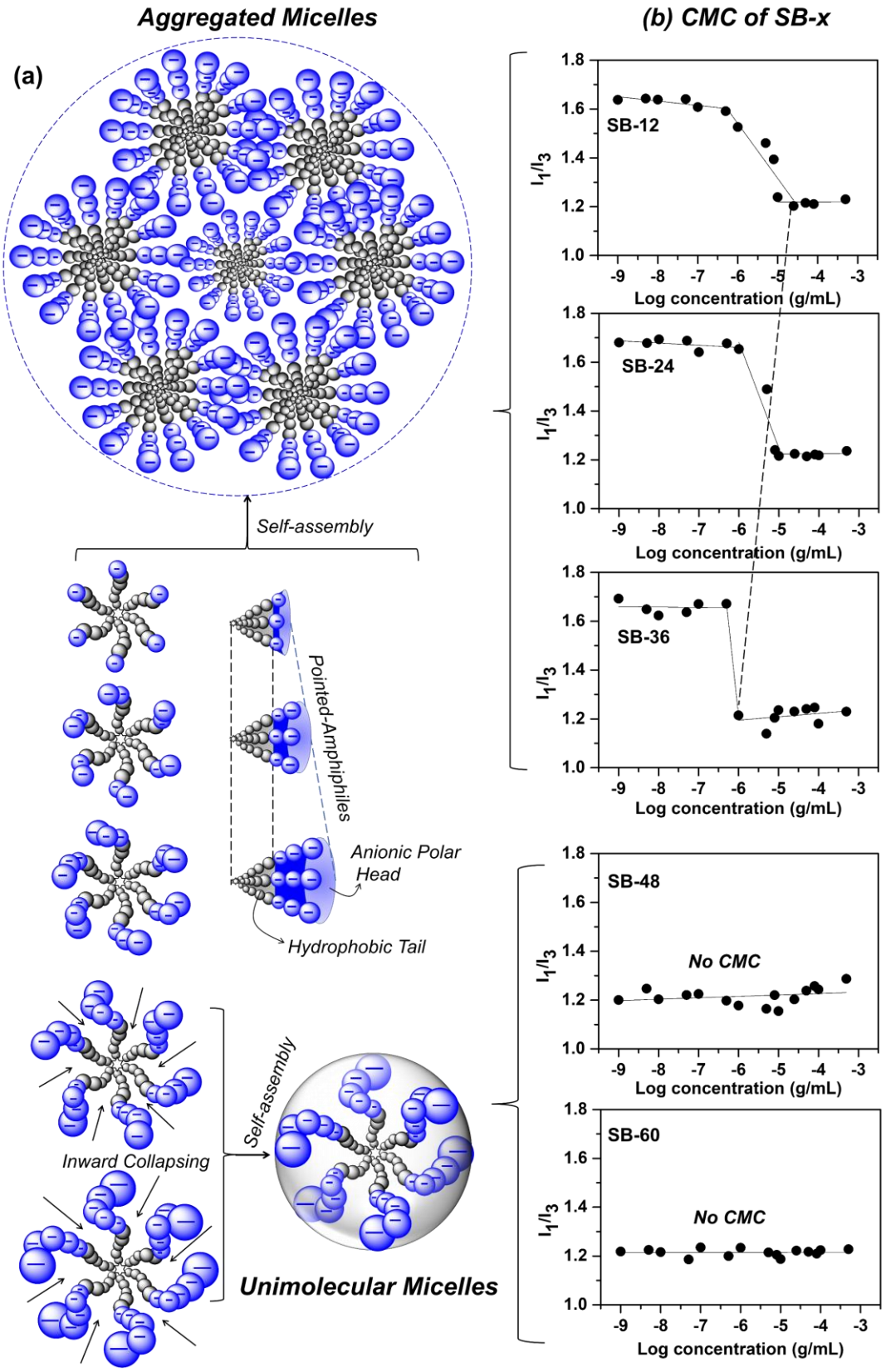

Figure 2.8. *(a) Pictorial representation of self-assembly of star block copolymers having varying number of carboxylic acid pendants units. (b) Pyrene encapsulation studies: CMC plots (I_1/I_3 vs Concentration) of star block copolymers.*

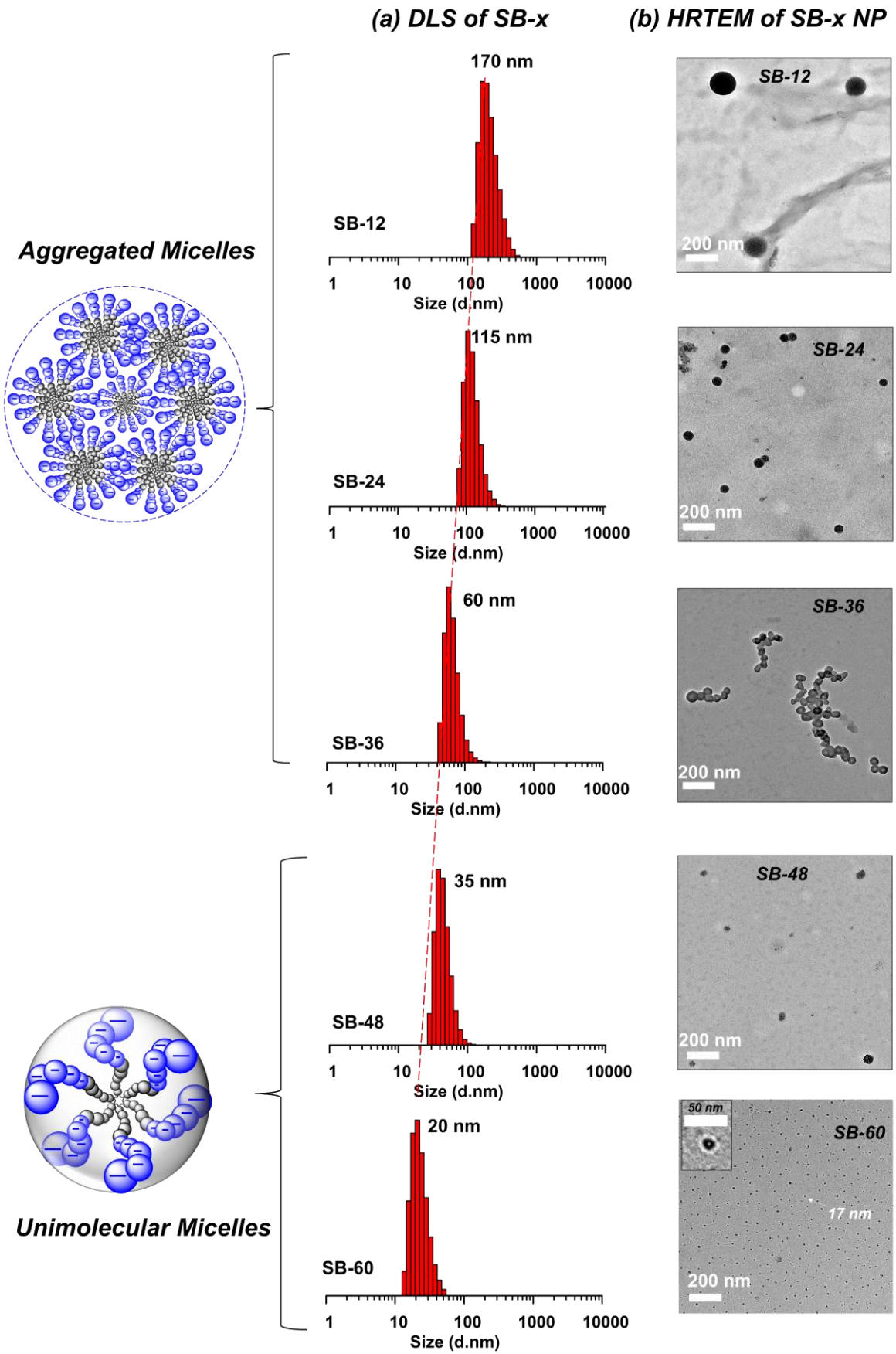

Figure 2.9. *(a) DLS histograms of star block nanoparticles (% Number plots, polymer concentration was 0.1mg/mL). (b) HR-TEM images of star block nanoparticles (scale bar 200 nm, nanoparticle concentration was 0.1mg/mL).*

The star carboxylic di-block polymers were subjected to aqueous self-assembly by dialysis method in which the polymers were dissolved in DMSO+ water solvent mixture and dialyzed against large excess of water using semi-permeable membrane having MWCO of 3.5 kDa. During the dialysis process, the gradual removal of DMSO leads to the phase segregation of hydrophobic and hydrophilic segments as shown in the Figure 2.8a. The carboxylic acid at the periphery is readily de-protonated into carboxylate anion (at pH > 4.0) and gain substantial hydrophilicity and become amphiphiles to self-assemble in aqueous medium. The segregation of hydrophobic PCL core and a negatively charged hydrophilic carboxylic PCL polar head in each star-polymer adopt pointed amphiphilic shape which underwent self-assembly to produce multimolecular or multiple polymer chains constituted aggregated micelles (AgM) as shown in Figure 2.8a. The formation of AgM is typically driven by the concentration gradient and such an event could be readily traced by pyrene fluorophore experiment to determine the CMC of the polymers. Pyrene fluorophore experiments in star-polymers SB-12, SB-24 and SB-36 showed break point in Figure 2.8b with respect to its CMC in the plot of I_1/I_3 against concentration as typically expected for multimolecular AgM. The CMC values determined from measurements are 8.0, 5.0 and 1.0 μg/mL for the SB-12, SB-24 and SB-36 respectively and mentioned in Table 2.1. The CMC of the SB-12 was found to be one order of magnitude higher concentration than the CMC of SB-36 indicating that the increase in the anionic charges in the periphery favors the stronger self-assembly of the star-polymers. The formation of micelles at lower concentration implies that only a few polymer chains are required to produce stable nano-assemblies in water. In contrast, each individual polymer chains in the higher star-polymer analogues SB-48 and SB-60 were found to undergo self-segregation to produce single chain micelle or unimolecular micelle (UMM) self-assembly as shown in Figure 2.8a. This ability of SB-48 and SB-60 to produce UMM is attributed to both the presence of large abundance of negative charges at the periphery as well as their large molar mass (> 20 kDa) (as similar to that of natural proteins which undergo individual globular self-assembly). To minimize the inter-arm electrostatic repulsion at the periphery in each star-polymer, these high molecular weight star systems are expected to undergo inward collapsing of the PCL core further to produce compact tiny particulates. As typically observed in anionic polyelectrolytes, these individual particles tend to stay apart in their own solvent cage (water in this case) to minimize the electrostatic repulsion by the neighboring chains or particles. As a net result, the UMM stays as individual entity in aqueous medium and it does not follow typical characteristics of AgM against concentration gradient. The existence of UMM is typically validated by the pyrene fluorophore experiments that do not show any break point in the plot

of I_1/I_3 against concentration since there is no concentration driven micelle formation. As anticipated, the pyrene fluorophore experiments for SB-48 and SB-60 did not show any break point in their I_1/I_3 plots in Figure 2.8b and directly evident for their existence as UMM in aqueous medium.

Sample	WCA (°)[a]	CMC (μg/mL)[b]	Size (nm)[c]	PDI[c]	ξ (mV)[c]	HRTEM (nm)[d]
SMI	106	-	-	-	-	-
SB-12	81	8.0	170 ± 12	0.31	-17.8 ± 1.0	148 ± 15
SB-24	68	5.0	115 ± 10	0.32	-22.8 ± 2.2	100 ± 10
SB-36	63	1.0	60 ± 6	0.22	-21.9 ± 4.1	55 ± 6
SB-48	55	-	35 ± 5	0.23	-22.9 ± 4.0	36 ± 4
SB-60	46	-	24 ± 3	0.26	-25.2 ± 1.3	17 ± 3

a) Water contact angle (WCA) measured by goniometry for drop-casted polymer films on glass substrate. b) Critical Micellar concertation was determined using Pyrene fluorescent probe. c) Size, PDI and Zeta potential were determined by dynamic light scattering in Britton-Robinson buffer at pH 7.4. d) HR-TEM images were recoded for dialyzed aqueous solution.

Table 2.1. *Tabulated details of molecular weight (M_n) based on ^{1}H-NMR analysis and SEC based molecular weights and polydispersity index in $CHCl_3$, and nanoparticle properties.*

To measure the size of the AgM and UMM, the dialyzed star-polymer aqueous solutions were subjected to dynamic light scattering (DLS) analysis and their DLS histograms are shown in Figure 2.9a, and the average sizes are given in Table 2.1. DLS histograms of SB-12 and SB-24 undoubtedly depicted the formation of larger hydrodynamic diameter of > 120 nm with respect to AgM. The SB-36 samples showed relatively smaller sized AgM of 60 nm in size. Interestingly, the SB-48 and SB-60 samples depicted much smaller hydrodynamic diameter in the range of 35 to 24 nm with respect to the formation of tiny UMM. The DLS histograms showed monomodal size distribution with narrow polydispersity in the range of 0.22 to 0.32 indicating the uniform size distribution (see Table 2.1). Interestingly the sizes of nanoparticles gradually decreased with the increase in hydrophilic block length (CPCL) depicting transition of sizes from 170 nm in the SB-12 (AgM) to 24 nm in SB-60 (UMM) which was further supported by CMC measurements. Upon dilution, the AGM are known to undergo disassembly below its CMC whereas UMM would not show any change in the size since it is produced by the individual polymer chain. Upon dilution, the AgM nanoparticle SB-36 exhibited a size reduction from 60 nm at 0.01 mg/mL to 20 nm at 0.025 mg/ML. On the other hand, the UMM nanoparticle SB-60 has retained its hydrodynamic diameter on serial dilution from 1.0 mg/mL to 0.001mg/mL as 20-25 nm with respect to its stable nature (see Figure 2.10). This clearly indicates that SB-60 produces unimolecular micellar assemblies which were consentient on

dilution and do not possess CMC or CAC concentrations at investigated range of concentrations. To study the shape and sizes of these nanoparticles, they were subjected to high resolution transmission electron microscopy (HR-TEM) imaging and images are shown in Figure 2.9b. HR-TEM depicted spherical morphologies of nanoparticles in all cases with uniform size distributions. AGM nanoparticles showed the existence of larger sized nanoparticles (AgM) of sizes ranging from 170 to 60 nm in SB-12 to SB-36 whereas tiny nanoparticles of ~ 20 nm were found in SB-60 validating the existence of tiny UMM. The surface charges of star block nanoparticles were measured by Zeta potential (ζ) in the pH 7.4 (Britton-Robinson buffer, 10mM) and details are shown in the Table 2.1. All the nanoparticles were found to be negatively charged due to the presence of carboxylic acid function group depicting ζ potential in the range of -17 to -25 mV. As anticipated the increase in negative ζ potential from SB-12 to SB-60 was observed due to increase in number of carboxylic acid functional entities. This transition of aggregated micelles to unimolecular micelles in 6-arm star block copolymer undoubtedly achieved by varying number of hydrophilic CPCL units and SB-48 was transition point suggesting that minimum 48 units of CPCL required produce the UMM nano-assembly.

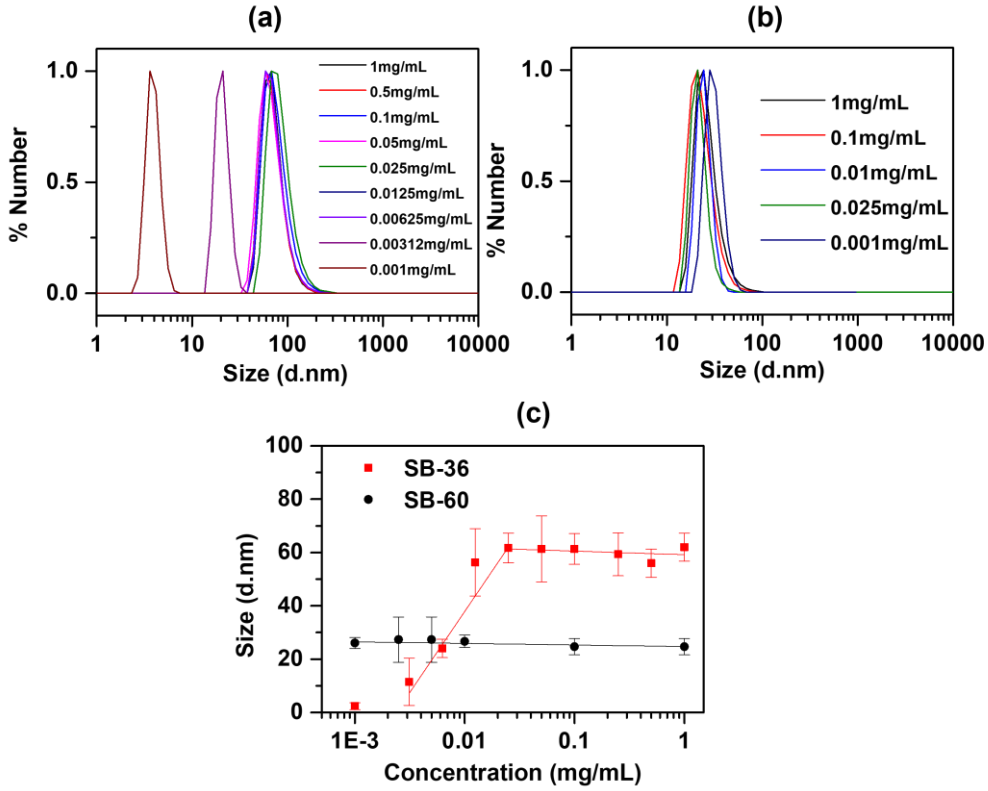

Figure 2.10: *(a) Plot of DLS histograms of AgM (SB-36) nanoparticles on serial dilution. (b) Plot of DLS histograms of UMM (SB-60) nanoparticles on serial dilution. (c) Plot of size vs concentration of AgM and UMM nanoparticles (n=3, Data represented as mean ± SD).*

2.3.4 Encapsulation studies

The encapsulation efficiency of polymer nanoparticles depends upon several factors such as compartmentalization of hydrophobic/hydrophilic segments, total hydrophobic content, core density and architecture, interchain-intrachain interactions, polymer-cargo interactions via either hydrophobic-hydrophobic interaction or electrostatic interactions and thermodynamic stability of nano-assemblies. Water soluble clinical Topoisomerase II anticancer drug doxorubicin (DOX) was selected to study the encapsulation in the AgM and UMM star block copolymer by dialysis method using semipermeable membrane of MWCO 3.5 kDa as described earlier. The encapsulated DOX was removed by continuous replenishing with water (MilliQ); the drug loading capacities (% DLC) and drug loading efficiencies (% DLE) were estimated by using absorbance spectroscopy. Different feed ratio of DOX have been used for optimization of maximum DLC (Appendix S2.4). The vials containing the DOX loaded samples SB-x+DOX are shown in Figures 2.11a-c along with the stack plot showing the DLC for various star-polymers. The SB-12 to SB-36 exhibited DLC > 3.0 % (see Figure 2.11c) for DOX due to insufficient amphiphilic balance and these values typically matched with that of the AGM reported for block copolymer nanoparticles, in general. In contrast, the better nano-compartmentalization in the SB-48 substantially increased DLC ~ 5.0 % and the loading further enhanced with superior encapsulating capability in the star-UMM SB-60 having DLC = 14 % for DOX (see Figure 2.11c). This is attributed primarily to balance amphiphilicity, compact size of the hydrophobic core for better stabilization of DOX in star-UMM. This trend of increase in DLCs while transitioning from aggregated to unimolecular micelles in the star block copolymer by tuning amphiphilicities was appreciable, suggesting the supremacy of unimolecular micelles. The TEM image of AgM+DOX (SB-36+DOX) is shown in Figure 2.11d exhibited larger size nanoparticles of 60 ± 5 nm confirming its existence as aggerated micelles. The TEM image of UMM+DOX (SB-60+DOX) in Figure 2.11e revealed the spherical shape with uniform distribution of sizes 20 ± 5 nm consistent with DLS data in Figure 2.11f. Hydrodynamic diameters of DOX loaded samples were measured by DLS and size histograms are shown in Figure 2.12a. The average size versus DLC plot is shown in Figure 2.12b, suggesting a direct correlation between decrease in size and increase in % DLC. Furthermore, all other DOX loaded SB-x nanoparticle samples exhibited comparable sizes to their non-loaded versions and monomodal size distribution having narrow PDI in the range of 0.29 to 0.37 and details are tabulated in Figure 2.12d. UMM (SB-60) was found to be superior in encapsulation of various cargoes such as DOX, HPTS, Sulforhodamin-B (SRhB), IR-780

and Cardio green (ICG) (see Figure 2.13 for encapsulation details and characterization); however, AgM (SB-36) could encapsulate DOX and IR-780 only. AgM and UMM exhibited 3.0 and 4.7 % DLC for IR780 dye, respectively (see table in Figure 2.11f). Sizes of UMM+dyes were in the range of 20-25 nm with narrow PDI (0.27-0.33) as shown in Figure 2.11f and 2.13. Dye or drug loaded UMM nanoparticles exhibited similar hydrodynamic sizes which further suggested the nature of cargo does not have effect on the self-assembly of unimolecular micelles. Further, the Zeta potential (ζ) potential values were obtained in the similar range (-17 to -23 mV) comparable to their nascent sample which further suggested the encapsulation retained the slightly anionic nature of the UMM periphery for hydrophilicity and stability in aqueous medium. Based on the above analysis, it can be categorized that SB-36, and SB-60-star polymers have distinct features as aggregated micelles (AgM) and unimolecular micelles (UMM) with substantial difference in their size and loading capabilities, and therefore, they are chosen further to study their drug delivering efficacies in vitro and in vivo. SB-36 will be referred to as AgM and SB-60 will be referred to as UMM from now onward.

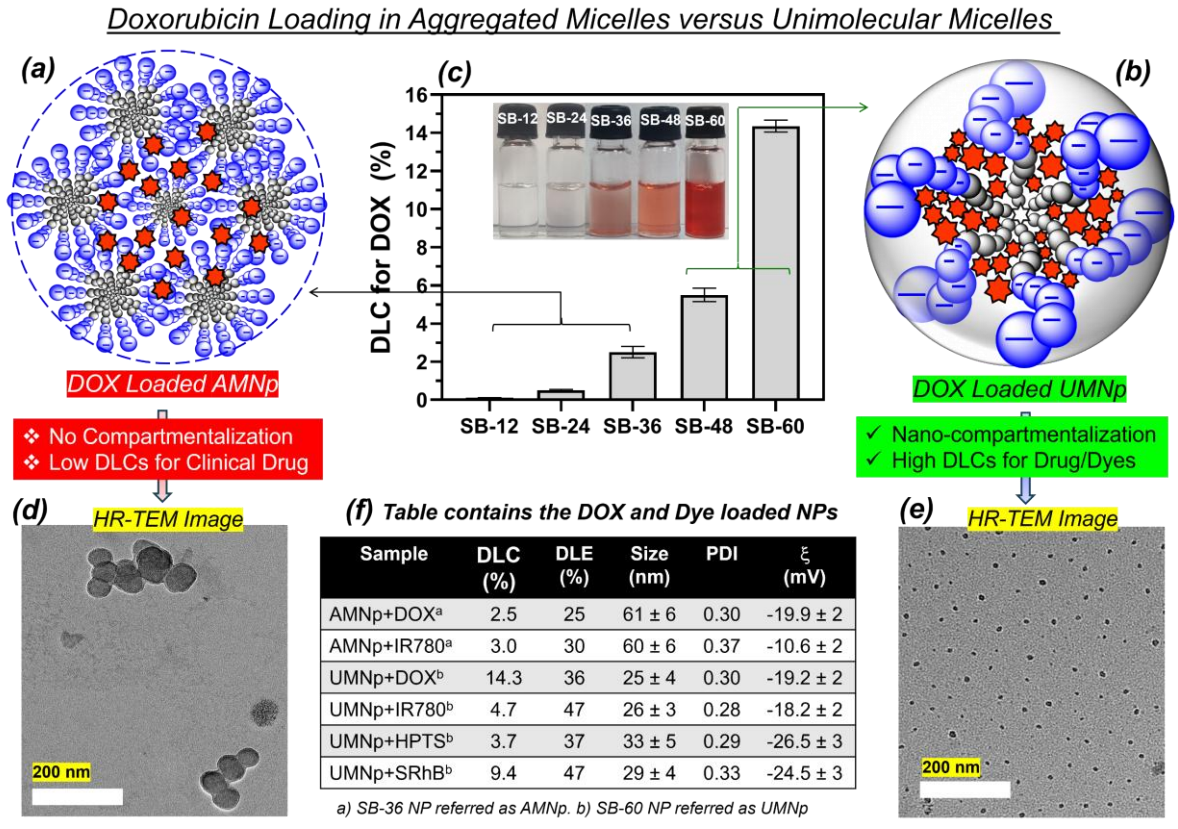

Sample	DLC (%)	DLE (%)	Size (nm)	PDI	ξ (mV)
AMNp+DOX[a]	2.5	25	61 ± 6	0.30	-19.9 ± 2
AMNp+IR780[a]	3.0	30	60 ± 6	0.37	-10.6 ± 2
UMNp+DOX[b]	14.3	36	25 ± 4	0.30	-19.2 ± 2
UMNp+IR780[b]	4.7	47	26 ± 3	0.28	-18.2 ± 2
UMNp+HPTS[b]	3.7	37	33 ± 5	0.29	-26.5 ± 3
UMNp+SRhB[b]	9.4	47	29 ± 4	0.33	-24.5 ± 3

Figure 2.11. *Encapsulation studies: (a) & (b) Pictorial representation DOX encapsulated star block copolymers AgM+DOX (SB-36) and UMM+DOX (SB-60) nanoparticles respectively. (c) The plot of % DLC for DOX loaded SB-x NP (n=3). (d) & (e) HR-TEM image of AgM+DOX and UMM+DOX nanoparticles respectively. (scale bar 200nm). (f) Tabulated details of DOX/dye loaded AgM and UMM nanoparticles (n=3, data represented as mean ± SD).*

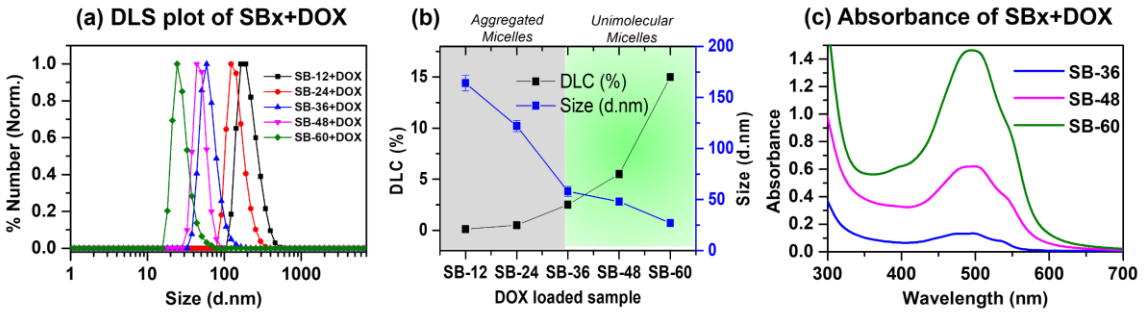

(d) Details of encapsulation

Entry	DOX loaded sample				
	DLC (%)	DLE (%)	DLS size (d.nm)	PDI	Zeta Potential (ζ) at pH 7.4 in mV
SB-12	0.11	1.1	160 ± 13	0.30 ± 0.01	17.2 ± 3.3
SB-24	0.50	5.0	112 ± 9	0.29 ± 0.03	-19.7 ± 1.8
SB-36	2.50	25.0	61 ± 6	0.3 ± 0.05	-19.9 ± 2
SB-48	5.50	25.0	47 ± 4	0.37 ± 0.09	-22.7 ± 3.6
SB-60	14.30	36.0	25 ± 4	0.30 ± 0.01	-19.2 ± 2

Figure 2.12: *Encapsulation studies: (a) DLS histograms DOX loaded star block copolymers. (b) Plot of % DLC for DOX vs sizes of star block copolymers. (c) Absorbance spectra of SBx-DOX. (d) Tabulated details DOX loaded SB-x nanoparticles (n>3, Data represented as mean ± SD).*

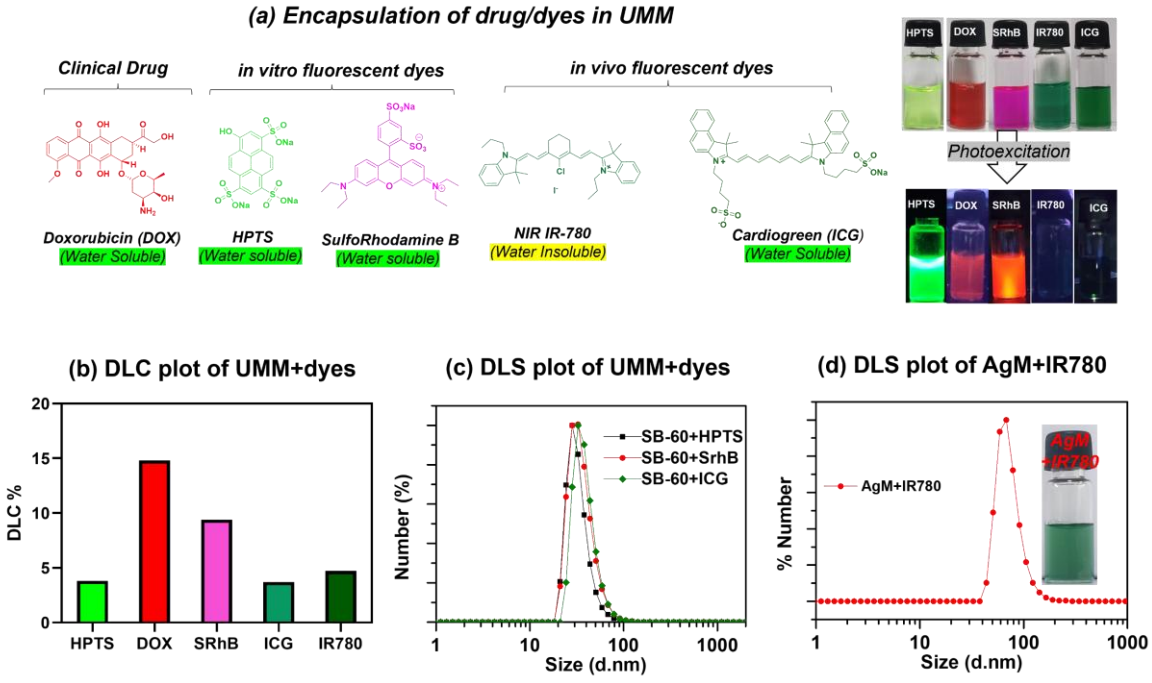

Figure 2.13: *Encapsulation studies: (a) Structures of different drug or fluorescent dyes encapsulated in UMM polymer. And photographs of dye loaded UMM nanoparticles under normal light and long UV excitation. (b) Plot of % DLC for UMM nanoparticles loaded with DOX and dyes. (c) DLS histograms of UMM+Dyes. (i) DLS plot of AgM+IR780. (NP concentration 0.1mg/mL)*

2.3.5 Enzyme-Responsive Drug Release

The release of drug from the nanocarriers largely depends on multiple factor such as physicochemical properties, stability, size, shape and charge of nanoparticles, pH, concentrations and temperature of surrounding environment. Currently designed star block copolymers are composed of aliphatic polyester (PCL) backbone rendering them suitable candidate for stimuli-responsive behavior. Nanoparticles derived from PCL or substituted PCL system are proven to be biodegradable by esterase enzyme-catalyzed hydrolysis resulting into complete scissoring of polymeric chain in the lysosomal compartments of the cells causing release of drug from polymeric matrix to the cytosol. The schematic of enzymatic biodegradation for UMM+DOX as a representative of star block copolymer is shown in Figure 2.14a. UMM+DOX nanoparticles are taken up by the cells via endocytosis and accumulated in the membrane derived vesicles called endosomes at intracellular level. After maturation of endosomal bodies further fuse with the lysosomes results into formation of endo-lysosomal compartments. The lysosomal esterase enzyme acts upon ester functional groups present on the fast degradable substituted PCL polymer backbone present on the outer shell resulting into cleavage or scissoring into smaller units leading to degradation of nanoparticles (see Figure 2.1a). In this process, very slow degradable PCL backbones are also chopped into smaller units simultaneously due to overall hydrophilicity of nanoparticles provided by the incorporation of hydrophilic substituted PCL shell in the nanoparticles. The overall hydrophilicity renders the penetration of water molecules into nanoparticles and makes them more available for esterase to act upon. This leads to cleavage/degradation of polymer matrix resulting in nanoparticles releasing the drug (DOX) molecules in controlled manner. The release DOX molecules from the lysosomal compartments then travel to their targeting side nucleus and intercalates with DNA to inhibit Topoisomerase II resulting into cell death as shown in Figure 2.14a.

To mimic the extracellular environment such as physiological pH, temperature and presence of various proteins, the stability of AgM+DOX and UMM+DOX was tested in the presence of 10% fetal bovine serum (FBS). The nanoparticles were incubated in FBS at 37 ºC in the physiological pH 7.4 (PBS buffer) and their sizes were monitored by DLS over the period of 5 days and the plot of sizes vs time is shown in Figure 2.14b. This revealed that no significant changes were observed in the sizes of AgM+DOX or UMM+DOX upon incubation with FBS which is source of various proteins at phycological pH and temperature. This result suggested that these nanoparticles can be stable and preserve the encapsulated DOX or any cargo for a longer period. Furthermore, aqueous stability of UMM+DOX was tested for 21 days and NP

were found very stable (see Appendix). In addition to this stability of UMM+DOX were examined against concentration gradient. The UMM+DOX were found to be stable against 1000 time dilution (Appendix). This stability is crucial factor *in vitro* as well as *in vivo* for sustained drug delivery because of the presence of larger pool of proteins in the blood stream in the body.

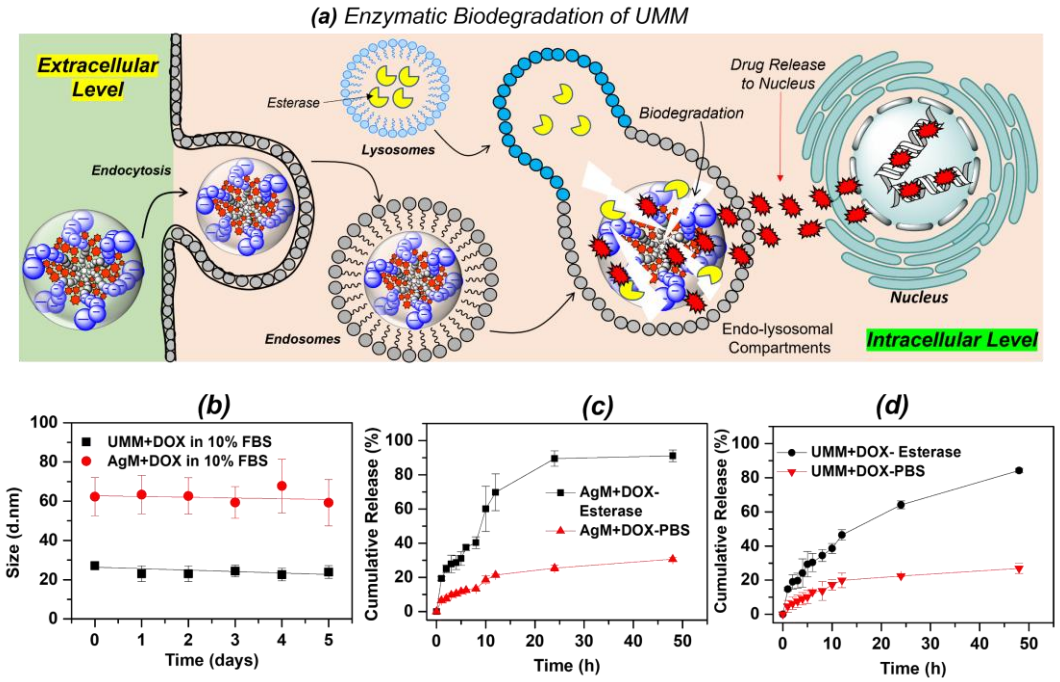

Figure 2.14. *(a) Schematic of enzymatic biodegradation. (b) Plot of DLS sizes versus time depicting the stability of AgM+DOX and UMM+DOX in 10% FBS (pH 7.4) at 37°C for 7 days. (c) and (d) Cumulative release profile of AgM+DOX and UMM+DOX in the presence and absence of esterase respectively (Data is represented as mean ±SD, n=3).*

Furthermore, to mimic the lysosomal conditions, AgM+DOX and UMM+DOX nanoparticles were incubated with esterase (Horse liver esterase) at physiological temperature and pH 7.4 and release of the DOX from the nanoparticles was monitored. The plots of cumulative DOX release for AgM+DOX and UMM+DOX in the presence or absence of esterase enzyme is shown in Figure 2.14c and 2.14d respectively. Both AgM+DOX and UMM+DOX exhibited triphasic release profiles in the presence of enzyme as shown in the plots. The AgM+DOX nanoparticles released approximately 60% of the loaded DOX at 12h due to faster release of DOX molecules occupying the intra-micellar spaces in the aggregated micelles attributed to surface erosion caused by polymer matrix degradation at outer shell by the enzyme compared to the drug molecules present in the core. Moreover, this drug release was also influenced by larger sizes of AgM+DOX which increases pH gradient. In contrast, only 40-50% of DOX released was observed in case of UMM+DOX after 12h attributed to presence of DOX molecules at the core and smaller sizes nanoparticles as shown in Figure

2.14d. Overall, 80-90% of DOX released observed in both nanoparticles after 48h of incubation with esterase and suggesting superior biodegradable nature of polymer backbone as shown in Figure 2.1a. In the absence of enzyme, only 20-25% of DOX was released when nanoparticles were incubated in the buffer (10mM PBS pH, 7.4) as shown in Figure 2.14c-d. This is attributed to the diffusion of the drug molecules from the nanoparticles to surrounding environment due to concentration gradient of salt molecules present in the buffer system driving osmolality. In addition to that UMM+DOX showed only <40% release in the pH 5.5 and pH 6.6 (Appendix). These overall results proved enzymatic biodegradation of star block nanoparticles.

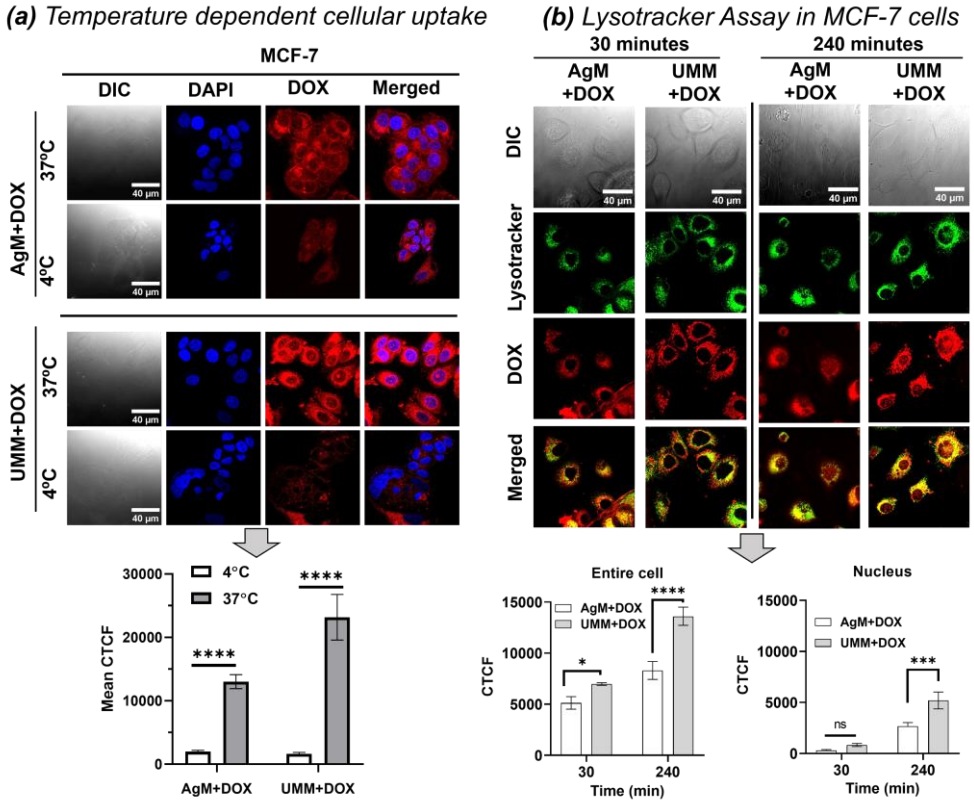

Figure 2.15. *(a) Endocytosis: CLSM images of temperature dependent cellular uptake of AgM+DOX and UMM+DOX in MCF-7 cells after 3h (scale bar 40µm, DOX concentration 2.5µg/mL) along with plot of CTCF for temperature dependent cellular uptake (n=3, Data represented as mean ± SD, ****p<0.0001, ANOVA test). (b) Lysotracker assay: Live cell CLSM images of AgM+DOX and UMM+DOX for 30 and 240 minutes in MCF-7 cells. (scale bar 40µm, DOX concentration 2.5µg/mL) along with plot of CTCF for uptake of DOX in entire cell and nucleus with respect to time (n=3, *p<0.05,*** p=0.0003, ANOVA test).*

2.3.6 Endocytosis and Live-Cell Biodegradation

To examine the pathway of intracellular entry (endocytosis) the AgM+DOX and UMM+DOX were given to MCF-7 (breast cancer) cells and incubated at 37 or 4 ºC and confocal images (CLSM) are shown in Figure 2.15a. Endocytosis is an energy-depending process (ATP-

mediated) only occurs at the physiological temperature (37 ºC) whereas this process does not take place when temperature lowered to 4 ºC. Both AgM+DOX and UMM+DOX exhibited higher fluorescence of DOX inside the cells when incubated at 37 ºC compared to 4 ºC which clearly indicates that these nanoparticles were taken up via endocytosis process. This was further confirmed by the estimated corrected total cell fluorescence (CTCF) which clearly suggested 6-8-fold higher DOX accumulation in case of cells incubated at 37 ºC for both nanoparticles as shown in Figure 2.15a. To further confirm the lysosomal colocalization of DOX loaded nanoparticles, live cell confocal imaging was performed by labelling lysosomes with lysotracker green (DND-26, 488nm) and confocal images are shown in Figure 2.15b. Live CLSM images were captured at 30 and 240 minutes after incubating MCF-7 cells with of AgM+DOX and UMM+DOX (2.5µg/mL). It was evident from CLSM images of 30 minutes that both nanoparticles were internalized in the cells via endocytosis process and colocalized with lysosomes elicited by yellow color in merged panel due colocalization of green (lysosomes) and red (DOX). As time progressed, lysosomal esterase enzymatic action initiated to degrade the polymer resulting in the release of DOX from nanoparticles toward the cytosol. The released DOX molecules were further started to accumulate in the nucleus evident from CLSM image of 240 minutes (4h). The merged panel of 4h clearly depicted fluorescence signal of DOX (red) in the nucleus as resulted from the partially degraded nanoparticles as well as remaining nanoparticles still internalized in the lysosomes evident from yellow color green and red fluorescence suggesting degradation of nanoparticles in the lysosomal compartment of the cells. This was further supported by CTCF in Figure 2.15b suggesting enhanced uptake in entire cell as well as in the nucleus at 4h compared to 30 min. Moreover, the uptake for UMM+DOX in the nucleus was higher compared to AgM+DOX suggesting better intracellular responsive behavior towards the lysosomal-enzyme. Live cell CLSM images for lysosomal colocalization and biodegradation for UMM+DOX in MIA PaCa2 (pancreatic cancer) cells from 30 minutes to 8 h are shown in Figure 2.16. It is clear from images of earlier timepoint that nanoparticles internalized by MIA PaCa2 cells and entered lysosomal compartment (merged image) in appreciable manner and further degraded by esterase to release DOX evident by higher fluorescence signal from nuclear regions.

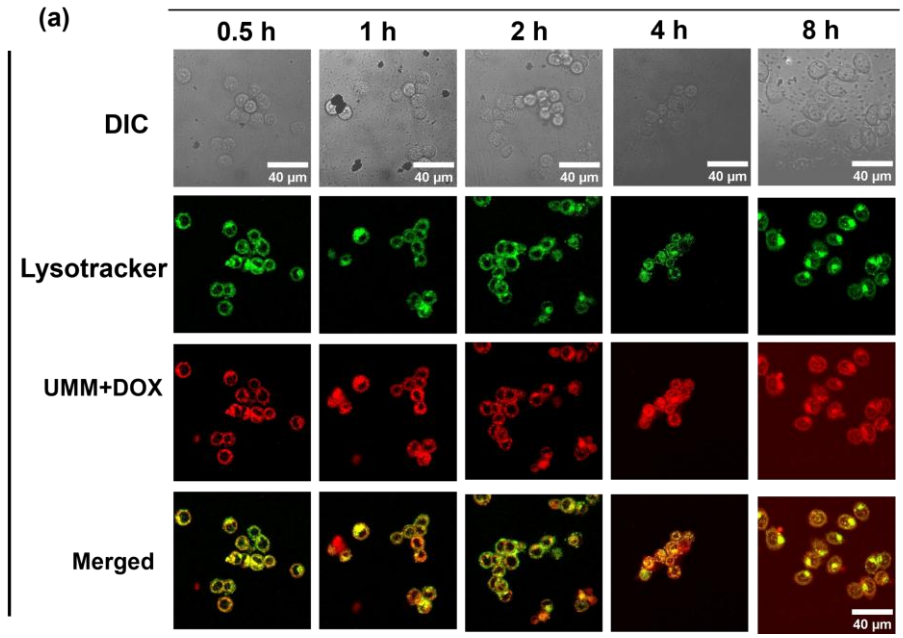

Figure 2.16: *Enzymatic biodegradation studies: Live cell CLSM images of UMM+DOX treated MIA PaCa 2 cells for different time of incubation.*

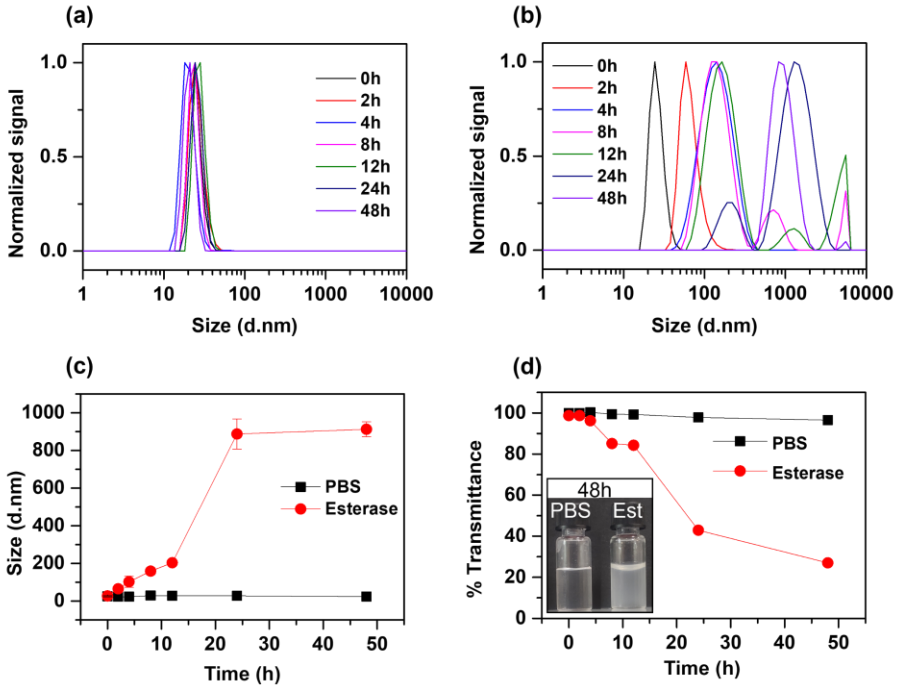

Figure 2.17: *Enzymatic biodegradation studies: (a) DLS histograms of UMM (SB-60) incubated in PBS (pH 7.4) at 37 ºC for 48h. (b) DLS histograms of UMM incubated in the presence of porcine liver esterase enzyme (in PBS, pH 7.4) at 37 ºC for 48h. (c) Plot of cumulative DLS size of UMM nanoparticles incubated with or without esterase in PBS pH 7.4. at 37 ºC. (d) Plot of % transmittance at 600 nm for UMM nanoparticles incubated with or without esterase in PBS pH 7.4 at 37 ºC (nanoparticle concentration 1.0 mg/mL). Photographs of nanoparticles incubated in PBS and esterase (EST) after 48h (concentration 1.0 mg/mL).*

Furthermore, the biodegradation of UMM star nanoparticle was evaluated using DLS size measurement, ^{1}H-NMR spectroscopy and MALDI-TOF Mass and these details are given in Figures 2.17 to 2.19. DLS size measurement was used for evaluating changes in sizes of nanoparticles owing to biodegradation and data is shown in Figure 2.17. For that purpose, the UMM nanoparticles were incubated with esterase and without esterase (control) in PBS pH 7.4 at 37 ºC for 48h. Sizes were measured by DLS, and the plot of size vs time is shown in Figure 2.17a-c. The UMM nanoparticles incubated with esterase exhibited significant change in sizes after 2h to 12h of incubation and further produced larger aggregates (100-200 nm) resultant from degraded polymer matrix which further increased to 800-1000 nm of size over the period of incubation. In contrast, UMM nanoparticles did not show any significant change in size when incubated with PBS buffer only. This clearly proved that star nanoparticles degraded with esterase enzymatic action and completely biodegradable. This was further supported by turbidity analysis by measuring % transmittance at 600 nm and plot is shown in Figure 2.17d. The turbidity of UMM in presence of esterase gradually increased as time of incubation progressed which is confirmed by gradual decrease in % transmittance from 98 to 30% in 48h. This turbidity is attributed to degradation of polymer resulting in the precipitation of oligomeric assemblies. However no visible turbidity was observed in case of nanoparticles incubated in PBS only evident from % transmittance values (>95 %) after 48h. The photographs of vials having UMM nanoparticles (1mg/mL) incubated with esterase and without esterase after 48h are shown in Figure 2.17d. Moreover, the UMM nanoparticles incubated with esterase were analyzed by ^{1}H-NMR spectroscopy and spectra are shown in Figure 2.18. A significant reduction in intensity of peaks at 3.90-4.15 and 2.30-2.45 ppm corresponding to -O-CO-C**H**$_2$- protons (ester backbone) and -CO-C**H**$_2$- protons (protons present on adjacent to carbonyl group) respectively was observed after 24 and 48h of esterase catalyzed degradation into small oligomeric units as shown in Figure 2.18. This was again supported by MALDI-TOF analysis depicting mass distribution of cleaved oligomeric units in Figure 2.19. MALDI-TOF analysis showed degradation of star block polymer into smaller oligomeric units. In the summery, the extracellular stability of nanoparticles in serum condition, *in vitro* release in the presence of esterase, endocytosis and live cell lysotracker colocalization assay and biodegradation confirmed the capabilities of AgM and UMM to undergo enzymatic degradation to release the DOX.

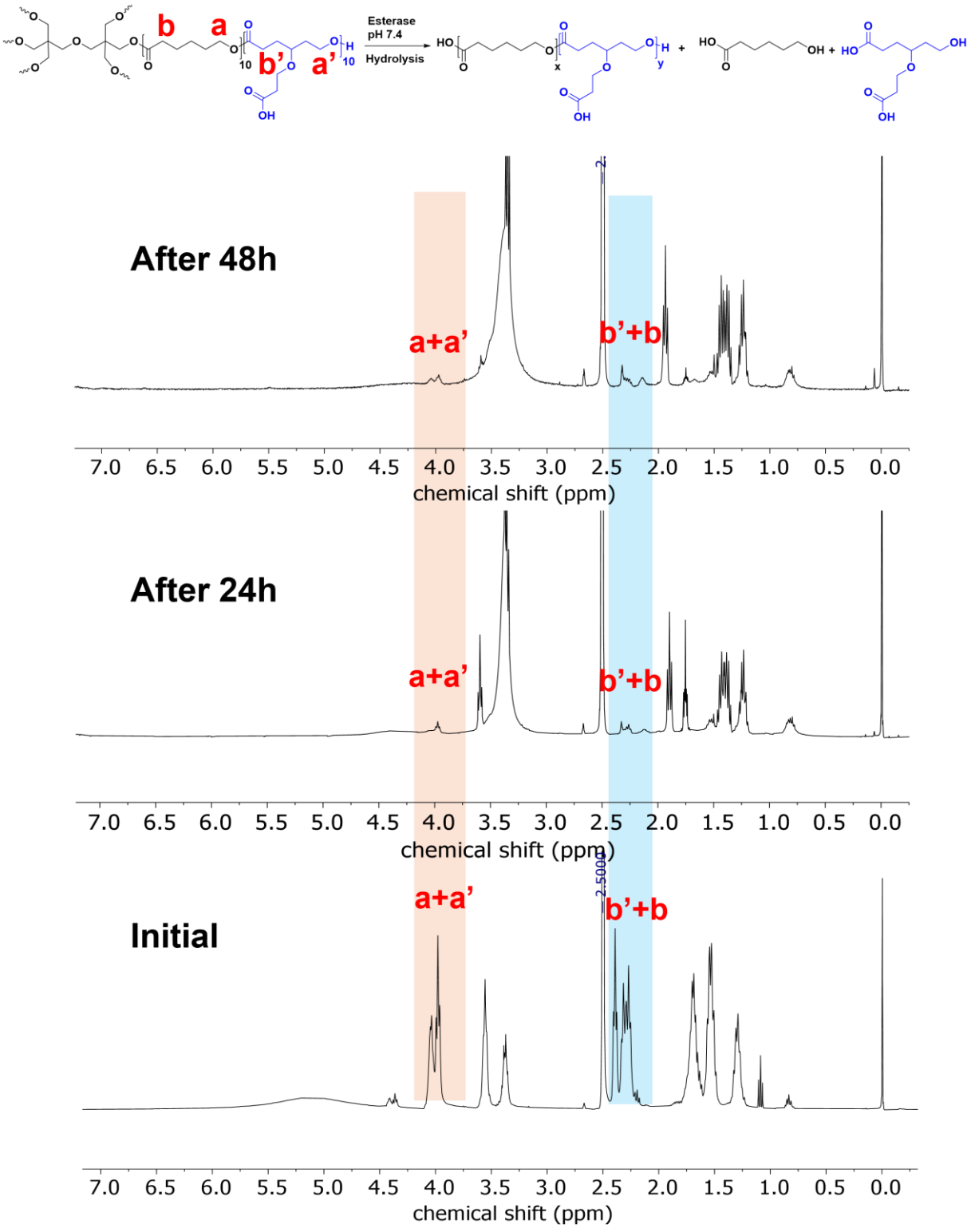

Figure 2.18: *^{1}HNMR plots SB-60 polymer in DMSO-d_6 incubated with esterase in PBS pH 7.4 at 37 ºC. The aliquots were collected at lyophilized at initial, 24h, 48h timepoints.*

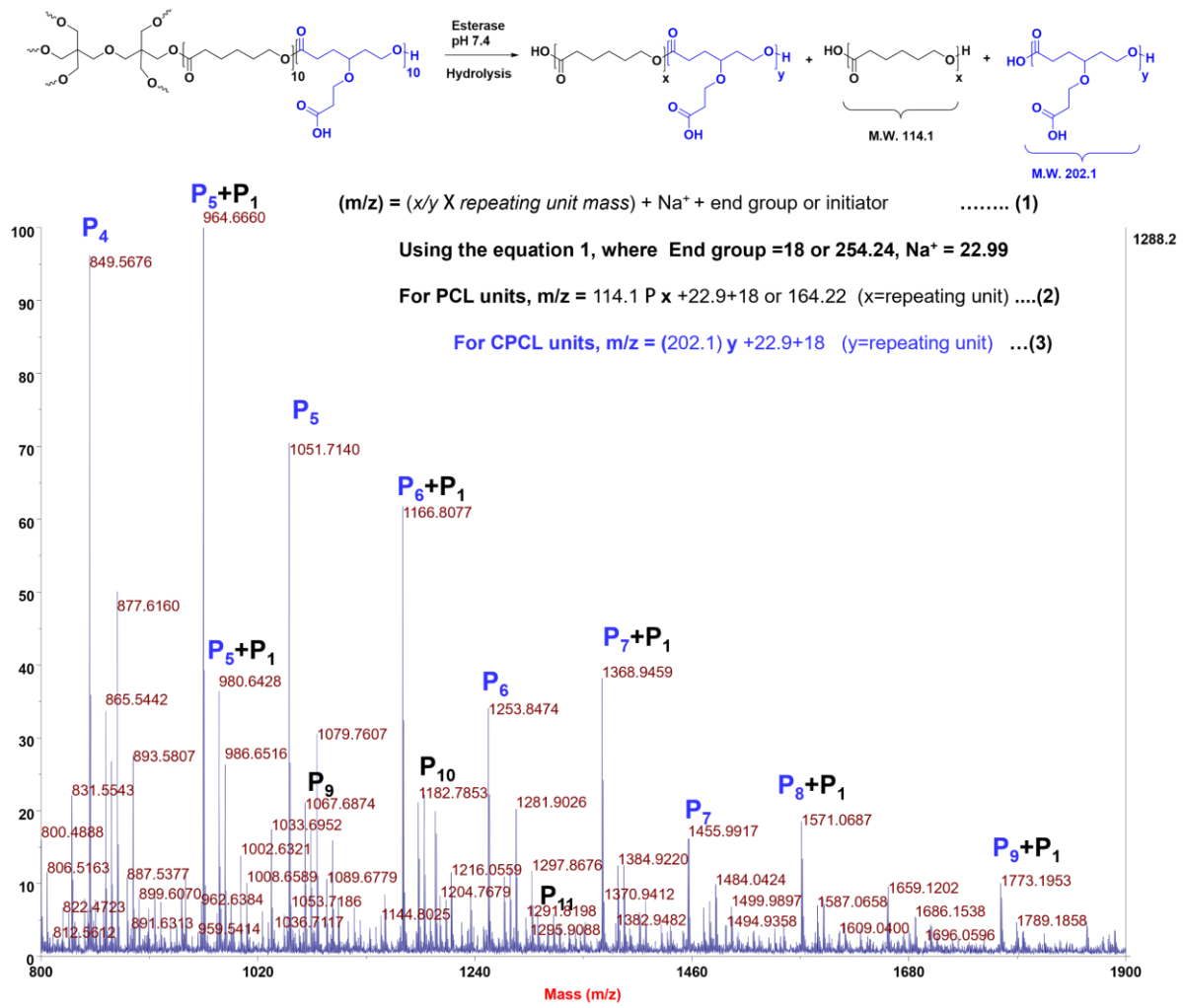

Figure 2.19: *MALDI-TOF spectra of SB-60 (UMM) polymer after incubation with esterase in PBS pH 7.4 at 37 ºC for 24h. The aliquots were collected at lyophilized at 24h, resolved in THF and subjected to MALDI-TOF analysis is reflectance mode. The fragmented peaks are assigned to degraded oligomers using aforementioned equations.*

.

2.3.7 Cytotoxicity

Toxicity of drug delivery system is of major concern since these nanocarriers should be able to not only deliver the cargo but also should not cause any adverse systemic toxicity after administration. Therefore, it is crucial to investigate the cytotoxicity of nascent nanoparticles and potency of their drug loaded versions *in vitro* prior to *in vivo* investigation. The cytotoxicity of nascent AgM and UMM nanoparticles were examined by MTT assays after treatment of 72h in MIA PaCa2 cell line is shown in Figure2.20a. Both the nanoparticles showed excellent compatibility with the MIA PaCa 2 cells (nearly 100% cell viability). Furthermore, the toxicity of AgM, UMM and other SB-x nanoparticles were examined in WT-MEF, MCF-7. MDA-MB-231 and MDA-MB-468 cell lines and data are shown in Figure 2.20b-2.20e. All the nascent nanoparticles depicted more than 80 % cell viability on highest concentrations (100 µg/mL) for 72h incubation in all the cancer and non-cancer cell lines studied as shown in Figure 2.20.

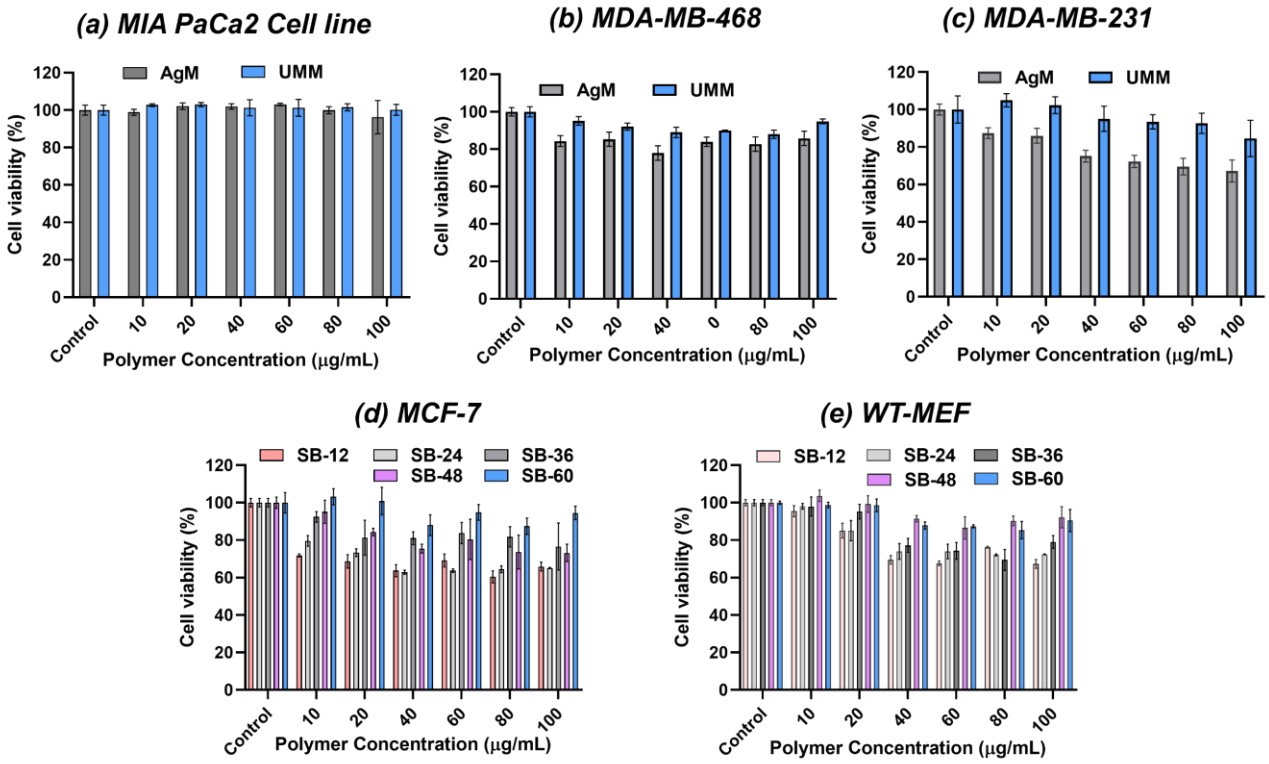

Figure 2.20. *Cytotoxicity by MTT assays for 72h incubation: Cytotoxicity of nascent AgM and UMM nanoparticles in (a) MIA PaCa2, (b) MDA-MB-468, (c) MDA-MB-231 cell lines for 72h incubation (n=3) respectively. (d) and (e) Plot of cell viability for nascent star block copolymers in MCF-7 cell line and WT-MEF (n=3, data represented as mean ± SD).*

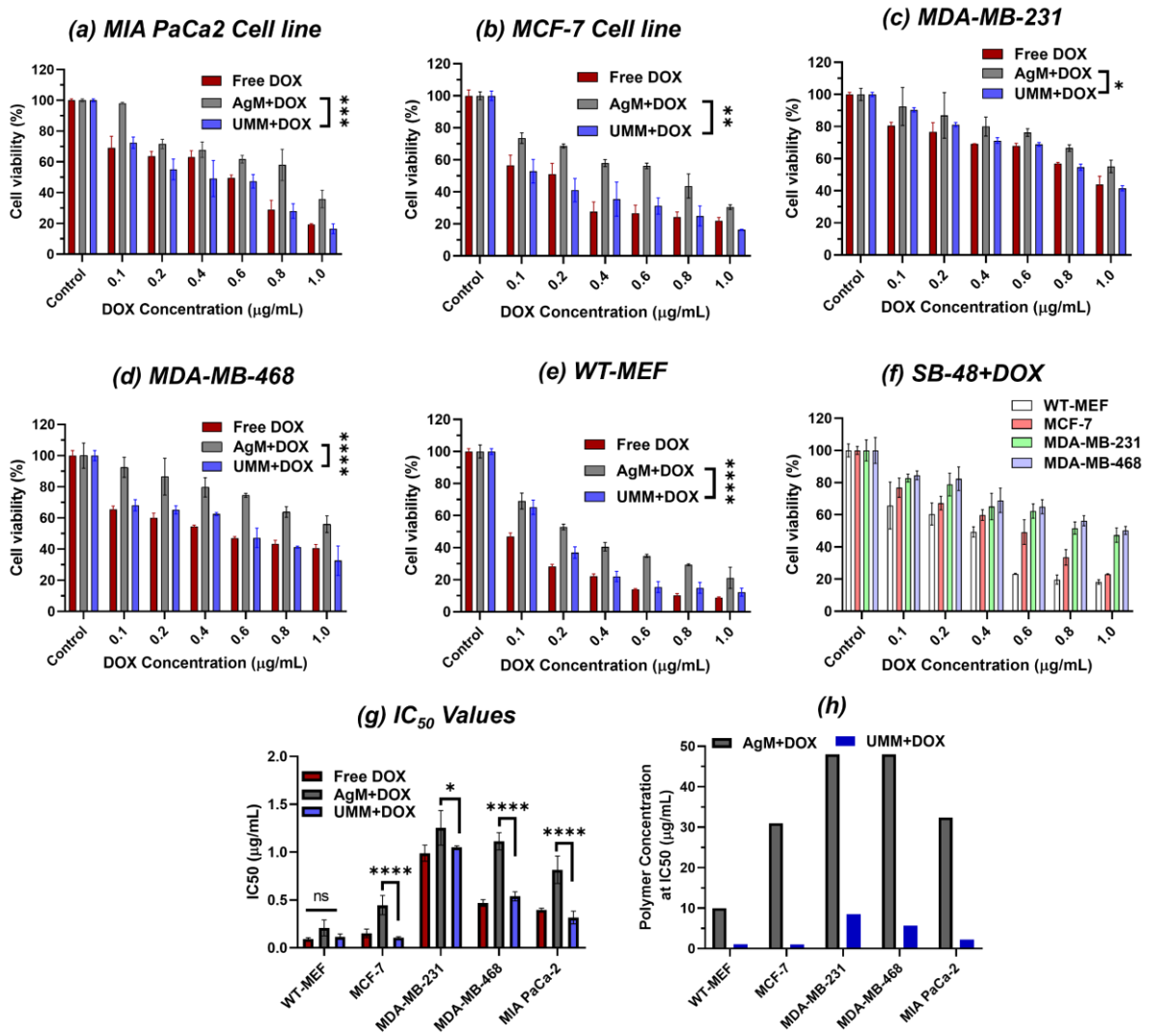

Figure 2.21. *Cytotoxicity by MTT assays for 72h incubation: (a) to (e) Cytotoxicity of free DOX (nascent DOX), AgM+DOX and UMM+DOX in MIA PaCa 2, MCF-7, MDA-231, MDA-MB-468 and WT-MEF cell lines after 72h incubation respectively (n=3, data represented as mean ± SD, **p=0.0043, ***p<0.001, ANOVA test). (f) Plot of cytotoxicity for SB-48+DOX nanoparticles in WT-MEF, MCF-7, MDA-MB-231, MDA-MB-cell lines after 72h (n=3, data represented as mean ± SD). (g) Plot of IC_{50} concentrations for AgM+DOX and UMM+DOX for various cell lines (n=3, *p<0.05, ****p< 0.0001, ns indicates non-significant, ANOVA test). (h) Plot of polymer concentration required to achieve IC_{50}.*

Investigating comparative efficacy of DOX loaded aggregated micelle (AgM+DOX) and unimolecular micelle (UMM+DOX), different cancer and non-cancer cell lines were chosen and results of MTT assay after treatment of 72h are shown in Figure 2.21. Both AgM+DOX and UMM+DOX showed concentration (dose) dependent killing in the similar manner to free DOX suggesting preservation of DOX activity (intercalating DNA and inhibition of Topoisomerase II) inside the nanocarriers. UMM+DOX showed superior cell killing ability in the MIA PaCa 2 (pancreatic cancer) and MCF-7 (breast cancer) where

UMM+DOX depicted >80% cell killing at highest concentration (1.0 μg/mL) compared to AgM+DOX which showed only 60-65% killings suggesting better efficacy of UMM+DOX as shown in Figure 2.21a and 2.21b. This superior killing ability was consistent for UMM in the DOX resistant breast cancer (MCF-7) and triple negative breast cancer cell lines (MDA-MB-231 and MDA-MB-468) compared to AgM+DOX on concentration range screened as shown in Figure 2.21c-2.21e. Data for evaluation of SB-48+DOX in multiple cancer cell lines is shown in Figure 2.22f. The plot of inhibitory concentration (IC_{50}) for free DOX (control), AgM+DOX and UMM+DOX is shown in Figure 2.21g. Significantly lower IC_{50} values were observed for all four cancer cell lines treated with UMM+DOX compared to AgM+DOX further indicated the superiority of unimolecular micelles. The amount of polymer needed to achieve IC_{50} concentration was estimated and revealed that 10-50-fold higher concentrations of AgM+DOX (aggregated micelles) required to achieve IC_{50} compared to UMM+DOX (unimolecular micelles) as shown in Figure 2.21h. Furthermore, the killing ability of DOX loaded NP were tested against MCF-7 and MIA PaCa2 on higher concentration of DOX (up to 3μg/mL). Data revealed better efficacy of UMM+DOX compared to AgM+DOX on high concentration of DOX (see Appendix). This is mainly attributed to high DLC, and superior killing ability of DOX loaded unimolecular micelles over aggregated micelles. These cytotoxicity results implied superior drug delivery ability of unimolecular micelles over aggregated micelles. The significant difference in the potent killing efficiency of DOX delivered from unimolecular micellar (UMM+DOX) platform over aggregated micelles (AgM+DOX) is very clearly seen in the MTT data.

2.3.8 Cellular Uptake studies

To comprehend the reason for different efficacy of DOX loaded unimolecular and aggregated micelles in the intracellular level, cellular uptake studies were performed in the WT-MEF, MCF-7 and MIA PaCa 2 cell lines. The CLSM images are shown in Figure 2.22a, along with CTCF estimated for free DOX (control), AgM+DOX, and UMM+DOX for the incubation of 6h in Figure 2.22b. The CLSM images in the from red channel clearly depicted intense fluorescence signal of DOX in the cells indicated the successful internalization of DOX loaded nanoparticle in the cells. The magenta color from nuclear region (merged panel) resulted from colocalization of DAPI (blue, nucleus stain) and DOX (red) clearly indicated the degradation of nanoparticles in the lysosomal compartment and release of the DOX to nucleus. The accumulation of DOX was much more significant in the case of UMM+DOX compared to

AgM+DOX indicated by intense DOX fluorescence signal in the nuclei from red channel or merged panel (magenta color, see Figure 2.22a). This is attributed to the fact that unimolecular micelle UMM+DOX are of small size (~20nm) can easily penetrate the cell membrane compared to large size aggregated micelles AgM+DOX (~60nm). Moreover, UMM has 6-fold high DLC compared to AgM therefore very few nanoparticles of UMM will carry significantly large amounts of drug molecules. In contrast, AgM+DOX, aggregated micelles of larger size and low DLC require 6-7-fold higher number of nanoparticles to compensate for the amount of DOX delivered by UMM. The estimated CTCF for WT-MEF, MCF-7 and MIA PaCa2 cell lines are shown in Figure 4.22b. CTCF calculations revealed significantly better cellular uptake of AgM+DOX compared to free DOX in cancer cell lines (MCF-7 and MIA PaCa2). Interestingly, a much superior uptake of UMM+DOX was observed compared to free DOX as well as AgM+DOX in WT-MEF, MCF-7 and MIA PaCa 2 cell lines. This is attributed to the fact that DOX molecules in the nascent form get efflux out of the cells due to action of integral membrane P-glycoprotein (Pgp) efflux pumps and these pumps are overexpressed in cancer cells resulting in multi-drug resistance (MDR). However, the nanoparticles can successfully avoid the efflux pumps and accumulate more in the cells resulting in higher cellular uptake compared to nascent drug (DOX) molecules. The CTCF values clearly showed significantly better cellular uptake of unimolecular micellar nanoparticles (UMM+DOX) compared to aggregated micelles (AgM+DOX) in all the cell lines examined. This result of cellular uptake provided evidence for the possible higher efficacy of UMM+DOX compared to AgM+DOX observed in MTT assays. Furthermore, capability of unimolecular micellar UMM+DOX nanoparticles was assessed for cellular uptake in time dependent manner in MCF-7 cells and CLSM images are shown in Figure 2.23a. It is evident from the CLSM images that the UMM+DOX showed significant enhancement with the progress in incubation time and further depicted accumulation of released DOX from the nanoparticle degradation afterward 4h timepoint (see Figure 2.23b for CTCF). In addition, UMM+DOX NPs were evaluated for cellular uptake capabilities in MDA-MB-231 and MDA-MB-468 (Triple negative breast cancer) cell lines, suggested excellent internalization of UMM+DOX NP compared to free DOX as shown in Figure 2.23c-d. UMM loaded with water soluble dyes such as 1,3,6,-trisulfonic acid trisodium salt (HPTS) and Sulforhodamine-B (SRhB) assessed for cellular uptake in WT-MEF (non-cancer) and MCF-7 (breast cancer) cell lines for 6h incubation and CLSM images are shown in Figure 2.24a-2.24d. The CLSM images revealed successful delivery of water soluble SRhB and HPTS indicating versatility of unimolecular micellar platform for various dye. Overall results obtained by assessment of cellular uptake studies

imply that the unimolecular micellar UMM nanoparticles are superior in cellular internalization and degradation compared to AgM nanoparticles. This positive data not only renders them suitable for drug delivery candidates for *in vivo* but also inspired to carry out further *in vivo* investigations to understand the performance of aggregate vs unimolecular micelles.

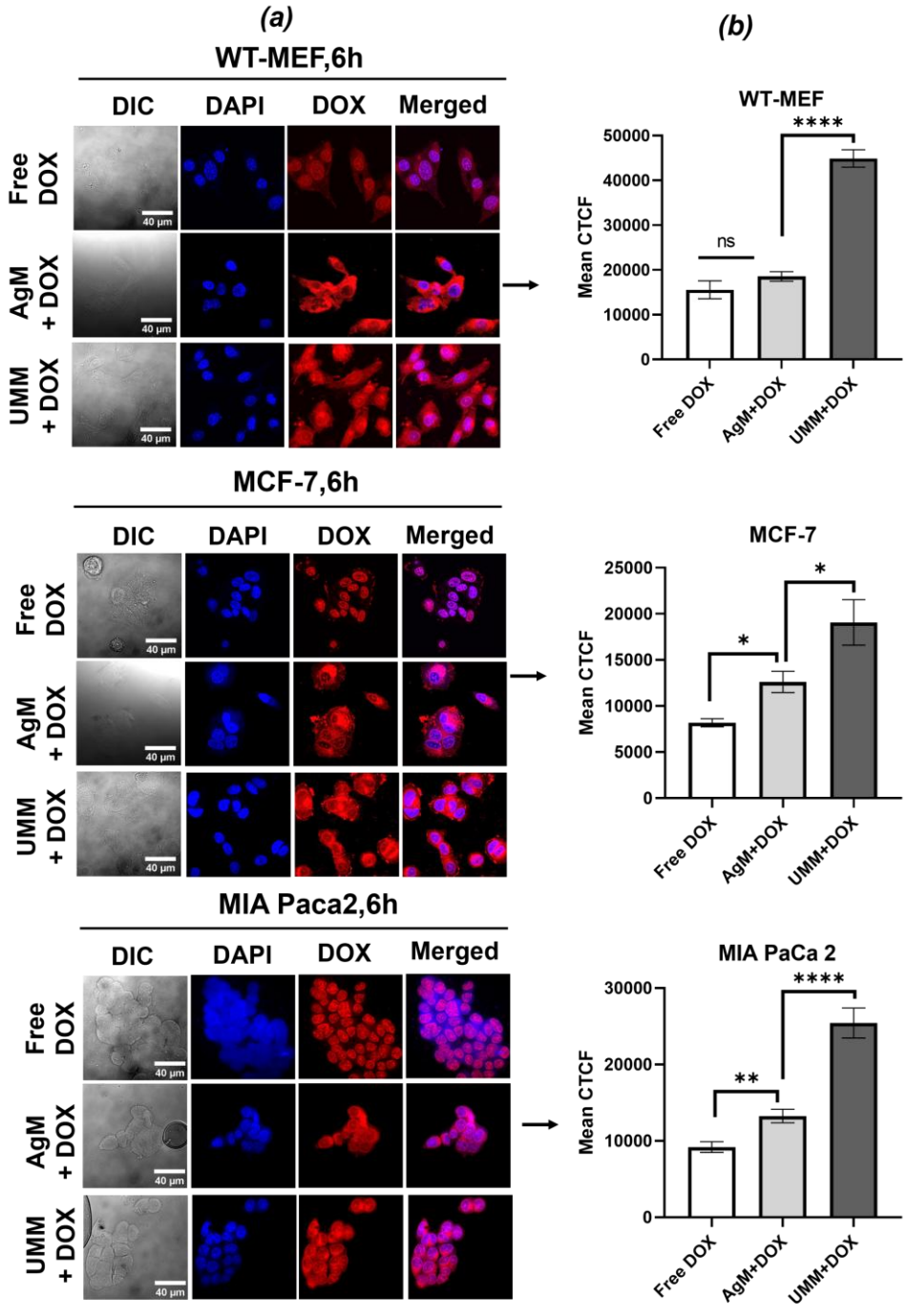

Figure 2.22. *Cellular uptake studies:(a)CLSM images of cellular uptake of Free DOX, AgM+DOX and UMM+DOX in WT-MEF, MCF-7 and MIA PaCa 2 cell lines for 6h incubation and (b) CTCF plots for uptake in respective cell lines. (scale bar 40µm, DOX concentration 2.5µg/mL, n>3, data represented as mean ± SD, ns=non-significant, *p<0.05, **p<0.0020, ***p<0.001,**** p<0.0001 ANOVA test).*

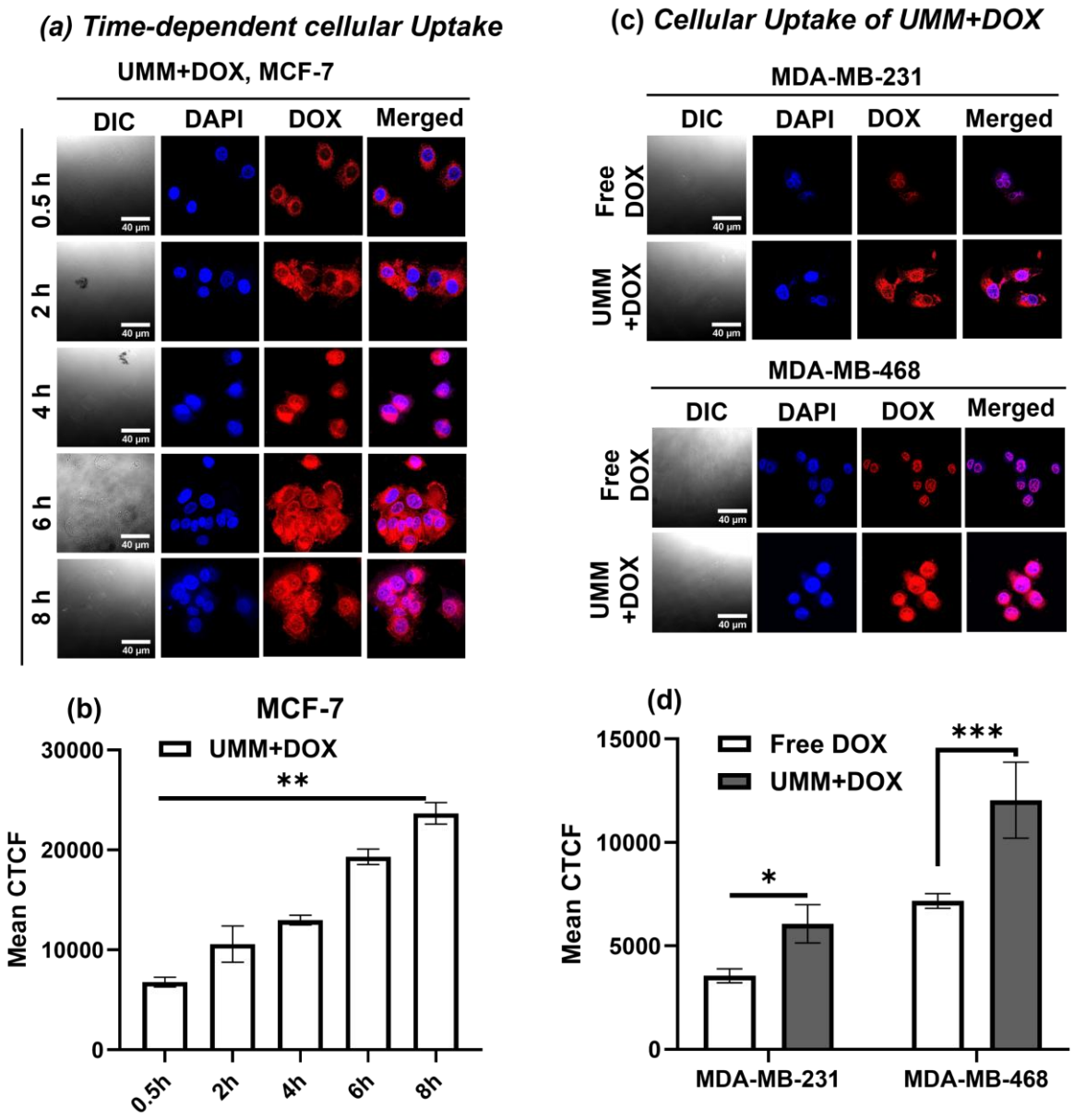

Figure 2.23. *(a) CLSM images for time dependent cellular uptake of UMM+DOX in MCF-7 cells (Scale bar 40µm, DOX concentration 2.5µg/mL). (b) Plot of CTCF for UMM+DOX for different timepoints (n=3, Data represented as mean ± SD, **p=0.0085). (c) CLSM images cellular uptake of free DOX and UMM+DOX in MDA-MB-231 and MDA-MB-468 cell lines after 6h (Scale bar 40µm, DOX concentration 2.5µg/mL). (d) Plot of CTCF for Free DOX and UMM+DOX in MDA-MB-231, MDA-MB-468 cell lines (n=3, data represented as mean ± SD, *p>0.05,*** p=0.001 ANOVA test).*

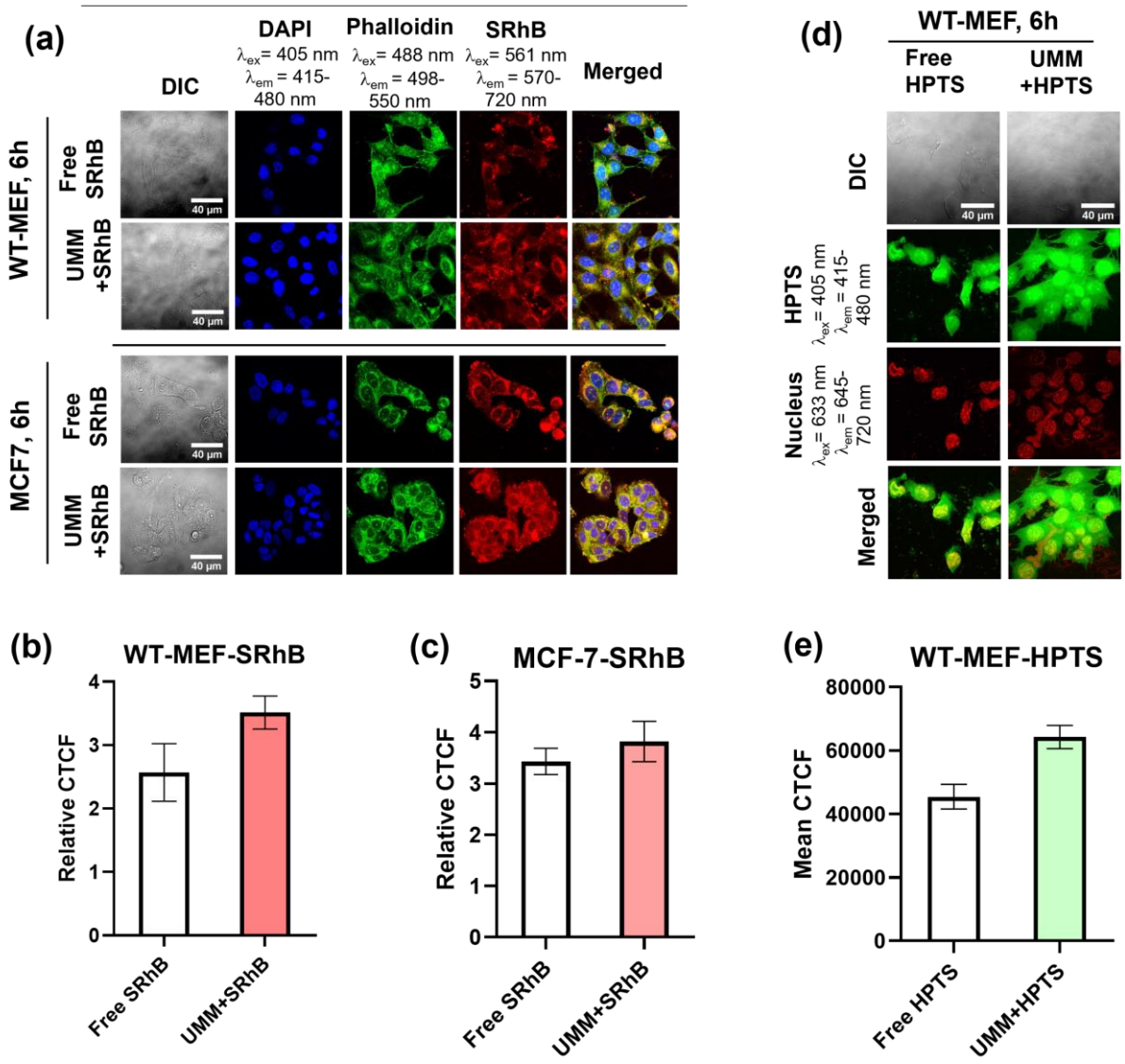

Figure 2.24. *(a) CLSM images of cellular uptake of Free sulforhodamine B (SRhB), UMM+SRhB nanoparticles in WT-MEF and MCF-7 cell lines for 6h incubation and CTCF plots. (scale bar 40µm, SRhB concentration 2.5µg/mL). (b) & (c) Plot of CTCF for free SRhB and UMM+SRhB in WT-MEF and MCF-7 cell lines respectively (n>3, data represented as mean ± SD). (d) CLSM images for time dependent cellular uptake of Free HPTS and UMM+HPTS in WT-MEF cells (Scale bar 40µm, DOX concentration 1.0 µg/mL). (e) Plot of CTCF for Free HPTS and UMM+HPTS in WT-MEF cell lines (n=3, data represented as mean ± SD).*

2.3.9 Hemolysis assay

Interaction of nanoparticles with circulating blood in the body is the first step of *in vivo* delivery aspect where the nanoparticles counters erythrocytes or red blood cells (RBC) as well as various proteins. It is therefore crucial to evaluate the nanoparticles for their non-hemolytic activity prior to administration as shown in Figure 2.25a. To investigate this all the nanoparticles were incubated with freshly collected RBCs for 1h and their hemolytic activity was measured as a function of RBC rupture. As anticipated, the complete rupture of RBCs was observed in case of Triton-X (100% hemolysis) treatment whereas no hemolysis was found for PBS (negative control) revealed by pellet of RBC at bottom in centrifuge tube. Surprisingly, all the nanoparticles exhibited excellent compatibility with RBC at highest concentration (1mg/mL) with no hemolytic evident from the pellet of RBC at the bottom of centrifuge tube in Figure 2.25a. These results implied that star block copolymer nanoparticles are safer for administration *in vivo* and further can be evaluated for biodistribution studies.

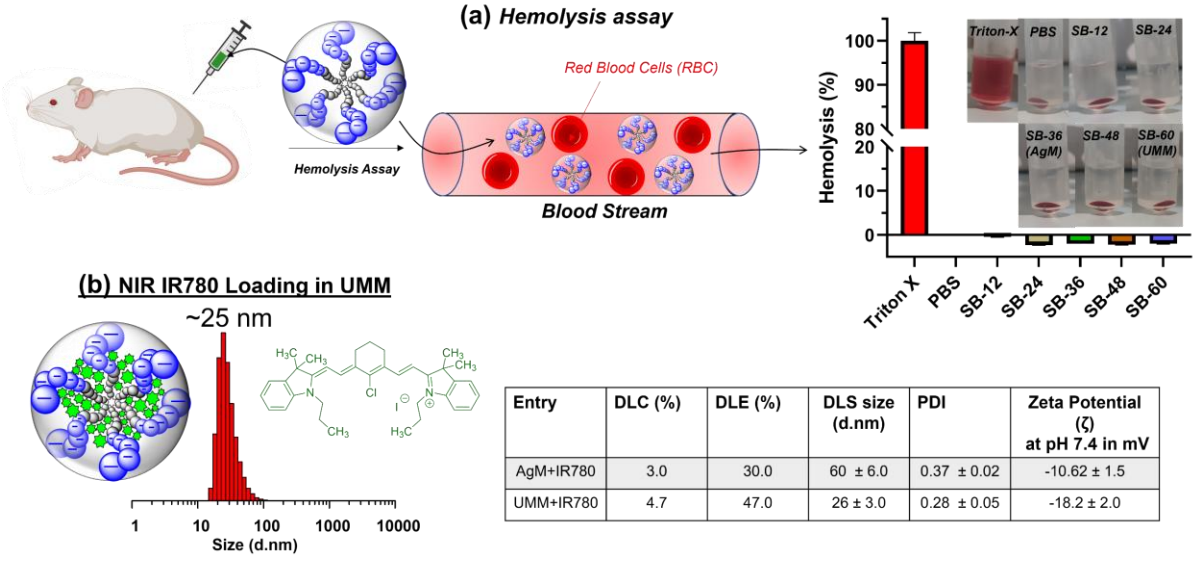

Entry	DLC (%)	DLE (%)	DLS size (d.nm)	PDI	Zeta Potential (ζ) at pH 7.4 in mV
AgM+IR780	3.0	30.0	60 ± 6.0	0.37 ± 0.02	-10.62 ± 1.5
UMM+IR780	4.7	47.0	26 ± 3.0	0.28 ± 0.05	-18.2 ± 2.0

Figure 2.25. *(a)Hemolysis assay, Plot of % hemolysis for SB-12, SB-24, SB-36, SB-48 and SB-60 (n=3, polymer concentration 1.0 mg/mL). Triton-X and PBS buffer were used as positive and 0negative control. (b) Pictorial representation of UMM+IR780 nanoparticle and DLS histogram and tabulated details of encapsulation.*

2.3.10 In Vivo Biodistribution assay

Near infrared fluorescence imaging (NIRF) was utilized to investigate the biodistribution of star block copolymer in animal model (mouse) owing to its non-invasive nature, minimal background emission and deep tissue penetration. For that purpose, infrared IR-780 dye was selected due to its high quantum yield and longer blood circulation time.[60] The schematic for UMM+IR780 nanoparticles and DLS histogram of UMM+IR780 nanoparticle is shown in Figure 2.25b. Details of encapsulation for near infrared dye IR780 encapsulations are tabulated in Figure 2.25b. To assess the biodistribution and tumor retention abilities of AgM and UMM nanoparticles in tumor bearing mouse model, pancreatic tumors were created (xenograft) in immune-compromised NOD-SCID mice and details are mentioned in experimental section. Briefly, MIA PaCa 2 cells (Human pancreatic cancer) were subcutaneously injected into right flanks of the mice and biodistributions analysis was carried out once tumor reached specific volumes. Pancreatic cancer tumors bearing NOD-SCID mice were injected with free IR-780 (positive control), AgM+IR780 (SB-36+IR780) and UMM+IR780 (SB-60+IR780) were injected ($n=3$, dose 0.7mg/kg) via intraperitoneal injection (100 μL PBS) and animals were imaged by IVIS for 96 h as shown in Figure 2.26a (experimental design). The animals injected with AgM+IR780 and UMM+IR780 depicted intense fluorescence from the whole body from 4h timepoint onwards compared to free IR-780 as shown in Figure 2.26b. Moreover, animals injected with free IR780 showed gradual reduction in fluorescence after 48h due to clearance of free IR780 from systemic circulation. In contrast the AgM+IR780 and UMM+IR780 did not show any significant reduction in fluorescence till 96h, which was attributed to longer blood circulation of nanoparticles compared to free IR780. Interestingly the signals were much more intense from the tumoral region due to high accumulation of AgM+IR780 and UMM+IR780 nanoparticles in the tumor compared to free IR780 as shown in Figure 2.26b (tumor marked with circles). The quantification of signals revealed the 2-4-fold higher signal intensity in case of animals injected with AgM+IR780 and UMM+IR780 nanoparticles compared to free IR780 for all time points and signals were persistent till 96h as shown in Figure 2.26c. Furthermore, significantly better whole-body signal (average radiance) was observed in the case of unimolecular micelles UMM+IR780 compared to aggregated micelles AgM+IR780 from 4h to 96h as shown in Figure 2.26c. In addition to that, IVIS images and quantification from the dorsal view depicted similar results as shown in Figure 2.26d-2.26e. This is attributed mainly to smaller size, greater stability, and better systemic circulation time of the unimolecular micelles compared to

aggregated micelles. This whole-body imaging results clearly suggested the slightly better performance of unimolecular micelles over aggregated micelles.

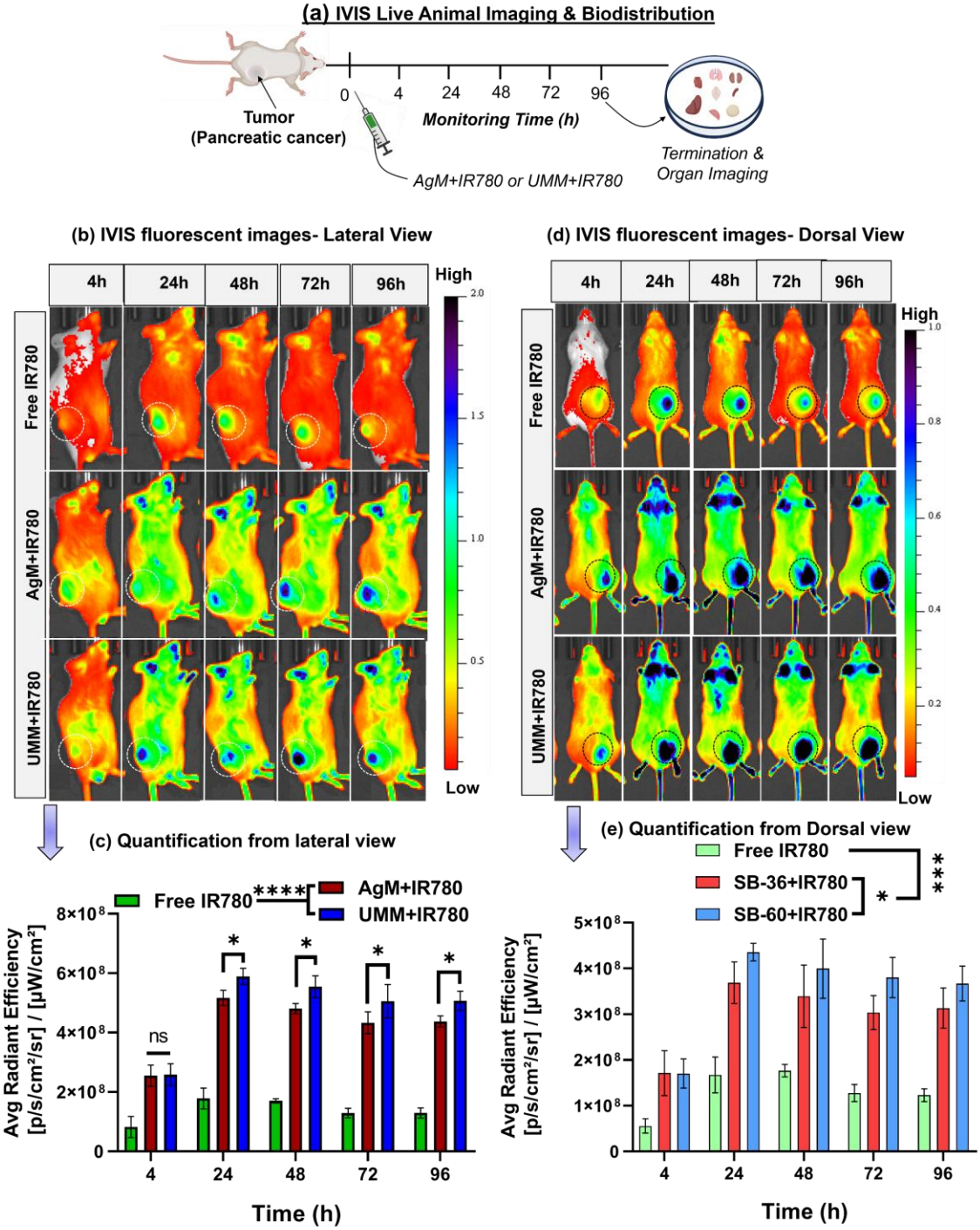

Figure 2.26. *(a) Experimental design for in vivo biodistribution studies in MIA PaCa 2 (pancreatic cancer) bearing NOD-SCID mice. (b) and (d) Representative whole body IVIS near infrared fluorescence images of lateral and dorsal view for animals intraperitoneally injected with Free IR780, AgM+IR780 and UMM+IR780 respectively. (c) and (e) Respective plot of quantified fluorescence signal from whole body images of lateral and dorsal view respectively (n=3, data represented as mean ± SD, *p<0.05,***p=0.0001, ****p<0.0001 ANOVA test).*

To investigate the retention and accumulation of IR780 loaded nanoparticles in the vital organs and tumors, the animals were euthanized after 96h of injection and their vital organs along with tumor were harvested. The harvested organs were subjected to IVIS infrared fluorescence imaging and images are shown in Figure 2.27a. Both AgM+IR780 and UMM+IR-780 nanoparticles depicted intense signals in excretory organs (lungs, kidneys and liver) and digestive organ (pancreas) compared to free IR780. Interestingly, IVIS images of tumor revealed appreciably more intense signal for both the nanoparticles compared to free IR780 in the tumor suggesting deep tissue penetration of nanoparticles. This is attributed to more retention and accumulation of nanoparticles in the tumor owing to passive targeting ability via enhanced permeability and retention (EPR) effect. The quantified for organ accumulation in Figure 2.26b revealed that both nanoparticles did not cause any significant cardiotoxicity or neurotoxicity (non-significant with free IR780) and showed more accumulation in lungs, liver, and kidney compared to free IR780. Interestingly, unimolecular micelles (SB-60+IR780) depicted significantly higher accumulation in tumor than aggregated micelles (SB-36+IR780) owing to their smaller size, better penetration ability, longer systemic circulation time and stability. This passive targeting ability and persistent accumulation after 96h of injection is significantly advantageous to maintain the effective concentration of drug into tumor site. Which further would result in reduction of dose frequency to achieve maximum effect and can avoid side effects caused by overdose.

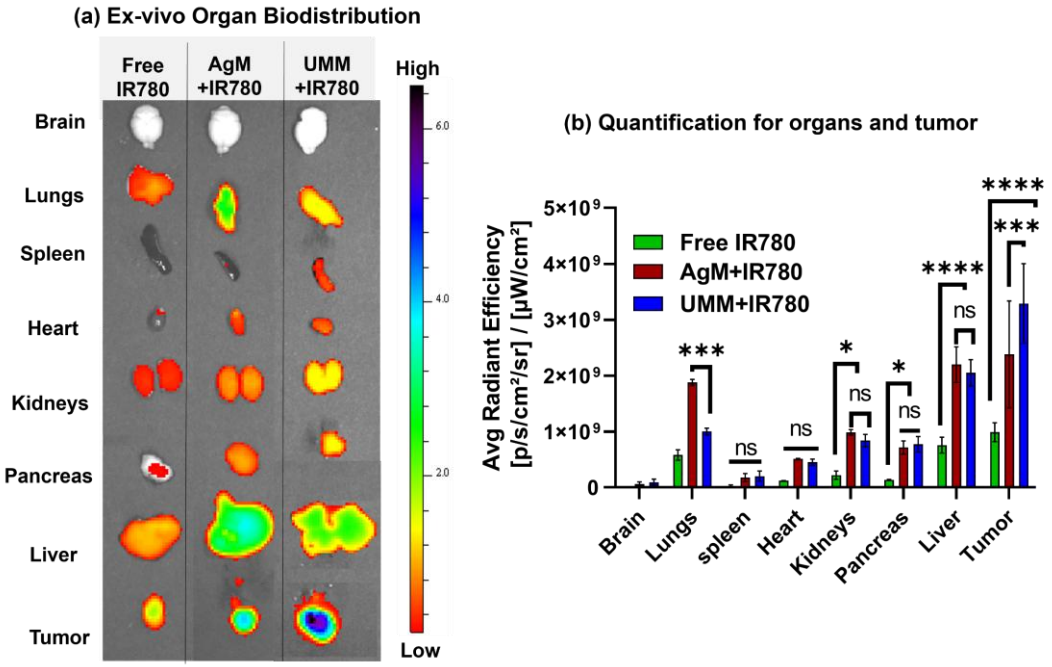

Figure 2.27. *(a) IVIS images of harvested organ 96h postinjection. (b) Respective plot of quantified fluorescence signal from harvested organs 96h postinjection (n=3, data represented as mean ± SD, ns=non-significant, *p<0.05, ***p=0.0004,**** p<0.0001 ANOVA test).*

2.3.11 Antitumor Efficacy in Xenograft Model

Encouraged by significantly better accumulation and retention of IR780 loaded nanoparticles into tumor owing to their excellent passive targeting ability, next we evaluated the antitumor efficacy of DOX loaded nanoparticles in subcutaneous xenograft mice model of pancreatic cancer (MIA PaCa2). The rationale of this study was to understand not only the antitumor efficacy of nanoparticle platform but also to evaluate comparative efficiencies of aggregated and unimolecular micellar platform. The experimental plan is shown in Figure 2.28a, when the tumor volume reached ~50 mm^3, the animals were randomly divided into 4 groups (*n=4*) and intraperitoneally injected with PBS (negative control), nascent DOX (positive control), AgM+DOX (aggregated micelles) and UMM+DOX (unimolecular micelles). As shown in Figure 2.28a, the injections were administered every fourth day (2mg/kg) for 16 days and tumor growth and body were monitored for 19 days. The body wights of animals treated with DOX showed drastic reduction in body weights after a week owing to systemic toxicity associated with of nascent DOX molecules as shown in Figure 2.28b. In contrast the animals treated with both DOX loaded nanoparticles did not show any significant change in body weights throughout the treatment revealed biocompatible characteristics of nanoparticles and currently designed platform possess satisfactorily biosafety. Individual tumor growth curves of all treated groups are shown in Figure 2.29a to 2.29d and tumor growth curves for all groups together are shown in Figure 2.29e. The group treated with PBS (negative control) depicted exponential growth in the tumor after a week tumor volume reached to ~1500 mm^3 in only 19 days as shown in Figure 2.29a and 2.29e. Whereas the group receiving DOX treatment showed significant suppression in tumor growth compared to PBS group and tumor volumes reached ~500 mm^3 towards the end of experiments as shown in Figure 2.29b and 2.29e. Similar results of tumor suppression were observed for the group treated with AgM+DOX suggesting equivalent efficacy of AgM+DOX and nascent DOX as shown in Figure 2.29c and 2.29e. Even though aggregated micelles could not perform significantly better than DOX, however AgM+DOX were better in biosafety aspects compared to nascent DOX. Interestingly, the unimolecular micelles UMM+DOX showed remarkably better suppression in tumor growth compared to DOX and AgM+DOX and tumor volumes observed in the range of ~225 mm^3 after 19 days of treatment as shown in Figure 2.29d and 2.29e. Superior anticancer efficacy of UMM+DOX (unimolecular micelles) is attributed to significantly higher retention and accumulation in tumor owing to smaller sized stable nanoparticles compared to aggregated micelles. Furthermore, all mice were euthanized at the end of experiment (19^{th} day) and tumor

tissue were harvested. The photograph of harvested tumors provided clear visual evidence of better tumor suppression in the group treated with unimolecular micelles (UMM+DOX) compared to aggregated micelles, DOX and PBS as shown in Figure 2.29f. The weights of harvested tumors were immediately measured and shown in the plot in Figure 2.29g. Quantitative analysis of tumor weights clearly indicated a remarkable suppression of tumor growth after treatment with unimolecular micellar (UMM+DOX) platform compared to aggregated micelles (AgM+DOX) control groups (Free DOX or PBS). These results revealed that star block copolymer nanoparticle platform displayed better anticancer efficacy in pancreatic cancer xenograft model along with considerable biosafety. This approach is not restricted to only pancreatic cancer models but can be exploited to other cancer models as well. Moreover, currently designed strategy of star block copolymers is also capable of encapsulating other chemotherapeutic drugs therefore unimolecular micelles can be used to deliver other chemotherapeutic drugs or combination therapies in future perspective.

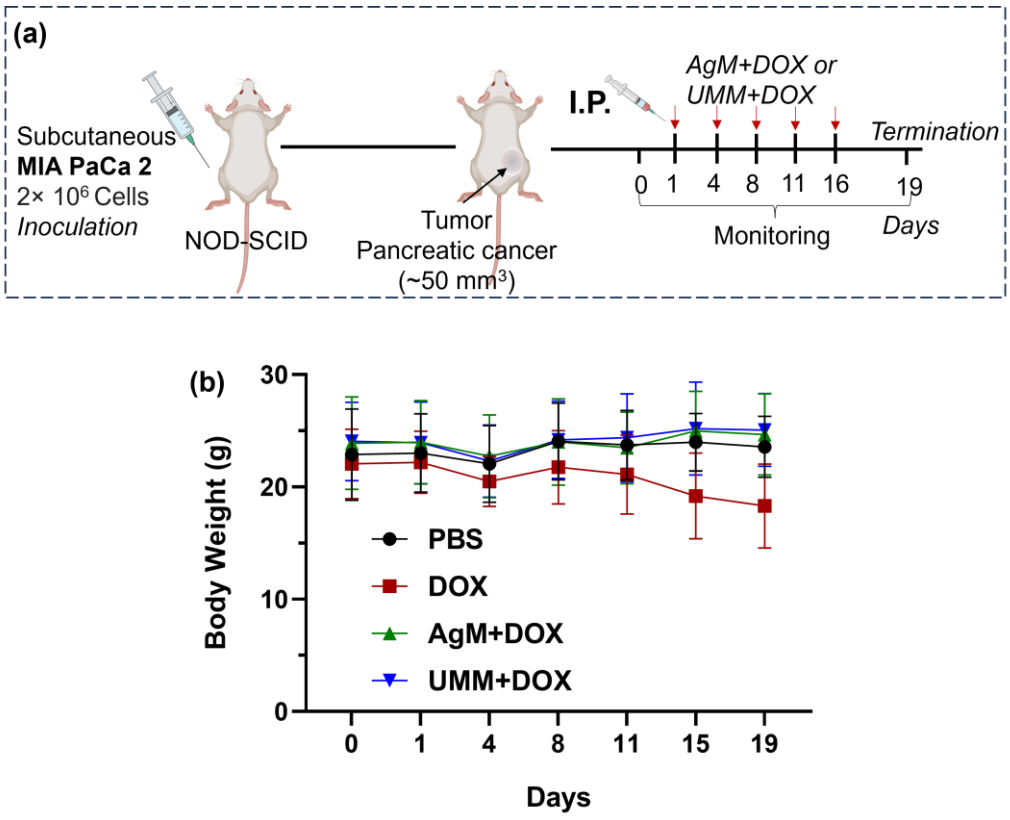

Figure 2.28. *(a) Experimental design for in vivo anticancer efficacy studies in MIA PaCa2 (pancreatic cancer xenograft model) bearing NOD-SCID mice. (b) Body weight variation curves of treated groups.*

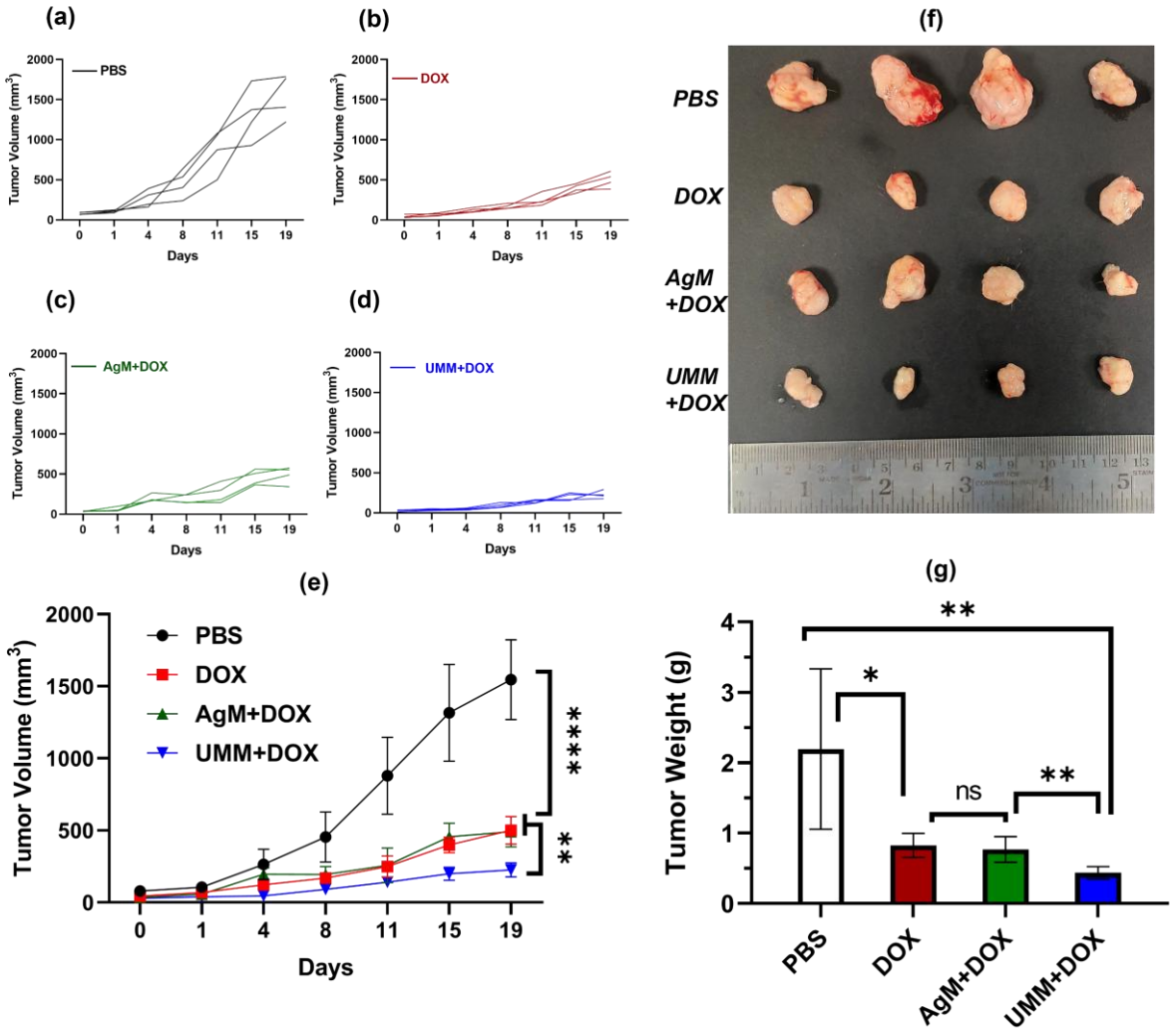

Figure 2.29. *(a) to (d)Tumor growth curves of PBS, DOX, AgM+DOX and UMM+DOX groups over 19 days. (e) Tumor suppression effect of 19-day treatment in PBS, Free DOX, AgM+DOX and UMM+DOX groups (Dose 2.0 mg/kg, n=4, data represented as mean ± SD, **p=0.0089, ****p<0.0001, ANOVA test). (f) Photographs of tumor harvested after 19 days of treatment. (g) Tumor weights of PBS, free DOX, AgM+DOX and UMM+DOX treated groups after 19 days of treatment (n=4, data represented as mean ± SD, *p<0.05, *p=0.007, t-test).*

2.4 Conclusion

In summary, we have successfully demonstrated the programming of the unimolecular micelles in the 6-arm star block copolymers by modulating the amphiphilicity. Self-assembly studies have proven that aggregated 60-200 nm or unimolecular micelles of 20 nm could be produced by tuning the size of hydrophilic block in the block copolymers. Unimolecular micelles depicted superior DLC for anticancer drug Doxorubicin (DOX) in the range of 15% compared to aggregated micelles (~2.5%). The in *vitro* drug release and live-cell lysotracker studies have proven truly biodegradable nature of star block copolymers. Anticancer efficacy of DOX loaded nanoparticles established the superior killing efficiency of unimolecular micellar platform compared to aggregated micelles in multiple cancer cells lines. The nanoparticles showed enhanced cellular uptake compared to nascent drug. The nascent nanoparticles were non-toxic and non-hemolytic nature. The *in vivo* biodistribution analysis via NIRF imaging revealed superior accumulation and retention of nanoparticles in the tumor tissues after 96h of injection in xenograft mice model. The DOX loaded unimolecular micelles (UMM+DOX) exhibited significant suppression in the tumor growth and depicted better anticancer efficacy compared to DOX or aggregated micelles in pancreatic cancer xenograft mice model. This approach is not restricted to only DOX or pancreatic cancer mice model but can be also exploited for other chemotherapeutic agents as well as other cancer models.

2.5 References

[1] Hwang, D.; Ramsey, J. D.; Kabanov, A. V., Polymeric Micelles for the Delivery of Poorly Soluble Drugs: From Nanoformulation to Clinical Approval. *Adv. Drug Deliv. Rev.* **2020,** *156*, 80-118.

[2] Peer, D.; Karp, J. M.; Hong, S. Farokhzad. O. C.; Margelit, R.; Langer, R. Nanocarriers as an Emerging Platform for cancer Therapy. *Nat. Nanotechnol.* **2007**, *2*, 751-760.

[3] Tarannum, M.; Vivero-Escoto, J .L. Nanoparticle-based Therapeutic Strategies targeting Major Clinical Challenges in Pancreatic Cancer Treatment. *Adv Drug Deliv. Rev*. **2022**, *187*, 114357.

[4] Wei, D.; Sun, Y.; Zhu, H.; Fu, Q. Stimuli-Responsive Polymer-Based Nano systems for Cancer Theragnostic. *ACS Nano* **2023** *17*, 23223–23261.

[5] Manzari, M.; Shamay, Y.; Kiyuchi, H.; Rosen, N.; Scaltiti, M.; Heller, D. A Targeted Drug Delivery Strategies for Precision Medicines. *Nat. Rev. Mater.* **2021**, *6*, 351–370.\

[6] El-Sawy, H.; Al-Abd, A. M.; Ahmed, T. A.; El-Say, K. M.; Torchilin, V. P. Stimuli-Respinsive Nano-Architecture Drug-Delivery Systems to Solid Tumor Micromilieu: Past, Present, and Future Perspectives. *ACS Nano* **2018**, *12*, 10636-10664.

[7] Wilhelm, S.; Tavares, A. T.; Dai, Q.; Ohta, S.; Audet, J.; Dvorak, H. F.; Chan, W. C. W. Analysis of Nanoparticle Delivery to Tumours. *Nat. Rev. Mater.* **2016**, 1, 16014.

[8] Song, C.; Li, Y.; Li, T.; Yang, Y.; Huang, Z. Martinez de la Fuente, M.; Ni, J.; Cui, D. Long-Circulating Drug-Dye-Based Micelles with Ultrahigh pH-Sensitivity for Deep Tumor Penetration and Superior Chemo-Photothermal Therapy. *Adv. Funct. Mater.* **2020**, *30*, 1906309.

[9] Kamley, N.; Yameen, B.; Wu, J.; Farokhzad, O. C. Degradable Controlled-Release Polymeric Nanoparticles; Mechanisms of Controlling Drug Release. *Chem. Rev.* **2016**, *116*, 2602–2663.

[10] Design of Nanocarriers Based on complex Biological Barriers In Vivo for Tumor Therapy. *Nano Today* **2017**, *15*, 56-60.

[11] Dai, Y.; Xu, C. Sun, X.; Chen, X. Nanoparticle Design Strategies for Enhanced Anticancer Therapy By Exploiting the Tumor Microenvironment. *Chem. Soc. Rev*. **2017**, *46*, 3830-3852.

[12] Shi, J.; Kantoff, P. W.; Wooster, R.; Farkokhzad O. C. Cancer Nanomedicine: Progress, Challenges and Opportunities. *Nat. Rev. Cancer* **2017**, *17*, 20-37.

[13] Liu, W.; Li, J.; Qin, Z.; Yao, M.; Tian, X.; Zhang, Z.; Zhang, L.; Guo, Q.; Zhang, L.; Zhu, D.; Yao, F., Zwitterionic Unimolecular Micelles with pH and Temperature Response: Enhanced In Vivo Circulation Stability and Tumor Therapeutic Efficiency. *Langmuir* **2020,** *36* (13), 3356-3366.

[14] Croy, S.; Kwon, G. Polymeric Micelles for Drug Delivery. *Curr. Pharm. Des.* **2006**, *12*, 466-4684.

[15] Cabral, H.; Matsumoto, Y.; Mizuno, K.; Chen, Q.; Murakami, M.; Kimura, M.; Terada, Y.; Kano, M. R.; Miyazono, K.; Uesaka, M.; Nishiyama, N.; Kataoka, K., Accumulation of Sub-100 nm Polymeric Micelles in Poorly Permeable Tumours Depends on size. *Nat. Nanotechnol* **2011,** *6* (12), 815-823.

[16] Luo, X.; Chen, M.; Zhang, Y.; Chen, Z.; Li, X. Pharmacokinetics and Antitumor Efficacy of Micelles Assembled from Multiarmed Amphiphilic Copolymers with Drug Conjugates in Comparison with Drug-Encapsulated Micelles. *Eur. J. Pharm. Biopharm.* **2016**, *98*, 9– 19.

[17] Qi, M.; Zhou, Y., Multimicelle Aggregate Mechanism for Spherical Multimolecular Micelles: from Theories, Characteristics and Properties to Applications. *Mater. Chem. Front.* **2019,** *3* (10), 1994-2009.

[18] Ghezzi, M.; Pescina, S.; Padula, C.; Santi, P.; Santi, Del Favero, E.; cantu, l.; Nicoli, S. Polymeric Micelles in Drug Delivery: An Insight of the techniques for Their Characterization and Assessment in Biorelevant Conditions. *J. Control Release* **2021***, 332,* 312-336.

[19] Torchilin, V. P. Micellar Nanocarriers: Pharmaceutical Perspectives. *Pharm. Res.***2007**, *24*, 1-16.

[20] Fan, X.; Li, Z.; Loh, X. j. Recent Development of Unimolecular Micelles as Functional Materials and Applications. *Polym. Chem.* **2016**, *7*, 5898-5919.

[21] Chen, W.; Liu, P. Facile Synthesis Of Pegylated Dendritic Polyurethanes As Unimolecular Micelles For Ultrasound-Triggered Localized Drug Delivery. *Polym. Chem.* **2022**, *13*, 80-84.

[22] Heise, A.; Hedrick, J. L.; Frank, C. W.; Miller, R. D. Starlike Block Copolymers With Amphiphilic Arms As Models For Unimolecular Micelles. *J. Am. Chem. Soc.* **1999**, *121*, 8647-8648.

[23] Kim, S.; Shi, Y.; Kim, J.; Park, K,; Cheng, J.; Overcoming The Barriers In Micellar Drug Delivery: Loading Efficiency, In Vivo Stability, And Micelle-Cell Interaction. *Expert Opin. Drug Deliv*. **2010**, *7*, 49-62.

[24] Takeda, K. M.; Yamasaki, Y.; Dirisala, A.; Ikeda, S.; Tockery, T. A.; Toh, K,; Osada, K.; Katoaka, K. Effect Of Shear Stress On Structure And Function Of Polyplex Micelles From Poly (Ethylene Glycol)-Poly(L-Lysine) Block Copolymers As Systemic Gene Delivery Carrier. *Biomaterials* **2017**, *126*, 31-38.

[25] Fox, M. E.; Szoka, F. C.; Fréchet, J. M. J. Soluble Polymer Carriers For The Treatment Of Cancer: The Importance Of Molecular Architecture. *Acc. Chem Res.* **2009,** *42* (8), 1141-1151.

[26] Nasongkla, N.; Chen, B.; Macargaeg, N.; Fox, M. E.; Frechet, J. M. J.; Szoka, F. C. Dependence of Pharmacokinetics and Biodistribution on Polymer Architecture: Effect of Cyclic versus Linear Polymers.

[27] Venkataraman, S.; Hedrick, J. L.; Ong, Z. Y.; Yang, C.; Ee, P. L. R.; Hammond, P. T.; Yang, Y. Y. The Effects Of Polymeric Nanostructure Shape On Drug Delivery. *Adv. Drug Deliv. Rev.***2011,** *63* (14), 1228-1246.

[28] Imran Ul-Haq, M.; Lai, B. F. L.; Chapanian, R.; Kizhakkedathu, J. N. Influence of Architecture of High Molecular Weight Linear And Branched Polyglycerols On Their Biocompatibility And Biodistribution. *Biomaterials* **2012,** *33* (35), 9135-9147.

[29] Kavand, A.; Anton, N.; Vandamme, T.; Serra, C. A.; Chan-Seng, D., Synthesis and Functionalization Of Hyperbranched Polymers For Targeted Drug Delivery. *J Control Release* **2020,** *321*, 285-311.

[30] Ohnsorg, M. L.; Prendergast, P. C.; Robinson, L. L.; Bockman, M. R.; Bates, F. S.;

Reineke, T. M. Bottlebrush Polymer Excipients Enhance Drug Solubility: Influence of End-Group Hydrophilicity and Thermoresponsiveness. *ACS Macro Lett.* **2021,** *10* , 375-381.

[31] Zhong, D.; Wu, H.; Wu, Y.; Li, Y.; Xu, X.; Yang, J.; Gu, Z., Rational Design and Facile Fabrication Of Biocompatible Triple Responsive Dendrimeric Nanocages for Targeted Drug Delivery. *Nanoscale* **2019,** *11*, 15091-15103.

[32] Dalal, R. J.; Ohnsorg, M. L.; Panda, S.; Reineke, T. M. Hydrophilic Surface Modification of Cationic Unimolecular Bottlebrush Vectors Moderate pDNA and RNP Bottleplex Stability and Delivery Efficacy. *Biomacromolecules* **2022**, *23*, 5179-5192.

[33] Liu, H.; Jiang, A.; Guo, J.; Uhrich, K. Unimolecular Micelles: Synthesis and Characterization of Amphiphilic polymer Systems. J. Polym. Sci.: Part A: Polym. Chem. 1999, 37, 703-711.

[34] Liu, H.; Farrell, S.; Uhrich, K., Drug Release Characteristics of Unimolecular Polymeric Micelles. *J Control Release* **2000,** *68* (2), 167-174.

[35] Jin, X.; Sun, P.; Tong, G.; Zhu, X., Star Polymer-Based Unimolecular Micelles and Their Application In Bio-Imaging And Diagnosis. *Biomaterials* **2018,** *178*, 738-750.

[36] Chen, G.; Wang, Y.; Xie, R.; Gong, S., A Review On Core–Shell Structured Unimolecular Nanoparticles For Biomedical Applications. *Adv. Drug Deliv. Rev.* **2018,** *130*, 58-72.

[37] Ren, J. M.; Mckenzie, T. G.; Fu, Q.; Wong, E. H. H.; Xu, J.; An, Z.; Shanmugam, S.; Davis, T. P.; Boyer, C.; Qiao, G. G., Star Polymers. *Chem. Rev* **2016,** *116* (12), 6743-6836.

[38] Chen, G.; Shi, X.; Wang, B.; Xie, R.; Guo, W-L.; Gong, S. Unimolecular Micelle-Based Hybrid System for Perivascular Drug Delivery Produces long-Term Efficacy for Neointima Attenuation in Rats. *Biomacromolecules* **2017**, *18*, 2205-2213.

[39] Zhao. P.; Liu, L.; Feng, X.; Wang, C.; Shuai, X.; Chen, Y. Molecular Nanoworm with PCL Core PEO Shell as a Non-Spherical Carrier for Drug Delivery. *Macromol. Rapid Commun.* **2012**, *3*, 1351-1355.

[40] Olemann, S. Meier, M. A. R. Synthesis of Unimolecular Micellar Behavior of Amphiphilic Star-Shaped Block Copolymers Obtained via the Passerini Three Component Reaction. *RSC Adv.* 2017, 7, 45195-45199.

[41] Bai, S.; Jia, D.; Ma, X.; Liang, M.; Xue, P.; Kang, Y.; Xu, Z. Cylindrical Polymer Brushes-Anisotropic Unimolecular Micelle Drug Delivery System for Enhancing the Effectiveness of Chemotherapy. *Bioactive Mater.* **2021**, *6*, 2894-2904.

[42] Du, F.; Honzke, S.; Neumann, F.; Kelitz, J.; Chen, W.; Ma, N.; Hedtrich, S.; Haag, R. Development of Biodegradable Hyperbranched Core-Multishell Nanocarriers for Efficient Topical Drug Delivery. *J. Control. Release* **2016**, *242*, 42-49.

[43] Prabaharan, M.; Grailer, J. J.; Pilla, S.; Steeber, Gong, S. Amphiphilic Multi-Arm Block Copolymer Based on Hyperbranched Polyester (Poly-L-Lactide) and Poly (ethylene glycol) as a Drug Delivery Carrier. *Macromol. Biosci.* **2009**, *8*, 871-881.

[44] Luo, S. Han, M.; Cao, Y.; Ling, C.; Zhang, y. Temperature-and pH-responsive Unimolecular Micelles with a Hydrophobic Hyperbranched Core. *Colloid Polym. Sci.* **2011**, *289*, 1243-1251.

[45] Kontoyianni, C.; Sideraou, Z.; Theodossiou, , T.; Tziveleka, L. A.; Tsiourvas, D.; Paleos, C M. A novel micellar PEGylated hyperbranched polyester as a prospective drug delivery system for paclitaxel. *Macromol. Biosci.* **2008**, *8*, 871-881.

[46] Prabaharan, M.; Grailer, J. J.; Pilla, S.; Steeber, Gong, S. Folate-Conjugated Amphiphilic Hyperbranched Block Copolymers Based on Boltorn® H40, poly (L-lactide) and poly (ethylene glycol) for Tumor-Targeted Drug Delivery. *Biomaterials* **2009**, *30*, 3009-3019.

[47] Tambe, P.; Kumar, P.; Paknikar, K. M.; Gajbhijye, V.; Smaar Triblock Dendritic Micelles as Pionieering Nanomaterials: Advancement Pertaining to Architecture and Biomedical Applications.

[48] Liu, F.; Wang, D.; Zhang, M.; Ma, L.; Yu, C-Y.; Wei, H. Synthesis of enzyme-Responsive Theranostic Amphiphilic Conjugated Bottlebrush Copolymers for Enhanced Anticancer Drug Delivery. *Acta Biomater.* **2022**, *144*, 15-31.

[49] Jia, T.; Huang, S.; Yang, C.; Wang, M. Unimolecular Micelles of pH-responsive Star-Loke Copolymers for Co-Delivery of Anticancer Drug and Small-Molecular Photothermal Agents: A New Drug-carrier for Combinational Chemo/Photothermal Cancer Therapy. *J. Mater. Chem. B.* **2017**, *5*, 8514-8524.

[50] Wang, Y.; Li, L.; Yang, B.; Wang, B.; Fang, W.; ji, F.; Wen, Y.; Yao, F. Stable and pH-Responsive Polyamidoamine Based Unimolecular Capped with a Zwitterionic Polymer Shell for Anticancer Drug Delivery. *RSC Adv.* **2016**, *6*, 17728-17739.

[51] Guo, J.; Hong, H.; Chen, G.; Shi, S.; Nayak, T. R.; Theuer, C. P.; Barnhart, T. E.; Cai, W.; Gong, S. Theranostic Unimolecular Micelles Based on Brush-Shaped Amphiphilic Block Copolymers for Tumor-Targeted Drug Delivery and Positron Emission Tomography Imaging. *ACS Appl. Mater. Interfaces* **2014**, *6*, 21769-21779.

[52] Surnar, B.; Jayakannan, M. Stimuli-responsive poly(caprolactone) Vesicles for Dual Drug Delivery under the Gastrointestinal Tract. *Biomacromolecules* **2013**, *14*, 4377-4387.

[53] Surnar, B.; Jayakannan, M. Triple-Block Nanocarrier Platform for Synergistic Cancer Therapy of Antagonistic Drugs. *Biomacromolecules* **2016**, *17*, 4075-4085.

[54] Kulkarni, B.; Surnar, B.; Jayakannan, M. Dual Functional Nanocarrier for Cellular Imaging and Drug Delivery in Cancer Cells based on π-Conjugated Core and Biodegradable Polymer Arms. *Biomacromolecules* **2016**, *17*, 1004-1016.

[55] Malhotra, M.; Surnar, B.; Jayakannan, M. Polymer Topology Driven Enzymatic Biodegradation in Polycaprolactone Block and Random Copolymer Architectures for Drug Delivery to Cancer Cells. *Macromolecules* **2016**, *49*, 8098-8112.

[56] Ghosh, R.; Malhotra, M.; Sathe, R. R. M.; Jayakannan, M. Biodegradable Polymer Theranostic Fluorescent Nanoprobe for Direct Visualization and Quantitative Determination of Antimicrobial Activity. *Biomacromolecules* **2020**, *21*, 2869-2912.

[57] Ghosh, R.; Jayakannan, M. Theranostic FRET Gate to Visualize and Quantify Bacterial Membrane Breaching. *Biomacromolecules* **2023**, *24*, 739-755.

[58] Surnar, B.; Jayakannan, M. Structural Engineering of Biodegradable PCL Block Copolymer Nanoassemblies for Enzyme-controlled Drug Delivery in Cancer Cells. *ACS Biomater. Sci. Eng.* **2016**, *2*, 1926-1941.

[59] Pranav, U.; Malhotra, M.; Pathan, S.; Jayakannan, M. Structural Engineering of Star

Block Biodegradable Polymer Unimolecular Micelles for Drug Delivery in Cancer Cells. *ACS Biomater. Sci. Eng.* **2023***, 9,* 743-759.

[60] Malhotra, M.; Pardasani, M.; Pathan, S.; Srikanth, P.; Shaw, K.; Abraham, N. M.; Jayakannan, M. Star-Polymer Unimolecular Micelle Nanoparticles to deliver a Payload Across the Blood-Brain Barrier. *Nanoscale* **2024**, *16*, 21582-21593.

Chapter 3

Impact of Size and Charge of Nanocarriers in Blood-Brain-Barrier Breaching

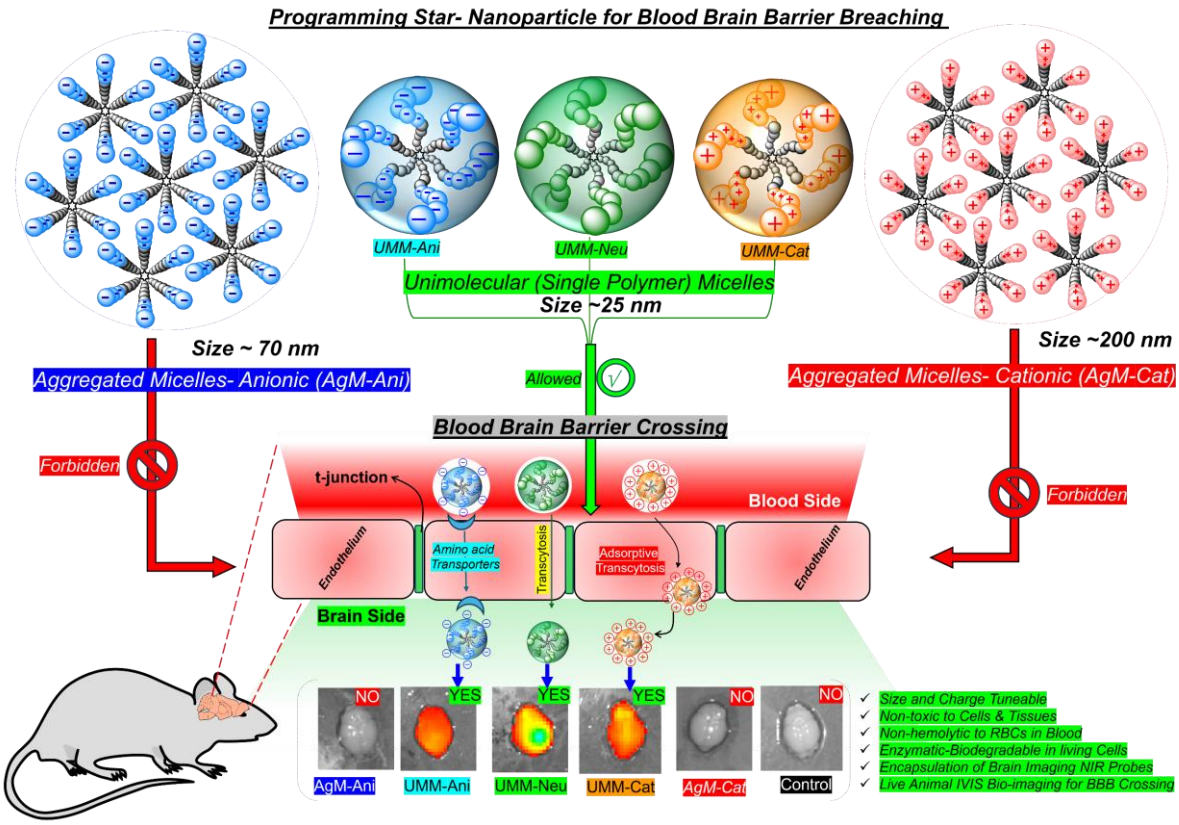

Abstract

Therapeutic delivery to the brain remained most difficult owing to tightly packed protective blood-brain barrier (BBB). To circumvent this barrier, drug delivery systems have been extensively explored in recent years aiming to develop efficient approach to alleviate therapy. However, non-biodegradability and systemic toxicity of delivery system is of major concern. Moreover, the influence of particle size and surface charge on the ability of nanocarrier to penetrate the BBB is rarely addressed for biodegradable delivery systems. To address this, we report on engineering of polycaprolactone based star shaped block copolymers consisting of hydrophobic PCL core and hydrophilic shell. The precise shell modifications with appropriate functionality resulted in the anionic, cationic and neutral (non-ionic) surface charged nano-assemblies having ζ potentials in the range of -30, +35 and -5mV respectively. Star shaped anionic and cationic designed to self-assembled into aggregated (AgM) or unimolecular micellar (UMM) nanoparticles (NP) depending on the molecular weight and the surface modifications on the shell respectively. AgM-Ani and AgM-Cat exist as spherical shaped NPs of 70 and 200 nm. In contrast, UMM-Ani, UMM-Cat and UMM-Neu existed as spherical shaped NP of sizes ~20-30 nm. AgM and UMM polymers exhibited high DLC (>15%) for drug and dye and NPs were non-toxic, non-hemolytic and precisely designed to be enzyme-stimuli responsive biodegradable in lysosomal compartment to deliver the payload at the intracellular level. Confocal microscopy analysis revealed excellent cellular uptake in the WT-MEF, MCF-7, HeLa and neuroblastoma SH-SY5Y cell lines. The NIRF imaging using IR780 dye loaded NPs enabled *in vivo* biodistribution and organ specific distribution analysis. Biodistribution evaluations depicted prolonged blood circulation of UMM NP for than 72h in mice. Additional whole brain imaging and quantification revealed efficient crossing of BBB for UMM NPs of size <40nm compared to AgM NP of sizes >50 nm substantiating the critical role of sizes in BBB breaching. The influence of surface charge among the UMM NP was not overly critical for crossing BBB compared to role of sizes implying different pathways of transcytosis functioning for each charged NPs. Star UMM demonstrates excellent stability, prolonging blood circulation and significant uptake in the brain proving promising candidatures as next generation nanocarriers for brain specific drug delivery application.

3.1 Introduction

Central nervous system (CNS) disease such as brains tumors, encephalopathy, epilepsy and neurodegenrative disoders are major cause of mortality due to failure of potentially effective therapeutics delivery across the barriers.[1-3] CNS is protected by three barriers: cerebral microvascular endothelium (blood-brain barrier, BBB), choroid plexus epithelium (blood-cerebrospinal fluid barrier, and the avascular arachnoid epithelium (cerebrospinal fluid-barrier (CSF)).[4-5] Delivery of pharmaceutics to the CNS is extremely difficult due to existence of these barriers, particularly BBB plays significant role in the controlling selective transport of molecules across the brain.[6-7] The BBB is dynamic interface composed of tightly packed endothelial cells linked together with tight junctions maintains CNS homeostasis by controlling the traverse of specific nutrients (fatty acid, glucose and amino acids) and by preventing the foreign substances or drug moelcules.[8-9] Two major strategies have adopted to treat the CNS diseases: (i) invasive techniques involving direct brain injections or surgeries and (ii) non-invasive techniques based on the biological mechanisms, intranasal brain delivery, nanoparticulate system and focus ultrasound.[10] Reports suggest that 98% conventional therapeutics including small molecules cannot traverse the BBB owing to presence of P-glycoprotein efflux pumps and large molecules of M.W. >1KD cannot penetrate BBB.[11-13]

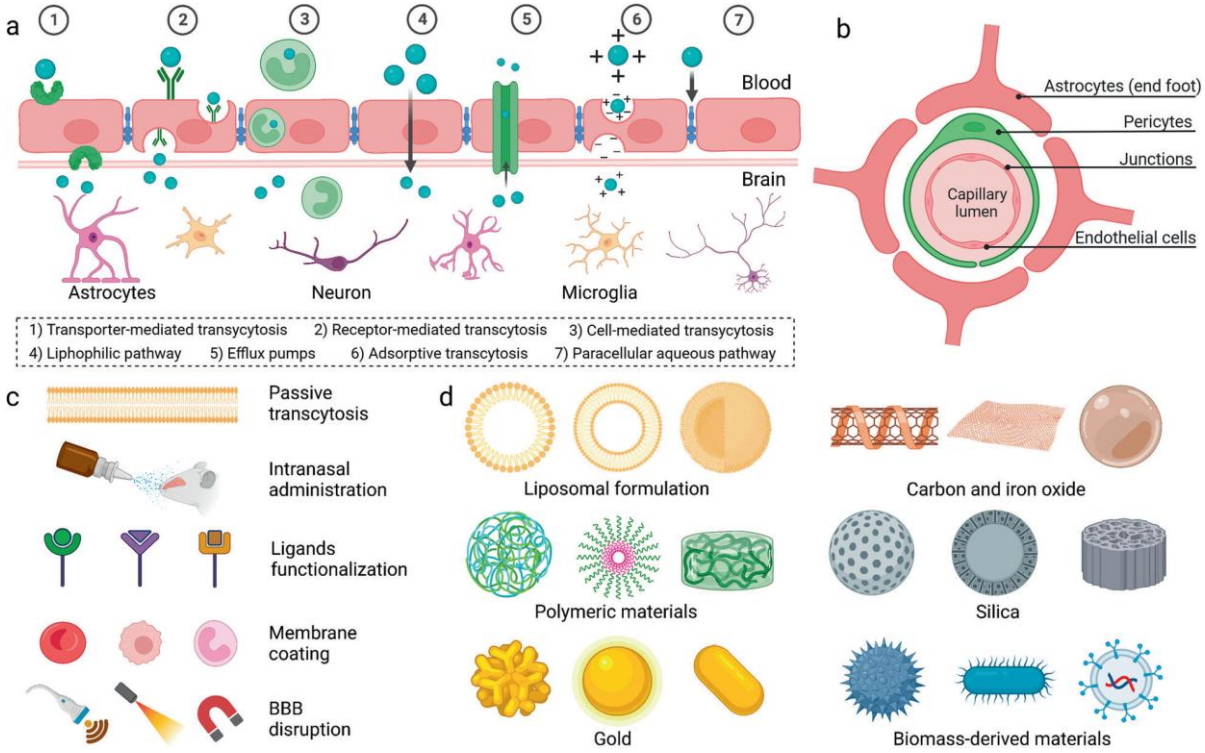

Figure 3.1. *Strategies and materials for delivery across the BBB. (a) Mechanism of transport across BBB. (b) BBB structure.(c)Strategies for brain delivery. (d)Designed materials for brain targeting (Adapted from Wu, D. et al, Signal Transduct. Target Ther.* **2023***, 8, 217).*

Drug delivery system (DDS) have gained attention in recent years to overcome the shortcomings related to CNS delivery.[14-15] Some of the strategies and nanomaterials which are being developed for delivery across the brain are shown in Figure 3.1.[16] There are different pathways of crossing BBB such as paracellular pathway and transcellular pathway involving receptor-mediated transcytosis, adsorptive-mediated transcytosis and so on.[17] The nanocarriers offers prolong blood circulation time due to reduced opsonization and further clearance from reticuloendothelial system (RES) uptake, hence increasing the bioavailability of drug at targeted site.[18] Solid-lipid nanoparticles, liposome-DOX formulations, dendrimers, acid-cleavable polymer coated Au NP, charge-reversal poly-L-lysine-siRNA nanoplexes, quantum dot derived NPs, polymersomes, polystyrene nanosphere and nanorods are some of the DDS recently explored for brain delivery.[19-28] Physiochemical properties of nanocarriers such as molecular weight, lipophilicity, chemical compositions shape, size and surface charge have critical influence on the BBB penetration ability (see Figure 3.2).[29] Molecules that are slightly hydrophobic or lipophilic in nature can cross BBB compared to completely hydrophilic moelcules.[30] Nanoparticles shapes like sphere, rod, cubical, star, disc, triangular etc., have been widely used in brain delivery. Among different shapes, rod-like shaped nanocarriers have proven to possess better BBB penetration abilities.[31-32] Although, some cases suggested better performance for spherical nanoparticle compared to rod-like counterparts.[33] Nevertheless, influence of shape is not fully understood yet due to lacking comparative studies involving thorough investigation of influence of shape.[34] Reports on architecture established the critical importance of branch or star-shaped (3-D) architecture of nanocarriers in prolonging blood circulation time via reducing renal clearance compared to linear (1-D) architectures.[35] 3-D polymer architectures such as hyperbranched, brush and star shaped, dendrimers, have shown better biodistribution aspect, longer half-life, increased efficacy.[36] Reports extensively revealed that nanoparticles (NP) having sizes <100 nm have better BBB penetration abilities compared to NP >100 nm.[37-39] NPs having larger sizes (>100nm) tend to clear from RES system (liver) while NP<10nm can be easily cleared from renal filtration therefore the most suitable choice of NP size are between 10-100nm.[40] The size comparison for PEG-PLGA based system having sizes 60, 90 and 120nm suggested only smaller NPs were able to cross the BBB most effectively compare to larger sized NP.[41] Another important parameter is the surface charge of nanoparticles which plays crucial role in overall biological activity including BBB penetration.[42] The BBB is negatively charged because surface of endothelium is composed of negatively charged lipids membrane and surface glycocalyx.[43] In general, cationic nanoparticles having zeta potential around +30mV are known to have better permeability

across the BBB than anionic or neutral nanoparticles.[44-45] The cationic bovine serum albumin modified PEG-PLGA, chitosan, cationic lipids , antibody-modified PEG-chitosan and cationic cell penetrating peptides have found better results in penetration of BBB via adsorptive-mediated trancytosis.[46-49] However most of the cationic system are known to cause disruption of BBB and cause the cytotoxicity, activates inflammatory responses and other severe systemic toxicities and hemolysis.[50-54] Moreover the cationic NP having zeta potential more than +35mV are tend to cleared easily via mononuclear phagocytic system (MPS) compared to negatively charged and neutral NP which show reduced opsonization, longer blood circulation providing safer approaches.[55-58] Mesoporous silica based NP of sizes 50 nm having charges ranging from -20 to -40 mV could penetrate BBB more effectively without need of targeting moieties than cationic charged NP and larger NP > 200nm.[59]

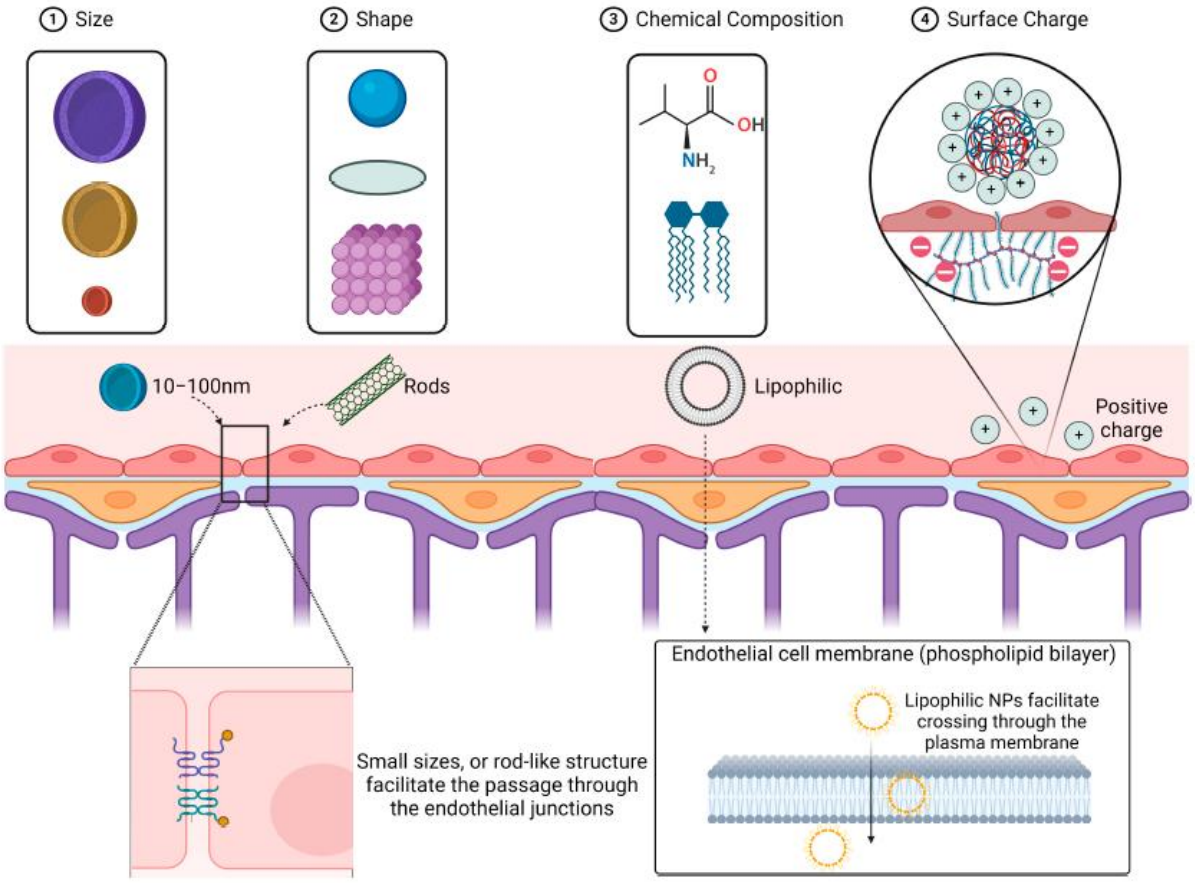

Figure 3.2. *Factors affecting nanoparticles penetration to BBB such as chemical composition, size, shape, and surface charge. (Adapted from Asimakidou, E. et al., Pharmaceuticals,* **2024**, *17, 612).*

Although extensive analysis of surface charges on nanocarriers based on lipid and biomimetic polymers are extensively studied for brain delivery. However careful investigation of reports suggests that in some cases cationic NP can penetrate BBB better than anionic or neutral NP while other cases suggest anionic and neutral charged NP are better than cationic.

Unfortunately, most of the inorganic or organic NP derived from the non-biodegradable polymers often suffer from limitations such as systemic toxicity and prolong accumulation in liver.[19] Therefore next generational nanocarriers must be precisely designed with biodegradable linkages and sufficient stability under concentration gradient in order to avoid toxicity and enable safer non-invasive approach for achieving successful delivery across the BBB. Nanoparticles that are biodegradable with control release profiles, possessing higher drug loading capacity and stable under blood circulation via reduced protein-corona formation, reduced opsonization and renal clearance are most desirable choice for the developing nanocarriers for BBB research.[60] Moreover clear role of size and surface charge for BBB permeability has not been fully understood yet for biodegradable macromolecular systems such as PCL based systems. One of the limitations for PCL based system is the very slow biodegradable nature which can take more than months.[61] Another important aspect is the stability of nanocarrier under the tremendous dilution in the blood stream and cardiac stress, which often leads to dis-assembly and premature release of cargo in before reaching to target site. Recent efforts suggested the discovery and investigation of unimolecular micellar nanoparticles to overcome the concentration gradient and stability against infinite dilution.[62]

To overcome these limitations, a fully biodegradable star unimolecular approach based on polycaprolactone (PCL) and substituted PCL system core-shell nano-architectures is developed and thoroughly investigated *in vivo* to understand the influence of size and surface charge on the BBB penetration in this chapter. Our recent studies demonstrated very first example of fully biodegradable star shaped substituted PCL based core-shell block copolymers capable of forming unimolecular micelles (UMM) with high drug loading content for DOX (>14%).[63] Furthermore our group successfully demonstrated the role of architecture by comparing anionic charged linear and star shaped polymers in the brain delivery concluded only star shaped UMM NP could be able to breach the BBB.[64] To further emphasize on the role of size and surface charges, the new concept is outlined in Figure 3.3 showing new PCL based strategy for *in vivo* BBB penetration and brain delivery. Chemical structures of star shaped (6-arm) block copolymers are shown in Figure 3.3b. Sizes of anionic and cationic nanoparticles tune as <30 nm and 60-200 nm by appropriate functionalization to understand the critical role of sizes on BBB penetration ability. The surface charges were tuned as cationic, anionic and neutral by shell modifications resulting in unimolecular micellar NP of sizes <30nm having surface charges in the range of +30 to -30 mV. Biodistribution analysis using NIR encapsulated larger aggregated micellar NP (AgM) and UMM NP suggested the critical importance of sizes

and surface charges in permeability of BBB as shown in Figure 3.3a. Larger sized NP (AgM) could not penetrate the BBB while UMM NP of sizes <30 nm effectively breach BBB. Among charges, small sized neutral, anionic and cationic NP were taken up by brain equally suggesting other factors besides charges also played significant roles in BBB penetration.

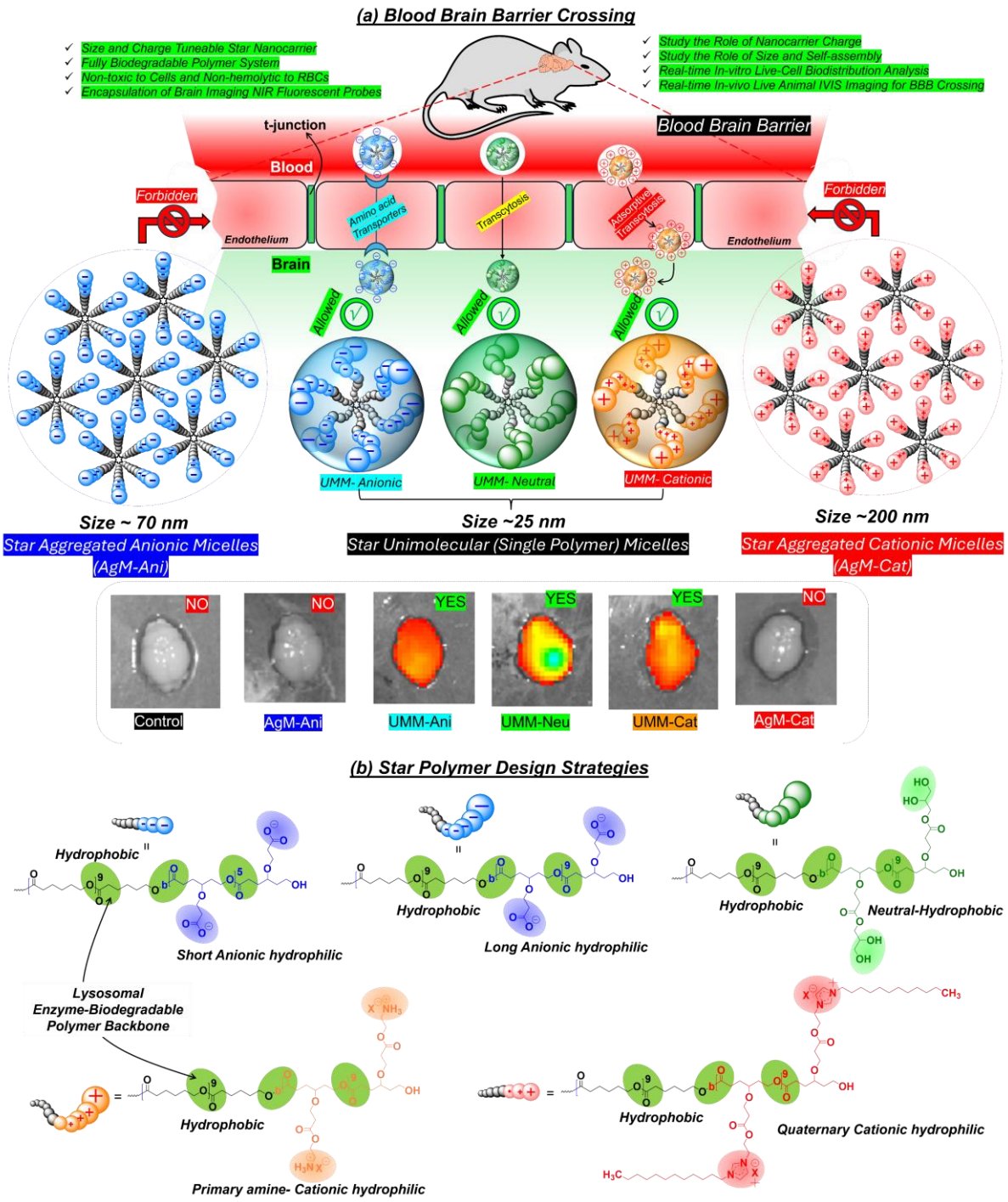

Figure 3.3. *(a) New strategy for breaching blood-brain-barrier and role of size and charges on star block copolymers. (b) Strategy for synthetic designs of fully biodegradable star polymer for breaching BBB.*

3.2 Experimental section

3.2.1 Materials

1,4-cyclohexanediol, tin Di octanoate (II), *t*Butyl acrylate, ε-CL, glycerol, 2-Aminoethanol, IR780 iodide, Doxorubicin HCl, 8-Hydroxypyren-1,3,6-trisulfonic acid trisodium salt (HPTS), Sulforhodamine B (SRhB), Thiazolyl blue tetrazolium bromide (MTT), esterase from horse liver and other chemicals were acquired form Sigma-Aldrich chemicals and used as received without further purification. All the solvents (analytical and HPLC grade) were purchased Finar chemicals and purified by standard methods. Cell culture reagents such as DMEM media, FBS, penstrep antibiotic and organelle staining dyes were obtained from Thermofisher Scientific. Semipermeable Spectra/Por membranes having molecular weight cut of 1KD and 3.5KD were purchased from ThermoFisher Scientific and used for dialysis.

3.2.2 Methods

Bruker 400 MHz spectrometer was used to record ^{1}H and ^{13}C NMR spectra. Gel permeation chromatography (GPC) or SEC analysis carried out using Viscotek GPC equipped with VE 3580 RI detectors having two columns' (Agilent PlGel 20μm Mixed-A) arranged in series with flow rate of 1.0mL/min. HPLC grade chloroform ($CHCl_3$) was used as eluent at 25 ºC for SEC analysis and calibration plot was generated using polystyrene standard obtained from Agilent. Dynamic light scattering (DLS) technique was used for size and surface charge measurement by Zetasizer ZS-90 instrument. HR-TEM images were captured by Joel JEM2200FS 200 KeV. Nanoparticle samples were prepared by drop casting on Formvar coated copper grids for TEM analysis. FE-SEM images were captured by Zeiss Ultra Plus scanning electron microscope. Samples were prepared by drop casting on silicon vapors for FESEM imaging. A Shimadzu UV-1900i spectrometer was utilized for absorbance measurement. EnSight microplate reader (Parkin-Elmer) was used for recording microplates. Confocal microscopes (Zeiss Anisotropy 710 and Multiphoton) were used to acquire the CLSM images. CLSM images were processed using ImageJ software. *In vivo* images were captured by using Perkin-Elmer IVIS spectrum instrument and images were processed using Live Imager software. Data was analyzed and processed using Origin 9.0 and Prism 8.01 software.

3.2.3 Synthetic procedures

Synthesis of compound 1 (Boc-ethanolamine): 2-Aminoethanol (5.0 g, 81.85 mmol) was dissolved in 60 mL tetrahydrofuran: water mixture (1:1, v/v) into a round bottom flask. Di-tert-butyl decarbonate (19.65 g, 90.0 mmol) and $NaHCO_3$ were (7.5g, 90.0 mmol) then added

slowly and reaction was stirred overnight at 25 ºC. The excess THF was removed by rotary evaporator and reaction was diluted with 50mL 0.1N HCl solution and 100 mL ethyl acetate. The crude product extracted 100 mL ethyl acetate (2 times) and washed with brine. Finally, the combined organic layer was dried over Na_2SO_4 and concentrated to yield Boc-ethanolamine. Yield = 12.50 g (94 %). ^{1}H NMR (400 MHz, $CDCl_3$) δ ppm: 5.02 (1, 1H), 3.69 (t, 2H), 3.28 (t, 2H), 1.43 (s, 9H) . ^{13}C NMR (100 MHz, $CDCl_3$) δ ppm: 157.0, 79.8, 62.7, 43.2, 28.4. ATR-FTIR (cm^{-1}): 3367, 2978, 2926, 1685, 1521, 1457, 1392, 1275, 1267, 1258, 1168, 1067, 866, 764. m/z ($M+Na^+$) for $C_7H_{15}NO_3$, calculated 184.0950: found 184.0949.

Synthesis of compound 2 ((2,2-dimethyl-1,3-dioxolan-4-yl)methanol): Glycerol (10.0 g, 108.0 mmol) was taken with p-toluene sulfonic acid (PTSA, 1.0 g, 0.058 mmol) in round bottom flask. Anhydrous acetone (60 mL) was added to it followed by 2,2-dimethoxy propane (16.96 g, 162 mmol). Reaction was continued under dry N_2 atmosphere for 24h at 25 ºC. After that excess acetone evaporated and crude mixture was dissolved in diethyl ether (50mL) washed with aqueous $NaHCO_3$ solution (50mL). Finally, the organic layer was dried over Na_2SO_4 and concentrated to yield compound 2. Yield = 8.3 g (58 %). ^{1}H NMR (400 MHz, $CDCl_3$) δ ppm: 4.23 (m, 1H), 4.03 (m, 1H), 3.378 (m, 1H), 3.17 (m, 1H), 3.60 (m, 1H), 1.19 (t, 1H), 1.43 (s, 3H), 1.36 (s, 3H). ^{13}C NMR (100 MHz, $CDCl_3$) δ ppm: 109.5, 76.2, 65.8, 63.1, 26.8, 25.3. ATR-FTIR (cm^{-1}): 3349, 2954, 2922, 2852, 1714, 1459, 1377, 1275, 1260, 1110, 1038, 909, 851, 764, 749, 617. m/z ($M+H^+$) for $C_6H_{12}O_3$ calculated 133.0786: found 133.0864.

Synthesis of SMI (Star-PCL Macroinitiator): ε-CL monomer M1 (1.0 g, 8.76 mmol with Di-pentaerythritol (37.12 mg, 0.14 mmol) were taken into custom-made melt reactor. The catalyst $Sn(Oct)_2$ (29 mg, 0.07 mmol) was then added followed by applying vacuum of 10^{-2} mbar for 45 min at 25 ºC to vacuum seal the tube. Polymerization was carried out at 110 ºC for 8 hours. After polymerization, the content was precipitated in large amount of methanol (70mL) in cold condition and filtered to yield white solid and dried in vacuo. Yield = 0.90 g (90%). ^{1}H NMR (400 MHz, $CDCl_3$) δ ppm: 4.05 (t, J = 6.7 Hz, 122H), 3.64 (t, J = 6.5 Hz, 12H), 3.37 (m, 4H), 2.30 (t, J = 7.5 Hz, 122H), 1.64 (m, 254H), 1.37 (m, 122H). ^{13}C NMR (100 MHz, $CDCl_3$) δ ppm: 173.70, 64.28, 62.89, 34.25, 32.46, 28.47, 25.66, 24.81. ATR-FTIR (cm^{-1}): 3041, 2864, 1724, 1462, 1419, 1365, 1294, 1161, 1104, 1045, 926, 749.

Synthesis of SB-60tBu diblock copolymer (Star-PCL60-*b*-*t*BuPCL-60): Monomer M2 (600 mg, 2.32 mmol) was taken with SMI macroinitiator (275 mg, 0.04 mmol) and $Sn(Oct)_2$ (47 mg, 0.11 mmol). Polymerization continued at 130 ºC for 12 hours followed by polymer

precipitation in a cold mixture of hexane in diethyl ether (1:3, v/v, 70mL). Yield = 0.85 g (90 %). ^{1}H NMR (400 MHz, $CDCl_3$) δ ppm: 4.15-4.11 (m, 122H), 4.05 (t, *J* = 6.7 Hz, 122H), 3.65 (m, 132H), 3.44 (bs, 64H), 2.44 (t, *J* = 6.3 Hz, 125H), 2.40 – 2.33 (t, 121H), 2.30 (t, *J* = 7.6 Hz, 123H), 1.80-1.72 (m, 244H), 1.64 (m, 248H), 1.44 (s, 555 H), 1.40-1.34 (m, 120H). ^{13}C NMR (100 MHz, $CDCl_3$) δ ppm: 173.70, 173.6, 171.0, 80.0, 75.60, 64.95, 64.30, 61.30, 46.8, 36.6, 34.2, 33.0, 28.50, 28.25, 25.75, 24.70. ATR-FTIR (cm^{-1}): 2931, 1728, 1366, 1157, 1103, 847.

Synthesis of SB-anionic diblock copolymer (SB-Ani or UMM-Ani): Star-PCL60-*b*-*t*BuPCL-60 (300 mg), TFA (3.0 mL), DCM (6 mL). After deprotection polymer was precipitated in cold mixture of hexane in diethyl ether (30mL). Yield = 250 mg. ^{1}H NMR (400 MHz, DMSO-d_6) δ ppm: 4.05 (m, 124H), 3.98 (t, 122H), 3.56 (m, 128H), 3.46 – 3.31 (m, 64 H), 2.39 (t, 119H), 2.32 (m, 120H), 2.27 (m, 120H), 1.71 (m, 220H), 1.54 (h, 236H), 1.30 (m, 124H). ^{13}C NMR (100 MHz, DMSO-d_6) δ ppm: 172.8, 172.7, 172.7, 74.9, 64.2, 60.7, 34.9, 33.4, 32.4, 29.4, 28.6, 27.8, 24.0. ATR-FTIR (cm^{-1}): 2952, 1729, 1712, 1356, 1259, 1166, 1102, 750. Deprotected diblock copolymer (50 mg) was dissolved in 5 mL of aqueous saturated $NaHCO_3$ solution and dialyzed against aqueous $NaHCO_3$ solution using dialysis membrane (MWCO 3.5KD) for 12h followed by water and lyophilized to yield sodium salt of star block copolymer (SB-Ani).

Synthesis of Boc-protected cationic diblock copolymer: The star diblock copolymer (200 mg, 0.521 mmol) was dissolved in 20 mL of DCM:DMF mixture (3:1, v/v) in two-neck round bottom flask. EDC.HCl (500.0 mg, 2.60 mmol), DMAP (32.0 mg, 0.26 mmol), DIPEA (542 µL, 3.13 mmol) were added into the reaction mixture followed by compound 1 (420 mg, 2.60 mmol). The reaction continued at 25 ºC for 96 h under inert N_2 atmosphere. Then DCM was evaporated, and the remaining content was transferred to dialysis membrane (MWCO 3.5KD) and dialyzed against water for 48 h followed by lyophilization. Yield=208 mg. ^{1}H NMR (400 MHz, $CDCl_3$) δ ppm: 4.14-4.11 (m, 245H), 4.05 (t, 120H), 3.70 (m, 146H), 3.45 (m, 68H), 3.39 (m, 123H), 2.54, (t, 116H), 2.35 (t, 125H), 2.30 (t, 118H), 1.85-1.78 (m, 291H), 1.66-1.61 (m, 279H), 1.43 (s, 470H), 1.39 (m, 126H). ^{13}C NMR (100 MHz, $CDCl_3$) δ ppm: 173.71, 171.66, 156.00, 79.61, 75.80, 64.69, 64.29, 63.97, 61.38, 39.70, 35.34, 34.25, 33.00, 29.77, 29.00, 28.48, 25.66, 24.71. ATR-FTIR (cm^{-1}): 2927, 1731, 1521, 1457, 1390, 1365, 1251, 1164, 1102, 1066, 860, 749.

Synthesis of SB-Cationic diblock copolymer (SB-Cat or UMM-Cat): Boc-protected cationic diblock copolymer (150 mg) was dissolved in 3 mL of DCM. 1.5 mL of TFA added in cold condition and reaction continued for 2h at ambient temperature. After deprotection reaction the polymer was precipitated in cold mixture of hexane in diethyl ether (30mL). Yield = 150 mg. ^{1}H NMR (400 MHz, DMSO-d_6) δ ppm: 4.20-3.98 (m), 3.58 (m, 143H), 3.39 (m, 72H), 3.09 (m, 133H), 2.31-2.27 (m, 259H), 1.68 (m, 242H), 1.52 (m, 267H), 1.29 (m, 122H). ATR-FTIR (cm^{-1}): 3459, 2951, 1784, 1714, 1682, 1537, 1537, 1435, 1353, 1275, 1260, 1190, 1180, 1067, 1014, 236, 764, 749.

Synthesis of Acetal-protected neutral diblock copolymer: The star diblock copolymer (220 mg, 0.63 mmol) was dissolved in 10 mL of DCM:DMSO mixture (1:1, v/v) in two-neck round bottom flask. EDC.HCl (1.21g, 6.30 mmol), DMAP (77.0 mg, 0.63 mmol), DIPEA (1.64 mL, 9.47 mmol) were added into the reaction mixture followed by compound 2 (835.0 mg, 6.3 mmol). The reaction continued at 25 ºC for 72 h under inert N_2 atmosphere. Then DCM was evaporated, and the remaining content was transferred to dialysis membrane (MWCO 3.5KD) and dialyzed against water for 48 h followed by lyophilization. Yield=254 mg. ^{1}H NMR (400 MHz, $CDCl_3$) δ ppm: 4.31 (m, 60H), 4.12-4.05 (m, 375H), 3.73-3.68 (m, 220H), 3.45 (m, 70H), 2.56 (m, 123H), 2.35-2.30 (m, 383H), 1.85-1.77 (m, 441H), 1.63 (m, 313H), 1.42 (m, 198H), 1.35 (m, 182H), 1.24 (m, 140H). ^{13}C NMR (100 MHz, $CDCl_3$) δ ppm: 173.69, 171.66, 73.69, 66.46, 64.85, 64.55, 64.28, 61.35, 35.21, 34.25, 32.99, 29.82, 28.85, 28.48, 26.84, 25.66, 25.53, 24.71. ATR-FTIR (cm^{-1}): 2927, 1732, 1530, 1458, 1371, 1259, 168, 1101, 842, 784, 749.

Synthesis of SB-Neutral diblock copolymer (SB-Neu or UMM-Neu): Acetal-protected neutral diblock copolymer (210 mg) dissolved in 5 mL of DCM and 0.1 mL of water was added to it. Into that 2.0 mL of TFA added in cold condition and reaction continued for 2h at ambient temperature. After deprotection reaction the polymer was precipitated in cold mixture of hexane in diethyl ether (35mL). Yield = 190 mg. ^{1}H NMR (400 MHz, DMSO-d_6) δ ppm: 4.36 (m, 68H), 4.02-3.98 (m, 314H), 3.86 (m, 133H), 3.58 (m, 166H), 3.32 (m, 133H), 2.75 (m, 86H), 2.27 (m, 247H), 1.68 (m, 244H), 1.54 (m, 1.54H), 1.29 (m, 122H). ATR-FTIR (cm^{-1}): 3459, 2927, 1784, 1731, 1462, 1360, 1275, 1260, 1173, 1103, 1061, 764, 749, 616.

3.2.4 Self-assembly and nanoparticle characterization

SB-Ani (UMM-Ani), SB-Cat (UMM-Cat) and SB-Neu (UMM-Neu) were self-assembled into nanoparticles using dialysis method as described previously. Briefly, 5 mg of polymer was dissolved in 0.8 mL of DMSO and slowly added to 4.2 mL deionized water with continuous

stirring for 4h. The DMSO+ water mixture of polymer was transferred to dialysis membrane (MWCO3.5KD) and dialyzed against deionized water for 24h with periodic replenishing of water. The nanoparticle solution was filtered (0.45μ) and stored at 4 ºC for further analysis. Dynamic light scattering (DLS) was used to measure hydrodynamic diameters and zeta (ζ) potential of nanoparticles at the concentration of 0.1 mg/mL in deionized water and Britton-Robinson (10 mM) buffer (pH 7.4). Data are expressed as mean ± SD of more than three independent measurements. Shape and size of nanoparticles were visualized using transmission electron microscopy (TEM) or field emission scanning electron microscopy (FE-SEM).

3.2.5 CMC determination using Pyrene probe

Critical micellar concentration (CMC) was determined by using pyrene as environmentally sensitive probe. The glass vials were uniformly coated with fixed concentration of pyrene (0.6 μmol, 3.6×10^{-7} g/mL). These vials then added with each polymer solutions in water having range of concentration 1.0×10^{-6} mg/mL to 0.5 mg/mL to prepare a total of 3mL solution. Resulting solutions were then sonicated for 3h at 25 ºC and kept overnight for equilibration under the dark. Prior to fluorescence measurement, the solutions were degassed by N_2 gas to remove dissolved air or oxygen. The solutions were subjected to fluorescence measurements using 337 nm excitation wavelength and emission was collected in the range of 350 nm to 500 nm. Fluorescence intensities corresponding to I_1 (372 nm) and I_3 (382 nm) for each respective solution were then used to estimate the CMC concentration. Ratios of I_1/I_3 were plotted against concentration and break point was regarded as CMC.

3.2.6 Encapsulation studies

HPTS, DOX, SRhB, ICG and IR780 were encapsulated in star block copolymers (UMM-Ani, UMM-Cat and UMM-Neu) by dialysis process. Drug/dye with varying feed of 0.5/1.0/2.0 mg were dissolved in 0.8mL of HPCL grade DMSO along with 5mg of polymer individually. The solutions were slowly dropped into 4.2 mL water with stirring for 4h. The resulting solution was transferred to dialysis tube (MWCO 3.5KD) and dialyzed against deionized water for 48h. Water was replenished periodically to remove the unencapsulated water soluble drug/dye and DMSO. Finally, the loaded nanoparticle solution was filtered (0.45 μ) to remove non-soluble dye and stored at 4 ºC until further use. The amount of loaded dyes/drug was estimated by absorbance which was further used for determination of drug loading content (DLC) and drug loading efficiency (DLE) as per previously described procedures in chapter 2.

3.2.7 *In vitro* release studies

To study the enzymatic degradation of polymer backbone to release loaded cargo, DOX loaded star block copolymers were chosen as candidates. 1mL solution of DOX loaded star block nanoparticles was taken into dialysis tube (MWCO 1KD) along with 3mg of esterase (Horse liver 3mg/U) and immersed in 3mL of PBS (pH 7.4) into a container at 37 ºC. For the control experiment, 1mL of the DOX nanoparticle solution was taken without esterase and immersed in PBS without any esterase. 2mL of solutions from container were withdrawn and subjected to absorbance measurement at regular intervals and put back into container. The amount of released drug from nanoparticles surrounding solution in container was estimated for each timepoints and used for estimation of cumulative release as described previously in the chapter 2. The cumulative release versus incubation time was plotted to generate the release profile for each sample.

3.2.8 Cell culture methods

The wild-type mouse embryonic fibroblast (WT-MEF), human breast cancer (MCF-7), and human cervical cancer (HeLa) and SH-SY5Y (neuroblastoma) cell lines were used for study. All the cells were cultured in 25 cm^2 flasks (Tarson) into an incubator at 37 ºC equipped with 5% CO_2 supply (humidified). Cell culture growth media Dulbecco modified eagle medium (DMEM, Gibcco) was supplemented with 10 % fetal bovine serum (FBS) and 1% pen-strep.

3.2.9 Cell viability by MTT assay

Cell viability was determined by well-known MTT (3-(4,5-dimethylthiazol-2-yl)-2,5-diphenyltetrazolium bromide), tetrazolium dye assay. For that purpose, 96-well plates were seeded with the cells with the density of 1000 cells/well in 100 µL media and incubated for 16 h to ensure adherence of cells. After that the media was aspirated and fresh media containing different concentrations of nanoparticles (UMM-Ani, UMM-Cat and UMM-Neu) were added to each and further incubated for 72h at similar conditions described earlier. One row in plate was added with only media and considered as control wells for determination of cell viability (100%). After 72h incubation compound containing media was aspirated and replaced with 100 µL MTT solutions (0.5mg/mL in) and incubated for 4h. During this incubation tetrazolium dye was reduced insoluble formazan crystal by the action of mitochondrial oxidoreductase enzyme. The media was aspirated, and formazan crystals were dissolved in DMSO (100 µL per well), and plates were subjected to absorbance measurement at 570 nm using microplate reader. Obtained absorbance values were used for estimation of cell viability. Using the

aforementioned protocol, cell viability of DOX loaded nanoparticles (UMM-Ani+DOX, UMM-Cat+DOX and UMM-Neu+DOX) were evaluated.

3.2.10 Temperature dependent cellular uptake via CLSM imaging

Temperature dependent cellular uptake was studied for understating the endocytosis phenomenon. A density of 1×10^5 WT-MEF cells was seeded onto each coverslip in 6-well plate in 2mL of media. The cells were incubated for 24h for complete adherence. After that the media was aspirated and replaced with 2mL of media containing SRhB loaded star nanoparticles or free SRhB (concentration 2.5 µg/mL for SRhB) and incubated at 4 ºC or 37 ºC for 4h. After that compound containing media was removed and cells were washed, fixed with 3.5 % PFA and counterstained with DAPI (nuclei). The coverslips were mounted on glass slides using 70% glycerol and air dried. The cells were visualized using =405 nm (blue channel for DAPI), λ=561 nm (red channel for SRhB) lasers in Zeiss confocal microscope (CLSM). Captured images were processed and CTCF (corrected total cell fluorescence) was estimated by using ImageJ software.

3.2.11 Cellular uptake via confocal laser scanning microscopy (CLSM) imaging

Cellular uptake drug/dye loaded nanoparticles in WT-MEF, MCF-7 and HeLa cell lines were studied by fixed cell method using CLSM imaging. Each well of 6-well plates having glass cover slips were seeded with 1×10^5 cells in 2mL media and incubated for 24h for complete adherence. After that the media was replaced with 2 mL of media containing drug/dye loaded star block nanoparticles or free drug/dye (for control) and incubated for 6h. Concentrations for HPTS, SRhB and DOX were kept at 1µg/mL, 2.5µg/mL and 2.5µg/mL respectively free form or in the nanoparticle loaded form. After the completion of incubation time, the compound containing media was aspirated and cells were washed with PBS buffer twice. The cells were fixed with 3.5% paraformaldehyde (PFA) solution (0.5mL/well) for 15min at room temperature. PFA solution was removed, and cells were washed with PBS twice. The fixed cells were counterstained with phalloidin green (cytoskeleton) and DAPI (nucleus) simultaneously for 15 min and 5 min respectively. Stained cells were washed with PBS twice. The coverslips having fixed stained cells were finally mounted on glass slides using 70% glycerol (mounting medium) and air dried. The glass slides were subjected to visualization using confocal microscope (Zeiss anisotropy). The lasers having excitation wavelength of λ=405 nm (blue channel for DAPI or HPTS), λ=488 nm (green channel for DOX or phalloidin) and λ=561 nm (for SRhB) was utilized. ImageJ software was used for image processing and CTCF estimation.

3.2.12 Lysotracker assay via CLSM Imaging

Live cell lysotracker assay was performed to investigate the enzymatic biodegradation of star block copolymer nanoparticles. The lysosomes were stained with Lysotracker green DND-26 (Invitrogen). For that purpose, MCF-7 cells (50,000) were seeded in each well of 4-well confocal chamber (Thermofisher) and incubate for 24h to ensure adherence. After that, the media was aspirated and replaced with 1 mL of fresh media containing DOX loaded star block nanoparticles (DOX concentration was 5.0 μg/mL) and incubated for 30 or 240 minutes. After that compound containing media was aspirated and cells were washed with PBS twice. 1mL of lysotracker solution (in media, 100nM) was added to each well and incubate at 37 ºC for 30 min for lysosomal staining. Afterwards, the lysotracker solution was removed and cells were washed with PBS twice and imaged using λ=488 nm (phalloidin) and λ=561 nm (DOX). CLSM images were processed using ImageJ software.

3.2.13 Animal handling and experimentation

The animal experiments were performed at National Facility for Gene Function in Health and Diseases (NFGFHD, IISER Pune, India) with the compliance of the guideline issued by Institutional Animal Ethics Committee India (IAEC). Balb-C (6-8-week-old) mice were taken, housed and experiments were carried out in NFGFHD IISER Pune.

3.2.14 Hemolysis assay

The compatibility of star block nanoparticles with red blood erythrocytes or cells (RBC) was evaluated by hemolysis assay. 0.5mL of was withdrawn into EDTA coated centrifuge tube by retro-orbital plexus puncture of an anesthetized healthy 6-8-week-old Balb-C mouse. The collected blood was centrifuged at 5000 rpm for 5 minutes for separating RBCs and plasma . Supernatant plasma was carefully aspirated, and RBC pellet was washed with PBS buffer twice. The RBC pellet was dispersed in PBS (pH 7.4) to make 5% v/v RBC solution. Each well of the 96-well was added with 100 μL of RBC solution. After that, 100 μL of the UMM-Ani, UMM-Cat and UMM-Neu nanoparticle solution in PBS (1 mg/mL) was added to it and incubated at 37 ºC for 1h. 1% Triton-X (100% hemolysis) and PBS (no-hemolysis) were used as positive and negative control respectively. After incubation the solutions from each well were withdrawn into centrifuge tube and subjected to centrifuge at 5000 rpm for 5 minutes and photographs were captured. The supernatant solutions were transferred to a new 96-well plate and subjected to absorbance measurement (λ =576 nm) using microplate reader. The % hemolysis was estimated by using absorbance values by using previously reported formula.

3.2.15 *In vivo* biodistribution studies

In vivo biodistribution was performed by whole body live animal imaging In-Vivo Imaging System (IVIS spectrum Perkin-Elmer) equipped with anesthesia and oxygen supply. Near infrared fluorescent dye IR780 was utilized owing to its longer blood circulation time, deep penetration ability and low background emission. The IVIS was set for excitation wavelength of 745 nm and emission filter was of 800 nm. 6-8-week-old healthy Balb-C mice were randomly divided into seven groups (*n=3*) and two mice injected with PBS only (negative control). Two groups were injected with free IR780 (dissolved in 5% DMSO in 100 µL PBS) and two groups were injected with UMM-Ani+IR780. And the remaining other groups were injected with AgM-Ani+IR780, UMM-Cat+IR780 and UMM-Neu+IR780 intraperitoneally. For all samples, the injection volume was 100 µL PBS and IR780 dose was 0.5 mg/Kg. The animals injected with PBS, Free IR780, AgM-Ani+IR780 and UMM-Ani+IR780 (*n=3*) were subjected to whole-body IVIS imaging at 2, 4, 6 and 24h postinjection. After 24h, the animals were anesthetized, pericardially perfused with PBS and organs were harvested. The harvested organs were imaged using IVIS. Other groups (*n=3*), Free IR780, UMM-Ani+IR780, UMM-Cat+IR780 and UMM-Neu+IR780 and PBS (one animal) were subjected to IVIS imaging at 4, 24, 48, 72 h postinjection. The blood (40-60µL) was withdrawn via retro-orbital sinus puncture using capillary tube into 5% EDTA coated vials from each group at similar times to extract the plasma. The plasma samples (10 µL) were diluted with PBS (90 µL) and added to the 96-well plate followed by IVIS fluorescence imaging for semi-quantitative pharmacokinetic analysis. After 72h, animals were euthanized, and organs were harvested and subjected to IVIS imaging. In similar way IVIS based biodistribution assay was carried out by using cardiogreen (Indocyanine green or ICG). Free ICG, UMM-Ani+ICG, UMM-Cat+ICG and UMM-Neu+ICG nanoparticles were injected intraperitoneally (dose 0.7mg/kg in 100-150 µL PBS) to the Balb-C mice (*n=3*) and imaged for 2, 4, 6, 24 hrs. After that, animals were euthanized, perfused and organs were harvested and imaged using IVIS. The IVIS images were processed using Living Image 4.7 software (PerkinElmer) software and data were analyzed by Prism 8.01 software.

3.2.16 Blood-brain barrier (BBB) integrity studies using Evan blue dye extravasation

Blood-brain barrier (BBB) integrity was assessed using Evans blue (EB) dye extravasation method. The EB is impermeable to BBB until its integrity is compromised. Therefore, the integrity of BBB can be assessed by injecting EB into a mouse and detecting its presence in

the brain. For this purpose, 8-10-week-old Balb-C mice are divided into two groups (n=3) and were injected with UMM-Ani (10mg/kg in 100 µL PBS) and PBS (control group) intraperitoneally and animals were left in normal habitat for 48h. After that, animals were injected intravenously with 100 µL of EB solution (2% w/v in saline) via lateral vein. Animals turned blue immediately and observed for 1h. After 1h postinjection animals were euthanized, pericardially perfused with 0.9% saline and their brains were harvested. Harvested brains were weighed using balance. Brain tissues were manually homogenized in 500 µL trichloroacetic acid (50% w/v in distill water) in tubes using tissue grinder. Homogenates were further centrifuged for 20 minutes at 10000 rpm and supernatants were carefully collected in fresh tubes. The freshly collected supernatants solutions having EB were diluted with ethanol (1:4) and 100 µL of each sample were added to 96-well plate (in triplicates) and subjected to absorbance measurements (632 nm). Standard curve for EB was generated by measuring absorbance of 100 µL of EB solutions in microplate at different concentrations (1000, 750, 500, 250 and 100 ng/mL of EB) in similar solvent. The amount of EB dye present in the brain samples was then estimated using standard curve and expressed in ng EB dye /mg of brain tissue.

3.2.17 Blood-brain barrier (BBB) integrity studies using BBB impermeable dye IR780

Integrity of BBB was confirmed by another brain impermeable dye IR780 iodide. The fluorescent dye IR780 iodide is normally impermeable to intact BBB. For that purpose, 8-12-week-old Balb-C female mice (total 9) were divided into 3 groups (n=3). The Ist group was injected with free IR780 (0.5mg/kg) and the IInd group was injected with UMM-Ani+IR780 intraperitoneally (in 100 µL PBS, IR780 dose 0.5mg/kg). Group I and II were subjected to IVIS fluorescence imaging and anesthetized, pericardially perfused with saline at 24h postinjection to harvest brain. Excised brains were washed with PBS and subjected to IVIS imaging. Group IIIrd was intraperitoneally injected with UMM-Ani nanoparticle solution in 100 µL PBS (10mg/kg) and kept for 24 hours and normal habitat to ensure complete circulation in body of mouse. After 24h the group IIIrd was injected with free IR780 intraperitoneally (0.5mg/kg) and kept for another 24h. Finally group IIIrd was anesthetized, pericardially perfused and their brains were harvested, washed with PBS and subjected to IVIS imaging. IVIS fluorescence images were processed using Living Image 4.7 software and data was analyzed using GraphPad Prism 8.0 software.

3.2.18 Statistical analysis

All the measurements are carried out at least three independent times and results are expressed as *mean* ± *SD or SEM* ($n \geq 3$). All the statistical analysis was performed using GraphPad Prism 8.0 software. The student t-test paired and unpaired t-test, One-way and Two-way ANOVA test were used for multiple comparisons. The statistical significance was considered for $p<0.05$.

3.3 Results and Discussion

3.3.1 Synthesis and characterization

The star block copolymers having different surface charges are synthesized by using ring opening polymerization (ROP) and post polymerization modifications as shown in scheme 3.1. Briefly, ROP of monomer **M1** with di-pentaerythritol initiator (M/I=60) using Sn(Oct)2 catalyst yielded star PCL macroinitiator (SMI). The formation of SMI was confirmed by ^{1}HNMR as shown in appendix. Degree of polymerization (DP) was estimated as described earlier by comparing peak intensities of initiator with ester protons of PCL chain. Subsequently, the ROP of monomer **M2** (γ-substituted caprolactone) using SMI macroinitiator yielded t-Butyl ester protected star block copolymer (SB-tBu). DP was obtained as 60 for t-BuPCL units SB-tBu. Subsequently SB-tBu was deprotected using mild acid (Trifluoracetic acid) to yield star block (SB) having carboxylic acid groups as pendant. ^{1}HNMR spectra of SB is shown in Figure 3.4a in which all the major peaks are assigned alphabetically in the structure and its respective ^{1}HNMR spectra. The carboxylic acid groups in SB were further coupled with compound **1** (Boc-ethanolanime) to yield Boc-protected cationic star block copolymer (SB-Cat-Boc) as shown in Scheme 3.1. Complete esterification was confirmed by the appearance of new peaks assigned with ***e*** (4.15 ppm), ***f*** (3.45) and ***g*** (1.43 ppm) corresponding to the -O-C**H$_2$**-, -CH2-C**H$_2$**-NHBoc and -C(C**H$_3$**)$_3$ protons respectively as shown in ^{1}HNMR spectra in Figure 3.4b. Subsequent acid catalyzed deprotection of t-Boc group yielded star block cationic (SB-Cationic) polymer as shown in Scheme 3.1. Removal of t-Boc group was confirmed by the disappearance of t-Boc peak (at 1.43 ppm) in ^{1}HNMR spectra as shown in Figure 3.4c. In similar manner the star block was reacted with compound **2** to give acetal protected star block neutral copolymer (SB-Neu-Acetal) which was further deprotected to yield star block neutral (SB-Neutral) polymer as shown in Scheme 3.1. Synthesis of SB-Neutral polymer was confirmed by ^{1}HNMR spectroscopy as shown in Appendix. The SB-Anionic was produced by treating star block (SB) with aqueous solution of $NaHCO_3$. The resulting solution was dialyzed against water to remove excess $NaHCO_3$ and finally sodium salt of star block (SB-Anionic) was lyophilized as powder. All the polymers are well characterized by ^{1}H and ^{13}C NMR and FTIR spectroscopy. In addition, one more star block anionic copolymer having 60-PCL units and shorter carboxylic PCL segment (36 unit) was synthesized, characterized and mentioned in chapter 2. Synthesis imidazole substituted quaternary ammonium cationic star block is mentioned in our earlier published report.[69]

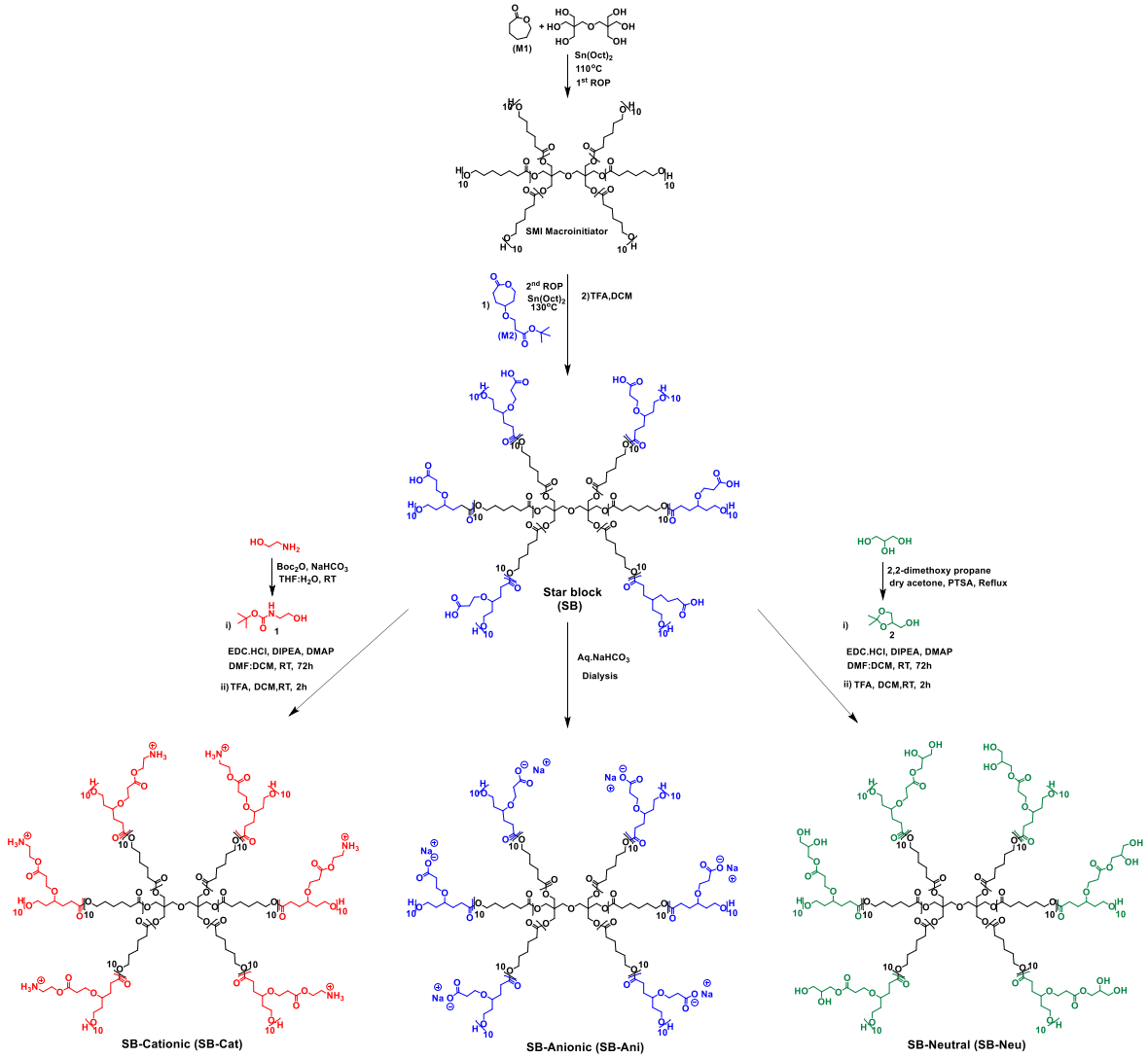

Scheme 3.1. *Synthesis of star block copolymer by ring opening polymerization (ROP) and post polymerization modifications. SB-Anionic, SB-Cationic and SB-Neutral are composed of similar backbone but only differ in surface functionalization.*

Size exclusion chromatography enabled molecular wight and polydispersity determination of SMI macroinitiator and SB-tBu in chloroform and SEC elution traces are shown in Figure 3.5. SEC chromatograms for SMI and SB-tBu were monomodal and narrow disperse with polydispersity in the range of 1.2-1.5. The SB-tBu eluted earlier compared to SMI suggested successful block copolymer formation on the top of SMI. The number average molecular weights (M_n) obtained from SEC were slightly overestimated compared to theoretical Mn (^{1}HNMR) owing to the use of polystyrene as standard and tabulated in Figure 3.5. Thermogravimetric analysis (TGA) of the star polymers revealed thermal stability of t-Butyl protected polymers up to ~290 ºC. In contrast, deprotected polymers showed stability up to ~260 ºC as shown in Figure 3.5. Thermal stabilities of t-butyl protected derivatives are much

higher compared to their deprotected versions. The deprotected polymers are carboxylic acid salts(TFA salts) which could affect the thermal stability in TGA studies. The reason for this unusual behaviour is not clear at present, more in-depth analysis is required in further investigation. Thermal analysis using differential scanning colorimetry (DSC) revealed semi-crystalline to amorphous nature of the star polymers with glass transition temperature in the range of -40 to -50 ºC as shown in Figure 3.5.

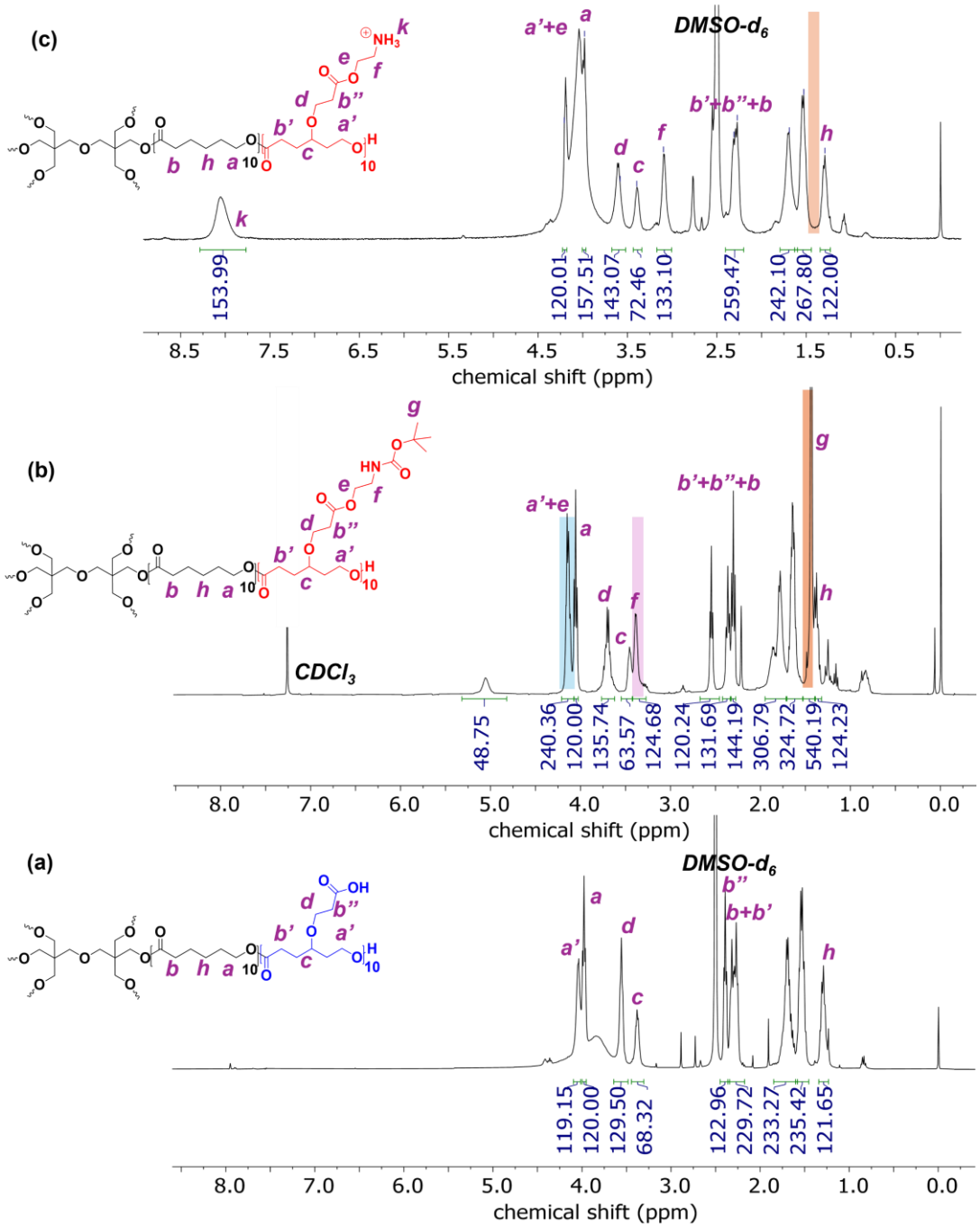

Figure 3.4. *1HNMR spectra of star block cationic copolymer: (a) Star block in DMSO-d_6. (b) Boc-protected star block cationic copolymer in $CDCl_3$. (c) SB-Cationic in DMSO-d_6. All the important peaks are highlighted in different color codes and assigned alphabetically.*

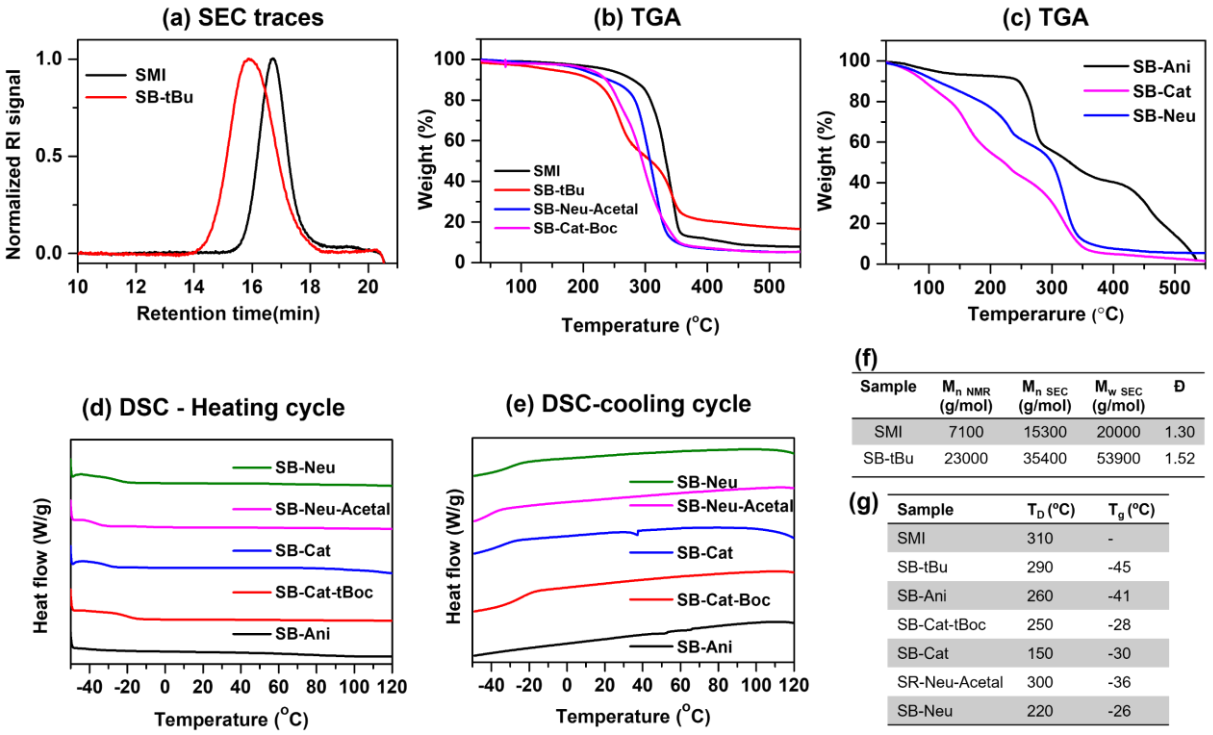

(f)

Sample	$M_{n\ NMR}$ (g/mol)	$M_{n\ SEC}$ (g/mol)	$M_{w\ SEC}$ (g/mol)	Đ
SMI	7100	15300	20000	1.30
SB-tBu	23000	35400	53900	1.52

(g)

Sample	T_D (°C)	T_g (°C)
SMI	310	-
SB-tBu	290	-45
SB-Ani	260	-41
SB-Cat-tBoc	250	-28
SB-Cat	150	-30
SR-Neu-Acetal	300	-36
SB-Neu	220	-26

Figure 3.5. *(a) SEC elution traces of SMI and SB-tBu in $CHCl_3$. (b) & (c) TGA plots of star polymers. (d) & (e) DSC profiles of heating and cooling cycles. (f) Details of molecular weights and polydispersity. (g) Thermal properties obtained from TGA and DSC.*

3.3.2 Self-assembly and drug encapsulation

Star polymers (SB-Ani, SB-Cat and SB-Neu) are inherently amphiphilic owing to presence of hydrophobic PCL core and hydrophilic shell in the six-arm structure as shown in Figure 3.1. Star polymers were self-assembled into core-shell nanostructures by the dialysis process as shown in Figure 3.6a. Pyrene encapsulation assay was performed to determine the critical micellar concentration (CMC) of the star polymer. The ratio of fluorescence intensities corresponding to I_1/I_3 vibronic levels of pyrene was plotted against the concentration and break point was considered as CMC as shown in Figure 3.6b-d along with PL intensity plot. The CMC plots revealed that SB-Ani, SB-Cat and SB-Neu polymers did not show any breakpoint suggesting existence of unimolecular micellar (UMM) assemblies. This is attributed to the fact that star block (SB) existed as UMM (Chapter 2) and modification on carboxylic group present in the shell with different functional groups (smaller chains of 2-3 carbon) having cationic or neutral charges did not affect its nature to self-assembled as unimolecular micelles. In contrast, star block anionic polymer having smaller shell size self-assembled into aggregated micelles

(AgM-Ani) and details are mentioned in chapter 2. SB-Anionic, SB-Cationic and SB-Neutral hereinafter will be referred to as UMM-Ani, UMM-Cat and UMM-Neu.

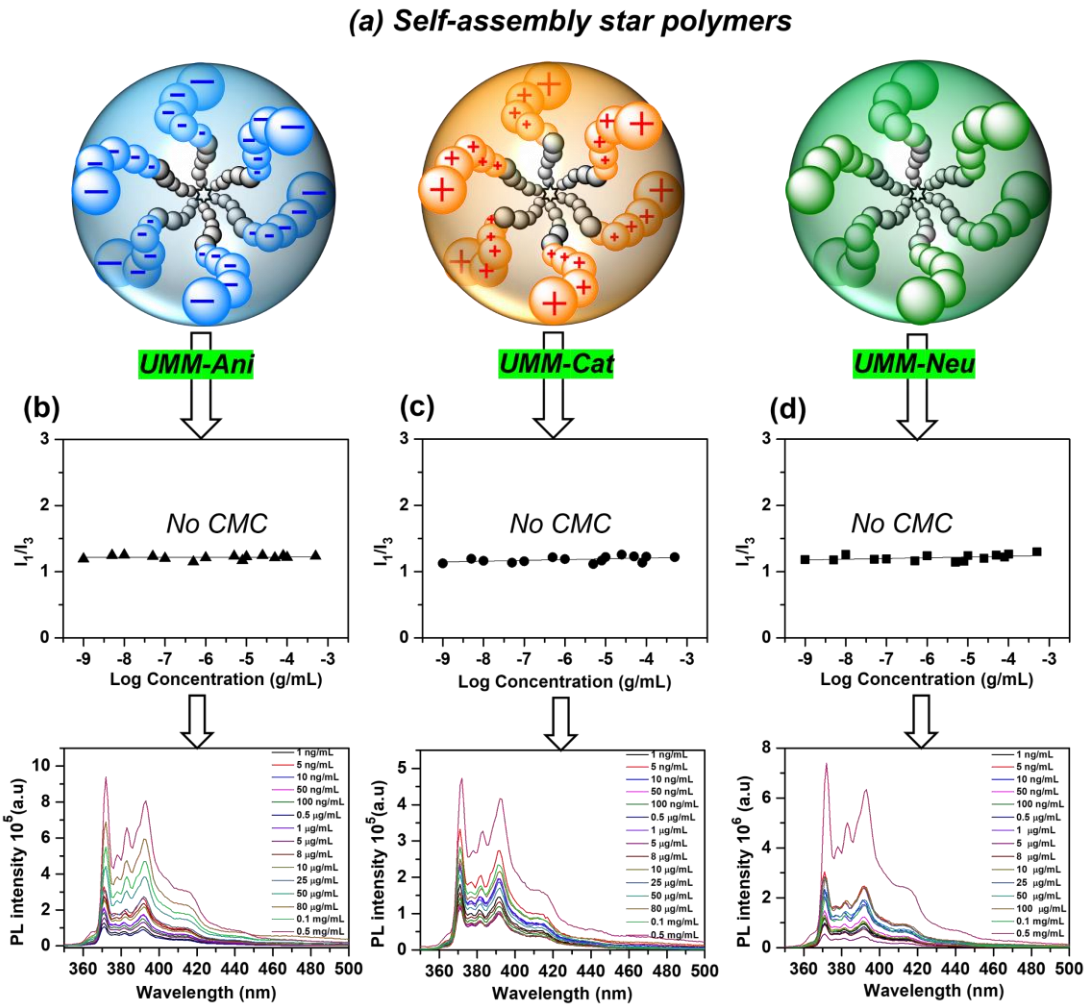

Figure 3.6. *(a) Self-assembly of star polymers. (b) to (d) Plots of I_1/I_3 vs concentrations for UMM-Ani, UMM-Cat and UMM-Neu for determination of CMC along with corresponding PL intensity plots.*

Next all UMM nanoparticles (NP) were assessed for sizes and charges by using dynamic light scattering (DLS) technique. The size histograms of UMM-Ani, UMM-Cat and UMM-Neu are shown in Figure 3.7 having monomodal size distribution. All the UMM depicted hydrodynamic diameters in the range of 25-35 nm with narrow polydispersity in the range of 0.3 to 0.4 and tabulated in Figure 3.7. Furthermore, the surface charges of UMM were measured in pH 7.4 by zeta (ζ) potential plot is shown in Figure 3.7. The ζ potential revealed the existence of anionic species (-28 mV) in UMM-Ani and cationic species in UMM-Cat (+40 mV) NP respectively. The UMM-Neu NP exhibited neutral charge (-3 mV), and all the details are tabulated in Figure 3.5. Self-assembled UMM NP were subjected to HR-TEM and FE-SEM

imaging analysis and images are shown in Figure 3.5f-h. HR-TEM images of UMM-Ani and UMM-Neu revealed the existence of smaller spherical nanoparticle of ~20-25 nm. Similarly, FE-SEM image analysis of UMM-Cat depicted formation of spherical nanoparticles of ~20 nm. CMC, DLS, HR-TEM and FE-SEM image analysis validated the existence of unimolecular micellar (UMM) nanoparticles for UMM-Ani, UMM-Cat and UMM-Neu.

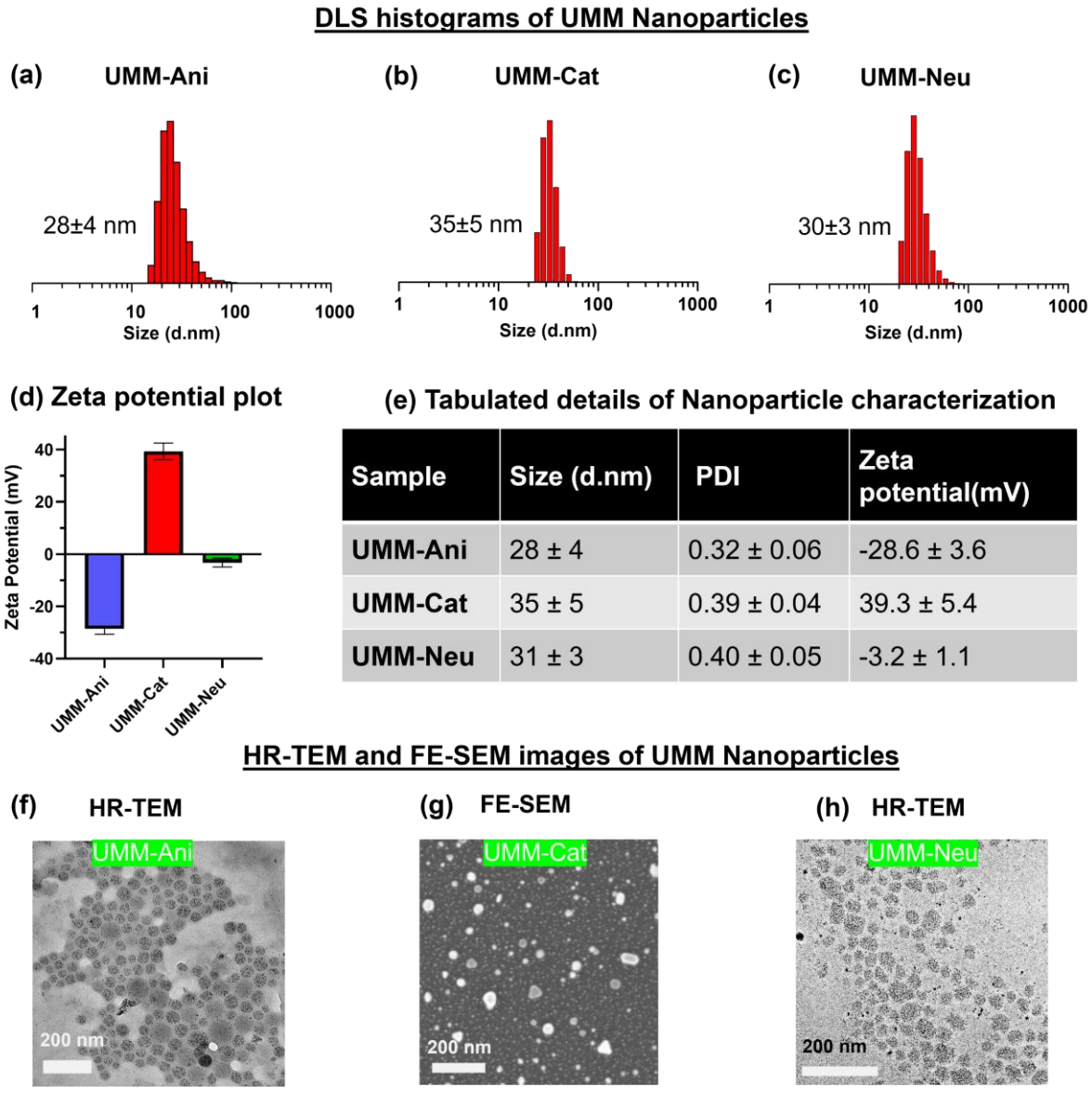

Sample	Size (d.nm)	PDI	Zeta potential(mV)
UMM-Ani	28 ± 4	0.32 ± 0.06	-28.6 ± 3.6
UMM-Cat	35 ± 5	0.39 ± 0.04	39.3 ± 5.4
UMM-Neu	31 ± 3	0.40 ± 0.05	-3.2 ± 1.1

Figure 3.7. *DLS histograms of (a) UMM-Ani. (b) UMM-Cat. (c) UMM-Neu nanoparticle. All the plots are % number vs size and nanoparticle concentration were kept as 0.1 mg/mL in the pH 7.4 (Britton-Robinson buffer).(d) Plot of zeta potential for UMM in pH 7.4. (e) Tabulated details of nanoparticle characterizations by DLS measurements. (f) HR-TEM image of UMM-Ani. (g) FE-SEM image of UMM-Cat. (h) HR-TEM image UMM-Neu. For recording HR-TEM images, aqueous NP solutions were drop-cast on copper grids and FE-SEM samples were prepared by drop casting on silicon vapor. Nanoparticle concentration was 0.1 mg/mL.*

UMM NPs were evaluated for their drug/ dyes loading capabilities. For that purpose, the anticancer drug Doxorubicin (DOX) and fluorescent dyes having absorbance and emission in visible range (HPTS, SRhB) for *in-vitro* visualization and in near infra-red (IR780 and ICG) region for *in-vivo* visualization were encapsulated by the dialysis process. The schematic of drug/dye encapsulation is shown in Figure 3.8. Interestingly all the UMM NP were able to encapsulate noticeable amount of drug/dye despite differences in surface charges. Photographs of vials containing drug/dye loaded UMM in Figure 3.8b provided visual evidence for large quantities of dyes/drug loaded in nanoparticles. Also, the nature of dyes did not affect the efficiency of UMM NP for encapsulation. The drug loading content (DLC) for all UMM NP was estimated by using absorbance technique. The plot of DLC for different dyes in UMM NP in Figure 3.8c revealed UMM-Neu NP could encapsulate the highest amount of hydrophilic dyes HPTS (7.3%) and SRhB (6.1%) compared to UMM-Cat and UMM-Ani. In contrast, UMM-Ani was able to encapsulate hydrophobic dye IR780 in highest amount (3.6%) compared to UMM-Cat and UMM-Neu and details are tabulated in table 3.1. Furthermore, UMM-Ani and UMM-Cat depicted outstanding 14% and 14.8 % DLC for DOX respectively; however UMM-Neu could only load ~9% DOX as shown in Figure 3.8d. Drug loading efficiency (% DLE) are tabulated in table 3.1. The PCL based systems have reported ~8-10% DLC for DOX in literature; However, our designed UMM has superior capabilities of loading not only drug but also different fluorescent dyes which can be used for *in vitro* and *in vivo* visualization. It is noteworthy that DLC for DOX obtained for currently designed UMM NP is one of the highest DLC reported and one of the first examples of fully biodegradable star UMM nanocarrier having more than 14% DLC for DOX. Encapsulation capabilities of UMM-Ani, Cat and Neu NP suggested great potential for *in vitro* and *in vivo* drug delivery applications. Drug/dye loaded NP will be hereinafter referred to as UMM-Ani/Cat/Neu+Dye/drug.

	DLC % *(DLE%)*[a]			DLS size (d.nm)[b]			PDI (DLS)[b]			Zeta Potential (mV)[b]		
Sample	**UMM-Ani**	**UMM-Cat**	**UMM-Neu**	**UMM -Ani**	**UMM -Cat**	**UMM -Neu**	**UMM-Ani**	**UMM-Cat**	**UMM-Neu**	**UMM-Ani**	**UMM-Cat**	**UMM-Neu**
HPTS	1.0 *(10)*	1.6 *(16)*	7.3 *(73)*	32±2	32±4	25±5	0.40±0.05	0.41±0.08	0.29±0.06	-26.2±2.3	27.8±2.1	-7.0±3.8
DOX	14.0 *(35)*	14.8 *(37)*	8.7 *(22)*	26±3	37±3	27±4	0.38±0.03	0.39±0.01	0.33±0.04	-20.0±1.0	29.0±2.4	-1.4±1.2
SRhB	3.6 *(36)*	3.8 *(38)*	6.1 *(61)*	28±5	32±3	32±4	0.34±0.05	0.31±0.05	0.28±0.02	-24.5±2.4	26.9±3.5	-4.8±1.2
IR780	3.6 *(36)*	0.8 *(8)*	2.0 *(20)*	32±2	36±4	34±3	0.34±0.04	0.38±0.01	0.40±0.09	-25.3±1.0	33.6±2.3	-6.2±3.2
ICG	4.3 *(43)*	3.3 *(33)*	4.5 *(45)*	31±2	36±2	29±4	0.38±0.06	0.37±0.05	0.29±0.03	-26.3±1.0	25.2±1.4	-4.7±1.0

a:Drug loading content (%DLC) and drug loading efficiency were estimated by absorbance. *b*: hydrodynamic diameters (sizes), PDI and zeta potential were measured by DLS for self-assembled samples in pH 7.4 (10mM Britton-Robinson buffer) at nanoparticle concentration of 0.1mg/mL.

Table 3.1. *Tabulated details of drug/dye loaded nanoparticles. % DLC and DLE. DLS sizes and zeta potentials were recorded in pH 7.4 buffer. Data is represented as mean ± SD (n=3).*

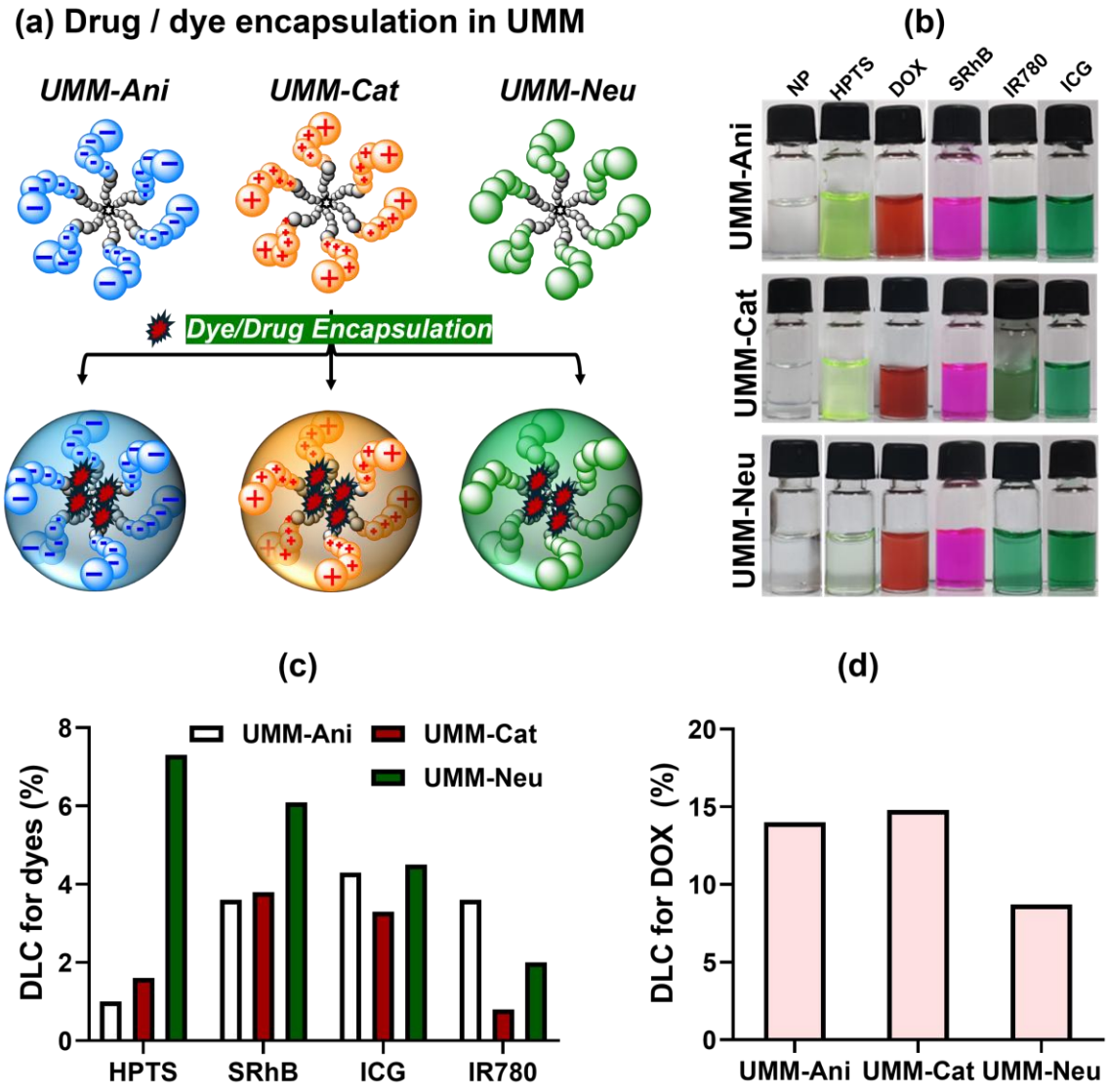

Figure 3.8. *(a) Schematic of drug /dye encapsulation in UMM Nanoparticles. (b) Photographs of vials containing drug/dye loaded UMM-Ani, UMM-Cat and UMM-Neu nanoparticle (Concentration 1.0mg/mL). (c) Plot of % DLC for different fluorescent dyes. (d) Plot of % DLC for DOX.*

The sizes of dye/drug encapsulated UMM-Ani, UMM-Cat and UMM-Neu nanoparticles were recorded by DLS in pH 7.4 and size histograms are shown in Figure 3.9a-c. All three UMM NP exhibited monomodal size distribution having hydrodynamic diameters in the range of 25-35 nm with narrow polydispersity of 0.2-0.4. The UMM NP. Interestingly sizes did not change after the encapsulation of drug or dye for UMM NP suggested that the cargoes were encapsulated and stabilized in the core region of NP only. Moreover, the pH of solution also did not alter the size of the UMM NP and all the data is tabulated in table 3.1. These results suggested that the UMM NP are stable in pH 7.4 and do not undergo any aggregation or precipitation. Furthermore, the surface charges for dye/drug loaded UMM-NP were recorded in pH 7.4 to assess the effect of charge of cargo on the nanoparticle. The zeta

potential plots are shown in Figure 3.9d-f. Interestingly no significant alteration in surface charges were observed after the encapsulation of dyes. Dye encapsulated UMM-Ani NP remained negatively charged (ζ -20 to -27 mV) and UMM-Cat remained positively charged (ζ +25 to +33 mV). In addition, dye-loaded UMM-Neu NP depicted ζ potential in the neutral range of -1 to -7 mV which is comparable to its blank NP. The ζ potential values further confirmed that cargoes were confined to the core of the UMM-NP only and did not have significant effect on the shell. Furthermore, the HR-TEM and FE-SEM imaging of all DOX loaded UMM NP suggested the spherical NP of sizes 20-30 nm as shown in Figure 3.9g-i.

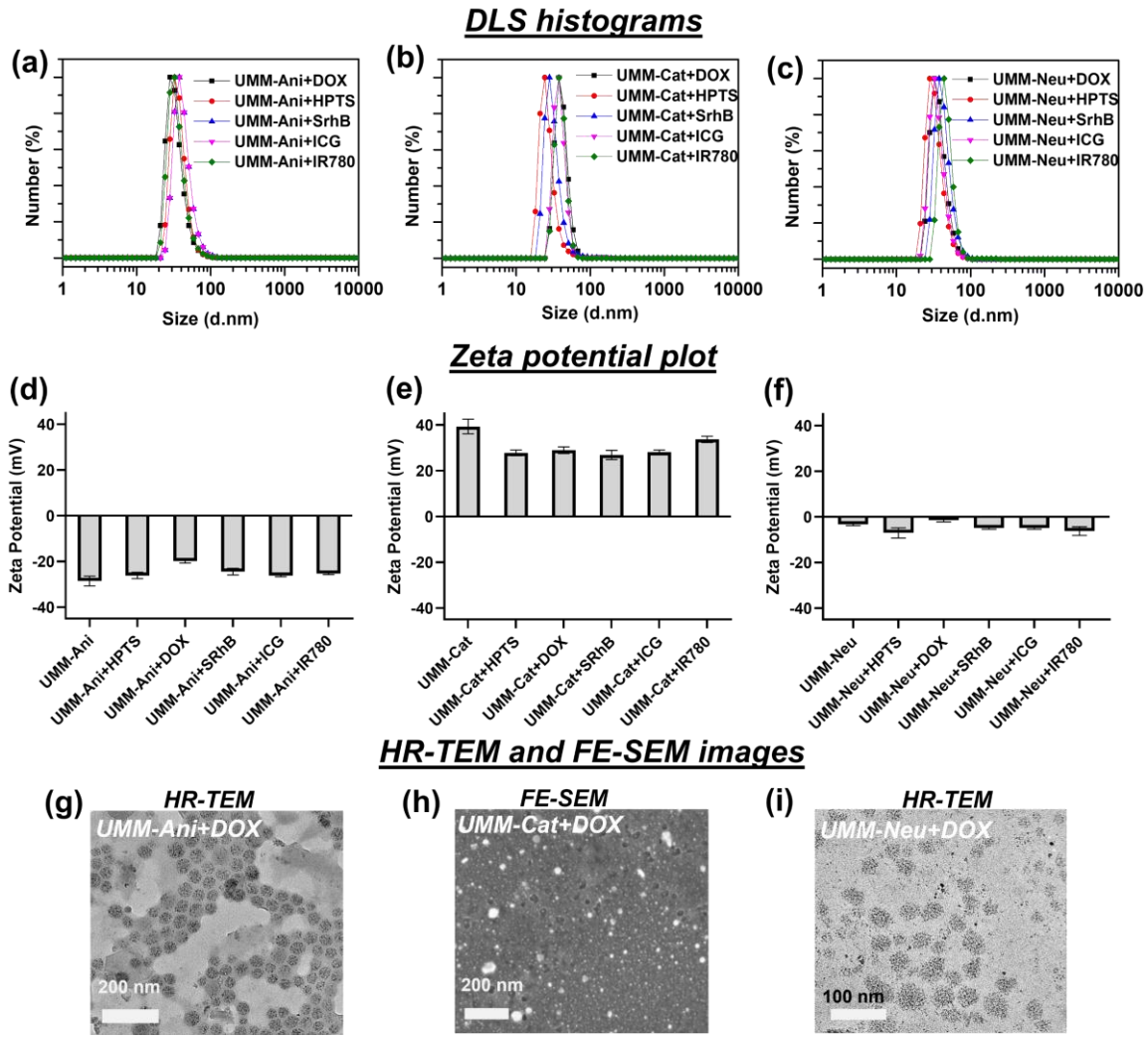

Figure 3.9. *DLS histograms of drug/dye loaded (a) UMM-Ani (b) UMM-Cat (c) UMM-Neu Nanoparticle (Concentration 1.0mg/mL). Zeta potentials plots of drug/dye loaded (d) UMM-Ani (e) UMM-Cat (f) UMM-Neu Nanoparticle (Concentration 1.0 mg/mL)in pH 7.4. Data is represented as mean ± SD (n=3). HR-TEM and FE-SEM images of (g) UMM-Ani+DOX (h) UMM-Cat+DOX (i) UMM-Neu+DOX nanoparticles. For recording HR-TEM images, aqueous NP solutions were drop-cast on copper grids and FE-SEM samples were prepared by drop casting on silicon vapor. Nanoparticle concentration was 0.1 mg/mL.*

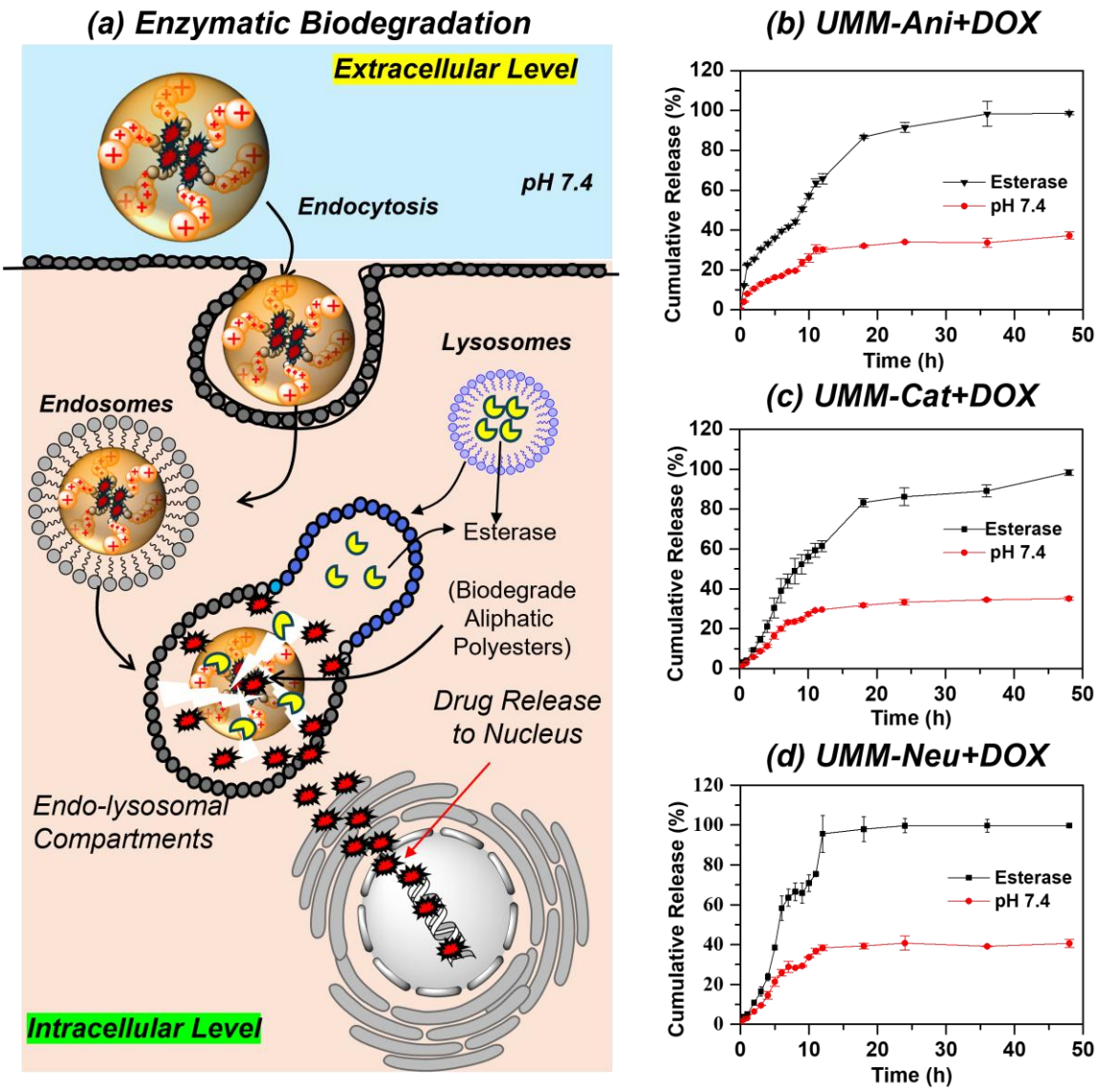

Figure 3.10. *(a) Schematic of enzymatic biodegradation. Release profiles of (b) UMM-Ani+DOX (c) UMM-Cat+DOX (d) UMM-Neu+DOX NP incubated in the presence of esterase (pH 7.4) and without esterase (only in PBS, pH 7.4) at 37°C for 48h.*

3.3.3 Enzymatic biodegradation, endocytosis and lysotracker assay

UMM-Ani, UMM-Cat and UMM-Neu NP are composed of esterase stimuli responsive aliphatic polyester backbone (PCL and substituted PCL) and assessed for enzymatic biodegradation. The representative schematic of enzymatic biodegradation for UMM-Cat+DOX NP is shown in Figure 3.10a. Briefly UMM NP undergoes endocytosis and engulfed by the membrane derived endosomal bodies in the intracellular compartment. Then the endosomes mature and fuse with lysosomes to form endo-lysosomal compartment where the esterase enzyme act on the aliphatic ester linkages of polymer which results in the hydrolysis

of ester bond. This process results in the degradation of high molecular weight UMM NP into smaller oligomeric units along with release of cargo (drug/dyes) into the cytosol. The released drug (DOX) then travels to nucleus and intercalates with DNA to interfere the DNA replication by inhibiting Topoisomerase enzyme and cause the cell death. To mimic the lysosomal condition the UMM-Ani+DOX, UMM-Cat+DOX and UMM-Neu+DOX NP were incubated in the presence of esterase enzyme (from horse liver) in PBS (10mM, pH 7.4) at 37ºC and release of the DOX was monitored. For the control experiment, NPs were only incubated in PBS , pH 7.4 without esterase enzyme. The plot of cumulative release for UMM NPs are shown in Figure 3.10b-d. The UMM-Ani+DOX and UMM-Cat+DOX NP showed controlled and slow release of DOX and about 80% of release was observed in 24h. In contrast, UMM-Neu+DOX NP exhibited slightly faster rate of degradation and depicted ~80% DOX release at 12h. Further incubation up to 48h did not cause very significant change in overall release and about 5-10% additional release was observed over the period of 48h. In the case of control experiment, UMM-Ani+DOX, UMM-Cat+DOX and UMM-Neu+DOX NP showed up to 25-30% release over the period of 48h incubation in absence of enzyme. This is attributed to the leaching of NP caused by high salt concentrations in PBS saline buffer. The release studies provided evidence of enzymatic biodegradation and validated the mechanism stated in Figure 3.10a.

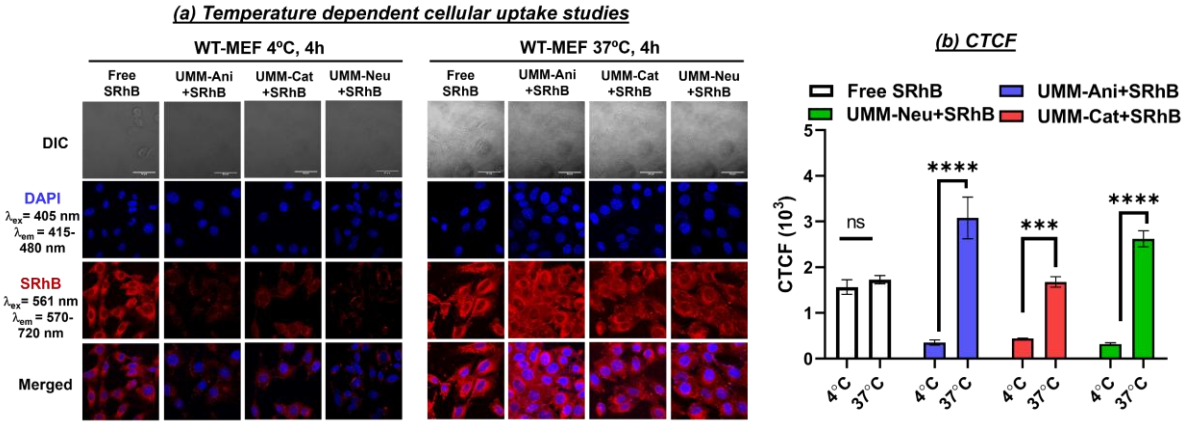

Figure 3.11. *(a) CLSM images of WT-MEF cells showing temperature dependent cellular uptake of free SRhB, UMM-Ani+SRhB, UMM-Cat+SRhB and UMM-Neu+SRhB NP incubated at 4 ºC and 37ºC for 4h. Scale bar 40µm. (b) Plot of CTCF for temperature dependent cellular uptake (n=3, Data is represented as mean ± SD, ****p<0.0001, ns=non-significant, ANOVA test).*

After validating enzymatic biodegradation of UMM NP and release of cargo subsequent endocytosis was assessed in WT-MEF (wild-type mouse embryonic fibroblast) cell line.

Endocytosis is an energy dependent process that occurs only at physiological temperature and inhibited at lower temperatures (4 ºC). To validate whether UMM NP were taken up via endocytosis or not, WT-MEF cells were incubated with Sulforhodamine B (SRhB) loaded UMM NP at 37 ºC and 4 ºC and confocal laser scanning microscopy (CLSM) images are shown in Figure 3.11a. The CLSM images provided direct evidence of endocytosis evident from intense fluorescence signal of UMM-Ani/Cat/Neu+SRhB NPs in the cells incubated at 37 ºC compared to negligible signal from the 4 ºC. In contrast free SRhB dye depicted similar signal from the cells incubated for both the temperatures suggested uptake of small molecule via diffusion pathway. Plot of corrected total cell fluorescence (CTCF) in Figure 3.11b suggested 3-4-fold higher cellular uptake at 37 ºC compared to 4 ºC. However, free SRhB dye showed similar uptake at both conditions. These results validated that all three UMM NP were taken up by cells via endocytosis process.

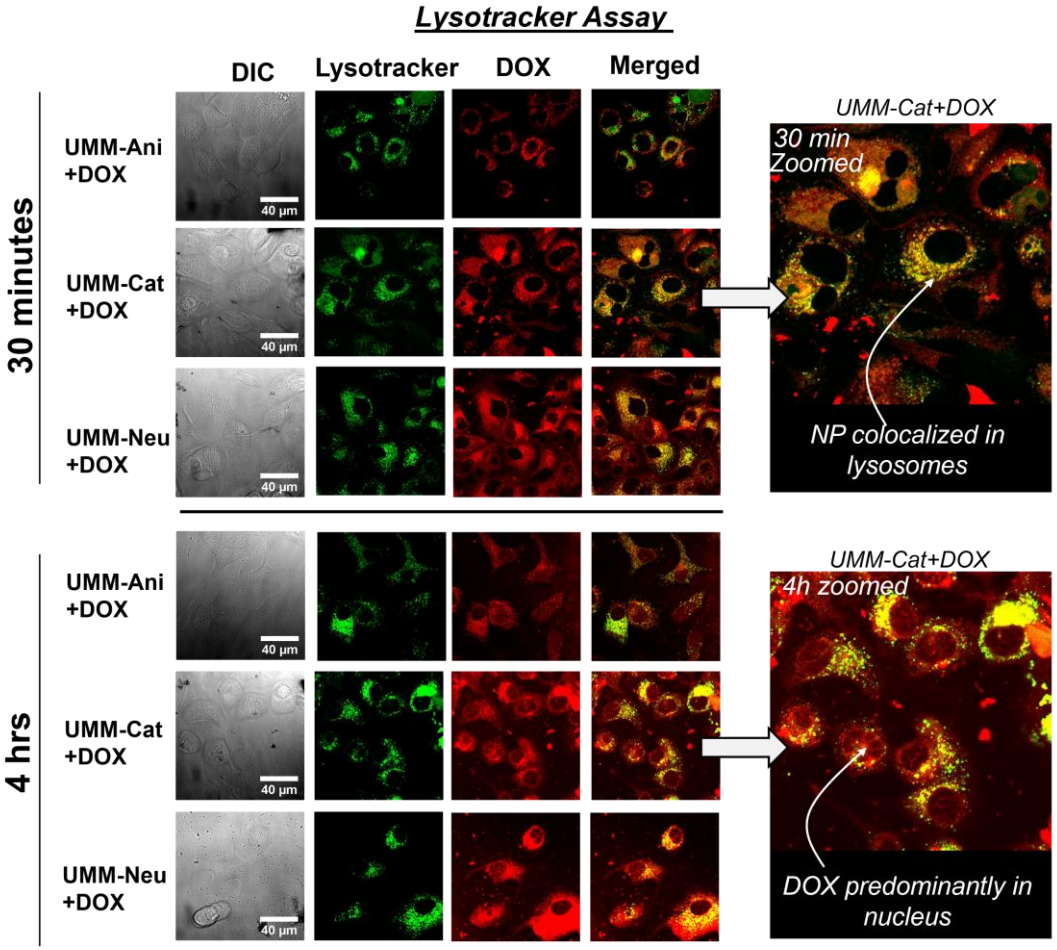

Figure 3.12. *Lysotracker assay. Real-time CLSM images of MCF-7 cells incubated with UMM-Ani+DOX, UMM-Cat+DOX and UMM-Neu+DOX NP at 30 minutes and 4h. The lysosomes are stained with lysotracker green DND-26 and visualized using 488nm laser. DOX was visualized using 561nm laser. Representative zoomed images of 30 min and 4h for UMM-Cat+DOX NP showed at right side.*

Real-time live lysosomal biodegradation in MCF-7 (breast cancer) cell line was evaluated by lysotracker assay. The MCF-7 cells were incubated with UMM-Ani+DOX, UMM-Cat+DOX and UMM-Neu+DOX NP and lysosomes were stained with lysotracker green DND-26. The CLSM images of 30min and 4h after incubation were captured and shown in Figure 3.12. At 30 minutes of incubation, all the UMM NP were significantly taken up by cell evident from the signal of DOX. Moreover, UMM NPs were colocalized with lysosomal evident from the yellow color in merged panel (resulted from lysotracker green + red DOX). The zoomed image of 30 min for UMM-Cat+DOX clearly shows that NPs are predominantly occupied in cytoplasm colocalizing with lysosomes. However, as the time progressed esterase enzyme degraded the polymer backbone to release the DOX to nucleus. At 4h timepoint, intense signal of DOX can be seen from nucleus for all NPs suggesting the degradation of NPs. Zoomed image of 4h for UMM-Cat+DOX NP provided clear visual evidence of biodegradation where DOX can be seen clearly predominantly from the nucleus. Moreover, signals from lysosomes at 4h suggested uptake and simultaneous biodegradation were in progress. These results validate the mechanism of lysosomal biodegradation mentioned in Figure 3.10.

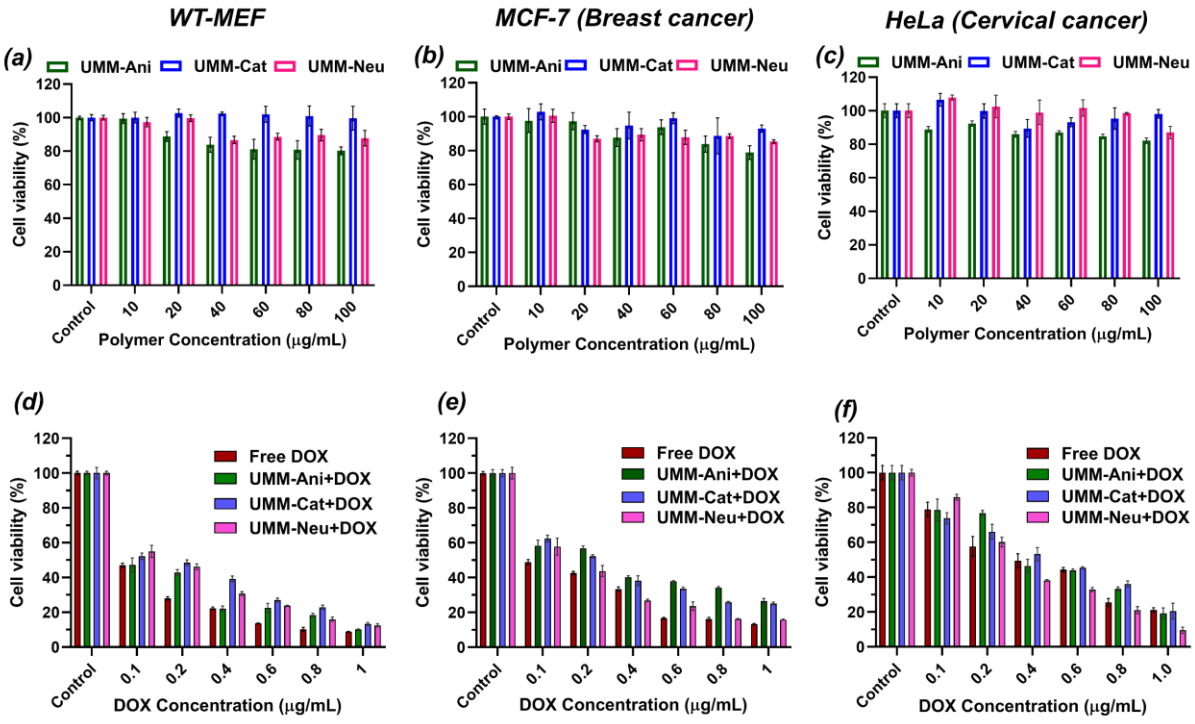

Figure 3.13. *Cytotoxicity by MTT assays for 72h of incubation. (a) to (c) Plot of cell viability for UMM-Ani, UMM-Cat and UMM-Neu nanoparticles in WT-MEF, MCF-7 and HeLa cell lines respectively. (d) to (f) Plot of cell viability for free DOX, UMM-Ani+DOX, UMM-Cat+DOX and UMM-Neu+DOX NP in WT-MEF, MCF-7 and HeLa cell line respectively. Data represented as mean ± SD (n=3).*

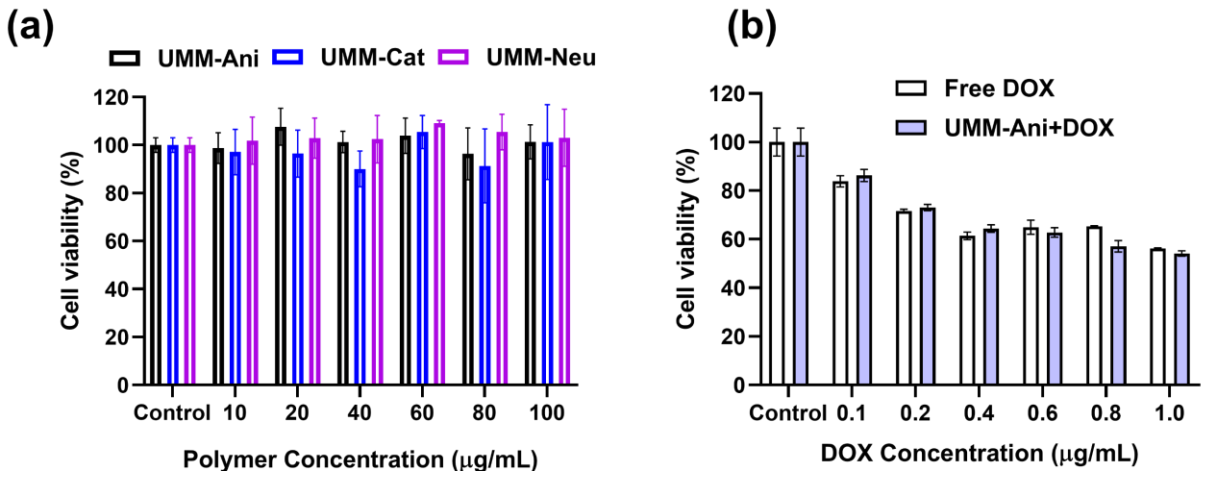

Figure 3.14. *Cytotoxicity by MTT assays 72h of incubation in SH-SY5Y cell line. (a) Plot of cell viability for UMM-Ani, UMM-Cat and UMM-Neu nanoparticles. (b) Plot of cell viability for free DOX, UMM-Ani+DOX NP. Data represented as mean ± SD (n=3).*

3.3.4 Cytotoxicity

Cytotoxicity of nascent UMM nanoparticles were tested in WT-MEF, MCF-7 and HeLa (cervical cancer) cell lines by MTT assay for 72h of incubation. The plots of cell viability for nascent UMM-Ani , UMM-Cat and UMM-Neu NP up to 100 μg/mL concentration for 72h incubation are shown in Figure 3.13a-c. All three UMM NP depicted excellent cyto-compatibility with >90% cell viability for longer period suggesting the safety of UMM NP. Next, DOX loaded UMM NPs were evaluated for their killing ability in WT-MEF, MCF-7 and HeLa cell line for 72h. The plots of cell viability of UMM-Ani+DOX, UMM-Cat+DOX and UMM-Neu+DOX NP for 72h incubation are shown in Figure 3.13d-f. DOX loaded UMM NP exhibited concentration-dependent killing ability equivalent to free drug suggesting the preservation of DOX structure inside nanocarriers. No significant difference was observed in killing efficiency among three UMM NP in WT-MEF cells. However, UMM-Neu+DOX showed slightly better killing ability in MCF-7 and HeLa compared to UMM-Ani+DOX and UMM-Cat+DOX NPs. Furthermore, the cytotoxicity of nascent UMM NP depicted excellent compatibility in SH-SY5Y (neuroblastoma) cell line for 72h with 100% cell viability as shown in Figure 3.14a. Moreover, UMM-Ani+DOX NP exhibited similar killing ability with free DOX as shown in Figure 3.14b suggesting the ability of UMM NP to degrade and release DOX in the neuroblastoma cells. The non-toxic nature of nascent UMM NP and killing ability of DOX loaded UMM NP in all the cell line tested signified that these UMM NP are excellent candidate for biomaterial application such as drug delivery.

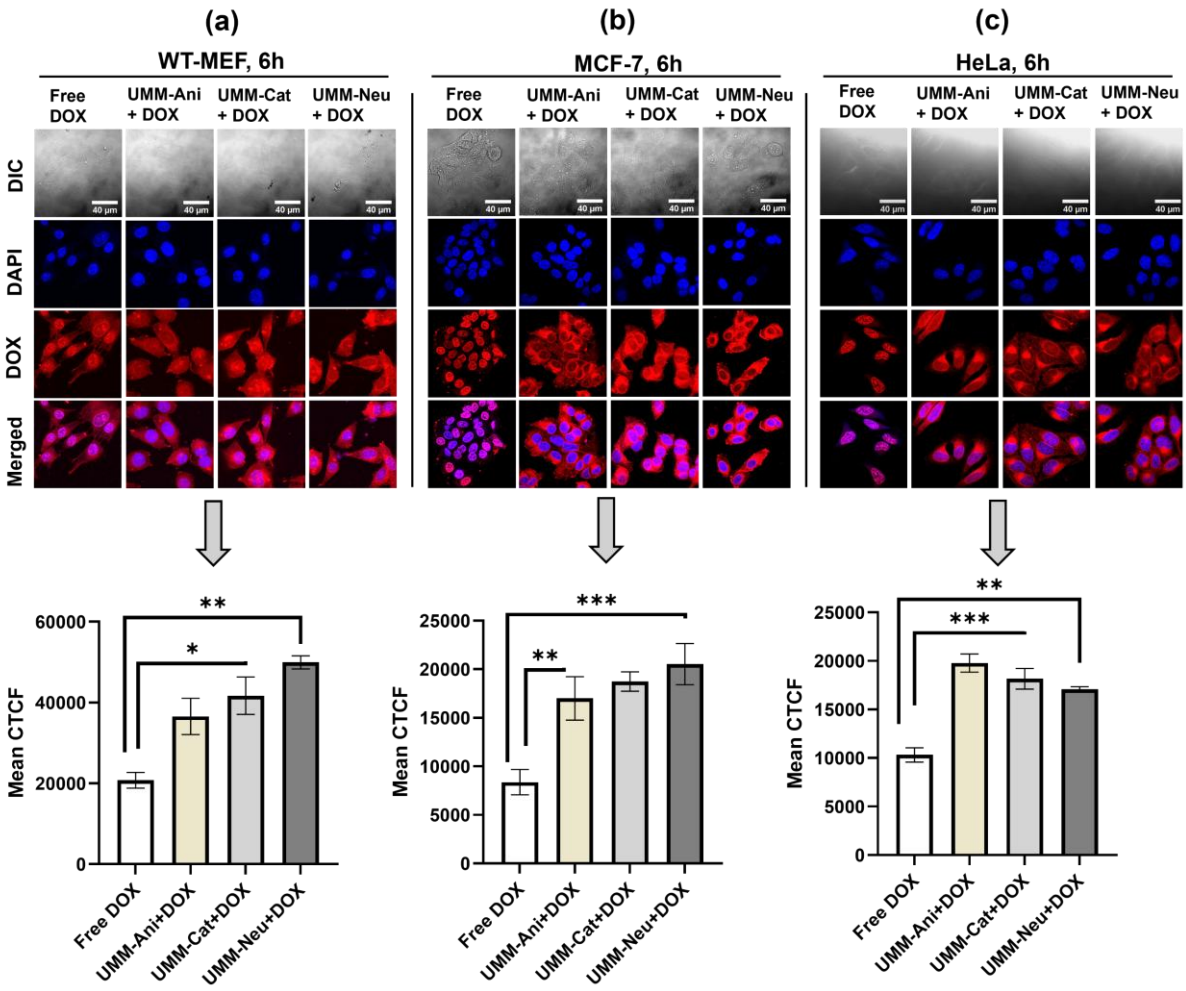

Figure 3.15. *CLSM images for cellular uptake of free DOX, UMM-Ani+DOX, UMM-Cat+DOX and UMM-Neu+DOX NP in (a) WT-MEF (b) MCF-7 and (c) HeLa for 6h incubation. Respective plot of CTCF for each cell line (n=3, Data is represented as mean ±SD, *p<0.05, **p=0.001, ***p=0.0001, ANOVA test). Nuclei were co-stained with DAPI and visualized using 405nm and DOX visualized using 488nm laser (DOX concentration=2.5µg/mL).*

3.3.5 Cellular uptake studies

DOX loaded UMM NP were evaluated for cellular uptake studies in the WT-MEF, MCF-7 and HeLa cell line for 6h incubation and CLSM images are shown in Figure 3.15. The CLSM images depicted strong intense fluorescence signal of DOX for UMM-Ani+DOX, UMM-Cat+DOX and UMM-Neu+DOX compared to free DOX suggested excellent uptake of NPs. The magenta color in the merged panel resulted from the colocalization DOX and DAPI in nucleus suggested degradation of NP and release of DOX to nucleus. The estimated CTCF revealed 1.5-2-fold higher cellular uptake in case of UMM NP compared to free DOX. This is attributed to fact that free drug molecules get effluxes out from the cells via P-glycoprotein

(Pgp) efflux pump. However, UMM NPs have superior ability to bypass the Pgp efflux pump and accumulate more and more in the cells as time progresses. Furthermore, no significant difference was observed among UMM-Ani, UMM-Cat and UMM-Neu NP at 6h timepoint.

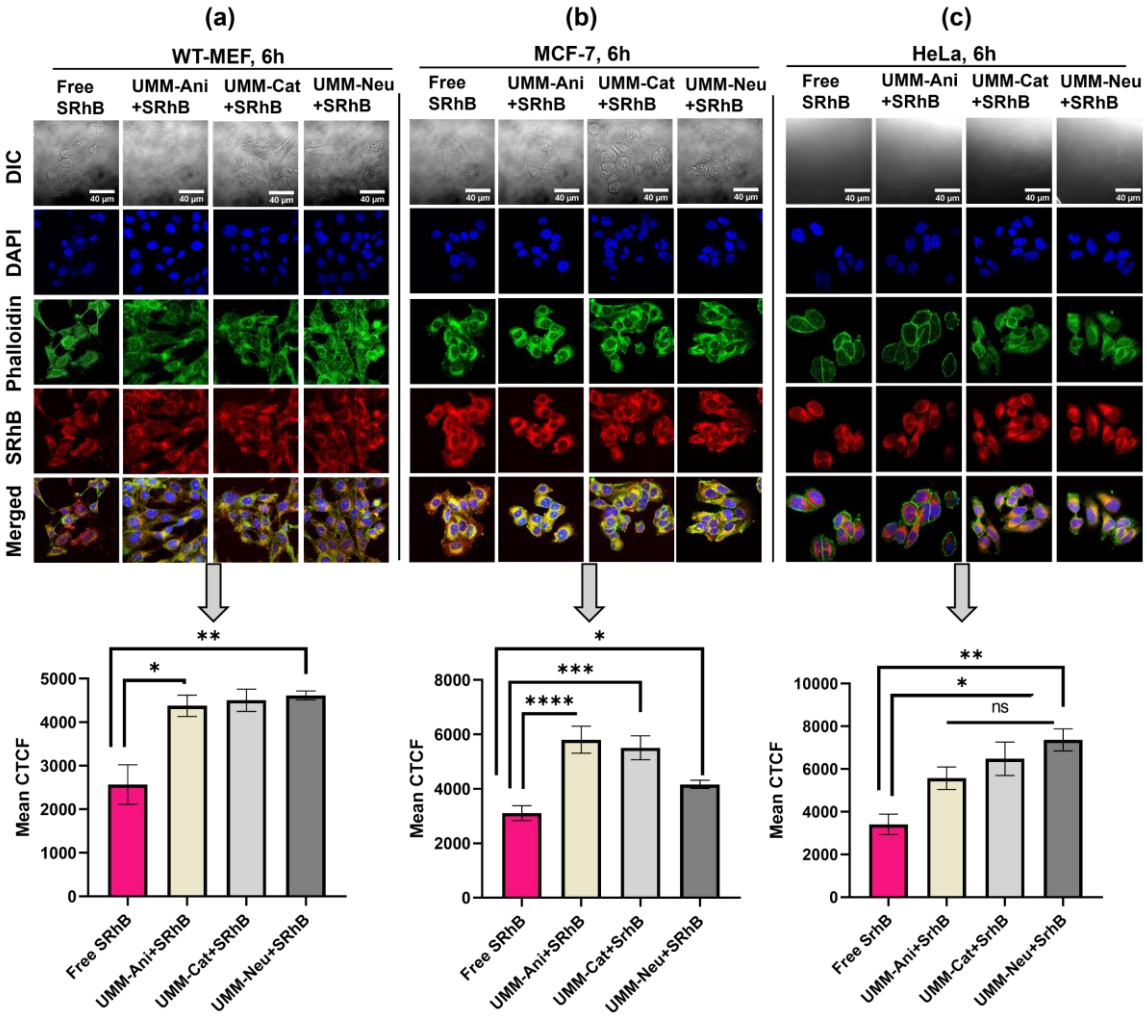

Figure 3.16. *CLSM images for cellular uptake of free SRhB, UMM-Ani+SRhB, UMM-Cat+SRhB and UMM-Neu+SRhB NP in (a) WT-MEF (b) MCF-7 and (c) HeLa for 6h incubation. Respective plot of CTCF for each cell line (n=3, Data is represented as mean ±SD, *p<0.05, **p=0.001, ** p=0.006, ***p=0.0001, ****p<0.0001, ANOVA test).Nuclei were co-stained with DAPI and phalloidin visualized using 405nm and 488nm respectively. SRhB was visualized using 561nm laser. (SRhB concentration=2.5µg/mL)*

The capability of UMM NP for delivering water soluble fluorescent dye (SRhB) to the cells was evaluated in WT-MEF, MCF-7 and HeLa cell lines. The CLSM images for cellular uptake of UMM-Ani+SRhB, UMM-Cat+SRhB and UMM-Neu+SRhB NP for 6h incubation timepoint are shown in Figure 3.16. The UMM NP exhibited excellent cellular uptake in all the cell lines evident from intense fluorescent signal in SRhB panel. The CTCF plots revealed a

1.5-2-fold higher uptake in case of UMM NP compared to free SRhB. In addition, another water-soluble dye HPTS was loaded in UMM NP and evaluated for cellular uptake of in WT-MEF cell line. CLSM images of UMM-Ani+HPTS, UMM-Cat+HPTS and UMM-Neu+HPTS NPs for 6h incubation in WT-MEF cells is shown in Figure 3.17a. All UMM NP exhibited excellent capability for delivering HPTS evident form intense signal of HPTS in CLSM images. CTCF plot in Figure 3.17b suggested that UMM NP were slightly better in cellular uptake compared to free HPTS dye. These cellular uptake studies depicted the potential of UMM NP to deliver the important anticancer drug DOX as well as water soluble dyes (HPTS and SRhB) in various normal and cancer cells lines which is remarkable. In addition, the delivery ability of UMM-Ani+DOX NP was assessed in neuroblastoma (SH-SY5Y) cell line and CLSM images are shown in Figure 3.17c. Interestingly UMM-Ani+DOX NP showed excellent ability to get internalized in neuroblastoma cells and cellular uptake linearly increased with increased time of incubation evident from CTCF estimation in Figure 3.17d. These results clearly suggest that the currently designed UMM NP are fully enzymatically biodegradable in the lysosomal compartment, non-toxic to various cells lines and have exceptional ability to deliver cargo in various cells line. Therefore, UMM NP are safer to use for *in vitro* drug delivery applications and can be examined for further *in vivo* assays.

3.3.6 Hemolysis assay

Interaction of nanocarriers with components such as blood cells and large pool of proteins is crucial when any noncarriers is administered to animals. Nanocarriers should not interfere with red blood cells (RBC) membrane to ensure the safety of animals. Therefor the hemolytic ability of nanoparticles should be assessed before *in vivo* experimentation. For that purpose, the freshly withdrawn blood form mouse was used to procure RBC. The UMM NPs were incubated with RBC for 1h to assess their safety. The incubated samples were centrifuged in fresh tube for visualization of RBC rupture. Surprisingly UMM NP were as safer as PBS evident from the formation of pellet of RBCs settled at the bottom of tube showed in Figure 3.18. In contrast, the complete rupture of RBCs was observed in case of 1% triton-100 (TrX), a non-ionic surfactant used as positive control for the experiment. The plot of % hemolysis showed in Figure 3.16 suggested that UMM NP were non-hemolytic nature even at very high concentrations of 1000 μg/mL and the values for hemolysis were even lower compared to PBS

(negative control). To our surprise UMM-Cat was also found to be non-hemolytic because cationic NPs are notorious for hemolytic activity reported in literature. Therefor currently designed UMM NP are suitable for further *in vivo* analysis. The self-assembly aspects, toxicity and delivery abilities of AgM-Ani NP are discussed in detail in chapter 2. Also, self-assembly and non-toxic nature and delivery capability of AgM-Cat NP are published in our recent work.[69]

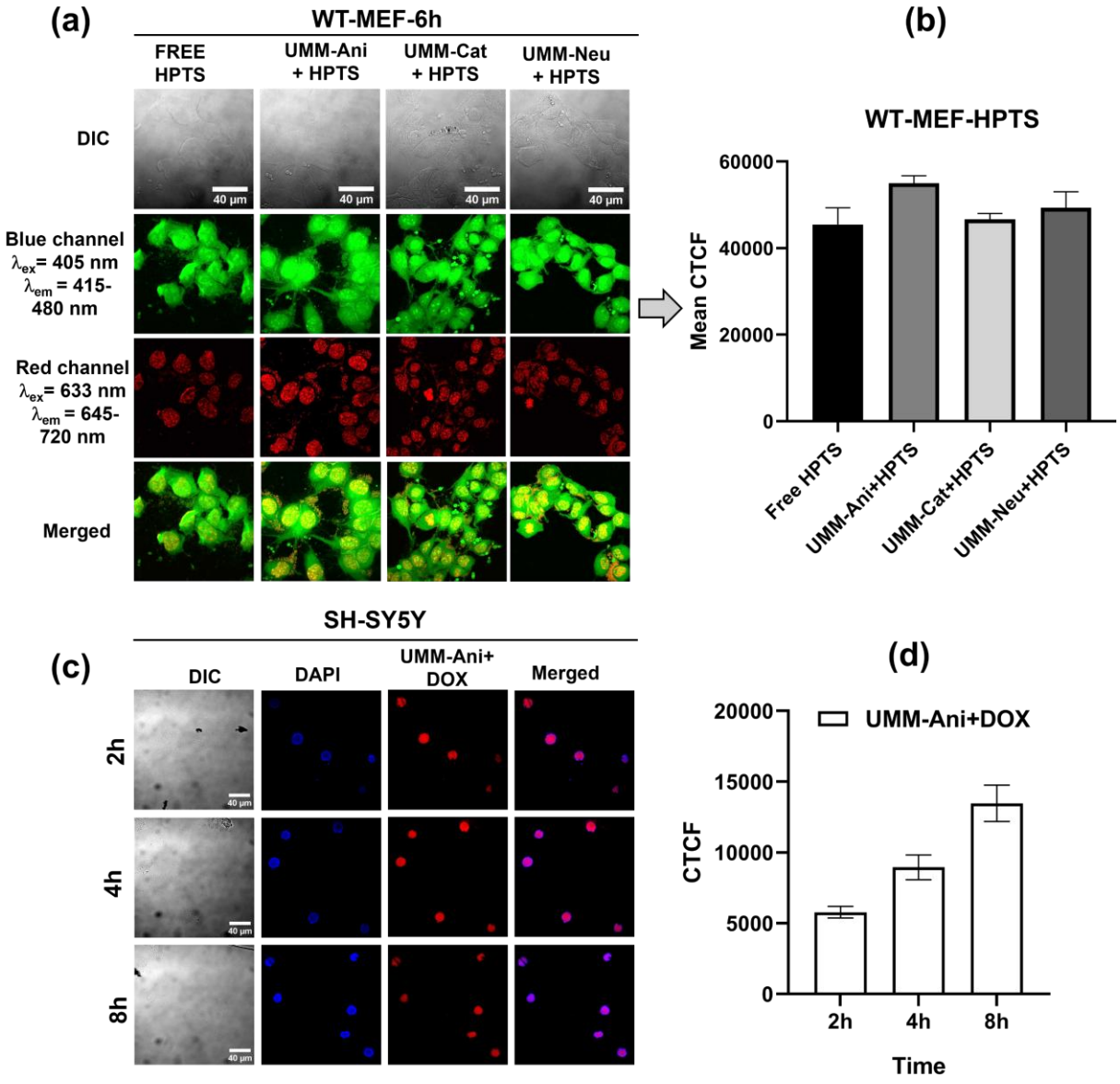

Figure 3.17. *(a) CLSM images for cellular uptake of free HPTS, UMM-Ani+HPTS, UMM-Cat+HPTS and UMM-Neu+HOTS NP in WT-MEF (b) Plot of CTCF for HPTS loaded UMM NPs in WT-MEF (n=3, Data is represented as mean ±SD. Nuclei were co-stained with SYTO red and visualized using 633nm and HPTS was visualized using 405nm laser respectively. (c) CLSM images of cellular uptake of UMM-Ani+DOX NP in SH-SY5Y cell line for various timepoints. Nuclei were stained with DAPI and visualized using 405nm laser. (d) Plot of CTCF for UMM-Ani+DOX NP in SH-SY5Y cells.*

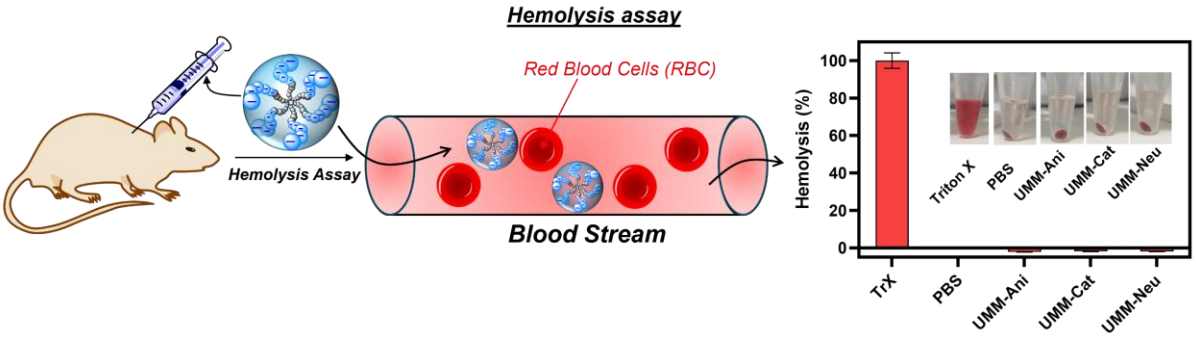

Figure 3.18. *Hemolysis assay. The fresh RBC were incubated with UMM NP. Plot of % hemolysis. Concentration of UMM NP was 1000µg/mL. PBS and triton X (TrX) were used as negative and positive control respectively.*

3.3.7 *In vivo* Biodistribution and BBB Breaching

Encouraged by non-toxic and non-hemolytic activity of UMM NP, we next evaluated them for biodistribution analysis and organ specific (particularly brain) distribution. The biodistribution studies were carried out using near infra-red fluorescence (NIRF) imaging owing to its non-invasive nature and low background noise. Moreover, infrared wavelength can penetrate deeper into tissue and give better signal to noise ratio. In-vivo imaging system (IVIS) was used for carrying out biodistribution studies. For that purpose, near infrared dye IR780 dye was chosen due to its high quantum yield and better circulation time owing to its lipophilic nature. The IR780 iodide was encapsulated in UMM NP and details are aforementioned in self-assembly. Details of IR780 loading in AgM-Ani are mentioned in chapter 2 and details of AgM-Cat+IR780 are mentioned in our published work.[69]

3.3.8 Role of sizes in BBB breaching: Aggregated vs unimolecular micelles

We first analyzed the role of sizes of NPs having similar charge only differ in sizes for the biodistribution and blood-brain-barrier (BBB) breaching. For that purpose, aggregated micellar anionic nanoparticles AgM-Ani+IR780 having sizes of ~70nm and unimolecular micellar NP UMM-Ani+IR780 having sizes of ~30 nm. The animals were intraperitoneally injected into Balb-C mice with AgM-Ani+IR780, UMM-Ani+IR780, free IR780 (n=3 for each group) and imaged for various time points till 24h. The IVIS florescence images of dorsal and lateral view of live-animals are shown in Figure 3.19a-b. The IVIS images revealed that the UMM-Ani+IR780 and AgM-Ani+IR780 NP were readily circulated in the whole body of mouse at 4h postinjection and depicted stronger signal compared to free IR780. The animal injected with only PBS (negative control) did not show any signal as expected. The

quantification of dorsal images in Figure 3.19c revealed that both AgM and UMM NP exhibited 2-3-fold higher signal compared to free IR780 owing to better circulation time of NP. However, UMM-Ani+IR780 NP were distributed slightly better on the dorsal side compared to AgM-Ani+IR780. In contrast, ventral side quantification in Figure 3.19d did not show significant differences among the free IR780, AgM and UMM distribution at earlier time points whereas significant difference was observed at 24h for both NP compared to free IR780. Interestingly, both AgM-Ani and UMM-Ani NP performed equally at 24h from whole body imaging data suggesting that minimum 24h are required to circulate complete NP throughout whole body of animals.

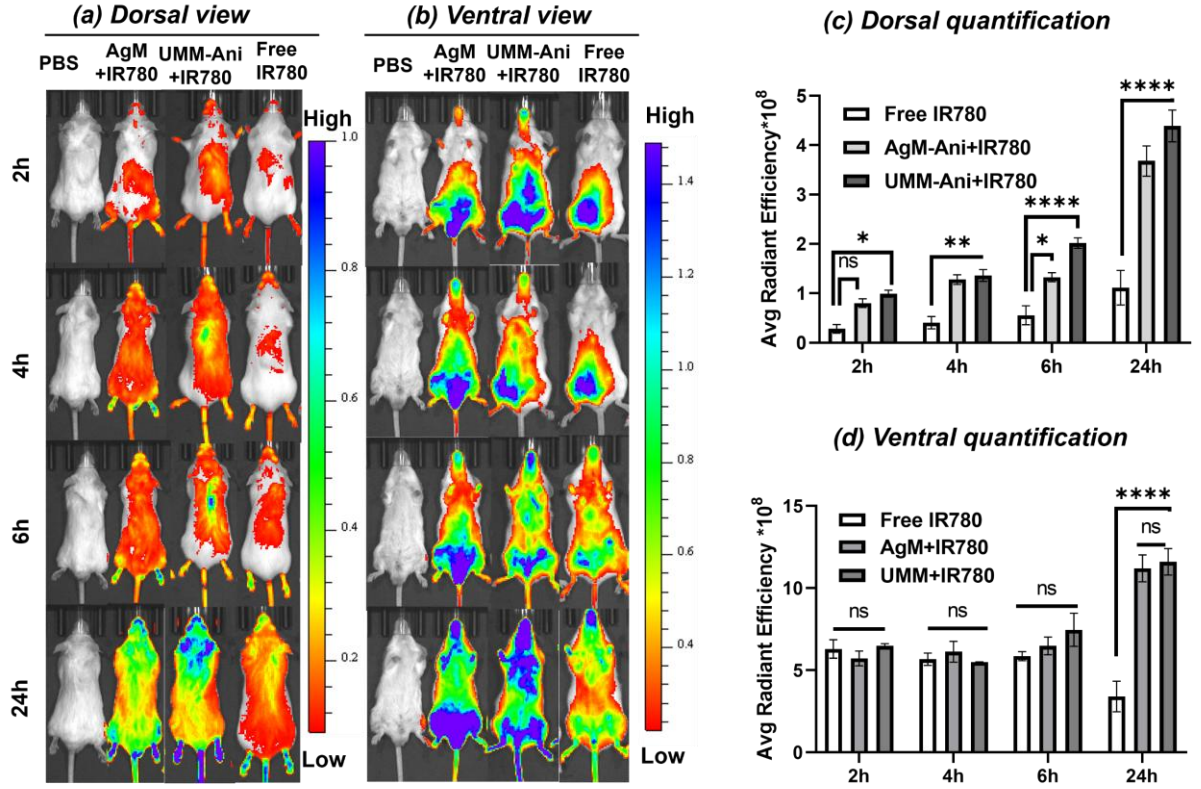

Figure 3.19. *Biodistribution using IVIS fluorescent bioimaging. Representative images of (a) dorsal & (b) ventral view for free IR780, AgM-Ani+IR780 and UMM-Ani+IR780 NP for various time points. Quantification of fluorescent signal from (c) dorsal (d) ventral images (Data is represented as mean ± SEM, n=3, *p<0.05, **p=0.003, ****p<0.0001,ns=non-significant, ANOVA test).*

At 24h postinjection animals were sacrificed and organs were excised and subjected to IVIS imaging to evaluate their performance in organ based biodistribution. Ex-vivo organ fluorescent images showed in Figure 3.20a depicted stronger signals from vital excretory organs harvested form the animals injected with UMM-Ani+IR780 NP compared to AgM-Ani+IR780 or free IR780. More importantly, free IR780 and AgM-Ani+IR780 did not show

any detectable fluorescent signal in the brains suggesting impermeability of free IR780 dye and AgM-Ani+IR780. This is attributed to the tightly controlled blood-brain-barrier consisting of tightly packed endothelial cells which allow only specific molecules to travel across the barrier. Hence the free IR780 dye cannot cross the barrier. In addition, the AgM-Ani+IR780 aggregated micellar nanoparticles of sizes ~70 nm also could not be able to cross the BBB evident from the images in 3.20a. In contrast, significant fluorescent signal was detected from the brain samples of animals injected with the UMM-Ani+IR780 NP of ~30nm size as shown in Figure 3.20a. Furthermore, quantification for signals obtained all vital organs in Figure 3.20b clearly suggested more retention and accumulation of UMM-Ani+IR780 in organs compared to AgM-Ani+IR780 NP and free IR780. Notably the quantified signal from brains clearly depicted that free IR780 dye and AgM+IR780 NP did cross the BBB as showed in Figure 3.20c. In contrast, UMM-Ani+IR780 NP could be able to cross the BBB and accumulated in appreciable amount in the brain suggested by quantification. These results clearly suggest that UMM-Ani NP possess the distinct ability of longer blood circulation, more accumulation and BBB crossing ability attributed to its smaller size. In conclusion, the NP having sizes <40 nm could be able to cross the BBB whereas the NP having sizes more than 50 nm cannot cross the BBB.

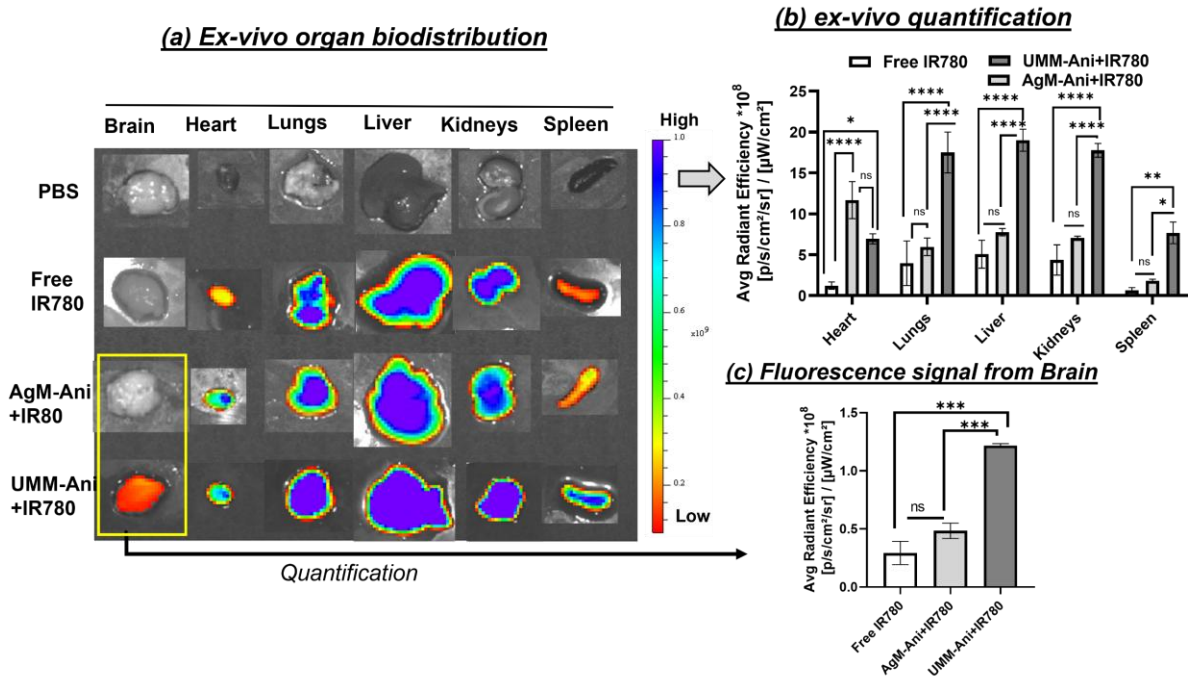

Figure 3.20. *(a) Ex-vivo IVIS fluorescent bioimaging organs for free IR780, AgM-Ani+IR780 and UMM-Ani+IR780 NP at 24 postinjection. (b) Quantifications for organs. (c) Signal from brains (data is represented as mean ± SEM, n=3, *p<0.05, **p=0.003, ***p=0.0001, p****<0.0001, ns=non-significant, ANOVA test).*

3.3.9 Role of surface charges in BBB breaching

After establishing the role of sizes in BBB crossing we next evaluated the role of surface charges of NP. For that purpose, UMM NPs of having sizes in similar range (25-35nm) but differ in the surface charges such as cationic (UMM-Cat, anionic (UMM-Ani) and neutral (UMM-Neu) were chosen. Balb-C mice were intraperitoneally injected with IR780 loaded UMM NPs and subjected to IVIS imaging. The IVIS fluorescence images of dorsal and ventral view from 4h to 72h are shown in Figure 3.21a-b. Images clearly depicted the intense signals throughout the whole body of mice injected with UMM NP compared to free IR780 dye. Intensities of signal were appreciably increased with time in case of UMM-Ani+IR780, UMM-Cat+IR780 and UMM-Neu+IR780 NP from 4h to 72h and almost remained steady till 72h suggesting the longer blood circulation time of UMM NPs. In contrast, animals injected with free IR780 dye depicted low signal owing to clearance of small molecular IR780 dye from the blood circulation. The quantification of signals from dorsal and ventral side in Figure 3.21c-d revealed that UMM NP depicted 2-3-fold higher intensities compared to free IR780 dye till 72h. However very small difference was observed among biodistribution of all UMM revealing performance of UMM-Cat+IR780 and UMM-Neu+IR780 NP was slightly better than UMM-Ani+IR780 NP. Whole body imaging clearly suggests that the UMM-Ani, UMM-Cat and UMM-Neu NP have exceptional ability to distribute all over the body compared to lipophilic free IR780 dye.

Plasma samples were extracted from the animals at different time points after injections and subjected to IVIS imaging for semi-quantitative pharmacokinetic evaluation. The IVIS images of plasma samples are shown in Figure 3.22 along with the quantification. The images depicted much intense signal for UMM NP compared to free IR780. The free IR780 showed diminishing signal till 72h suggesting clearance from the blood circulation. On other hand the UMM-Ani+IR780 showed intense signal till 48h postinjection and further slightly decreased at 72h. In case of UMM-Cat+IR780 and UMM-Neu+IR780 signals were steadily intense till 72h suggesting longer blood circulation time. The quantified data suggested that UMM NP have 2-3-fold higher signals compared to free dye. Moreover, all the samples depicted highest signal at earliest time point (4h) and further signals started to decrease till 72h. UMM-Cat and UMM-Neu performed slightly better compared to UMM-Ani+IR780 at longest time point of 72h. In summary, semi-quantitative pharmacokinetic evaluation validated that UMM NP are excellent candidates owing to long blood circulation time compared to small molecules.

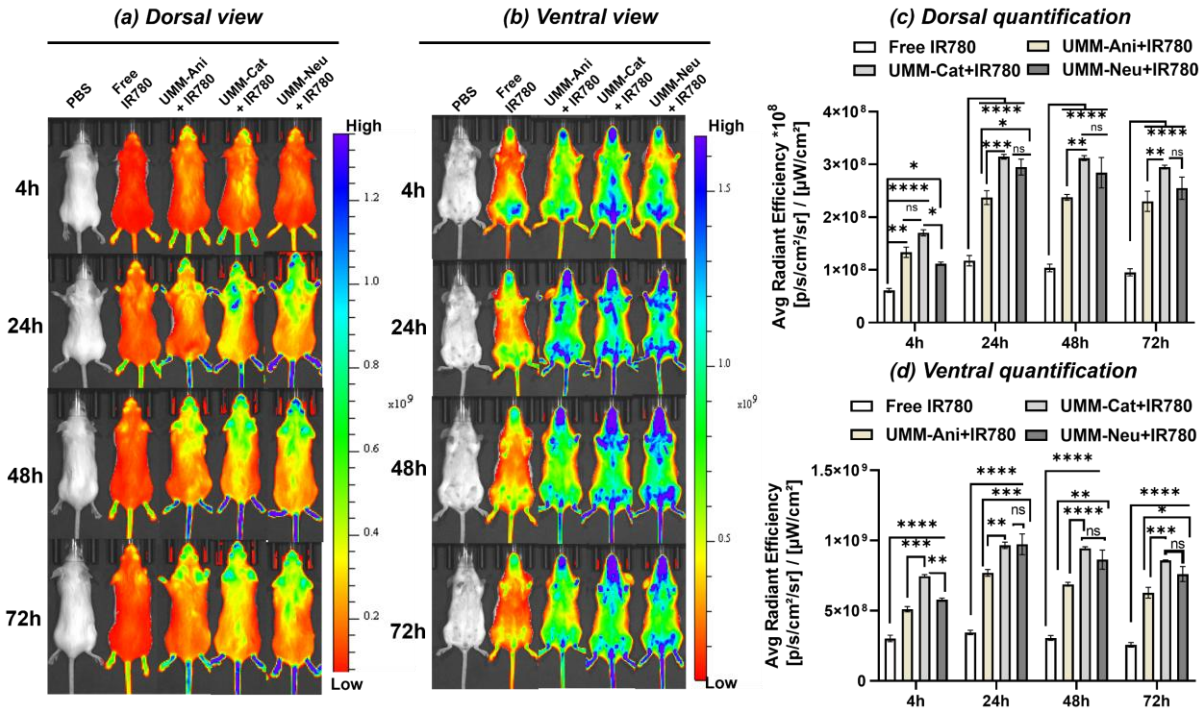

Figure 3.21. *Biodistribution using IVIS fluorescent bioimaging. Representative images of (a) dorsal & (b) ventral view for free IR780, UMM-Ani+IR780, UMM-Cat+IR780 and UMM-Neu+IR780 NP for various time points. Quantification of fluorescent signal from (c) dorsal (d) ventral view (Data is represented as mean ± SEM, n=3, *p<0.05, **p=0.0014, ***p=0.006 ****p<0.0001,ns=non-significant, ANOVA test).*

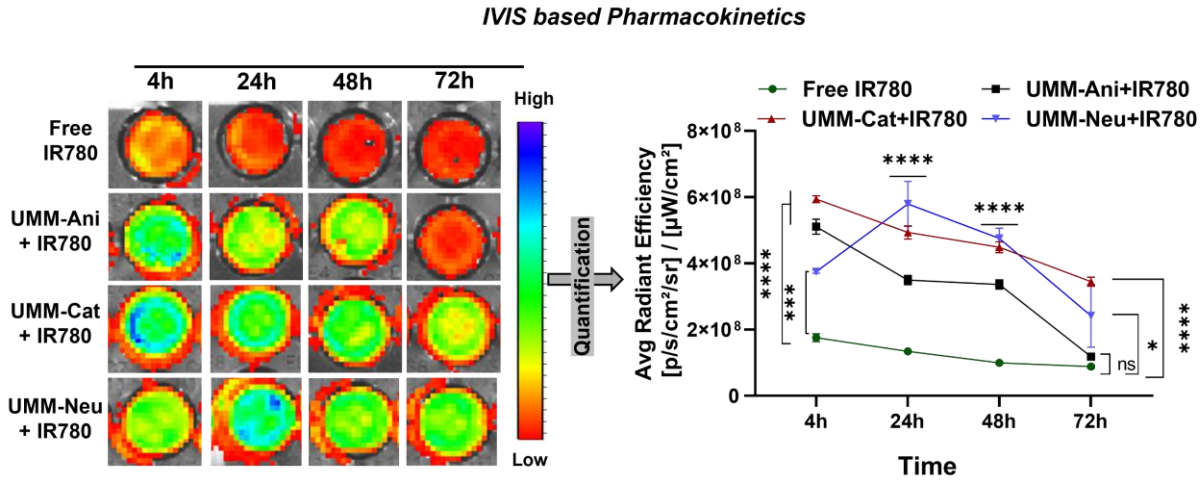

Figure 3.22. *IVIS fluorescent bioimaging based pharmacokinetics. IVIS images of plasma samples extracted from animals injected with free IR780, UMM-Ani+IR780 and UMM-Cat+IR780 and UMM-Neu+IR780 NP at different time points. Plot of quantified signal from plasma samples (data is represented as mean ± SEM, n=3, *p<0.05, ****p<0.0001, ns=non-significant, ANOVA test).*

Organs were harvested and subjected to IVIS imaging at 72h postinjection to evaluate the organ based biodistribution and IVIS images of excised organs are shown in Figure 3.22a. IVIS images revealed much more intense signals from excretory organs such as liver, kidneys, spleen and lungs in case of UMM NPs compared to free IR780. In addition, the quantification for all other organs in Figure 3.22b revealed 2-4-fold higher accumulation of UMM NPs in excretory organs compared to free IR780. Lungs, kidneys and liver showed highest accumulation for UMM-Ani+IR780, UMM-Cat+IR780 and UMM-Neu+IR780 groups as expected. However, there was no significant difference observed among for accumulation and retention in organs all three UMM NPs suggesting that sizes played crucial roles in accumulation. In summary all three differently charged UMM NP are excellent candidates organ based in-vivo delivery application.

Brains of animals injected with PBS or free IR780 did not show any detectable fluorescence signal as expected. Surprisingly brains of animals injected with UMM-Ani+IR780, UMM-Cat+IR780 and UMM-Neu+IR780 NP showed excellent fluorescent signal as shown in Figure 3.23a. The signal was much intense from brain for UMM-Neu+IR780 group compared to UMM-Ani and UMM-Cat group as shown in Figure 3.23b. The quantified data for brains suggested the 8-10-fold higher uptake and accumulation of UMM NPs compared to free IR780. This suggested that all the UMM NP were able to breach the BBB and could be able to accumulate in the brain in significant amount. However, very small differences among all three UMM NP were observed upon quantifying which was statistically non-significant. This result is indeed surprising because all three UMM NP are of approximately similar sizes (25-35nm) only differ in shell modification resulting in anionic (-26mV), cationic (+33mV) and neutral (-6mV) surface charge. This could be attributed to fact that mechanism of uptake for all different charged nanoparticles is different which will be discussed in coming section. Therefore, all three UMM NP could have been taken up and accumulated equally in the brains.. The organ based biodistribution suggests that the UMM NP are excellent candidates for BBB breaching and delivering the cargo to the brain. Noticeably anionic, cationic and neutral charged UMM NP performed equally in BBB breaching indicates that the charges of UMM NP did not have significant role in crossing BBB in this particular case. Moreover, only size of NP is the deciding factor whether NP would cross the BBB or not. Unimolecular micelle NPs having sizes <40 nm can cross the BBB and accumulate in the brain while aggregated micellar NP >40-50 nm cannot cross the BBB. While surface charges did not influence the delivery ability of UMM NP across the brain.

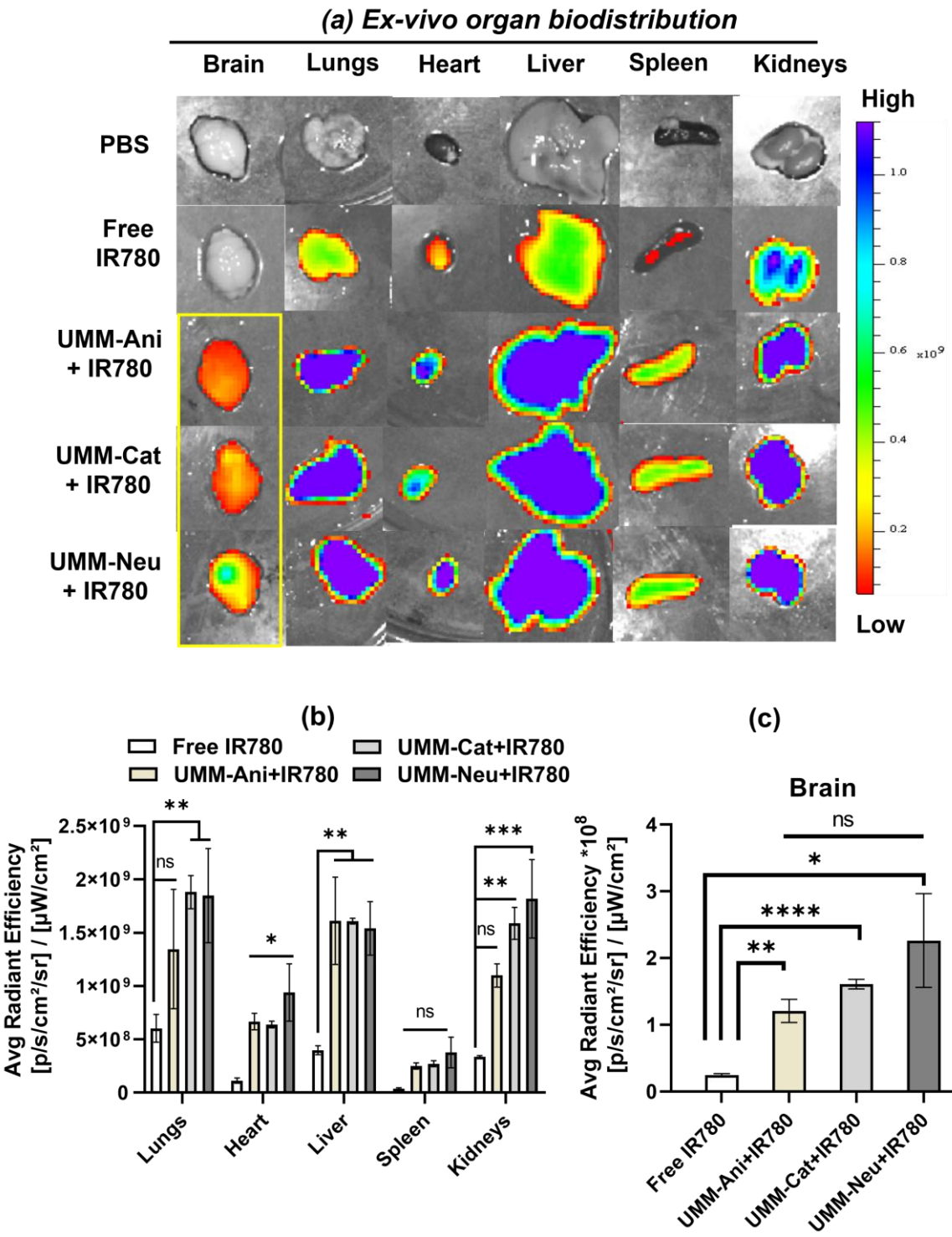

Figure 3.23. *(a) Ex-vivo IVIS fluorescent bioimaging organs for free IR780, UMM-Ani+IR780 and UMM-Cat+IR780 and UMM-Neu+IR780 NP at 72h postinjection. (b) Quantified signal from brain (data is represented as mean ± SEM, n=3, *p<0.05, **p=0.005, ****p<0.0001, ns=non-significant, t-test). (c) Quantified signal from other vital organs (data is represented as mean ± SEM, n=3, *p<0.05, **p=0.0003, ns=non-significant, ANOVA test).*

3.3.10 Role of sizes of cationic nanoparticles in BBB breaching

After understanding the role of sizes and surface charges in breaching BBB, we further validated the effectiveness of sizes for cationic NP. For that purpose, we have selected the star shaped aggregated micellar NP AgM-Cat having size of 200 nm and one unimolecular micellar NP UMM-Cat of size ~30 nm. Aforementioned analysis proved that UMM-Cat can cross the BBB and accumulate in the brain therefore we further compared it to the large size cationic NP. The structure of AgM-Cat and UMM-Cat polymers are shown in Figure 3.24a. AgM-Cat block copolymer is functionalized with substituted imidazolium ion at periphery (quaternary ammonium ion, +28mV) while UMM-Cat is functionalized with primary amines (+33mV).

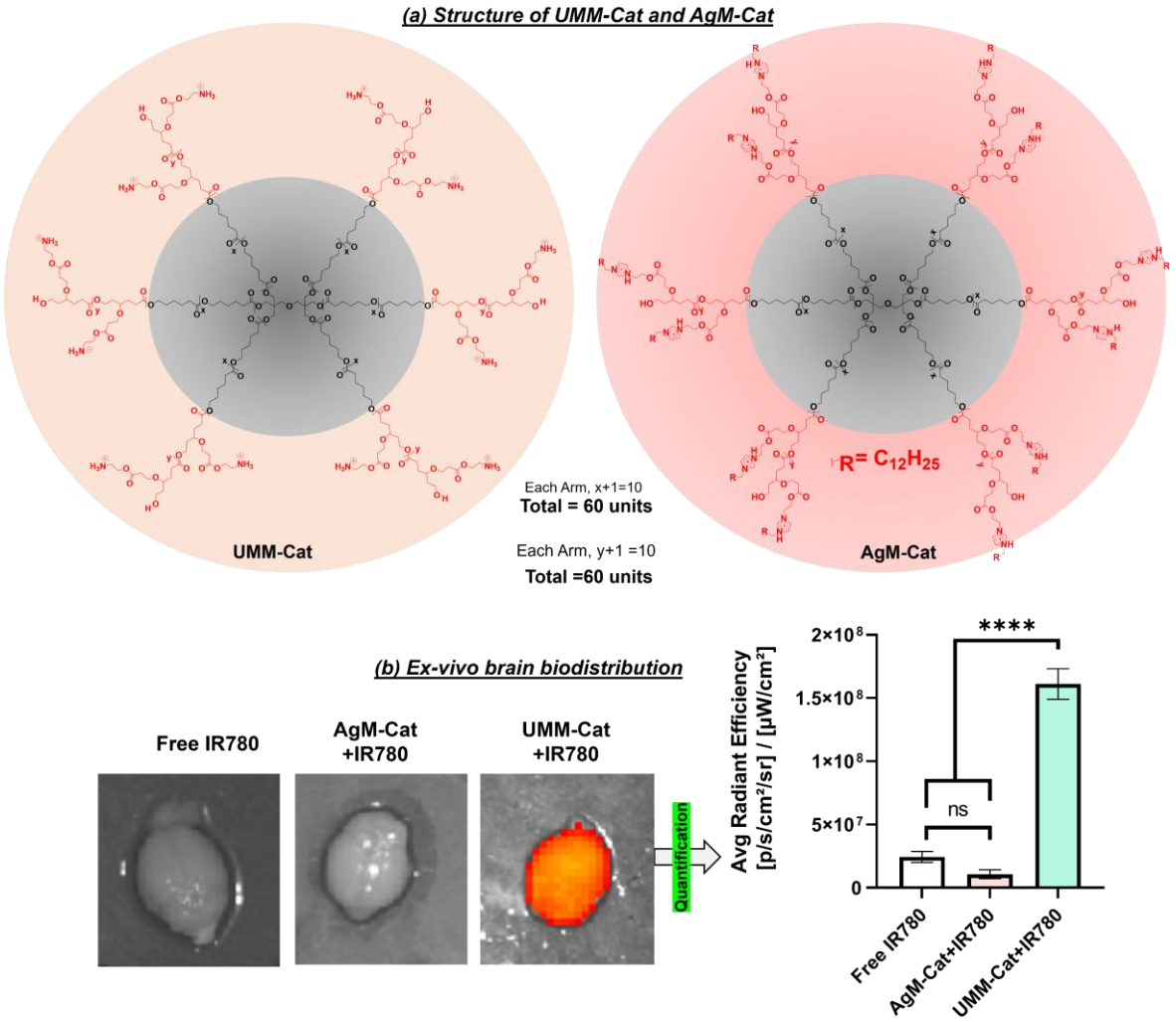

Figure 3.24. *(a)Structure of UMM-Cat (SB-Cat) having primary amines at periphery and AgM-Cat polymer having quaternary ammonium at periphery. (b) The representative IVIS images of brain harvested at 72h postinjection from the animals injected with free IR780, AgM+IR780 and UMM+IR780 NP along with quantification of fluorescent signal from brain region (n=3, ****p<0.0001, ANOVA test).*

The IR780 loaded UMM-Cat and AgM-Cat were intraperitoneally injected into the Balb-C mice (n=3) and animals were sacrificed at 72h postinjection to harvest their brains. The IVIS images of brains in Figure 3.24b revealed that the aggregated micellar AgM+IR780 did not show any detectable signals from brain region. In contrast the UMM-Cat+IR780 showed appreciable signal. To our surprise, only UMM-Cat (~30nm) could be able to cross the BBB while AgM-Cat (200nm) could not despite the NP carrying positive surface charge. Quantified signal in Figure 3.24b depicted 10-12-fold higher uptake of UMM-Cat+IR780 NP compared to AgM-Cat+IR780 NP in the brain suggesting only UMM-Cat NP can cross BBB. These results further substantiated our earlier results obtained for size comparison for anionic charge NP. Size comparison for both anionic and cationic charged NP further proved that NP having sizes <40 nm are only suitable candidates for crossing BBB and delivering the cargo to the brain. In contrast NPs having sizes more than 50 nm are not capable of crossing BBB.

3.3.11 Biodistributions analysis using ICG loaded UMM NP

Indocyanine green (ICG) or cardio green is FDA approved dye used in diagnostic purposes such as cardiac output, liver and hepatic function determination. But ICG is highly water soluble and unstable dye known to have half-life less than 30 min in body of animals and also it has very low quantum yield. Therefore, using ICG for biodistribution studies is very challenging despite being near-infrared dye. An attempt was made using ICG and NIR fluorophore to understand behavior of UMM NP toward the BBB. For that purpose, ICG loaded UMM NP were chosen and details of encapsulation and sizes are mentioned in earlier sections. The Balb-C mice were intraperitoneally injected with UMM-Ani+ICG, UMM-Cat+ICG and UMM-Neu+ICG NP and free ICG and subjected to IVIS fluorescence imaging for different time points till 24h and images are shown in Figure 3.25a-b. Whole-body images revealed better distribution of UMM NP till 6h compared to free ICG which started to eliminate from blood circulation after 2h onwards. However very faint signal was observed for 24h timepoint due to low quantum yield and instability of ICG. At 24h timepoint, it can be clearly seen from ventral images that free ICG almost cleared form the blood circulation. However, noticeable signals were observed for UMM-Ani+ICG, UMM-Cat+ICG and UMM-Neu+ICG NP from the peritoneal region of the animals as shown in Figure 3.25b. The quantification for dorsal and ventral sides in Figure 3.25c-d suggested slightly better signals for 2h and later timepoints were equivalent for all cases. However, in case of ventral side quantification, UMM-cat was slightly better at all timepoint compared to other NPs and free ICG.

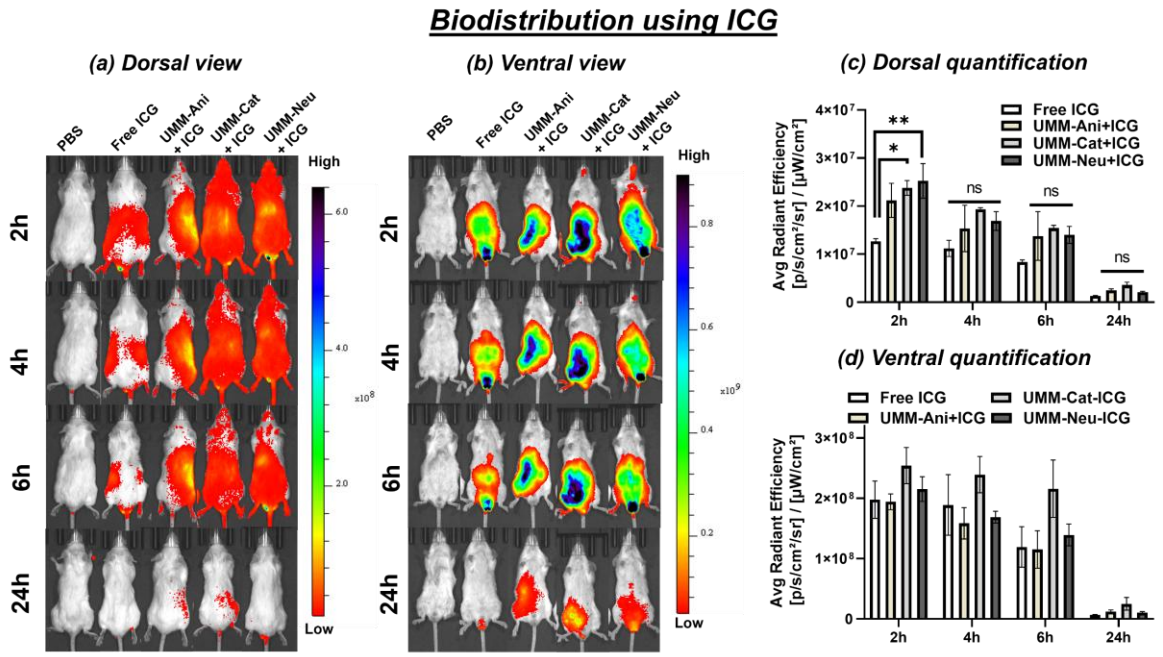

Figure 3.25. *IVIS fluorescent bioimaging using ICG. Images of (a) dorsal & (b) ventral view for free ICG, UMM-Ani+ICG, UMM-Cat+ICG and UMM-Neu+ICG NP for various time points. Quantification of fluorescent signal from (c) dorsal (d) ventral view (Data is represented as mean ± SEM, n=3, *p<0.05, **p=0.0014, ns=non-significant, ANOVA test).*

At 24h postinjection animals were sacrificed and their organs were harvested, washed with PBS and subjected to IVIS imaging. The ex-vivo organs IVIS images in Figure 3.26a suggested that ICG and UMM+ICG NPs were mostly accumulated in liver and kidneys. Notably UMM NP were able to cross the BBB and accumulated in the brain. The quantified data for vital organs in Figure 3.26b suggested 2-3-fold higher accumulation of UMM-NP in the lungs, liver and kidneys compared to free ICG. Interestingly signal for heart was very low suggesting negligible cardiotoxicity of UMM NPs. Among UMM NP, the UMM-Neu+ICG NP showed better retentions in organs. In addition, the quantification for brain in Figure 3.26c revealed all UMM NP were taken up by brains equally. However, no significant difference in the brain uptake was observed for free ICG and UMM NP. This is attributed to permeability of ICG to BBB. In contrast to free IR780 which is impermeable to BBB and cannot accumulate in the brain. These results of biodistribution using ICG further supported the role of sizes and charge of NPs in BBB breaching. Accumulation of ICG loaded UMM NP in the brains further proved that the UMM NPs have the ability to cross the BBB, and it does not depend on the nature of cargo. Biodistribution studies using water insoluble (IR780) and soluble (ICG) loaded UMM NP, demonstrated excellent ability of UMM to deliver the cargo across the brain.

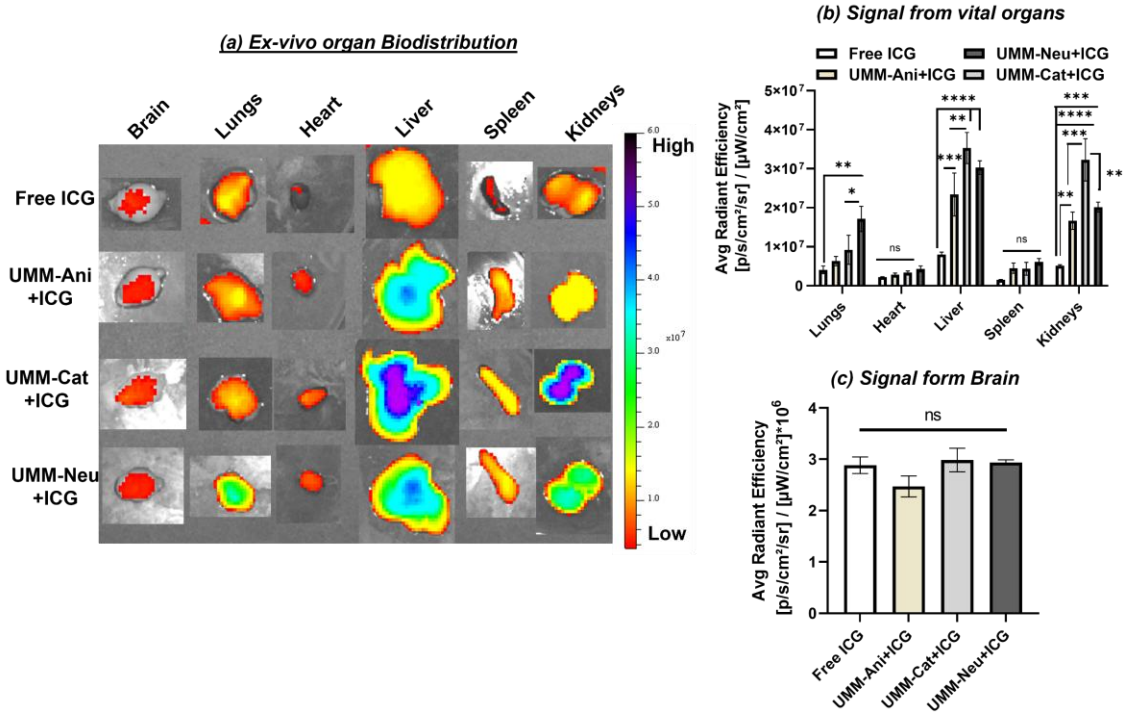

Figure 3.26. *(a) Ex-vivo IVIS fluorescent images of organs for free ICG, UMM-Ani+ICG and UMM-Cat+ICG and UMM-Neu+ICG NP at 24h postinjection. (b) Quantified signal vital organs (data is represented as mean ± SEM, n=3, *p<0.05, **p=0.005, ***p=0.0001, ****p<0.0001, ns=non-significant, t-test). (c) Quantified signal from brains (data is represented as mean ± SEM, n=3, ns=non-significant, ANOVA test).*

3.3.12 Mechanism of BBB crossing

Mechanism illustrating the ability of UMM NP to penetrate the blood-brain-barrier (BBB) and accumulate in the brain compared to free drug/dye is proposed in Figure 3.27. BBB is protective layer between blood and brain parenchyma composed of tightly packed endothelial cells of the cerebral microvessels which allows only selective molecules to traverse the tight junctions.[4-6] The restricted entry of the selective molecules across the BBB is largely controlled to maintain the homeostasis and avoid any systemic toxicity. Several factors such as molecular weight, size, charge, lipophilicity and so on dictate transcytosis of the molecules across the BBB. Furthermore, undesirable molecules are efflux out via P-glycoprotein (Pgp) efflux pump to protect CNS.[6,7,11] The two major mechanisms for transport across the BBB have been identified in literature mainly paracellular pathway and transcellular pathway (transcytosis). Macromolecules have been known to adopt the transcytosis pathway through brain microvascular endothelial cells (BMECs) for BBB crossing. Transcytosis can take place via different pathways such as receptor-mediated endocytosis (RMT) and adsorptive-mediative endocytosis (AMT). Sizes less than 50nm, appropriate lipophilicity and surface

charge near neutral are crucial parameters in order to penetrate the BBB for any nanoparticles. For present investigation, we proposed the plausible mechanism of BBB crossing for UMM-Ani NP to be receptor-mediated endocytosis (RMT).[16-17] This could be further attributed to sub-pathways of RMT such as amino-acid receptor (glutamate rector) or caveolae-mediated transcytosis. The UMM-NP are anionic charged and exhibit affinity towards amino acids receptors or towards caveolae receptors. Negative-charged lipid nanoparticles exhibited RMT pathway further emphasizing two major factors such as hydrophobic interaction between the caveolae invaginations and NP along with negative surface charge which avoided non-specific interactions of membranes.[65-67] UMM-Cat NP could have been taken by adsorptive-mediated endocytosis pathway, which has been known to be taken up by cationic NPs. In case of UMM-Neu NP which are neutral in surface charge could have been taken up transcytosis most likely caveolae-mediated endocytosis. Currently designed UMM NP showed the ability of breaching the BBB can be attributed to several factors such as stability and longer blood circulation time, small size (<40nm), high DLC and presence of different surface charges for AMT or RMT pathways and ability to avoid to Pgp efflux pumps. All these factors contribute to the ability of UMM NP to breach BBB and brain delivery.

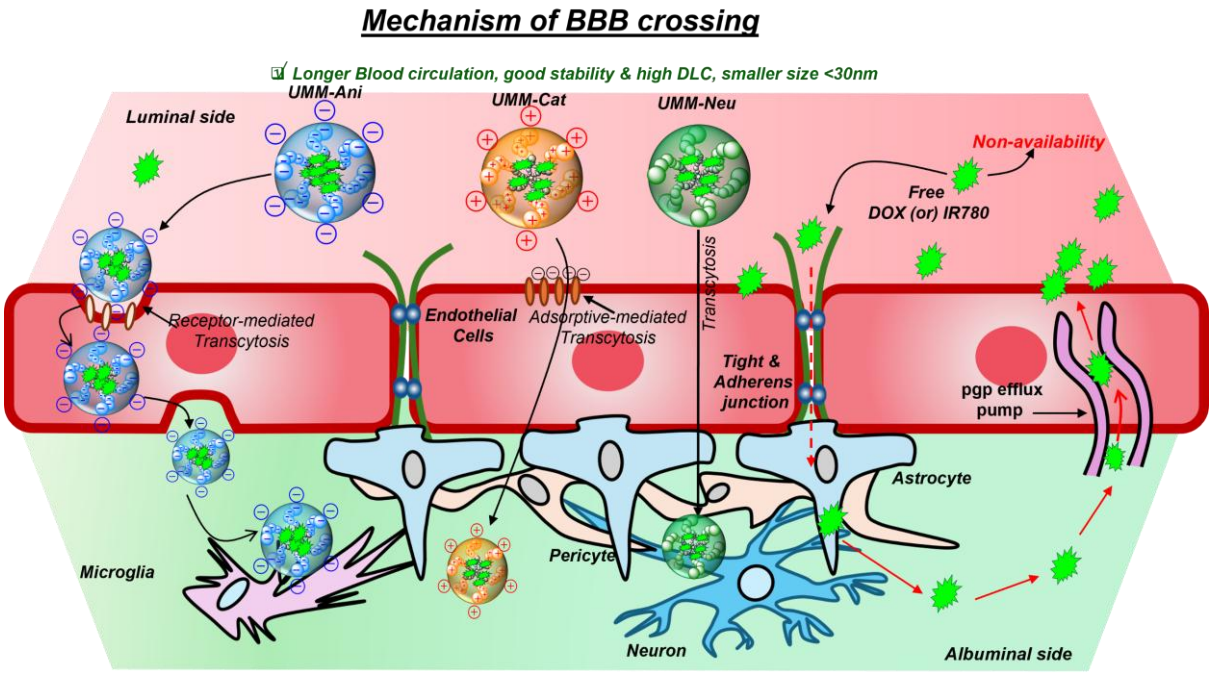

Figure 3.27. *Proposed mechanism for illustrating the ability of UMM NP to penetrate into blood-brain-barrier and deliver to brain.*

3.3.13 Integrity of blood-brain-barrier (BBB) using EB dye

The structural and functional integrity of BBB is pivotal in order to maintain the homeostasis and regular function of transcytosis. Disruption to BBB can lead to severe side effects and brain injury therefore macromolecules crossing BBB should not interfere with the structural integrity of BBB. After successful assessment of BBB breaching ability of UMM NP, integrity of BBB was evaluated using Evans blue (EB) assay.[68] The EB dye is impermeable to brain at normal conditions until BBB is compromised. The disrupted BBB can allow the EB dye to accumulate in the brain. Hence the integrity of BBB can be assessed by detecting the presence of EB via qualitative and quantitative measurements. For that purpose, we have selected one of the representatives UMM-Ani out of all structures for assessment. The UMM-NPs (10mg/kg) were intraperitoneally injected into Balb-c mice (n=3) and animals were monitored for 48h to ensure complete circulation of NP through whole body as well as into the brain. PBS (pH 7.4) was injected into mice (n=3) at similar conditions and this group was used as control because the PBS do not cause any disruptions to BBB. After 48h the 2% EB (in saline) dye was intravenously injected via tail vein into all the mice as shown in Figure 3.28a. After EB injection, animals started to turn blue immediately as shown in Figure 3.28b. At 1h postinjection of EB, animals were anesthetized and pericardially perfused using 0.9 % saline (50mL). The internal organs such appeared dark blue before and after injection due to presence of EB suggesting complete circulation of EB dye. Brains were then harvested to visualize the blue coloration if any. Surprisingly, no blue coloration was observed in the brains of the animals injected with UMM-Ani NP as well as with PBS as shown in Figure 3.28d. Note that blue coloration is the indication of uptake of EB which occurs only if integrity of BBB is compromised. Absence of blue coloration is direct evidence of intact BBB suggested by photographs of brain in Figure 3.28d. Subsequently, brains were homogenized, and EB was extracted from the tissue homogenates as described in the experimental section. The extracted EB dye was subjected to absorbance measurement and the amount of dye (EB) leaked into brains were then estimated by using standard curve generated for EB given in Figure 3.28c. The plot in Figure 3.28d revealed the similar amount of EB dye leaked into the brains of animals injected with UMM-Ani NP compared to PBS (negative control) suggesting the integrity of BBB was not compromised. These results indeed confirmed the biosafety of UMM NP toward the BBB integrity and therefore the UMM NP are safer to use for brain delivery applications.

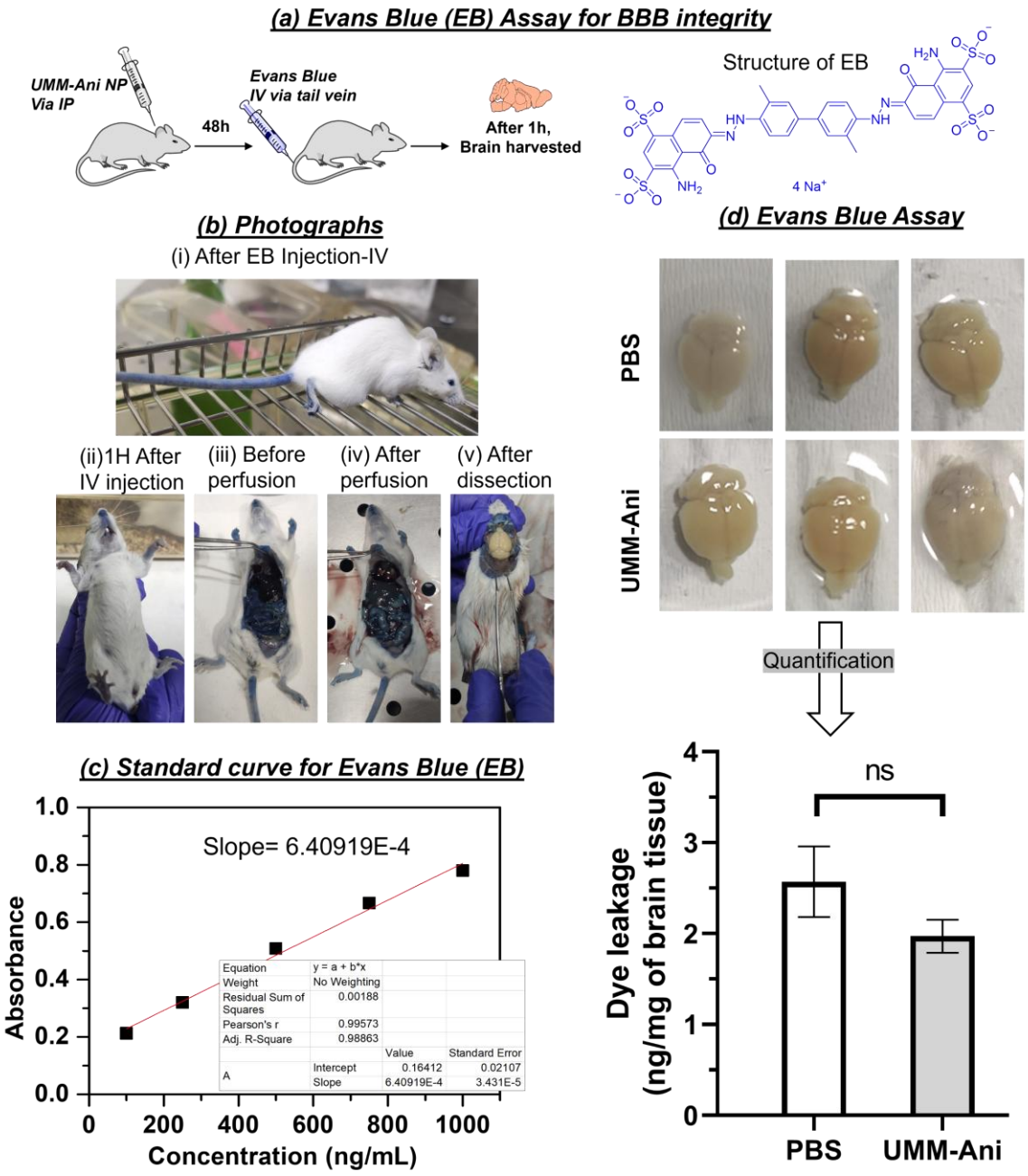

Figure 3.28. *Integrity of BBB by Evans blue (EB) assay: (a) Outline of experimental set up for EB assay. (b) Photographs of Balb-C mouse after EB injection via tail vein. (c) standard curve for EB. (d) EB assay, photographs of brain harvested form the animals injected with PBS and UMM-Ani NP followed by EB along with the plot of amount of dye (EB) in brain.*

3.3.14 Integrity of blood-brain-barrier (BBB) using IR780

We further examined the integrity of BBB by using brain impermeable dye IR780. For that purpose,. Groups I and II (n=3) of Balb-c mice were injected with free IR780 and UMM-Ani+IR780 respectively and animals left for 24h as shown in Figure 3.29a. After 24h animals

were euthanized, brains were harvested and subjected to IVIS imaging. The IVIS images of brains of the animal with free IR780 and UMM-Ani+IR780 in Figure 3.29b revealed that free IR780 did not depict any fluorescent signal in brain demonstrating impermeability of IR780 towards BBB. In contrast, UMM-Ani+IR780 NP depicted very intense signal in brain suggesting the ability of UMM-Ani NP to cross the BBB. The group III was injected with blank or nascent UMM-Ani NP (10mg/kg) and left for 24h to circulate the NP through whole body. At this point if blank UMM-Ani NP could have caused any disruption to integrity of BBB during crossing then free IR780 dye would easily enter the brain parenchyma by crossing disintegrated BBB. To test this hypothesis, we further sacrificed the animals of group I and harvested their brains and subjected to IVIS imaging. Surprisingly we did not see any fluorescence signal of free IR780 form the brains of animals injected with UMM-Ani NP followed by IR780 as shown in Figure 3.29b. Further quantified data in Figure 3.29c revealed only UMM-Ani+IR780 NP could accumulate in the brain showing 6-8-fold higher signal compared to free IR780. Interestingly, there was no significant difference observed among free IR780, and UMM-Ani followed by free IR780 suggesting the integrity of BBB was retained. These results clearly signify that the UMM-Ani NP can cross the BBB without affecting the integrity of the blood-brain barrier.

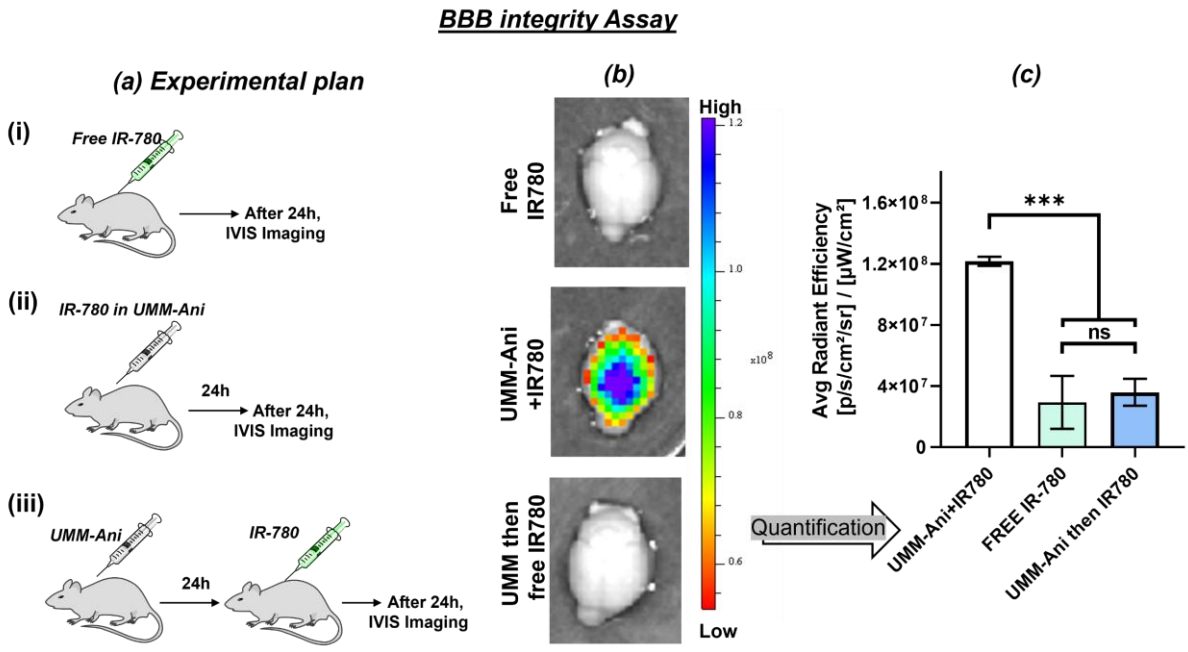

Figure 3.29. *Integrity of BBB by IR780 dye: (a) Experimental plan. (b) IVIS fluorescent images of brain at 24h postinjection. (c) Plot of fluorescent signal measured from the brains (Data is represented as mean ±SEM, n=3, ***p =0.0001, ns=non-significant, ANOVA).*

3.4 Conclusion

In summary, to investigate the impact of sizes and surface charge on the ability to cross blood-brain barrier (BBB), we successfully engineered the 6-arm star shaped polycaprolactone based polymer architectures having anionic, cationic or neutral surface charges by modifying shell's functionalization. The star shaped anionic polymers were self-assembled into aggregated (AgM) or unimolecular micellar (UMM) nanoparticles (NP) based on the amount of carboxylic PCL units in the shell. Similarly cationic polymers were self-assembled into AgM or UMM depending on the post-functionalization with quaternary or primary amine moieties respectively. AgM-Ani and AgM-Cat depicted spherical shaped NP of sizes 70 and 200 nm respectively. While UMM-Ani, UMM-Cat and UMM-Neu self-assembled into unimolecular micelles of sizes of 20-30 nm. The AgM-Ani and UMM-Ani showed ζ potentials in the range of -30mV while the AgM-Cat and UMM-Cat NP exhibited ζ potentials in the range of +30 mV. UMM-Neu NP were found neutral with ζ potential of -5mV. All the AgM and UMM NPs exhibited appreciable drug/dye encapsulation abilities for HPTS, DOX, SRhB, IR780 and ICG. The AgM and UMM NP were fully enzymatic biodegradable in the lysosomal compartment of the cells. The NPs were found to be non-toxic and non-hemolytic in nature. Confocal imaging studies revealed the excellent capabilities of UMM NPs to internalize and deliver the cargo in various cell lines. Biodistribution analysis using NIRF imaging showed that the IR780 loaded AgM and UMM NPs can circulate in mice for more than 72h and accumulate in the major organs. The comparison of the ability to traverse the BBB among UMM and AgM nanoparticles uncovered substantial results. In particular, AgM-Ani and AgM-Cat NP, exceeding sizes > 50 nm were unable to penetrate the BBB. In contrast, UMM-Ani NP having sizes < 30 nm demonstrated capability to effectively breach BBB, emphasizing the critical importance of particle size on the barrier crossing. In addition, impact of surface charge on brain delivery was evaluated by examining the BBB breaching capabilities of UMM-Ani, UMM-Cat and UMM-Neu NP (non-ionic) having ζ potentials of -30mV, +30mV, and -5mV respectively. All three differently charged UMM NP depicted comparable uptake in the brain, which can be attributed to varying uptake mechanisms or other factors. UMM-Ani and UMM-Neu NP possibly entered brain via receptor-mediated transcytosis or caveolae mediated transcytosis, while UMM-Cat NP appeared to breach BBB through adsorptive-mediated transcytosis. Remarkably, integrity of BBB remained intact following successful brain delivery suggesting biosafety of UMM NP. The UMM NPs exhibit considerable promise for delivering drugs for treatments of various neurological disorders including glioma, Alzheimer's disease and Parkinsons disease.

3.5 References

1) Zhao, Y.; Gan, L.; Ren, L.; Lin, Y.; Ma, C.; Lin, X. Factors Influencing the Blood-Brain Barrier Permeability. *Brain Research* **2022**, *1788*, 147937.
2) Khare, P.; Edgecomb, S. X.; Hamadani, C. M.; Tanner, E. E. L.; Manickam, D. S. Lipid Nanoparticle-Mediated Drug Delivery to the Brain. *Adv. Drug Deliv. Rev.* **2023**, *197,* 114861.
3) Jena, L.; McErlean, E.; McCarthy, H. Delivery Across the Blood-Brain Barrier: Nanomedicine for Glioblastoma Multiforme. *Drug Deliv. Transl. Res.* **2020**, *10*, 304-318.
4) Wilhelm, I.; Nyul-Toth, A.; Suciu, M.; Hermenean, A.; Krizbai, I. A. Heterogeneity of the Blood-Brain Barrier. *Tissue Barriers*, **2016**, *4*, e1143544.
5) Zhang, W.; Mehta, A.; tong, Z.; Esser, L.; Voelcker, N. H. Development of Polymeric Nanoparticles for Blood-Brain Barrier Transfer– Strategies and Challenges. *Adv. Sci.* **2021**, *8*, 2003937.
6) Chen, Y.; Liu, L. Modern Methods for Delivery of Drugs across the Blood-Brain Barrier. *Adv. Drug Deliv. Rev.* **2012**, *64*, 640–665.
7) Zhou, Y.; Peng, Z.; Seven, E. S.; Leblanc, R. M. Crossing the Blood-Brain Barrier with Nanoparticles. *J. Control. Release* **2018**, 270, 290–303.
8) Terstappen, G. C.; Meyer, A. H.; Beli, R. D.; Zhang, W. Strategies for Delivering Therapeutics Across the Blood-Brain Barrier. *Nat. Rev. Drug Discov.* **2021**, *20*, 362–383.
9) Tang, W.; Fan, W.; Lau, J.; Deng, L.; Shen, Z.; Chen, X. Emerging Blood-Brain-Barrier-Crossing Nanotechnology for Brain Cancer Theranostics. *Chem. Soc. Rev.* **2019**, *48*, 2967–3014.
10) Power, E. A.; Rechberger, J. S.; Gupta, S.; Schwartz, J. D.; Daniels, D. J.; Khatua, S. Drug Delivery Across the Blood-Brain Barrier for the Treatment of Pedatric Brain Tumors–an Update. *Adv. Drug Deliv. Rev.* **2022**, *185,* 114303–114322
11) Wohlfart, S.; Gelperina, S.; Kreuter, J. Transport of Drugs across the Blood-Brain Barrier by Nanoparticles. *J. Control. Release* **2012**, *161*, 264–273.
12) Seko, I.; Sahin, A.; Tonbul, H.; Capan, Y. Brain-Targeted Nanoparticles to Overcome the Blood-Brain Barrier. *J. Pharm. Technol*. **2020**, *1*, 25–39.
13) Qiao, L.; Yang, H.; Shao, X-X.; Yin, Q.; Fu, X-J.; Wei, Q.; Research Progress on Nanoplatforms and Nanotherapeutic Strategies in Treating Glioma. *Mol. Pharmaceutics* **2022**, *19*, 1921–1951.
14) Tsou, Y-H.; Zhang X-Q.; Zhu, H.; Syed, S.; Xu, X. Drug Delivery to the Brain Across the Blood-Brain Barriers Using Nanomaterials. *Small* **2017**, *13*, 1701921.
15) Ayub, A.; Wettig, S.; An Overview of Nanotechnologies for Drug Delivery to the Brain. *Pharmaceutics* **2022**, *14*, 224.
16) Zha, S.; Liu, H.; Li, H.; Wong, K-L.; All, A. H. Functionalized Nanomaterials Capable of Crossing the Blood-Brain Barrier. *ACS Nano* **2024**, *18*, 1820-1845.
17) Wu, D.; Chen, Q.; Chen, X.; Han, F.; Chen, Z.; Wang, Y. The blood-brain barrier; Structure, Regulation and Drug Delivery. *Signal Transduct. Target Ther.* **2023**, *8*, 217.
18) Lombardo, S.M.; Schneider, M.; Tureli, A. E.; Tureli, N. G. Key for crossing the BBB with nanoparticles with rational design. *Beilstein J. Nanotechnol*. **2020**, *11*, 866-883.
19) Kreuter, J. Drug Delivery to the Central Nervous System by Polymeric Nanoparticles: What Do We Know? *Adv. Drug Deliv. Rev.* **2014**, *71*, 2–14.
20) Sharma, A.; Porterfield, J. E.; Smith, E.; Sharma, R.; Kannan, S.; Kannan, R. M. Effect of Mannose Targeting of Hydroxyl PAMAM Dendrimers on Cellular and Organ Biodistribution in a Neonatal Brain Injury Model. *J. Control. Release* **2018**, *283*, 175–189.

21) Zhang, F.; Nance, E.; Zhang, Z.; Jasty, V.; Kambhampati, S. P.; Mishra, M. K.; Burd, I.; Romero, R.; Kannan, S.; Kannan, R. M. Surface Functionality Affects the Biodistribution and Microglia-Targeting of Intra-Amniotically Delivered Dendrimers. *J. Control. Release* **2016**, *237*, 61–70.
22) Clark, A. J.; Davis, M. E. Increased Brain Uptake of Targeted Nanoparticles by Adding an Acid-Cleavable Linkage between Transferrin and the Nanoparticle Core. *Proc. Natl. Acad. Sci. U. S. A.* **2015**, *112*, 12486–12491.
23) Liu, Y.; Zou, Y.; Feng, C.; Lee, A.; Yin, J.; Chung, R.; Park, J. B.; Rizos, H.; Tao, W.; Zheng, M.; Farokhzad, O. C.; Shi, B. Charge Conversional Biomimetic Nanocomplexes as a Multifunctional Platform for Boosting Orthotopic Glioblastoma RNAi Therapy. *Nano Lett.* **2020**, *20*, 1637–1646.
24) Morad, G.; Carman, C. V.; Hagedorn, E. J.; Perlin, J. R.; Zon, L. I.; Mustafaoglu, N.; Park, T. E.; Ingber, D. E.; Daisy, C. C.; Moses, M. A. Tumor-Derived Extracellular Vesicles Breach the Intact Blood-Brain Barrier via Transcytosis. *ACS Nano* **2019**, *13*, 13853–13865.
25) Lundy, D. J.; Lee, K. J.; Peng, I. C.; Hsu, C. H.; Lin, J. H.; Chen, K. H.; Tien, Y. W.; Hsieh, P. C. H. Inducing a Transient Increase in Blood-Brain Barrier Permeability for Improved Liposomal Drug Therapy of Glioblastoma Multiforme. *ACS Nano* **2019**, *13*, 97–113.
26) Ohta, S.; Kikuchi, E.; Azuma, T.; Sakuma, I.; Ito, T. Investating the Optimum Size of Nanoparticles for their Delivery into the Brain Assisted by Focus Ultrasound-Induced Blood–Brain Barrier Opening. *Sci Rep.* **2020**, *10*, 18220.
27) Xu, G.; Yong, K-T.; Roy, I.; Mahajan, S. D.; Ding, H.; Scwartz, S. A.; Parsad, P. N. Bioconjugated Quantum Rods as Targeted Probes for Effeicnet Transmigration Across an *in vitro* Blood-Brain Barrier. *Bioconjugate chem.* **2008**, *19*, 1179-1185.
28) Gastaldi, L.; Battaglia, L.; Peira, E.; Chirio, D,; Muntoni, E.; Solazzi, I.; Gallarate, M.; Dosio, F. Solid Lipid Nanoparticles as Vehicles of Drug to the Brain: Current State of the Art. *Eur. J. Pharm. Biopahrm.* **2014**, *87*, 433–444.
29) Asimakidou, E.; Kok Soon Tan, J.; Zeng, J.; Hung Lo, C. Blood-Brain Barrier-targetiong Nanoparticles: Biomaterial Properties and Bimedical Applications in Translational Neuroscence. *Pharmaceuticals* **2024**, *17*, 612.
30) Mikitsh, J. L.; Chacko, A-M. Pathways for Small Molecule Delivery to the Central Nervous System across the Blood-Brain Barrier. *Perspect Medicin Chem.* **2014**, *166*, 11–24.
31) Kolhar, P.; Anselmo, A. G.; Gupta, V.; Pant, K.; Prabhakarpandian, B.; Ruoslahti, E.; t al. Using Shape Effects to Target Antibody-Coated Nanoparticles to Lung and Brain Endothelium. *Proc. Natl. Acad. Sci. U.S.A.* **2013**, *110*, 10753.
32) Da Silva-candal, A.; Brown, T.; Krishnan, V.; Lopez-Loureiro, L.; Avila-Gomez, P.; Castillo, J.; et al. Shape effect in Active Targeting of Nanoparticles to Inflamed cerebral Endothelium under Static and Flow Conditions. *J. Control. Release* **2019**, *309*, 94–105.
33) Liu, X.; Sui, B.; Sun, J. Size- and Shape-Dependent Effects of Titanium Dioxide Nanoparticles on the Permeabilization of the Blood-Brain Barrier. *J Mater. Chem. B* **2017**, *5*, 9558–9570.
34) Song, Y. H.; De, R.; Lee, K. T. Emerging Strategies to Fabricate Polymeric Nanocarriers for Enhanced Drug Delivery across the Blood-Brain Barrier: An Overview. *Adv. Colloid Interface Sci.* **2023**, *320*, 103008.
35) Fox, M. E.; Szoka, F. C.; Frechet, J. M. J. Soluble Polymer Carriers for the Treatment of Cancer: The Importance of Molecular Architecture. *Acc Chem Res.* **2009**, *42*, 1141–1151.
36) Yang, D-P.; Nwe Linn Oo, M. N.; Roshan Deen, G.; Li, Z.; Jun Loh, X. Nano-Star

Shaped Polymers for Drug Delivery Applications. *Macromol. Rapid Commun.* **2017**, *38*, 1700410.
37) Hanada, S.; Fujioka, K.; Inoue, K.; Monome, Y.; Yamamoto, K.; Cell-Based *in vitro* Blood-Brain Barrier Model can Rapidly Evaualte Nanoparticls's Brain Permeability in Association with Particle Size and Surafce Modification. *Int. J. Mol. Sci.* **2014**, *15*, 1825-1825.
38) Daglar, B.; Ozgur, E.; Corman, M. E.; Uzan, L.; Demirel, G. B. Polymeric Nanocarriers for Expected Nanomedicine: Current Challenges and Future Prospects. *RSC Adv.* **2014**, *4*, 48639-48659.
39) Bourquin, J.; Milosevic, A.; Hauser, D.; Lehner, R.; Blank, F.; Petri-Fink, A. Biodistribution, Clerance, and Long-Term Fate of Clinically Relevent Nanomaterials. *Adv. Mater.* **2018**, *30*, 1-31.
40) Shilo, M.; Sharon, A.; Baranes, K.; Motiei, M.; Lelluuche, J. P. M.; Popavtzzer,, R. The Effect of Nnaoparticle Size on the Probability to Cross the Blood-Brain Barrier:An in vutro Endothelial Cell Model. *J. Nanobiotechnol.* **2015**, *13*, 19.
41) Meng, Q.; Meng, H.; Pan, Y.; Liu, J.; Li, J.; Qi, Y. et al. Influence of Nanoparticle Size on Blood-Barain Barrier Penetration and the Accumulation of Anti-Seizure Medicines in the Brain. *J. Mater Chem B.* **2022**, *10*, 271-281.
42) Wu, J .R.; Hernandez, Y. ;Miyasaki, K. F.; Kwon, E. J. Engineered Nanomaterials that Exploit Blood-Brain Barrier Dysfunction for Delivery to the Brain. *Adv. Drug Deliv. Rev.* **2023**, *197*, 114820.
43) Walter, F. R; Santa-Maria, A. R.; Meszaros, M.; Veszelka, S.; Der, A.; Deli, M. A. Surface Charge, Glycocalyx, and Blood-Brain Barrier Function. *Tissue Barriers* **2021**, *9*, 1904773.
44) Mailnder, V.; Landfester, K. Interaction of Nanoparticles with Cells. *Biomacromolecules **2009***, *10*, 2379-2400.
45) Balnco, E.; Shen, H.; Ferrari, M. Principles of Nanoparticle Design for Overcoming Biological Barriers to Drug Delivery. *Nat. Biotechnol.* **2015**, *33*, 941-951.
46) Lu, W.; Tan, Y-Z.; Hu, K-L.; Jiang, X-G. Cationic Albumin Conjugated Pegylated Nanoparticle with its Transcytosis Ability and Little Toxicity against Blood-Brain Barrier. *Int. J. Pharm.* **2005**, *295*, 247-260.
47) Gabal, Y. M.; Kamel, A. O.; Sammour, O. A.; Elshafeey, A. H. Effect of Surafce charge on the Brain Delivery of Nanostructured Lipid Carriers in situ Gels via the Nasal Route. *Int. J. Pharm.* **2014**, *473*, 442-457.
48) Harve, F.; Ghinea, N.; Scherrmann, J-M. CNS Delivery via Adsorptive Transcytosis. *AAPS J.* **2008**, *10*, 455-472.
49) Monsalve, Y.; tosi, G.; Ruozi, B.; Belletti, D.; Vilella, A.; Zoli, M.; Vendelli, A.; Forni, F.; Lopez, L.; Sieraa, L. PEG-g-Chitosan Nanoparticles Fucntionalized with the Monocolonal Antibody OX26 for Brian Drug Targeting. *Nanomedicine* **2015**, *10*, 1735-1750.
50) Knudsen, K. B.; Northeved, H.; Kumar EK, P.; Permin, A.; Anderson, T. L.; :arsen, S.; Wegner, K. M.; Rye Lam, H.; Lykkesfeldt, J. Differential Toxicological Response to Postively and Negatively Charged Nanoaprticles in the Rat Brain. *Nanotoxicology* **2014**, *8*, 764-774.
51) Moller, P.; Lykkesfeldt, J. Postive Charge, Negative Effect: the Imapact of Cationic Nanoparticles in the Brain. *Nanomedicine* **2014**, *9*, 1441-1443.
52) Bexiga, M. G.; Varela, J. A.; Wang, F.; Fenaroli, F.; Salvati, A.; Lynch, I.; Simpson, J. C.; Dawson, K .A. Cationic Nanoaprticles Induces Caspase 3-, 7- and 9-mediated Cytotoxicity in Human Astrocytoma Cell Line. *Nanotoxicology* **2011**, *5*, 557-567.
53) Lockman, P. A.; Koziara, J .M.; Mumper, R.; Allen, D. D. Nanoaprticle Surface Charges

Alter Blood-Brain Barrier Integrity and Permeability. *J. Drug Target*. **2004**, *12*, 635-641.
54) Hwang, T-L.; Aljuffali, I .A.; Lin, C-F.; Chang, Y-T.; Fang, J-Y. Cationic Additives in Nanosystems Activate Cytotoxicity and Inflammatory Response of human Neutrophils; lipid Nanoaprticles verses polymeric Nanoparticles. *Int. J. Nanomed.* **2015**, *10*, 371-385.
55) Blanco, E,; Shen, M.; Ferrari, M. Principles of Nanoparticle Design for Overcoming Biological Barriers to the Drug delivery. *Nat Biotechnol*. **2015**, *33*, 941-951.
56) Alexis, F.; Pridgen, E.; Molnar, L. K.; Farokhzad, O. C.; Factors affecting the Clearance and Biodistribution of Polymeric Nanoparticles. *Mol. Pharmaceutics* **2008**, *5*, 505-515.
57) Madani, F.; Esnnashri, S. S.; Bergonzi, M .C.; Webster, T. J.; Younes, H. M.; Khosravani, M. Paclitaxel/Methotrezate co-Loaded PLGA Nanoparticles in Glioblastoma Treatment:Formulation Development and *in vitro* Antitumor Activity Evaluation. *Life Sci.* **2020**, *256*, 117943.
58) Ramalho M. J.; Bravo, M.; Loureiro, J. A.; Pereira, M. C. Transferrin-Modifed Nanoparticles for Targeted Delivery of Asiatic Acid to Gliblastoma Cells. *Life Sci*. **2022**, *296*, 120435.
59) Chen, Y-P.; Chou, C-M.; Chang, T-Y.; Ting, H.; Dembele, J.; Chu, Y-T.; Changou, C. A.; Liu, C-W.; Chen, C-T. Bridging Size and Charge Effects pf Mesoporous Silica Nanoparticles for Crossing the Blood-Brain Barrier. *Front. Chem*. **2022**, *10*, 931584.
60) Kamley, N.; Yameen, B.; Wu, J.; Farokhzad, O. C. Degradable Controlled-Release Polymeric Nanoparticles/; Mechanisms of Controlling Drug Release. *Chem. Rev.* **2016**, *116*, 2602-2663.
61) Ulery, B. D.; Nair, L. S.; Laurencin, C. T. Biomedical Applications of Biodegradable Poymers. *J. Polym. Sci. Part B. Polym. Phys.* **2011**, *49*, 832-864.
62) Chen, G.; Wang, Y.; Xie, R.; Gong, S. A Review on Core-Shell Structured Unimolecular Nanoparticles for Biomedical Applications. *Adv. Drug Deliv. Rev.* **2018**, *130*, 58-72.
63) Uppendra, P.; Malhotra, M.; Pathan, S.; Jayakannan, M. Structural Engineering of Star Block Biodegradable Polymer Unimolecular Micelles for Drug Delivery in Cancer Cells. *ACS Biomater. Sci. Eng*. **2023**, *9*, 743-759.
64) Malhotra, M.; Pardasani, M.; Pathan, S.; Srikanth, P.; Shaw, K.; Abraham, N. M.; Jayakannan, M. Star-Polymer Unimolecular Micelle Nanoparticles to Deliver a Payload across the Blood-Brain Barrier. *Nanoscale* **2024**, *16*, 21582-21593.
65) Pulicherla, K. K.; Kumar Verma, M. Targeting Therapeutics across the Blood-Brain Barrier (BBB), Prerequisite towards Thrombolytic Therapy for Cerbraovascular Disorder-An Overview and advancements. *AAPS PharmSciTech* **2015**, *16*, 223.
66) Zhou, M.; Shi, S. X.; Liu, N.; Jiang, Y.; Karim, M. S.; Vodovoz, S.J.; Wang, X.; Zhang, B.; Dumont, A. S. Caveolae-Mediated Endothelial Transcytosis across the Blood-Brain Barrier in Acute Ischemic Stroke. *J. Clin. Med.* **2021**, *10*, 3795.
67) Ayloo, S.; Du, C. Transcytosis at the Blood-Brain Barrier. *Curr. Opin. Neurobiol.* **2019**, *57*, 32.
68) De Souza Goldim, M. P.; Giustina, A. D.; Petronilho, F. Using Evans Blue Dye to Determine Blood-Brain Barrier Integrity in Reports. *et al*, *Current Protocols in Immunology*, **2019**, *126*, e83.
69) Ghosh, R.; Pathan, S.; Jayakannan, M. Structural Engineering of Cationic Block Copolymer Architectures for Selective Breaching of Prokaryotic and Eukaryotic Biological Species. *ACS Appl. Bio Mater.* **2024**, *7*, 7062-7075.

Chapter 4

Zwitterionic Strategy to Stabilize Self-Immolative Polymer Nanoarchitecture under Physiological pH for Drug Delivery In Vitro and In Vivo

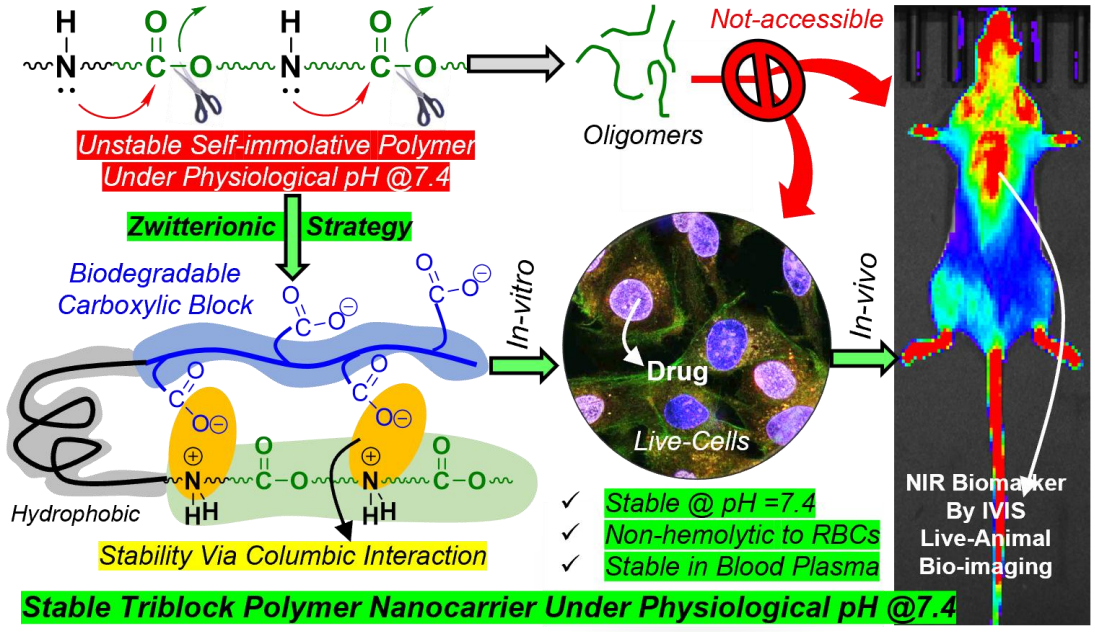

Abstract

The major bottleneck in employing polymer nano-vectors for biomedical application, particularly those based on self-immolative poly(amino ester) (PAE)s lies in their uncontrolled auto-degradation at physiological pH before they can reach the intended target. Here, an elegant triblock-copolymer strategy is designed to stabilize the unstable PAE chains via zwitterionic interactions under physiological pH (pH 7.4) and precisely program their enzyme-responsive biodegradation specifically within the intracellular compartments, ensuring targeted delivery of the cargoes. To achieve this goal, biodegradable polycaprolactone (PCL) platform is chosen, and structure-engineered several di-and triblock architectures to arrive the precise macromolecular geometry. The hydrophobic-PCL core and hydrophilic anionic-PCL block at the periphery shielded PAEs against auto-degradation, thereby ensuring stability under physiological pH in PBS, FBS, cell culture-medium and blood-stream. The clinical anticancer drug doxorubicin and deep-tissue penetrable near-infrared IR-780 biomarker is encapsulated to study their biological actions by in vitro live-cancer cells and in vivo bioimaging in live-animals. These zwitterions are biocompatible, non-hemolytic, and real-time *in vitro* live-cell confocal studies have confirmed their internalization and enzymatic-biodegradation in the endo-lysosomal compartments to deliver the payload. *In vivo* bioimaging established their prolonged blood-circulation for over 72 h, and the biodistribution analysis revealed the accumulation of nanoparticles predominantly in the excretory organs.

4.1 Introduction

Self-immolative macromolecules are important classes of synthetic biomaterials owing to their unique ability to undergo auto-degradation of long polymer chains into oligomeric subunits while employing them for biomedical applications.[1-4] Self-immolation is typically achieved by incorporating light, pH, enzyme or redox-responsive functional handles in the polymer backbone, as pendants or at the chain ends to accomplish the desired polymer degradation pattern at the cellular level for the delivery of the payloads.[5-10] Electron-delocalization assisted 1,4-, 1,6- or 1,8-elimination mechanism in benzylic-amines and phenols is one of the most commonly chosen degradation pathways in self-immolating dendrimers, linear and hyperbranched polymers, etc.[11] Acid-catalyzed polyglyoxylamides and polyacetals are other important self-immolating polymers that experience degradation under physiological pH or mild acidic conditions.[12-15] Among the self-immolative polymers, poly(amino esters)s (PAE)s (both α and β derivatives) have a special place in the literature because of their unique auto-degradation mechanism under physiological pH=7.4 by the nucleophilic attack of the amine on the ester-carbonyl atom in the backbone (see Figure 4.1a).[16] Under acidic pH < 4.0, the protonated amine does not facilitate nucleophilic attack; however, at neutral pH the amine (in the de-protonated form) attack the ester carbonyl that triggered the chopping of the long polymer chains into oligomeric units. As a consequence, the self-immolative PAEs are not found to be suitable for biomedical application wherein the stability of the polymer matrix or nanocarriers is vital at pH=7.4 such as intravenous or intraperitoneal drug delivery. PAEs were complexed with DNA and mRNA to minimize the amine de-protonation,[17-22] and the resultant polyplex underwent endosomal escape allowing it to internalize in the cytoplasm. This process is crucial for mRNA transfection efficiencies and it facilitated by the charge-altering releasable transporting (CART)s mechanism.[23-24] A similar protocol was employed for several other amine-functionalized aliphatic polyesters for gene-delivery applications.[25-29] Several efforts have been taken to design hydrophobized PAEs based on Michael-addition type condensation route which were explored for biomedical applications.[30-31] These Michael-type PAEs are predominately stable under neutral pH (they are not self-immolative polymers); and they exhibit pH responsiveness for payloads delivery at the cellular level.[30-31] Recently, supramolecular strategies were reported for anticancer drug delivery, cancer immunotherapy, and membrane transports, etc.,[32-34] Though the PAEs have been employed for gene delivery, the auto-degradation of the nascent PAE macromolecular chains or their nano-assemblies under physiological pH are still uncontrollable and unresolved for intravenous or intraperitoneal drug

delivery *in vitro* and *in vivo*. Polymer nanoparticle drug delivery is typically governed by the endocytosis across cell membranes, intracellular migration via endosomal compartments, and subsequent biodegradation at the endo-lysosomal compartments (see Figure 4.1b). Therefore, the success of the self-immolative polymer like PAEs for intravenous drug delivery is highly dependent on its stability at extracellular level and its ability to undergo intracellular digestive pathways to deliver the payloads. This emphasizes the need for new synthetic strategies to leverage the unique self-immolation characteristics of PAEs for drug delivery applications under physiological pH.

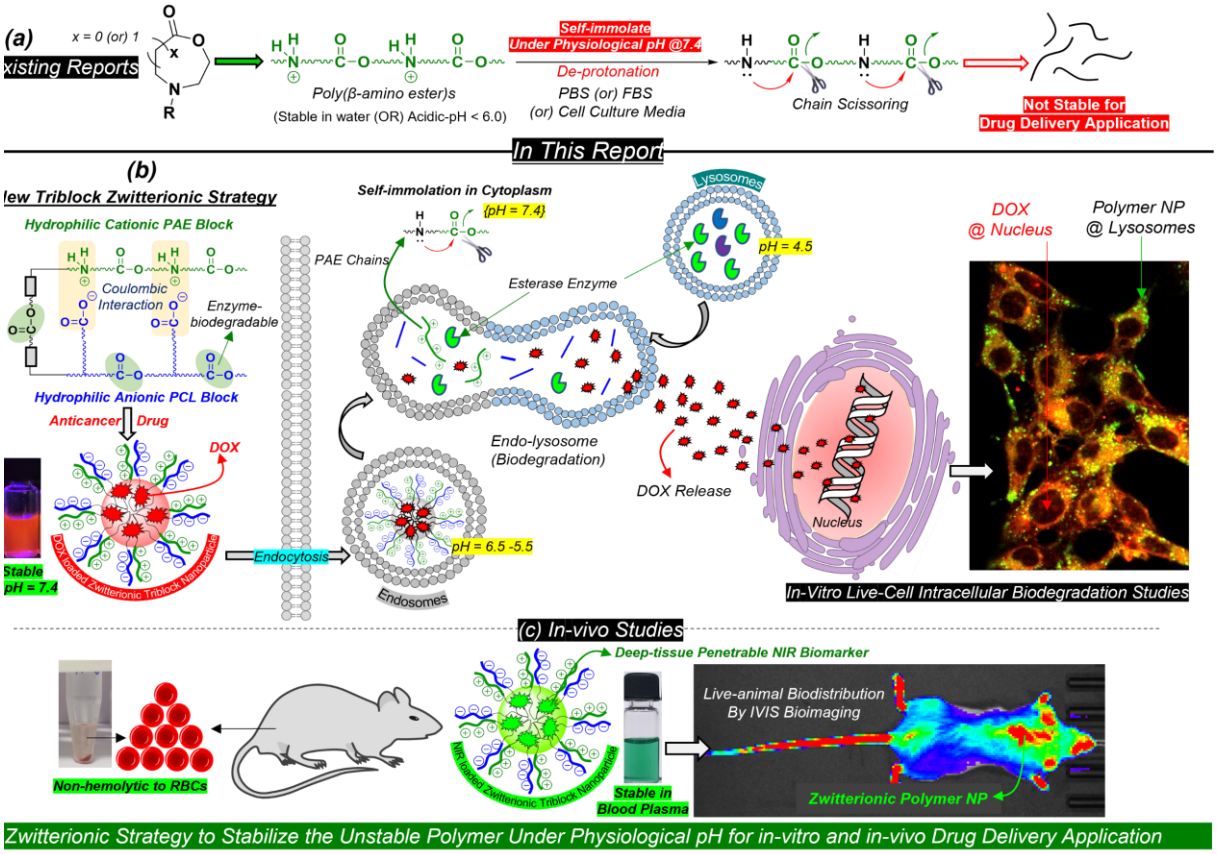

Figure 4.1. *Strategies to stabilize the unstable self-immolate poly(amino ester): (a) Cationic PAEs under acidic pH in the protonated-form and nucleophilic attack of the amine on the ester carbonyl at neutral pH. (b) Zwitterionic triblock strategy for PAEs and lysosomal enzymatic-biodegradation of the zwitterionic nanoparticles at the endo-lysosomal compartment for drug delivery in live-cells. (c) Tissue penetrable NIR-bio probe loaded Zwitterionic triblock for in vivo biodistribution in mice.*

In this study, a novel zwitterionic triblock copolymer strategy was introduced that was designed to stabilize the unstable PAEs by cleverly incorporating enzyme-biodegradable polycaprolactone (PCL) platform as illustrated in Figure 4.1. Zwitterionic polymers[35-41] were reported to be readily hydrated in water, pH responsive, exhibiting anti-polyelectrolyte effect in solution, enhanced cellular uptake and reduced opsonization towards plasma protein adsorption (antifouling).[43-48] Polyacrylate based zwitterionic polymers having anionic and cationic block or random sequences, and polybetaines were reported as pH responsive micellar system for biomedical antifouling and they were also explored in drug or gene delivery.[49-53] Unfortunately, these polyacrylate system has rigid C-C bond backbone which makes them less attractive for biodegradation aspects under physiological conditions. Building on our previous experience with PCL systems,[54-62] the present study has undertaken systematic efforts to explore various cationic AB di-block, anionic AC di-block, zwitterionic BC di-block, and zwitterionic BAC or ACB tri-blocks to reach appropriate macromolecular architectures necessary for stabilizing the self-immolative PAEs. Moreover, PCL based nanocarriers have been known to undergo enzymatic biodegradation. [54-63] and therefore, the idea of development of zwitterionic triblock strategy to stabilize the unstable self-immolative cationic PEAs by enzymatic-biodegradable and anionic carboxylic PCL seems to be appropriate. At neutral pH, the triblock zwitterionic nanovector experiences Coulombic interaction between the carboxylic substituted anionic PCL and the cationic PAE backbone that prevents de-protonation and stabilize the PAE chains. The hydrophobic PCL blocks seem to play a crucial role to impart right amphiphilicity for the successful encapsulation of anticancer drug doxorubicin and tissue penetrable near-infra red IR-780 biomarkers (Figure 4.1c). The utility of the newly designed zwitterionic nanovector in biological system is demonstrated both in vitro live cells and in vivo live animal bioimaging.

4.2 Experimental Section

4.2.1 Materials

1,4-cyclohexanediol, 4-piperidone monohydrate hydrochloride, PCC, mCPBA, ε-CL, tin (II) 2-ethylhexanoate, Doxorubicin hydrochloride, near infra-red NIR IR780 iodide, HPTS, thiazolyl blue tetrazolium bromide (MTT), Esterase from Horse liver (HLE) and other chemicals were purchased from Sigma Aldrich. Other chemicals and solvents were purchased locally and purified or used as it was. Biological reagents and media were obtained from ThermoFisher Scientific. Cell culture reagents, DMEM media, GIBCO fetal bovine serum, pen strep, Lysotracker DND-26, DAPI and Spectra/Por semi-permeable membrane (MWCO 1KD and 3.5KD) dialysis tubing materials were purchased from ThermoFisher Scientific.

4.2.2 Methods

NMRs were recorded in deuterated solvents ($CDCl_3$, DMSO-d_6 and D_2O) using Brucker 400 MHz NMR spectrometer and tetramethyl silane (TMS) as internal standard. Size exclusion chromatography (SEC) performed using Viscotek VE 3580 RI detector and Agilent PlGel 20μm Mixed-A column in THF as eluent and polystyrene as standard for calibration. Thermogravimetric analysis (TGA) was performed using PerkinElmer thermal analyzer STA 6000. Thermal analysis was performed using TA Q20 Differential Scanning Calorimeter (DSC) utilizing N_2 atmosphere with 10°C/min heating/cooling rate. A Zetasizer ZS-90 instrument was utilized for all dynamic light scattering (DLS) measurements with 633 nm laser light and 90^0 angles scattering. Hydrodynamic diameter was obtained using Stoke-Einstein equation utilizing diffusion coefficient (D) which was determined from correlation function [$g^2(t)$]. pH dependent DLS and zeta potential measurements were done using Britton-Robinson buffers (10mM). All the UV-visible absorbance measurements were recorded using Shimadzu UV-1900i absorbance spectrophotometer. FE-SEM and TEM images were captured using Zeiss Ultra Plus scanning electron microscope and Joel JEM2200FS 200 KeV systems. Silicon vapors were used for drop-casting FE-SEM samples and copper grids for TEM (Concentration 0.1mg/mL) and. Agilent AFM was used to obtain AFM images by drop casting samples onto mica sheets. Wild-type mouse embryonic fibroblast (WT-MEF) cells, human ovarian cancer cells (SKOV-3) and human breast cancer cells (MCF-7) were cultured in DMEM media containing 10% FBS and 1% penicillin-streptomycin in cell culture flasks (Eppendorf) into incubator with humidified 5% CO_2. MTT assays and other assays were performed using 96-well plates and 6-well plates (Eppendorf) with flat bottom. Absorbance of microplates were recorded using A Perkin-Elmer Ensight microplate reader. Zeiss multiphoton and Anisotropy

microscopes were used to capture CLSM images. CLSM images were processed using ImageJ software. Perkin-Elmer IVIS spectrum was used for Live animal whole body imaging. All the data reported as average of three or more independent measurements with standard deviation of mean.

4.2.3 Synthetic procedures

Synthesis of *tert*-butyl 4-oxopiperidine-1-carboxylate (Compound 1): Piperidin-4-one monohydrate hydrochloride (5.0 g, 32.54 mmol) in 80 mL THF: H_2O mixture (1:1 v/v) was taken in round bottom flask, and $NaHCO_3$ (5.5 g, 65.10 mmol) was added, and the mixture was stirred for 15 minutes at 25 °C. Di-tert-butyl dicarbonate (8.8 g, 39.08 mmol) was added dropwise and reaction was proceeded by stirring for 12 h at 25 °C. After completion of reaction, the THF was evaporated using rotary evaporator, the reaction mixture was diluted using diethyl ether (50 mL) and washed with 5 % $KHSO_4$ (50 mL). Product was extracted with diethyl ether (50 mL) and washed with 5 % $KHSO_4$ (50 mL) multiple times. Finally, the collected organic layers combined together and dried over anhydrous Na_2SO_4 and concentrated on rotary evaporator and crude product was purified using column chromatography using 5% ethyl acetate in pet ether system. Solvent was evaporated to obtain the product as solid. Yield = 6.4 g (98 %). ^{1}H NMR (400 MHz, $CDCl_3$) δ ppm: 3.71(t, J = 6.2 Hz, 4H), 2.43(t, J = 6.3 Hz, 4H), 1.46 (s, 9H). ^{13}C NMR (100 MHz, $CDCl_3$) δ ppm: 208.04, 154.64, 80.62, 43.16, 41.31, 28.50. ATR-FTIR (cm^{-1}): 2980.62, 1695.45, 1479.57, 1424.45, 1368.08, 1314.88, 1241.59, 1165.94, 1125.89, 1038.60, 986.04, 860.98, 770.75, 636.15. HRMS (ESI): [M+Na] calcd for $C_{10}H_{17}NO_3$ 222.1106; found, 223.0367.

Synthesis of *tert*-butyl 7-oxo-1,4-oxazepane-4-carboxylate (Monomer M1): $NaHCO_3$(7.6 g, 90.45 mmol) and mCPBA (3-cholorperbenzoic acid, 15.6 g, 90.45 mmol) were added into a compound 1 (5.5 g, 27.40 mmol) dissolved dry DCM (180 mL). The reaction mixture was stirred at 25 °C under N_2 atmosphere for 24 h. After completion, the turbid solution was added into saturated aqueous solution of $NaHCO_3$ (100 mL) and stirred for 30 minutes until it became phase separated into two layers. The organic layer was washed with $NaHCO_3$ solution (3 times) and with brine (100 mL). Organic layer was dried over anhydrous Na_2SO_4 and the solvent evaporated. Crude products were purified by column chromatography using 10% v/v Ethyl acetate/pet ether system. The product was obtained as white solid. Yield = 3.4 g (57 %). ^{1}H NMR (400 MHz, $CDCl_3$) δ ppm: 4.25 (m, 2H), 3.77 (m, 2H), 3.66 (m, 2H), 1.49 (s, 9H). ^{13}C NMR (100 MHz, $CDCl_3$) δ ppm: 173.98, 154.47, 81.15, 77.16, 69.56, 47.41, 41.11, 37.61,

28.44. ATR-FTIR (cm^{-1}): 2982, 1773, 1693, 1423, 1368, 1251, 1161, 1121, 1040, 982, 921, 856, 770, 636. HRMS (ESI): [M+Na] calcd for $C_{10}H_{17}NO_4$, 238.1056; found, 238.1055.

Synthesis of Polymers-General procedure for Ring opening polymerization (ROP): All the polymers synthesized via melt route (without solvent) using ring opening polymerization (ROP) strategy. $Sn(Oct)_2$ was employed at catalyst for ROP. Typically, Flame dried Schlenk's tube was charged with monomer and initiator (Tri-ethylene glycol monomethyl ether), $Sn(Oct)_2$ was added to it in inert atmosphere and vacuum (10^{-2} mbar) was applied for 45 minutes with constant stirring. After that tube was vacuum sealed and immersed in preheated oil bath (110 °C or 130 °C) and stirred for desired time. After completion polymers were purified using precipitation technique. Briefly, polymers were dissolved in THF (2 mL) and precipitated in mixture (60 mL) of diethyl ether /hexane (4:1 v/v) at cold condition, further solvent was decanted and polymer dried in vacuo.

Synthesis of Poly(amino-ester) macroinitiator (PAE): Typical ring opening polymerization synthetic route was explained in detail for PAE. Flame dried Schlenk's tube was charged with monomer **M1** (700 mg, 3.25 mmol), tri-ethylene glycol monomethyl ether (initiator, 13.40 mg, 0.08 mmol), and $Sn(Oct)_2$ (catalyst, 16.45 mg, 0.04 mmol). The polymerization mixture was degassed by applying vacuum (10^{-2} mbar) for 45 minutes with constant stirring. The tube was sealed (with high vacuum stop-cock) and immersed in preheated oil bath (110 °C), and polymerization continued for 4 h. The solid polymer mass was dissolved in THF (2.0 mL) and precipitated into large amount (60 mL) of diethyl ether + hexane (4:1 v/v) solvent mixture at 4 °C. The powder was dried and stored in vacuo. Yield = 0.64 g (90%). ^{1}H NMR (400 MHz, $CDCl_3$) δ ppm: 4.1 (bs, 90H), 3.70-3.63 (m, 10H), 3.47 (s, 183H), 2.59 (s, 96H), 3.36 (s, 3H), 1.44 9s, 414H). ^{13}C NMR (100 MHz, $CDCl_3$) δ ppm: 171.18, 155.32, 80.34, 70.68, 62.95, 46.95, 46.76, 44.32, 33.98, 33.42, 27.12. ATR-FTIR (cm^{-1}): 2985, 1737, 1657, 1481, 1395, 1164, 1029, 767. $M_{n\ NMR}$=9200 g/mol.

Synthesis of Polycaprolactone macroinitiator (PCL): Monomer **M3** (1000 mg, 8.76 mmol), initiator (tri-ethylene glycol monomethyl ether, 24.0 mg, 0.14 mmol), and catalyst $Sn(Oct)_2$ (30 mg, 0.07 mmol) were taken, and the polymerization was done at 110 °C for 2 hours as described for PAE. Polymer was purified by dissolving in THF and precipitated into cold methanol (60 mL). Yield = 0.92 g (92 %). ^{1}H NMR (400 MHz, $CDCl_3$) δ ppm: 4.21 (m, 2H), 4.05 (t, *J*=6.7 Hz, 121H), 3.69-3.54 (m, 10H), 3.37 (m, 2Hz, 3.37 (s. 3H), 2.30, (t, *J*=7.6 Hz, 120H), 1.68-1.59 (m, 279H), 1.41-1.33 (m, 122 H). ^{13}C NMR (100 MHz, $CDCl_3$) δ ppm: 173.65, 64.28,

34.25, 28.45, 25.69, 24.64. ATR-FTIR (cm^{-1}): 2942, 1723, 1470, 1396, 1369, 1294, 1242, 1192, 1037, 769, 732. $M_{n\ NMR}$=7000 g/mol.

Synthesis of Polycaprolactone-*b*-Poly(amino-ester) di-block (PCL-*b*-PAE): PCL macroinitiator (PCL, 270 mg, 0.04 mmol), monomer **M1** (500 mg, 2.32 mmol), and $Sn(Oct)_2$ (8 mg, 0.02 mmol) were polymerized at 110 °C for 2 h and purified as described for PAE. Yield = 0.62 g (80%).^{1}H NMR (400 MHz, $CDCl_3$) δ ppm: 4.15 (s, 82H), 4.05 (t, *J*=6.7 Hz, 120H), 3.71-3.63 (m, 10H), 3.48 (s, 170H), 3.37 (s, 3H), 2.59 (s, 87H), 2.31 (t, *J*=7 Hz, 121H), 1.64 (m, 275H), 1.44 (s, 371H), 1.31 (m, 121H). ^{13}C NMR (100 MHz, $CDCl_3$) δ ppm: 173.70, 155.31, 80.34, 64.20, 62.95, 47.0, 44.29, 34.25, 29.39, 25.66, 24.71. ATR-FTIR (cm^{-1}): 2984, 1733, 1657, 1396, 1370, 1164, 1035, 770. $M_{n\ NMR}$=15600 g/mol.

Synthesis of Polycaprolactone-*b*-^{t}Butyl-polycparolactone di-block (PCl-b-tBuPCL): PCL macroinitiator (PCL, 226 mg, 0.03 mmol), monomer **M2** (500 mg, 1.93 mmol), and $Sn(Oct)_2$ (6.6 mg, 0.1 mmol) were polymerized at 130 °C for 4 h and purified as described for PAE. Yield = 0.58 g (80%). ^{1}H NMR (400 MHz, $CDCl_3$) δ ppm: 4.19-4.09 (m, 110H), 4.05 (t, *J*= 6.7 Hz, 122H), 3.65 (m, 122H), 3.42 (m,56H), 3.37 (s, 3H), 2.43 (t, *J*= 6.3 Hz, 10H), 2.36 (td, 110H), 2.30 (t, *J*=7.5 Hz, 122H), 1.88-1.71 (m, 266H), 1.71-1.59 (m, 277H), 1.43 (s, 510H), 1.39-1.33 (m, 120H). ^{13}C NMR (100 MHz, $CDCl_3$) δ ppm: 173.70, 173.61, 170.98, 80.69, 75.56, 64.91, 61.35, 36.58, 34.58, 33.03, 29.79, 29.01, 28.47, 28.20, 25.60, 24.69. ATR-FTIR (cm^{-1}): 2934, 1730, 1368, 1161, 1031, 768. $M_{n\ NMR}$=21200 g/mol.

Synthesis of Poly(amino-ester)-*b*-^{t}Butyl-polycaprolactone di-block (PAE-*b*-tBuPCL): PAE macroinitiator (P1-OH, 318 mg, 0.034 mmol), monomer **M2** (400 mg, 1.55 mmol), and $Sn(Oct)_2$ (7 mg, 0.018 mmol) were polymerized at 130 °C for 4 h and purified as described for PAE. Yield = 0.7 g (95%) Viscous solid. ^{1}H NMR (400 MHz, $CDCl_3$) δ ppm: 4.15-4.11 (m, 180H), 3.66-3.61(m, 137H), 3.45 (bs, 205H), 3.37 (s, 3H), 2.57, (s, 86H), 2.41 (t, *J*=6.3 Hz, 122H), 2.37(m, 110H), 1.89-1.72 (m, 262H), 1.44 (s, 874H). ^{13}C NMR (100 MHz, $CDCl_3$) δ ppm: 173.61, 171.96, 170.97, 155.14, 80.69, 80.37, 75.57, 64.91, 61.35, 46.89, 44.35, 36.58, 33.03, 29.81, 29.02, 28.50, 28.20, 22.74. ATR-FTIR (cm^{-1}): 2983, 1730, 1657, 1369, 1161, 1033, 770. $M_{n\ NMR}$=21200 g/mol.

Synthesis of Poly(amino-ester)-*b*-Polycaprolactone di-block (PAE-*b*-PCL): PAE macroinitiator (PAE, 500 mg, 0.05 mmol), monomer **M3** (372 mg, 3.26 mmol), and $Sn(Oct)_2$ (11 mg, 0.03 mmol) were polymerized at 110 °C for 2 h and purified as described for P1-OH.

Yield = 0.72 g (82%). ^{1}H NMR (400 MHz, $CDCl_3$) δ ppm: 4.15 (s, 82H), 4.05 (t, *J*=6.7 Hz, 124H), 3.71-3.63 (m, 10H), 3.48 (s, 168H), 3.37 (s, 3H), 2.59 (s, 87H), 2.31 (t, *J*=7 Hz, 137H), 1.64 (m, 276H), 1.44 (s, 394H), 1.31 (m, 131H). ^{13}C NMR (100 MHz, $CDCl_3$) δ ppm: 173.70, 155.31, 80.34, 64.20, 62.95, 47.0, 44.29, 34.25, 29.39, 25.66, 24.71. ATR-FTIR (cm^{-1}): 2984, 1733, 1657, 1396, 1370, 1164, 1035, 770. $M_{n\ NMR}$=16700 g/mol.

Synthesis of Poly(amino-ester)-*b*-Polycaprolactone*e*-*b*-^{t}Butyl-polycaprolactone- tri-block (PAE-*b*-PCL-*b*-tBuPCL): PAE-*b*-PCL macroinitiator (420 mg, 0.026 mmol), monomer **M2** (300 mg, 1.18 mmol), and $Sn(Oct)_2$ (6 mg, 0.013 mmol) were polymerized at 130 °C for 4 h and purified as described for PAE. Yield = 0.6 g (82 %) ^{1}H NMR (400 MHz, $CDCl_3$) δ ppm: 4.16-4.11 (m, 162H), (t, *J*= 6.7 Hz, 122H), 3.63 (m, 116H), 3.48 (s, 187H), 3.37 (s, 3H), 2.58 (s, 88H), 2.43 (t, *J*= 6.7 Hz, 92H), 2.36 (m, 88H), 2.30 (t, *J*= 7.6 Hz, 132H), 1.85-1.73 (m, 267H), 1.68-1.59 (m, 314H), 1.41 (s, 748H), 1.37 (m, 122H). ^{13}C NMR (100 MHz, $CDCl_3$) δ ppm: 173.69, 173.60, 170.98, 80.70, 80.60, 75.58, 64.92, 64.28, 61.37, 47.72, 36.60, 34.25, 33.04, 29.82, 29.03, 28.50, 28.48, 28.22, 25.66, 24.70. ATR-FTIR (cm^{-1}): 2986, 1731, 1730, 1369, 1164, 1035, 767. $M_{n\ NMR}$=26800 g/mol.

Synthesis of Polycaprolactone-*b*-^{t}Butyl-Polycaprolactone-*b*-Poly(amino-ester) tri-block tri-block (PCL-*b*-tBuPCL-*b*-PAE): PCL-*b*-tBuPCL macroinitiator (360 mg, 0.016 mmol), monomer **M1** (200 mg, 0.93 mmol), and $Sn(Oct)_2$ (3.5 mg, 0.01 mmol) were polymerized at 130 °C for 4 h and purified as described for PAE. Yield = 0.45 g (80%). ^{1}H NMR (400 MHz, $CDCl_3$) δ ppm: 4.20-4.05 (m, 170H), 4.05 (t, *J*= 6.7 Hz, 122H), 3.66-3.62 (m, 122H), 3.47 (m, 197H), 3.37 (s, 3H), 2.58 (s, 92H), 2.43 (t, *J*= 6.7 Hz, 102H), 2.36 (t, *J*=7.5 Hz, 100H), 2.30 (t, *J*= 7.5 Hz, 132H), 1.88-1.70 (m, 224H), 1.68-1.59 (m, 271H), 1.44 (s, 774H), 1.39-1.33 (m, 130H). ^{13}C NMR (100 MHz, $CDCl_3$) δ ppm: 173.57, 173.49, 170.86, 80.58, 75.46, 64.79, 64.16, 61.12, 36.47, 34.12, 32.92, 29.69, 28.90, 28.35, 28.35, 25.53, 24.58. ATR-FTIR (cm^{-1}): $M_{n\ NMR}$=30900 g/mol.

General procedure for deprotection: Typical procedure for deprotection of all polymers were followed as mentioned here. Briefly, di-block or tri-block polymers were taken in round bottom flask and dissolved in DCM and reaction mixture was cooled to 0 °C. Trifluoroacetic acid (TFA) was added slowly into the polymer solution. Reaction was stirred for 30 minutes or 2 hours at cold conditions and brought to ambient temperature. TFA was removed by azeotropic distillation with dichloromethane (DCM) multiple times. The polymer was purified by dissolving into DCM (2 mL) and precipitated into mixture (60 mL) of diethyl ether/hexane (4:1

v/v) at cold condition and kept at cold condition (0 °C) for 2 hours, then solvent decanted. The precipitation repeated at least twice, and polymer was dried in vacuo.

Synthesis of Cationic AB di-block (Cat-AB): PCL-*b*-PAE di-block (250 mg), TFA (2.5 mL), DCM (5 mL). Reaction was done for 2 hours. Yield = 0.21 g. ^{1}H NMR (400 MHz, DMSO-d_6) δ ppm: 9.21 (s, 93H), 4.37-4.30 (m, 96H), 3.98 (t, *J*=6.5 Hz, 122H), 3.65-3.58 (m, 15H), 3.28-3.23 (m, 183H), 2.84 (t, *J*=7.2 Hz, 95H), 2.27 (t, *J*=7.3 Hz, 122H), 1.53(h, *J*=7.1 Hz, 251H), 1.35-1.25 (m, 127H). ^{13}C NMR (100 MHz, DMSO-d_6) δ ppm:172.74, 169.90, 158.67, 118.00, 115.06, 67.02, 63.48, 59.98, 56.31, 45.29, 42.29, 33.36, 33.36, 30.07, 27.80, 24.89, 24.08. ATR-FTIR (cm^{-1}): 2986, 1732, 1166, 1038, 764.

Synthesis of Anionic AC di-block (Ani-AC): PCL-*b*-tBuPCL (130 mg), TFA (1.3 mL), DCM (3 mL). Reaction was done for 30 minutes. Yield = 0.08 g. ^{1}H NMR (400 MHz, DMSO-d_6) δ ppm: 4.03 (m, 115H), 3.98 (t, *J*=6.5 Hz, 122H), 3.55 (m, 117H), 3.38 (m, 62H), 3.32 9s, 3H), 2.39 (m, 104H), 2.33-2.24 (m, 212H), 1.74-1.61 (m, 212H), 1.55-1.48 (m, 217H), 1.32-1.25 (m, 120H). ^{13}C NMR (100 MHz, DMSO-d_6) δ ppm: 172.89, 172.76, 172.69, 74.56, 64.22, 63.49, 60.77, 34.91, 33.36, 32.38, 29.27, 28.60, 27.80, 24.89, 24.09. ATR-FTIR (cm^{-1}): 2986, 1699, 1167, 1037, 766.

Synthesis of Zwitterionic BC di-block (Zw-BC): PAE-*b*-tBuPCL (350 mg), TFA (3.5 mL), DCM (5 mL). Reaction was done for 2 hours. Yield = 0.33 g. ^{1}H NMR (400 MHz, D_2O) δ ppm: 4.45 (s, 86H), 4.17 (s, 96H), 3.76 (bs, 148H), 3.57 (bs, 54H), 3.46 (m, 182H), 2.95-2.91 (m,90H), 2.60-2.44 (m, 247H), 1.18 (bs, 235H). ^{1}H NMR (400 MHz, DMSO-d_6) δ ppm: 9.30-8.47 (m, 51H), 4.32-4.25 (m, 96H), 4.03 (m, 117H), 3.63-3.55 (m, 179H), 3.37 (bs, 84H), 3.27-3.17 (m, 120H), 3.03-3.01 (m, 43H), 2.67-2.65 (m, 52H), 2.39-2.23 (m, 213H), 1.74-1.60 (m, 224H). ^{13}C NMR (100 MHz, DMSO-d_6) δ ppm: 174.54, 172.93, 172.74, 171.82, 158.57, 74.97, 64.23, 60.82, 56.33, 49.01, 45.52, 34.95, 32.39, 30.27, 29.36, 28.62. ATR-FTIR (cm^{-1}): 2971, 1699, 1396, 1166, 1034, 765, 635.

Synthesis of Zwitterionic BAC tri-block (Zw-BAC): PAE-*b*-PCL-*b*-CPCL (480 mg), TFA (4.8 mL), DCM (5 mL). Reaction was done for 2 hours. Yield = 0.39 g. ^{1}H NMR (400 MHz, DMSO-d_6) δ ppm: 9.13 (bs, 97H), 4.32-4.25 (m, 88H), 4.04 (m, 102H), 3.98 (t, *J*=6.5 Hz, 122H), 3.60-3.29 (m, 132H), 3.40-3.36 (m, 58H), 3.29-3.16 (m, 158H), 2.80 (t, *J*=7.3 Hz, 86H), 2.39 (t, *J*=6.1 Hz, 96H), 2.31-2.24 (m, 203H), 1.75-1.61 (m, 194H), 1.58-1.48 (m, 240H), 1.32-1.27 (m, 120H). ^{13}C NMR (100 MHz, DMSO-d_6) δ ppm: 172.91, 172.79, 172.71,

169.91,25869, 158.52, 117.55, 114.91, 74.88, 67.03, 64.24, 63.50, 60.78, 60.01, 45.51, 42.30, 34.93, 33.37, 32.39, 30.02, 29.29, 28.62, 27.81, 25.81, 24.90, 24.10. ATR-FTIR (cm^{-1}): 2917, 1697, 1395, 1166, 1033, 819, 766.

Synthesis of Zwitterionic ACB tri-block (Zw-ACB): PCL-*b*-tBuPCL-*b*-PAE (270 mg), TFA (2.7 mL), DCM (3 mL). Reaction was done for 2 hours. Yield = 0.24 g. ^{1}H NMR (400 MHz, DMSO-d_6) δ ppm: 9.09-8.66 (m, 52H), 4.32-4.26 (m, 93H), 4.04, (m, 100H), 3.98 (t, *J*=6.5 Hz, 120H), 3.60-3.51 (m, 114H), 3.39-3.35 (m, 56H), 3.32-3.16 (m, 162H), 2.81-2.27 (m, 84H), 2.39 (t, *J*=6.1 Hz, 105H), 2.34-2.21 (m, 219H), 1.77- 1.61(m, 194H), 1.58-1.48 (m, 286H), 1.32-1.25 (m, 125H). ^{13}C NMR (100 MHz, DMSO-d_6) δ ppm: 172.93, 127.84, 172.72, 169.92, 158.67, 158.32, 117.52, 114.87, 74.89, 64.25, 63.53, 60.79, 60.02, 49.04, 45.53, 42.31, 34.95, 33.55, 33.39, 32.40, 32.17, 29.30, 28.63, 27.83, 24.91, 24.11. ATR-FTIR (cm^{-1}): 2912, 1697, 1395, 1166,1033, 765.

Synthesis of Poly(amino-ester) macroinitiator (PAE-30): Monomer **M1** (300 mg, 1.40 mmol), tri-ethylene glycol monomethyl ether (initiator, 7.60 mg, 0.046 mmol), and $Sn(Oct)_2$ (catalyst, 9.40 mg, 0.023 mmol). The polymerization was done for 3h at 110 °C. Polymer was purified by precipitation similar to PAE. Yield = 0.300 g (97%). ^{1}H NMR (400 MHz, $CDCl_3$) δ ppm: 4.1 (bs, 30H), 3.70-3.63 (m, 10H), 3.47 (s, 120H), 3.36 (s, 3H), 2.59 (s, 60H), 1.44 (s, 275H).

Synthesis of Polycaprolactone macroinitiator (PCL-45): Monomer **M3** (1000 mg, 8.76 mmol), initiator (tri-ethylene glycol monomethyl ether, 33.0 mg, 0.20 mmol), and catalyst $Sn(Oct)_2$ (41.0 mg, 0.10 mmol) were taken, and the polymerization was done at 110 °C for 1.5 hours as described for PCL. Polymer was purified by dissolving in THF and precipitated into cold methanol (60 mL). Yield = 0.94 g (93 %). ^{1}H NMR (400 MHz, $CDCl_3$) δ ppm: 4.21 (m, 2H), 4.05 (t, *J*=6.7 Hz, 90 H), 3.69-3.54 (m, 10H), 3.5 (m, 2Hz), 3.37 (s. 3H), 2.30 (t, *J*=7.6 Hz, 92H), 1.68-1.59 (m, 189H), 1.41-1.33 (m, 94H).

Synthesis of Poly(amino-ester)-*b*-Polycaprolactone di-block (PAE-*b*-PCL-30): PAE macroinitiator (PAE-30, 300 mg, 0.046 mmol), monomer **M3** (240 mg, 2.10 mmol), and $Sn(Oct)_2$ (10 mg, 0.02 mmol) were polymerized at 110 °C for 2 h and purified as described for PAE. Yield = 0.545 g (97%).

Synthesis of Poly(amino-ester)-*b*-Polycaprolactone*e*-*b*-^{t}Butyl-polycaprolactone- tri-block (PAE-*b*-PCL-*b*-tBuPCL-30): PAE-*b*-PCL macroinitiator (545 mg, 0.047 mmol), monomer **M2** (362 mg, 1.40 mmol), and $Sn(Oct)_2$ (10 mg, 0.024 mmol) were polymerized at 130 °C for 4 h and purified as described for PAE. Yield = 0.75 g (83 %) ^{1}H NMR (400 MHz, $CDCl_3$) δ ppm: 4.16-4.11 (m, 120 H), (t, *J*= 6.7 Hz, 90H), 3.63 (m, 64H), 3.48 (s, 126H), 3.37 (s, 3H), 2.58 (s, 60H), 2.43 (t, *J*= 6.7 Hz, 62H), 2.36 (m, 61H), 2.30 (t, *J*= 7.6 Hz, 88H), 1.85-1.73 (m, 120H), 1.68-1.59 (m, 200 H), 1.41 (s, 477H), 1.37 (m, 90H).

Synthesis of Polycaprolactone-*b*-^{t}Butyl-polycaprolactone di-block (PCl-b-tBuPCL-30): PCL macroinitiator (PCL-45, 200 mg, 0.038 mmol), monomer **M2** (400 mg, 1.55 mmol), and $Sn(Oct)_2$ (8.0 mg, 0.02 mmol) were polymerized at 130 °C for 3 h and purified as described for PAE. Yield = 0.50 g (80%). ^{1}H NMR (400 MHz, $CDCl_3$) δ ppm: 4.13 (m, 72H), 4.06 (t, *J*= 6.7 Hz, 90H), 3.65 (m, 73H), 3.45 (m, 34 H), 3.37 (s, 3H), 2.44 (t, *J*= 6.3 Hz, 60 H), 2.37 (td, 60H), 2.30 (t, *J*=7.5 Hz, 88 H), 1.88-1.71 (m, 147H), 1.71-1.59 (m, 178H), 1.44 (s, 232H), 1.39-1.33 (m, 87H).

Synthesis of Polycaprolactone-*b*-^{t}Butyl-Polycaprolactone-*b*-Poly(amino-ester) tri-block tri-block (PCL-*b*-tBuPCL-*b*-PAE-30): PCL-*b*-tBuPCL macroinitiator (344 mg, 0.023 mmol), monomer **M1** (200 mg, 0.93 mmol), and $Sn(Oct)_2$ (4.8 mg, 0.01 mmol) were polymerized at 110 °C for 4 h and purified as described for PAE. Yield = 0.43 g (80%). ^{1}H NMR (400 MHz, $CDCl_3$) δ ppm: 4.13 (m, 139H), 4.05 (t, *J*= 6.7 Hz, 90H), 3.66 (m, 77H), 3.48 (m, 145H), 3.37 (s, 3H), 2.58 (s, 78H), 2.42 (t, *J*= 6.7 Hz, 60H), 2.37 (t, *J*=7.5 Hz, 60H), 2.30 (t, *J*= 7.5 Hz, 102H), 1.83-1.78 (m, 175H), 1.64 (m, 244H), 1.44 (s, 527H), 1.36 (m, 95H).

Synthesis of Zwitterionic ACB tri-block (Zw-ACB-30): PCL-*b*-tBuPCL-*b*-PAE-30 (225 mg), TFA (2.0 mL), DCM (4 mL). Reaction was done for 2 hours. Yield = 0.21 g. ^{1}H NMR (400 MHz, DMSO-d_6) δ ppm: 4.32-4.26 (m, 64H), 4.04, (m, 70H), 3.98 (t, *J*=6.5 Hz, 91H), 3.60-3.51 (m, 105H), 3.39-3.35 (m, 42H), 3.32-3.16 (m, 140H), 2.81-2.27 (m, 84H), 2.39 (t, *J*=6.1 Hz, 105H), 2.34-2.21 (m, 103H), 1.77- 1.61(m, 174H), 1.58-1.48 (m, 244H), 1.32-1.25 (m, 89H).

Synthesis of Zwitterionic BAC tri-block (Zw-BAC-30): PAE-*b*-PCL-*b*-tBuPCL (300 mg), TFA (3.0 mL), DCM (4 mL). Reaction was done for 2 hours. Yield = 0.31 g. ^{1}H NMR (400 MHz, DMSO-d_6) δ ppm: 4.32-4.26 (m, 61H), 4.04, (m, 67H), 3.98 (t, *J*=6.5 Hz, 90H), 3.60-

3.51 (m, 70H), 3.39-3.35 (m, 48H), 3.32-3.16 (m, 132H), 2.81-2.67 (m, 67H), 2.39-2.21 (m, 226H), 1.77- 1.61(m, 110 H), 1.58-1.48 (m, 256H), 1.32-1.25 (m, 91H).

4.2.4 Self-assembly, nanoparticle characterization

All the deprotected polymers were self-assembled using dialysis method. Typically, polymer solution (5.0 mg in 0.8 mL in DMSO) added dropwise into 4.2 mL of deionized water with moderate stirring at room temperature for 4 hours. Then polymer solution was dialyzed using semipermeable membrane (MWCO 3.5 KD) against deionized water for 48 hours with replenishing water at regular interval to remove DMSO. Self-assembled nanoparticles were lyophilized and stored at 4 ºC. The hydrodynamic diameters (sizes) and surface zeta potential (ζ) of self-assembled polymeric NP were measured by DLS at the concentration of 0.1 mg/mL using Zetasizer ZS-90 particle analyzer. pH-dependent sizes and zeta potential of NP were measured by DLS using Britton-Robinson (10 mM) buffer of varying pH (2.0 to 11). All measurements were conducted at least three independent times and results are represented as mean ± SD. The NP were visualized using transmission electron microscopy (TEM). For pH dependent- self-assembly analysis 10 mM Britton-Robinson saline buffers (pH 2 to 14) were freshly prepared and used for pH dependent DLS and Zeta potential measurement. Self-assembled nanoparticles were dispersed in different buffers (0.5mg/mL) and solutions were subjected to size and zeta potential measurements. For Ani-AC and Cat-AB mixture equimolar concentration of polymers were taken and final concentration was maintained as 0.5 mg/mL. Zeta potentials and sizes were plotted against pH for corresponding polymers.

4.2.5 CMC determination

Pyrene was used as probe to determine the critical micellar concentration (CMC) of polymers. Self-assembled polymers with various concentrations ranging from $1.0x10^{-6}$ mg/mL to 0.5 mg/mL and fixed concentration of Pyrene (0.6 μmol, $3.6x10^{-7}$ g/mL) were prepared. Polymer solutions were added to pyrene precoated vials and sonicated for 3 hours at room temperature under dark, further equilibrated overnight. Samples were purged with N_2 prior to fluorescence measurement to remove the dissolved oxygen. Fluorescence spectrum was recorded using excitation wavelength 337 nm and emission was collected from 350 nm to 500 nm using 1 nm slit width. The ratios of PL intensity corresponding to I_1 (372 nm) and I_3 (382 nm) vibrionic levels were plotted against concentration to determine the CMC.

4.2.6 Polymer degradation studies

Degradation studies for Cat-AB diblock, Zw-BC diblock, Zw-ACB and Zw-BAC triblock were performed by using ^{1}HNMR spectroscopy, DLS and UV-visible absorbance (transmittance mode) measurements. Cat-AB polymer (54 mg) was dissolved in 6mL 1x (10mM) PBS buffer (pH 7.4) and incubated at 37 °C. Aliquots were taken out on predetermined interval and immediately lyophilized. Lyophilized content was dissolved in DMSO-d_6 and ^{1}HNMR was recorded for all the aliquots. Similar experiment was repeated for Zw-BAC triblock. For DLS and transmittance measurement, self-assembled Cat-AB diblock, Zw-BC diblock, Zw-ACB triblock, Zw-BAC triblock and Ani-AC+Cat-AB mixture were incubated separately in 10mM PBS (pH 7.4) buffer (1 mg/mL) as well as in deionized water at 37 °C. At regular interval sizes and transmittances of the nanoparticles were measured.

4.2.7 Encapsulation and stability studies

Doxorubicin (DOX) as therapeutic drug, HPTS and NIR IR-780 iodide as bioimaging dyes were used for encapsulation studies. General procedure for DOX encapsulation for all polymers is as follows. Typically, 0.5 or 1 mg DOX (pre-neutralized with triethyl amine) was taken along with 5 mg polymer and dissolved in 0.8 mL DMSO, and solution was added dropwise to 4.2 mL water. Further mixture stirred for 4 hours at room temperature then dialyzed against deionized water for 48 hours to remove unencapsulated drug and DMSO. Water was periodically changed each hour. Amount of drug/dye encapsulated in nanoparticles was determined by measuring absorbance of loaded sample at 488 nm and concentration of DOX calculated using Beer-Lambert equation. Drug loading content and drug loading efficiencies were determined following our earlier reports.[61-62] DOX loaded samples were lyophilized at stored at 4 ºC for further use. Similar procedures were followed for encapsulation of HPTS and IR-780 iodide. The serum stability of DOX loaded nanoparticles (NP) were determined by incubating NP in 10% FBS (fetal bovine serum) in PBS (pH 7.4) at 37 ºC for 5 days. The sizes of NPs were measured by DLS for more than 5 days.

4.2.8 *In vitro* enzymatic release studies

DOX loaded nanoparticles were subjected to *in vitro* release kinetic studies to investigate enzymatic biodegradability of block-co-polymers containing aliphatic polyester backbone. Horse liver Esterase (3 U) enzyme was employed for the study. Typically, DOX loaded nanoparticle solution (1 mL), and esterase enzyme were occupied in dialysis tube (1 kD) immersed in reservoir containing PBS, pH 7.4 (3 mL) and incubated at 37 °C. In the control

experiment only, DOX loaded nanoparticles were taken without Esterase and incubated similarly. At regular intervals of time, solution from reservoir was taken and out and its absorbance was recorded. Similarly release kinetics studies were carried out using pH 5.5 (Britton-Robinson saline buffer, 100mM) for all DOX loaded nanoparticles. Cumulative drug release was estimated following our earlier reports.[61-62] Drug release kinetics were investigated by using DLS as reported earlier.[58,61] For this purpose, DOX loaded nanoparticles (2 mL in PBS buffer pH 7.4) were taken in vial along with esterase enzyme and incubated at 37 °C and periodically monitored for their sizes using DLS. For the control DOX loaded nanoparticles were incubated in PBS buffer pH 7.4. Results are expressed as average of three independent measurements.

4.2.9 Enzymatic degradation studies

Enzymatic degradation of aliphatic polyester was studied by incubating polymers with esterase enzyme at physiological pH and temperature. Briefly, the polymers (Zw-BAC, Zw-ACB and Zw-BC) were taken 40 mg each and dissolved in 4 mL of PBS buffer (7.4 pH, 1x) in a container. Esterase, 8.5 mg (esterase from Porcine liver, 28 units/mg) was added to each of the polymer solutions and incubated at 37ºC. Aliquots were collected at specific intervals (24, 48 and 72 hrs.) and lyophilized. Lyophilized aliquots were THF for MALDI-TOF analysis (DHB and dithranol used as matrix. Solutions were centrifuge and supernatant solution were analyzed by MALDI-TOF.

4.2.10 Cell culture methods

The cells were cultured in an incubator with a humidified 5% CO_2 atmosphere at 37 ºC. Cells were grown in complete media consist of Dulbecco modified eagle medium (DMEM, Gibcco) supplemented with 10% fetal bovine serum (FBS, Thermofisher) and 1% penicillin-streptomycin (PenStrep, Thermofisher) antibiotics into twenty-five cm^2 flasks (Tarson). Wild-type mouse embryonic fibroblast (WT-MEF), Human breast cancer (MCF-7), Human ovarian cancer (SKOV3) cells used for studies.

4.2.11 Cell viability by MTT assay

The cytotoxicity of the nascent nanoparticles and cytotoxicity of DOX loaded nanoparticles were examined using MTT assays (cell viability assays) in WT-MEF (wild type-Mouse embryonic fibroblast), MCF-7 (Human breast cancer) and SKOV-3 (Human ovarian cancer) cell lines. MTT (3-(4,5-dimethylthiazol-2-yl)-2,5-diphenyltetrazolium bromide), tetrazolium dye reduced by cellular mitochondrial to insoluble formazan crystals, which was quantified.

The assays were performed in a 96 well plate (Eppendorf), wherein each well was seeded with 1000 cells in DMEM media containing 10%FBS and 1% pen-strep (100 µL). Cells were incubated at 37 °C with humidified CO_2 (5%) atmosphere for 16 h to adhere prior to compound treatment. After 16 h incubation media was aspirated and fresh media containing required concentrations of nascent nanoparticles, free DOX and DOX loaded nanoparticles were added to wells containing cells and incubated for 72 hours at aforesaid conditions. Correspondingly, a column containing cells was added only fresh DMEM and incubated for similar time and condition. And this was considered as control column for assay (100% cell viability). After desired period of incubation media was aspirated and replaced with MTT solution (in DMEM media, 100 µL, 0.5mg/mL) and incubated for a further 4 hours. Finally, media containing MTT aspirated and DMSO (100 µL) was added into each well to dissolved purple formazan crystals. Microplates were subjected to absorbance measurements in PerkinElmer Ensight microplate reader using maxima at 570 nm. Absorbance values obtained for control wells were considered as 100% cell viability and values obtained from other wells were compared to calculating cell viabilities.

4.2.12 Cellular uptake via confocal microscopy imaging (CLSM)

WT-MEF, MCF-7 and SKOV-3 cell lines investigated for cellular uptake of DOX loaded nanoparticles. 1 X 10^5 Cells were seeded using DMEM media in each well of 6 well plate containing sterile glass cover slip and incubated at 37 °C with 5 % CO_2 for 16 hours prior to experiments. Afterward media was replaced with fresh media containing free DOX and DOX loaded nanoparticles (DOX concentration 2.5 µg/mL) and incubated for different time points to investigate cellular uptake. After compound treatment media containing DOX and DOX loaded nanoparticles were aspirated and coverslips washed with 1x PBS twice. Furthermore, cells were fixed using 3.5% PFA solution followed by washing with PBS and nuclei were stained with DAPI. For Phalloidin staining, fixed cells treated with phalloidin solution for 15 min and further washed with PBS to remove excess dye. Coverslips were mounted on clean and sterile glass slides using 70% glycerol mounting media and dried under dark for an hour at room temperature. Cells were visualized via confocal microscope using λ=405 nm (blue channel), λ=488 nm (green channel) and λ=561 nm (red channel) for DAPI, Phalloidin and DOX respectively. All the images were processed using ImageJ software and CTCF (corrected total cell fluorescence) were calculated.

4.2.13 Temperature dependent Cellular uptake studies through CLSM

Temperature dependent cellular uptake studies by using confocal laser microscopy (CLSM) were utilized to understand the mechanism of cellular uptake and internalization of nanoparticles. Generally cellular uptake of nanoparticles occurs via energy mediated endocytosis process, which occurs only at physiological temperature. Therefore, whether nanoparticles are taken up by cells via endocytosis pathway or diffusion (usual pathway for small molecules) can be understood via temperature dependent cellular uptake studies. For this purpose, MCF-7 cells line was utilized which was cultured in 5% CO_2 in DMEM media supplemented with 10% FBS and 1% penicillin-streptomycin. Into 6-well plate, 10^5 cells were seeded onto glass cover slip per well in 2 mL medium and incubated for 16 h prior to treatment. Then cells treated with DOX loaded nanoparticles (DOX concentration 2.5µg/mL) and plate were incubated at 37 °C for 3h, similarly for the control, cells were incubated at 4ºC cellular processes are arrested) after DOX nanoparticle addition for 3h. After incubation time cells were fixed using 3.5% PFA and nuclei were stained with DAPI, and coverslips were mounted in glass slide. Cells were visualized via confocal microscope using λ=405 nm (blue channel), λ=488 nm (green channel) for DAPI and DOX respectively and further images were processed using ImageJ software.

4.2.14 Time dependent Cellular uptake studies through CLSM

To understand the cellular uptake in time dependent manner MCF-7 cell line was utilized. Cells (10^5) were seeded onto each glass cover slip in 6-well plate and incubated for 16 h. After adherence of cells, they were treated with DOX loaded nanoparticles (DOX concentration 2.5µg/mL) and further incubated for different time point from 30 min to 9 h at 37 ºC. After desired time of incubation cells were further fixed using 3.5% PFA and nuclei were stained with DAPI and mounted onto glass slide. Further they were visualized using λ=405 nm (blue channel), λ=488 nm (green channel) for DAPI and DOX respectively in confocal microscope. Images were further processed in ImageJ software.

4.2.15 Live cell imaging using CLSM

Live cell imaging was carried out using CLSM to track the fate of nanoparticles in the cytoplasm after endocytosis. The DOX loaded nanoparticles were employed to understand the interaction of the polymer with lysosomal compartment. For this purpose, 30,000 WT-MEF cells were seeded in each well of 4-well live cell imaging chamber and incubated for 16h at 37 °C in growth media (5% CO_2 in DMEM media supplemented with 10% FBS and 1% penicillin-

streptomycin to adhere. After 16h media was aspirated and fresh media (0.5mL corresponding to 20μM DOX concentration) containing DOX (DOX concentration 5μg/mL) loaded zwitterionic ABC, ACB and Cationic AC nanoparticles were added for different time points such as 30 min, 2h, 4h and 6h. Media was again aspirated, and cells were washed with 1x PBS buffer then fresh media (0.8mL) containing Lysotracker green DND-26 (100nM) was added and incubated for another 30 minutes. Lastly the lysotracker solution as removed and cells were washed twice with PBS and 0.3mL DMEM was added, and live cells were imaged using confocal laser microscope for various time points. Cells were visualized via confocal microscope using λ=488 nm (green channel) for Lysotracker green λ=561 nm (red channel) for DOX and further images were processed using ImageJ software.

4.2.16 Animal handling, Experimentation and Hemolysis assay

All the animal experiments were carried with compliance of Institutional Animal Ethics Committee India (IAEC) guidelines. Animals were housed in the same NFGFHD, IISER Pune and experimentation work were conducted at the same facility. Hemolysis assay was carried out to investigate compatibility of nanoparticles with RBCs (erythrocytes). 8 weeks old C57BL/6 mice were used to investigate hemolysis studies. Mice were anesthetized using Isoflurane I.P. and blood was collected into 5% EDTA precoated centrifuge tubes by puncturing retro-orbital sinus with thin sterile capillary tube. Freshly withdrawn blood was centrifuge at 5000 rpm for 10 minutes to separate RBC from plasma. Supernatant plasma was removed, and RBC pellet was washed multiple times with PBS. Additionally, RBCs were diluted with PBS buffer (5% v/v). A total 100 μL RBC solution was added in each well of a Microplate (96 well plate) followed by addition of nascent nanoparticle solution (100 μL) in PBS buffer (1mg/mL) in each well containing RBCs and microplate was incubated at 37 °C under dark for an hour. Wells treated with Triton X-100 (1% v/v) and 1x PBS buffer were used as positive and negative controls respectively. After incubation microplate was centrifuged (5000 rpm, 10 minutes) and 100 μL supernatant transferred to fresh microplate and absorbance recorded using microplate reader (λ=576 nm). Percentage of ruptured RBCs were calculated based on our earlier reports.[59]

4.2.17 *In vivo* biodistribution via IVIS imaging

Biodistribution studies were carried out in 8-10-week-old female Balb-C mice(20-25g). IR-780 iodide has been used as near IR probe for visualization of nanoparticles via IVIS whole body imaging. Nanoparticles encapsulated with IR-780 were used for this study. The dosage amount of IR-780 dye utilized for injection was 0.5mg/kg all the mice. Mice were divided into

four groups (n=3), and injected with PBS, Free IR-780, Zw-BAC+IR780 nanoparticles, Zw-ACB+IR-780 nanoparticles respectively. All the samples were injected intraperitoneally into 1x PBS (100µL). Fluorescence images were acquired multiple times by anesthetizing animals using Isoflurane. Similarly, blood samples were collected by puncturing retro-orbital sinuses of animals at desired timepoints in EDTA coated centrifuge tubes. The collected blood samples were centrifuged at 5000 rpm for 5 minutes to separate plasma from RBCs. The collected plasma samples then were taken in 96 well plate diluted with PBS and fluorescence were recorded with IVIS instrument. At the end point of experiment animals were euthanized using overdose of anesthesia (Isoflurane) and pericardially perfused using PBS saline buffer and organs have been harvested for further imaging (IVIS). Images were analyzed using IVIS software Living Imager.

4.2.18 Statistical analysis

All the Statistical analysis were performed using GraphPad prism 8.1 software. T-test (one-tail test, two-tailed t-test), ANOVA test and two-way ANOVA tests were used to perform statistical analysis. Statistical significance considered if $P<0.05$. Results of analysis are represented as *mean ±SEM* (*n=3 or more)*.

4.3 Results and Discussion

4.3.1 Synthesis and Characterization

Two caprolactone monomers were synthesized starting from commercial sources piperidin-4-one and 1,4-cyclohexane diol, and the details are given in Scheme 4.1. Briefly, monomer M1 was synthesized by protecting the amine-unit in piperdin-4-one using acid-labile *t*-Boc unit and subsequent Baeyer-Villiger oxidation to seven-member cyclic-monomer. ^{t}Butyl carboxylic ester γ-substituted ε-caprolactone monomer M2 was synthesized through multi-step organic synthesis by selectively protecting mono-hydroxyl unit in 1,4-cyclohexane diol, PCC oxidation, and Baeyer-Villiger reaction. The characterization details of monomers by ^{1}HNMR analysis are given in the Figures 4.2 and in appendix for M1. Ring opening polymerization (ROP) strategy was employed for the synthesis of homopolymers, di- and the tri- block copolymers using $Sn(Oct)_2$ as the catalyst and triethylene glycol monomethyl ether as the initiator under solvent-free melt (or neat) condition at 110-130 °C. The ROP of commercial caprolactone monomer M3 yielded polycaprolactone (PCL) which was used as a macro-initiator for the ROP of M1 to get polycaprolactone-b-poly(amino-ester) (referred as PCL-*b*-PAE, see Scheme 4.2). The ROP of M2 by the PCL macroinitiator produced PCL-*b*-^{t}butyl carboxylic ester PCL di-block copolymer (referred as PCL-*b*-tBuPCL). The ROP of monomer M1 yielded PAE which was employed as a macroinitiator for the ROP of monomer M2 to yield new poly(amino-ester)-*b*-^{t}butyl carboxylic ester PCL (referred as PAE-*b*-^{t}BuPCL).

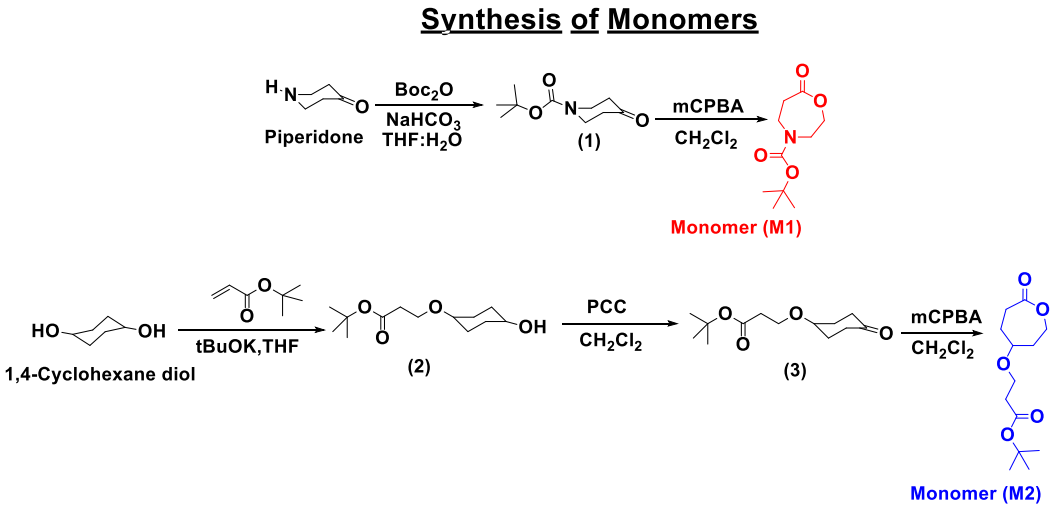

Scheme 4.1. *Synthesis of monomers M1 and M2.*

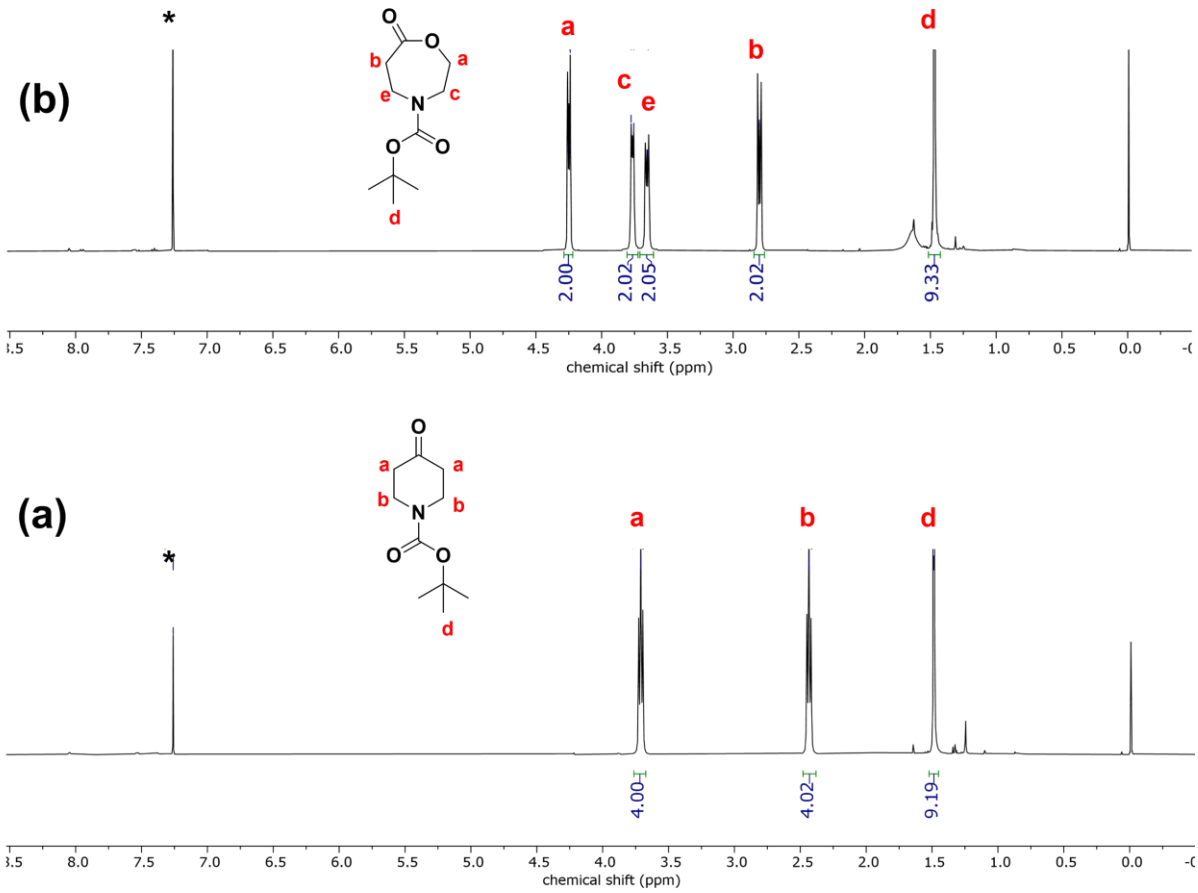

Figure 4.2: *^{1}HNMR of (a) Compound **1.** (b) Monomer **M1** in $CDCl_3$. Peaks are assigned alphabetically for each type of protons.*

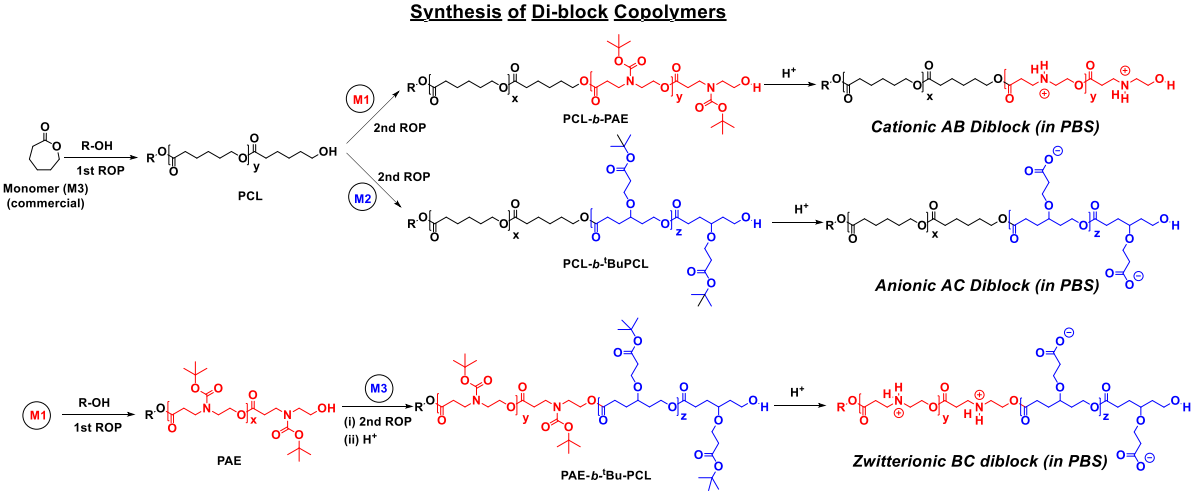

Scheme 4.2. *Synthesis cationic, anionic and zwitterionic diblock copolymers based on poly(amino-ester), polycaprolactone and carboxylic substituted polycaprolactones.*

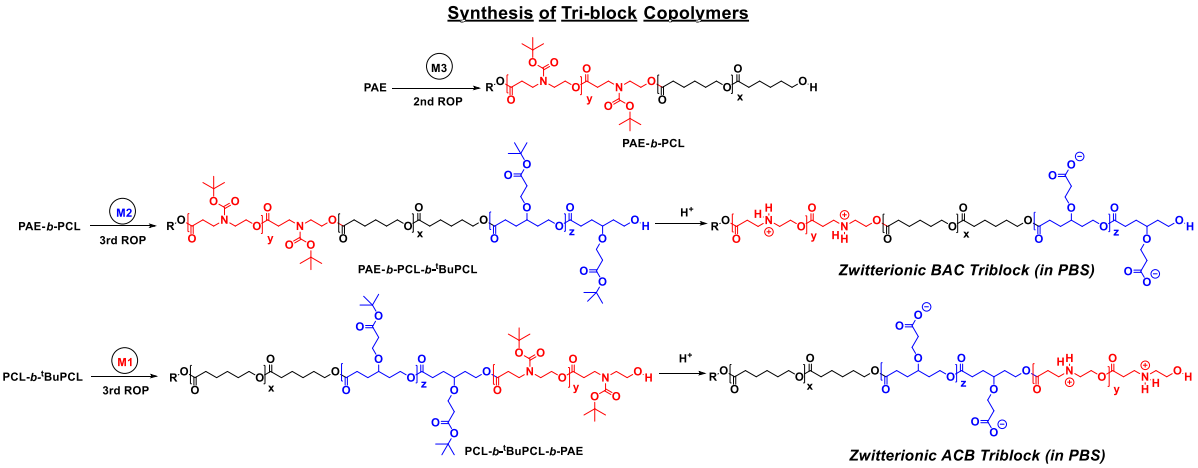

Scheme 4.3. *Synthesis of zwitterionic tri-block copolymers based on poly(amino-ester), polycaprolactone and carboxylic substituted polycaprolactones*

Additionally, two triblock-co-polymers were synthesized by employing the di-block copolymers PAE-*b*-PCL and PCL-*b*-^{t}BuPCL as macro-initiators for the ROP of monomers M2 and M1 to yield PAE-*b*-PCL-*b*-^{t}BuPCL and PCL-*b*-^{t}BuPCL-*b*-PAE, respectively (see Scheme 4.3). ^{1}HNMR analysis enabled the determination of the degree of polymerization in each of the blocks and the all the detailed spectra ^{1}HNMR are given in appendix. A specific example is discussed in detail for the zwitterionic BAC triblock copolymer in Figure 4.3. The degree of polymerization (DP) in PAE is estimated as 44, by comparing integration of initiator protons ***i*** corresponding to -O-C**H**$_3$ to the ***b*** protons adjacent to the carbonyl of PAE corresponding to -CO-C**H**$_2$- as shown in Figure 4.3a. Similarly, DP in PAE-b-PCL block was estimated by comparing integration of ***i*** initiator protons with ***a'*** protons of PCL corresponding -C**H**$_2$OCO- and DP estimated as ~60 as shown in Figure 4.3b. The PAE-*b*-PCL-*b*-tBuPCL triblock copolymer coincidentally showed distinct signals for the -C**H**$_2$COO- protons in the PAE, PCL, and ^{t}BuPCL units at 2.58, 2.29 and 2.43 ppm, respectively (assigned by proton-**b**, **b'** and **b"**) as shown in Figure 4.3c. Similarly, the -COOC**H**$_2$-ester protons (**a**, **a'** and **a"**) appeared separately and they were distinguishable from 4.05 to 4.15 ppm. The comparison of intensities of the initiator peak -OC**H**$_3$ (***i***) at 3.37 ppm to that of either -C**H**$_2$COO- or COOC**H**$_2$- in the chain backbone enabled the estimation of degree of polymerization (DP or n) in the PAE, PCL and ^{t}BuPCL block segments as 44, 60, 45, respectively (see Figure 4.3c). By applying the above method, the number of each unit in other di- and tri-block copolymers were determined by ^{1}H-NMR and summarized in Table 4.1. Deprotection in triblock copolymer was confirmed by disappearance of t-Boc peak at ~1.45 ppm as shown in Figure 4.3d.

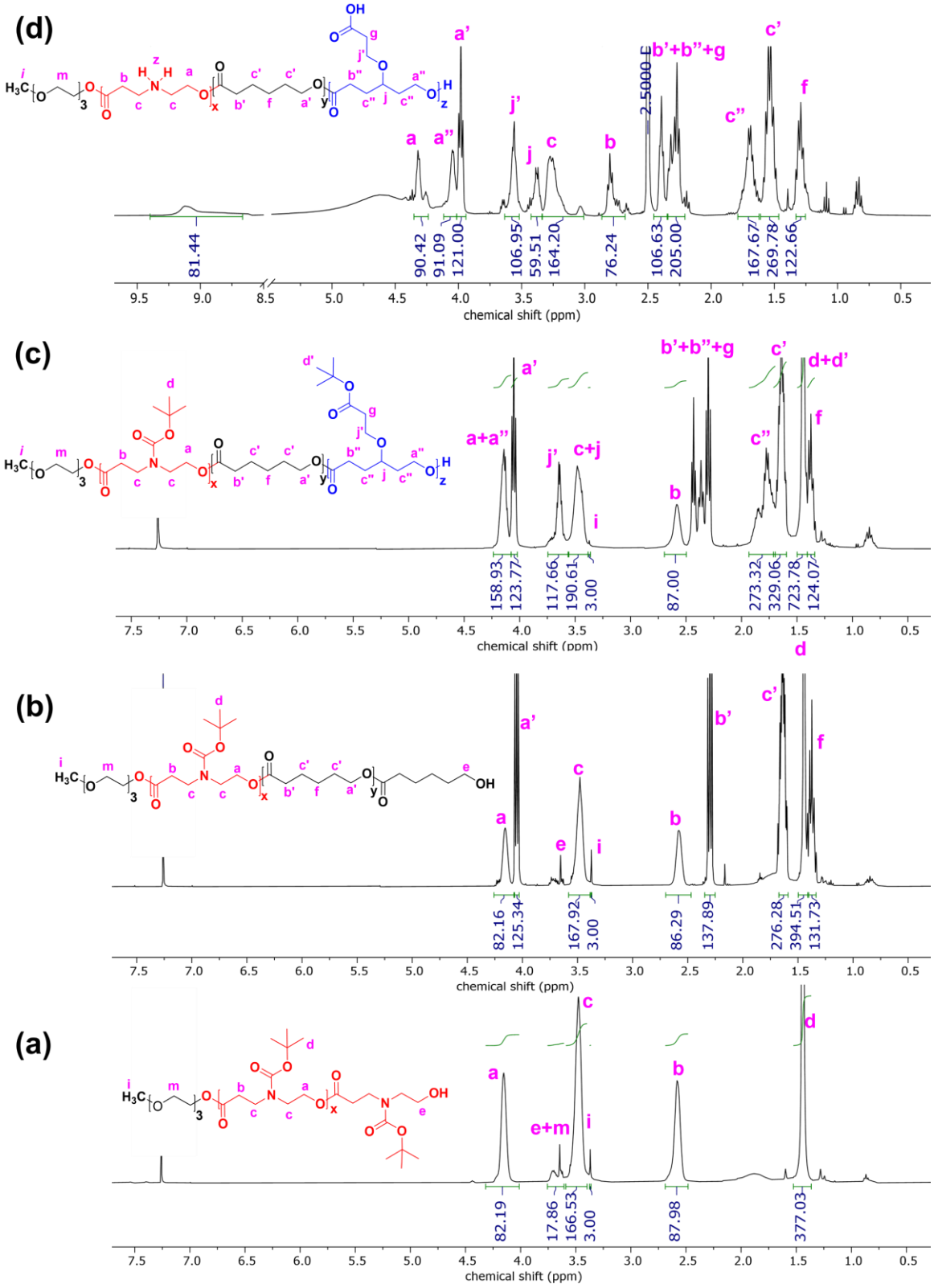

Figure 4.3. *[1]HNMR stack plot of (a) PAE macroinitiator. (b) PAE-b-PCL diblock polymer. (c) PAE-b-PCL-b-tBuPCL triblock polymer. (d) Zwitterionic BAC triblock polymer in DMSO-d_6. The peaks corresponding to different protons in the chemical structure are assigned alphabetically.*

Sample[a]	PCL[b] (x)	PAE[b] (y)	tBuPCL[b] (z)	M_n [c] (g/mol)	M_n [d] (g/mol)	M_w [d] (g/mol)	Đ	T_D [e] (°C)	T_g [f] (°C)	T_m [f] (°C) [ΔH_m]
PCL	60	-	-	7000	9400	11700	1.24	300	-	54 (74.4 J/g)
PCL-*b*-PAE	60	44	-	16700	13300	16600	1.24	250	-40	36.1 [5.2 J/g]
PCL-*b*-^{t}BuPCL	60	-	55	21200	18100	23700	1.30	270	-36	43.7 [18.4 J/g]
PAE	-	44	-	9200	8400	10600	1.26	245	-6	-
PAE-*b*-^{t}BuPCL	-	44	50	23800	10700	16600	1.55	255	-29	-
PAE-*b*-PCL-*b*-^{t}BuPCL	60	44	45	26800	16800	26300	1.56	265	-32	-
PCL-*b*-^{t}BuPCL-*b*-PAE	60	45	55	30900	11800	18600	1.57	264	-30	39.7

[a] The polymers represent the Boc or t-butyl ester derivatives of the corresponding block copolymers. Detail chemical structures are given in the Scheme S1 and S2. [b] Degree of polymerizations (DP) determined by ^{1}H-NMR analysis. [c] Number average molecular weight (Mn) determined by ^{1}H-NMR analysis following the equation: Mn = Repeating unit mass x DP. [d] SEC molecular weight determined in THF at 25 ° C using polystyrene for calibration. [e] Thermogravimetric analysis was carried out at 10 °/min heating under nitrogen atmosphere. [f] Differential scanning calorimetry analysis was carried out at 10 °/min heating/cooling under nitrogen atmosphere.

Table 4.1. *Table containing the degree of polymerization, Molecular weights and thermal properties of polymers*

The number average molecular weight (M_n) was estimated based on ^{1}HNMR spectra and is summarized in the Table 4.1 (details provided in appendix). Acid-catalyst-deprotection of these tailor-made di-block and tri-block copolymers yielded new classes of cationic AB diblock (Cat-AB), anionic AC diblock (Ani-AC), zwitterionic BC diblock (Zw-BC), zwitterionic BAC triblock (Zw-BAC), and zwitterionic ACB triblock (Zw-ACB) polymers as shown in Scheme 1 (A, B, C blocks represent PCL, PAE and carboxylic PCL blocks, respectively). ^{1}HNMR spectral analysis of the de-protected polymers confirmed the disappearance of *t*-butyl ester and *t*-Boc units in the ^{t}BuPCL and PAE blocks; further, the degree of polymerization was also not affected by the post-polymerization de-protection step (Figure 4.3d and appendix). The size exclusion chromatography (SEC) in THF enabled the determination of the molecular weights (M_n and weight average molecular weight M_w) and polydispersity index (Đ). Representative SEC plots of polymers are shown in Scheme 1d, and all these chromatograms exhibit mono-modal distribution (more SEC plots in Figures 4.4 and molecular weights in Table 4.1) having the polydispersity in the range of 1.2-1.5. Thermogravimetric analysis (TGA) studies of the polymers established thermal stability stable up to 250 to 300 ºC (Figure 4.5). The differential scanning colorimetry (DSC) analysis revealed semi-crystalline nature of the PCL-containing di-blocks PAE-*b*-PCL and PCL-*b*-tBuPCL copolymers whereas all other polymers were found to be amorphous. The glass transition temperature (T_g) was found to be in the of ranges from -6 to -40 ºC (detailed analysis is given Figure 4.6).

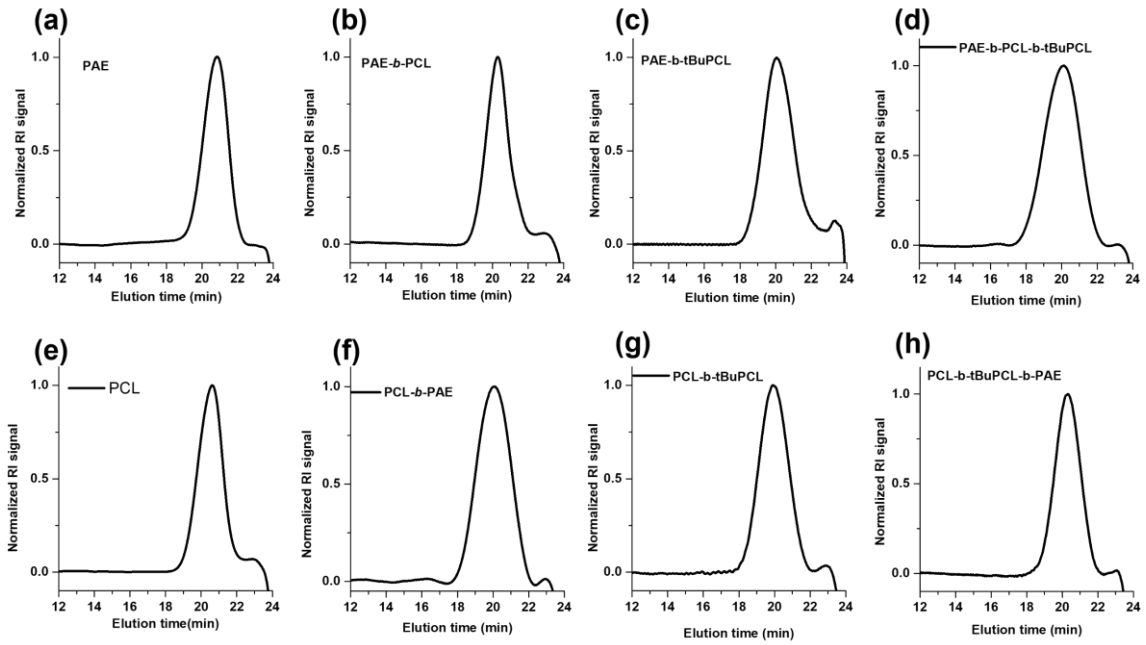

Figure 4.4. *(a) to h) SEC plots of the PAE, PAE-b-PCL, PAE-b-tBuPCL, PAE-b-PCL-b-tBuPCL, PCL, PCl-b-PAE, PCL-b-tBuPCL, and PCL-b-tBuPCL-b-PAE homopolymers, diblock copolymers and triblock copolymers in tetrahydrofuran at 25 ℃.*

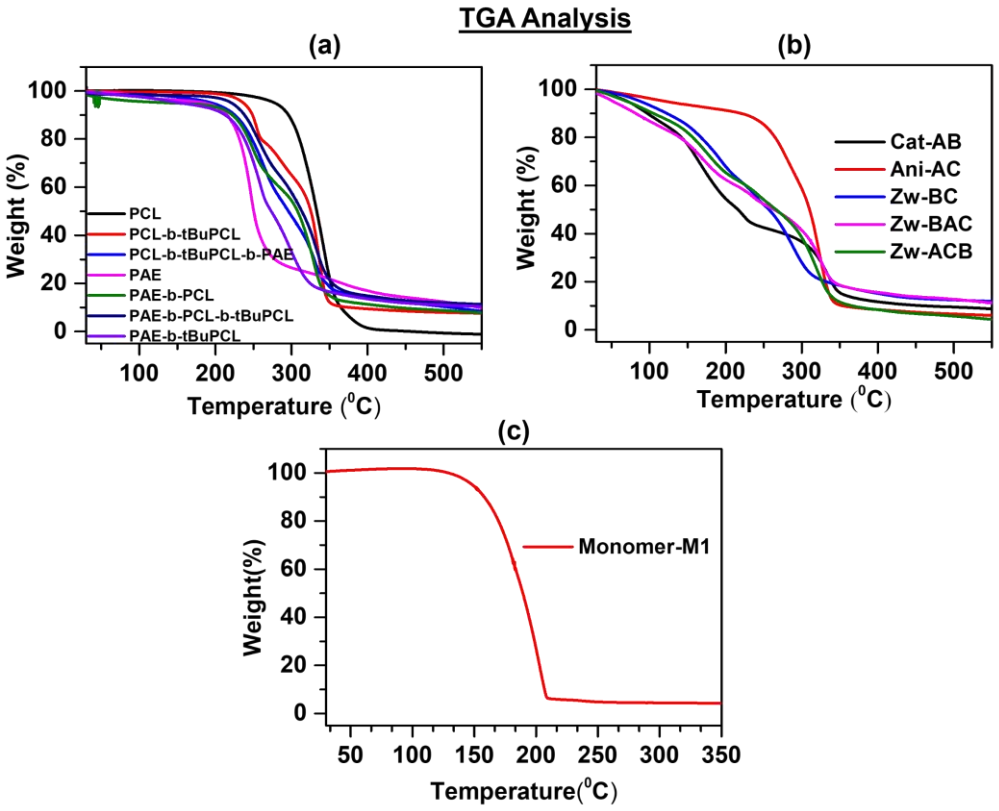

Figure 4.5. *TGA(thermogravimetric analysis) plots: (a) TGA plot of t-butyl derivative for homopolymers, diblock copolymers and triblock copolymers. (b) TGA plot of anionic, cationic and zwitterionic polymers. (c) TGA plot for Monomer M1.*

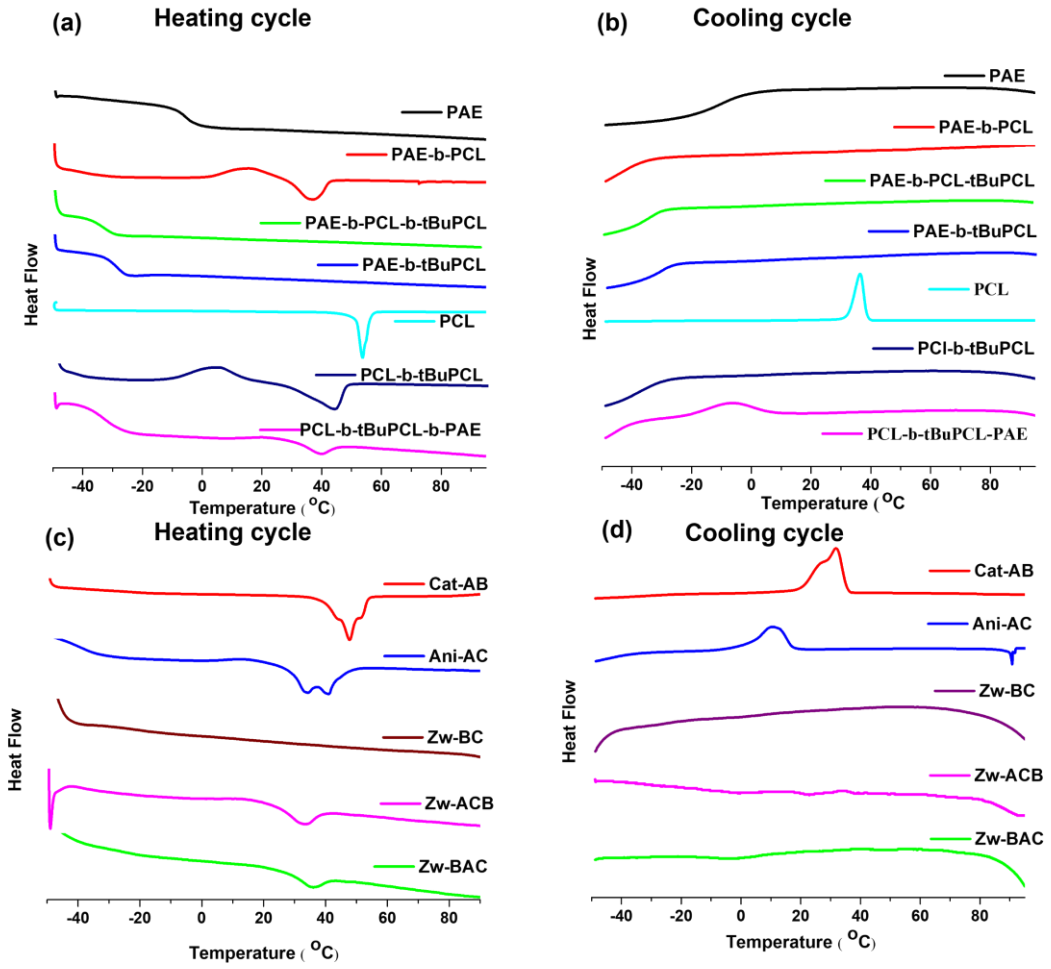

(e)

Polymer	DSC				
	T_g(°C)	T_m(°C)	T_c(°C)	ΔH_m(J/g)	ΔH_c (J/g)
PAE	-6.0	-	-	-	-
PAE-b-PCL	-40.0	36.1	-	14.2	-
PAE-b-PCL-tBu PCL	-32.0	-	-	-	-
PAE-tBu PCL	-28.0	-	-	-	-
PCL	-	53.6	30.0	74.4	74.1
PCL-tBu PCL	-36.0	43.7	-	17.1	-
PCL-b-tBu PCL-b-PAE	-30.0	39.7	-	-	-

(f)

Polymer	DSC				
	T_g(°C)	T_m(°C)	T_c(°C)	ΔH_m(J/g)	ΔH_c (J/g)
Cat-AB	-43.0	47.74	29.04	28.92	28.44
Ani-AC	-46.0	41.02	10.49	13.57	9.07
Zw-BC	-45.6	-	-	-	-
Zw-ACB	-42.0	32.75	-	-	-
Zw-BAC	-45.0	42.24	-	-	-

Figure 4.6: *DSC analysis was performed at 10°C/min under nitrogen atmosphere. Plots of heat flow vs temperature (a) heating cycle, (b) cooling cycle and (e) Table showing T_g,T_m,T_c, ΔH_m and ΔH_c for t-butyl derivative for homopolymers, diblock copolymers and triblock copolymers. Plots of heat flow vs temperature (c) heating cycle, (d) cooling cycle and (f) Table showing T_g,T_m,T_c, ΔH_m and ΔH_c for deprotected anionic, cationic and zwitterionic polymer.*

4.3.2 Self-Assembly and Self-Immolation of Cat-AB

The Cat-AB diblock polymer acquires inherent amphiphilicity due to combination of hydrophobic PCL segment and hydrophilic self-immolative cationic PAE units which enables it to self-assemble into a micellar structure (Figure 4.7a or its aggregated micelles). At acidic pH =3 to pH = 6.0, the cationic-AB nanoparticles exist in the protonated amine-form with Zeta potential of +40 mV (Figure 4.7b). At neutral pH = 7.4, the Zeta potential gradually reduced to +20 mV and further increase in pH resulted in the de-protonation of the amine (-20 mV). The DLS size in Figure 4.7c indicated that the Cat-AB nanoparticles were stable in acidic pH having hydrodynamic diameters < 250 nm, but at neutral to basic pH (> pH =7.0), the nanoparticles degraded and appeared as a turbid solution having size in the μm-range. The self-immolative aspects of the Cat-AB were examined by turbidity measurements. The plot of % transmittance versus incubation time for Cat-AB in PBS (pH = 7.4, at 37 °C) in Figure 4.7d and 4.7f depicted a gradual reduction and became fully turbid at 8h (see spectra in Figure 4.7d). In contrast, the % transmission of Cat-AB in deionized water (no self-immolation occurs in pure water) did not show any turbidity that confirmed the stability of the polymer up to 120 h (see Figure 4.7e). In Figure 4.7h, the Cat-AB was further subjected to encapsulation of clinical anticancer drug doxorubicin (DOX) and the drug loading content (DLC) was obtained as 2.2 %. The *in vitro* drug release kinetics in Figure 4.7i showed that nearly 90 % DOX released under physiological pH=7.4 in PBS (pH =7.4, 37 °C). In contrast, only 30% DOX release was observed at pH 5.5 suggesting that the nanoparticle was relatively more stable under acidic pH (Figure 4.7j).In addition release of DOX was monitored by incubating Cat-AB+DOX nanoparticles in PBS, pH 7.4 with esterase enzyme at 37°C; however similar release pattern was observed in presence of enzyme to that of only PBS, pH 7.4 as shown in Figure 4.7j. This suggested DOX was released because of self-immolation even in the presence of enzymes. Further, the stability of the DOX loaded nanoparticles was monitored by DLS and the plots and photographs of vials in Figure 4.7k clearly showed that the nanoparticle was not stable and precipitated in less than 10 h in PBS. The mechanism of self-immolation of poly(amino-ester) segments was further studied by ^{1}HNMR spectroscopy by incubating Cat-AB in PBS (pH 7.4) at 37 ºC for 24 h and subjecting the aliquots for analysis. The schematic of self-immolation mechanism is shown in Figure 4.8a. The Cat-AB has 44 self-immolative PAE units and stable 60 PCL units, and therefore, the peak ratio of these subunits could be employed as a measure of self-immolation in PBS buffer at pH=7.4. The peak corresponding to proton-***a*** in the PCL segments (stable segment) was intact even after 24h of incubation in PBS. The peaks corresponding to the

protons ***b*** and ***c*** in the PAE self-immolative segments drastically reduced with incubation time in PBS buffer. Stack plot of ^{1}HNMR spectra is provided in Figure 4.8b for time-dependent incubation and important peaks are highlighted. The zoomed region from 3.8 to 4.5 ppm showing integration of PCL and PAE protons is shown in Figure 4.8c. Upon comparing the decrease in the intensity proton ***b*** of PAE with respect to proton ***a*** of PCL revealed that nearly 50 % of PAE underwent auto-degradation in 24h as shown in Figure 4.8d. This suggests that the Cat-AB di-block was not suitable for biomedical application for *in vitro* and *in vivo* analysis despite it has amphiphilicity to self-assembled and load anticancer drug molecules.

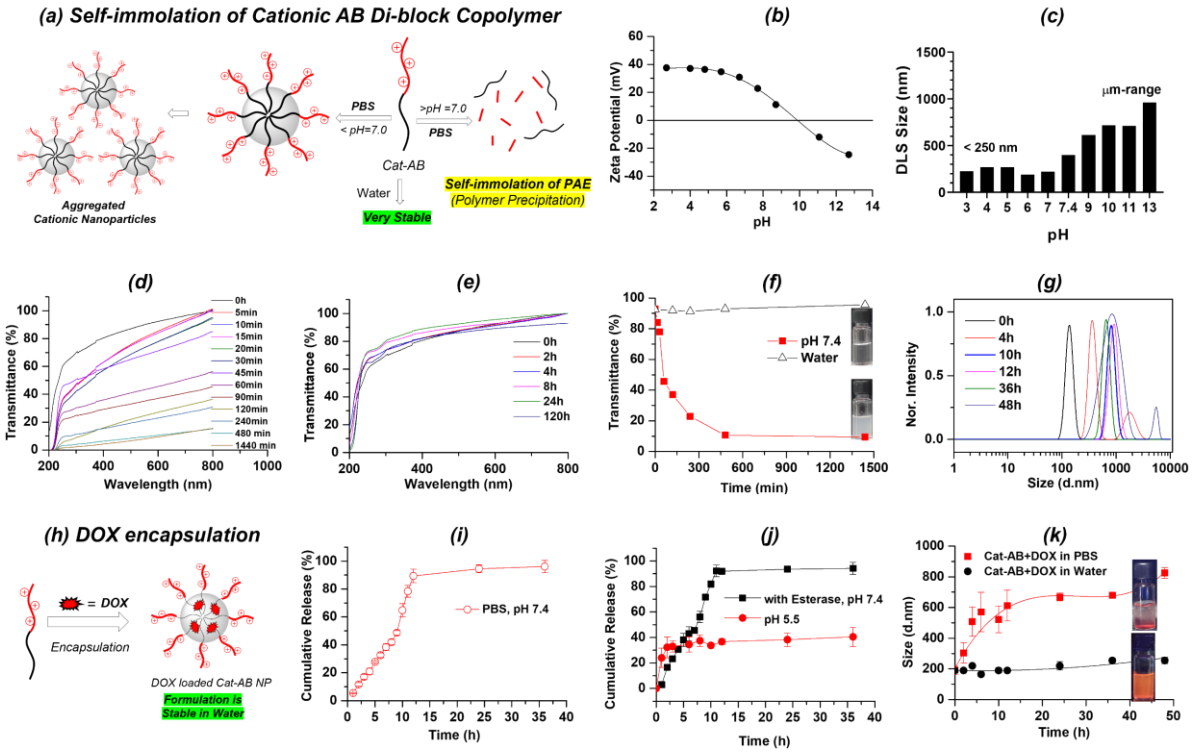

Figure 4.7. *(a) Schematic representation of pH dependent self-assembly of Cat-AB di-block polymer. (b) Zeta potential and (c) DLS size of the Cat-AB nanoparticles in various pH in Briton-Robinson buffer at 25 ℃. (d) and (e) Plot of transmittance (%) spectra of the Cat-AB nanoparticles incubated in PBS at pH=7.4 at 37 ℃ and in water at 37 ℃ (concentration of the polymer is 1.0 mg/mL) respectively. (f) Cumulative transmittance (%) of the Cat-AB nanoparticles incubated in PBS at pH=7.4 at 37 ℃ and in water at 37 ℃ (at 600 nm). (g) Plot of DLS histograms of Cat-AB nanoparticles incubated in pH 7.4 at 37 ℃. (h) Schematic representation of DOX loaded Cat-AB nanoparticles. Drug release profile of Cat-AB+DOX in (i) PBS, pH=7.4 at 37 ℃, (j) in presence of esterase at pH 7.4 and in pH 5.5 without esterase respectively. (k) Plot of sizes of Cat-AB+DOX nanoparticles incubated in PBS, pH 7.4 and in water at 37 ℃ at various time. Inset photographs represent Cat-AB+DOX in PBS, pH 7.4 (upper vial) and in water (lower vial) after 24h of incubation.*

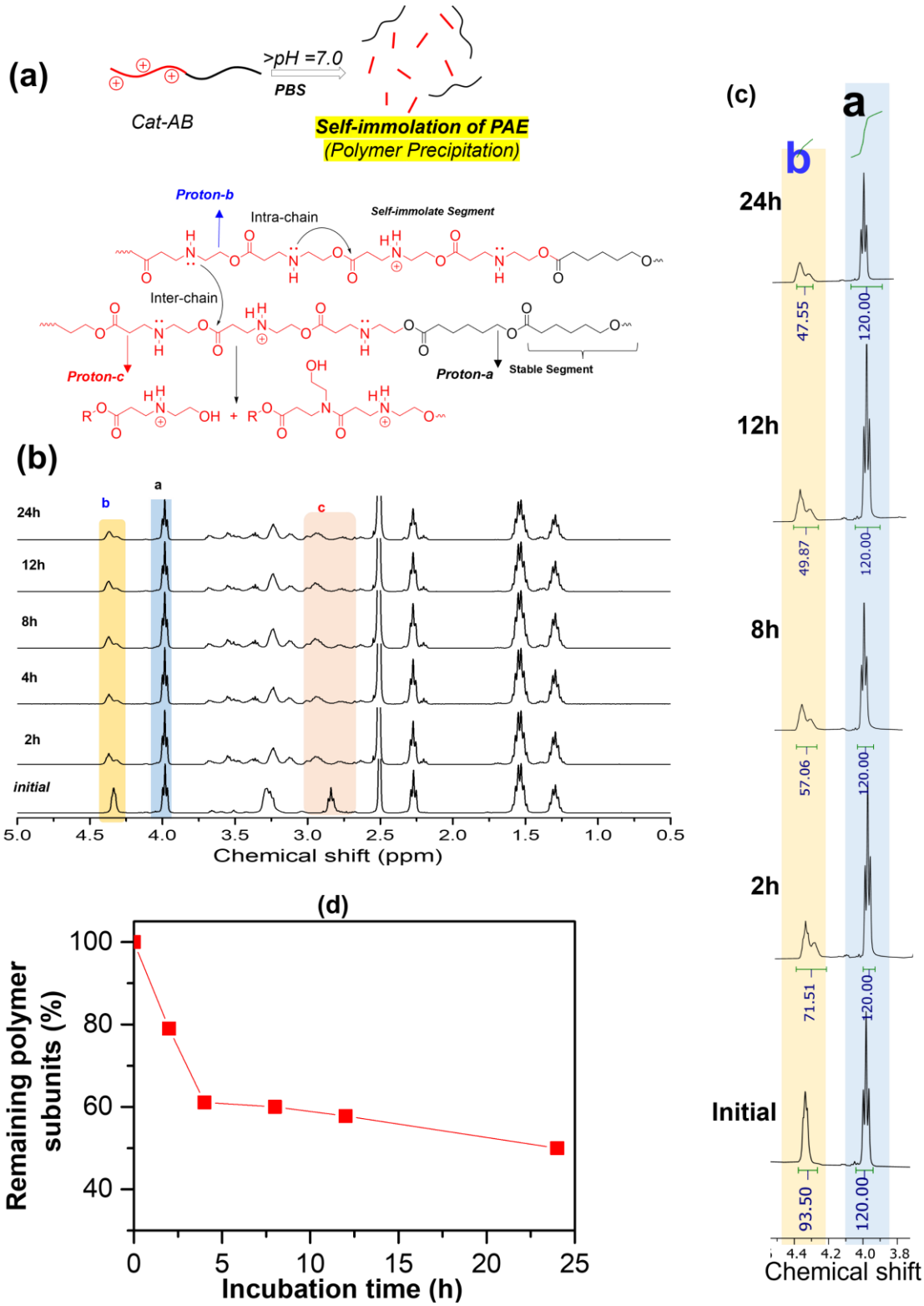

Figure 4.8. *(a) Schematic for self-immolation of Cat-AB polymer at pH 7.4. (b) ^{1}HNMR spectra of the aliquots of the Cat-AB nanoparticles incubated in PBS at pH=7.4 at 37 ℃ various time points of incubation. (c) Zoomed region of ^{1}HNMR 3.8 to 4.5ppm with integration. The aliquots were lyophilized and recorded for ^{1}HNMR spectroscopy in DMSO-d_6. Various protons in the chemical structure are assigned with alphabets. (d) Plot of % degradation of Self-immolative PAE units.*

4.3.3 Electrostatic Strategy to Stabilize Self-Immolation of Cat-AB

Electrostatic interaction strategy is an elegant approach to retain the PAE segments in the $R_2NH_2^+$ form in PBS buffer to resist the self-immolation. The zwitterionic di-block polymer Zw-BC has carboxylic acid and amine functional groups in the PCL and PAE blocks, respectively. At acidic pH (pH< 5.0), the PCL segments predominantly exist in the carboxylic acid-form rendering them hydrophobic and consequently they occupy at the core of the micelles as shown in Figure 4.9a. Under this condition, the amines in the PAE chains are protonated and hydrophilic that occupy at periphery. At basic conditions, the reverse self-assembly is observed in which the PCL carboxylic anion and hydrophobic amine-functionalized PAE occupied at the periphery and core, respectively, as shown in Figure 4.9a. This is further evident in Figure 4.9b while the pH of the solutions varied from 3.0 to 12 that the zeta potential values changed from cationic (+40 mV) to anionic (-40 mV) with an isoelectric point around pH 7. In Figure 4.9c, the DLS data revealed the formation of large, sub-micron sized assemblies (0.5 to 0.7 μm) in acidic pH. Interestingly, above pH=5.0, the carboxylate anion not only imparts the amphiphilicity to the block copolymer but also stabilize the amine in its protonated form. This cooperativity among the amine and carboxylic functional groups stabilizes the PAE backbone against self-immolation at neutral pH and basic conditions. The resultant nanoparticles attained excellent stability at physiological pH=7.4 with zeta potential of -8 mV and size under 200 ± 20 nm.

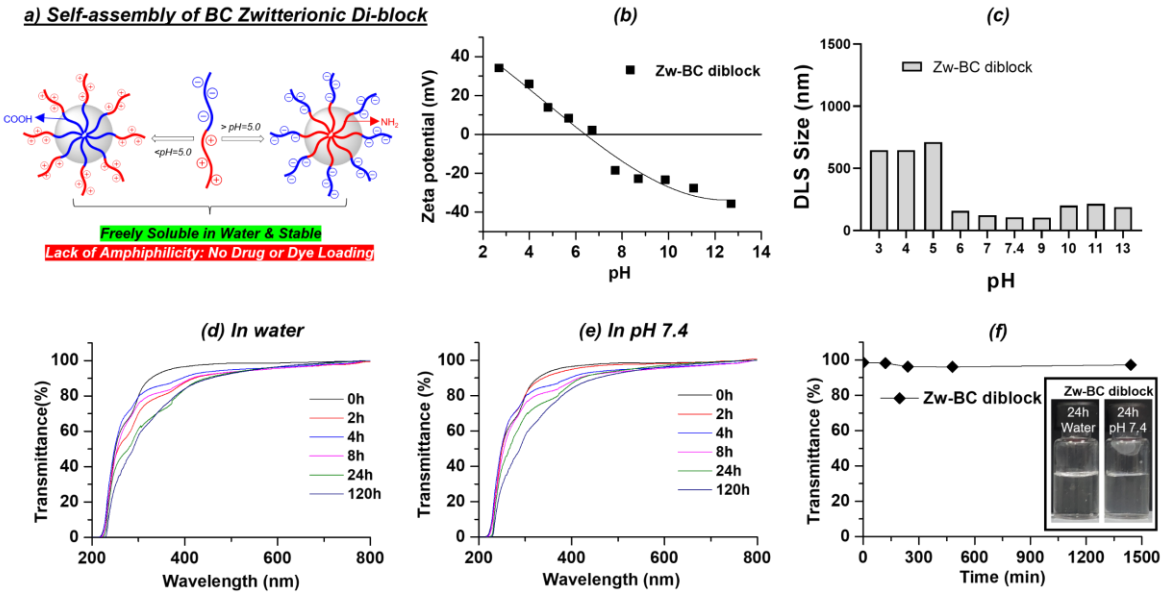

Figure 4.9. *(a) Schematic representation of pH dependent self-assembly of Zw-BC di-block polymer. (b) Zeta potential and (c) DLS sizes of the Zw-BC di-block in Briton-Robinson buffer at 25 ℃. Transmittance (%) of the Zw-BC di-block incubated in (d) In water (e) In PBS at*

pH=7.4 at 37℃. (f)Cumulative % transmission plot of Zw-BC incubated in pH 7.4 (PBS) at 37℃ (at 600 nm). Photograph of vials containing Zw-BC diblock after 24h incubation in water and PBS, pH 7.4.

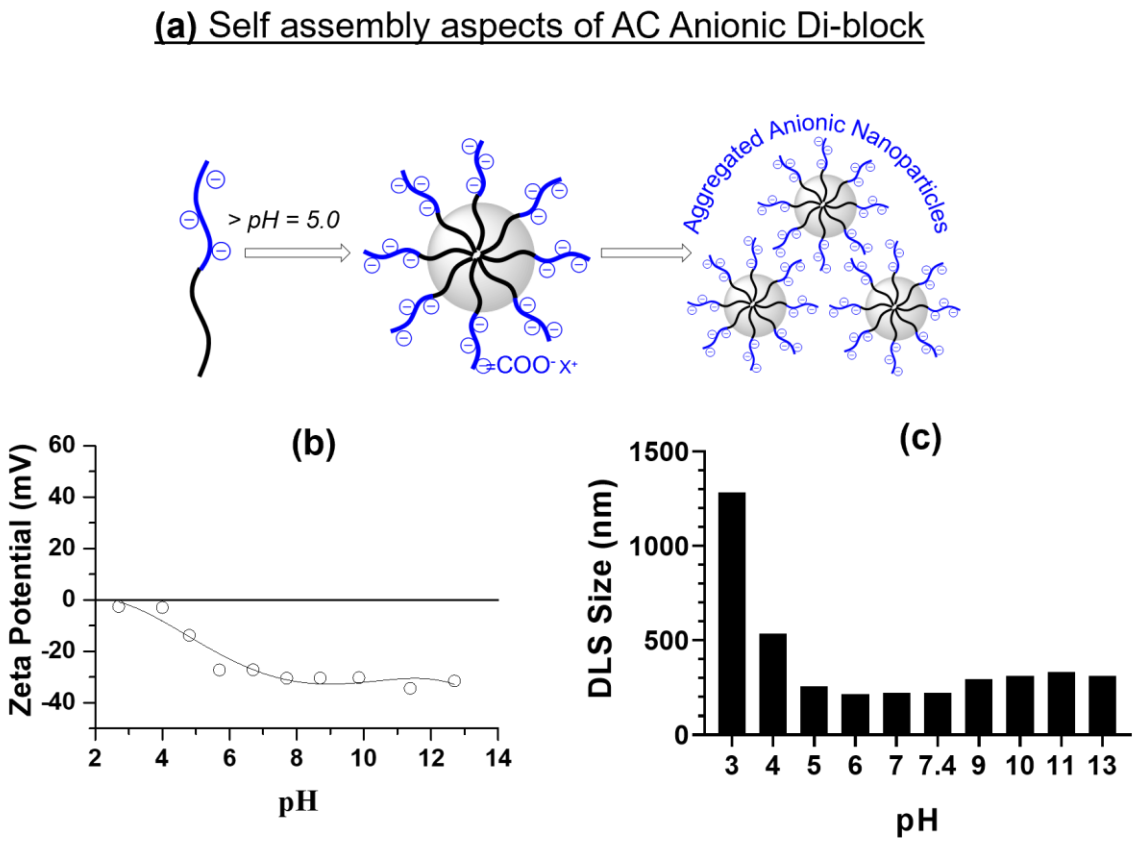

Figure 4.10: *(a) Pictorial representation of pH dependent self-assembly aspects of Anionic-AC diblock copolymer. (b) Zeta potential (c) DLS size of Ani-AC copolymer nanoparticles in different pH (Briton-Robinson buffer 10mM).*

This was further supported by the % transmittance plot in Figure 4.9d-4.9f that the stability of the Zw-BC was retained in PBS (pH = 7.4, 37 °C) for more than 24 h. Interestingly Zw-BC diblock was very stable and did not show any precipitation in PBS, pH 7.4 even after longer incubation time evident from % transmittance in Figure 4.9e. The photographs of vials provided visual evidence of stability (clear solution) in Figure 4.9f. To investigate whether the block copolymer architecture is necessary to imbibe the stability in PAE chains at neutral pH; a control experiment was carried out to study the stability for equimolar mixtures of Cat-AB+Ani-AC diblock (synthesized following reported procedure [57] and self-assembly data in Figure 4.10). The resultant mixed zwitterionic species shown in Figure 4.11a exhibited zeta potential and DLS size similar to that of the Zw-BC (Figure 4.11b and 4.11c for Cat-AB+Ani-AC mixture and Figure 4.9 for Zw-BC data). The transmittance studies in Figure 4.9f, proved

the stability of Zw-BC diblock at pH 7.4 in PBS without any phase separation; however, the Cat-AB+Ani-AC mixture exhibited 40 % reduction in transmission (Figure 4.11e) due to the uncontrolled self-immolation by the cationic PAE units in the Cat-AB (for spectra, see Figure 4.11d). This was further supported by DLS size measurements, as shown in Figure 4.11f, revealed the formation of larger aggregates having multimodal size distribution over the period of time. This signified that mixture was stable for longer period and photographs of vials provided visual evidence of precipitation in Figure 4.11g. These results clearly demonstrate that physical mixture of Cat-AB and Ani-AC is not stable for longer time period in PBS, pH 7.4. This validates the necessity of zwitterionic diblock nanoarchitectures to be essential for the stabilization of the PAE blocks against the uncontrolled self-immolation at neutral pH. Unfortunately, the Zw-BC di-block was found to be inferior to encapsulate therapeutics drugs or biomarkers, and this is attributed to the high solubility of the polymer in water.

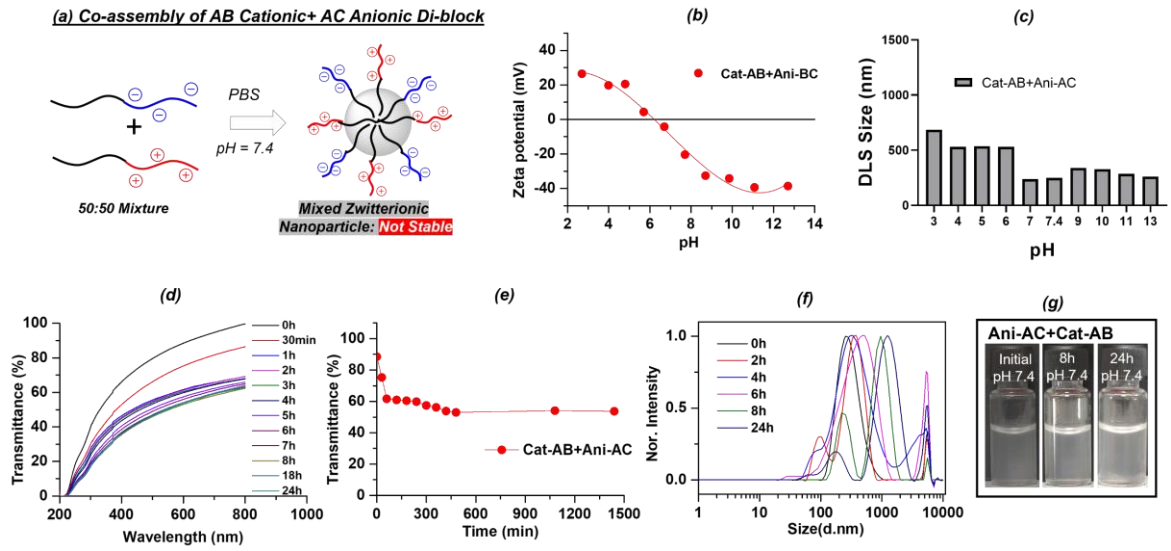

Figure 4.11. *(a) Schematic representation of pH dependent self-assembly aspects of co-assembling Cat-AB +Ani-AC di-blocks.(b)Zeta potential and (c) DLS size of the Cat-AB+Ani-AC di-blocks mixture in Briton-Robinson buffer at 25 ℃. (d) Transmittance plot of Cat-AB+Ani-AC mixture in PBS at various incubation time.(e) Cumulative % transmission plot of Zw-BC incubated in pH 7.4 (PBS) at 37℃ (at 600nm). (f) DLS histogram of Cat-AB+Ani-AC mixture in PBS at various incubation time. (g) Photograph of vial containing of Cat-AB+Ani-AC mixture in PBS at various incubation time.*

4.3.4 Self-Assembly and Encapsulation studies of Zwitterionic Triblock polymers

Incorporation of appropriate hydrophobic segments in the zwitterionic polymer design was comprehended to be a crucial factor to enhance their encapsulation capabilities while retaining their stability at neutral pH. To accomplish this task, two zwitterionic tri-block copolymers were structure-engineered: (i) placing the hydrophobic PCL block in between the anionic carboxylic PCL and cationic PAE block (referred as Zw-BAC), and (ii) placing the hydrophobic PCL block kept away from the zwitterionic PAE and carboxylic PCL units (referred Zw-ACB) (see Scheme-4.3). The PCL segments in the tri-block copolymers brought excellent hydrophilic-hydrophobic balance and enabled them to self-assemble into stable nanoparticles. The strong-electrostatic attraction among the anionic-cationic species and the hydrophobic PCL middle segments induced formation of U-shaped amphiphiles as shown in Figure 4.12a for Zw-BAC triblock. Self-assembly of Zw-ACB triblock is given in Figure 4.12b. In Figure 4.12c, the zeta potential data suggests that the zwitterionic triblock-polymers act in a similar way to that of their di-block counterparts, and the values varied from +57 mV to -35 mV with isoelectric point around pH 7 while increasing the pH from 3.0 to 13.0. Most astonishingly, these factors stabilized the zwitterionic triblock nanoparticles and the DLS sizes were controlled well below < 200 nm in the entire pH range as seen in Figure 4.12d. It is noteworthy that the stability of the triblock copolymer was not influenced by the sequence of the units in the Zw-BAC or Zw-ACB triblock. In addition, time-dependent DLS size measurement of Zw-BAC triblock revealed monomodal size distribution indicating stability as shown in Figure 4.12e. Furthermore, the % transmittance studies in Figure 4.12f revealed that the Zw-BC and Zw-BAC or Zw-ACB nanoparticles solution was transparent throughout the period of incubation of 120 h in PBS, pH 7.4 at 37 ºC (for spectra and more details see Figure 4.12g, 4.12h, and appendix). The stability of the Zw-BAC triblock was further confirmed by ^{1}HNMR spectral analysis in PBS at pH=7.4 and more details are summarized in Figure 4.13. The proposed mechanism of stabilization of unstable PAE units by carboxylic PCL units is shown in the Figure 4.13a. The carboxylate ions of carboxylic-PCL interact electrostatically with the protonated amines of PAE units forming a strong zwitterion pair at pH 7.4. This zwitterionic complex gets highly hydrated and prevents deprotonation of amines by buffer anions. Therefore, amines of PAE cannot attack on its carbonyl carbons of backbone and overall self-immolation process is restricted. Moreover, carboxylate anions also help to restrict the penetration of other buffer anions towards amines of PAE and provide overall shielding of PAE units at pH 7.4. ^{1}HNMR spectra are shown in Figure 4.13b for Zw-BAC triblock suggested

no noticeable changes in peaks. The peak ***b*** and ***c*** corresponding to C**H**$_2$-O-C=O and C**H**$_2$-C=O of amino ester backbone respectively in zwitterionic BAC triblock did not show any reduction or change in intensity with increase in incubation time in pH 7.4, PBS buffer compared to its original intensity which is clear indication that of cationic segment did not undergo any auto-degradation caused by buffer action at pH 7.4 and stabilized by anionic segment (carboxylate anions) by zwitterionic interaction. The % degradation was estimated from NMR, and it was found that Zw-BAC polymer did not show any degradation as shown in Figure 4.13c.

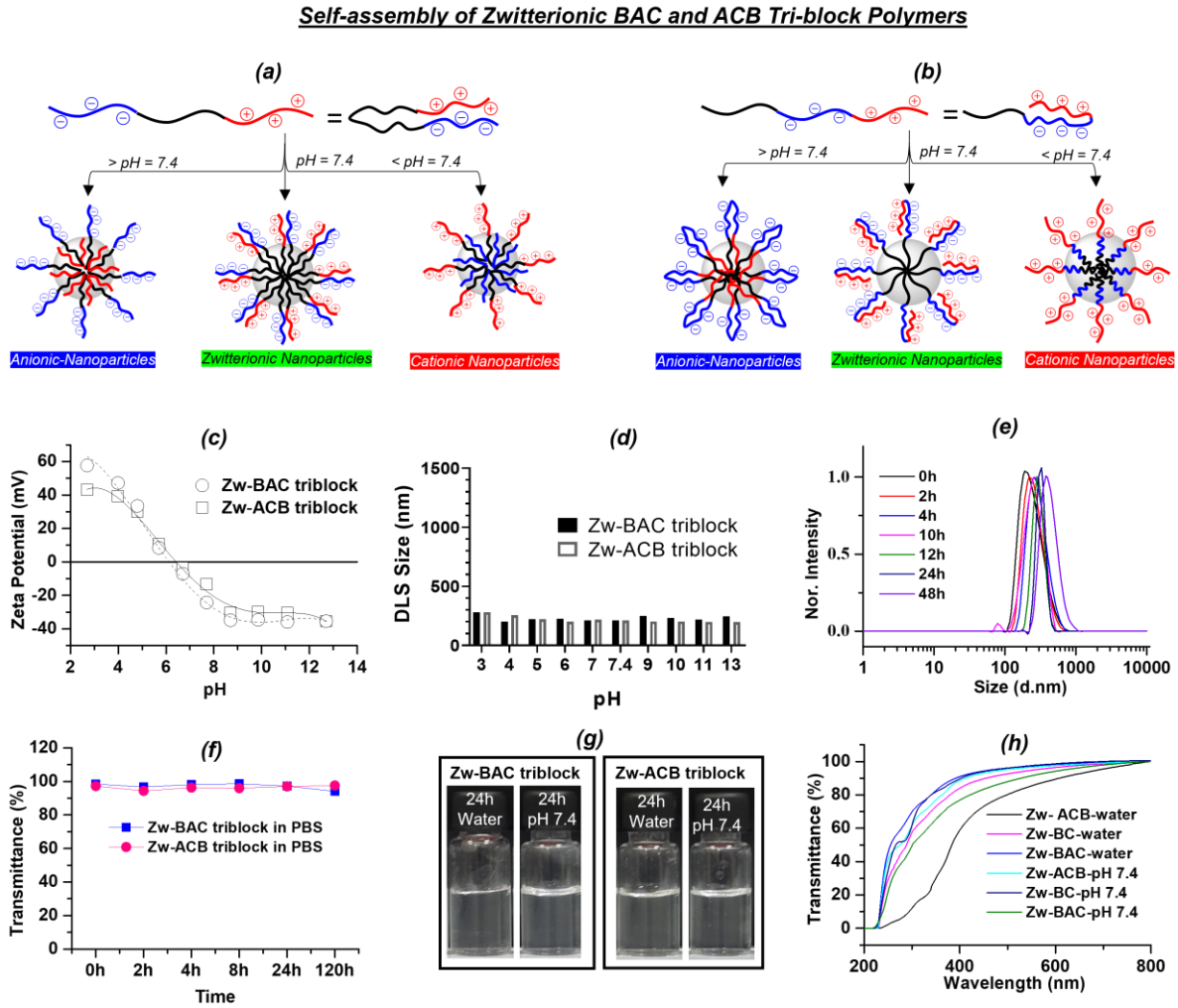

Figure 4.12. *(a) and (b) Schematic representation of pH dependent self-assembly aspects of Zw-BAC and Zw-ACB triblock polymers respectively in different pH. (c) Zeta potential and (d) DLS sizes of the Zw-BAC and Zw-ACB nanoparticles at various pH in Briton-Robinson buffer at 25 ℃. (e) Plot of DLS size histograms of Zw-BAC nanoparticles incubated in PBS, pH 7.4. (f) Transmittance (%) of the Zw-BAC and Zw-ACB nanoparticles incubated in PBS at pH=7.4 at 37℃ (at 600 nm). (g) Photographs of vials containing Zw-BAC and Zw-ACB triblock after 24h of incubation in water and PBS, pH 7.4. (h) Plot of transmittance spectra for Zw-BAC and Zw-ACB triblock incubated in water and PBS, pH 7.4 after 120h incubation.*

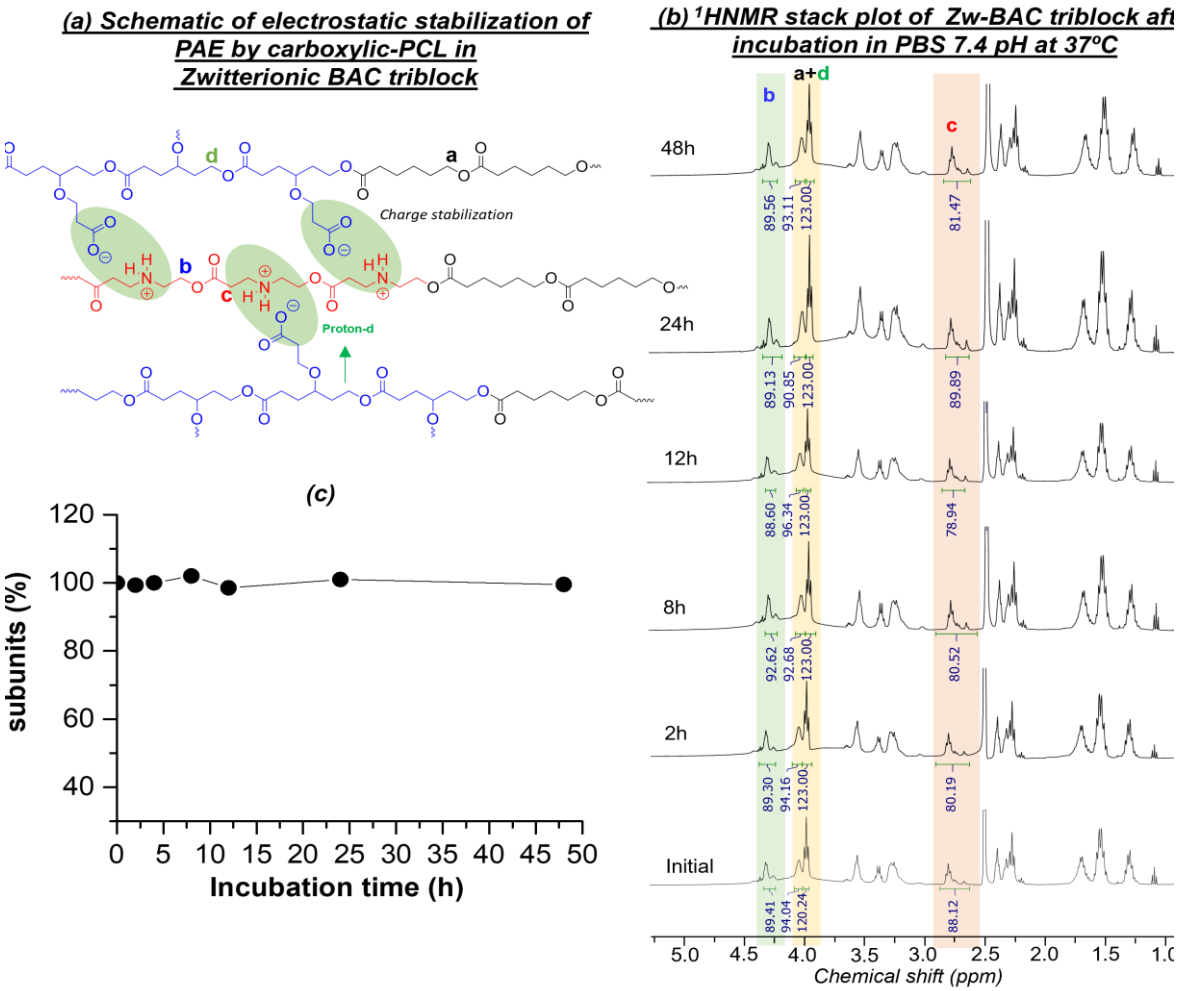

Figure 4.13: *(a) Schematic representation of zwitterionic stablization in Zw-BAC triblock polymer at pH 7.4. (b) Stack plot of ^{1}H-NMR spectra of the aliquots of the Zw-BAC triblock incubated in PBS, pH=7.4 at 37℃ for 24h of incubation. The aliquots were lyophilized and recorded for ^{1}H-NMR in d_6-DMSO. Various protons in the chemical structure are assigned with alphabets. (c) % Degradation of Zw-BAC analyzed by ^{1}HNMR.*

Critical micellar concentration (CMC) of the polymers were in the range of 1.0 to 10 µg/mL suggesting excellent ability to self-assemble in aqueous medium to produce stable micellular nanoparticles in Figure 4.14. Further zwitterionic BAC and ACB triblock were subjected to cargo encapsulations by dialysis process. The structures of cargos (DOX, HPTS ad IR780) are shown in Figure 4.15a and photographs of cargo loaded nanoparticles are shown in Figure 4.15b proving visual evidence of remarkable loadings. In Figure 4.15c, the DLC for DOX and HPTS loading was compared to zwitterionic triblock Zw-BAC and Zw-ACB with Cat-AB and Ani-BC diblock (see Table 4.2, and 4.3 for more details). The Zw-BAC and Zw-ACB tri-block copolymers exhibited excellent DLC of 6-8 % for DOX, which are better than

their di-block counterparts. Previous reports on polyacrylate based zwitterionic polymers exhibited very good DLC for DOX in the range of 5-10 % which is comparable to that of the present PCL triblock nanoparticle design.[64-66] Further, the zwitterionic triblock copolymer DLC values are also comparable to other substituted PCL polymers (non-zwitterionic system).[67] The detailed nanoparticle characterization of Zw-BAC+DOX nanoparticle is shown in Figure 4.15d. The DLS histograms showed mono-modal distribution having average hydrodynamic diameter of 220 ± 8 nm, FE-SEM and AFM images depicted spherical nanoparticles of 210 ± 7 nm and 210 ± 8 nm, respectively. Absorbance spectra of DOX , HPTS and IR780 loaded nanoparticles in Figure 4.15e revealed preservation of spectral properties of cargo upon encapsulations. Furthermore, Zw-BAC+DOX nanoparticles showed no sign of precipitation after 24h of incubation in PBS, pH 7.4 at 37 ℃ as shown in Figure 4.15f. The detailed characterization of all cargo loaded nanoparticles by DLS, AFM, FE-SEM and TEM is shown in Figure 4.16 to 4.18. Triblock with varying number of PCL, PAE and carboxylic PCL chain lengths were synthesized to study the role of the composition of triblock on the self-assembly and their encapsulation capabilities. The CMC, size and DLCs are shown in Table 4.4. It was observed that the nanoparticle sizes, CMC, and colloidal stability (for 5 days) were not affected by changing the block lengths. A slightly lower DLC was observed for DOX loaded samples in shorter block lengths, and therefore, the triblock copolymers having longer block lengths are chosen for further analysis.

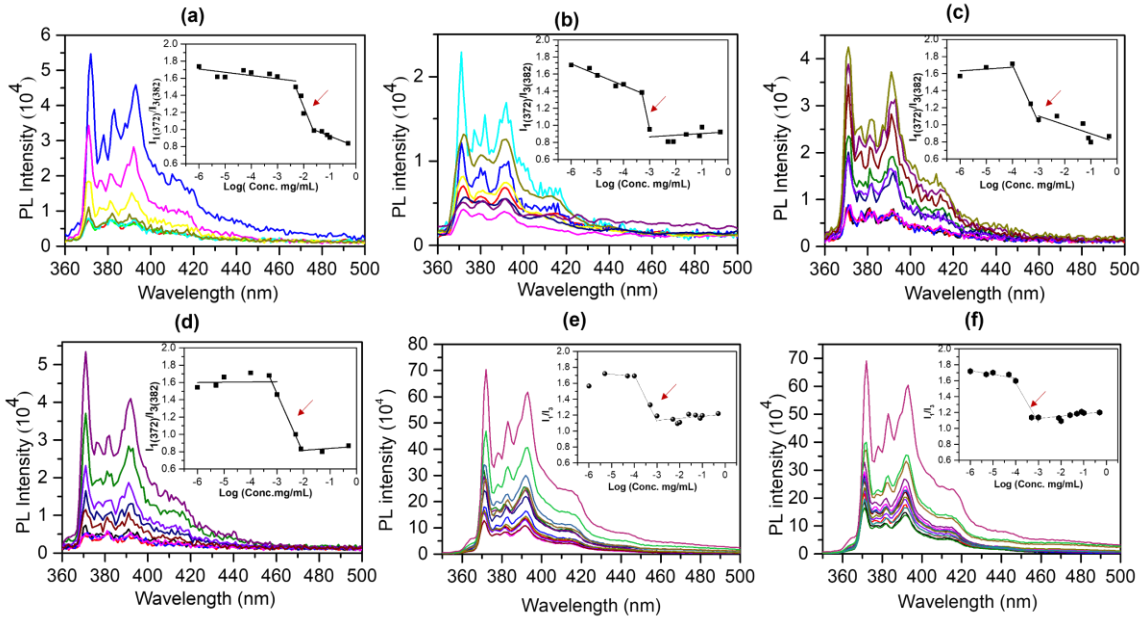

Figure 4.14: *CMC determination using pyrene as probe. Fluoroscence plots of pyrene in polymers, respective plots of I_1/I_3 are shown in insets. (a) Cat-AB (b) Zw-BC (c) Zw-ACB (d) Zw-BAC. (e) Zw-ACB-30. (f) Zw-BAC-30.*

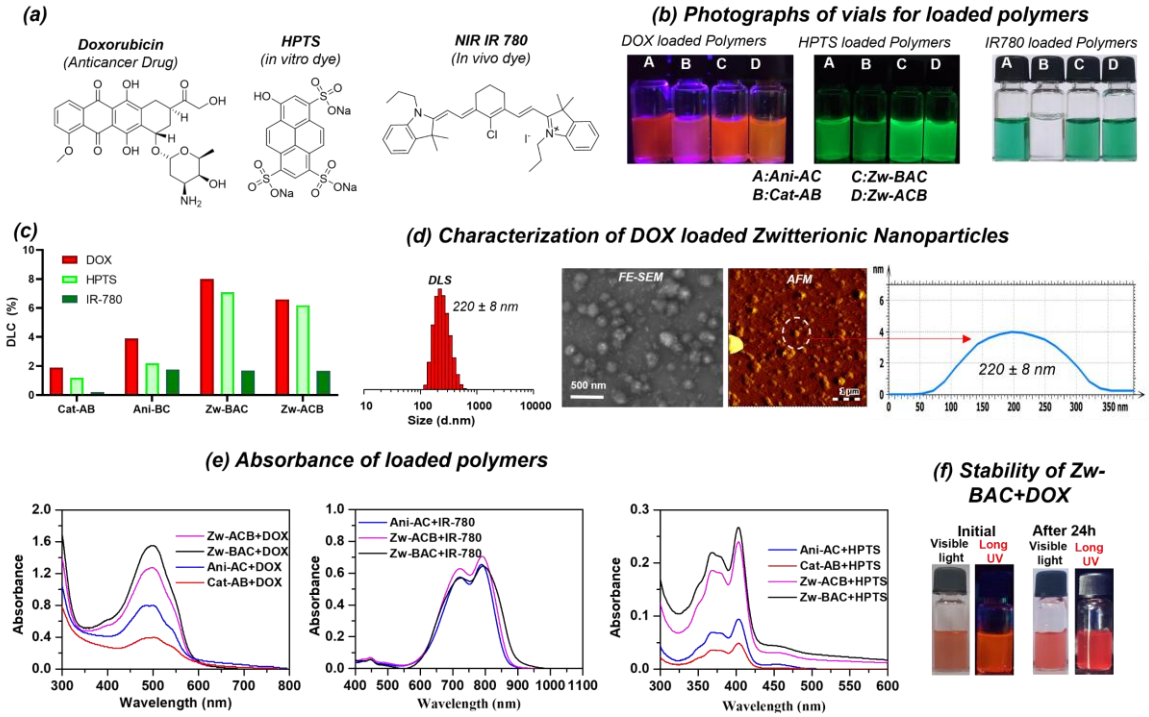

***Figure 4.15**: (a) Structure of cargoes used for encapsulation studies. (b) photographs of vials containing DOX, HPTS and IR780 loaded Nanoparticles. (c) Plot of % DLC for DOX, HPTS and NIR IR-780 loaded nanoparticles. (d) DLS histogram, FE-SEM and AFM image and height profile of Zw-BAC+DOX nanoparticles (concentration = 0.1 mg/mL). (d) Absorbance spectra of DOX, IR780 and HPTS loaded nanoparticles. (e) Photographs of vials containing Zw-BAC+DOX nanoparticles incubated in PBS, pH 7.4 at initial and after 24 hours of incubation under normal light and UV light (Concentrations of NP 1.0 mg/mL).*

Sample	CMC (mg/mL)	DLS Size (d.nm)	PDI	ξ (mV)	DOX loaded Polymers			IR 780 loaded Polymers			HPTS loaded Polymers		
					Size (d.nm)	PDI	ξ (mV)	Size (d.nm)	PDI	ξ (mV)	Size (d.nm)	PDI	ξ (mV)
Cat-AB	0.010	114 ± 2	0.32±0.02	+20.9 ± 1.5	125± 5	0.40±0.01	18.8± 0.9	-	-	-	197± 12	0.65±0.07	-9.9±0.4
Ani-AC	-	190 ± 4	0.38±0.01	-23.4 ± 1.4	200± 6	0.20±0.01	-25.5± 0.7	221± 5	0.47±0.02	-20± 2	256± 15	0.41±0.06	-26±2
Zw-ACB	0.001	215 ± 6	0.25±0.04	-8.1 ± 0.5	200± 5	0.30±0.01	-19.5± 0.7	200± 2	0.25±0.04	-18.1± 1	160± 9	0.18±0.01	-18±1
Zw-BAC	0.002	220 ± 7	0.21±0.01	-11.2± 0.6	220± 7	0.31±0.01	-22± 0.4	220± 6	0.21±0.01	-15.2± 0.4	156± 9	0.36±0.01	-15±0.5
Zw-BC	0001	90±4	0.50±0.04	-7.18 ±1.7	-	-	-	-	-		-	-	

***Table 4.2**: Tabulated details of CMC values, nascent and cargo loaded nanoparticles characterizations such as sizes, polydispersity (PDI, Zeta potentials at pH 7.4.*

Sample	DOX Loaded Polymers		IR-780 loaded Polymers		HPTS loaded Polymers	
	DLC (%)	DLE (%)	DLC (%)	DLE (%)	DLC (%)	DLE (%)
Cat-AB	2.0	20	0.2	2	1.2	12
Ani-AC	4.0	40	1.7	17	2.2	22
Zw-ACB	6.6	33	1.6	16	6.6	66
Zw-BAC	8.0	40	1.7	17	7.1	71
Zw-BC	-	-	-	-	-	-

***Table 4.3**: Tabulated details of DLC and DLE for cargo loaded nanoparticles .*

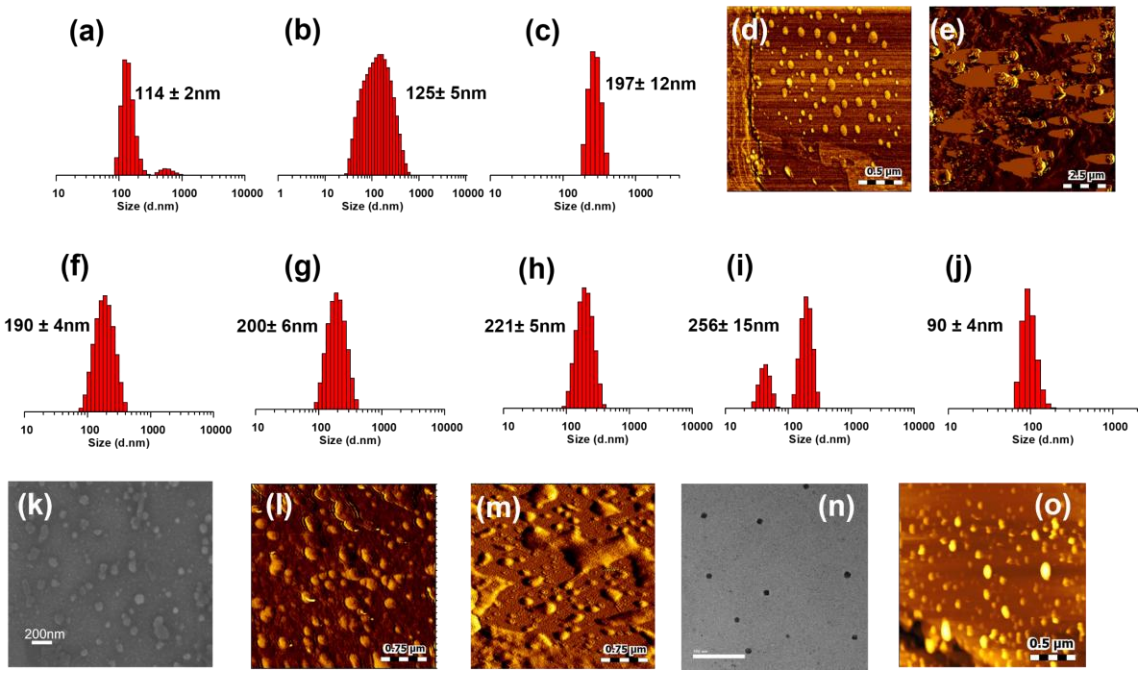

***Figure 4.16:** Self-assembly studies: DLS histogram of (a) Cat-AB nanoparticles, (b) Cat-AB+DOX and (c) Cat-AB+HPTS. AFM images of (d) Cat-AB nanoparticles and (e) Cat-AB+DOX. DLS histograms of (f) Ani-AC nanoparticles, (g) Ani-AC+DOX, (h) Ani-AC+IR-780, (i) Ani-AC+HPTS and (j) Zwitterionic BC nanoparticles. (k) FE-SEM, (l) AFM images of Ani-AC nanoparticles and (m) AFM image of Ani-AC+DOX. (n) HR-TEM (scale bar 0.5µm) and (o) AFM images of zwitterionic BC nanoparticles (Nanoparticles were drop cast at 0.1mg/mL concentration for all imaging analysis and all DLS histograms shown here are % intensity plot or % number plot).*

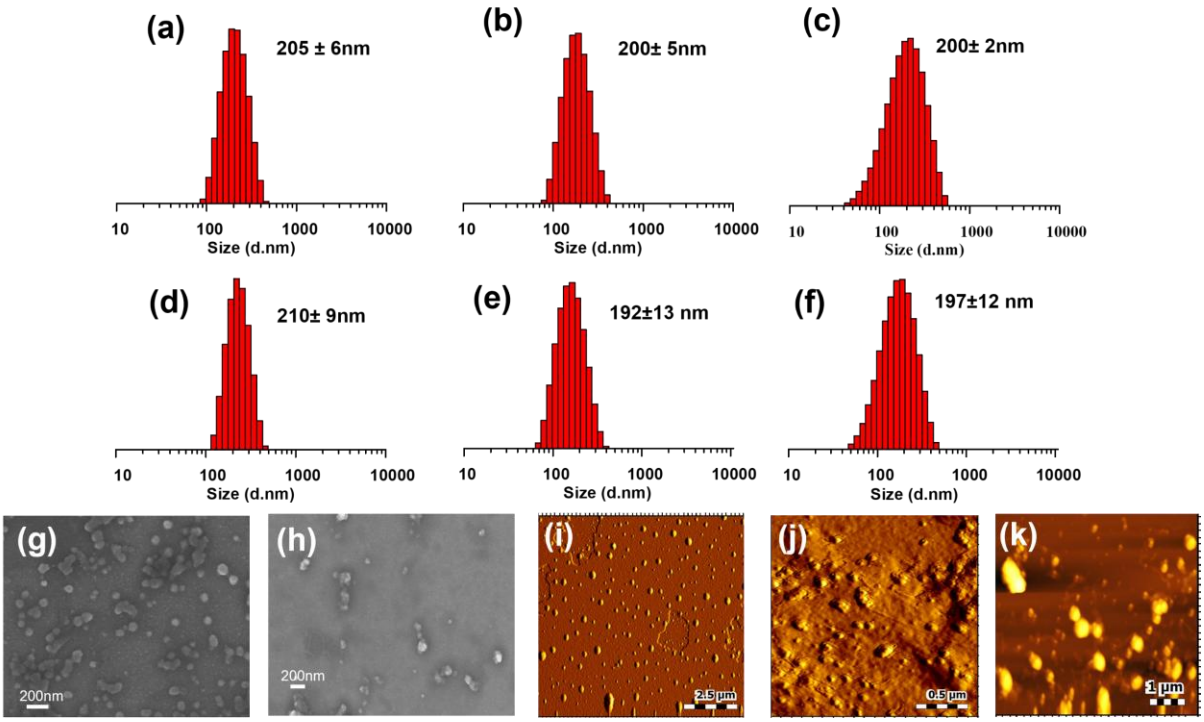

Figure 4.17: *Self-assembly studies: DLS histogram of (a) Zw-ACB nanoparticles, (b) Zw-ACB +DOX, (c) Zw-ACB +IR-780 and (d) Zw-ACB +HPTS, (e) Zw-ACB-30 nanoparticles, (f) Zw-ACB-30+DOX. FE-SEM images of (g) Zw-ACB nanoparticles and (h) Zw-ACB +DOX. AFM images of (i) Zw-ACB nanoparticles, (j) Zw-ACB and (k) Zw-ACB +IR-780. (Nanoparticles were dropcasted at 0.1mg/mL concentration for all imaging analysis and all DLS histograms shown here are % intensity plot or % number plot).*

Sample	Composition			CMC (mg/mL)	Size (d.nm)	PDI	DOX loaded samples			
	PCL (x)	PAE (y)	tBuPCL (z)				DLC (%)	DLE (%)	Size (d.nm)	PDI
Zw-ACB	60	55	45	0.001	215 ± 6	0.25±0.04	6.6	33	200± 5	0.30±0.01
Zw-ACB30	45	35	35	0.001	192±13	0.33±0.01	5.0	25	197±12	0.32±0.01
Zw-BAC	60	44	45	0.002	220 ± 7	0.21±0.01	8.0	40	220± 7	0.31±0.01
Zw-BAC30	45	30	30	0.001	221±14	0.30±0.01	4.0	20	222±14	0.26±0.01

Table 4.4*: Table summarizes the compositions, CMC, DLS sizes and DLCs of triblock copolymers.*

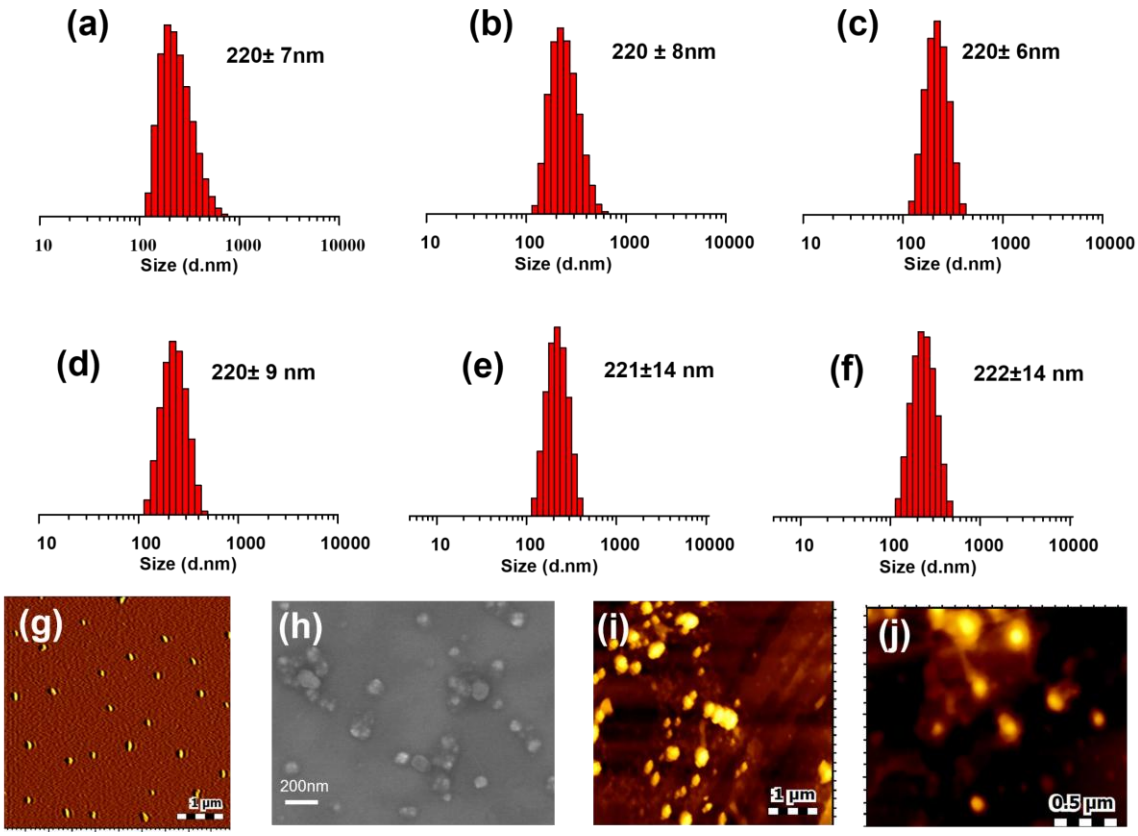

Figure 4.18: *Self-assembly studies: DLS histogram of (a) Zw-BAC nanoparticles, (b) Zw-BAC +DOX, (c) Zw-BAC +IR780 and (d) Zw-BAC +HPTS, (e) Zw-BAC-30 nanoparticles, (f) Zw-BAC-30+DOX. (g) AFM image of Zw-BAC nanoparticles. (h) FE-SEM image of Zw-BAC+DOX . AFM images of (p) Zw-BAC+IR-780 and (q) Zw-BAC+HPTS. (Nanoparticles were dropcasted at 0.1mg/mL concentration for all imaging analysis and all DLS histograms shown here are % intensity plot or % number plot).*

4.3.5 Extracellular Stability and Enzyme-Responsive Drug Release

Upon endocytosis by the cells, the zwitterionic nanoparticles transported via the acidic-endosomal and enzyme-rich lysosomal compartments as shown in Figure 4.19a. The zwitterionic nanoparticle encounter two scenarios in endo-lysosomal compartments: (i) the acidic pH environment stabilizes the cationic PAE chains in the amine-protonated form; thus, the nanoparticles are stable, and they do not undergo self-immolation, and (ii) the aliphatic ester linkages in the anionic carboxylic PCL backbone would readily undergo biodegradation by the lysosomal esterase-enzymes. The second process would indeed create zwitterionic

imbalance followed by the degradation of anionic PCL units and disturbed the overall self-assembly of the nanoparticles. This would facilitate the release the DOX from the endo-lysosomal compartments as shown in Figure 4.19a (also Figure 4.1b). In the event of PAE blocks escaping to cytosol pool, the self-immolation mechanism is expected to set in (as earlier reported in the CARTs)[19-21] for complete chopping up into non-toxic oligomeric species. Thus, the entire zwitterionic triblock would be biodegraded by the combination of lysosomal enzymatic-digestion and self-immolation mechanisms.

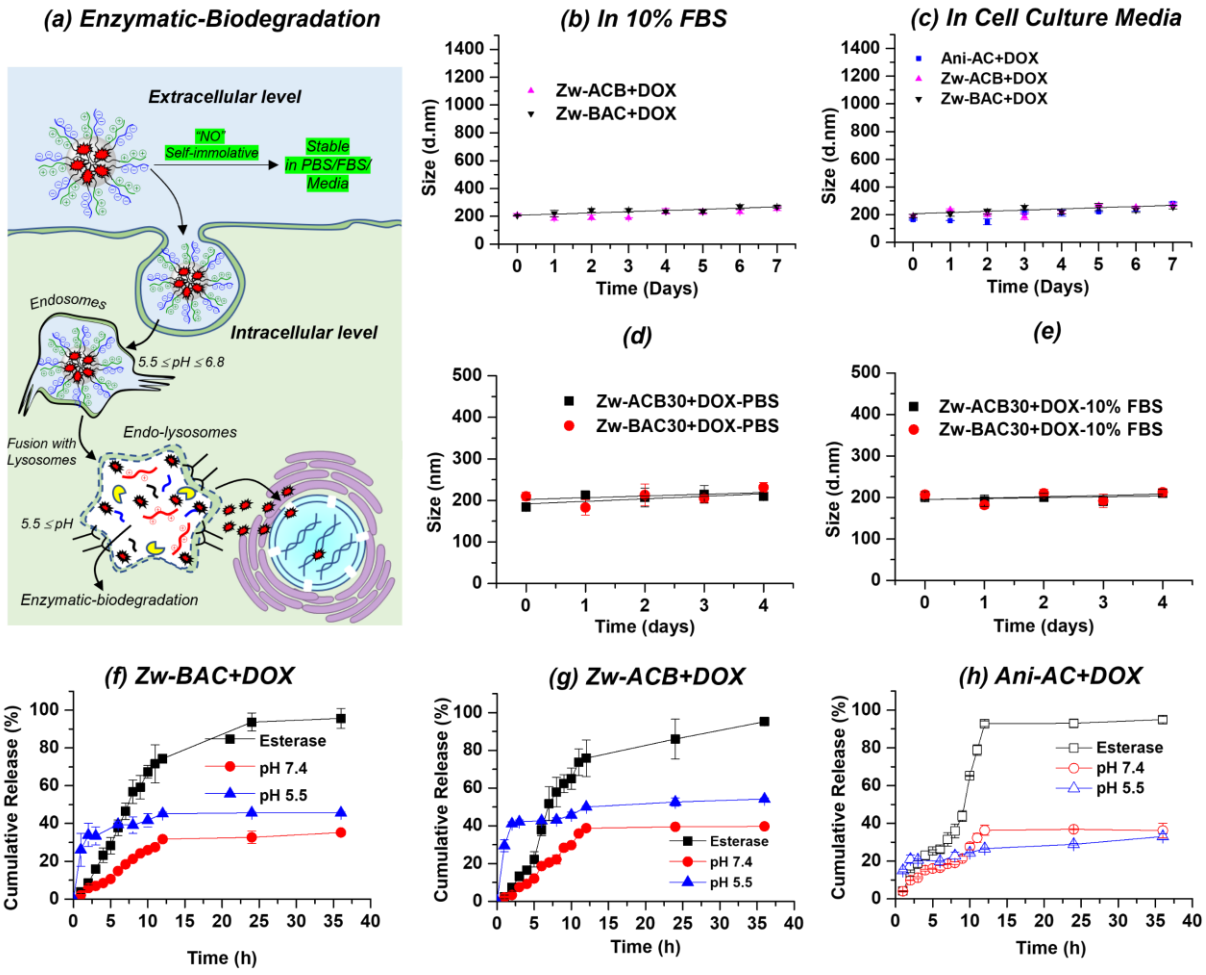

Figure 4.19. *(a) Schematic representation of intracellular delivery and release of DOX loaded nanoparticles. Colloidal stability: (b) Plot of DLS size of Zw-BAC+DOX and Zw-ACB+DOX nanoparticles incubated in 10% FBS in PBS, pH 7.4 at 37 ℃ for 7 days. (c) DLS plot of sizes of DOX loaded nanoparticles obtained after incubating them for 7 days at 37℃ in cell culture media (10% FBS in DMEM). (d) and (e) Plot of colloidal stability for Zw-ACB and Zw-BAC-30+DOX nanoparticles. (f) to (h) In vitro drug release profile of Zw-BAC+DOX nanoparticles in the presence of 3 U/mg of horse liver esterase enzyme or in the absence of enzyme in PBS, pH=7.4 and pH 5.5 at 37 ℃ respectively.*

To study the extracellular stability of the zwitterionic nanoparticles, they were subjected to stability analysis by DLS in PBS, pH=7.4 at 37 °C, 10 % FBS in PBS, DMEM media for more than a week and the data is shown in Figure 419b-4.19e . Interestingly, the DOX-loaded zwitterionic triblock copolymer nanoparticles (Zw-BAC+DOX and Zw-ACB+DOX) exhibited excellent stability for more than 7 days without any trace of precipitation or degradation. The in vitro drug release kinetics were conducted in presence of horse liver esterase enzyme (HLE, 3 U/mg) in PBS, pH 7.4 at 37ºC and absence of esterase (control experiment) and the plot is shown in Figure 4.19f. Zw-BAC+DOX nanoparticles exhibited 80-90% drug release in 24h of incubation in presence of esterase. The release study was done by dialysis method in the absence of enzyme (only in PBS at 37 °C). The initial drug release reached maximum 28 % (± 5 %) in 12 h and continued to be stable for 36 h. The drug leaching in PBS in the absence of the enzyme was attributed to the influence of high salt concentration on the nanoparticles which are routinely observed by earlier investigations.[62] The drug release profiles of Zw-ACB+DOX and Ani-AC+DOX are reported in Figure 4.19g-h. Moreover, DOX loaded triblock nanoparticles did not show significant release in presence of pH 5.5 as shown in Figure 4.19f-4.19h, suggesting that currently designed zwitterionic nanoparticles are only enzyme-responsive. The enzymatic-biodegradation aspects were also investigated by DLS in the absence of the enzyme (only in PBS at 37 °C) and in the presence of horse liver esterase enzyme (HLE, 3 U/mg) in PBS, pH 7.4 at 37ºC as shown in Figure 4.20. In the presence of the enzymes (in PBS at 37 °C), the hydrophilic carboxylic PCL undergo biodegradation which in turn expected to impart imbalance in the charge neutralization on the PAE segments for self-immolation. As a result, the overall self-assembly of the polymer nanoparticle is disturbed and the degraded debris precipitates in the medium to give large size aggregates as seen in DLS in the Figure 4.20. The increase in the DLS size followed almost a similar kinetics as shown in the absorbance-based data (in Figure 4.19f-h). The enzyme-degraded polymer aliquots were also subjected to MALDI-TOF analysis, and the data for Zw-BAC triblock is shown in Figure 4.21 and appendix. The degraded polymer samples showed peaks corresponding to oligomeric units of < 5-8 confirming both the enzymatic biodegradation of PCL units and hydrolytic degradation of PAE units.

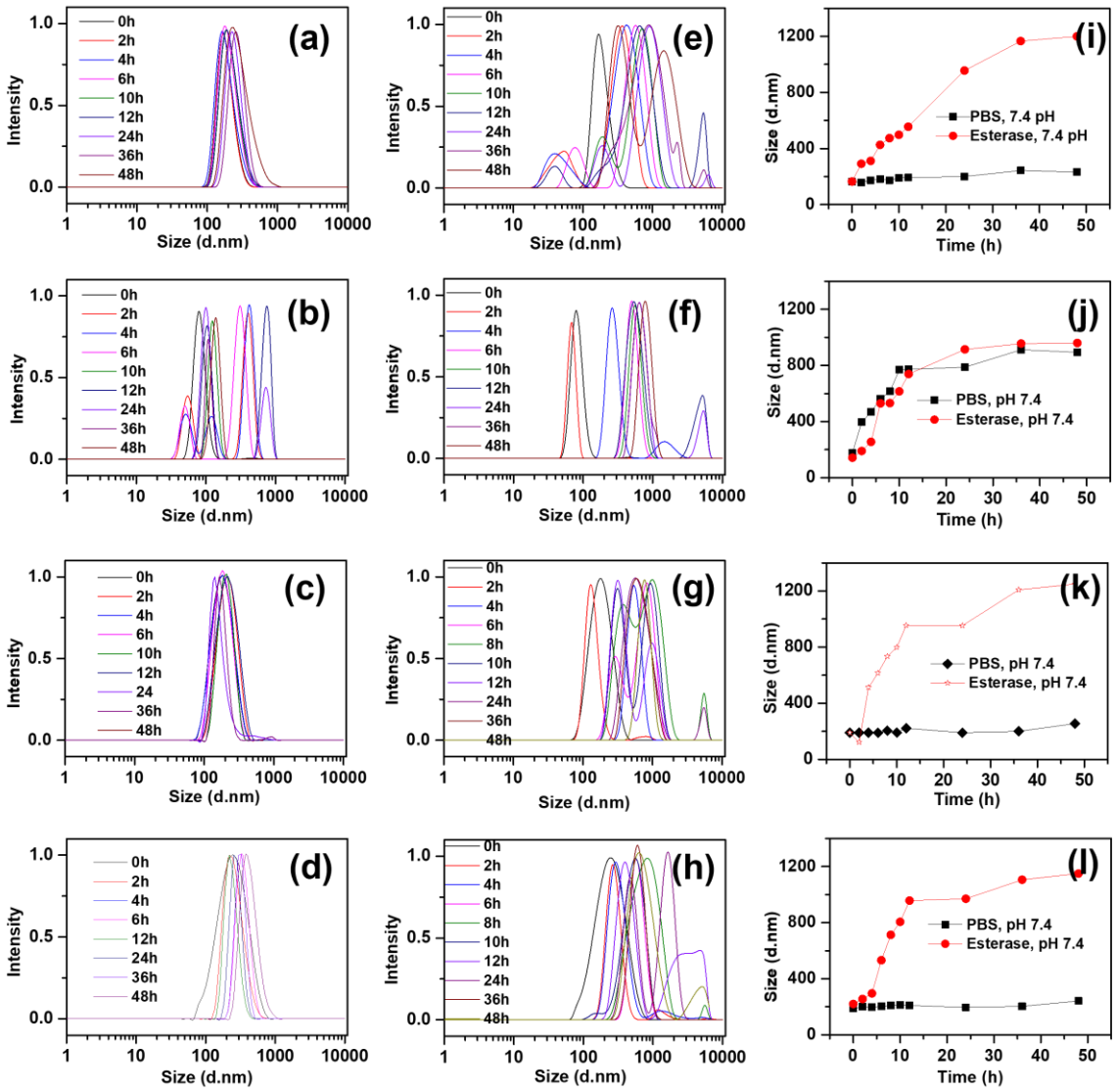

Figure 4.20: Enzymatic degradation study of DOX loaded nanoparticles by DLS*; DOX loaded nanoparticles were incubated in PBS (pH 7.4) and in presence of Esterase enzyme (pH 7.4, PBS) at 37ºC for 48h b: Plots of DLS histogram of DOX loaded nanoparticles in pH 7.4 at 37ºC (a) Ani-AC+DOX, (b) Cat-AB+DOX, (c) Zw-ACB+DOX and (d) Zw-BAC+DOX. Plots of DLS histogram of DOX loaded nanoparticles in presence of Esterase enzyme at 37ºC (e) Ani-AC+DOX, (f) Cat-AB+DOX, (g) Zw-ACB+DOX and (h) Zw-BAC+DOX. Cumulative size plots of (i) Ani-AC+DOX, (j) Cat-AB+DOX, (k) Zw-ACB+DOX and (j) Zw-BAC+DOX.*

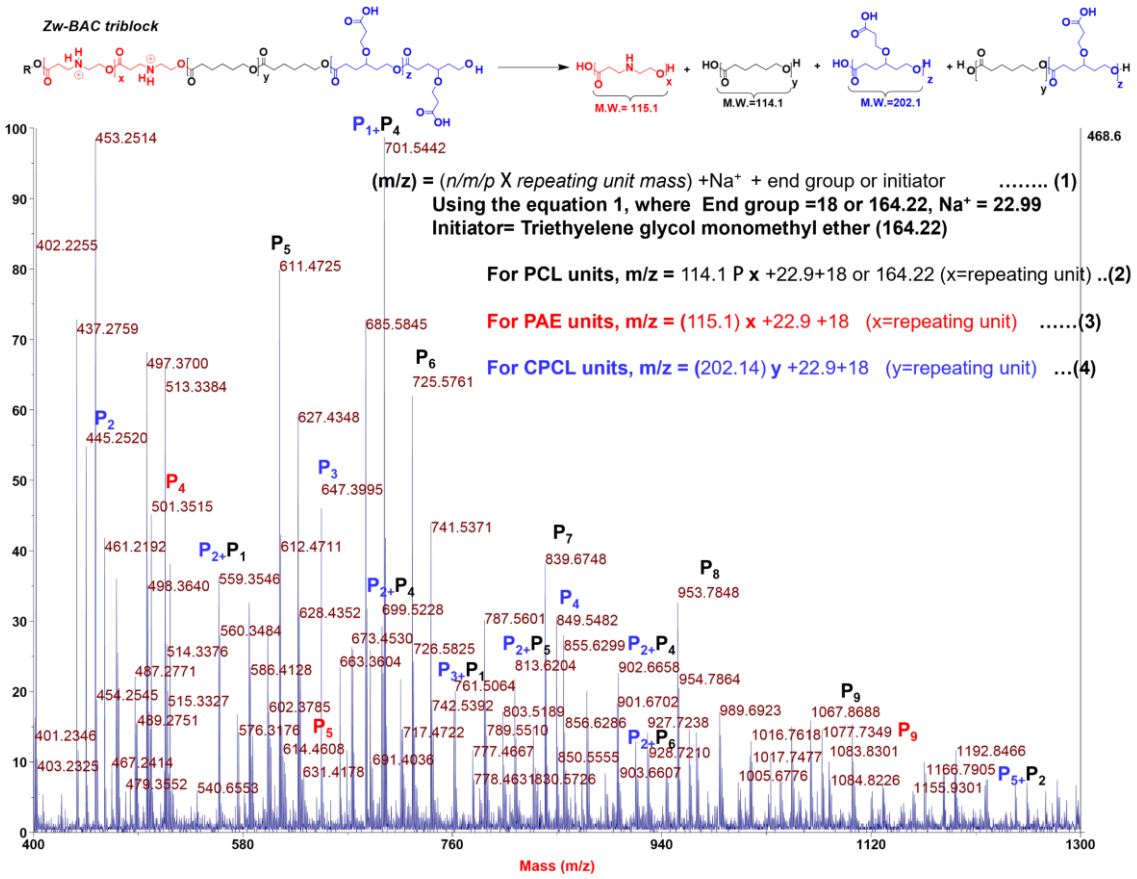

Figure 4.21: *MALDI-TOF spectra of Zw-BAC triblock after incubating with esterase enzyme in pH 7.4. at 37ºC for 24h. Peaks are assigned for degraded oligomers in spectra.*

4.3.6 Endocytosis and Live-Cell Biodegradation

Endocytosis of the polymer nanoparticle is an energy driven process;[68-69] thus, the cellular uptake of zwitterionic particles was studied at 37 ºC and 4 ºC in MCF-7 cell line. Both Zw-BAC+DOX and Zw-ACB+DOX nanoparticles were incubated for 3h at both these temperatures and the cells were fixed for CLSM imaging and are shown in Figure 4.22. The corrected total cell fluorescence (CTCF) values in Figure 4.22b and 4.22d depicted 7-10-fold higher cellular uptake for DOX loaded nanoparticles at 37 ºC compared to 4 ºC. This result proved that these nanoparticles were taken up by endocytosis pathway which occurs predominantly only at physiological temperature. To provide direct proof of lysosomal colocalization and lysosomal enzymatic biodegradation of DOX loaded nanoparticles, live cell confocal imaging[62] was done for Zw-BAC+DOX nanoparticles in WT-MEF cells using lysotracker as shown in Figure 4.23. Zw-BAC+DOX nanoparticles were readily taken up by cells and they were predominately co-localized in the cytosol and appeared as yellow color due to colocalization of green (lysotracker DND-26) and red (DOX). At initial time points (30 min zoomed image), there is no DOX present in the nucleus; however, with the progress of

incubation time, one could clearly notice the accumulation of DOX at the nucleus (at 120 min zoomed image). After 8h incubation (480 min zoomed image), the DOX predominately accumulated in the nucleus. DOX loaded Zw-ACB triblock also exhibited lysosomal biodegradation as similar to zwitterionic BAC triblock system and images are shown in Figure 4.24. It was revealed in Figure 4.24 that the Zw-ACB+DOX underwent lysosomal degradation evident from the co-localization (yellow) in the cytoplasm of lysotracker (green) with DOX (red) from 30 min to 120 min images. Further DOX can be seen in the nucleus at 180 min or higher timepoints suggests that Zw-ACB+DOX underwent lysosomal bio-degradation. In contrast, live-cell imaging of free DOX under the identical conditions showed direct diffusion pathway without going through the lysosomal compartment as depicted in Figure 4.25. The live-cell real-time drug release kinetics, thus strongly supports the co-localization of zwitterionic nanoparticles in the lysosome for the enzymatic-biodegradation to release the cargoes (DOX) to the nucleus and a validation the mechanism given in Figure 4.19a.

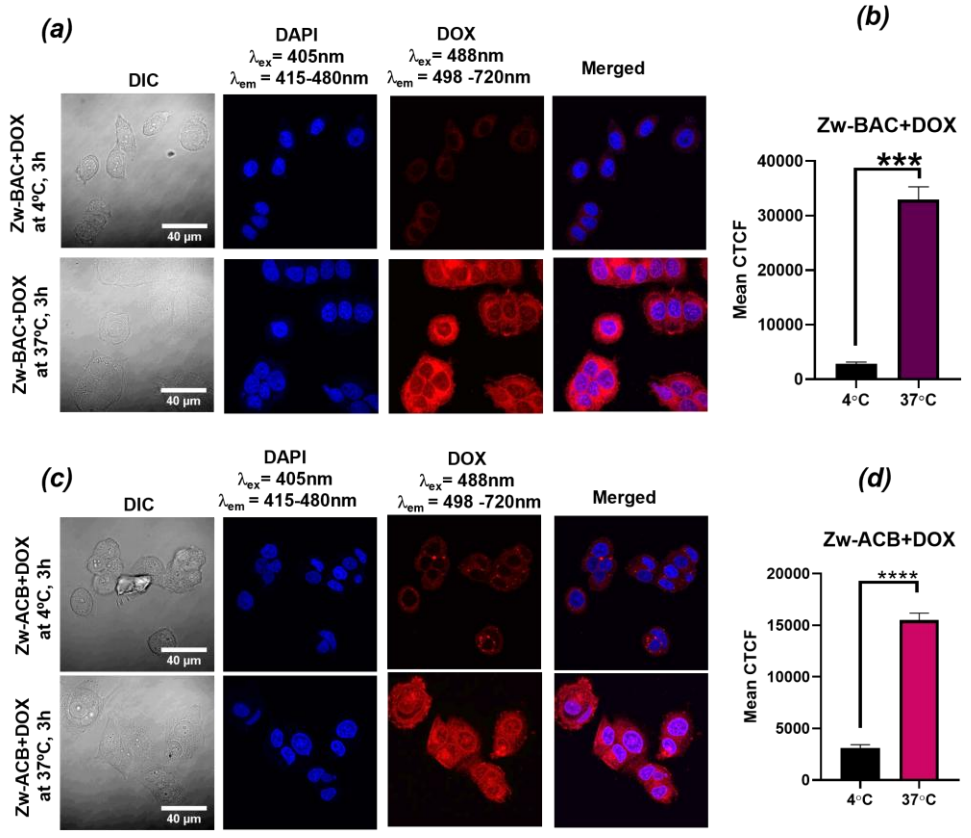

Figure 4.22. *(a) Energy-dependent CLSM images of cellular uptake of the Zw-BAC+DOX at 37 ℃ and 4℃ in MCF 7 cell line (3h incubation, DOX concentration 2.5µg/mL). (b) Plot of CTCF (n=3) for 37 ℃ and 4℃ incubated samples in MCF 7 cell line (n=3, ***P=0.0003). (c) CLSM images of temperature dependent cellular upatke studies of Zw-ACB+DOX nanoparticles at 4℃ and 37℃ for 3h incubation in MCF-7 cells. (d) mean CTCF plot for Zw-ACB+DOX (n=3,****p<0.0001).*

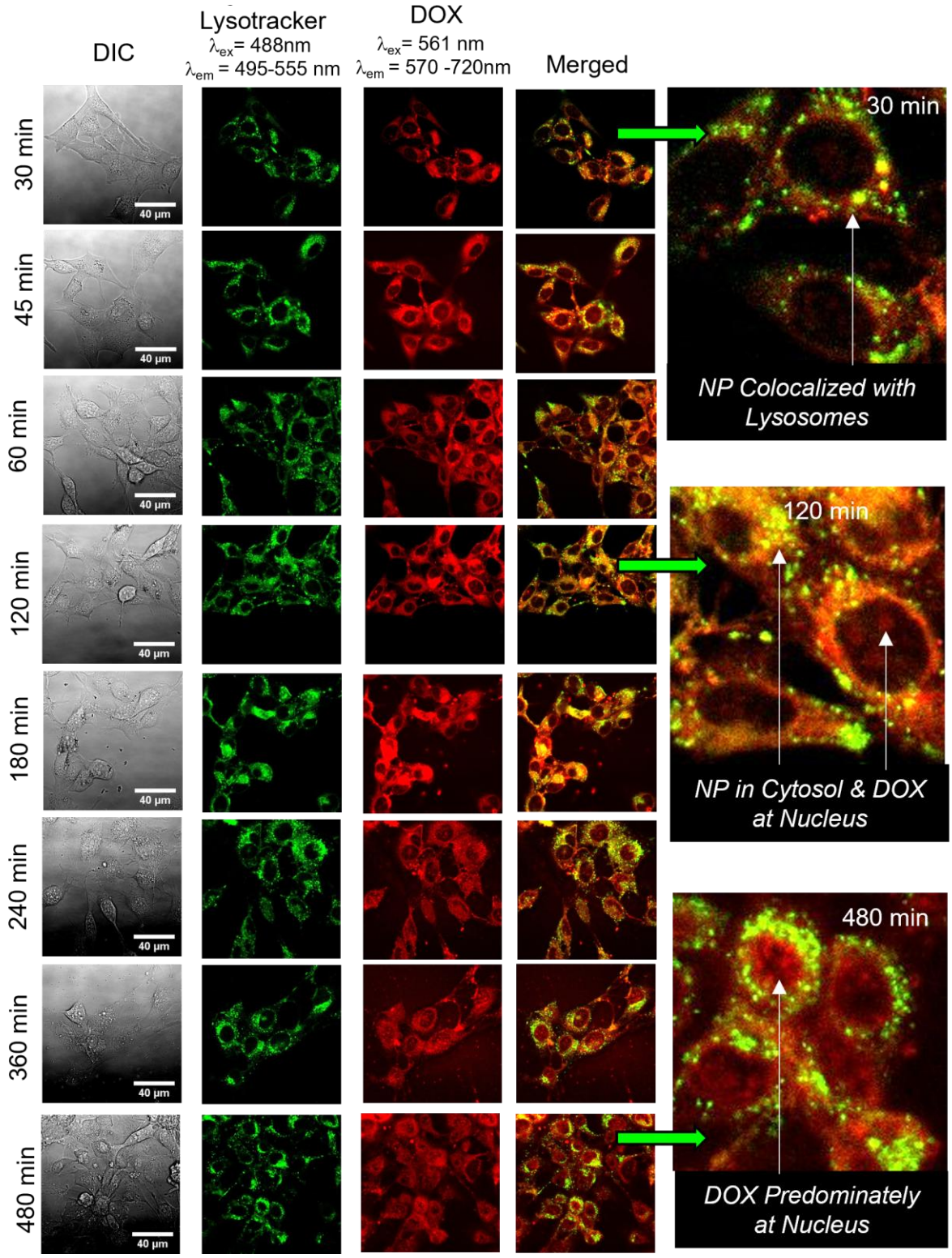

Figure 4.23. *Time dependent live-cell images using lysotracker for Zw-BAC+DOX nanoparticles (scale bar 40µm) in WT-MEF cells. Cells were visualized using 488 nm (green channel for Lysotracker green DND-26) and 561 nm (red channel for DOX) channel respectively. (DOX concentration 5 µg/mL).*

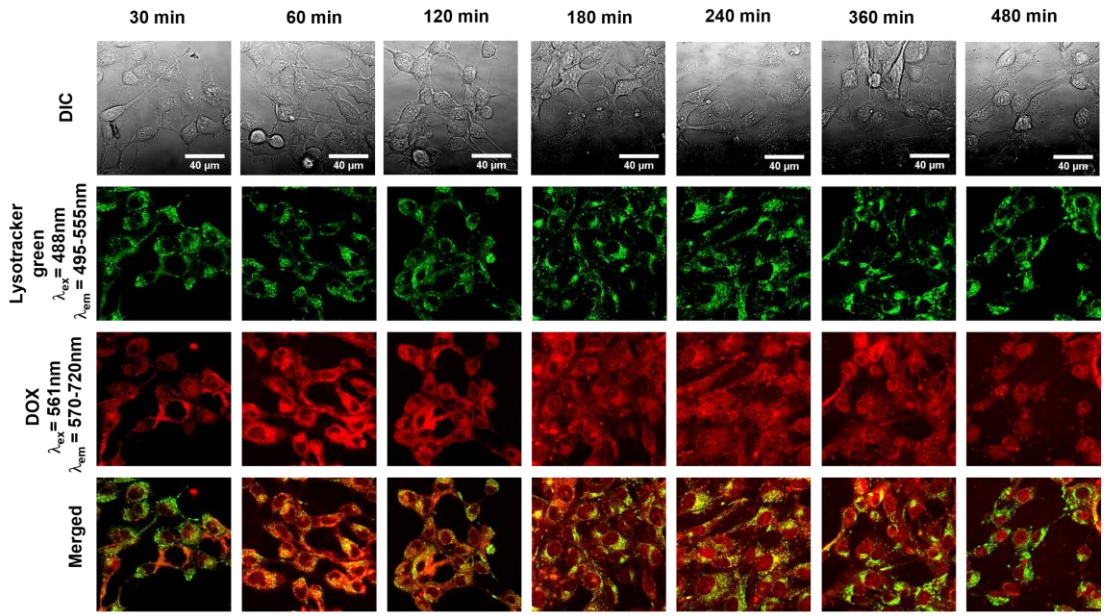

Figure 4.24: *CLSM images of time dependent live cell imaging carried out for Zw-ACB +DOX nanoaprticles in presence of lysotracker in WT-MEF cells. Cells were visualized using 488 nm (green channel for Lysotracker green DND-26) and 561 nm (red channel for DOX) channel respectively. (DOX concentration 5µg/mL).*

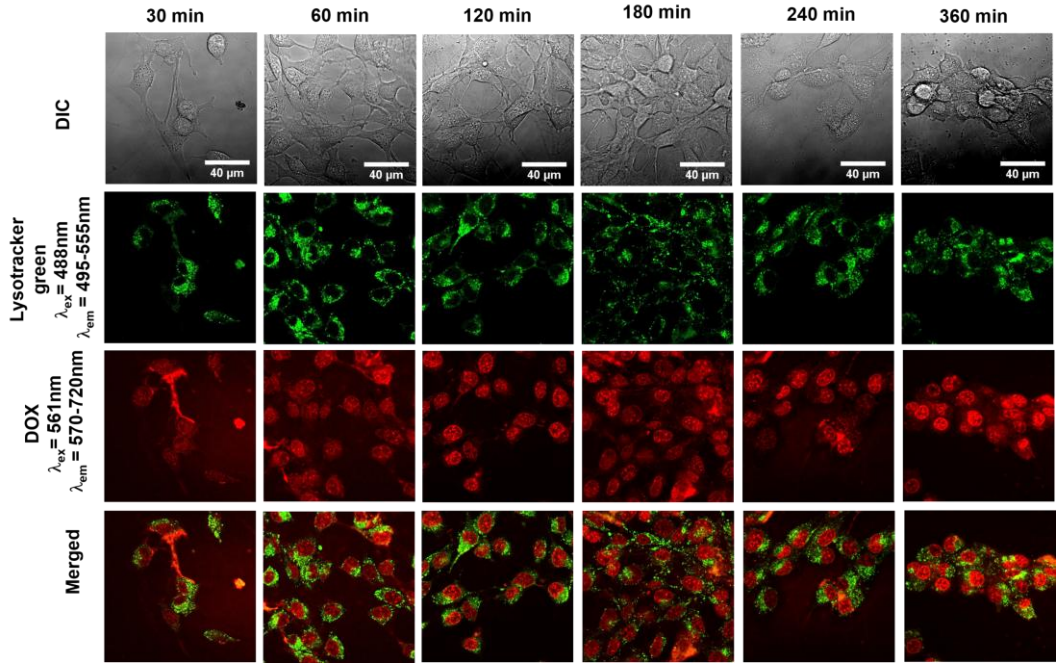

Figure 4.25: *CLSM images of time dependent live cell imaging carried out for free DOX in presence of lysotracker in WT-MEF cells. Cells were visualized using 488 nm (green channel for Lysotracker green) and 561 nm (red channel for DOX) channel respectively. (DOX concentration 5µg/mL).* ***Note:*** *Free DOX did not show any co-localization with lysotracker suggests that it has been taken up cells via diffusion pathway (common pathway for small molecules).*

4.3.7 Cytotoxicity and Cellular Uptake Studies

The zwitterionic polymer nanoparticles were evaluated for their cytocompatibility in non-cancerous cell line (WT-MEF), breast cancer cell line (MCF-7) and ovarian cancer cell line (SKOV-3) by MTT assay in Figures 4.26a to 4.26c. The nascent Zw-BAC and Zw-ACB triblock nanoparticles exhibited excellent cytocompatibility up to 100 μg/mL having 90 % cell viability. Doxorubicin (DOX) is a Topoisomerase II inhibitor which acts by DNA intercalation, interfering with the DNA replication process causing cell apoptosis. From the Figure 4.26a, in WT-MEF cell line, the IC_{50} values for Zw-BAC+DOX and Zw-ACB+DOX were obtained at 0.1-0.2 μg/mL concentration which is comparable to that of free DOX. More than 90 % of cells underwent apoptosis suggesting that DOX could be efficiently delivered from zwitterionic nanoparticles. From the plot shown in Figure 4.26b and 4.26c, the cell killing efficiency was observed to be high in MCF-7 and SKOV-3 cell lines indicating ability of Zw-BAC+DOX and Zw-ACB+DOX in DOX resistant cancer lines and their IC_{50} was obtained at a concentration 0.4 μg/mL. The cellular uptake of Zw-BAC+DOX and Zw-ACB+DOX was further studied in SKOV-3 cell line by CLSM and shown in Figure 4.27a. The magenta color at nucleus and yellowish color at cytoplasm of cells in the merged image in Figure 4.27a, resulted from colocalization of DOX with DAPI (blue) and phalloidin (green) indicating that DOX reached the nucleus predominantly as well as in the cytoplasm. A slight difference was noticed among these two Zw polymer nanoparticles in Figure 4.27a. The Zw-ACB polymer has hydrophobic PCL at one-end of the triblock design; thus, it resulted in better segregation for hydrophobic PCL and hydrophilic chains constituted by carboxylic PCL and PAE together. Therefore, hydrophilic periphery was readily exposed to enzyme for faster degradation in aqueous medium. In case of Zw-BAC, the hydrophobic PCL chains located at the middle of triblock design rendered relatively slow degradation compared to Zw-ACB. This difference in the architectures account for the variation in the release profiles among the triblock copolymers and the Zw-ACB seems to be a better candidate to release the drugs at the intracellular level. The CTCF values in Figure 4.27b supported that DOX delivery was more efficient while delivery from zwitterionic platform; however, a slight difference could be noticed among the two triblock as well as the types of cancer cell lines. SKOV-3 cell line showed much higher uptake of DOX compared to MCF-7. Based on image quantification as shown in Figure 4.27b, mean CTCF calculation suggested 1.5 to 3-fold higher uptake for Zw-BAC+DOX and Zw-ACB+DOX compared to free DOX, which is noteworthy.

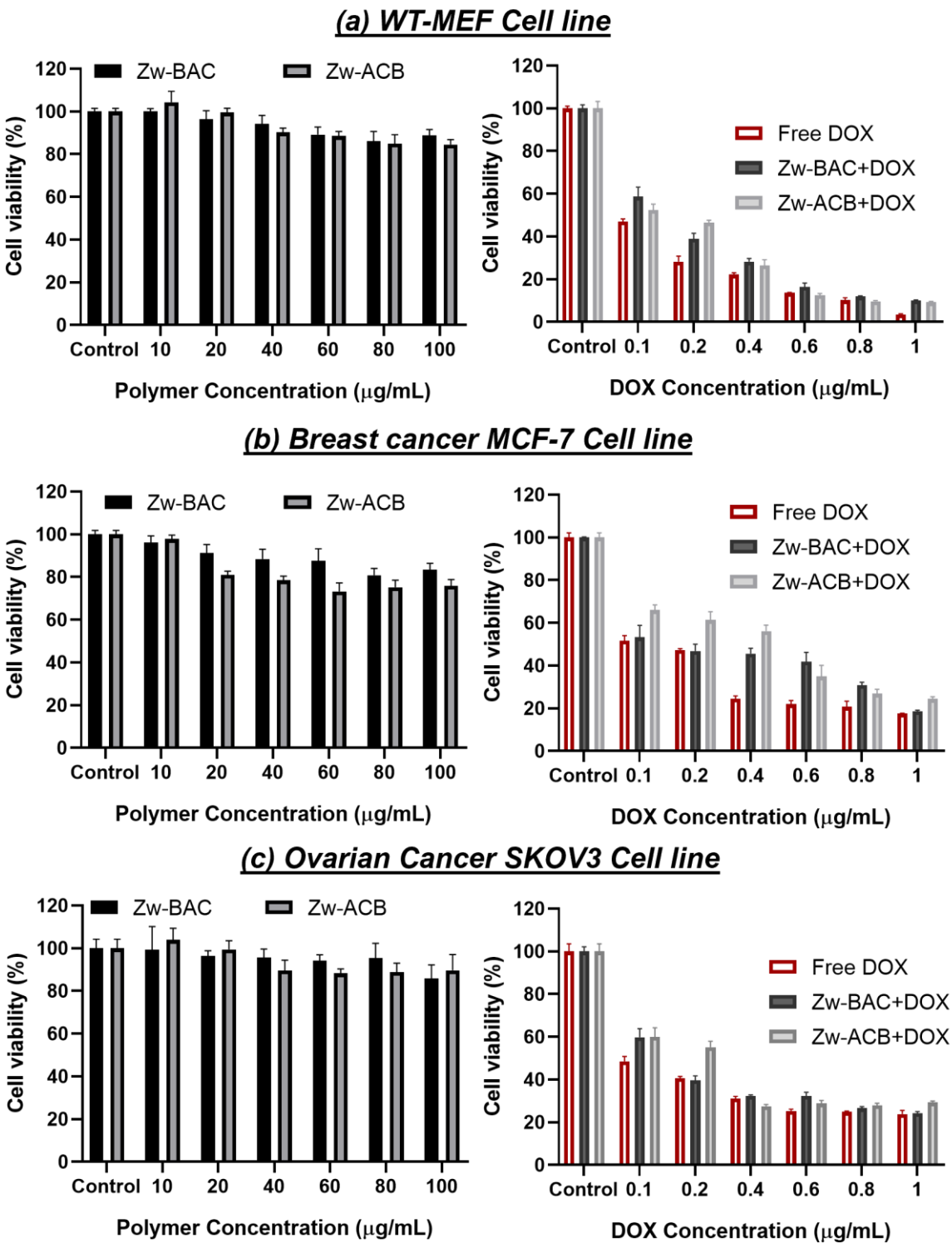

Figure 4.26. *Cytotoxicity of nascent Zw-BAC and Zw-ACB nanoparticles, and their DOX loaded samples, and free DOX in (a) WT-MEF, (b) breast cancer MCF-7, and (c) ovarian cancer SKOV-3 cell lines for 72 h incubation (DOX concentration of 0.1 – 1.0 μg/mL). Results are expressed as mean ± SEM (n=3).*

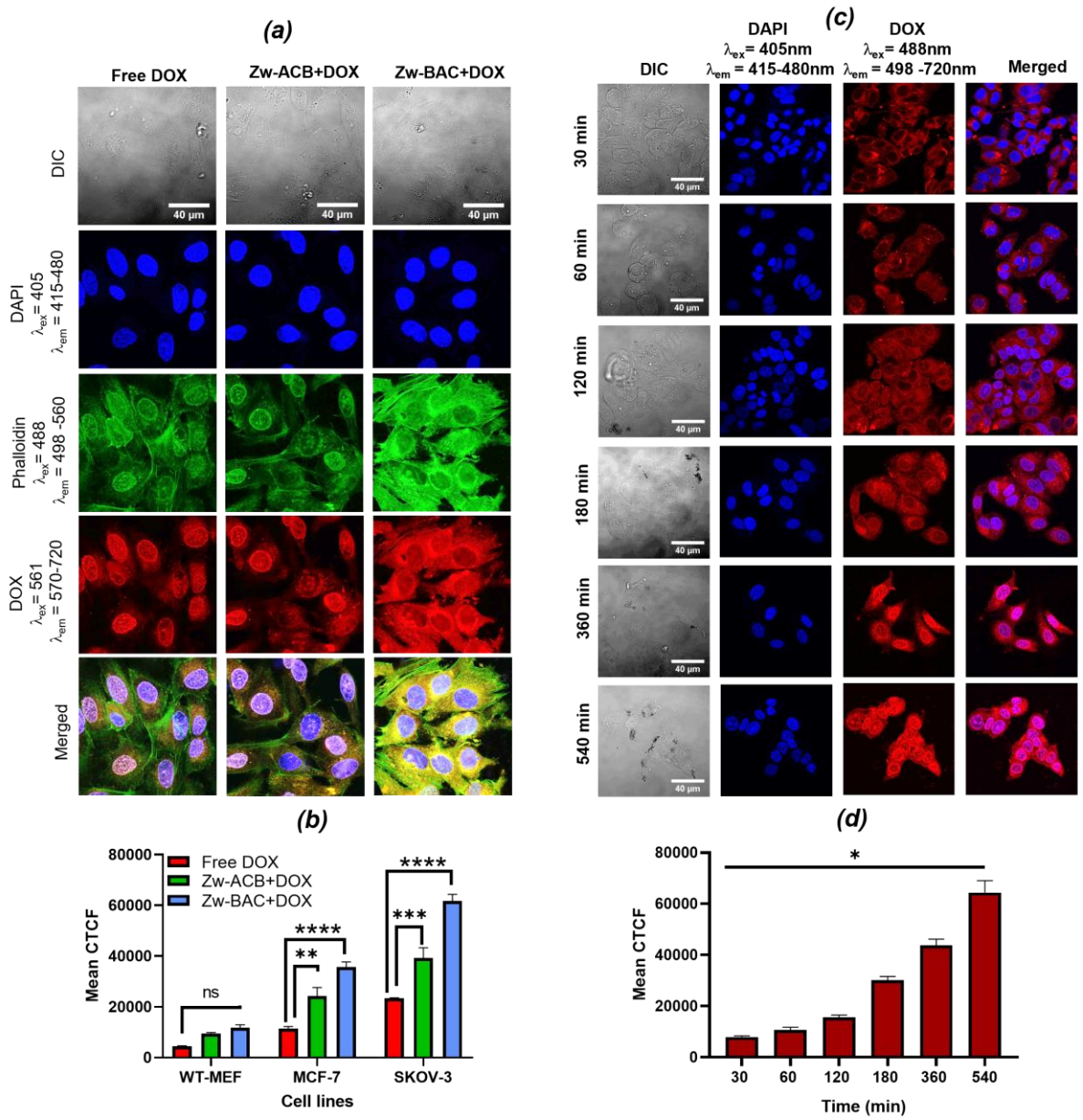

Figure 4.27. *(a) CLSM images of cellular uptake in SKOV-3 cell line incubated with free DOX, Zw-BAC+DOX and Zw-ACB+DOX for 4h (DOX concentration 2.5 µg/mL). (b) Plot of CTCF for DOX, Zw-BAC+DOX and Zw-ACB+DOX in WT-MEF, MCF-7 and SKOV-3 (4h incubation). All results are expressed as mean±SEM (n>6) (**P = 0.0012, ***P = 0.0001, **** P < 0.0001). (c) Time-dependent CLSM images of Zw-BAC+DOX nanoparticles in MCF 7 cell line for various incubation period (DOX concentration 2.5µg/mL). (d) Plot of CTCF for DOX uptake for time dependent cellular uptake. (*P<0.05) (Note: CLSM images were captured with 63X, and scale bar is 40 µm for all CLSM images).*

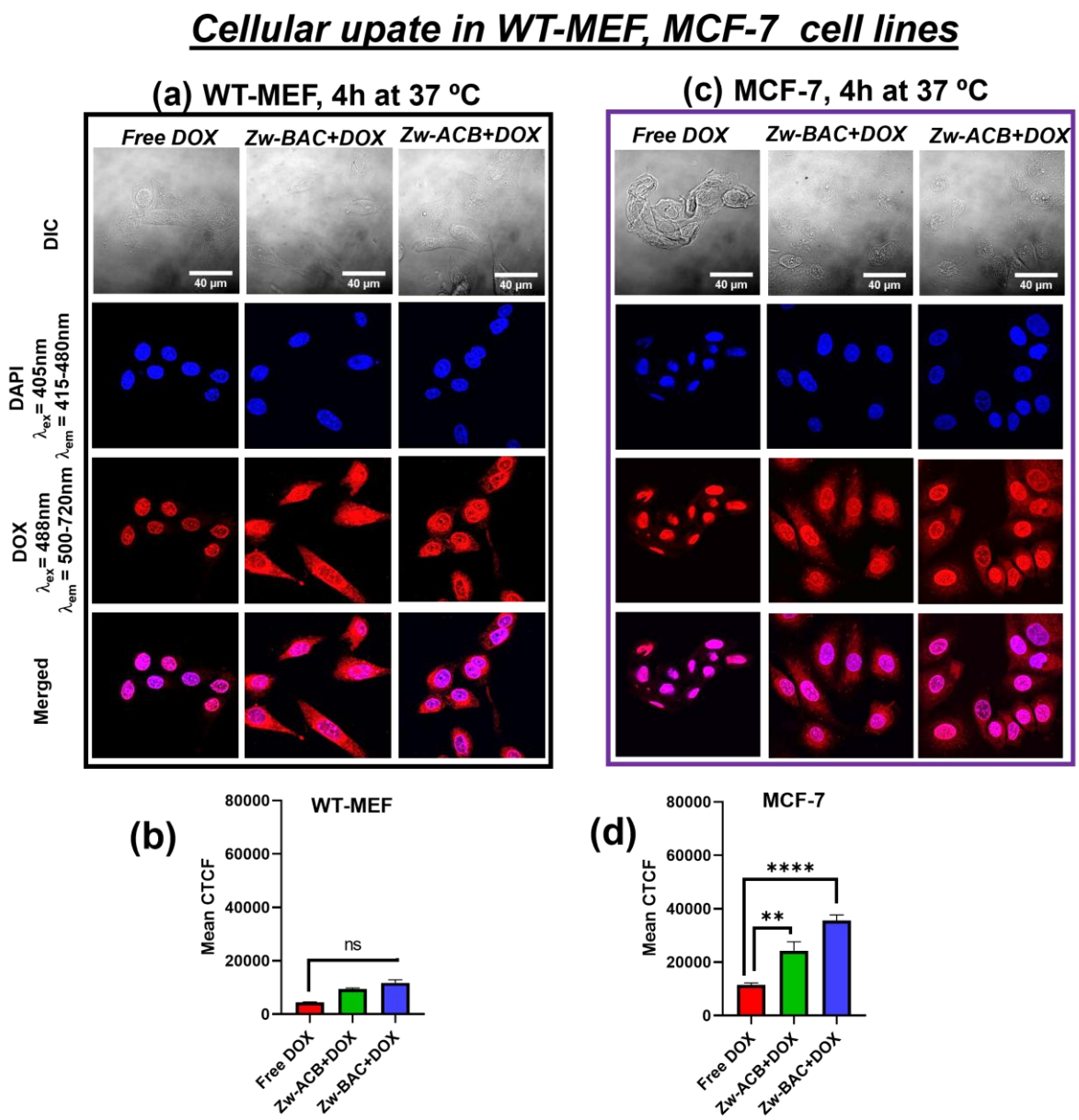

Figure 4.28: *CLSM images of cellular uptake of free DOX, Zw-BAC+DOX and Zw-ACB+DOX nanoparticles at 37ºC for 4h incubation in WT-MEF cells and MCF-7 cell lines. Images were counterstained with DAPI (nuclei).DAPI and DOX visualized using 405nm and 488nm channel respectively: (a) Imaging panel showing cellular upatke of nanoparticles. Merge panel represents colocalized images of DAPI and DOX channels in WT-MEF cell line. (b) Plot showing CTCF for DOX , Zw-BAC+DOX and Zw-ACB+DOX nanoparticles in WT-MEF cells for 4h incubation. (c) Imaging panel showing cellular upatke of free DOX , Zw-BAC+DOX and Zw-ACB+DOX nanoparticles in MCF-7 cell line. Merge panel represents colocalized images of DAPI and DOX channel. (d) Plot showing CTCF for DOX , Zw-BAC+DOX and Zw-ACB+DOX nanoparticles in MCF-7 cells for 4h incubation. (**p<0.05, ****p<0.0001).*

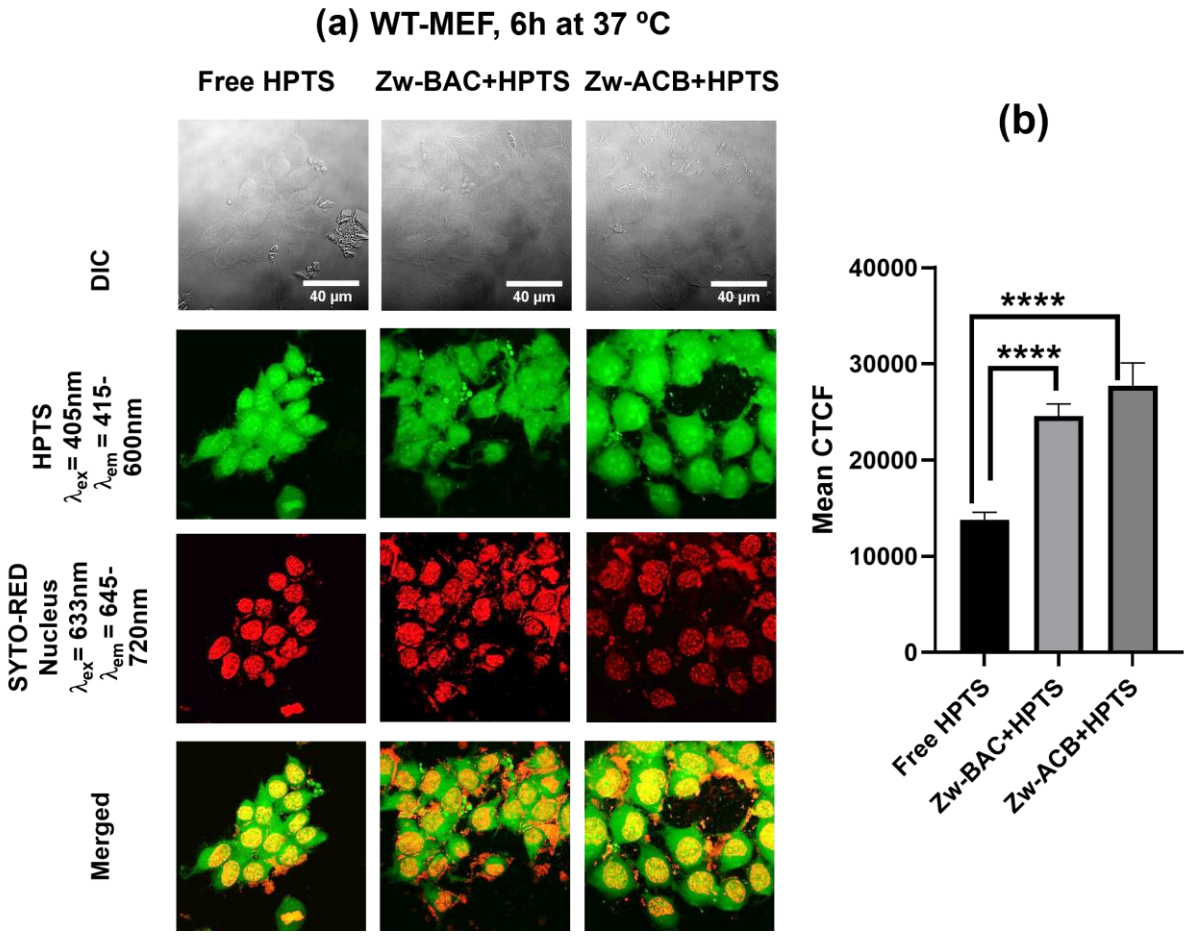

Figure 4.29: *(a) CLSM images of cellular upatke studies of HPTS loaded Zw-BAC+HPTS and Zw-ACB+HPTS nanoparticles and free HPTS at 37ºC for 6h incubation in WT-MEF cells. Images were counterstained with SYTO-deepRed 633 (nuclei). SYTO and HPTS visualized using 633 nm and 405 nm channel respectively, at 37ºC for 6h incubation. (b) Mean CTCF plot for the same. (****p<0.0001).*

Time dependent cellular uptake studies were performed in MCF-7 cells. Cells were incubated with Zw-BAC+DOX nanoparticles from 30 min to 9 h and their corresponding CLSM images are shown in Figure 4.27c. In the initial stages, the DOX fluorescence signal was predominately observed in the cytoplasm and with increasing incubation the DOX emission enhanced in the nucleus. The CTCF values suggested that cellular uptake for DOX loaded nanoparticles increased linearly with time as shown in in the CTCF plot in Figure 4.27d. This trend further confirmed that the DOX loaded nanoparticles successfully cleaved in the lysosomal compartment and released the DOX to nucleus, which supported the mechanism in Figure 4.19a. Based on the time-dependent cellular uptake both in live-cell real-time analysis (Figure 4.23, and 4.24) and fixed cell line (in Figure 4.27), we can conclude that the tailor-

made zwitterionic polymers are very stable at extracellular environment at neutral pH and the design evaded the self-immolation of the PAE segments. This enabled them to be readily internalized to undergo lysosomal enzymatic-biodegradation to deliver the loaded cargoes such as DOX and HPTS. In the event PAE escaped to the cytoplasm from the endo-lysosomal compartment, it has inherent ability to undergo self-immolation at the intracellular level. CLSM images for cellular uptake of Zw-BAC+DOX and Zw-ACB+DOX nanoparticles in WT-MEF and MCF-7 cell lines are shown in Figure 4.28. Furthermore, the efficiency of the Zw-BAC and Zw-ACB nanoparticles to deliver water-soluble biomarker HPTS was also examined in WT-MEF cells in Figure 4.29.

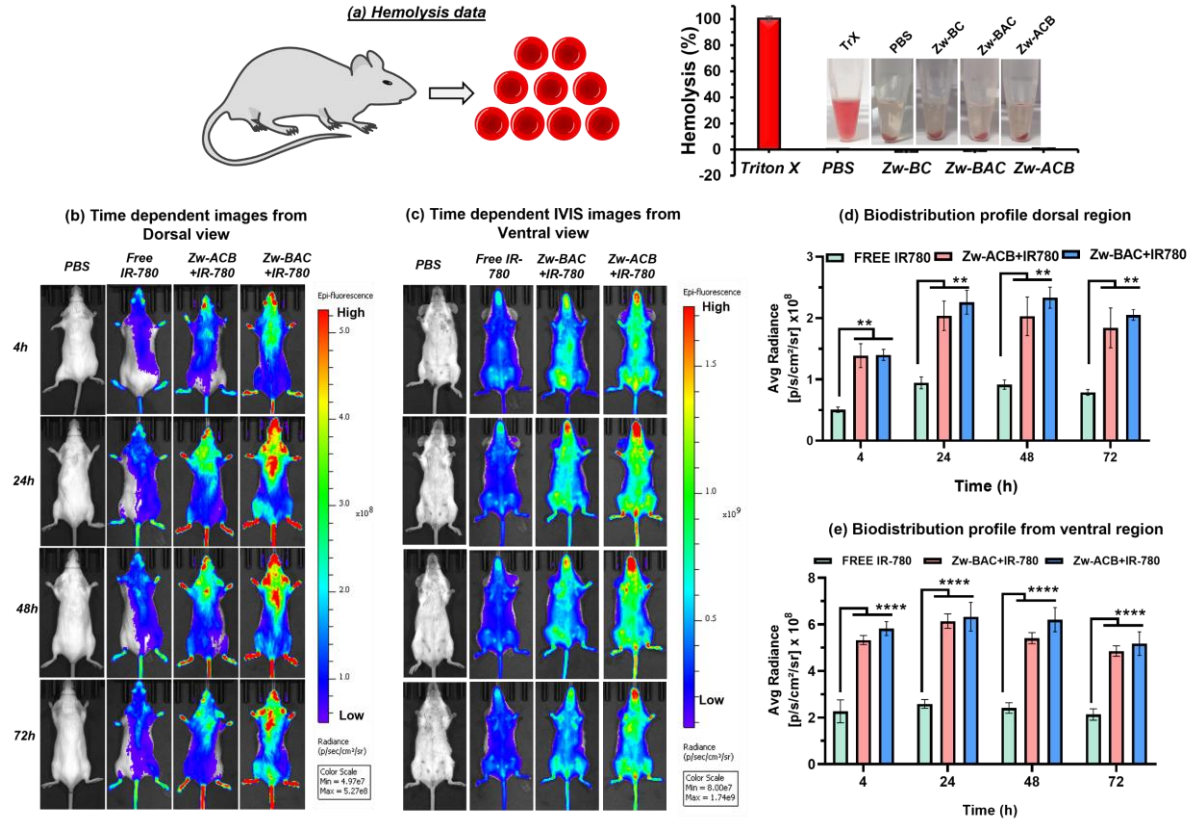

Figure 4.30. *(a) Hemolysis data for Zw-BC, Zw-BAC and Zw-ACB nanoparticles (polymer concentration 1.0 mg/mL) along with TrX as positive control and PBS saline buffer as negative control at pH 7.4. IVIS mediated live animal whole body fluorescence bioimaging showing the panel of time dependent images for (b) dorsal view and (c) ventral view for mice intraperitoneally injected with PBS, Free IR-780, Zw-BAC+IR780 and Zw-ACB+IR780. (d) and (e) Real time quantificational plot of average radiance vs time calculated from dorsal and ventral images respectively. All data point represented as mean±SEM (n=3) (** P = 0.0036, ** P = 0.0012, ****p<0.0001, ANOVA test).*

4.3.8 Hemolysis and In Vivo Biodistribution Studies

The hemolysis data shown in Figure 4.30a, depicted that these zwitterionic nanoparticles were completely non-hemolytic in nature at 1 mg/mL concentration without any % hemolysis and further can be employed for *in vivo* analysis. Deep tissue penetrable near infrared IR-780 iodide probe loaded nanoparticles were utilized for biodistribution analysis via IVIS in adult female Balb-C mice by intraperitoneal administration. The NIR IR-780 loaded Cat-AB di-block polymer nanoparticle was not stable in PBS due to self-immolation of polymer backbone; thus, the mice experiments could not be performed. Zw-BC di-block polymer was freely soluble in water, and it did not load NIR IR-780 biomarkers. Therefore, Cat-AB and Zw-BC polymers were not subjected to in vivo analysis. PBS and free IR-780 were used as control. The whole-body images at various time points are shown in Figure 4.30b and for dorsal images (for ventral images, see Figure 4.30c). From the images it can be seen that Zw-BAC+IR780 and Zw-ACB+IR780 depicted higher fluorescence signals compared to free IR-780 dye. All the mice injected with nanoparticles showed signals from early 4h timepoint throughout whole body indicating uptake of zwitterionic nanoparticles in entire body and the intensity enhanced with time and signals were persistent up to 72h for both the systems indicating prolonged circulation of nanoparticles in dorsal as well as ventral images attributed to zwitterionic nature of polymer. Image-based quantification for dorsal and ventral images are shown in the form of plot in Figure 4.30d (for ventral image, see Figure 4.30e), which suggested that Zw-BAC+IR780 and Zw-ACB IR780 system exhibited 2 to 3-fold higher signal compared to free IR780 dye (statistically significant) due to their prolonged circulation. The animals injected with Zw-BAC+IR780 and Zw-ACB+IR780 exhibited much more intense signals in plasma compared to free IR780 dye at both the timepoints (24 and 72h) attributed to prolonged circulation in blood (Figure 4.31a). Quantified data suggests 2-3-fold higher signal in Zw-BAC+IR780 and Zw-ACB+IR780 system compared to free IR 780 as shown in Figure 4.31b. Further *ex-vivo* organ biodistribution study was carried out and the images are shown in Figure 4.31c. Quantified data for organ biodistribution seen in Figure 4.31d suggested accumulation of nanoparticles in major excretory organs such as liver and kidney. It can be concluded form the biodistribution analysis that Zw-BAC+IR780 and Zw-ACB+IR780 nanoparticles system demonstrated enhanced blood circulation for prolonged time in mice body and they did not excrete completely out of the body even at longer period of 72h due to their stability in blood and their enzymatic biodegradable nature. Therefore, they are promising candidates for various drug delivery applications *in vivo*. In a nutshell, the present investigation demonstrates the

potential of zwitterionic triblock strategy to stabilize the otherwise unstable self-immolative PAEs under physiological pH and established their ability to function as a potential drug delivery vector by in vitro real-time live-cell bioimaging and in vivo biodistribution analysis in mice. The strategy further opened new opportunities to combine the enzyme-biodegradable polycaprolactone with self-immolative polymers in drug delivery research. The approach is not restricted to the selection of polymer candidates, anticancer drugs or NIR probes, or 1D linear block copolymer architectures; in principle, this strategy can be expanded to other polymeric systems including 3D macromolecular systems.

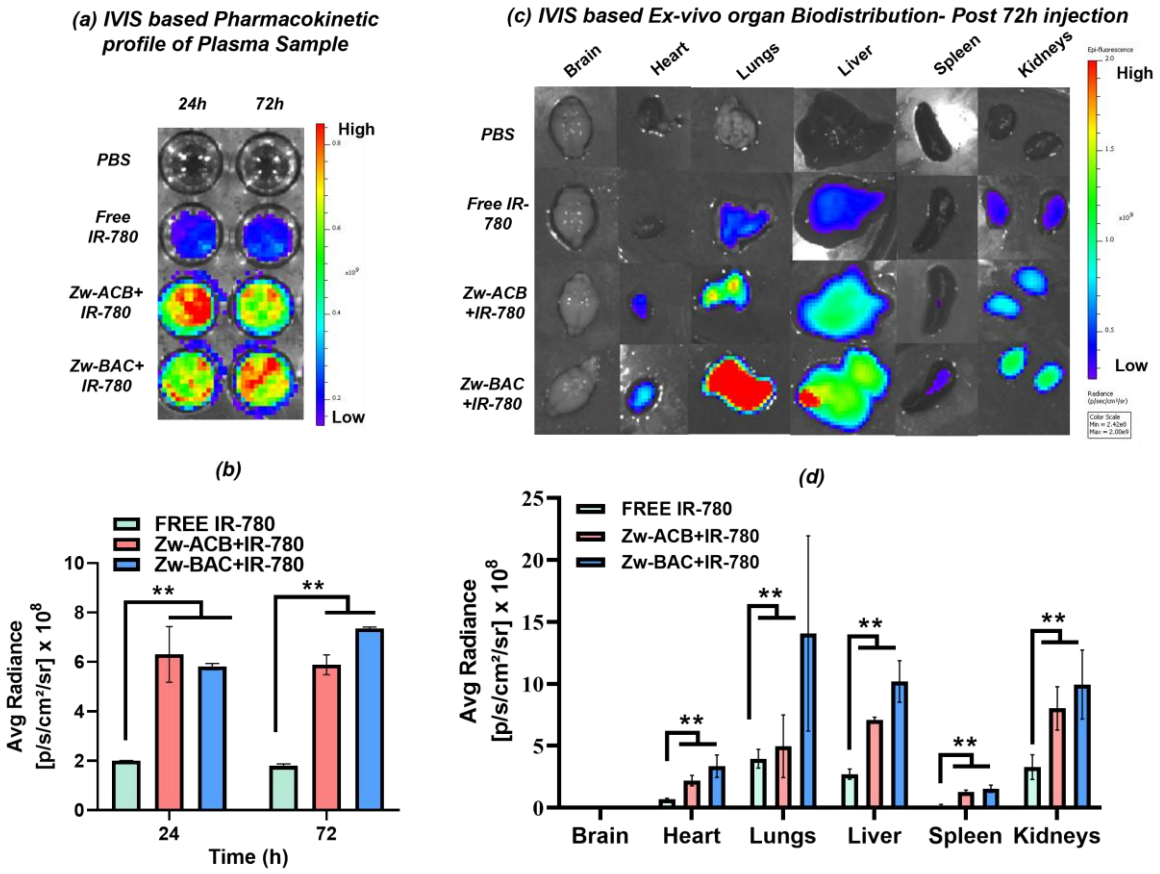

Figure 4.31: *IVIS based pharmacokinetics:(a) Compiled IVIS fluorescent images of plasma sample at 24 h and 72h. (b) Plot of average radiances vs time quantified from fluorescence images of plasma samples for 24h and 72h timepoint. All data point represented as mean±SEM (n=3) (** P = 0.0014).(c) Compiled IVIS images of organs harvested after pericardial perfusion post 72h of injection. (d) Plot of average radiance vs time representing organ specific biodistribution for free IR-780, Zw-BAC+IR780 and Zw-ACB+IR780 nanoparticles. All data point represented as mean±SEM (n=3) (** P = 0.0025).*

4.4 Conclusion

We demonstrate a strategy to stabilize self-immolative PAEs through electrostatic interactions by incorporating fully enzyme- biodegradable carboxylic acid-PCL into a zwitterionic block-copolymer. The pH dependent self-assembly studies revealed excellent stability of these spherical nanoparticles across a pH range of 3-11. Notably, they retained their size during this pH variation. They were able to efficiently encapsulate DOX, IR780 and HPTS with appreciable DLCs. Which remained stable in PBS, FBS and cell culture media at physiological pH. The zwitterions underwent enzymatic biodegradation releasing 90 % DOX within 24h and exhibited biocompatibility with WT-MEF, MCF-7 SKOV-3 and they were also found to be non-hemolytic RBCs (red blood cells) up to 1.0 mg/mL concentration. The DOX loaded nanoparticles were efficient in killing cells and they were internalized via endocytosis and underwent lysosomal biodegradation. Live-cell lysotracker mediated imaging exhibited controlled release of DOX loaded zwitterionic polymers and 3-4 -fold higher cellular uptake compared to free DOX in breast cancer and ovarian cancer cell lines. *In vivo* biodistribution studies using near IR-780 biomarker loaded nanoparticles exhibited prolonged blood circulation and longer retention in organs over a period of 72h period compared to free IR780. The current strategy showcases the engineering of fully biodegradable zwitterionic diblock and triblock copolymer and their self-assembly and drug delivery aspects. Consequently, these zwitterionic nanoparticles hold great promise as drug delivery systems for treating various cancer and other diseases in long-term in biomedical field.

4.5 References

1) Roth, M. E.; Green, O.; Gnaim, S.; Shabat, D. Dendritic, Oligomeric, And Polymeric Self-Immolative Molecular Amplification. *Chem. Rev.* **2016**, *116*, 1309-1352.
2) Yardley, R. E.; Kenaree, A. R.; Gillies, E. R. Triggering Depolymerization: Progress and Opportunities for Self-Immolative Polymers. Macromolecules 2019, 52, 6342-6360.
3) Wong, A. D.; Dewit, M. A.; Gillies, E. R. Amplified Release Through the Stimulus Triggered Degradation of Self-Immolative Oligomers, Dendrimers, And Linear Polymers. *Adv. Drug Delivery Rev.* **2012**, *64*, 1031-1045.
4) Sirianni, Q.E.A.; Gillies, E. Self-Immolative Hydrogels Via in Situ Gelation. *Polymer* **2020**, *202*, 122638.
5) Liu, G.; Zhang, G.; Hu, J.; Wang, X.; Zhu, M.; Liu, S.; Hyperbranched Self-Immolative Polymers (Hsips) For Programmed Payload Delivery and Ultrasensitive Detection. *J. Am*. *Chem. Soc*. **2015**, *137*, 11645-11655.
6) Liu, G.; Wang, X.; Hu, J.; Zhang, G.; Liu, S. Self-Immolative Polymersomes for High Efficiency Triggered Release and Programmed Enzymatic Reactions. *J. Am. Chem. Soc.* **2014**, *136*, 7492-7497.
7) Sagi, A.; Weinstein, R.; Karton, N.; Shabat, D. Self-Immolative Polymers. *J. Am. Chem. Soc*. **2008**, *130*, 5434-5435.
8) Shelef, O.: Gnaim, S.; Shabat, D. Self-Immolative Polymers: An Emerging Class of Degradable Materials with Distinct Disassembly Profiles. *J. Am. Chem. Soc.* **2021**, *143*, 21177-21188.
9) Gao, J.; Dutta, K.; Zhuang, J.; Thayumanavan, S. Cellular- And Subcellular-Targeted Delivery Using Simple All-In-One Polymeric Nanoassembly. *Angew. Chem. Int. Ed.* **2020**, *59*, 23466-23470.
10) Deng, Z.; Liang, X.; Gillies, E. Clock Oy Self-Immolation: A "Click" Functionalization Strategy Towards Triggerable Self-Immolative Homopolymers and Block Copolymers. *Angew. Chem. Int. Ed.* **2023**, 63, E202317063.
11) Alouane, A.; Laubruere, R.; Saux, T. L.; Schmidt, F.; Jullien, L. Self-Immolative Spacers: Kinetic Aspects, Structure-Property Relationships, And Applications. *Angew. Chem. Int. Ed.* **2015**, 54, 7492-7509.
12) Sirianni, Q. E. A.; Liang, X.; Such, G. K.; Gillies, E. R. Polyglyoxylamides with A Ph-Mediated Solubility and Depolymerization Switch. *Macromolecules* **2021**, *54*, 10547-10556.
13) Sirianni, Q. E. A.; Wang, T.; Borecki, A.; Deng, Z.; Ronald, J. A.; Gillies, E. R. Self-Immolative Polyplexes for DNA Delivery. *Biomater. Sci*. **2022**, *10*, 2557-2567.
14) Miller, K. A.; Morado, E. G.; Samanta, S. R.; Walker, B. A.; Nelson, A. Z.; Sen, S.; Tran, D. T.; Whitaker, D. J.; Ewoldt, E. H.; Braun, P. V.; Zimmerman, S. C. Acid-Triggered, Acid-Generating and Self-Amplifying Degradable Polymers. *J. Am. Chem. Soc.* **2019**, *141*, 2838-2842.
15) Chattarji, S.; Ramakrishnan, S. Hyperbranched Polyacetals with Tunable Degradation Rates. *Macromolecules* **2011**, *44*, 4658-4664.

16) Blake, T. R.; Ho, W. C.; Turlington, C. R.; Zang, X.; Huttner, M. A.; Wender, P. A.; Waymouth, R. M. Synthesis and Mechanistic Investigations of Ph-Responsive Cationic Poly (Aminoester)S. *Chem. Sci*. **2020**, *11*, 2951-2966.
17) Lynn, D. M.; Langer, R. Degradable Poly (B-Amino Esters): Synthesis, Characterization, And Self-Assembly with Plasmid DNA. *J. Am. Chem. Soc*. **2000**, *122*, 10761-10768.
18) Keenely, M.; Ong, S-G.; Padila, A.; Yao, Z.; Goodman, S.; Wu, J. C.; Yang, F. Development of Poly (B-Amino Esters)-Based Biodegradable Nanoparticles for Nonviral Delivery of Minicircle DNA. *ACS Nano* **2013**, *7*, 7241-7250.
19) Mckinlay, C. J.; Vargas, J. R.; Blake, T. R.; Hardy, J. W.; Kanada, M.; Contag, C. H.; Wender, P. A.; Waymouth, R. M. Charge-Altering Releasable Transporters (Carts) For the Delivery and Release of mRNA In Living Animals. *Proc. Natl. Acad. Sci USA.* **2017**, *114*, E448-E456.
20) Mckinlay, C. J.; Banner, N. L.; Haabeth, O. A.; Waymouth, R. M.; Wender, P. A. Enhanced mRNA Delivery into Lymphocytes Enabled by Lipid-Varied Libraries of Charge-Altering Releasable Transporters. *Proc. Natl. Acad. Sci USA.* **2018**, *115*, E5859-E5866.
21) Haabeth, O. A.; Blake, T. R.; Mckinlay, C. J.; Waymouth, R. M.: Wender, P. A.; Levy, E. mRNA Vaccination with Charge-Altering Releasable Transporters Elicit Human T Cell Responses and Cures Established Tumors in Mice. *Proc. Natl. Acad. Sci USA.* **2018**, *115*, E9153-E9161.
22) Wang, X.; Hadjichristidis, N. Poly (Amino-*Co*-Ester)S By Binary Organocatalytic Ring-Opening Polymerization Of *N*-Boc-1,4-Oxazepan-7-One: Synthesis, Characterization, And Self-Assembly. *Macromolecules* **2020**, *53*, 223-232.
23) Haabeth, O. A.; Lohmeyer, J. Sallets, A.; Blake, T. R.; Sagiv-Barfi, I.; Czerwinski, D. K.; Mccarthy, B.; Powell, A. E.; Wender, P. A.; Waymouth, R. M.; Levy, R. An Mrna SARS-Cov-2 Vaccine Employing Charge-Altering Releasable Transporters with a TLR-9 Agonist Induces Neutralizing Antibodies And T Cell Memory. *ACS Cent. Sci.* **2021**, *7*, 1191-1204.
24) Lu, H.; Hu, Z.; Chen, H.; Yan, Y.; Le, Z.; Wei, C.; Cao, W.; Chen, T.; Chen, Y.; Liu, L. Self-Degradable Poly (B-Amino Ester) S Promote Endosomal Escape of Antigen Ad Agonist. *J. Control. Release.* **2022**, *345*, 91-100.
25) Banner, N. L.; Near, K. E.; Bachman, M.; Contag, C. H.; Waymouth, R. M.; Wender, P. A. Functional DNA Delivery Enabled by Lipid-Modified Charge-Altering Releasable Transporters (Carts). *Biomacromolecules* **2018**, *19*, 2812-2824.
26) Banner, N. L.; Mcclellan, R. L.; Turlington, C. R.; Haabeth, O. L.; Waymouth, R. M.; Wender, P. A. Oligo (Serine Ester) Charge-Altering Releasable Transporters: Organocatalytic Ring-Opening Polymerisation and Their Use *In Vitro* And *In Vivo* Mrna Delivery. *J. Am. Chem. Soc.* **2019**, *141*, 8416-8421.
27) Sun, J.; Jung, D.; Schoppa, T.; Andreski, J.; Picker, M-T.; Ren, Y.; Mulac, D.; Stein, N.; Langer, K.; Kuckling, D. Lightt-Responsive Serinol-Based Polycarbonate as Polyester as Degradable Scaffolds. *ACS Appl. Bio Mater.* **2019**, *2*, 3038-3051.
28) Lim, Y-B.; Choi, Y. H.; Park, J-S. A Self-Destroying Polymer; Biodegradable Poly (4-Hydroxy-L-Proline Ester). *J. Am. Chem. Soc.* **1999**, *121*, 5633, 5639.

29) Liu, Y.; Li, Y.; Keskin, D.; Shi, L. Poly (B-Amino Esters): Synthesis, Formulations, And Their Biomedical Applications. *Adv. Healthcare Mater.* **2019**, *8*, 1801359
30) Deng, X., Zheng, N.; Song, Z.; Yin, L.; Cheng, J. Trigger-Responsive, Fast-Degradable Poly(B-Amino Ester)S for Enhanced DNA Unpackaging And Reduced Toxicity. *Biomaterials* **2014**, *35*, 5006-5015.
31) Rui, Y.; Wilson, D. R.; Choi, J.; Varanasi, M.; Sanders, K.; Karlsson, J.; Lim, M.; Green, J. J. Carboxylated Branched Poly (B-Amino Esters) Nanoparticles Enable Robust Cytosolic Protein Delivery and CRISPR-Cas9 Gene Editing. *Sci. Adv.* **2019**, *5*, Eaay3255.
32) Yang, J.; Yu, X.; Song, J-I.; Song, Q.; Hall, S. C. L.; Yu, G.; Perrier, S. Aggregation-Induced Emission Featured Supramolecular Tubisomes for Imaging-Guided Drug Delivery. *Angew. Chem. Int. Ed.* **2022**, *61*, E202115208
33) Yang, J.; Yu, G., Sessler, J. L., Shin, I., Gale, P. A., Huang, F. Artificial Transmembrane Ion Transporters as Potential Therapeutics. *Chem* **2021**, *7*, 3256-3291.
34) Liang, H.; Lu, Q.; Yang, J.; Yu, G. Supramolecular Biomaterials for Cancer Immunotherapy. *Research* **2023**, *6*, 0211.
35) Lowe, A. B.; Mccormick, C. L. Synthesis and Solution Properties of Zwitterionic Polymers. *Chem. Rev.* **2002**, *102*, 4177-4189.
36) Blackman, L. D.; Gunatillake, P. A.; Cass, P.; Locock, K. E. S. An Introduction to Zwitterionic Polymer Behaviour and Application in Solution and At Surface. *Chem. Soc. Rev*. **2019**, *48*, 757-770.
37) Erfani, A.; Seaberg, J.; Aichele, C. P.; Ramsey, J. D. Interactions Between and Zwitterionic Moieties: A Review. *Biomacromolecules* **2020**, *21*, 2557-2573.
38) Li, B.; Yuan, Z.; He, Y.; Hung, H-C.; Jiang, S. Zwitterionic Nanoconjugates Enables Safe and Efficient Lymphatic Drug Delivery. *Nano Lett.* **2020**, *20*, 4693-4699.
39) Jackson, M. A.; Werfel, T. A.; Curvino, E. J.; Yu, F.; Kavanaugh, T. E.; Serett, S. M.; Dockery, M. D.; Kilchrist, K. V.; Jackson, A. N.; Giorgio, T. D.; Duvall, C. L. Zwitterionic Nanocarrier Surface Chemistry Improves siRNA Tumor Delivery and Silencing Activity Relative to Polyethylene Glycol. *ACS Nano* **2017**, *11*, 5680-5696.
40) Venkataraman, S., Tan, J. P. K., Ng, V. W. L., Tan, E. W. P., Hedrick, J. L., Yang. Y. Y. Amphiphilic and Hydrophilic Block Copolymers from Aliphatic *N*-Substituted 8-Membered Cyclic Carbonates: A Versatile Macromolecular Platform for Biomedical Applications. *Biomacromolecules* **2017**, *18*, 178-188.
41) Delgado, J. D.; Schlenoff, J. B. Static and Dynamic Solution Behaviour of a Polyzwitterion Using a Hofmeister Salt Series. *Macromolecules* **2017**, *50*, 4454-4464.
42) Liu, S.; Wang, X.; Yu, X.; Cheng, Q.; Johnson, L. T.; Chatterji, S.; Zhang, D.; Lee, S. M.; Sun, Y.; Lin, T-C.; Liu, J. L.; Siegwart, D. J. Zwitterionic Phospholipidation of Cationic Polymers Facilitates Systemic mRNA Delivery to Spleen and Lymph Nodes. *J. Am. Chem. Soc.* **2021**, *143*, 21321-21330.
43) Zhang, M.; Yu, P.; Xie, J.; Li, J. Recent Advances of Zwitterionic-Based Topological Polymers for Biomedical Applications. *J. Mater. Chem. B*. **2022**, *10*, 2338-2356.
44) Kim, Y.; Binauld, S.; Stenzel, M. H. Zwitterionic Guanidine-Based Oligomers Mimicking Cell-Penetrating Peptides as A Nontoxic Alternative to Cationic Polymers to Enhance the Cellular Uptake. *Biomacromolecules* **2012**, *13*, 3418-3426.

45) Keefe, A. J.; Jiang, S. Poly (Zwitterionic) Protein Conjugate Offer Increased Stability Without Sacrificing Binding Affinity or Bioactivity. *Nat. Chem* **2012**, *4*, 59-63.
46) Yesilyurt, V. Veiseh, O. Doloff, J. C. Li, J. Bose, S. Xie, X. Bader, A. R. Chen, M. Webber, M. J. Vegas, A. J. Langer, R. Anderson, D. G. A Facile and Versatile Method to Endow Biomaterial Devices with Zwitterionic Surface Coating. *Adv. Healthcare Mater.* **2017**, 6, 1601091.
47) Pelegri-O'Day, E. M.; Bhattacharya, A.; Theopold, N.; Ko, J. H.; Maynard, H.D. Synthesis of Zwitterionic and Trehalose Polymers with Variable Degradation Rates and Stabilization of Insulin. *Biomacromolecules* **2020**, *21*, 2147-2154.
48) Saha, S.; Klein-Hitpaß, M.; Vallet, C.; Knauer, S. K.; Schmuck, C.; Voskuhl, J.; Giese, M. Smart Glycopolymeric Nanoparticles for Multivalent Lectin Binding a Stimuli-Controlled Guest Release. *Biomacromolecules* **2020**, *21*, 2356.
49) Du, J.; Tang, Y.; Lewis, A. L.; Armes, S. P. pH-Sensitive Vesicles Based on a Biocompatible Zwitterionic Diblock Copolymer. *J. Am. Chem. Soc.* **2005**, *127*, 17982-17983.
50) Zhao, D.; Rajan, R.; Matsumura, K. Dual Thermo-and pH-Responsive Behavior of Double Zwitterionic Graft Copolymers for Suppression of Protein Aggregation and Protein Release. *ACS Appl. Mater. Interfaces* **2019**, *11*, 39459-39469.
51) Bengani-Lutz, P.; Converse, E.; Cebe, P.; Asatekin, A. Self-Assembling Zwitterionic Copolymers as Membrane Selective Layers with Excellent Fouling Resistance: Effect of Zwitterion Chemistry. *ACS Appl. Mater. Interfaces* **2017**, *9*, 20859–20872.
52) Ladd, J.; Zhang, Z.; Chen, S.; Hower, J. C.; Jiang, S. Zwitterionic Polymers Exhibiting High Resistance to Nonspecific Protein Adsorption from Human Serum and Plasma. *Biomacromolecules* **2008**, *9*, 1357–1361.
53) Li, M.; Zhuang, B.; Yu, J. Functional Zwitterionic Polymers on Surface: Structures and Applications. *Chem Asian J.* **2020**, *15*, 2060-2075.
54) Surnar, B.; Jayakannan, M. Stimuli-Responsive Poly(Caprolactone) Vesicles for Dual Drug Delivery Under the Gastrointestinal Tract. *Biomacromolecules* **2013**, *14*, 4377-4387.
55) Surnar, B.; Jayakannan, M. Triple-block nanocarrier platform for synergistic cancer therapy of antagonistic drugs. *Biomacromolecules* **2016**, *17*, 4075-4085.
56) Kulkarni, B.; Surnar, B.; Jayakannan, M. Dual functional nanocarrier for cellular imaging and drug delivery in cancer cells based on π-conjugated core and biodegradable polymer arms. *Biomacromolecules* **2016**, *17*, 1004-1016.
57) Malhotra, M.; Surnar, B.; Jayakannan, M. Polymer Topology Driven Enzymatic Biodegradation in Polycaprolactone Block and Random Copolymer Architectures for Drug Delivery to Cancer Cells. *Macromolecules* **2016**, *49*, 8098-8112.
58) Ghosh, R.; Malhotra, M.; Sathe, R. R. M.; Jayakannan, M. Biodegradable Polymer Theranostic Fluorescent Nanoprobe for Direct Visualization and Quantitative Determination of Antimicrobial Activity. *Biomacromolecules* **2020**, *21*, 2869-2912.
59) Ghosh, R.; Jayakannan, M. Theranostic FRET Gate to Visualize and Quantify Bacterial Membrane Breaching. *Biomacromolecules* **2023**, *24*, 739-755.

60) Surnar, B.; Jayakannan, M. Structural Engineering of Biodegradable PCL Block Copolymer Nanoassemblies for Enzyme-Controlled Drug Delivery in Cancer Cells. *ACS Biomater. Sci. Eng.* **2016**, *2*, 1926-1941.
61) Pranav, U.; Malhotra, M.; Pathan, S.; Jayakannan, M. Structural Engineering of Star Block Biodegradable Polymer Unimolecular Micelles for Drug Delivery in Cancer Cells. *ACS Biomater. Sci. Eng.* **2023***, 9,* 743-759.
62) Saxena, S.; Jayakannan, M. Development of L-Amino Acid-Based Hydroxyl Functionalized Biodegradable Amphiphilic Polyesters and Their Drug Delivery Capabilities to Cancer Cells. *Biomacromolecules* **2020**, *21*, 171-187.
63) Chali, S. P.; Azhdari, S.; Galstyan, A.; Groschel, A. H.; Ravoo, B. J. Biodegradable Supramolecular micelles via host-guest interaction of cyclodextrin-terminated polypeptide admantane-terminated polycaprolactones. *Chem. Commun.,* **2021**, *57*, 9446.
64) Cao, J.; Xie, X.; Lu, A.; He, B.; Chen, Y.; Gu, Z.; Luo. X. Cellular Internalization of Doxorubicin loaded Star-Shaped Micelles with Hydrophilic Zwitterionic Sulfobetaine Segments. *Biomaterials* **2014**, *35,* 4517–4524.
65) Chen, Y.; Han, H.; Tong, H.; Chen, T.; Wang, H.; Ji, J.; Jin, Q. Zwitterionic Phosphorylcholine-TPE conjugate for pH-Responsive Drug Delivery and AIE Active Imaging. *ACS Appl. Mater. Interfaces* **2016**, *8*, 21185–21192.
66) Huang, P.; Song, H.; Wang, W.; Sun, Y.; Zhou, J.; Wang, X.; Liu, J.; Liu, J.; Kong, D.; Dong, A. Integrin-Targeted Zwitterionic Polymeric Nanoparticles with Acid-Induced Disassembly Property for Enhanced Drug Accumulation and Release in Tumor. *Biomacromolecules* **2014**, 15, 3128–3138.
67) Karmegam, V.; Kuruppu, S. S.; Udamulle Gedara, C. M.; Biewer, M. C.; Stefan, M. C., Enhanced DOX Loading in Star-Like Benzyl Functionalized Polycaprolactone Micelles. *J Polym Sci.* **2021**, *59*, 3040-3052.
68) Deshpande, N. U.; Jayakannan, M. Biotin-Tagged Polysaccharide Vesicular Nanocarriers for Receptor-Mediated Anticancer Drug Delivery in Cancer Cells. *Biomacromolecules* **2018**, *19*, 3572-3585.
69) Khuddus, M.; Jayakannan, M. Strategy for Amide-Functionalized L-Aspartic Acid Amphiphilic Polyester Nano-Assemblies and Enzyme-Responsive Drug Delivery in Cancer Cells. *Biomacromolecules* **2023**, *24*, 2643-2660.

Chapter 5

Star Shaped Zwitterionic Block and Random Copolymer for In Vitro and In Vivo Drug Delivery to Pancreatic Tumor

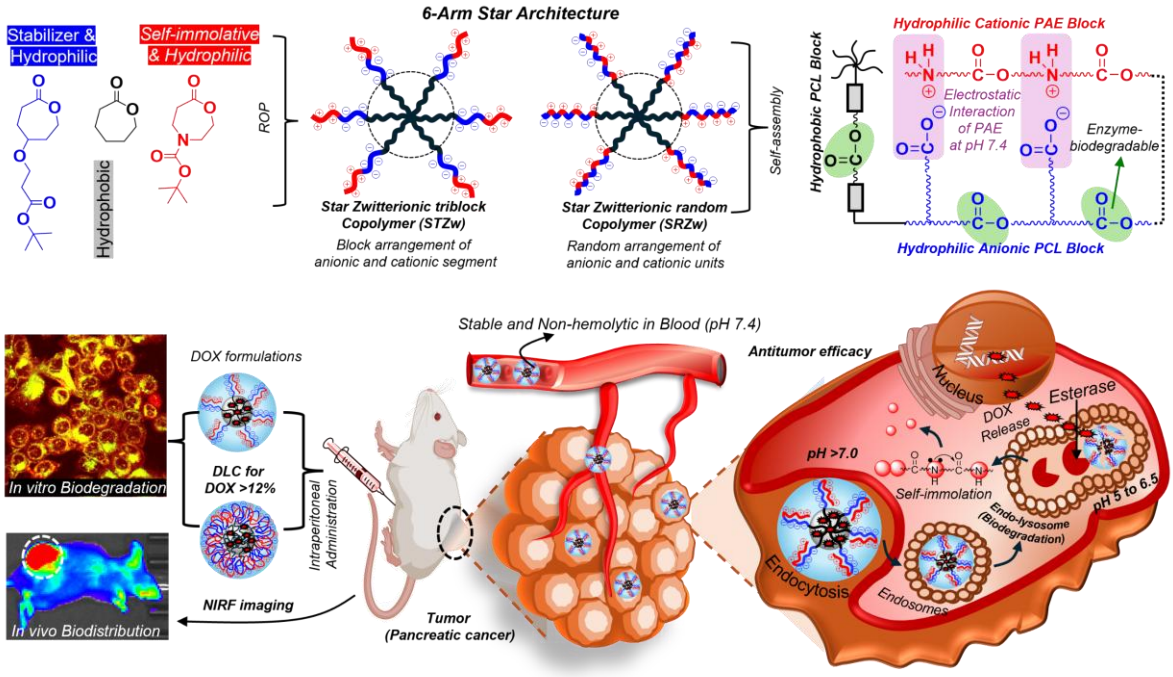

Abstract

Pancreatic is one of the lethal malignancies having >10% survival rate owing to chemoresistance and poor penetration of drugs. Nanomedicine have been emerging to overcome the limitations of free drugs and improving therapeutic efficacy. Unfortunately, non-biodegradable polymer based nanocarriers posed the safety problem in long term use despite being promising candidates. Here we report 6-arm star shaped polycaprolactone (PCL) and self-immolative poly(βamino esters)s (PAE) based zwitterionic block and random copolymers. Aqueous self-assembly of diblock or triblock copolymers depict formation of tiny nanoparticles (NP) of sizes ~20-25nm with nearly neutral zeta potential at pH 7.4, while random copolymers produce larger NPs of 100nm. The zwitterionic NP demonstrated high DLC for DOX >12% and great serum stability. pH dependent studies showed stabilization of PAE against self-immolation at physiological pH 7.4, while on-demand enzymatic biodegradation in the intracellular (lysosomal) compartment facilitated release of DOX to the nucleus evident form CLSM imaging. Zwitterionic NPs were excellent biocompatible, non-hemolytic in nature. The NIRF imaging of IR780 loaded NP in MIA PaCa2 (human pancreatic cancer) tumor bearing xenograft mice model demonstrated longer blood circulation and retention in tumor for more than72h. DOX loaded NP showed significant tumor suppression at lower dosage suggesting effective delivery via passive targeting (EPR) effect. This approach is not only restricted for delivery of one type of chemotherapeutic but also can be applied to other combinations of drugs and different type of cancer models.

5.1 Introduction

Pancreatic cancer is one of the most lethal malignant cancer having less than 10% survival rate worldwide.[1] Gemcitabine, Paclitaxel, 5-Flurouracil, Irinotecan and Oxaliplatin are most commonly used first line chemotherapy in the treatment of PC.[2] However poor solubility and retention, shorter half-life non-targeting abilities of these drugs results in less effective therapeutic efficacy and systemic toxicities.[3] Moreover pancreatic cancer is relatively resistant to chemotherapeutics suggesting urgent need of new treatment modalities.[4] To overcome this, nanoplatform have been emerging which can solubilize drugs, increased blood circulation time and accumulate more in tumor sites via active or passive targeting (EPR effect).[5-6] Recently various examples of nanoplatforms including dendrimers, hydrogel, lipid and mesoporous silica nanoparticles, polyacrylates-polymers, supramolecular nanodots based approaches have been explored for delivery of drugs and genes to Pancreatic tumors.[7-12] Another new strategies have been developed to facilitate the infiltration of drug across the stromal barrier using gemcitabine loaded pH-sensitive cellular membrane disruptive molecule derived nanoparticles.[13] Unfortunately most the reported promising nanoparticles for drug delivery to pancreatic tumors are derived from non-biodegradable polymers which can cause prolong accumulation and result in the system toxicities. Therefore, biodegradable and biocompatible polymers urgently need to be developed and evaluated to circumvent the side-effects. The stimuli responsive biodegradable polymers having pH, light, redox, thermal, enzyme, ultrasound, etc.; responsiveness is desirable owing to degradation of nanocarriers upon trigger by these stimuli resulting in release of drug at targeted side.[14-15] An important class of stimuli-responsive materials known as self-immolative polymers have been emerging as new generational smart polymer for biomedical applications which can be auto-degraded into oligomers or small molecules by triggering with specific stimuli such pH, redox, enzyme, light, etc.; .[16-17] Among pH -responsive self-immolative polymers, poly(amino esters)s (PAE)s (both α and β derivatives) have been explored for gene delivery due to their rapid auto-degradation into non-toxic molecule at pH >7.0, achieving faster transfections of mRNA and plasmic DNA.[18-19] Unfortunately PAEs are not suitable to be used for intraperitoneal or intravenous drug delivery administration due to uncontrolled degradation and instability at physiological pH 7.4. To circumvent this limitation of PAEs, our group have recently developed a strategy to stabilize PAEs using electrostatic interaction between carboxylate ions from carboxylic PCL units with ammonium ions of PAE at pH 7.4 (physiological pH) at extracellular level.[20] This electrostatic strategy not only enabled stabilization of PAEs but also provided the zwitterionic

properties, high DLC content for DOX~8% and enzyme responsiveness followed by self-immolation of remaining PAE units at intercellular compartment.

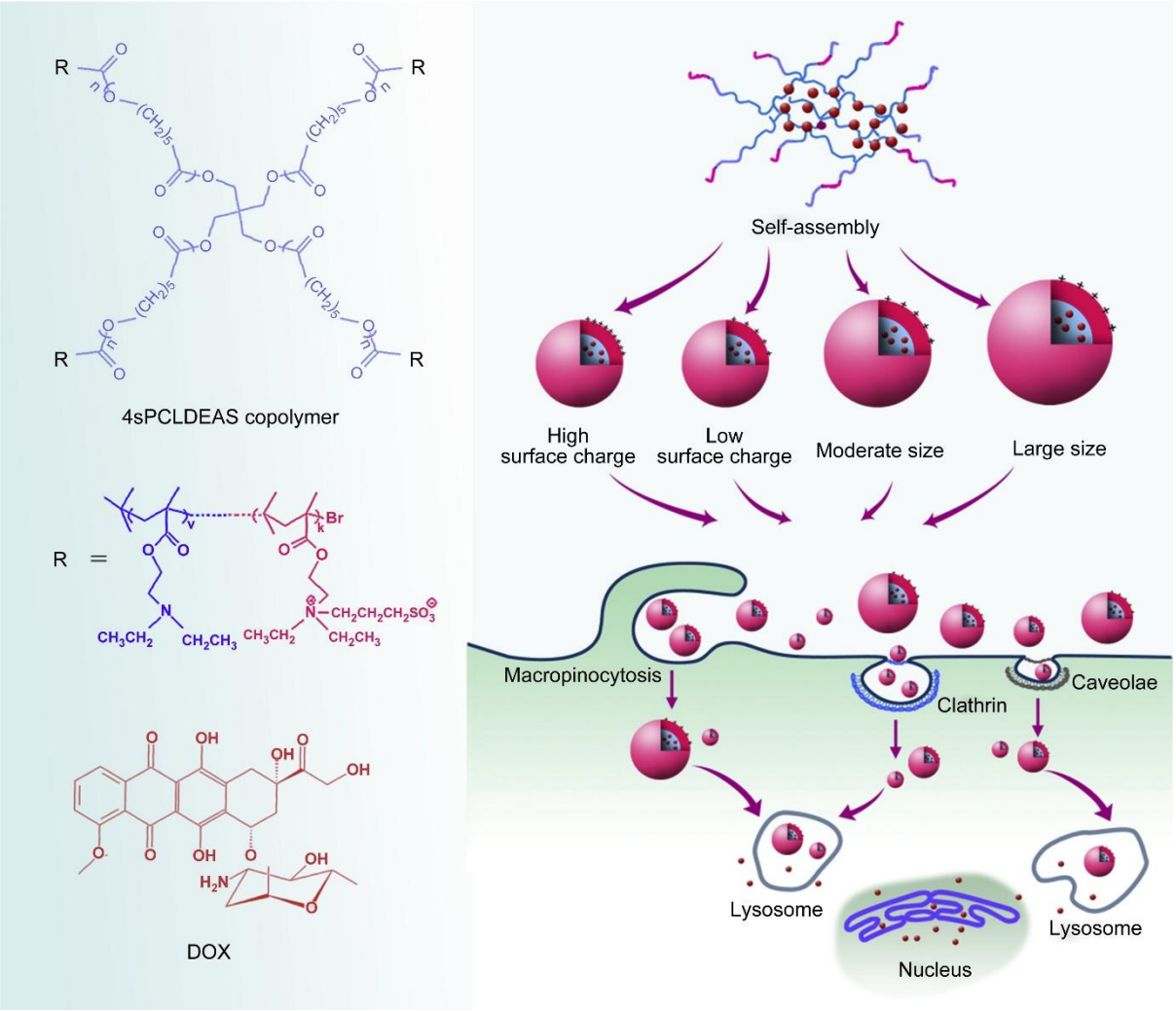

Figure 5.1: *Illustration of star-shaped self-assembly of 4sPCLDEAS copolymers and cellular internalization pathways (Adapted from Cao, J., et al, Biomaterials* ***2014****, 35, 4517–*4524*).*

Zwitterionic polymers including polyampholyte and polybetaines, an important class of smart materials composed of anionic and cationic units are very well explored in the literature for their excellent hydration in water, pH responsiveness and anti-polyelectrolytic effect in solution.[21-22] Exploiting super hydrophilic nature, zwitterionic polymers exhibit excellent antifouling properties, resistance to non-specific adsorption to human serum and plasma proteins, and reduced opsonization, enhanced cellular uptake, and increase blood circulation time.[23-26] Polyacrylate based zwitterionic polymers having linear and star-shaped architectures have been widely explored for drugs, genes, proteins delivery and other biomedical applications.[27-33] Recent reports based on polyacrylate (polybetaine)-zwitterionic

system derived nanocarriers exhibited drug loading content (DLC) in the range 5-12% for anticancer drug Doxorubicin.[34-35] One of the examples of 4-star-shaped micelles composed of PCL-sulfobetaine segment has been studied for size specific DOX loading and cellular internalization as shown in Figure 5.1 depicted DLC in the range of 4-12% for DOX.[36] Unfortunately most of the zwitterionic system derived from polyacrylate polymers are constructed be C-C rigid carbon bonds hence they are non-biodegradable in nature makes them less desirable for long-term use *in vivo* applications owing to induced systemic toxicities induced by non-specific longer accumulation in animals. Moreover, the mechanism of degradation and clearance of these non-biodegradable polymers has not been clearly understood yet.

To overcome these limitations, in this chapter we report novel star-shaped zwitterionic polymer based on enzyme-biodegradable polycaprolactone (PCL) and self-immolative poly(βamino esters)s as shown in Figure 5.2. Based on our expertise in PCL and substituted anionic carboxylic PCL systems,[37-44] 6-arm star shape block and random copolymers with or without hydrophobic PCL core were synthesized as shown in Figure 5.2a to understand the role of topology or architecture. The star-shaped and branch architectures have been proven promising in the literature for longer blood circulation time and stability against renal filtration compared to linear architectures.[45-47] Therefore the combination enzymatic-biodegradability from anionic PCL units and self-immolation form cationic PAEs not only makes the structure zwitterionic in nature but also provide stability at physiological pH at extracellular conditions as shown in Figure 5.2b. The star shaped block or triblock copolymer showed formation of ~25nm nanoparticles while random copolymers of similar composition aided formation of lager NP of sizes 100nm. Moreover, on-demand enzymatic biodegradation followed by self-immolation at intracellular level results in the complete degradation of polymer matrix preventing systemic toxicity. The star shaped zwitterionic system exhibited high DLC >12% for DOX depicted crucial role of PCL core. NIRF imaging of IR780 loaded star zwitterionic nanoparticles (NP) demonstrated superior accumulation and retention in pancreatic tumor bearing mice model. DOX loaded NPs depicted excellent suppression in tumor growth as shown in Figure 5.2c.

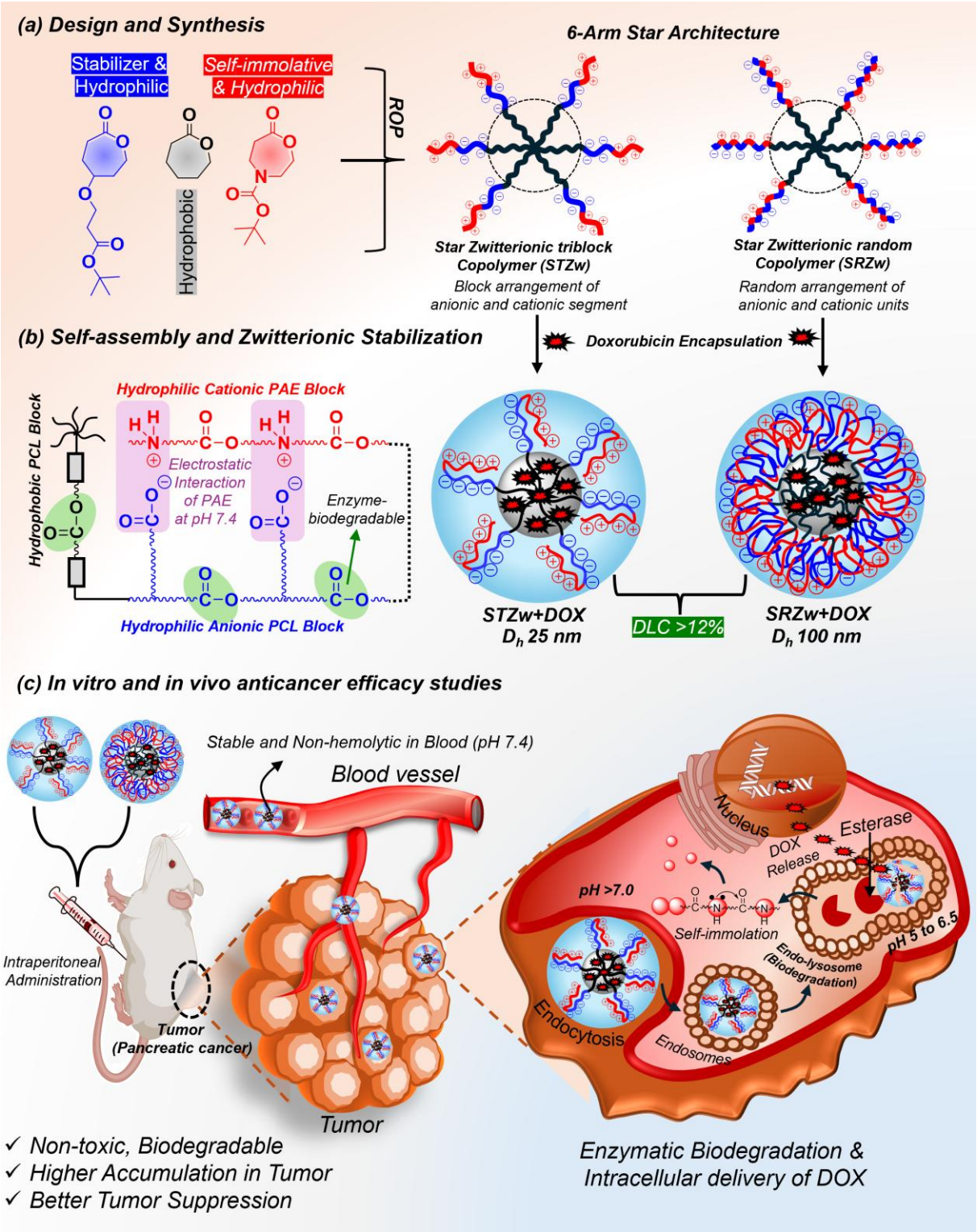

Figure 5.2. *(a) Synthetic strategy for Star shaped zwitterionic triblock and random copolymers. (b) Self-assembly and Doxorubicin encapsulation. (c) Role of topology and architecture in star zwitterionic block copolymers for in vitro and in vivo tumor drug delivery.*

5.2 Experimental Section

5.2.1 Materials

4-Piperidinone hydrochloride monohydrate, PCC, mCPBA, 1,4-cyclohexanediol, tin Di octanoate (II), *t*Butyl acrylate, ε-CL, IR780 iodide, Doxorubicin HCl, MTT, Esterase from porcine liver and other chemicals were purchased form Sigma-Aldrich chemicals. HPLC grade and analytical grade solvents were purchased from Sigma-Aldrich or Finar. Cell culture reagents, DMEM media, GIBCO fetal bovine serum, pen strep, Lysotracker DND-26, DAPI and Spectra/Por semi-permeable membrane (MWCO 1KD and 3.5KD) dialysis tubing materials were purchased from ThermoFisher Scientific.

5.2.2 Methods

^{1}H and ^{13}C NMR spectra were recorded using Bruker 400 MHz spectrometer. Gel permeation chromatography (GPC) or size exclusion chromatography (SEC) was performed using Agilent PlGel 20μm Mixed-A column with Viscotek GPC equipped with VE 3580 RI detectors, Tetrahydrofuran (THF) and polystyrene was used as eluent and calibration standard, respectively. Zetasizer ZS-90 instrument was utilized for size measurements by dynamic light scattering (DLS) with 633 nm laser light and 90° angles scattering. Joel JEM2200FS 200 KeV was used to acquire transmission electron microscopy (TEM) images. Absorbance and transmission spectra were recorded using Shimadzu UV-1900i spectrometer. A Perkin-Elmer Ensight microplate reader was utilized for recording absorbance for microplates. Zeiss Anisotropy 710 microscope was used to capture CLSM images and ImageJ software used for processing. Perkin-Elmer IVIS spectrum instrument was utilized for live animal whole body imaging and IVIS Live Imager software was used for image analysis. Origin 9.0, Prism 8.01 software used for data analysis.

5.2.3 Synthetic procedures

Synthesis of Star Poly(amino-ester) macroinitiator (SPAE): Ring opening polymerization (ROP) synthetic route is typically explained for SPAE. Monomer **M1** (900.0 mg, 4.18 mmol) was taken in flame dried custom-made polymerization tube along with Di pentaerythritol (initiator, 17.80 mg, 0.07 mmol, M/I=60), and $Sn(Oct)_2$ (catalyst, 85 mg, 0.21 mmol). The tube was connected with an overhead stirrer (Heidolph) and vacuum sealed by applying vacuum (10^{-2} mbar) for 45 min. Then the tube was immersed in preheated oil bath (110 °C) and stirring was applied (150rpm) for 8h. After polymerization, the tube was brought to room temperature and dissolved in THF (2.0 mL) and precipitated into large amount of diethyl ether + hexane

(60 mL, 4:1 v/v) solvent mixture at cold condition for 1h. The solvent was decanted carefully, and polymer was dried in vacuo. Yield = 0.750 g (84 %). ^{1}H NMR (400 MHz, $CDCl_3$) δ ppm: 4.15 (bs, 108H), 3.71 (bs, 12H), 3.48 (bs, 215H), 2.59 (bs, 110H), 1.44 (s, 483H). ATR-FTIR (cm^{-1}): 2973, 1735, 1691, 1468, 1411, 1390, 1365, 1277, 1247, 1157, 1130, 860, 771, 641.

Synthesis of Star Poly(amino-ester)-*b*-^{t}Butyl-Polycaprolactone (SPAE-b-^{t}BuPCL): Monomer **M2** (350 mg, 1.35 mmol), SPAE macroinitiator (300 mg, 0.023 mmol) and $Sn(Oct)_2$ (28.0 mg, 0.07 mmol) were taken in polymer tube. Polymerization was done for 12 hours at 130 ºC using similar strategy described for SPAE. After polymerization, the polymer was dissolved in THF (2.0 mL) and precipitated into large amount of diethyl ether + hexane (60 mL, 4:1 v/v) solvent mixture at cold condition for 1h. The solvent was decanted carefully, and polymer was dried in vacuo. Yield = 0.49 g (75%). ^{1}H NMR (400 MHz, $CDCl_3$) δ ppm: 4.17-4.07 (bs, 213H), 3.69-3.61 (m, 135H), 3.47-3.44 (m, 279H), 2.57 (bs, 110H), 2.42 (t, 127H), 2.36 (t, 112H), 1.87-1.70 (m, 243H), 1.43 (s, 1019H). ^{13}C NMR (100 MHz, $CDCl_3$) δ ppm: 173.61, 170.98, 155.13, 80.70, 80.32, 75.59, 65.99, 64.92, 61.37, 46.94, 44.34, 36.60, 33.05, 29.82, 29.03, 28.51, 28.22, 15.39, 0.12. ATR-FTIR (cm^{-1}): 2973, 1729, 1695, 1468, 1412, 1392, 1365, 1250, 1156, 1104, 847, 764.

Synthesis of Star Poly(amino-ester)-r-^{t}Butyl-Polycaprolactone (SPAE-*r*-^{t}BuPCL): Monomer **M2** (450.0 mg, 1.74 mmol) and monomer **M3** (375.0 mg, 1.74 mmol) were taken in 1:1 ratio, Di pentaerythritol (initiator, 11.80 mg, 0.03 mmol, M/I=120) and $Sn(Oct)_2$ (35.30 mg, 0.087 mmol) was taken in polymer tube. Polymerization was done for 12 hours at 130 ºC using similar strategy described for SPAE. After polymerization, the polymer was dissolved in THF (2.0 mL) and precipitated into large amount of diethyl ether + hexane (60 mL, 4:1 v/v) solvent mixture at cold condition for 1h. The solvent was decanted carefully, and polymer was dried in vacuo. Yield = 0.55 g (66%). ^{1}H NMR (400 MHz, $CDCl_3$) δ ppm: 4.15-4.10 (bs, 211H), 3.72-3.63 (m, 133H), 3.48-3.43 (m, 247H), 2.58 (bs, 110H), 2.43 (t, 115H), 2.36 (t, 112H), 1.85-1.76 (m, 348H), 1.44 (s, 988H). ^{13}C NMR (100 MHz, $CDCl_3$) δ ppm: 173.82, 171.00, 155.35, 80.72, 80.65, 75.58, 64.92, 61.19, 36.59, 33.28, 29.71, 29.04, 28.52, 28.22. ATR-FTIR (cm^{-1}): 2970, 1730, 1694, 1463, 1412, 1365, 1251, 1156, 847, 758.

Synthesis of Star Polycaprolactone Macroinitiator (Star-PCL or SMI60): ε-Caprolactone monomer **M3** (1.0 g, 8.77 mmol), Di-pentaerythritol (32.0 mg, 0.12 mmol) and catalyst $Sn(Oct)_2$ (30 mg, 0.08 mmol) were taken in polymerization tube. Then polymerization (ROP) was conducted for 8 hours at 110 ºC and after that the content was cooled to room temperature.

Crude polymer was dissolved in 2mL tetrahydrofuran (THF) and precipitated in cold methanol (70mL) for 1h. After precipitation, the polymer was filtered through and dried in vacuo to obtain white solid. Yield = 0.91 g (90%). ^{1}H NMR (400 MHz, $CDCl_3$) δ ppm: 4.05 (t, *J* = 6.7 Hz, 144H), 3.64 (t, *J* = 6.5 Hz, 12H), 3.37 (m, 4H), 2.30 (t, *J* = 7.5 Hz, 145H), 1.64 (m, 301H), 1.37 (m, 145H). ^{13}C NMR (100 MHz, $CDCl_3$) δ ppm: 173.70, 64.28, 62.89, 34.25, 32.46, 28.47, 25.66, 24.81. ATR-FTIR (cm^{-1}): 3041, 2864, 1724, 1462, 1419, 1365, 1294, 1161, 1104, 1045, 926, 749.

Synthesis of Star Polycaprolactone-*b*-^{t}Butyl-Polycaprolactone (Star-PCL-*b*- ^{t}BuPCL): Monomer **M2** (650 mg, 2.71 mmol), SMI60 macroinitiator (302 mg, 0.04 mmol, M/I=60) and $Sn(Oct)_2$ (9.0 mg, 0.02 mmol) were taken in polymerization tube and polymerized for 12 hours at 130 ºC as described for PAE. After the polymerization, the polymer was dissolved in THF (2mL) and precipitated in a cold mixture of hexane in diethyl ether (70mL). Yield = 0.9 g (82%). ^{1}H NMR (400 MHz, $CDCl_3$) δ ppm: 4.15-4.11 (m, 120H), 4.05 (t, 144H), 3.66 (m, 129H), 3.43 (bs, 68H), 2.43 (t, 125H), 2.33 (t, 112H), 2.29 (t, 154H), 1.80-1.74 (m, 284H), 1.64-1.60 (m, 356H), 1.39 (s, 555H), 1.39-1.35 (m, 145H). ^{13}C NMR (100 MHz, $CDCl_3$) δ ppm: 173.70, 173.6, 171.0, 80.0, 75.60, 64.95, 64.30, 61.30, 46.8, 36.6, 34.2, 33.0, 28.50, 28.25, 25.75, 24.70. ATR-FTIR (cm^{-1}): 2931, 1728, 1366, 1157, 1103, 847.

Synthesis of Polycaprolactone-*b*-^{t}Butyl-Polycaprolactone-*b*-^{t}Butyl-Polycaprolactone-Poly(amino-ester) (SPCL-*b*-^{t}BuPCL-*b*-PAE): Monomer **M1** (300 mg, 1.39 mmol), Star-PCL-*b*-*t*BuPCL macroinitiator (552 mg, 0.023 mmol, M/I=60) and $Sn(Oct)_2$ (28.20 mg, 0.07 mmol) were taken in polymerization tube and polymerized for 8 hours at 110 ºC as described for PAE. After the polymerization, the polymer was dissolved in THF (2mL) and precipitated in a cold mixture of hexane in diethyl ether (70mL). Yield = 0.74 g (86%). ^{1}H NMR (400 MHz, $CDCl_3$) δ ppm: 4.15-4.12 (m, 216H), 4.05 (t, 144H), 3.68 (m, 121H), 3.48 (bs, 268H), 2.58, (bs, 118H), 2.43 (t, 118H), 2.36 (t, 110H), 2.29 (t, 140H), 1.80-1.74 (m, 321H), 1.68-1.60 (m, 244H), 1.44 (s, 1019H), 1.39-1.33 (m, 142H). ^{13}C NMR (100 MHz, $CDCl_3$) δ ppm: 173.71, 173.62, 170.99, 155.16, 80.71, 80.63, 75.60, 64.93, 64.29, 61.37, 36.61, 34.26, 33.05, 29.82, 29.04, 28.52, 28.23, 25.67, 24.72. ATR-FTIR (cm^{-1}): 2931, 1730, 1694, 1463, 1412, 1391, 1365, 1249,1155, 1104, 847, 764.

Synthesis of Polycaprolactone-*b*-(*r*-^{t}Butyl-Polycaprolactone-*r*-^{t}Butyl-Polycaprolactone-Poly(amino-ester)) (SPCL-*b*-(^{t}BuPCL-*r*-PAE)): Monomer **M2** (360 mg, 1.40 mmol), monomer **M1** (300 mg, 1.40 mmol), SMI-60 macroinitiator (193.0 mg, 0.023 mmol, M/I=120)

and $Sn(Oct)_2$ (14.20 mg, 0.035 mmol) were taken in polymerization tube and polymerized for 12 hours at 130 ºC as described for PAE. After the polymerization, the polymer was dissolved in THF (2mL) and precipitated in a cold mixture of hexane in diethyl ether (70mL). Yield = 0.61 g (72%). ^{1}H NMR (400 MHz, $CDCl_3$) δ ppm: 4.15-4.12 (m, 198H), 4.05 (t, 145H), 3.68 (m, 117H), 3.48 (bs, 261H), 2.58, (bs, 110H), 2.43 (t, 101H), 2.36 (t, 110H), 2.29 (t, 153H), 1.80-1.74 (m, 260H), 1.68-1.60 (m, 333H), 1.44 (s, 1010H), 1.39-1.33 (m, 137H). ^{13}C NMR (100 MHz, $CDCl_3$) δ ppm: 173.71, 173.62, 170.99, 155.16, 80.71, 80.63, 75.60, 64.93, 64.29, 61.37, 36.61, 34.26, 33.05, 29.82, 29.04, 28.52, 28.23, 25.67, 24.72. ATR-FTIR (cm^{-1}): 2931, 1730, 1694, 1463, 1412, 1391, 1365, 1249,1155, 1104, 847, 764.

General procedure for deprotection: Typically, the star block or random copolymer was dissolved into dichloromethane (DCM) in round bottom flask and reaction was cooled to 0^0C. Trifluoracetic acid (TFA) was slowly added to reaction mixture and then stirred for 2h in cold condition. After completion of the reaction, excessive TFA was evaporated using rotary-evaporator and deprotected polymer was dispersed in DCM was precipitated in cold mixture of hexane in diethyl ether mixture (3:1 v/v, 30-40mL) in cold condition for 1h. After the precipitation solvent was decanted and polymer dried in vacuo.

Synthesis of Star-PAE-NH_2-*b*-CPCL (SZw-diblock): SPAE-*b*- *t*BuPCL (200 mg), TFA (2.0 mL), DCM (4 mL). After deprotection polymer was precipitated in cold mixture of hexane in diethyl ether (30mL). Yield = 200 mg. ^{1}H NMR (400 MHz, DMSO-d_6) δ ppm: 4.32-4.25 (m, 110H), 4.10-4.03 (bs, 112H), 3.65-3.56 (m, 131H), 3.38 (m, 100H), 3.27 (bs, 194H), 2.79 (m, 110), 2.39 (t, 110H), 2.32 (t, 96H), 1.70 (m, 213H). ^{13}C NMR (100 MHz, DMSO-d_6) δ ppm: 172.93, 172.72, 169.92, 64.23, 45.52, 41.95, 34.94, 32.39, 28.61, 15.19. ATR-FTIR (cm^{-1}): 2921,1717, 1671, 1407, 1258, 1178, 835, 196, 751, 721.

Synthesis of Star-PAE-NH_2-*r*-CPCL (SZw-RanCo): SPAE-*r*-^{t}BuPCL (280 mg), TFA (2.8 mL), DCM (4 mL). After deprotection polymer was precipitated in cold mixture of hexane in diethyl ether (40 mL). Yield = 270 mg. ^{1}H NMR (400 MHz, DMSO-d_6) δ ppm: 4.32-4.26 (m, 106H), 4.10-4.05 (bs, 115H), 3.68-3.55 (m, 150H), 3.38 (m, 214H), 2.78 (m, 110H), 2.40-2.32 (m, 215H), 1.70 (m, 221H). ^{13}C NMR (100 MHz, DMSO-d_6) δ ppm: 172.93, 172.72, 169.92, 64.23, 45.52, 41.95, 34.94, 32.39, 28.61, 15.19. ATR-FTIR (cm^{-1}): 2921,1717, 1671, 1407, 1258, 1178, 835, 196, 751, 721.

Synthesis of Star-PCL-*b*-PAE-NH_2-*b*-CPCL (STZw): SPCL-*b*-^{t}BuPCL-*b*-PAE (300 mg), TFA (3.0 mL), DCM (6 mL). After deprotection polymer was precipitated in cold mixture of

hexane in diethyl ether (50 mL). Yield = 310 mg. ^{1}H NMR (400 MHz, DMSO-d_6) δ ppm: 4.41-4.30 (m, 121H), 4.05 (bs, 125H), 3.98 (t, 144H), 3.56 (bs, 164H), 3.38 (m, 122H), 3.27 (bs, 270H), 2.79 (m, 122H), 2.40 (m, 92H), 2.31-2.23 (m, 272H), 1.68 (m, 254H), 1.53 (m,358H), 1.29 (m, 189H). ^{13}C NMR (100 MHz, DMSO-d_6) δ ppm: 174.51, 172.71, 169.92, 74.91, 63.52, 56.33, 45.53, 42.14, 34.94, 33.38, 27.82, 24.90, 24.11. ATR-FTIR (cm^{-1}): 2954, 1784, 1727, 1673, 1402, 1172, 836, 798, 749, 721.

Synthesis of Star-PCL-*b*-(PAE-NH$_2$-*r*-CPCL) (SRZw): SPCL-*b*-(^{t}BuPCL-*r*-PAE) (300 mg), TFA (3.0 mL), DCM (6 mL). After deprotection polymer was precipitated in cold mixture of hexane in diethyl ether (50 mL). Yield = 300 mg. ^{1}H NMR (400 MHz, DMSO-d_6) δ ppm: 4.32-4.24 (m, 122H), 4.04, (bs, 123H), 3.98 (t, 144H), 3.56, (bs, 139H), 3.37(m, 68H), 3.26, (bs, 221H), 2.79-2.74 (m, 110H), 2.38 (m, 175H), 2.32-2.25 (m, 220H), 1.68 (m, 229H), 1.52 (m, 334H), 1.29 (m, 142H). ^{13}C NMR (100 MHz, DMSO-d_6) δ ppm: 174.51, 172.71, 169.92, 74.91, 63.52, 56.33, 45.53, 42.14, 34.94, 33.38, 27.82, 24.90, 24.11. ATR-FTIR (cm^{-1}): 2955, 1785, 1726,1726, 1675, 1410, 1275, 1260, 1186, 1104, 833, 798, 764, 749, 722, 607.

5.2.4 Self-assembly and nanoparticle characterization

Zwitterionic polymers were self-assembled into NP by modified dialysis method. The DMSO solution (0.8 mL) of polymer (5.0 mg) was dropped into 4.2 mL deionized water with moderate stirring and kept for 4h. Then mixture was transferred to dialysis membrane (MWCO 3.5KD) and dialyzed against fresh deionized water for 24h. The water was replaced each hour to ensure the removal of DMSO. Dialyzed polymer solution (NP) was filtered using 0.45μ (PES) filter and stored at 4 ºC until further analysis. The hydrodynamic diameters (sizes) and surface zeta potential (ζ) of self-assembled polymeric NP were measured by DLS at the concentration of 0.1 mg/mL using Zetasizer ZS-90 particle analyzer. pH-dependent sizes and zeta potential of NP were measured by DLS using Britton-Robinson (10 mM) buffer of varying pH (2.0 to 11). All measurements were conducted at least three independent times and results are represented as mean ± SD. The NP were visualized using transmission electron microscopy (TEM). CMC measurements were done using protocols described in earlier chapters.

5.2.5 Encapsulation and stability studies

Anticancer agent Doxorubicin (DOX) was encapsulated in zwitterionic polymers by dialysis process. 1.0 or 2.0 mg of neutralized DOX and 5mg of the polymer and were dissolved in 0.8mL of HPCL grade DMSO. This DMSO solution was slowly added to the deionized water for mixing with moderate stirring at room temperature. The DMSO+water solution of

polymer+DOX was transferred to dialysis membrane (MWCO 3.5KD) and dialyzed against deionized water for 24h with replenishing water each hour to remove DMSO and unencapsulated DOX. The loaded solutions were filtered using 0.45µ PES filters. A similar strategy was used to encapsulate the IR780 iodide. The amount of encapsulated DOX or IR780 was calculated by absorbance using Lambert-Beer law. Drug loading content (DLC) and Drug loading efficiency (DLE) were determined as described in earlier reported procedure (Chapter 2). The serum stability of DOX loaded STZw+DOX and SRZw+DOX NP were determined by incubating NP in 10% FBS (fetal bovine serum) in PBS (pH 7.4) at 37 ºC for 5 days. The sizes of STZw+DOX and SRZw+DOX NP were measured by DLS for 5 days.

5.2.6 *In vitro* enzymatic release investigations

The release of DOX from NP was investigated for enzymatic biodegradation of zwitterionic polymers using esterase (from porcine liver, 28U/mg) enzyme at physiological pH and temperature (pH 7.4, 37 ºC). For that purpose, 1 mL solution of STZw+DOX or SRZw+DOX NP (1mg/mL) were taken in dialysis tube (MWCO 1KD) along with 2.0 mg of esterase enzyme and immersed into total of 3mL of PBS, pH 7.4 in reservoir incubated at 37 °C. For the control experiment, 1.0 mL of STZw+DOX or SRZw+DOX NP were incubated without esterase in PBS at similar conditions. At regular intervals, 2mL solutions from reservoir were taken out and subjected for absorbance measurements and the amount of DOX released at each timepoint was calculated. The total amount of DOX released was plotted against time of incubation as release profile.

5.2.7 Enzymatic biodegradation studies

The zwitterionic polymers are composed of aliphatic polyester backbone (PCL). Their enzymatic biodegradation was investigated by different techniques (turbidity measurements, DLS, NMR and MALDI-TOF) to understand the stimuli-responsive behavior towards esterase enzyme. The porcine liver esterase (28U/mg) was used as an enzyme to catalyze the hydrolysis of ester bonds in the polymer backbone to degrade the polymer backbones. The transmission of the polymer solutions was recorded to determine the turbidity of the polymer solution as a measure of degradation. For that purpose, the 5mg of zwitterionic polymer (STZw and SRZw) were incubated in PBS (5mL, pH 7.4,) with esterase (5mg) or without esterase (control) at 37 ºC for 48h. Transmittance of these solutions was recorded at regular interval till 48h. The % transmittance at 600 nm was plotted against time to determine the turbidity as measure of degradation. Similar solutions were subjected to size measurement by DLS for 48h. In another similar experiment, 10mg of STZw or SRZw polymers were incubated with 7.5 mg of esterase

enzyme at 37 ºC for 48h. Aliquots were removed at predetermined intervals and lyophilized immediately to get powder samples. Lyophilized samples were redispersed in DMSO-d_6 and subjected to ^{1}HNMR analysis.

5.2.8 Cell culture methods

The cells were cultured in an incubator with a humidified 5% CO_2 atmosphere at 37 ºC. Cells were grown in complete media consist of Dulbecco modified eagle medium (DMEM, Gibcco) supplemented with 10% fetal bovine serum (FBS, Thermofisher) and 1% penicillin-streptomycin (PenStrep, Thermofisher) antibiotics into twenty-five cm^2 flasks (Tarson). Human embryonic kidney (HEK293), Human pancreatic cancer (MIA PaCa2), Human urinary bladder cancer (T24) cells used for studies.

5.2.9 Cell viability assay

Cell viability was measured by well-known MTT assay using(3-(4,5-dimethylthiazol-2-yl)-2,5-diphenyltetrazolium bromide), tetrazolium dye (MTT). The cytotoxicity of nascent NP or DOX loaded NP were determined in HEK293, MIA PaCa2 and T24 cell lines. 96-well plates were seeded with density of 1000 cells per well in100 µL media and incubated for 16h for complete adherence. After adherence, the media was aspirated and replaced with fresh 300 µL media containing the NP or DOX loaded NP of desired concentrations and further incubated for desired time points (24h, 48h and 72h). A column in each 96-well plate was added only with 300 µL fresh media and considered as a control. After incubation, the compound containing media was aspirated and replaced by 100 MTT solution (0.5mg/mL) and further incubated for 4h. Thereafter MTT solution was removed with100 µL HPLC grade DMSO to dissolve the purple formazan crystals. After that the media was aspirated and replaced by MTT solution (100 µL, 0.5mg/mL in media) and further incubated for 4h. Finally, the MTT solution was aspirated and DMSO (100 µL) was added to each well to dissolve the purple formazan crystals. The plates were subjected to absorbance measurements at 570 nm using microplate reader and cell viability was estimated.

5.2.10 Cellular uptake via confocal microscopy imaging (CLSM)

Cellular uptake of free DOX, STZw+DOX and SRZw+DOX NP in MIA PaCa 2 and T24 cell lines were performed by using confocal laser scanning microscopy (CLSM). For that purpose, 1×10^5 cells seeded onto glas cover slip in each well of 6-well plate (Tarson) in 2mL of complete media and incubated for 24h for adherence. Then the media was aspirated and replaced with 2mL of fresh media containing free DOX, STZw+DOX and SRZw+DOX

nanoparticle (concentration of DOX 2.5 μg/mL) and incubated for desired timepoints (0.5, 2, 4 and 8h). After incubation time, media was removed and cells were washed two times with PBS (1x, pH 7.4) and fixed with 3.5% paraformaldehyde (PFA). Nuclei were stained with DAPI (1x) for 5 min and coverslips were mounted on sterilized glass slides. Cells were visualized and imaged using confocal microscope (Zeiss anisotropy) utilizing lasers of λ=405 nm (blue channel for DAPI), λ=488 nm (green channel for DOX). All the captured CLSM images were processed using ImageJ software and CTCF (corrected total cell fluorescence) were calculated and analyzed using Prism 8.01.

5.2.11 Endocytosis: Temperature dependent cellular uptake

Endocytosis phenomenon was investigated by temperature dependent cellular uptake. MIA PaCa 2 cells with density of 1×10^5 were seeded onto glass cover slip per well in 6-well plate 2 mL medium and incubated for 24h. After ensuring complete adherence, the media was aspirated and replaced with 2mL of fresh media containing STZw+DOX and SRZw+DOX (DOX concentration was 2.5 μg/mL). The compound treated 6-well plates then incubated at 37 °C and 4 ºC for 3h. Afterwards the cells were fixed and co-stained with DAPI (nucleus) using similar protocol mentioned for cellular uptake. Cells were imaged using Zeiss microscope and images were processed using ImageJ software.

5.2.12 Live-cell Lysotracker CLSM Imaging

To investigate enzymatic biodegradation of zwitterionic polymers in endo-lysosomal compartment of cells, live cell lysotracker imaging was performed using Zeiss Anisotropy confocal microscope. For that purpose, a density of 50,000 MIA PaCa 2 cells was seeded in multi-well confocal chamber (Thermofisher) and incubated for 24h. After the complete adherence of cells, media was replaced by 1mL of fresh media containing STZw+DOX and SB36+DOX NP (DOX 2.5μg/mL) and incubated for desired timepoints. After incubation, the media was replaced with 1mL of fresh media containing lysotracker green DND-26 (100 nM) and further incubated for another 30 minutes to stain the lysosomes. Then, media containing lysotracker was removed and cells were washed with PBS (1x) twice and imaged using Zeiss Anisotropy microscope in live condition. The lasers of excitation wavelength λ=488 nm and λ=561 nm was used to visualize lysotracker green-DND and DOX, respectively. The captured CLSM images were further processed and analyzed using ImageJ software.

5.2.13 Animal handling and experimentation

All the animal experiments were carried with compliance of Institutional Animal Ethics Committee India (IAEC) guidelines. Balb-C (6-8-week-old) and NOD-SCID (6-8-week-old) mouse strains were acquired from National Facility for Gene Function in Health and Diseases (NFGFHD, IISER Pune, India). Animals were housed in the same NFGFHD, IISER Pune and experimentation work were conducted at the same facility.

5.2.14 Hemolysis assay

The healthy Balb-C mouse (6–8-week-old) was used as source of fresh blood to conduct the hemolysis. Fresh blood (0.5) was withdrawn from anaesthetized mouse by retro-orbital plexus puncture using capillary into EDTA (5%) pre-coated centrifuge tube. RBCs were separated by centrifugation at 5000rpm for 10min supernatant carefully removed. The RBC pellet was washed with PBS buffer(pH 7.4) 2-3 times and resuspended in PBS (5% v/v) which was then used for further assay. Each well of the 96-well plate was then added with 100 µL RBC solutions. The stock solution of zwitterionic polymeric NP in PBS (100 µL, 1mg/mL) was then added to wells containing RBC solutions. Wells added with PBS buffer and Triton-X (1% v/v) were considered as negative (no-hemolysis) and positive control (100% hemolysis) respectively for the assay and the plate was incubated at 37 ºC for 1h. After the incubation period, the content from each well was transferred to centrifuge tubes and centrifuged at 5000 rpm for 5 min to visualize the pellet formation. The supernatant (100 µL) from each tube was then transferred to wells in 96-well plate and subjected to absorbance measurement using 570 nm excitation wavelength (heme) in microplate reader. Percentage hemolysis was calculated using the absorbance values based on our earlier reports (chapter 2).

5.2.15 Pancreatic cancer Xenograft Tumor model

Immuno-compromised NOD-SCID (6-8-week-old) mice were obtained from NFGFHD, IISER Pune, India for the xenograft model study. To create the subcutaneous tumor, 2×10^6 MIA PaCa2 cells (human Pancreatic Carcinoma) in 100 µL PBS buffer were injected subcutaneously to right flanks of the mice. The mice showed significant tumor growth after 10-15 days of injection and further studies were conducted once tumor reached a certain volume.

5.2.16 *In Vivo* biodistribution studies

Biodistribution analysis was performed in the MIA PaCa2 tumor bearing NOD-SCID mice (~100 mm^3) conducted using In-Vivo Imaging System (IVIS spectrum Perkin-Elmer)

employing near infrared fluorescence imaging (NIRF). The near infrared dye IR780 and IR780 labeled NP were used for imaging owing to deep penetration ability, high quantum yield, and less background emission. IR780 was excited using wavelength 740 nm and emission was collected at 800 nm using filter of 25 nm. Mice were divided into three groups (*n=3*) and intraperitoneally injected with IR780, STZw+IR780 and SRZw+IR780 NP respectively and one animal was injected with PBS only as negative control. The dosage of IR780 was kept at 0.7mg/kg for nascent IR780 or IR780 loaded NP based on our earlier studies. Due to the insolubility of IR780 in PBS, 5% DMSO in PBS (100 µL) was used for injection of nascent IR780. Whereas IR780 loaded NP were injected using PBS (100 µL) only. Whole body live animal images were captured at 4, 24, 48, and 72 by anesthetizing animals using inbuild system equipped with isoflurane I.P. and oxygen inlet. After 72h, experiment was terminated by euthanizing animals using an overdose of isoflurane and animals were pericardially perfused using PBS buffer (40-50mL). Organs were harvested and washed with PBS and subjected to IVIS imaging for quantifying organ-based accumulation of NP. Living Image 4.7 software (PerkinElmer) was used to process the capture images for quantification.

5.2.17 Anticancer Efficacy of STZw+DOX and SRZw+DOX

6-8-week-old healthy NOD-SCID having subcutaneous human Pancreatic Carcinoma (Xenograft model) was used for study. Once the tumor reached ~70 mm^3 volume, all animals were randomly divided into four groups (*n=5*). The animals were intraperitoneally injected with PBS, DOX, STZw+DOX and SRZw+DOX in 100 µL PBS buffer every 6^{th} day for 28 days. The tumor growth and body were monitored for every fourth day for 28 days. Tumor volume was measured by caliper and estimated by using the formula [$0.5 \times (\text{length} \times \text{width}^2$. At the end of the 28th day of treatment, the animals were sacrificed using CO_2 and tumors were collected for visualization and gravimetric analysis (weights). Harvested tumor tissue were fixed with 4% neutral formalin (NBF) for further studies.

5.2.18 Statistical analysis

GraphPad Prism 8.01 software was used to perform all the statistical analysis. Results are expressed as mean ± SD ($n \geq 3$). t-tests, one-way ANOVA test and two-way ANOVA tests were used for multiple comparisons using GraphPad Prism 8.0. $p < 0.05$ was considered statistically significant.

5.3 Results and Discussion

5.3.1 Synthesis and Characterization

The star zwitterionic diblock and copolymer were synthesized using ring opening polymerization (ROP) as shown in Scheme 5.1. ROP of monomer M1 (chapter 4) using 6-arm alcohol initiator (dipentaerthryitol) and tin (II) di-octanoate keeping M/I ratio as 60 yielded star poly(amino-ester) or SPAE macroinitiator. Degree of polymerization (DP) for SPAE was obtained as 60 by HNMR as shown in Figure 5.3a. The degree of polymerization (DP) for SPAE was estimated by comparing integration of end group protons (**e**) with the proton corresponding to -C**H**$_2$-O-CO- ester backbone **(a)**. The second ROP using monomer M2 and SPAE as a macroinitiator resulted in SPAE-*b*-tBuPCL diblock copolymer. DP was confirmed as 60 for tBuPCL block by ^{1}H NMR analysis and data is shown in Figure 5.3b. DP in SPAE-b-tBuPCL was estimated by comparing integration of proton **c** (PAE) to proton **h** (tBuPCL). Acid catalyzed deprotection of SPAE-*b*-tBuPCL further yielded star zwitterionic diblock copolymer (SZw-Di) as shown in Scheme 5.1a which was further confirmed by ^{1}H NMR analysis as shown in Figure 5.3c by disappearance of **d** and **d'** protons (tButyl groups) in SZw-Di. To understand the role of arrangement of anionic and cationic repeating units in the copolymer, the random counterpart of diblock copolymer was synthesized. Star zwitterionic copolymer (S-RanCo) was synthesized by one step ROP of monomer M1 and M2 together (M1:M2, 1:1, M/I=120) using dipentaerthryitol as an initiator followed by deprotection as shown in Scheme 5.1b and characterized by NMR as shown in Appendix. Synthesis of triblock copolymer was conducted by sequential ROP followed by deprotection as shown in Scheme 2a. 1st ROP of monomer M3 (ε-caprolactone) yielded star polycaprolactone (SPCL) which was further utilized as macroinitiator for 2nd ROP with monomer M2 to obtained SPCL-b-tBuPCL diblock copolymer. The diblock SPCL-b-tBuPCL was further utilized as macroinitiator for 3rd ROP with monomer M1 to yield SPCL-b-tBuPCL-b-PAE triblock copolymer which was further deprotected to obtain star zwitterionic triblock (STZw) copolymer. The formation of each block in triblock copolymer was confirmed by ^{1}H NMR analysis and data is shown in Figure 5.4. DP for SPCL was estimated by comparing integration of initiator (***i***) with the proton corresponding to -C**H**$_2$-O-CO- ester backbone ***(a)*** as shown in Figure 5.4a. DP in SPCL-*b*-*t*BuPCL was estimated by comparing integration of proton ***a*** (PCL) to proton ***a' (tBuPCL)*** as shown in Figure 5.4b. DP in SPCL-*b*-tBuPCL-*b*-PAE was estimated by comparing integration of proton ***b"*** of PAE with protons ***a*** of PCL as shown in Figure 5.4c. Deprotection was successfully confirmed by the disappearance of ***d*** and ***d'*** protons (tButyl groups) in STZw as shown in Figure 5.4d.

The random counterpart of triblock copolymer was synthesized by ROP of monomer M1 and M2 together (M1:M2, 1:1, M/I=120) using hydrophobic SPCL as macroinitiator as shown in Scheme 5.2b. DP was estimated 55:55 for PAE and tBuPCL units by ^{1}HNMR analysis in similar manner to that of triblock. tButyl groups were further removed by acid catalyzed deprotection to yield star zwitterionic random copolymer (SRZw) and well characterized by NMR analysis. The ^{1}HNMR spectra for star zwitterionic random copolymer for each step is shown is shown in Appendix.

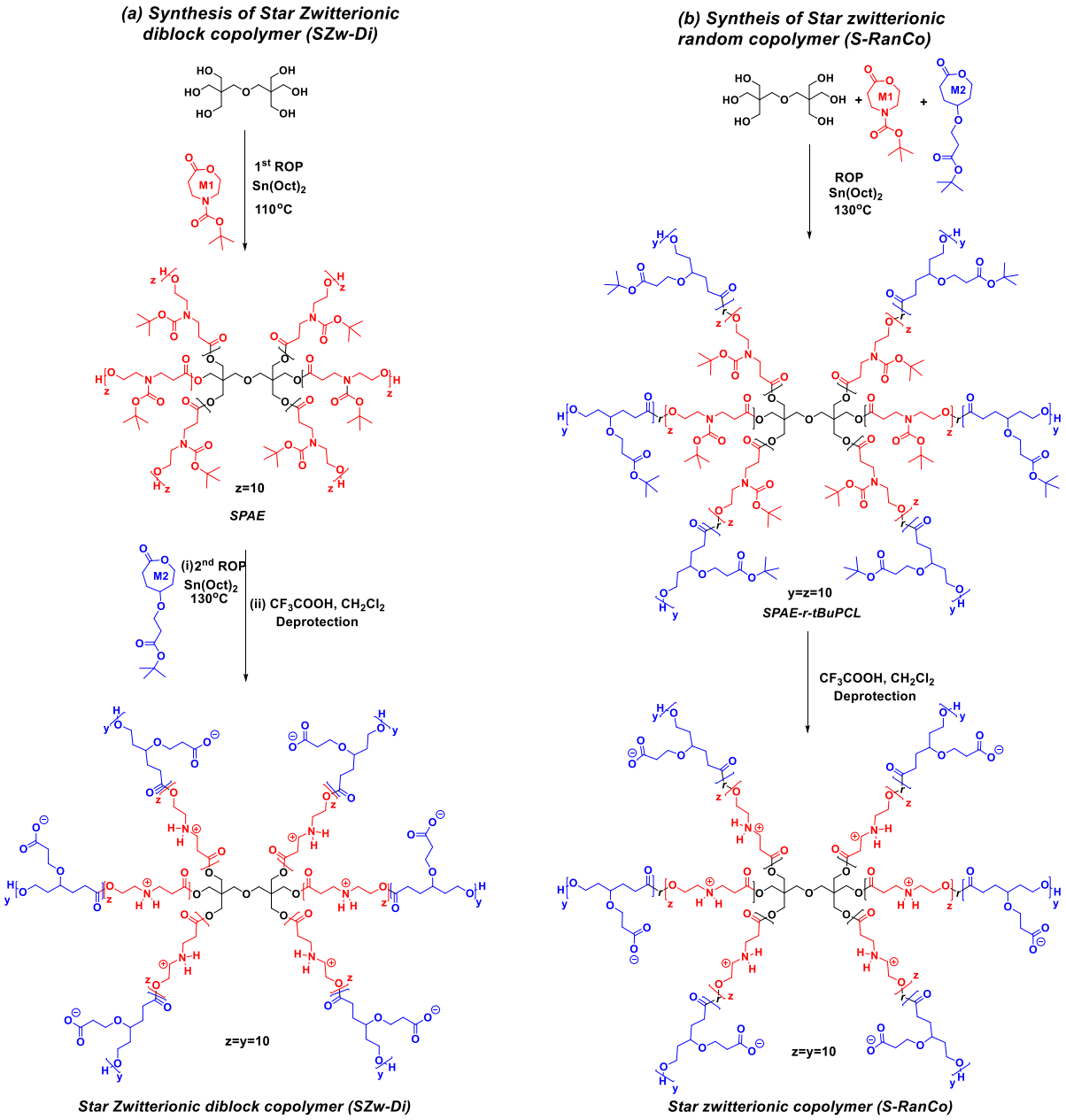

Scheme 5.1. *(a) Synthesis of star zwitterionic diblock copolymer by ROP. (b) Synthesis of star zwitterionic random copolymer by ROP.*

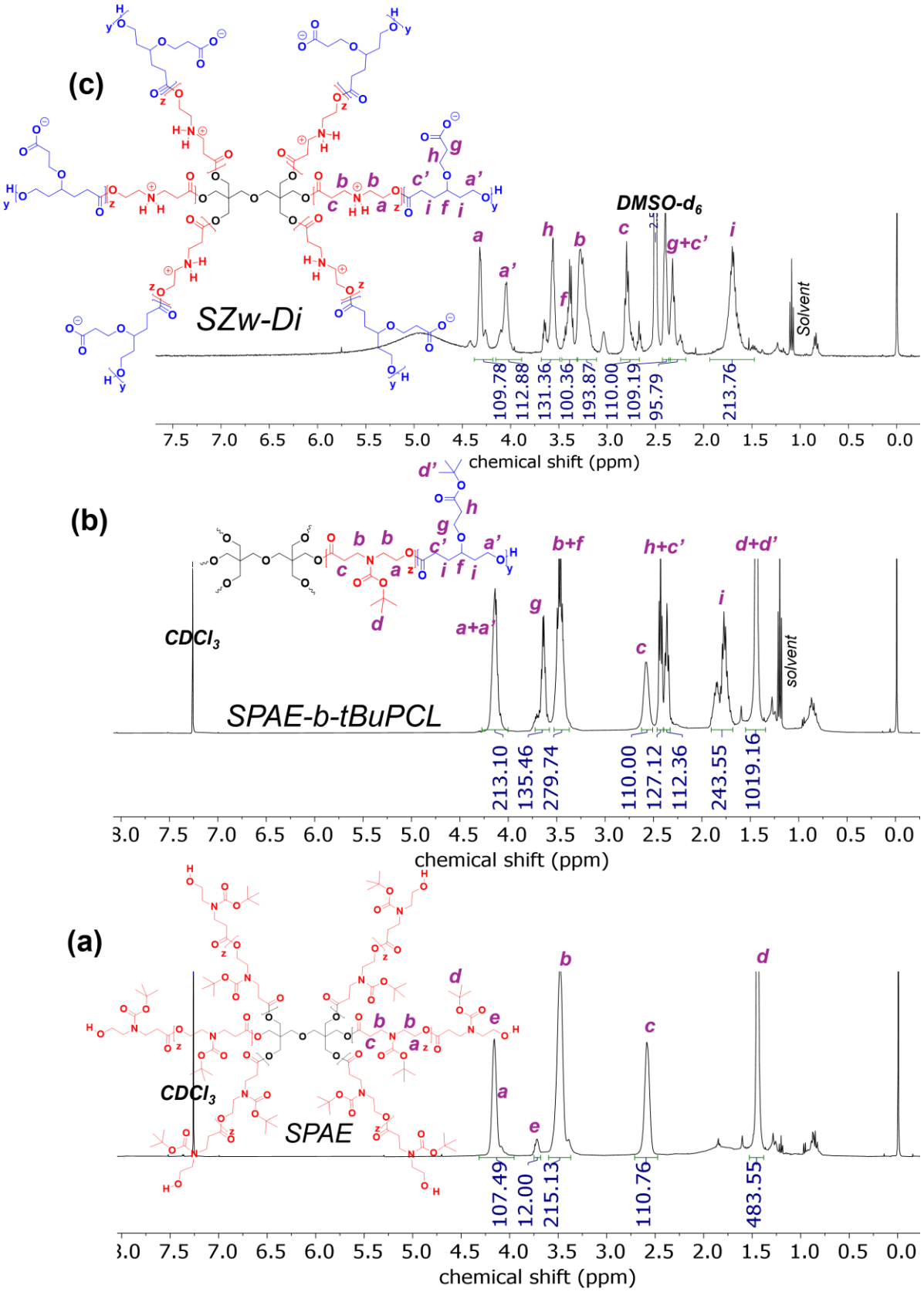

Figure 5.3. *^{1}HNMR plots of (a) SPAE in $CDCl_3$. (b) SPAE-b-tBuPCL in $CDCl_3$. (c) SZw-Di in DMSO-d_6.* ***Note:*** *Peaks are assigned alphabetically.*

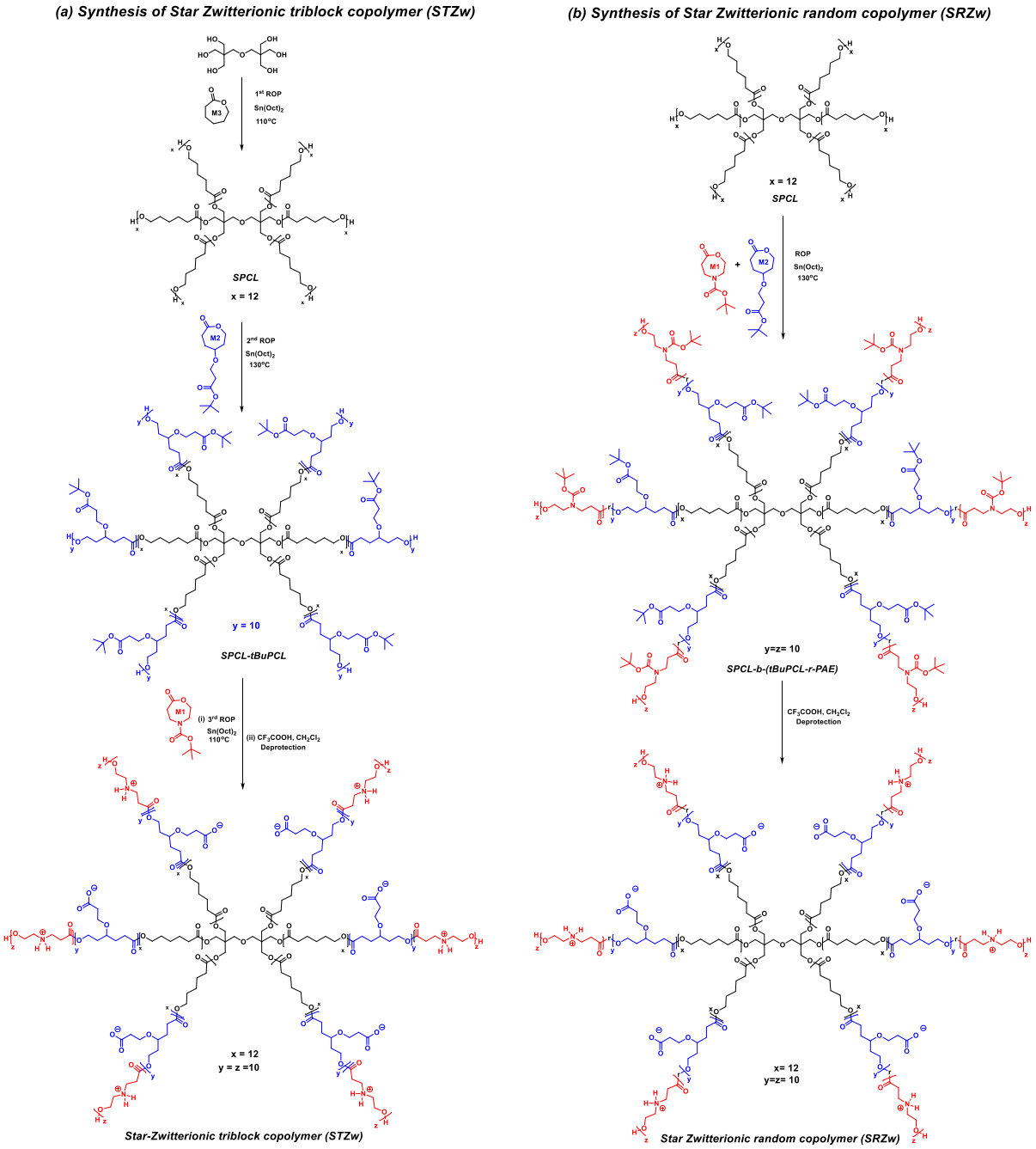

Scheme 5.2. *(a) Synthesis of star zwitterionic triblock copolymer by sequential ROP followed by acid catalyzed deprotection. (b) Synthesis of star zwitterionic random copolymer by ROP followed by acid catalyzed deprotection.*

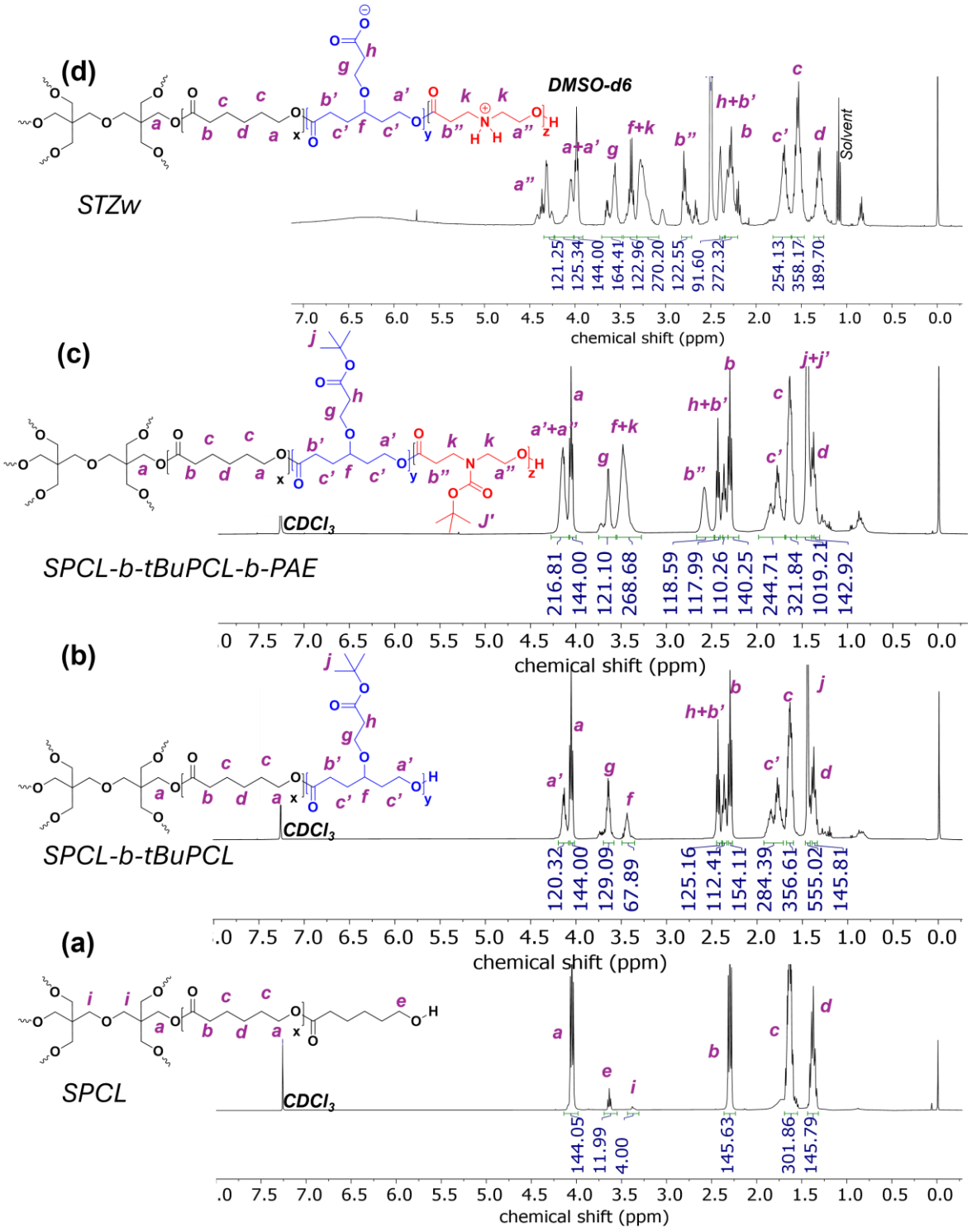

Figure 5.4: *^{1}HNMR plots of (a) SPCL in $CDCl_3$. (b) SPCL-b-tBuPCL in $CDCl_3$. (c) SPCL-b-tBuPCL-b-PAE triblock copolymer in $CDCl_3$. (d) STZw triblock in DMSO-d_6.* ***Note:*** *Peaks are assigned alphabetically.*

Molecular wights (M_n and M_w) and polydispersity index (Đ) of the tButyl derivative of the star block and random copolymers were estimated by gel permeation chromatography (GPC) or size exclusion chromatography (SEC) using THF as eluent. The SEC elution traces of t-Butyl protected star diblock, triblock and random copolymers are shown in Figure 5.5a-c. Details of number of repeating units of each block, ^{1}HNMR derived molecular weights and SEC derived molecular weights are tabulated in Figure 5.5d. All the polymers exhibited monomodal molecular wight distribution with the narrow Đ ranging from 1.1 to 1.6. The estimated number average molecular weights (M_n) from SEC were very well accorded with theoretical molecular weights (M_n from ^{1}HNMR) for homopolymers and diblock copolymers. However, the SEC based M_n and weight average molecular weights (M_w) for triblock was slightly underestimated owing to the use of polystyrene standard as shown in Figure 5.5d.

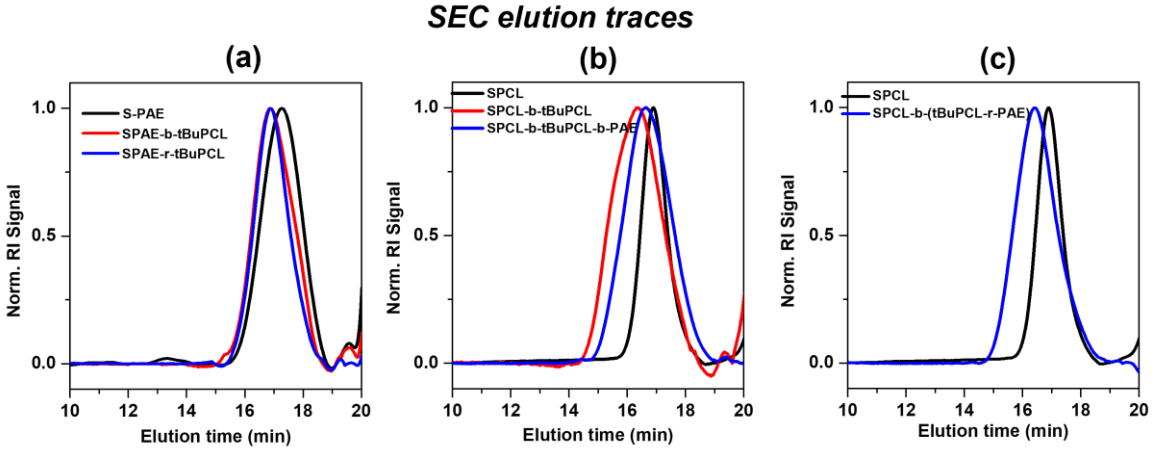

(d) Details of Molecular Weights

Sample[a]	PCL[b] (x)	PAE[b] (y)	tBuPCL[b] (z)	M_n [c] (g/mol)	M_n [d] (g/mol)	M_w [d] (g/mol)	Đ[d]
SPCL	72	-	-	8500	12900	14900	1.15
SPCL-*b*-*t*BuPCL	72	-	60	24000	29200	45900	1.57
SPAE	-	54	-	11900	8900	12000	1.34
SPAE-*b*-*t*BuPCL	-	54	56	26300	12500	18200	1.45
SPAE-*r*-*t*BuPCL	-	55	55	26100	13500	19100	1.41
SPCL-*b*-*t*BuPCL-*b*-PAE	72	60	60	36900	20000	32200	1.60
SPCL-*b*-(*t*BuPCL-*r*-PAE)	72	55	55	34500	24000	38600	1.61

a:tButyl protected samples. b: Number of repeating units were estimated by ^{1}HNMR analysis. c: Molecular weights estimated by ^{1}HNMR. d: Molecular weight and polydispersity was estimated by SEC analysis in THF for tButyl protected samples. Polystyrene was used as calibration standard.

Figure 5.5: *Size exclusion chromatography (SEC) profiles of (a) SPAE macroinitiator, SPAE-b-tBuPCL diblock copolymer and, SPAE-r-tBuPCL copolymer. (b) SPCl macroinitiator, SPCL-b-tBuPCL diblock copolymer and SPCL-b-tBuPCL-b-PAE triblock copolymer. (c) SPCL macroinitiator and SPCL-b-(tBuPCL-r-PAE) random copolymer. (d) Details of molecular weights.*

5.3.2 Self-Assembly and Drug Encapsulation

The novel star-zwitterionic triblock (STZw) copolymer consists of hydrophobic core composed of PCL segment and shell made up of hydrophilic self-immolative PAE segment and carboxylic acid substituted PCL (CPCL) segment in block arrangement. On other hand, star random copolymer (SRZw) the core is composed of hydrophobic PCL segment and shell is composed of PAE and CPCL segment in random manner. Both STZw and SRZw are core-shell star amphiphilic structures consisting of pH sensitive amine groups in PAE and carboxylic acid pendent groups in CPCL units, respectively. To understand comprehensively the self-assembly of STZw triblock copolymer, the STZw polymer was self-assembled in solutions of varying pH from 2.0 to 11 and resulting nano-assemblies of STZw are shown in Figure 5.6a. The phase segregation of hydrophobic and hydrophilic segments resulted in the energetically most stable anionic, cationic or zwitterionic nano-assemblies based on pH of the solution. The STZw self-assembled into cationic Nanoparticles (NP) below pH~5.0 owing to protonation of PAE segment and carboxylic acid units (in CPCL) in the shell evident from positive zeta (ζ) potential (+40 to +20 mV) as shown in Figure 5.6b . This resulted in the inward collapsing of CPCL (COOH form) units into core along with PCL and cationic shell ($^{+}NHR_2H$). When the pH of solution increased above 7.4, the PAE segment deprotonated into neutral amine (NHR_2) form and confined to the core of NP while CPCL units oriented towards outer layer being in deprotonated form COO^- constituted shell of the core-shell anionic NP as shown in Figure 5.6a. Formation of anionic NP was confirmed by highly negative ζ potential (-20 to -35 mV) as pH was elevated from 8 to 11 as shown in Figure 5.6b. Interestingly, the NP remained in the zwitterionic state in the pH range ~6.5 to 7.4 evident from the neutral ζ potential (+10 to -10 mV) as shown in Figure 5.6b. Isoelectric point was observed around neutral pH (7.0) resulted from existence of protonated PAE ($^{+}NHR_2H$) and deprotonated CPCL (COO^-) segments in the shell of NP. Surprisingly, the hydrodynamic diameters (DLS size) of STZw were observed in the range of 25 nm irrespective of pH of the solution as shown in Figure 5.6b. This clearly indicated that the NP were stable irrespective of pH of the solution and surface charge (anionic, cation or zwitterionic). Interestingly, the CPCL units stabilized the unstable PAE (self-immolation) at neutral pH via electrostatic (zwitterionic) interaction among the COO^- of CPCL and $^{+}NHR_2H$ of PAE segments in the analogous manner to our earlier report.[20] The DLS histogram of STZw NP exhibited monomodal size distribution having hydrodynamic diameter of ~25 nm with narrow polydispersity (PDI) of 0.28 as shown in Figure 5.6c. HR-TEM analysis revealed spherical shape of STZw NP as shown in Figure 5.6d.

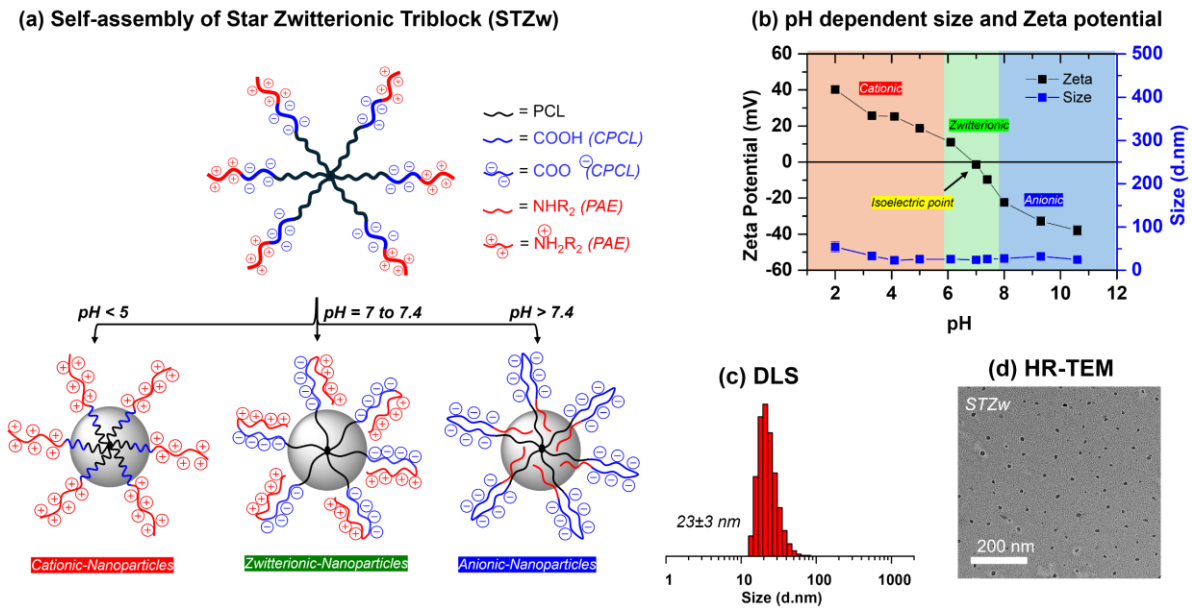

Figure 5.6. *pH-dependent self-assembly: (a) Schematic representation of self-assembly of zwitterionic star triblock copolymer (STZw) in varying pH. (b) Plot of DLS sizes and Zeta potential of the STZw NP in Briton-Robinson buffer(10mM) at 25 ℃. (c) DLS histogram (% Number plot) and (d) HR-TEM image of STZw NP. (scale bar 200nm, NP concentration was 0.1 mg/mL).*

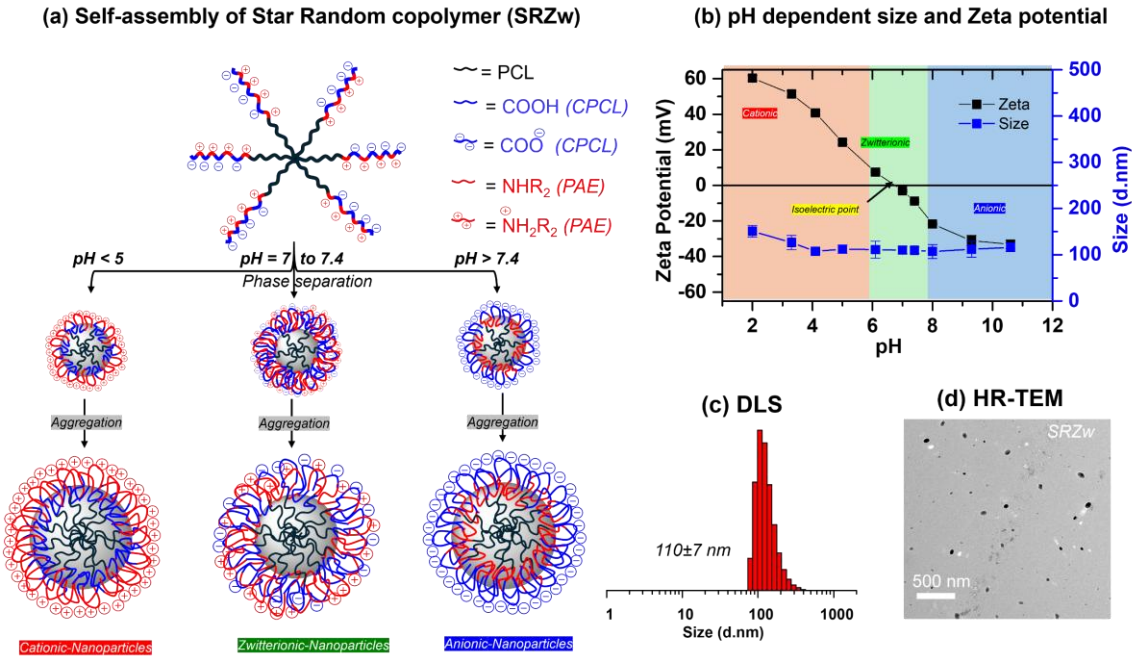

Figure 5.7. *pH-dependent self-assembly: (a) Schematic representation of self-assembly of zwitterionic star random copolymer (SRZw) in varying pH. (b) Plot of DLS sizes and Zeta potential of the SRZw NP in Briton-Robinson buffer(10mM) at 25 ℃. (c) DLS histogram (% Number plot) and (d) HR-TEM image of SRZw NP. (scale bar 500nm, NP concentration was 0.1 mg/mL).*

In addition, we further evaluated pH dependent self-assembly of star-zwitterionic random copolymer (SRZw) as shown in Figure 5.7a. Resulting nano-assemblies of SRZw depicted identical behaviour to that of STZw NP on varying pH. The surface charges (ζ potential) of SRZw were observed in similar trend to that of STZw as shown in Figure 5.7b depicting isoelectric point at pH~7. In contrast to STZw, the sizes of SRZw NP were observed in the range of ~100 nm at pH 3 to 11 as shown in Figure 5.7b. This is attributed to the formation of larger aggregated micellar NP in case of SRZw owing to the random arrangement of anionic and cationic units. This random arrangement facilitated the intra and inter polymeric chain interaction in the phase segregation process based on the pH of solution resulting in larger aggregates. The DLS histogram of SRZw NP exhibited monomodal size distribution having hydrodynamic diameter of ~110 nm with narrow polydispersity (PDI) of 0.29 as shown in Figure 5.7c. SRZw NP existed as spherical shaped nano assemblies revealed by HR-TEM imaging as shown in Figure 5.7d. Both STZw and SRZw NP exhibited neutral to slightly negative ζ potential of -9.6 and -8.9 mV at pH 7.4 and details are shown in Figure 5.8c. Details of nanoparticle characterization for the zwitterionic diblock and copolymer are mentioned in Figure 5.8d. DLS histograms of star zwitterionic diblock (SZw-Di) and copolymer (S-RanCo) in Figure 5.8a,b revealed monomodal size distribution. The pH-dependent self-assembly of star zwitterionic diblock (SZw-Di) and copolymer (S-RanCo) exhibited similar trends as of STZw and SRZw respectively as shown in Figure 5.9. However, both SZw-Di and S-RanCO NP showed larger aggregates at pH <5.0 due to protonation of CPCL and PAE. This is attributed to lack of hydrophobic PCL core which is essential in phase-segregation at lower pH. In contrast, above pH 5.0, stable nano-assemblies were observed as shown in Figure 5.9c and 5.9d. pH dependent trend in surface charges was observed revealed by zeta potential measurements depicting isoelectric points at pH ~6 to 6.5 in SZw-Di and S-RanCo nanoparticles. Size details are mentioned in Figure 5.8c. Critical micellar concentration (CMC) was obtained in the range of 1.0 to 8.0 µg/mL(see Appendix).

(a) DLS histogram of SZw-Di

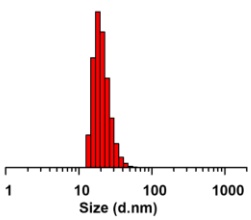

(b) DLS histogram of S-RanCo

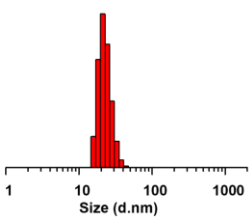

(c) Details of nanoparticle characterization

Entry	Nanoparticles		
	DLS size (d.nm)	PDI (Đ)	Zeta Potential (ζ) in mV at pH 7.4
SZw-Di	22 ± 4	0.39 ± 0.04	-30.7 ± 1.6
S-RanCO	122 ± 12	0.45 ± 0.10	-23.4 ± 1.2
STZw	23 ± 3	0.28 ± 0.05	-9.6 ± 1.3
SRZw	110 ± 7	0.29 ± 0.06	-8.9 ± 1.0

Figure 5.8: *DLS histograms of (a) SZw-Di NP and (b) S-RanCo NP (Nanoparticle concentration was 0.1mg/mL). (c) Tabulated details of nanoparticle characterization at pH 7.4.*

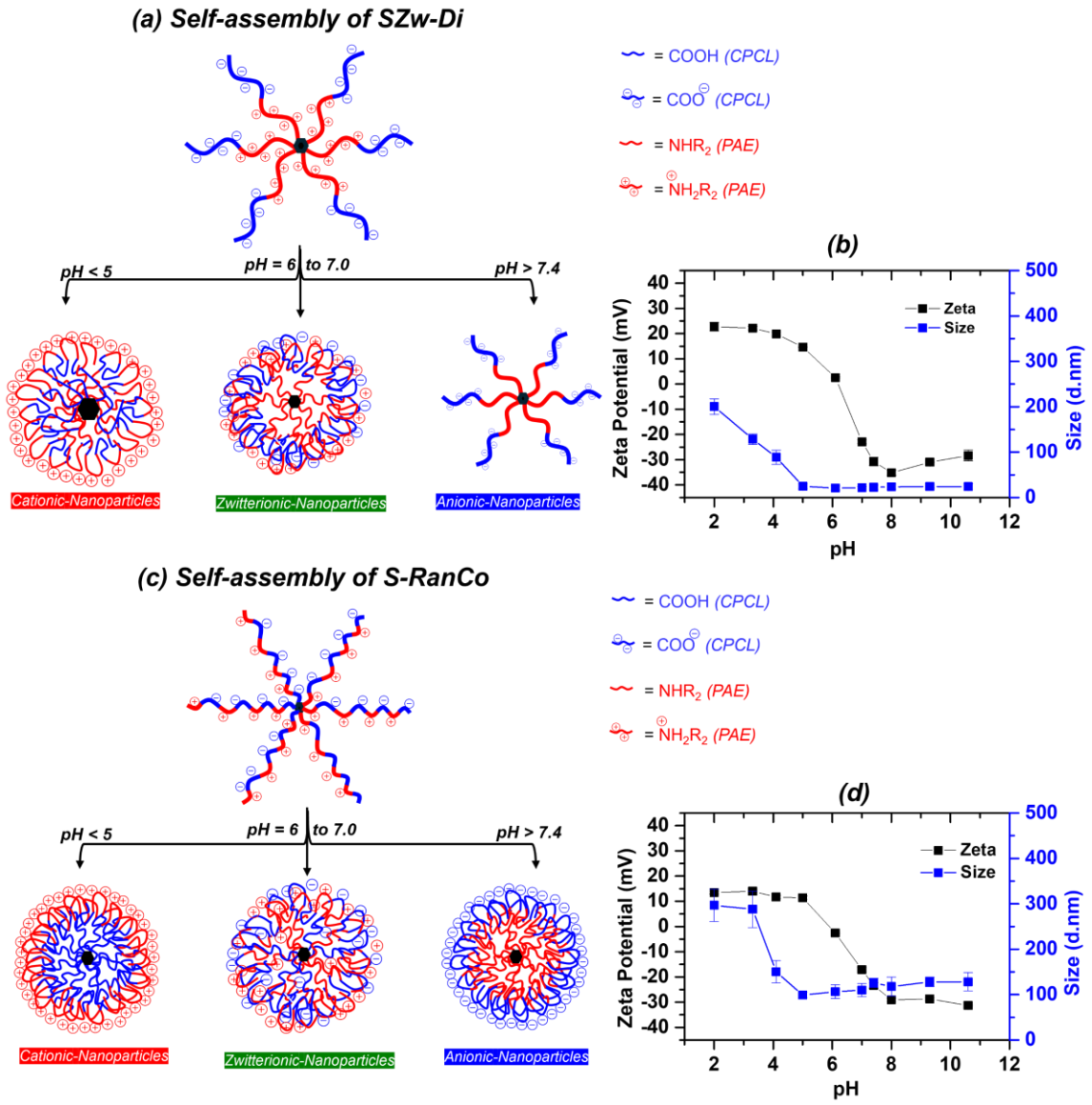

Figure 5.9: *(a) Schematic representation of self-assembly of star zwitterionic random copolymer (SRZw) in various pH (Britton-Robinson buffer, 10 mM) resulting in cationic, anionic and zwitterionic nanoparticles. (b) Plot of pH dependent size and zeta potential of star diblock (SZw-Di). (c) Self-assembly S-RanCO on various pH and (d) Plot of size and zeta potential at various pH of S-RanCo.*

The antineoplastic agent Doxorubicin (DOX, Topoisomerase II) was encapsulated in the STZw and SRZw NP by dialysis process and details are mentioned in experimental procedures. The pictorial representation of DOX encapsulation in triblock copolymer (STZw) is shown in Figure 5.10a. Photographs of vials in Figure 5.10b containing DOX loaded nanoparticles provided visual evidence of high drug loading content. DOX loaded STZw and SRZw NP will be referred as STZw+DOX and SRZw+DOX from here onward, respectively. Schematic of SRZw+DOX NP is given in Figure 5.10c. Interestingly, DLC plot in the Figure 5.10d revealed that both star STZw and SRZw exhibited 13.0 and 12.75 % drug loading

content (DLC) for DOX respectively despite of formation of different sized nano-assemblies. In contrast, the other two structures zwitterionic diblock (SZw-Di) and copolymer (S-RanCo) depicted DLC >5% attributed to lack of proper compartmentalization of hydrophobic and hydrophilic segment due to absence of PCL core. This result indeed indicates that the inner PCL hydrophobic core in the zwitterionic polymer is essential for better entrapment efficiency and stabilization in the nano-assemblies. The DLE values were obtained in the range of ~33% indicating robustness of currently designed scaffold for entrapment of DOX and all details are tabulated in Figure 5.10g.The sizes of STZw+DOX and SRZw were observed in the similar range of their respective nascent NP and DLS histograms is given in Figure 5.10e. HR-TEM analysis suggested existence of spherical NP and sizes were well correlated with DLS as shown in Figure 5.10f. More importantly, the star architecture (STZw and SRZw) enabled twice drug loading content compared to our previously reported[20] linear architecture of similar composition (see Appendix). These results clearly indicated the importance of star architecture in the process of drug stabilization.

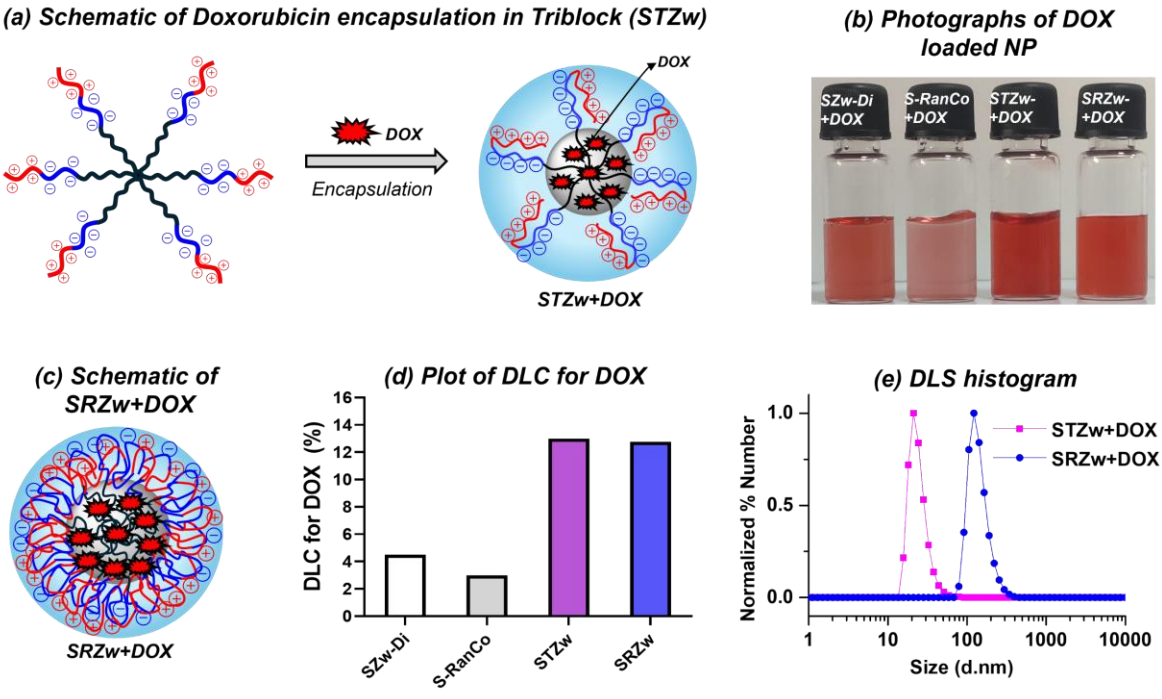

(f) HR-TEM images

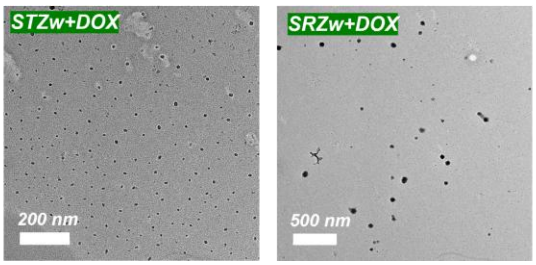

(g) Details of DOX encapsulation

Entry	DOX loaded sample				
	DLC (%)	DLE (%)	DLS size (d.nm)	PDI	Zeta (ζ) Potential in mV at pH 7.4
SZw-Di	4.5	22.5	23 ± 5	0.50 ± 0.03	-25.5 ± 2.3
S-RanCO	3.0	15.0	131 ± 10	0.54 ± 0.08	-18.6 ± 1.0
STZw	13.0	32.5	26 ± 2	0.35 ± 0.05	-8.2 ± 1.8
SRZw	12.75	31.7	111 ± 8	0.25 ± 0.05	-9.4 ± 1.0

Figure 5.10. *(a) Schematic of DOX encapsulation in STZw triblock copolymer. (b) Photographs of vials containing DOX loaded nanoparticles. (c) Schematic of SRZw+DOX nanoparticles. (d) Plot of DLC for DOX. (e) DLS histograms of STZw+DOX and SRZw+DOX NP (concentration 0.1mg/mL, % Number plot) (f) HR-TEM of STZw+DOX and SRZw+DOX NP (NP concentration was 0.1 mg/mL). (g) Details of DLC, DLE, sizes, and surface charges of DOX loaded NP at pH 7.4 (Data represented as mean ±SD, n=3).*

5.3.3 Enzymatic-Responsive Biodegradation and Drug Release

The star zwitterionic triblock and random copolymers are composed of esterase enzyme-responsive aliphatic polyester linkages in the backbone. The overall polymer structure is designed meticulously by incorporating hydrophobic PCL units which are slow biodegradable, faster biodegradable carboxyl PCL (CPCL) units and self-immolative PAE. The self-immolative PAE alone has unique ability to undergo self-destruction at pH > 7.0 via nucleophilic attack of amine lone pair onto next carbonyl of ester linkages. Since PAE are unstable at physiological pH, they cannot be used alone as drug carrier. Our previous strategy of combining the unstable PAE units with CPCL units enabled the stabilization of unstable PAE units via zwitterionic interactions between COO^- of CPCL and $^+NH_2R_2$ of PAE at physiological pH. The schematic of enzymatic biodegradation is depicted in Figure 5.11a, showing the endocytosis of DOX loaded NP and enzymatic biodegradation of NP to release the encapsulated cargoes. Briefly, the NP are taken up by the cells via endocytic pathway and internalize within endosomes which transport the NP to endo-lysosomal compartments encounters three scenarios. First, the abundant esterase enzyme acts upon the ester linkages of carboxylic acid PCL units and hydrolyzes into smaller units (degradation) causing the release of DOX. Second, the imbalance in the zwitterions caused due to biodegradation of carboxylic acid PCL units facilitates disassembly of NP resulting in the release of DOX. Third, in the event of enzymatic biodegradation, partially biodegraded PAE units could escape from endo-lysosomal compartment to cytosol where they encounter the pH 7.4 (cytosolic pH) and undergo self-immolation rendering complete degradation of polymer chains into small molecules. These overall processes render star zwitterionic NP completely biodegradable at the intracellular level which is essential to avoid the systemic toxicity due to longer accumulation of polymer matrix, making them superior candidates for drug delivery. Prior to endocytosis, NP encounter various proteins and salts at extracellular level having pH of 7.4. Therefore, the stability of DOX loaded NP is crucial for sustaining blood circulation. To mimic the extracellular conditions, the DOX loaded NP were incubated in 10% FBS (in PBS, pH 7.4) at 37 ºC and subjected to size measurement using DLS over 6 days. The plot of cumulative hydrodynamic sizes versus

incubation time for the STZw+DOX and SRZw+DOX is shown in Figure 5.11b. Both DOX loaded NP did not depict any change in sizes over the period of 6 days in the presence of FBS serum and exhibited great stability which is a prerequisite for in vitro and in vivo evaluations.

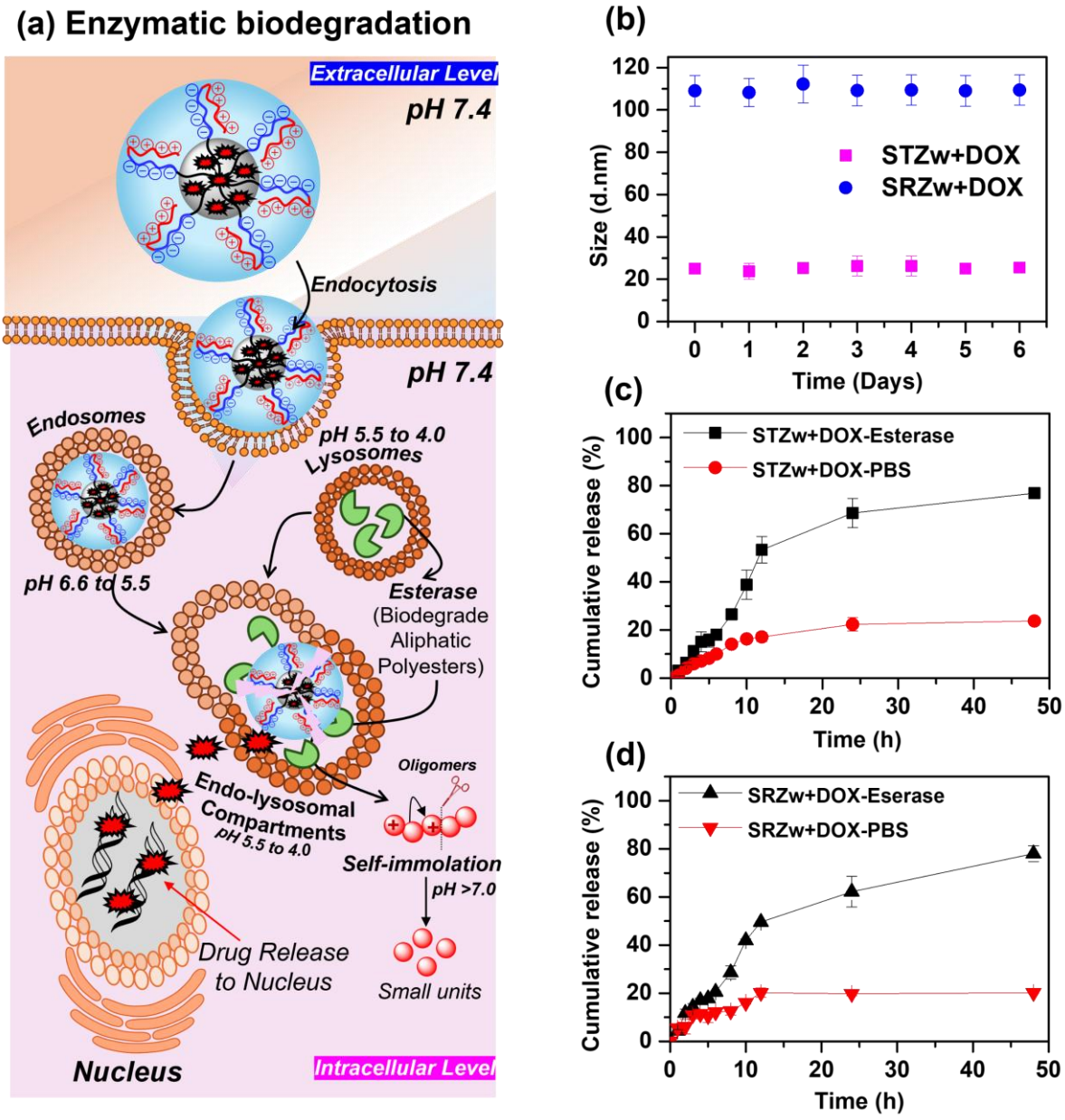

Figure 5.11. *(a) Diagrammatic representation of intracellular enzymatic biodegradation. (b) Plot of DLS sizes versus time for the stability of STZw+DOX and SRZw+DOX NP incubated in 10% FBS at 37°C for 6 days. (c) and (d) Plots of cumulative release of STZw+DOX and SRZw+DOX NP in the presence and absence of esterase, respectively.*

Furthermore, the release of DOX from NP by enzymatic biodegradation was evaluated using the porcine liver esterase. The DOX loaded NP were incubated in the presence of esterase in PBS (pH 7.4) at 37 ºC and only in PBS (without esterase) for the control experiment. The release profiles for STZw+DOX and SRZw+DOX are shown in Figure 5.11c and 5.11d, respectively. STZw+DOX and SRZw+DOX NP depicted well controlled time-dependent enzymatic degradation leading to ~60% drug release in 24h. Further incubation resulted in ~ 80% DOX release in the presence of esterase over the period of 48 h for both cases; however, only 15-23% release of DOX was observed without enzyme as shown in Figure 5.11c and 5.11d. These results clearly validate the hypothesis mentioned in Figure 5.11a and the newly designed zwitterionic polymers are completely biodegradable at the intracellular level. Therefore, combining the enzymatic biodegradable ability of carboxylic PCL with self-immolative PAE in star architecture is not only facilitate to stabilize the unstable PAE but also make the whole polymer chain completely biodegradable at intracellular level into non-toxic smaller units.

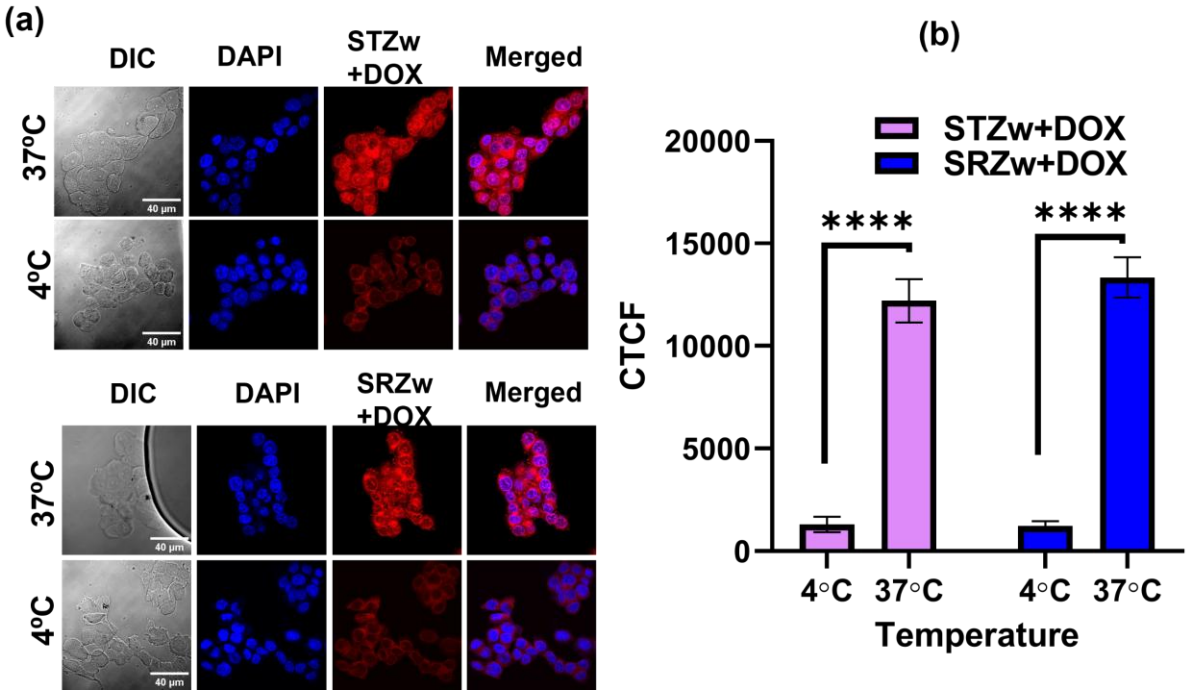

Figure 5.12. *Endocytosis: (a) CLSM images for cellular uptake of STZw+DOX and SRZw+DOX NP in MIA PaCa 2 cell lines at different temperatures after 3h (scale bar 40µm, DOX concentration 2.5µg/mL). (b) Plot of estimated CTCF for temperature dependent cellular uptake of STZw+DOX and SRZw+DOX (n>3, ****p<0.0001).*

5.3.4 Endocytosis

Endocytosis is an energy dependent process, occurring at physiological temperatures. To validate the pathway of cellular uptake for DOX loaded star zwitterionic NP (STZw+DOX and SRZw+DOX) into the cells, temperature dependent uptake assay in MIA PaCa 2 cell line (pancreatic cancer) has been conducted and confocal laser microscopy images (CLSM) are shown in Figure 5.12a. The STZw+DOX and SRZw+DOX NP exhibited significant cellular uptake only at physiological temperatures (37 ºC) clearly evident from the highly intense fluorescence of DOX (see 37 ºC panel in Figure 5.12a). In contrast, negligible fluorescence was observed in the case of cells incubated at 4 ºC where no endocytosis occurred. The corrected total cell fluorescence (CTCF) for temperature dependent cellular uptake was estimated and shown in Figure 5.12b revealed that both STZw+DOX and SRZw+DOX NP have been taken up by cells via endocytosis pathway.

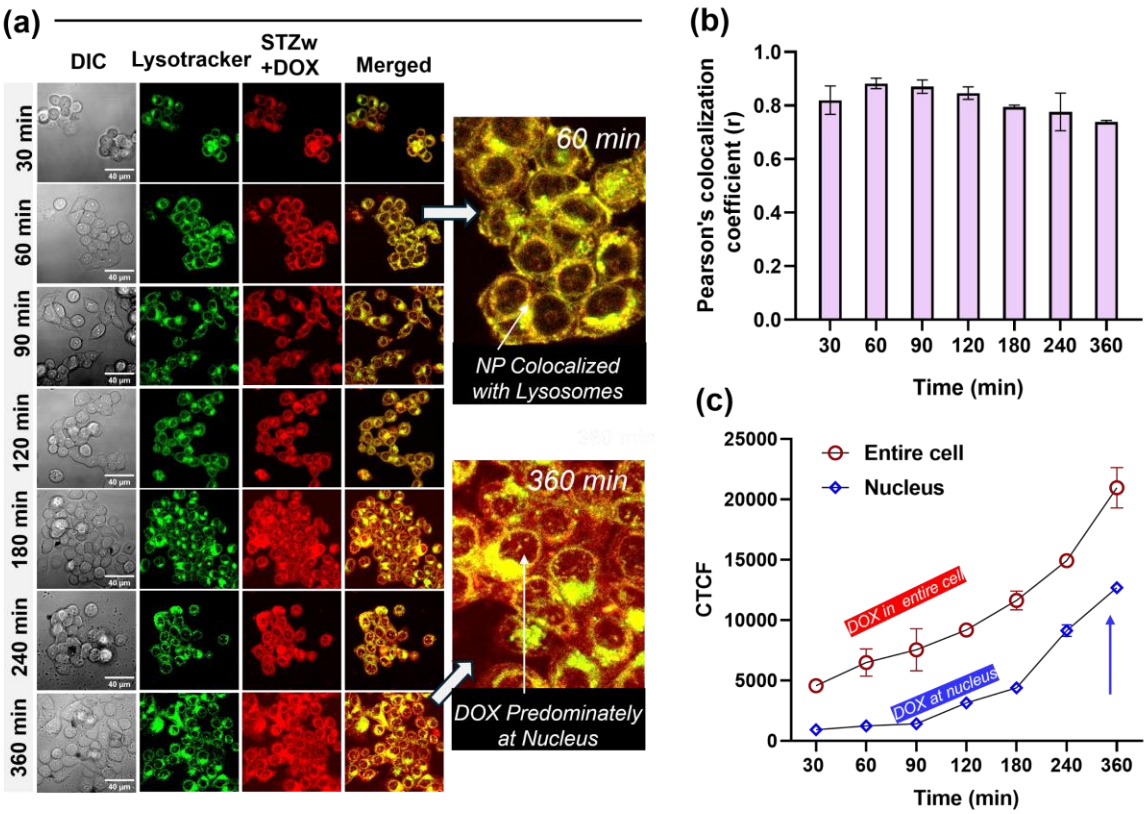

Figure 5.13. *Live cell biodegradation: (a) Real time live cell CLSM images of STZw+DOX NP treated MIA PaCa 2 cells for different time points. (scale bar 40µm, DOX concentration 2.5µg/mL, zoomed images of 60 min and 300 min). (b) Plot of Pearson's colocalization coefficient versus time for lysosome-STZw+DOX NP colocalization. (c) Plot of CTCF for cellular uptake of STZw+DOX NP in live MIA PaCa 2 cells showing uptake in entire cell and at the nucleus.*

5.3.5 Real time Live-cell Enzymatic Biodegradation

To further validate the mechanism of intracellular lysosomal colocalization and enzymatic biodegradation as mentioned in Figure 5.11a, the MIA PaCa 2 cells were treated with DOX loaded NP and subjected to real time live cell confocal imaging co-stained with lysotracker green (Lysosomes) and CLSM images are shown in Figure 5.13a. The STZw+DOX NP readily exhibited cellular uptake and internalized in the cytoplasm evident from the red color of DOX from 30 min incubation time can be seen from images in Figure 5.13a. Moreover, the NP were colocalized with lysosomes evident form yellow color in merged panel resultant from fluorescence signals of DOX (red) and lysotracker (green) in the zoomed image of 60 min incubation. At the initial timepoints of incubation, the NP were observed at cytoplasm (in the lysosomes); however, as the incubation time progressed the lysosomal enzymatic biodegradation resulted in the release and enhancement of DOX at the nuclear region (see images from 180 min onwards). The intense red fluorescence signal of DOX can be seen predominantly from the nucleus from the images of 360 min (zoomed) is direct evidence of esterase catalyzed degradation of polymer backbone to release the drug. Pearson's coefficient colocalization supported the colocalization of STZw+DOX NP with lysosomes as shown in Figure 5.13b. CTCF estimation of real time live-cell images revealed the enhancement in cellular uptake with the progression of incubation time as shown in Figure 5.13c. Interestingly, the uptake at the nucleus also enhanced with incubation time suggested the biodegradation of NP and release of DOX as shown in Figure 5.13c. In analogous manner, the SRZw+DOX NP also subjected for live-cell lysotracker imaging and CLSM images in MIA PaCa 2 are shown in Figure 5.14a. SRZw+DOX NP exhibited similar biodegradation profile as STZw+DOX NP. Zoomed images of 60 min revealed NP colocalization in lysosomes and further biodegradation resulted DOX accumulation in nucleus in 300 min zoomed images as shown in Figure 5.14a. Pearsons colocalization coefficient in Figure 5.14b supported co-localization of SRZw+DOX NP with lysosomes. Further CTCF calculations given in Figure 5.14c suggested time-dependent enhancement of DOX accumulation in nucleus resulted from enzymatic biodegradation. Surprisingly, STZw+DOX and SRZw+DOX did not show significant differences in uptake for entire cell as shown in Figure 5.14d ; however, noticeable difference among both structures was observed for live-cell biodegradation and accumulation of DOX in nucleus at 360 min timepoint as shown in Figure 5.14e. However, overall performance of both NP for internalization and colocalization remained same suggesting that both zwitterionic NP have similar behavior towards MIA PaCa2 cells.

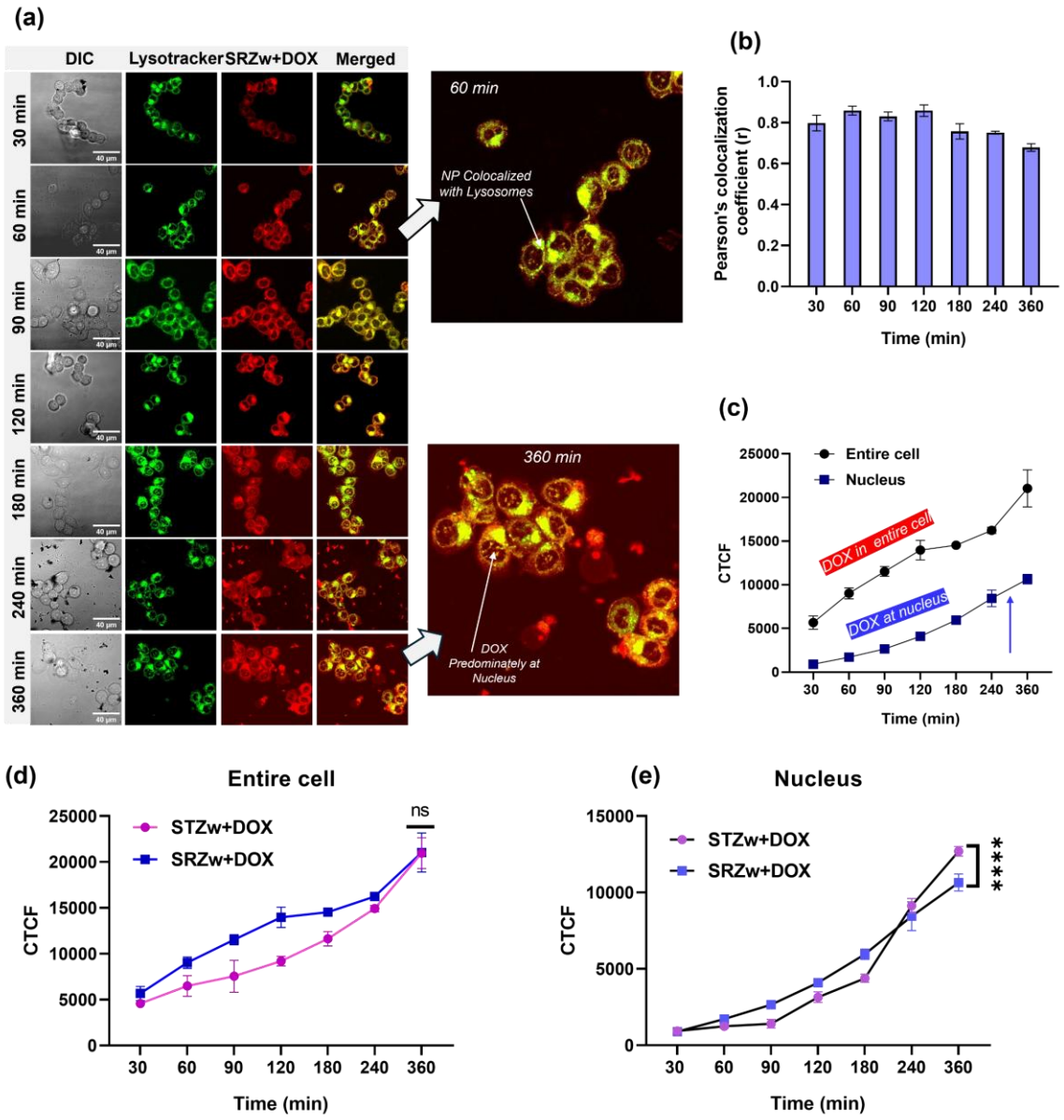

Figure 5.14. *Live cell biodegradation: (a) Real time live cell CLSM images of SRZw+DOX NP treated MIA PaCa 2 cells for different time points. (scale bar 40µm, DOX concentration 2.5µg/mL, zoomed images of 60 min and 300 min). (b) Plot of Pearson's colocalization coefficient versus time for lysosome-SRZw+DOX NP colocalization. (c) Plot of CTCF for cellular uptake of SRZw+DOX NP in live MIA PaCa 2 cells showing uptake in entire cell and at the nucleus. (d) Comparative CTCF of STZw+DOX and SRZw+DOX NP quantified from entire cell. (e) Comparative CTCF of STZw+DOX and SRZw+DOX NP quantified from nucleus (n=3, ***p=0.001, ANOVA test).*

5.3.6 Enzymatic Degradation Studies of Polymers

Furthermore, the enzymatic biodegradation was validated by turbidity, DLS and ^{1}HNMR techniques. The STZw and SRZw NP incubated with esterase (from porcine liver) enzyme in PBS (pH 7.4) at 37 ºC showed gradual increase in turbidity evident from the reduction in % transmittance up to 50 % during 48h of incubation as shown in Figure 5.15a-b. The photographs of vials in Figure 5.15c revealing turbidity clearly provided visual evidence of the enzymatic biodegradation of polymer backbone in the case of NP incubated with esterase and appeared to be turbid. This is attributed to enzymatic degradation of aliphatic ester bonds in the backbone of the polymer resulting in the precipitation of chopped oligomeric aggregates. In contrast no turbidity was observed in case of NP incubated in PBS only (without esterase) and % transmittance was > 90 % for 48h of incubation and further supported by transparent NP solution in photograph as shown in Figure 5.15c.

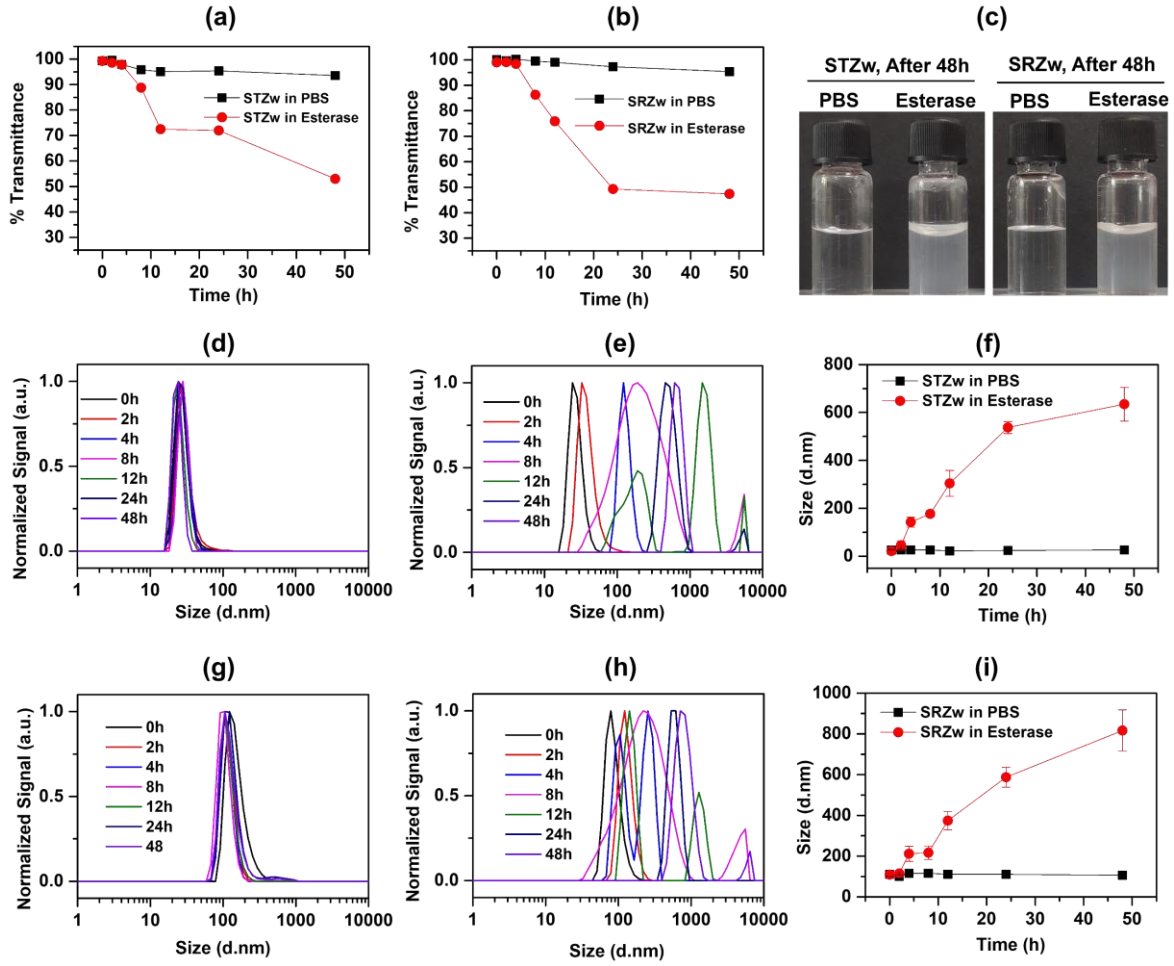

Figure 5.15. *Enzymatic biodegradation studies for STZw and SRZw nanoparticles: (a) and (b) Plots of % transmittance vs incubation time for STZw and SRZw nanoparticles incubated with esterase (porcine liver esterase, 1mg/mL) or without esterase in PBS (pH 7.4) at 37 ºC*

(NP concentration was 1mg/mL) respectively. (c) Photographs of vials containing STZw and SRZw nanoparticles (1mg/mL) in PBS and esterase after 48h incubation at 37 ºC. Plot of DLS histogram of STZw nanoparticles (1mg/mL) incubated (d) in PBS (e) in PBS with esterase at 37 ºC for various timepoint. (f) Plots of cumulative DLS sizes vs incubation time for STZw nanoparticles incubated with or without esterase (Data represented as mean ± SD, n=3). Plot of DLS histogram of SRZw nanoparticles (1mg/mL) incubated (g) in PBS (h) in PBS with esterase at 37 ºC for various timepoint. (i) Plots of cumulative DLS sizes vs incubation time for SRZw nanoparticles incubated with or without esterase (Data represented as mean ± SD, n=3).

We further validated this by size measurement (DLS), the both NP incubated with esterase (in PBS at 37 ºC) depicted a gradual increase in size attributed to hydrolysis of ester bonds resulting in the multimodal size distribution of micrometer sized aggregates over the period of 48h as shown in Figure 5.15e and 5.15h. On other hand sizes remained constant with monomodal size distribution while NP incubated in PBS (without esterase) for 48h indicating stability of NP in PBS and did not show any sign of self-immolation of PAE units as shown in Figure 5.15d and 5.15g. The cumulative size plots of STZw and SRZw NP incubated with or without esterase supported the degradation process in presence of enzyme only as shown in Figure 5.15f and 5.15i. This result indeed indicates that the star zwitterionic NP can only be degraded by applying esterase stimuli while stabilizing the NP in PBS at 37 ºC which is prerequisite for *in vitro* and *vivo* studies. It is important to note that the PAE units are capable of self-immolation at pH >7 alone but when combined with carboxylic PCL units in copolymer, PAE indeed gets stabilized due to zwitterionic interaction between amine of PAE and carboxylic acid of CPCL as shown in Figure 5.2b and only can be degraded by creating imbalance in zwitterions by enzymatic degradation. In another experiment, the STZw and SRZw star zwitterionic polymers were incubated with esterase for 48h in PBS (pH 7.4) at 37 ºC, aliquots lyophilized and subjected to ^{1}HNMR analysis. The ^{1}HNMR spectra of STZw and SRZw clearly depicted degradation of ester backbone in the presence of enzyme evident from the disappearance or reduction of ester peaks at 4.5 to 4 ppm as shown in Figure 5.16a-5.16d. This results further supported the transmission and DLS evaluation. The stability, live-cell lysosomal enzymatic biodegradation investigation supported the mechanism mentioned in Figure 5.11a and was coherent with our earlier report on fully biodegradable linear zwitterionic systems.

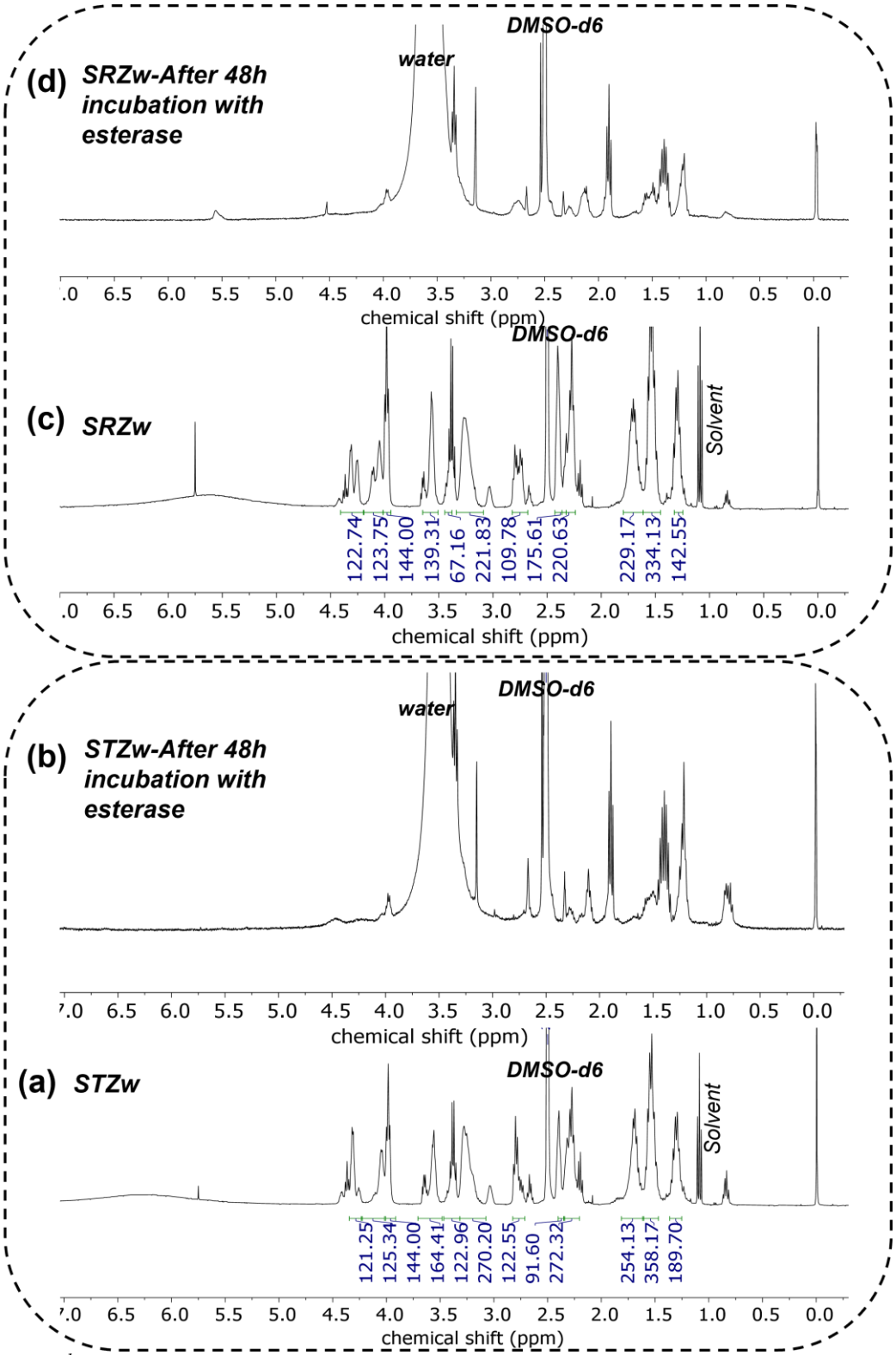

Figure 5.16: *^{1}HNMR stacks plots of STZw before (a) and after (b) incubation with esterase in PBS (pH 7.4) at 37 ºC for 48h in DMSO-d_6. ^{1}HNMR stack plots of SRZw before (c) and after (d) incubation with esterase in PBS (pH 7.4) at 37 ºC for 48h in DMSO-d_6. Aliquots were taken after 48h of incubation and lyophilized. Lyophilized samples were dissolved in DMSO-d_6 for NMR analysis.*

5.3.7 Cytotoxicity Studies

Cytotoxicity of nascent zwitterionic NP was assessed in multiple cell lines by MTT assay for 72h of incubation. Nascent zwitterionic nanoparticles were evaluated for biocompatibility in WT-MEF (wild-type mouse embryonic fibroblast), HEK293T (human embryonic kidney), MIA PaCa 2 (pancreatic cancer) and T24 (urinary bladder cancer) cell lines for 72h incubation and cell viability plots are shown in Figure 5.17a-d. All the nascent NP showed excellent cell viability in WT-MEF cell. We continued with STZw and SRZw NP for evaluation of cell viability in other cell lines. Zwitterionic STZw and SRZw NP showed excellent cell compatibility with 100% cell viability in Hek293T, MIA PaCa 2 and T24 cell line as shown in Figure 5.17b-d. Next we assessed the killing efficiency of STZw+DOX and SRZw+DOX NP in HEK293T, and T-24 cell lines for 72h incubation and data is shown in Figure 5.17e and 5.17f. Both DOX loaded NP depicted excellent dose dependent killing ability similar to DOX in both non cancer (HEK) and cancer cell (T24) lines suggesting the efficiency of NP to deliver the DOX. Notably the STZw+DOX and SRZw+DOX NP were slightly non-toxic to HEK293T cells compared to DOX implying selective efficacy towards cancer cells as shown in Figure 5.17e. However, the both NPS were equally efficient in killing T24 cells and showed similar efficiency with free DOX. Next we evaluated STZw+DOX and SRZw+DOX NP for their killing efficiency in MIA PaCa2 cell line for two different time points of incubation such as 48h and 72h. The plot of cell viability for 48h and 72h in MIA PaCa 2 cell line is shown in Figure 5.17g and 5.17h respectively. Interestingly at 48h incubation efficient cell killing was observed only at higher concentrations, however at 72h incubation excellent killing ability was observed. In addition, STZw+DOX and SRZw+DOX NP exhibited similar killing efficiency compared to free DOX in MIA PaCa 2 cells suggesting successful delivery of DOX in the pancreatic cancer cells. The half-maximal inhibitory concentrations (IC_{50}) were obtained in the range of 0.1 to 0.6 μg/mL as shown in Figure 5.17i. IC_{50} values revealed significant differences between triblock (STZw) and random (SRZw) structures; however, at higher concentrations the efficacy of both NP remained similar. The DOX loaded NP showed better efficacy in MIA PaCa 2 among all cell lines examined.

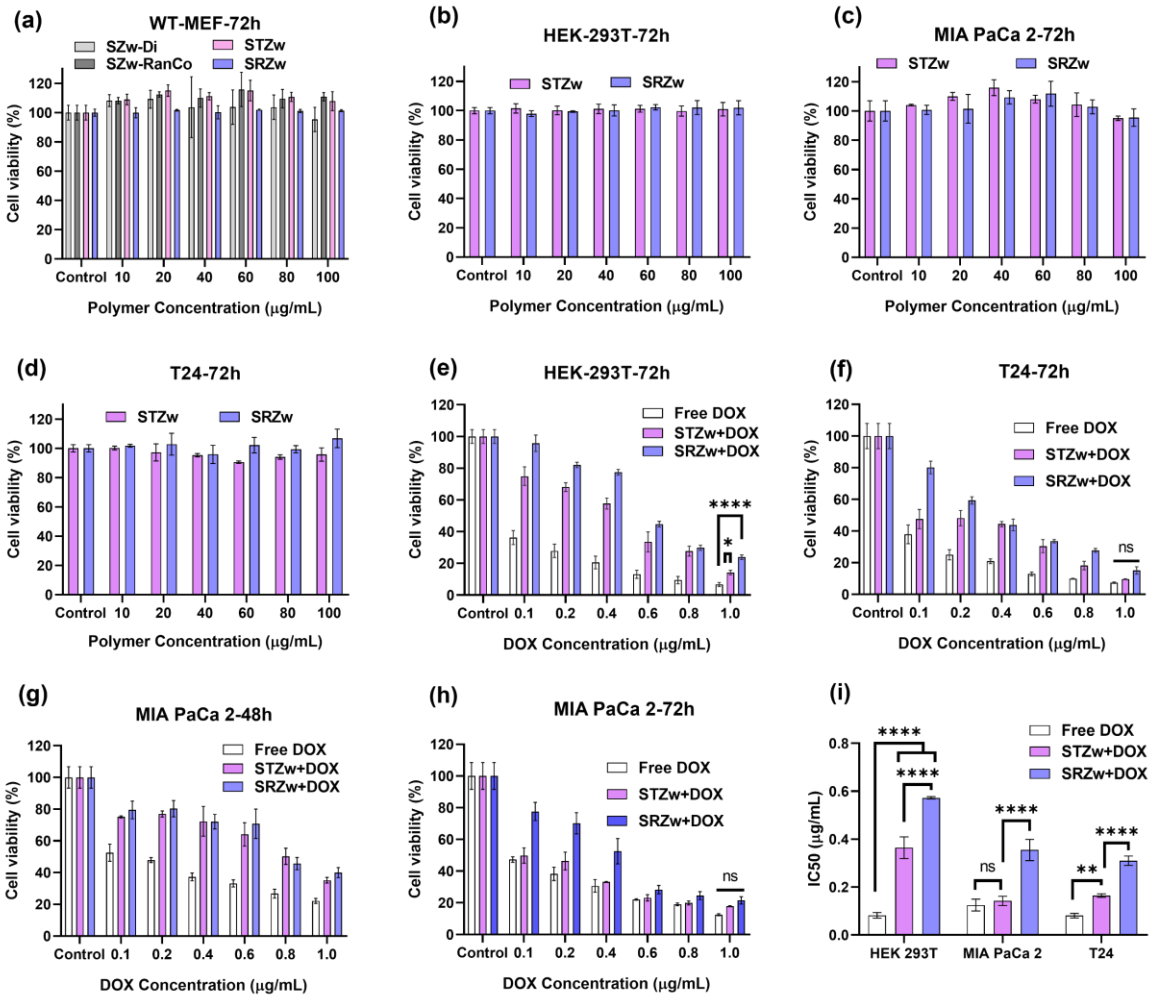

Figure 5.17. *Cytotoxicity by MTT assays: (a) Plot of cell viability (MTT assay) for nascent SZw-Di, S-RanCO, STZw and STZw NP in WT-MEF cell line for 72h incubation. (b) to (d) Plot of cell viability (MTT assay) for nascent STZw and STZw NP in HEK293T, MIA PaCa 2 and T24 cell lines for 72h incubation. (e) to (f) Cytotoxicity of free DOX, STZw+DOX and SRZw+DOX NP in HEK293T and T24 cell lines for 72h incubation (n=3, data represented as mean ± SD, ***p<0.0001, ns=non-significant). (g) and (h) Cytotoxicity of free DOX, STZw+DOX and SRZw+DOX NP in MIA PaCa 2 cell lines for 48h and 72h incubation respectively (n=3, data represented as mean ± SD). (i) The plot of IC_{50} concentrations of free DOX, STZw+DOX and SRZw+DOX NP for different cell lines (n=3, data represented as mean ± SD, **p=0.0021, ****p< 0.0001, ns= non-significant, ANOVA test).*

5.3.8 Cellular uptake studies

Cellular uptake studies in MIA PaCa 2 cell line in a time-dependent manner revealed that the STZw+DOX and SRZw+DOX were efficiently taken up by the cells and CLSM images for 2h-8h incubation are shown in Figure 5.18a. CLSM images showed strong fluorescence signal of DOX at the cytoplasm at 30 min and 2h incubation as shown in Figure 5.18a. Whereas at higher timepoints (4h and 8h), NP cleaved and released DOX to nucleus evident form the

intense signal from the nucleus evident from the magenta color in merged images in Figure 5.18a. The CTCF values in Figure 5.18b revealed enhancement in cellular uptake with increase in time and 1.5 to 2-fold higher uptake was observed in case NP compared to DOX in MIA PaCa 2 cell line at higher time points. To assess the efficiency of STZw+DOX and SRZw+DOX NP in another cancer cell line, cellular uptake in T24 cell line was performed for 4h and 8h incubation and CLSM images are shown in Figure 5.19a. Both DOX loaded NP showed better uptake in T24 cells evident from intense fluorescence signal of DOX from nucleus owing to accumulation of DOX in the nuclei in merged images. A similar trend in CTCF plot in Figure 5.19b was observed for T24 cell treated with STZw+DOX and SRZw+DOX NP and depicted 1.5-fold higher uptake compared to free DOX. Noticeably both structures did not show significant difference in cellular uptake suggesting that the block or random arrangement of cationic and anionic units in polymer did not affect endocytosis and biodegradation. These results suggest that currently designed NP are effective against multiple cancer cell lines.

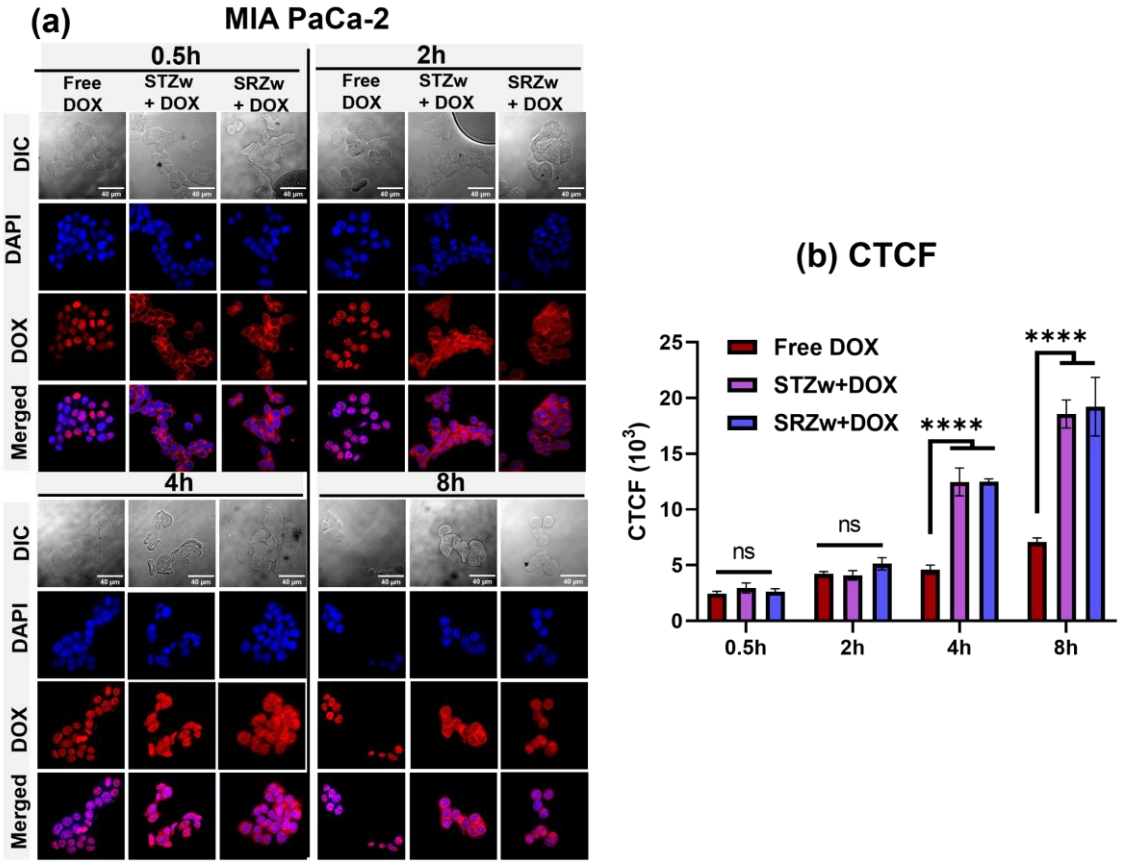

Figure 5.18. *(a) CLSM images of MIA PaCa 2 cells incubated with free DOX, STZw+DOX and SRZw+DOX NP for time-dependent incubation. Cells were fixed and nuclei counter-stained with DAPI (scale bar 40µm, DOX concentration 2.5µg/mL). (b) Plot of CTCF for cellular uptake of various time points of incubation in MIA PaCa 2 cell line incubated with free*

*DOX, STZw+DOX and SRZw+DOX NP (n>3, data represented as mean ± SD, ****p<0.0001 ANOVA test).*

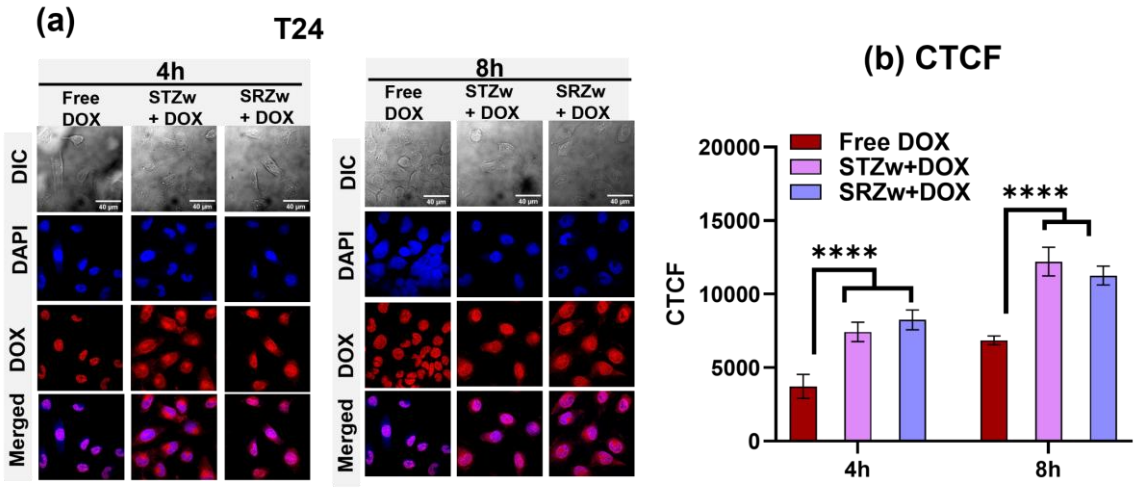

Figure 5.19. *(a) CLSM images of T24 cells incubated with free DOX, STZw+DOX and SRZw+DOX NP for 4h and 8h incubation. (b) The plot of CTCF for 4h and 8h time points of incubation of free DOX, STZw+DOX and SRZw+DOX in T24 cell lines. (n>3, data represented as mean ± SD, ****p<0.0001 ANOVA test).*

5.3.9 Hemolysis assay

Next we evaluated the non-hemolytic ability of star zwitterionic NP prior to administering into mice. Photographs of tubes in Figure 5.20 depicted the RBC pellet formation suggesting the intact RBCs when treated with NP solutions similar to negative control PBS. However, RBCs were completely ruptured when treated with positive control Triton-x (1% v/v). The plot of % hemolysis in Figure 5.20 revealed no hemolysis of NP at 1.0 mg/mL concentration suggesting excellent compatibility of NP with RBCs.

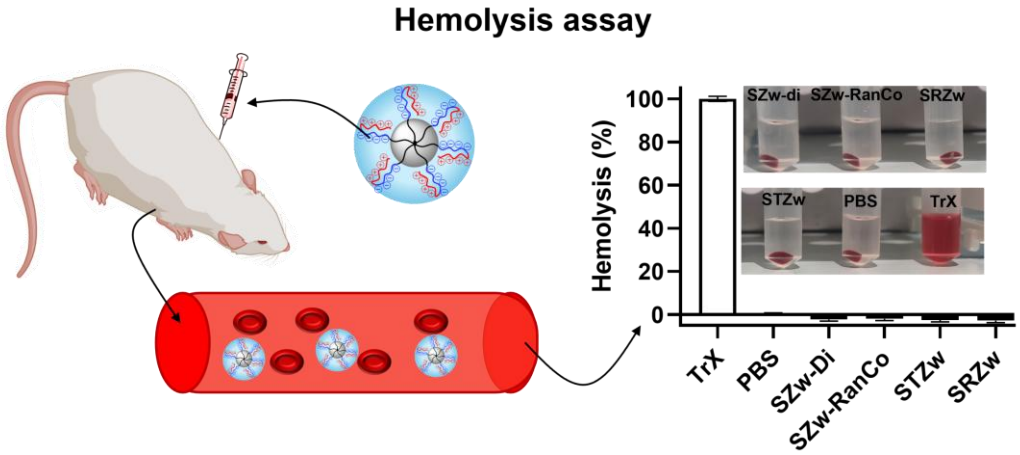

Figure 5.20. *Hemolysis assay: Plot of % hemolysis for the different zwitterionic NP. (Polymer concentration was 1.0mg/mL, Triton-X and PBS were used as positive and negative control. Inset photograph showing the tubes having RBCs in polymer solution).*

5.3.10 In Vivo Biodistribution studies

Successful in vitro investigation and non-hemolytic nature of star zwitterionic polymers encouraged to evaluate for in vivo biodistribution studies prior to antitumor efficacy investigations. Understanding the circulation behavior, accumulation in major organ and tumor (biodistribution) is crucial step for developing any new drug delivery vehicle. For that purpose, near infra-red fluorescence (NIRF) imaging technique was chosen owing to its non-invasive, low background emission and deep penetration ability. Therefore, NIR dye IR780 iodide was encapsulated in STZw and SRZw and DLC were obtained as 1.0 % and 0.5 % respectively and as shown in Figure 5.21a-b. IR780 loaded STZw and SRZw NP hereinafter will refer to as STZw+IR780 and SRZw+IR780. The hydrodynamic diameters of STZw+IR780 and SRZw+IR780 were found to be 25± 8 nm and 110 ± 8 nm with ζ-potential of -8 to -10 mV respectively as shown in Figure 5.21c.

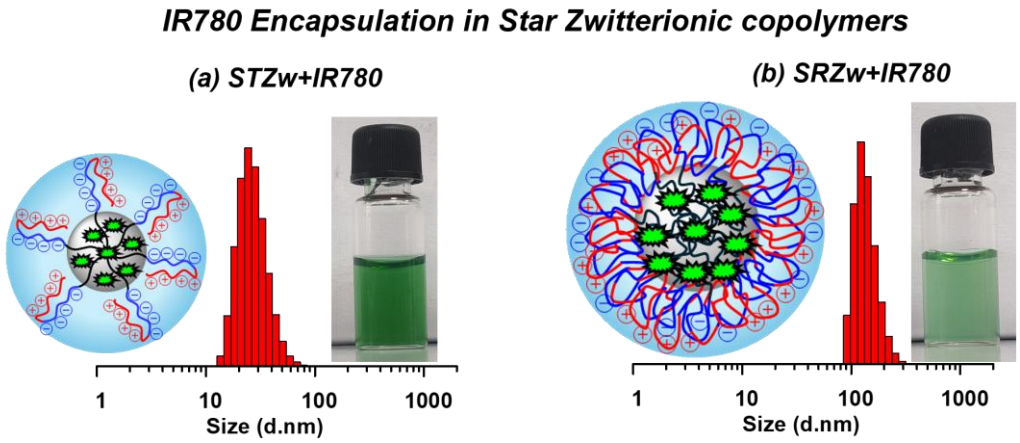

(c) Details of IR780 encapsulation

Entry	IR780 loaded sample				
	DLC (%)	DLE (%)	DLS size (d.nm)	PDI	Zeta Potential (ζ) in mV at pH 7.4
STZw+IR780	1.0	10	25 ± 5	0.35 ± 0.05	-8.4 ± 0.96
SRZw+IR780	0.5	5	110 ± 8	0.25 ± 0.05	-10.1 ± 1.0

Figure 5.21: *IR780 encapsulation in STZw and STZw zwitterionic polymers: (a) DLS histogram (% number) and photograph of vial containing STZw+IR780 nanoparticles (1mg/mL). (b) DLS histogram and photographs of SRZw+IR780 nanoparticles (1mg/mL). (c) Tabulated characterization details of IR780 loaded nanoparticles.*

NOD-SCID mice were subcutaneously inoculated with MIA PaCa 2 cells to create pancreatic cancer xenograft model. Once the tumor reached ~100 mm^3, the animals were randomly divided into three groups (n=3), intraperitoneally injected with free IR780, STZw+IR780 and SRZw+IR780. One extra mouse was used as negative control injected with PBS only where no signal is expected, and the outline of the experiment is shown in Figure 5.22a. All the groups were subjected to IVIS fluorescence imaging (λ=745nm), and images of lateral view are shown in Figure 5.22b. Animals injected with STZw+IR780 and SRZw+IR780 NP showed strong fluorescence signal from all over the body from 4h postinjection onwards and signals were persistent till 72h suggesting longer blood circulation in blood stream compared to free IR780. Noticeably the signals were very intense from the tumoral region and persistent till longer period in case of STZw+IR780 and SRZw+IR780 groups compared to free IR780. The quantified signals in Figure 5.22c revealed 2-3-fold higher signals of NP in the mouse body compared to free IR780. Surprisingly, STZw and SRZw did not show any differences in whole body image-based quantification. Plasma samples subjected to IVIS provided visual evidence of stronger fluorescence for groups treated with NP compared to free IR780 in Figure 5.23a. Interestingly signals from groups treated with free IR780 were almost diminished at longer time (72h) suggesting its clearance from the blood. In contrast, the NP did persist for 72h suggesting longer blood circulation time owing to zwitterionic nature of the polymer. The plot of semi-quantitative pharmacokinetics based on IVIS fluorescence in Figure 5.23b revealed the 2-3-fold higher signals in the plasma of NP groups compared to free IR780 owing to prolonged blood circulation. Ex-vivo IVIS images of organs harvested 72h postinjection are shown in Figure 5.23c depicted much more intense signals in the excretory organs and tumors in case of STZw+IR780 and SRZw+IR780 groups than free IR780. Quantified signals for organs in Figure 5.23d suggested 2-3-fold higher accumulation of NP in excretory organs such as lungs, liver, kidney, and tumor compared to free IR780. More importantly STZw+IR780 and SRZw+IR780 NP exhibited the highest accumulation in tumor even after 72h postinjection which is a remarkable result suggesting passive targeting ability of currently designed star zwitterionic NP. Higher accumulation and retention in tumor for star zwitterionic NP is attributed to enhanced permeability and retention (EPR) effect. Moreover, both the star shape zwitterionic polymers have 6-arms which make it difficult to excrete out from renal membranes therefore increasing retention time in blood circulation resulting in better passive targeting ability compared to linear structures.

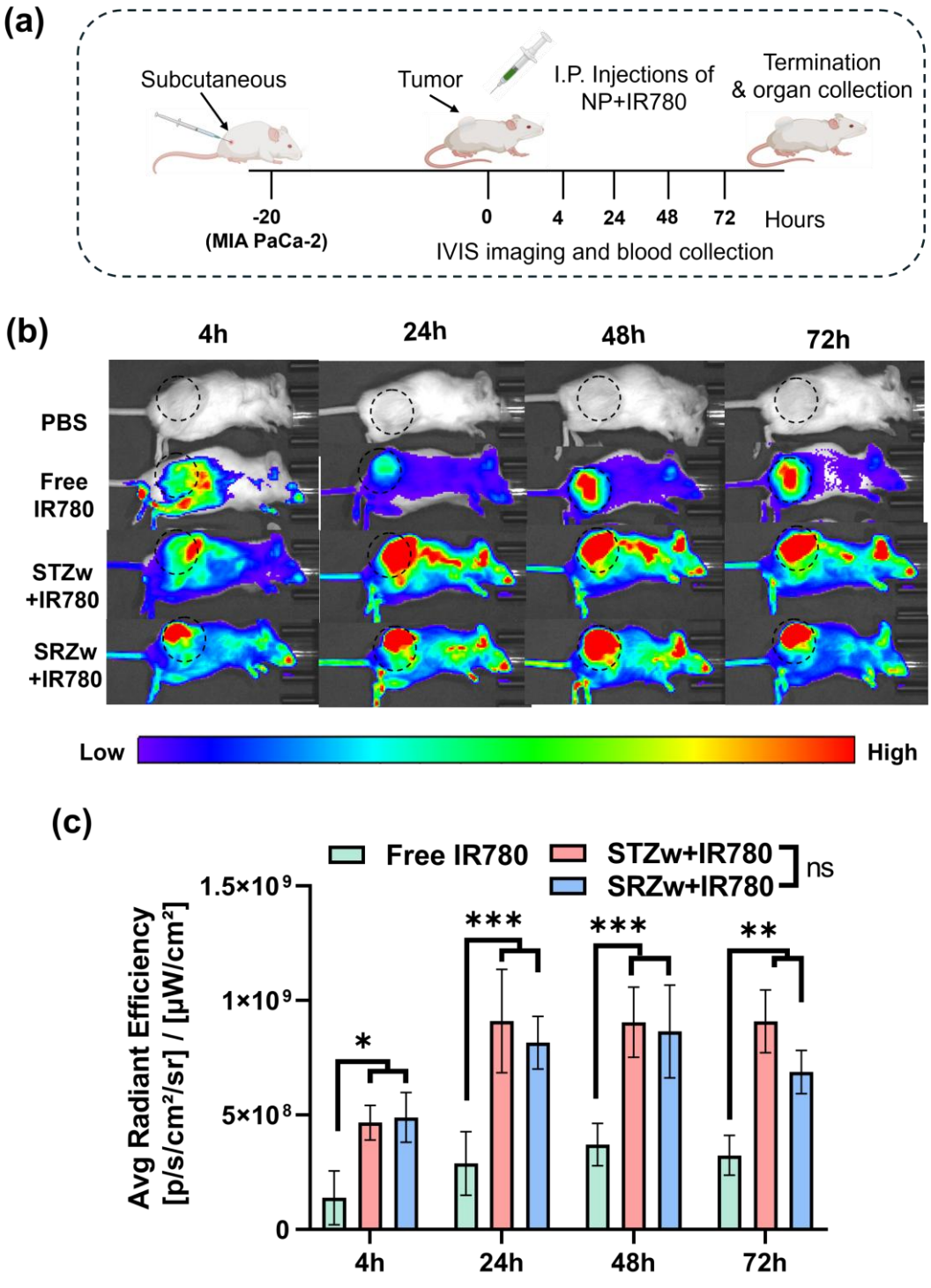

Figure 5.22. *(a) Experimental plan for in vivo biodistribution in NOD-SCID mice xenograft model (pancreatic cancer). (b) Representative IVIS whole body fluorescence images of tumor bearing NOD-SCID mice injected with PBS, free IR780, STZw+IR780 and SRZw+IR780 for 72h. Tumors are highlighted with black circles for visualization. (c) Quantified fluorescence signal obtained from whole body images (n=3, data represented as mean ± SD, *p<0.05, **p=0.0088, ***p=0.0002, ****p< 0.0001, ANOVA test).*

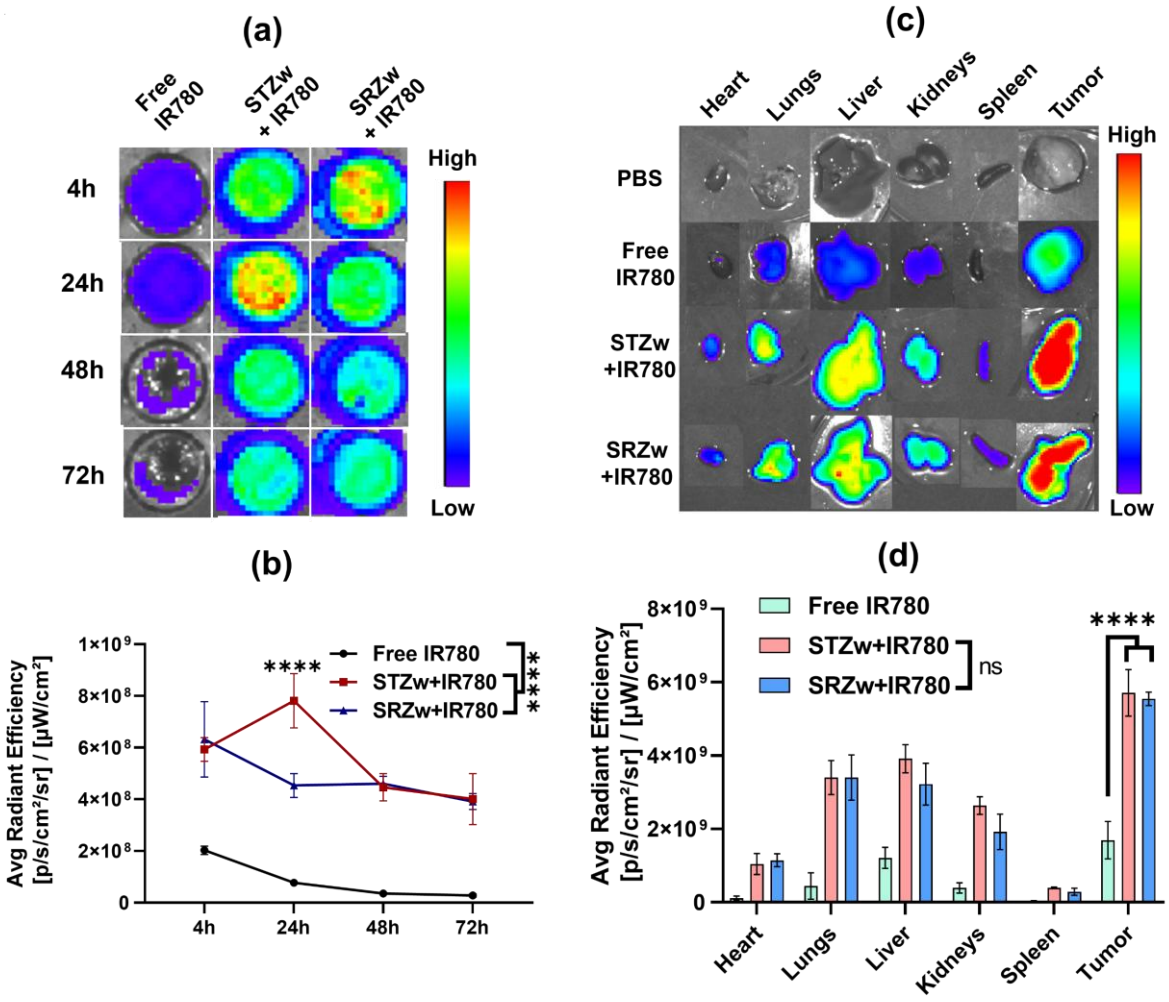

Figure 5.23. *(a) IVIS fluorescence images of plasma samples for 72h. (b) Quantified fluorescence signal obtained from plasma samples (n=3, data represented as mean ± SD, ****p< 0.0001, ANOVA test). (c) ex-vivo IVIS fluorescence images organs harvested after 72h of injections. (d) Quantified fluorescent signal for organs harvested after 72h of injections (n=3, data represented as mean ± SD, ****p< 0.0001, ANOVA test).*

5.3.11 Antitumor Efficacy in Xenograft mouse model

Antitumor efficacy of DOX loaded Zwitterionic NP was evaluated in MIA PaCa2 (pancreatic cancer) tumor bearing NOD-SCID mice (subcutaneous xenograft mouse model) and the experimental plan is shown in Figure 5.24a. Once the tumor reached ~70 mm^3, animals were randomly divided into four groups (*n=5*) and intraperitoneally injected with PBS, free DOX, STZw+DOX and SRZw+DOX every week 6^{th} day (total 5 dosage of 2.0 mg/kg in 100 µL PBS) for 28 days. The body weights were monitored every fourth day to assess the biosafety of zwitterionic NP and plot of variation is shown in Figure 5.24b. The body weight variation

curve of the treated group did not show any drastic changes and revealed good compatibility of zwitterionic NP with animals suggesting potential of star zwitterionic NP as promising candidate for drug delivery. The tumor growth was monitored, and growth curves are shown in Figure 5.24c to 5.24f and cumulative tumor volume plot is shown in Figure 5.24g. Group treated with PBS showed tremendous growth in tumor volume and tumor reached ~2500 mm^3 toward the end (28^{th} day) of treatment owing to highly metastatic nature of pancreatic cancer. The DOX treated group exhibited moderate suppression in tumor growth and volume were controlled below ~1000 mm^3. Interestingly the STZw+DOX and SRZw+DOX treated groups showed better suppression in tumor growth owing to prolonging blood circulation and passive targeting ability (EPR effect) compared to free DOX group. Tumor sizes were well controlled below 500 mm^3 in the case of NP treated group as shown in Figure 5.24g. Surprisingly STZw+DOX and SRZw+DOX NP did not show significant difference in tumor inhibition effect despite being differ in sizes. This result indicates that the arrangement of anionic and cationic units in the star zwitterionic polymer has less or no effect on their delivery ability *in vivo* system.

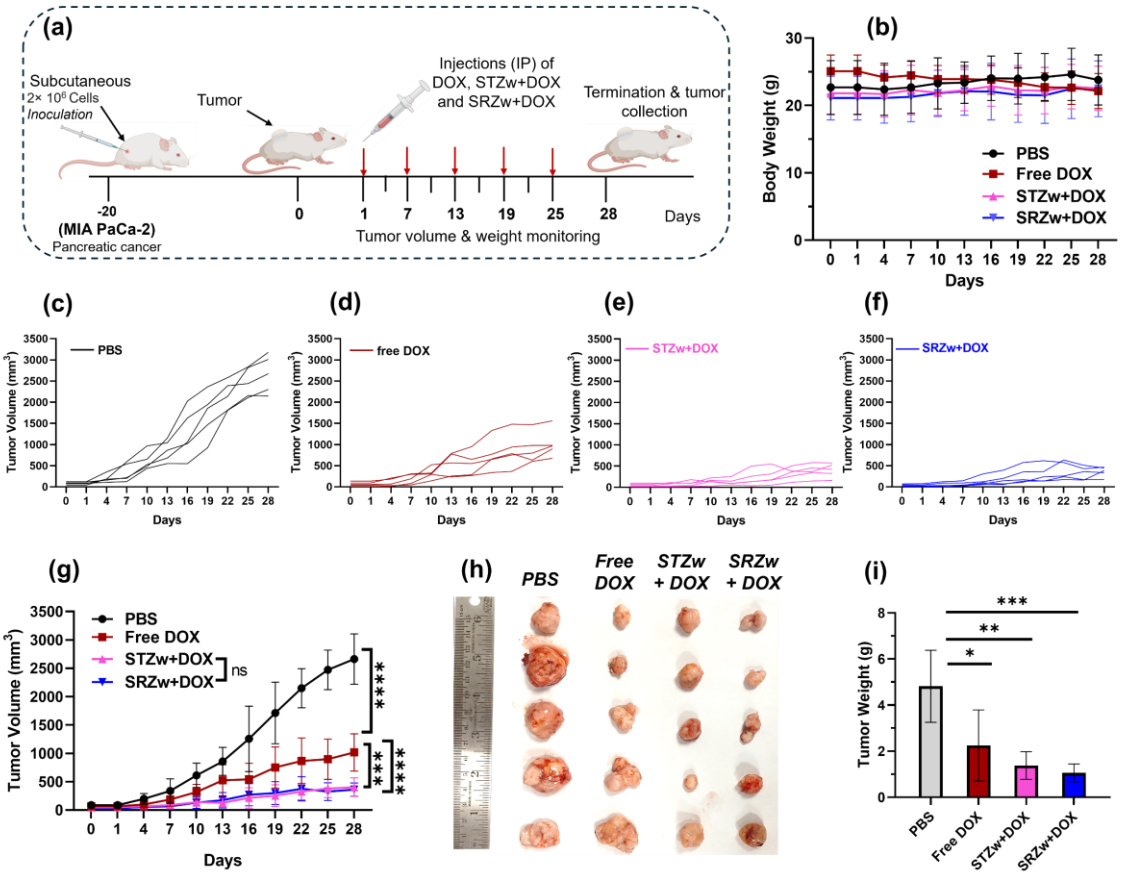

Figure 5.24. *(a) Experimental plan for in vivo antitumor efficacy studies of free DOX, STZw+DOX and SRZw+DOX in NOD-SCID mice xenograft model (pancreatic cancer). (b)*

*Plot of body weight variation of treated groups (n=5). (c) to (f) individual tumor growth curves of animals treated with PBS, free DOX, STZw+DOX and SRZw+DOX for 28 days (DOX dose 2.0mg/kg, n=5). (g) Tumor inhibition effect over 28-day treatment for PBS, free DOX, STZw+DOX and SRZw+DOX groups (n=5, data represented as mean ± SD, ***p=0.0002, ****p<0.0001, ANOVA). (h) Photograph of pancreatic tumor harvested after 28-day treatment. (i) Tumor weights of treated groups (n=5, data represented as mean ± SD, *p<0.05, **p=0.0016, ***p=0.0006, ANOVA).*

The experiment was terminated after 28th day by euthanizing animals and tumors were excised. Photographs of harvested tumor tissue are shown in Figure 5.24h. The photographs provided visual evidence of tumor suppression in STZw+DOX and SRZw+DOX NP treated groups. The weights of excised tumor were measured, and the plot is shown in Figure 5.24i. The tumor weights revealed that the groups treated with STZw+DOX and SRZw+DOX showed significantly better tumor growth inhibition compared to PBS and free DOX; however, among STZw and SRZw no significant difference was observed. In summery the zwitterionic NP showed better prolonged blood circulation time, tumor accumulation, and superior tumor suppression effect compared to controls and exhibited considerable biosafety in animal models. Therefore, the currently designed completely biodegradable star zwitterionic system based on self-immolative PAE and anionic-PCL system are promising candidates for drug delivery *in vitro* and in *vivo*.

5.4 Conclusion

We have successfully constructed four biodegradable star-shaped zwitterionic systems based on polycaprolactone, anionic PCL (CPCL) and poly(amino ester)s (PAE) systems. The diblock (SZw-Di) and copolymers (S-RanCo) composed of anionic PCL and PAEs based NP depicted DLC > 6% for DOX, while triblock (STZw) and its random version (SRZw) of it depicted DLC >12% for DOX. STZw and SRZw depicted great serum stability for more than 5 days at pH 7.4. Live-cell lysotracker studies demonstrated enzymatic biodegradation facilitated release of DOX in the lysosomal compartment at intracellular level. The cytotoxicity evaluation demonstrated excellent compatibility of NPs in multiple cells lines such as MIA PaCa 2, HEK298T, T24. While DOX loaded congeners depicted excellent killing efficiency in all cell lines with lower IC50 and exhibited excellent cellular uptake capabilities confirmed by CLSM imaging. NPs were non-hemolytic at high concentration of 1.0mg/mL. NIRF imaging suggested retention of zwitterionic NPs in blood circulation for more than 72h in pancreatic tumor bearing mice. Ex-vivo tumor analysis by NIRF IVIS imaging demonstrated superior accumulation of STZw+IR780 and SRZw+IR780 NP compared to free IR780. STZw+DOX and SRZw+DOX NP showed significant tumor suppression and along with appreciable biosafety in xenograft mice model. This approach opens up new avenue for developing biodegradable zwitterionic polymers based on electrostatic strategy stabilized self-immolative PAE polymers for various biomedical applications.

5.5 References

1) Siegel, R. I.; Miller, K. D.; Fuchs, H. E.; Jemal, A. Cancer Statistics, 2021. *CA, Cancer J. Clin*. **2021**, *71*, 7–33.
2) Tarannum, M.; Vivero-Escoto, J .L. Nanoparticle-based Therapeutic Strategies targeting Major Clinical Challenges in Pancreatic Cancer Treatment. *Adv Drug Deliv. Rev*. **2022**, *187*, 114357.
3) Thapa, R. K.; Oh Kim, J. Nanomedicine-based Commercial Formulations: Current Developments and Future Prospects. *J. Pharm. Investig*. **2023**, *53*, 19–33.
4) Manzari, M.; Shamay, Y.; Kiyuchi, H.; Rosen, N.; Scaltiti, M.; Heller, D. A. targeted Drug Delivery Strategies for Precision Medicines. *Nat. Rev. Mater.* **2021**, *6*, 351–370.
5) Mitchell, M. J.; Billingsley, M. M.; Haley, R. M.; Weschsler, M.E.; Peppas, N. A.; Langer, R. Engineering Precision Nanoparticles for Drug Deliver. *Nat. rev. Drug Discov.* **2021**, *20*, 101–124.
6) Vand der Meel, R.; Sulhelm, E.; Shi, Y.; Klessling, F.; Mulder, W. J. M.; Lammers, T. Smart Cancer Nanomedicine. *Nat. Nanotechnol.* **2019**, *14*, 1007–1017.
7) Wang, G.; Zhaou, Z.; li, Q>; Wu, Y.; Yan, S.; Shen, Y.; Huang, P. Enzyme-Triggered Transcytosis of Dendrimer-Drug Conjugate for Deep Penetration into Pancreatic Tumors. *ACS Nano* **2020**, *14*, 4890–4904.
8) Chen, X.; Gao, H.; Deng, Y.; Jin, Q.; Ji, J.; Ding, D. Supramolecular Aggregation-Induced Emission Nanodots with Programmed Tumor Microenvironment Responsiveness for Image-Guided Pancreatic Cancer Therapy. *ACS Nano* **2020**, *14*, 5121–5134.
9) Meng, H.; Wang, M.; Huiyu, L.; Liu, X.; Situ, A.; Wu, B.; Ji, Z.; Hyun Chang, C.; Nel, A. E. Use of a Lipid-Coated Mesoporous Silica Nanoparticle Platform for Synergistic Gemcitabine and Paclitaxel Delivery to Human Pancreatic cancer in Mice. *ACS Nano* **2015**, *9*, 3540–3557.
10) Mondal, G.; Almawash, Chaudhary, A. K.; Mahato, R. I. EGFR-Targeted Cationic Polymeric Mixed Micelles for Codelivery of Gemcitabine and miR-205 for Targeting Advanced Pancreatic cancer. *Mol. Pharmaceutics* **2017**, *14*, 3121–3133.
11) Gao, C.; Cheng, K.; Li, Y.; Gong, R.; Zhao, X.; Neiw, G.; Ren, H. Injectable Immunotherapeutic Hydrogen Containing RNA-Loaded Lipid Nanoparticles Reshapes Tumor Microenvironment for Pancreatic Cancer Therapy. *Nano Lett.* **2022**, *22*, 8801–8809.
12) Zhang, M.; Xhang, W.; Tang, G.; Wang, H.;Wu, M.; Yu, W.; Zhou, Z.; Mou Y.; Liu, X. Targeted Codelivery of Docetaxel and Atg7 siRNA for Autophagy Inhibition and Pacreatic Cancer Treatment. *ACS Appl. Bio. Mater.* **2019**, *2*, 1168–1176.
13) Fan, F.; jin, L.; Yang, L. pH-Sensitive Nanoparticles Composed Solely of of Membrane-Disruptive Macromolecules for Treating Pancreatic Cancer. *ACS Appl. Mater. Interfaces* **2021**, 13, 12824–12835.
14) Kamley, N.; Yameen, B.; Wu, J.; Farokhzad, O. C. Degradable Controlled-Release Polymeric Nanoparticles; Mechanisms of Controlling Drug Release. *Chem. Rev.* **2016**, *116*, 2602–2663.

15) Wei, D.; Sun, Y.; Zhu, H.; Fu, Q. Stimuli-Responsive Polymer-Based Nano systems for Cancer Theragnostic. *ACS Nano* **2023** *17*, 23223–23261.
16) Sherif, O.; Gnaim, S.; Shobat, D. Self-Immolative Polymers: An Emerging Class of Degradable Materials with Distinct Disassembly Profiles. *J. Am. Chem. Soc.* **2021**, *143*, 21177–21188.
17) Xio, Y.; Tan, X.; Li, Z.; Zhang, K. Self-Immolative Polymers in Biomedicine. *J. Mater. Chem. B.* **2020**, *8*, 6697–6909.
18) McKinlay, C. J.; Vargas, J. R.; Blake, T. R. J.; Hardy, W.; Kanada, M.; Contag, C. H.; Wender, P. A.; Waymouth, R. M. Charge-Altering Releasable Transporter (CARTs) for the Delivery and Release of mRNA in Living Animals. *Proc. Natl. Acad. Sci USA.* **2017**, *114*, E448.
19) Lynn, D. M.; Langer, R. Degradable Poly(β-amino esters): Synthesis, Characterization, and Self-Assembly with Plasmid DNA. *J. Am. Chem. Soc.* **2000**, *122*, 10761–10768.
20) Pathan, S.; Jayakannan, M. Zwitterionic Strategy to Stabilize Self-immolative Polymer Nanoarchitecture under Physiological pH for Drug Delivery In Vitro and In Vivo. *Adv. Healthcare Mater.* **2024**, *13*, 2304599.
21) Blackman, L. D.; Gunatillake, P. A.; Cass, P.; Locock, K. E. S. An Introduction to Zwitterionic polymer Behaviour and Applications in Solution and at Surface. *Chem. Soc. Rev*. **2019**, *48*, 757–770.
22) Lowe, A. B.; McCormick, C. L. Synthesis and Solution Properties of Zwitterionic Polymers. *Chem. Rev.* **2002**, *102*, 4177–4189.
23) Zhang, M.; Peng, Y.; Li, J.; Recent Advances of Zwitterionic-based topological Polymers for Biomedical Applications. *J. Mater. Chem. B.* **2022**, *10*, 2338–2356.
24) Erfani, A.; Seaberg, J.; Aichele, C. P.; Ramsey, J. D. Interaction between Biomolecules and Zwitterionic Moieties: A Review. *Biomacromolecules* **2020**, *21*, 2557–2573.
25) Bengani-Lutz, P.; Converse, E.; cebe, P.; Asatekin, A. Self-Assembling Zwitterionic Copolymers as Membrane Selective Layers with Excellent Fouling Resistance: Effect of Zwitterion Chemistry. *ACS Appl. Mater. Interfaces* **2017**, *9*, 20859–20872.
26) Ladd, J.; Zhang, Z.; Chen, S.; Hower, J. C.; Jiang, S. Zwitterionic Polymers Exhibiting High Resistance to Nonspecific Protein Adsorption from Human Serum and Plasma. *Biomacromolecules* **2008**, *9*, 1357–1361.
27) Li, B.; Yuan, Z.; He, Y.; hung, H-C.; Jiang, S. Zwitterionic Nanoconjugates Enables Safe and Efficient Lymphatic Drug Delivery. *Nano Lett.* **2020**, *20*, 4693–4699.
28) Jackson, M. A.; Werfel, T. A.; Curvino, E. J.; Yu, F.; Kavanaugh, T. E.; Serett, S. M.; Dockery, M. D.; Kilchrist, K. V.; Jackson, A. N.; Giorgio, T. D.; Duvall, C. L. Zwitterionic Nanocarrier Surface Chemistry Improves siRNA Tumor Delivery and Silencing Activity Relative to Polyethylene glycol. *ACS Nano* **2017**, *11*, 5680–5696.
29) Liu, S.; Wang, X.; Yu, X.; Cheng, Q.; Johnson, L. T.; Chatterji, S.; Zhang, D.; Lee, S. M.; Sun, Y.; Lin, T-C.; Liu, J. L.; Siegwart, D. J. Zwitterionic Phospholipidation of Cationic Polymers Facilitates Systemic mRNA Delivery to Spleen and Lymph Nodes. *J. Am. Chem. Soc.* **2021**, *143*, 21321–21330.
30) Zhang, M.; Yu, P.; Xie, J.; Li, J. Recent Advances of Zwitterionic-based Topological Polymers for Biomedical Applications. *J. Mater. Chem. B*. **2022**, *10*, 2338–2356.

31) Kim, Y.; Binauld, S.; Stenzel, M. H. Zwitterionic Guanidine-based Oligomers Mimicking Cell-Penetrating Peptides as a Nontoxic Alternative to Cationic Polymers to Enhance the Cellular Uptake. *Biomacromolecules* **2012**, *13*, 3418-3426.
32) Keefe, A. J.; Jiang, S. Poly (Zwitterionic) Protein Conjugate Offer Increased Stability without Sacrificing Binding Affinity or Bioactivity. *Nat. Chem* **2012**, *4*, 59–63.
33) Li, Y.; Xu, B.; Bai, T.; Liu, W. Co-Delivery of Doxorubicin and Tumor-Supressing p53 Gene using a POSS-based Star-Shaped polymer for Cancer Therapy. *Biomaterials* **2015**, *55*, 12–23.
34) Chen, Y.; Han, H.; Tong, H.; Chen, T.; Wang, H.; Ji, J.; Jin, Q. Zwitterionic Phosphorylcholine-TPE conjugate for pH-Responsive Drug Delivery and AIE Active Imaging. *ACS Appl. Mater. Interfaces* **2016**, *8*, 21185–21192.
35) Huang, P.; Song, H.; Wang, W.; Sun, Y.; Zhou, J.; Wang, X.; Liu, J.; Liu, J.; Kong, D.; Dong, A. Integrin-Targeted Zwitterionic Polymeric Nanoparticles with Acid-Induced Disassembly Property for Enhanced Drug Accumulation and Release in Tumor. *Biomacromolecules* **2014**, 15, 3128–3138.
36) Cao, J.; Xie, X.; Lu, A.; He, B.; Chen, Y.; Gu, Z.; Luo. X. Cellular Internalization of Doxorubicin loaded Star-Shaped Micelles with Hydrophilic Zwitterionic Sulfobetaine Segments. *Biomaterials* **2014**, *35,* 4517–4524.
37) Surnar, B.; Jayakannan, M. Stimuli-responsive poly(caprolactone) Vesicles for Dual Drug Delivery under the Gastrointestinal Tract. *Biomacromolecules* **2013**, *14*, 4377-4387.
38) Surnar, B.; Jayakannan, M. Triple-Block Nanocarrier Platform for Synergistic Cancer Therapy of Antagonistic Drugs. *Biomacromolecules* **2016**, *17*, 4075-4085.
39) Kulkarni, B.; Surnar, B.; Jayakannan, M. Dual Functional Nanocarrier for Cellular Imaging and Drug Delivery in Cancer Cells based on π-Conjugated Core and Biodegradable Polymer Arms. *Biomacromolecules* **2016**, *17*, 1004-1016.
40) Malhotra, M.; Surnar, B.; Jayakannan, M. Polymer Topology Driven Enzymatic Biodegradation in Polycaprolactone Block and Random Copolymer Architectures for Drug Delivery to Cancer Cells. *Macromolecules* **2016**, *49*, 8098-8112.
41) Ghosh, R.; Malhotra, M.; Sathe, R. R. M.; Jayakannan, M. Biodegradable Polymer Theranostic Fluorescent Nanoprobe for Direct Visualization and Quantitative Determination of Antimicrobial Activity. *Biomacromolecules* **2020**, *21*, 2869-2912.
42) Ghosh, R.; Jayakannan, M. Theranostic FRET Gate to Visualize and Quantify Bacterial Membrane Breaching. *Biomacromolecules* **2023**, *24*, 739-755.
43) Surnar, B.; Jayakannan, M. Structural Engineering of Biodegradable PCL Block Copolymer Nanoassemblies for Enzyme-controlled Drug Delivery in Cancer Cells. *ACS Biomater. Sci. Eng.* **2016**, *2*, 1926-1941.
44) Pranav, U.; Malhotra, M.; Pathan, S.; Jayakannan, M. Structural Engineering of Star Block Biodegradable Polymer Unimolecular Micelles for Drug Delivery in Cancer Cells. *ACS Biomater. Sci. Eng.* **2023***, 9,* 743-759.
45) Fox, M. E.; Szoka, F. C.; Frechet, J. M. J. Soluble Polymer Carriers for the Treatment of Cancer: The Importance of Molecular Architecture. *Acc Chem Res.* **2009**, *42*, 1141–1151.
46) Yang, D-P.; Nwe Linn Oo, M. N.; Roshan Deen, G.; Li, Z.; Jun Loh, X. Nano-Star

Shaped Polymers for Drug Delivery Applications. *Macromol. Rapid Commun.* **2017**, *38*, 1700410.

47) Daglar, B.; Ozgur, E.; Corman, M. E.; Uzan, L.; Demirel, G. B. Polymeric Nanocarriers for Expected Nanomedicine: Current Challenges and Future Prospects. *RSC Adv.* **2014**, *4*, 48639-48659.

Summery and Future direction

To summarize, fully biodegradable 6-arm star shaped PCL block copolymers have been designed by ROP varying M/I ratio to produce amphiphilicity variation. The self-assembly analysis revealed formation of aggregated micellar NP of having size in the range of 60-200 nm and unimolecular micelles of 20 nm depending on carboxyl PCL content in the block copolymer. Star-shaped unimolecular micelles (UMNp) have proved superior compared to star shaped aggregated micelles (AMNp) for encapsulation abilities for Doxorubicin (>14 wt% for UMM) and other fluorescent dyes. *In vitro* and live-cell confocal imaging analysis proven enzymatic biodegradation and lower IC_{50} of DOX loaded UMNp in multiple cancer cell lines. Both aggregated and unimolecular micelles have been found to be biocompatible and non-hemolytic. Near infrared fluorescence (NIRF) imaging using IR780 labeled UMNp and AMNp NP based biodistribution suggested longer blood circulation and better accumulation of UMNp in tumor surpassing AMNp further proving efficient drug delivery reducing >90% pancreatic tumor volume. Furthermore, new class of unimolecular micelles based on star-shaped PCL block copolymer have been synthesized by ROP and pos-functionalization into anionic, cationic and neutral surface charges. Detailed analysis of self-assembly *in vitro* biodegradation demonstrated superior encapsulation capability compared to their aggregated counterparts and enzymatic biodegradation in the lysosomal compartments. Surface charge modified unimolecular micelles emphasized the critical importance of particle size and charge on the barrier crossing suggested unimolecular micellar nanoparticles of sizes >35nm could only cross the BBB and particles having sizes more than 50 nm were ineffective. In addition, impact of surface charge on brain delivery was evaluated by examining the BBB breaching capabilities of unimolecular micelles anionic, cationic and neural (non-ionic) having ζ potentials of -30mV, +30mV, and -5mV respectively. All three differently charged UMM NP depicted comparable uptake in the brain suggesting only sizes played important role. Further employment of carboxylic acid functionalized PCL in the stabilization of unstable self-immolative PAEs through electrostatic interactions resulting zwitterionic nanoparticles have been proven to stabilize the Doxorubicin formulation at extracellular conditions. This next generational zwitterionic nanoparticle exhibited lysosomal biodegradation and release of Dox to nucleus achieving efficient killing in breast and ovarian cancer cells and in vivo biodistribution confirmed stability of nanoparticles in longer blood circulation. Their star shape versions (zwitterionic) demonstrated higher accumulation in pancreatic tumor substantiated by NIRF

imaging and showed significant suppression in tumor growth by the treatment of DOX loaded zwitterionic nanoparticles.

All these block copolymers demonstrated excellent biocompatibility, biosafety, non-hemolytic ability and promising results in the doxorubicin delivery for in vitro and in vivo mouse tumor model (xenograft). All the polymeric architectures reported here showed excellent biocompatibility and non-hemolytic abilities. Furthermore, the cellular internalization for each system was investigated thoroughly using confocal microscopy in multiple cancers and non-cancer cell lines suggested enhanced uptake of 2-6-fold nanocarriers compared to small molecules. The biodistribution analysis in mice having tumor and in mice without tumor depicted longer blood circulation of all the star and zwitterionic system designed for this thesis work. Moreover, the star unimolecular micelles and star shaped zwitterionic triblock or random copolymer derived nanocarriers demonstrated excellent tumor targeting ability and showed higher retention and accumulation in the pancreatic tumor (xenograft model) by passive targeting. Furthermore, DOX loaded star and zwitterionic nanocarriers demonstrated significant suppression in tumor growth suggesting these biodegradable polymers based system can be utilized for further exploration inn drug delivery application.

The work resented in thesis highlighted the importance of the biodegradable PCL and PAE based polymeric star and linear architecture for in in vivo drug delivery application. This work has opened up new opportunities for further exploration of new PCL and PAE based higher order architectures for preclinical investigations. One way to further enhance the targeting ability is to conjugate the star nanocarriers with specific targeting ligand for achieving active targeting. Another way to enhance the efficacy of therapeutic is by using combinational therapy of two or more drugs together for synergistic treatment of multi-drug resistant tumors. Furthermore, brain specific delivery has been shown by star shaped block copolymer unimolecular micelles in healthy mice model. However, delivery of specific drug for the specific CNS disorder including glioblastoma, Alzheimer, and Parkinson's disease yet be evaluated. For that purpose, decoration of star nanocarrier with targeting ligand would have active targeting ability and might be useful for deep understanding of mechanistic aspects. Fluorophore tagging onto structure can help in real time monitoring by direct visualization of polymer fate in *vitro* and *in vivo.* The star shaped polymeric nanocarriers are not only restricted for one type of drug or tumor and they can be utilized for delivering various type of drugs, inhibitor into tumors. Finally, in the context of zwitterionic polymers composed of self-

immolative PAE and enzymatic degradable carboxylic PCL, exploration of other architecture including, brush, miktoarm need to done to understand structure-property relationship. Moreover, self-immolation of PAE can be utilized in the field surface coating materials or antibacterial coating and device fabrication. The future aspect have been diagrammatically represented in Figure 6.1.

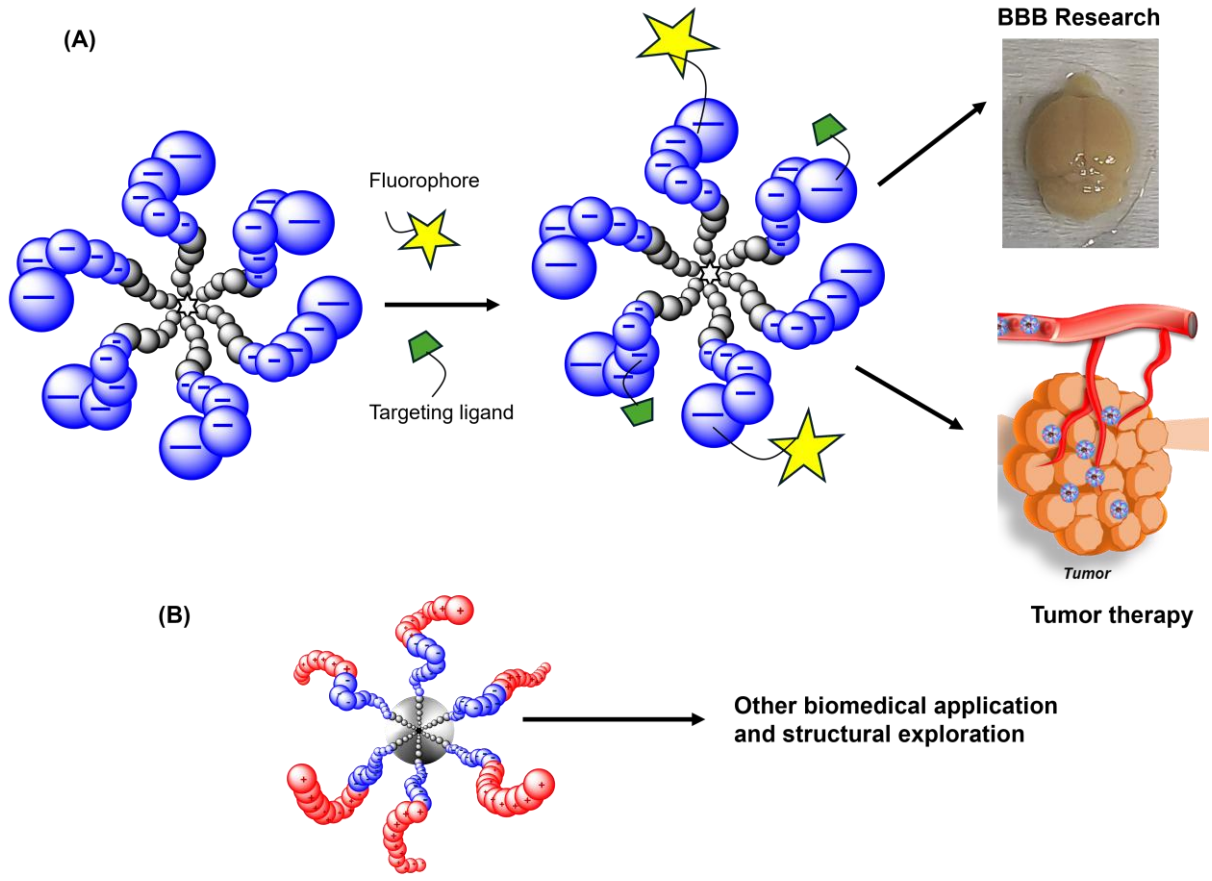

Figure 6.1. *Diagrammatic representation of future aspect of star shaped anionic and zwitterionic polymer architecture.*

List of Publication

1) **Pathan, S.;** Jayakannan, M. Zwitterionic Strategy to Stabilize Self-Immolative Polymer Nanoarchitecture under Physiological pH for Drug Delivery In Vitro and In Vivo. *Adv. Healthcare Mater.* **2024**, *13*, 2304599.

2) Malhotra, M.; Pardasani, M.; **Pathan, S**.; Srikanth, P.; Shaw, K.; Abraham, N. M.; Jayakannan, M. Star-Polymer Unimolecular Micelle Nanoparticles to Deliver a Payload across the Blood-Brain Barrier. *Nanoscale* **2024**, *16*, 21582.

3) Ghosh, R.; **Pathan, S**.; Jayakannan, M. Structural Engineering of Cationic Block Copolymer Architectures for Selective Breaching of Prokaryotic and Eukaryotic Biological Species. *ACS Appl. Bio Mater.* **2024**, *7*, 7062-7075.

4) Pranav, U.; Malhotra, M.; **Pathan, S**.; Jayakannan, M. Structural Engineering of Star Block Biodegradable Polymer Unimolecular Micelles for Drug Delivery in Cancer Cells. *ACS Biomater. Sci. Eng.* **2023**, *9*, 743-759.

5) Virmani, M.; Deshpande, N. U.; **Pathan, S.;** Jayakannan, M. Self-Reporting Polysaccharide Polymersome for Doxorubicin and Cisplatin Delivery to Live Cancer Cells. *ACS Polym. Au* **2022**, *2*, 181-193.

6) **Pathan, S.;** Jayakannan, M. Tweaking Unimolecular Micellar Nanoarchitecture for Drug Delivery in Tumor Xenograft. (*Manuscript under review*)

7) Singh, K.; **Pathan, S**.; Jayakannan, M.; Balasubramanian, N. Targeting Aurora Kinase A with MLN8237-Loaded Unimolecular Micelle Polymer Nanoparticles: AURKA-RalA Mediated Tumor Suppression in Ras-Independent and Ras-Dependent Cancers. (*Manuscript under review*)

8) Nisal, R.; Kambale, P.; **Pathan, S**.; Jayakannan, M. ROPISA Strategy for In-situ Encapsulation of Fluorescent Dyes in Polypeptide Nanoparticles and their Intracellular Bio-Imaging. (*Manuscript under review*)

9) **Pathan. S**.; Jayakannan, M. Influence of Size and Surface Charge of Nanoparticles on Blood-Brain Breaching. (*Manuscript under preparation)*

10) **Pathan. S**.; Singh, K.; Jayakannan, M. Star-Shaped Zwitterionic Polymeric Nanoarchitecture for Drug delivery to Solid Tumors. (*Manuscript under preparation)*

11) Nisal, R.; **Pathan, S**.; Kambale, P.; Jayakannan, M. β-Sheet Polypeptide Block Copolymers for Drug Delivery. (*Manuscript under preparation)*

12) **Pathan. S**.; Jayakannan, M. Unimolecular Micellar Nanoarchitecture for Camptothecin delivery to Breast Cancers. (*Manuscript under preparation)*

13) **Pathan. S**.; Jayakannan, M. AIE Chromophore Conjugated Zwitterionic Block Copolymer for Real-Time Monitoring Drug Delivery and Release in Live Cancer Cells . (*Manuscript under preparation)*

Check for updates

RESEARCH ARTICLE

ADVANCED HEALTHCARE MATERIALS
www.advhealthmat.de

Zwitterionic Strategy to Stabilize Self-Immolative Polymer Nanoarchitecture under Physiological pH for Drug Delivery In Vitro and In Vivo

*Shahidkhan Pathan and Manickam Jayakannan**

The major bottleneck in using polymer nanovectors for biomedical application, particularly those based on self-immolative poly(amino ester) (PAE), lies in their uncontrolled autodegradation at physiological pH before they can reach the intended target. Here, an elegant triblock-copolymer strategy is designed to stabilize the unstable PAE chains via zwitterionic interactions under physiological pH (pH 7.4) and precisely program their enzyme-responsive biodegradation specifically within the intracellular compartments, ensuring targeted delivery of the cargoes. To achieve this goal, biodegradable polycaprolactone (PCL) platform is chosen, and structure-engineered several di- and triblock architectures to arrive the precise macromolecular geometry. The hydrophobic-PCL core and hydrophilic anionic-PCL block at the periphery shield PAEs against autodegradation, thereby ensuring stability under physiological pH in PBS, FBS, cell culture medium and bloodstream. The clinical anticancer drug doxorubicin and deep-tissue penetrable near-infrared IR-780 biomarker is encapsulated to study their biological actions by in vitro live cancer cells and in vivo bioimaging in live animals. These zwitterions are biocompatible, nonhemolytic, and real-time in vitro live-cell confocal studies have confirmed their internalization and enzymatic biodegradation in the endo-lysosomal compartments to deliver the payload. In vivo bioimaging establishes their prolonged blood circulation for over 72 h, and the biodistribution analysis reveals the accumulation of nanoparticles predominantly in the excretory organs.

1. Introduction

Self-immolative macromolecules are important classes of synthetic biomaterials owing to their unique ability to undergo autodegradation of long polymer chains into oligomeric subunits while using them for biomedical applications.[1] Self-immolation is typically achieved by incorporating light, pH, enzyme, or redox-responsive functional handles in the polymer backbone, as pendants or at the chain ends to accomplish the desired polymer degradation pattern at the cellular level for the delivery of the payloads.[2] Electron delocalization assisted 1,4-, 1,6-, or 1,8-elimination mechanism in benzylic-amines and phenols is one of the most commonly chosen degradation pathways in self-immolating dendrimers, linear, and hyperbranched polymers, etc.[3] Acid-catalyzed polyglyoxylamides and polyacetals are other important self-immolating polymers that experience degradation under physiological pH or mild acidic conditions.[4] Among the self-immolative polymers, poly(amino esters)s (PAEs) (both α and β derivatives) have a special place in the literature because of their unique autodegradation mechanism under physiological pH = 7.4 by the nucleophilic attack of the amine on the ester-carbonyl atom in the backbone (see **Figure 1a**).[5] Under acidic pH < 4.0, the protonated amine does not facilitate nucleophilic attack; however, at neutral pH the amine (in the deprotonated form) attack the ester carbonyl that triggered the chopping of the long polymer chains into oligomeric units. As a consequence, the self-immolative PAEs are not found to be suitable for biomedical application wherein the stability of the polymer matrix or nanocarriers is vital at pH = 7.4 such as intravenous or intraperitoneal drug delivery. PAEs were complexed with DNA and mRNA to minimize the amine deprotonation,[6] and the resultant polyplex underwent endosomal escape allowing it to internalize in the cytoplasm. This process is crucial for mRNA transfection efficiencies and it facilitated by the charge-altering releasable transporting (CART) mechanism.[7] A similar protocol was used for several other amine-functionalized aliphatic polyesters for gene-delivery applications.[8] Several efforts have been taken to design hydrophobized PAEs based on Michael-addition type condensation route which were explored for biomedical applications.[9] These Michael-type PAEs are predominately stable under neutral pH (they are not self-immolative polymers); and they exhibit pH responsiveness for payloads delivery at the cellular level.[9] Recently, supramolecular strategies were

S. Pathan, M. Jayakannan
Department of Chemistry
Indian Institute of Science Education and Research (IISER Pune)
Dr. Homi Bhabha Road, Pune, Maharashtra 411008, India
E-mail: jayakannan@iiserpune.ac.in

The ORCID identification number(s) for the author(s) of this article can be found under https://doi.org/10.1002/adhm.202304599

DOI: 10.1002/adhm.202304599

 © 2024 Wiley-VCH GmbH

Nanoscale

ROYAL SOCIETY OF CHEMISTRY

PAPER

View Article Online
View Journal | View Issue

Check for updates

Cite this: *Nanoscale*, 2024, **16**, 21582

Star-polymer unimolecular micelle nanoparticles to deliver a payload across the blood–brain barrier†

Mehak Malhotra,[a] Meenakshi Pardasani,[b] Shahidkhan Pathan,[a] Priyadharshini Srikanth,[b] Karishma Shaw,[b] Nixon M. Abraham *[b] and Manickam Jayakannan *[a]

Received 26th June 2024,
Accepted 13th October 2024

DOI: 10.1039/d4nr02636e

rsc.li/nanoscale

Nanocarrier-mediated therapeutic delivery to brain tissue is impeded by tightly controlled transportation across the blood–brain barrier (BBB). Herein, we report a well-defined core–shell star-shaped unimolecular micelle (star-UMM; a single polymer entity) as an efficient BBB-breaching nanoparticle for brain-specific administration of the fluorescent anticancer drug doxorubicin and *in vivo* mapping of brain tissues by the near-infrared biomarker IR780 in mice. The star-UMM was engineered by precisely programming the polymer topology having hydrophobic and hydrophilic polycaprolactone blocks and in-built with lysosomal enzyme-biodegradation stimuli to deliver the payloads at intracellular compartments. *In vivo* imaging in mice revealed prolonged circulation of star-UMM in blood for >72 h, and whole-organ image-quantification substantiated its efficient ability to breach the BBB. Star UMM exhibited excellent stability in blood circulation and reduced cardiotoxicity, was non-hemolytic, had substantial uptake in the cortical neurons of the mouse brain, had lysosomal enzymatic-biodegradation, and exhibited negligible immunogenicity or necrosis. This newly designed star-UMM could have long-term applications in brain-specific drug delivery.

Introduction

Drug delivery across the tightly regulated vasculature of the blood–brain barrier (BBB) in treating tumors and neurodegenerative diseases has been a major bottleneck.[1–3] The BBB maintains the homeostatic balance by regulating the transport of small-molecule nutrients and ions through the vasculature into the brain; thus, restricting the transportation of larger size and extraneous species across this biological barrier.[4] Nano-prodrug development has clearly identified that carriers <50 nm in size can penetrate the BBB and enable drug accumulation in the brain.[5–9] Polypeptide nanoparticles (NPs), tumor-derived extracellular vesicles, synthetic protein NPs, nano-antioxidants, liposomes, dendrimers, worm-like micelles, and T cell-mediated polymer NPs are some of the important examples reported for BBB research.[10–23] Intranasal[24] and gut-to-brain oral drug-delivery models[25] have also been developed to overcome BBB challenges encountered by intravenous delivery pathways. Near infrared (NIR)-assisted fluorescent NPs have been utilized for image-guided therapy for Parkinson's disease[26] and glioblastoma.[27] Uncontrollable glomerular renal filtration of smaller (<15 nm) nanocarriers, and splenic and hepatic filtration of bigger NPs (>200 nm) in the body limits the drug concentration of the NP formulation upon intravenous administration which, in turn, reduces the bioavailability of NPs for BBB crossing.[28,29] Thus, the next generation of BBB-crossing nanocarriers is mandatorily designed to be substantially stable to evade disassembly in body fluidics *in vivo*, tiny-size sub-nanometer objects (<50 nm) for penetrating tightly regulated *t*-junctions, high drug-loading content, reduced cardiotoxicity and, most importantly, biodegradable for safe use in BBB research.[30–34] Among the many synthetic NPs, branched macromolecular architectures such as "star block" copolymers exhibit resistance against renal filtration and retain the drug NP formulation in the blood for prolonged periods.[29] Star-block copolymers provide excellent structural control to build well-defined core–shell NPs.[35–40] Persistent to their three-dimensional globular core–shell

[a]*Department of Chemistry, Indian Institute of Science Education and Research (IISER Pune), Dr Homi Bhabha Road, Pune 411008, Maharashtra, India. E-mail: jayakannan@iiserpune.ac.in*

[b]*Laboratory of Neural Circuits and Behaviour (LNCB), Department of Biology, Indian Institute of Science Education and Research (IISER Pune), Dr Homi Bhabha Road, Pune 411008, Maharashtra, India. E-mail: nabraham@iiserpune.ac.in*

†Electronic supplementary information (ESI) available: Synthesis, structural characterization and additional biological data are provided. See DOI: https://doi.org/10.1039/d4nr02636e

This journal is © The Royal Society of Chemistry 2024

ACS APPLIED BIO MATERIALS

www.acsabm.org Forum Article

Structural Engineering of Cationic Block Copolymer Architectures for Selective Breaching of Prokaryotic and Eukaryotic Biological Species

Published as part of ACS Applied Bio Materials special issue "Celebrating the 25th Anniversary of the Chemical Research Society of India".

Ruma Ghosh, Shahidkhan Pathan, and Manickam Jayakannan*

Cite This: ACS Appl. Bio Mater. 2024, 7, 7062−7075 Read Online

ACCESS | Metrics & More | Article Recommendations | Supporting Information

ABSTRACT: Positively charged antimicrobial polymers are known to cause severe damage to biological systems, and thus synthetic strategies are urgently required to design next-generation nontoxic cationic macromolecular architectures for healthcare applications. Here, we report a structural-engineering strategy to build cationic linear and star-block copolymer nanoarchitectures having identical chemical composition, molar mass, nanoparticle size, and positive surface charge, yet they differ distinctly in their biological action in breaching prokaryotic species such as *E. coli* (Gram-negative bacteria) without affecting eukaryotic species like red-blood and mammalian cells. For this purpose, linear and star-block structures are built on a polycaprolactone biodegradable platform having an imidazolium positive handle. Under physiological conditions, the linear architecture exhibits toxicity indiscriminately to all biological species, whereas its star counterpart is remarkably selective in membrane breaching action toward bacteria while maintaining inertness toward eukaryotic species. Confocal microscopy analysis of HPTS fluorescent dye-loaded star-polymer nanoparticles substantiated their antimicrobial action in *E. coli*. Tissue-penetrable near-infrared fluorescent dye (IR-780) loaded NP aided the *in vivo* biodistribution analysis and *ex vivo* quantification of cationic species' accumulations in vital organs in mice. Azithromycin, a clinical water-insoluble macrolide, is delivered from the star platform to accomplish synergistic antimicrobial activity by the combination of bactericidal−bacteriostatic action of the polymer carrier and drug together in a single system.

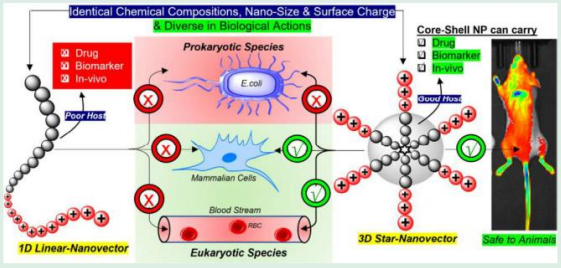

KEYWORDS: *Block polymers, Biodegradable polymers, Drug Delivery, Cationic Polymers, Antimicrobial Agents*

INTRODUCTION

Direct encounter of a cationic antimicrobial polymer with prokaryotic and eukaryotic species is important to study for safe treatment of microbial infections without affecting the healthy tissues and organs in the body.[1−3] Single-celled prokaryotic microbes like *E. coli* (Gram-negative bacteria), and eukaryotic red-blood cells (RBCs) and mammalian cells coexists in our biological body. Therefore, it is essential to design next-generation macromolecular antimicrobial agents that are less toxic or nontoxic to RBCs and healthy cells when they are employed for antimicrobial activity against bacteria.[4] Positively charged synthetic macromolecules are emerging as important classes of artificial antimicrobial agents due to their ability to self-assemble into drug delivery vehicles to carry substantial amounts of payloads to overcome multidrug resistance in combination therapy.[5−12] Prokaryotic cell membranes (e.g., in *E. coli*) are multilayered, rigid, and anionic in nature ($\xi = -22 \pm 3.0$ mV); thus, cationic polymers having appropriate amphiphilicity become a natural choice to electrostatically adhere, leading to membrane disruption in bacterial cells.[13−15] RBC membranes are slightly less negative ($\xi = -15 \pm 0.1$ mV)[16] compared to microbial membranes, whereas mammalian cell membranes are zwitterionic (ξ = neutral).[17] Therefore, cationic polymers need to navigate through these different membrane potentials to avoid unwanted toxicity toward RBCs and healthy cells or tissues.[18−20] Efforts have been made in the past to study the role of hydrophilic−hydrophobic content,[21] block versus random copolymers,[22−26] dendritic[27,28] and star polymers,[29−33] and cross-linked polymeric resins[34] to establish

Received: July 5, 2024
Revised: October 3, 2024
Accepted: October 7, 2024
Published: October 18, 2024

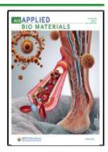

ACS Publications © 2024 American Chemical Society

https://doi.org/10.1021/acsabm.4c00913
ACS Appl. Bio Mater. 2024, 7, 7062−7075

16)

ACS Biomaterials SCIENCE & ENGINEERING

pubs.acs.org/journal/abseba Article

Structural Engineering of Star Block Biodegradable Polymer Unimolecular Micelles for Drug Delivery in Cancer Cells

Upendiran Pranav, Mehak Malhotra, Shahidkhan Pathan, and Manickam Jayakannan*

Cite This: ACS Biomater. Sci. Eng. 2023, 9, 743−759 Read Online

ACCESS | Metrics & More | Article Recommendations | Supporting Information

ABSTRACT: The present investigation reports the structural engineering of biodegradable star block polycaprolactone (PCL) to tailor-make aggregated micelles and unimolecular micelles to study their effect on drug delivery aspects in cancer cell lines. Fully PCL-based star block copolymers were designed by varying the arm numbers from two to eight while keeping the arm length constant throughout. Multifunctional initiators were exploited for stepwise solvent-free melt ring-opening polymerization of ε-caprolactone and γ-substituted caprolactone to construct star block copolymers having a PCL hydrophobic core and a carboxylic PCL hydrophilic shell, respectively. A higher arm number and a higher degree of branching in star polymers facilitated the formation of unimolecular micelles as opposed to the formation of conventional multimicellar aggregates in lower arm analogues. The dense core of the unimolecular micelles enabled them to load high amounts of the anticancer drug doxorubicin (DOX, ∼12−15%) compared to the aggregated micelles (∼3−4%). The star unimolecular micelle completely degraded leading to 90% release of the loaded drug upon treatment with the lysosomal esterase enzyme *in vitro*. The anticancer efficacies of these DOX-loaded unimolecular micelles were tested in a breast cancer cell line (MCF-7), and their IC_{50} values were found to be much lower compared to those of aggregated micelles. Time-dependent cellular uptake studies by confocal microscopy revealed that unimolecular micelles were readily taken up by the cells, and enhancement of the drug concentration was observed at the intracellular level up to 36 h. The present work opens new synthetic strategies for building a next-generation biodegradable unimolecular micellar nanoplatform for drug delivery in cancer research.

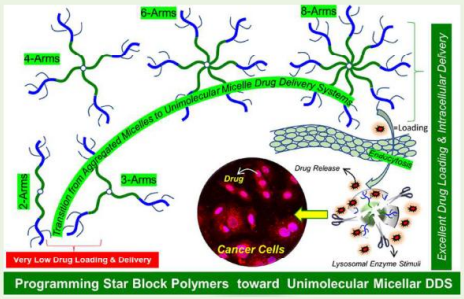

KEYWORDS: *block copolymers, star polymers, unimolecular micelles, polycaprolactone, enzymatic biodegradation, drug delivery*

INTRODUCTION

Synthetic macromolecular architectures have been emerging as an essential part of biomaterial research both in the development of diagnostic probes for early detection of diseases[1−3] and function as an efficient vehicle to deliver an ampule of therapeutic drugs with minimum or no side effects in the treatment of malignant tumors.[4−6] Conventional polymeric nanocarriers are typically produced by the aggregation of hydrophilic and hydrophobic polymeric segments in aqueous medium that are at thermodynamic and kinetic equilibrium with their unimers.[7] More often, the aggregated micellar polymer nanoassemblies were observed to disassemble by the concentration gradient in the body fluidics while administrating intravenously and exhibited premature leakage of drug formulations in the bloodstream.[8,9] Further, polymeric nanoparticles were also found to encounter heavy stress in the renal filtration apparatus in the body, and tiny nanoparticles of <5 nm in size or feebly stable rigid-rod-type micellar aggregates were routinely filtered out.[10] High-molecular-weight macromolecular (polymer) nanocarriers having branched and flexible architectures were found to withstand the pressure in a renal apparatus, thus imparting them prolonged blood circulation to enhance the therapeutic efficiency.[11] Dendrimers,[12,13] hyperbranched polymers,[14,15] polymer brushes,[16−18] and star polymers[19,20] are some of the most sought-after nonlinear branched polymer architectures to serve the above requirement in drug delivery. Among them, star polymers were found to be particularly important owing to their ease of synthesis, structural diversity, and most importantly their ability to self-assemble into unimolecular micelles, i.e., single-chain polymer nanocarriers.[21] Unimolecular micelles (UMM) are promising candidates due to their high thermodynamic stability against a concentration gradient owing to their unique core−shell structure.[22] The density of the UMM core enables them to load humongous amounts of a

Received: October 13, 2022
Accepted: December 16, 2022
Published: December 29, 2022

ACS Publications © 2022 American Chemical Society

17)

ACS POLYMERS Au
AN OPEN ACCESS JOURNAL OF THE AMERICAN CHEMICAL SOCIETY

pubs.acs.org/polymerau Article

Self-Reporting Polysaccharide Polymersome for Doxorubicin and Cisplatin Delivery to Live Cancer Cells

Mishika Virmani, Nilesh Umakant Deshpande, Shahidkhan Pathan, and Manickam Jayakannan*

Cite This: *ACS Polym. Au* 2022, 2, 181−193 Read Online

ACCESS | Metrics & More | Article Recommendations | Supporting Information

ABSTRACT: We report self-reporting fluorescent polysaccharide polymersome nanoassemblies for enzyme-responsive intracellular delivery of two clinical anticancer drugs doxorubicin (DOX) and cisplatin to study the real-time drug-releasing aspects by fluorescent resonance energy transfer (FRET) bioimaging in live cancer cells. Fluorescent polymersomes were tailor-made by tagging an aggregation-induced emission (AIE) optical chromophore, tetraphenylethylene (TPE), and a plant-based vesicular directing hydrophobic unit through enzyme-biodegradable aliphatic ester chemical linkages in the polysaccharide dextran. The blue-luminescent polymersome self-assembled in water and exhibited excellent encapsulation capability for the red-luminescent anticancer drug DOX. FRET between the AIE polymersome host and DOX guest molecules resulted in a completely turn-off probe. At the intracellular level, the lysosomal enzymatic disassembly of the polymersome restored the dual fluorescent signals from DOX and TPE at the nucleus and the lysosomes, respectively. Live-cell confocal microscopy coupled with selective photoexcitation was employed to study the real-time polymersome disassembly by monitoring the turn-on fluorescent signals in human breast cancer cell lines. Alternatively, carboxylic acid-functionalized AIE polymersomes were also tailor-made for cisplatin stitching to directly monitor Pt drug delivery. The polymersome nanoassemblies exhibited excellent structural tolerance for the chemical conjugation of the Pt drugs, and the fluorescence signals were unaltered. An in vitro drug release study confirmed that the cisplatin-stitched fluorescent polymersomes were very stable under physiological conditions and underwent lysosomal enzymatic degradation to inhibit the cancer cell growth. A lysosomal colocalization experiment using confocal microscopy substantiates the enzyme-responsive degradation of these polymersomes to release both the encapsulated and conjugated drugs at the intracellular level. The present design provides a unique opportunity to deliver more than one anticancer drug from a single polymersome platform in cancer research.

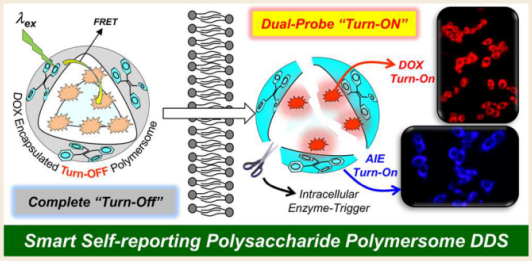

KEYWORDS: *drug delivery, fluorescent probes, polymersomes, enzyme-responsive, polysaccharides, cisplatin, doxorubicin*

INTRODUCTION

Enlarging therapeutic effects of anticancer drugs has become the holy grail of oncotherapy, thereby paving the way for the development of drug-delivery systems (DDSs) in cancer treatment.[1−4] Multitudes of delivery scaffolds ranging from liposomes,[5] microspheres,[6] dendrimers,[7] polymeric drug conjugates,[8] polymeric micelles,[9] and polymersomes[10−12] have been a subject of extensive clinical research. The rationale of loading therapeutics in delivery vehicles is to reduce systemic toxicity by shielding the drug against a plethora of plasma components during its transport via the bloodstream and later accumulating inside the target site leading to enhanced efficacy.[13] The choice of the delivery scaffold and its concomitant effects on drug efficacy is worth paying attention to improve the cancer treatment.[14] For instance, liposomal encapsulation of the chemotherapy drug doxorubicin (DOX) has shown considerable reduction in cardiotoxicity, simultaneously maintaining a high level of efficacy.[15,16] Surprisingly, liposomal formulation of cisplatin-conjugated drug (SPI-77 or stealth cisplatin) showed rather poor efficacy owing to slow release inside the tumor.[17,18] The problem of reduced efficacy due to poor uptake can be mitigated by a thoughtful choice of engineering the structural aspects of the nanoscaffold. Sugars are ubiquitous to cell membranes, and hence, polysaccharide-based scaffolds such as dextran become candidates of choice as they are easily taken up by the cells owing to like−like interactions.[8,19−21] Tagging the scaffold with a fluorophore can further help shed light on its uptake mechanism at the cellular level and also enable the tracking of the polymer nanocarriers.[22,23] Therefore, next-generation polymer nanocarriers are required to create a smart self-

Received: September 30, 2021
Revised: December 11, 2021
Accepted: December 13, 2021
Published: December 28, 2021

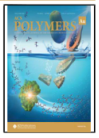

ACS Publications
© 2021 The Authors. Published by American Chemical Society

https://doi.org/10.1021/acspolymersau.1c00042
ACS Polym. Au 2022, 2, 181−193

19)

Indian Institute of Science Education and Research
(IISER – PUNE)

Dr. Homi Bhabha Road, Pashan, Pune 411 008.

Certificate

This is to certify that the project **"In Vivo Studies of Theranostic Block Copolymer Polymer Nanoparticles" (IISER_Pune/IAEC/2022_01/15)** from **Prof. M. Jayakannan** has been approved by the IAEC.

Authorized by	Name	Signature	Date
Chairman:	Dr. Nixon Abraham		04 Mar 2022
Member Secretary:	Dr. Suraj Ingle		04 Mar 2022
Main Nominee of CPCSEA:	Dr. Shital Suryavanshi	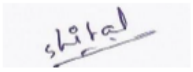	04 Mar 2022

Indian Institute of Science Education and Research
(IISER – PUNE)

Dr. Homi Bhabha Road, Pashan, Pune 411 008.

Certificate

This is to certify that the project proposal number **IISER_Pune/IAEC/2022_02/02** entitled **Star Block Copolymer Polymer Nanoparticles in Tumour bearing mice (in vivo)** submitted by **Prof. M. Jayakannan** has been approved/recommended by the IAEC of **IISER, Pune** in its meeting held on **03/08/2022**.

Authorized by	Name	Signature	Date
Chairman:	Dr. Nixon Abraham		03 Aug 2022
Member Secretary:	Dr. Suraj Ingle	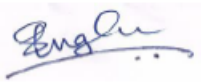	03 Aug 2022
Main Nominee of CPCSEA:	Dr. Shital Suryavanshi	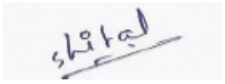	03 Aug 2022

Appendix

Chapter2

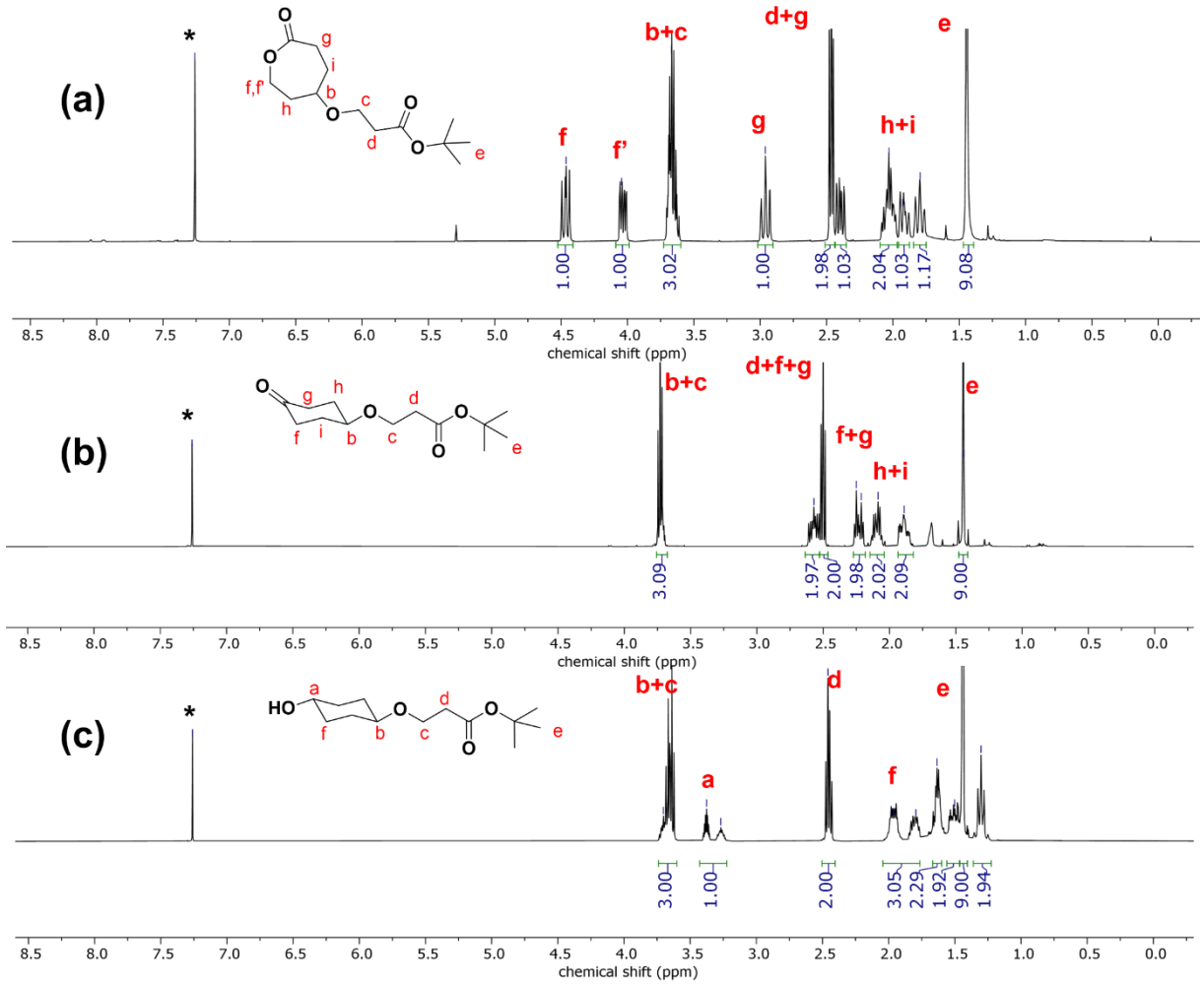

Figure S2.1: ^{1}HNMR of (a) Monomer **M2.** (b) Compound **2**. (c) Compund **1** in $CDCl_3$.

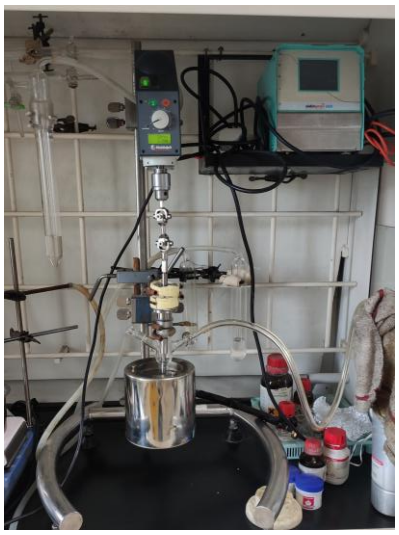

.

Photograph of In-house build ROP reactor with overhead stirrer and heating setup for melt polymerization

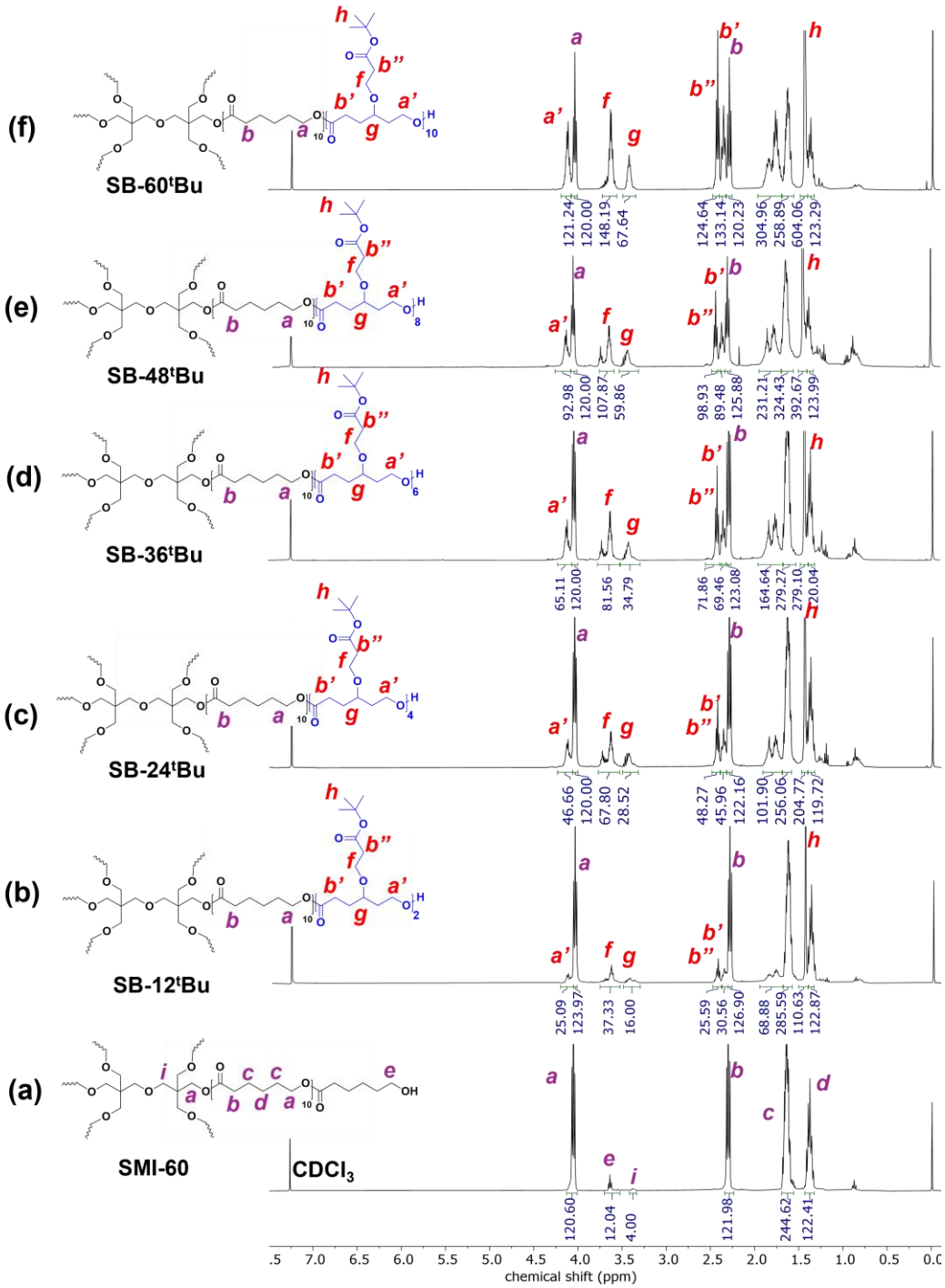

Figure S2.2: [1]HNMR plots of SMI-60, SB-12*t*Bu, SB-24*t*Bu, SB-36*t*Bu, SB-48*t*Bu, SB-60*t*Bu in *CDCl*$_3$.

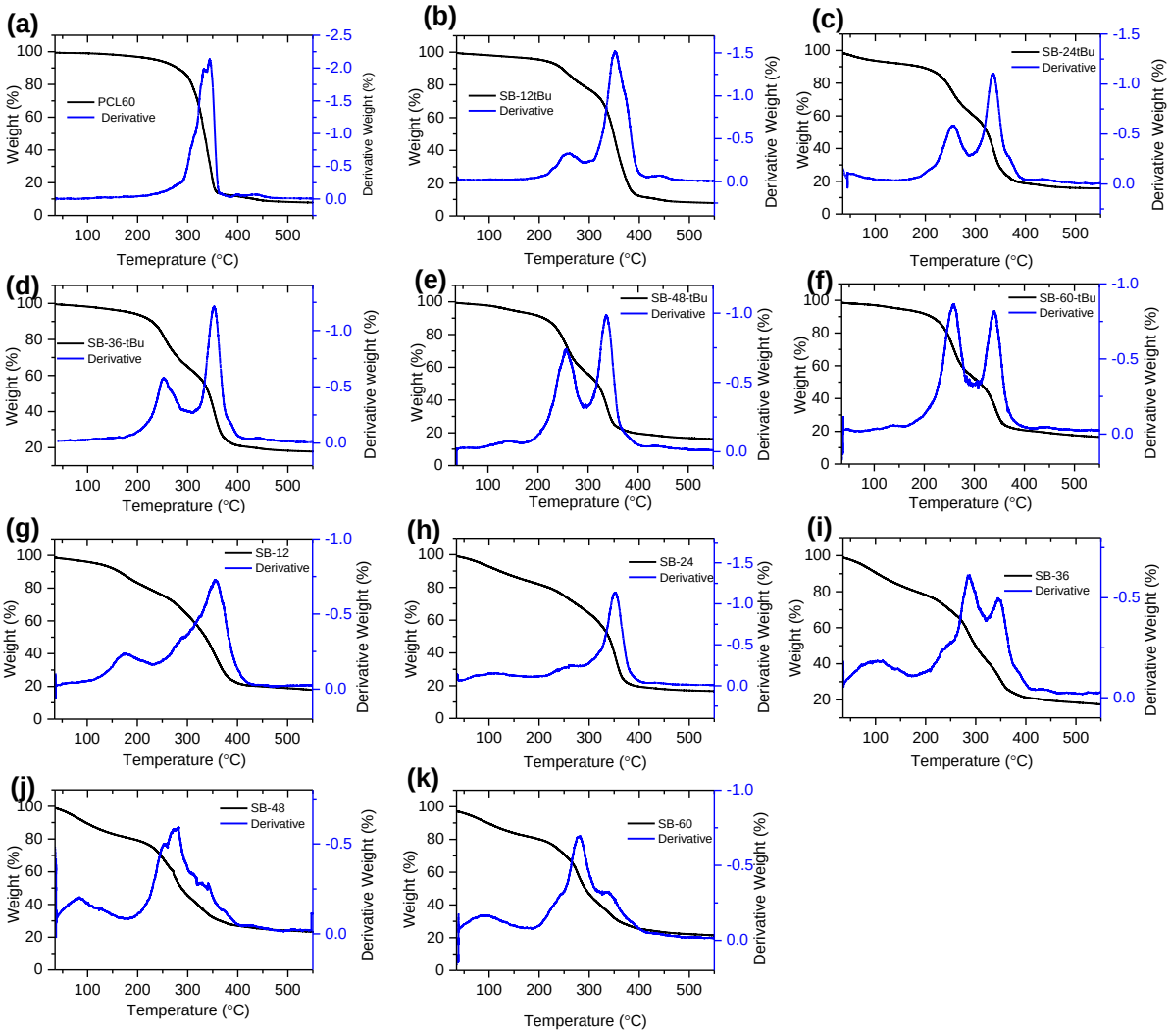

Figure S2.3: Derivative weight loss TGA plots of Star block polymers.

(a)

Sample[a]	DOX (0.5 mg)[b]		DOX (1.0 mg)[b]		DOX (2.0 mg)[b]	
	DLC (%)	DLE (%)	DLC (%)	DLE (%)	DLC (%)	DLE (%)
SB-12	0.11	1.1	-	-	-	-
SB-24	0.5	5	0.7	3.5	-	-
SB-36	2.5	25	2.6	13	2.8	7.0
SB-48	2.9	30	5.5	27.5	5.8	14.5
SB-60	5	50	8.2	41	14.3	36

a) Polymer weight was 5.0 mg for every sample. b) Feed of DOX in mg.

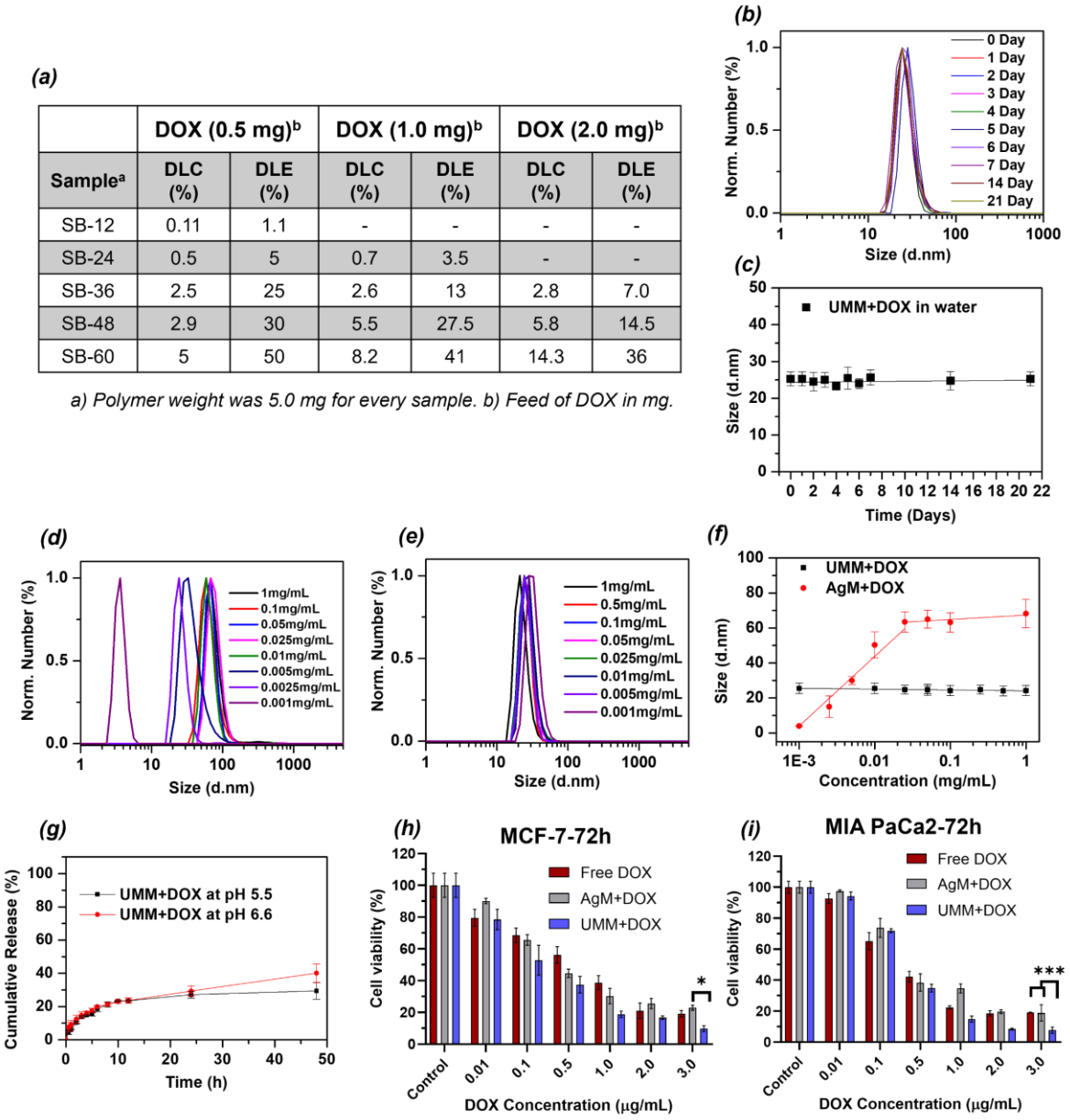

Figure S2.4: (a) Tabulated details of DOX encapsulation showing feed ratio and obtained DLC and DLE values. (b) DLS histogram of UMM+DOX in water for 21 days. (c) Cumulative size versus incubation time of UMM+DOX for 21 days incuabtion in water. (d) DLS histograms of AgM+DOX on serial dilution in water. (e) DLS histograms of UMM+DOX on serial dilution. (f) Cumulative size versus concentration of AgM+DOX and UMM+DOX on dilution. (g) Release profile of UMM+DOX in pH 5.5 and pH 6.6 at 37 ºC (Data represented as mean ± SD). Cytotoxicity by MTT assays for 72h incubation: (h) and (i) Cytotoxicity of AgM+DOX and UMM+DOX nanoparticles in MCF-7 and MIA PaCa 2 cell lines (n=3, data represented as mean ± SD, *p<0.05, ***p<0.001, ANOVA test).

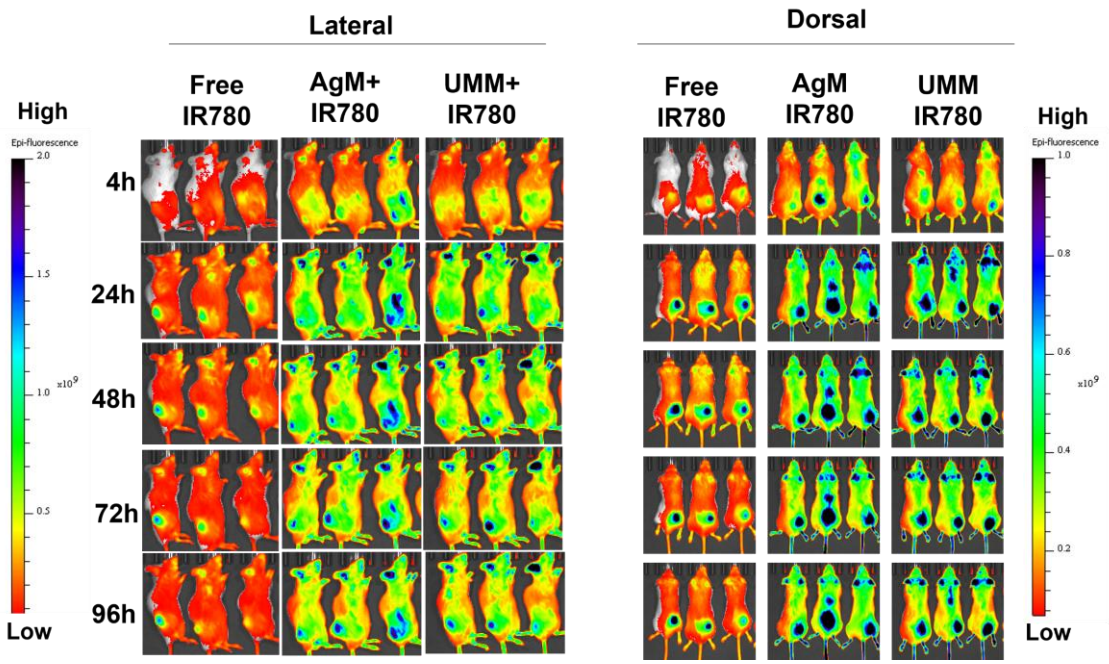

Figure S2.4: IVIS images of tumor bearing mice injected with free IR, AgM+IR780 and UMM+IR780.

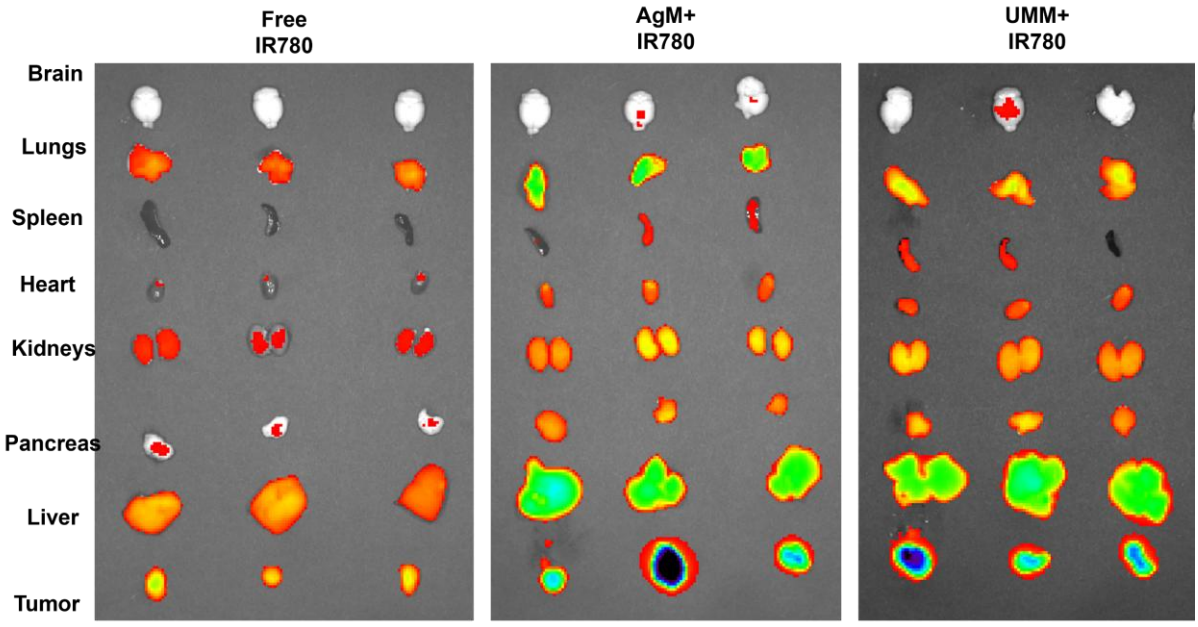

Figure S2.5: IVIS images of tumor after 96h of injection with free IR, AgM+IR780 and UMM+IR780.

Chapter 3

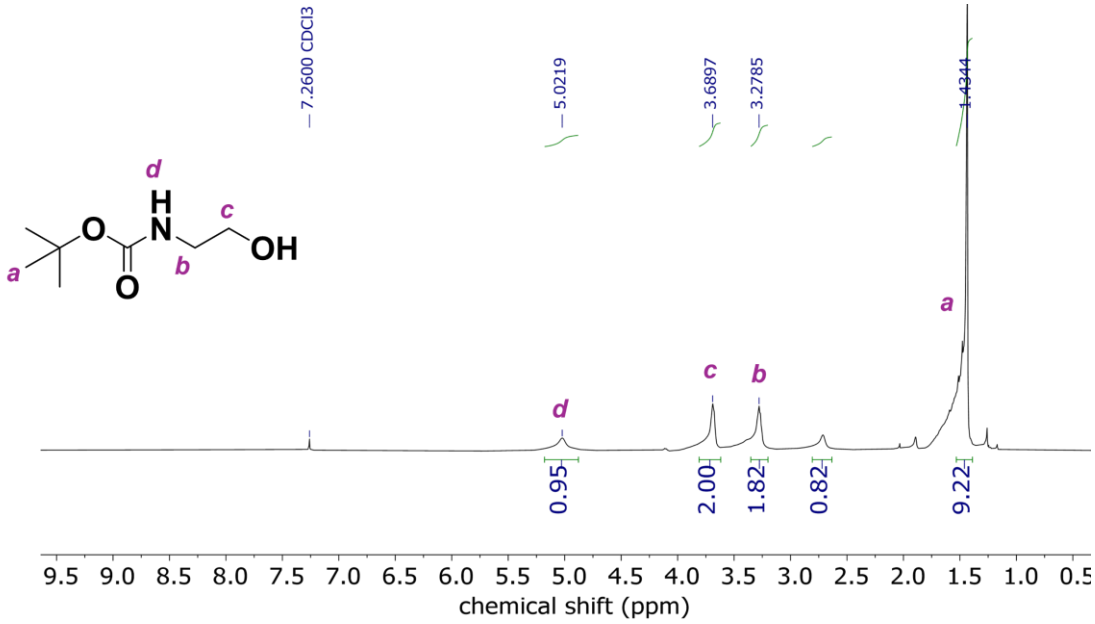

Figure S3.1: ^{1}HNMR of t-boc protected ethanolamine in $CDCl_3$.

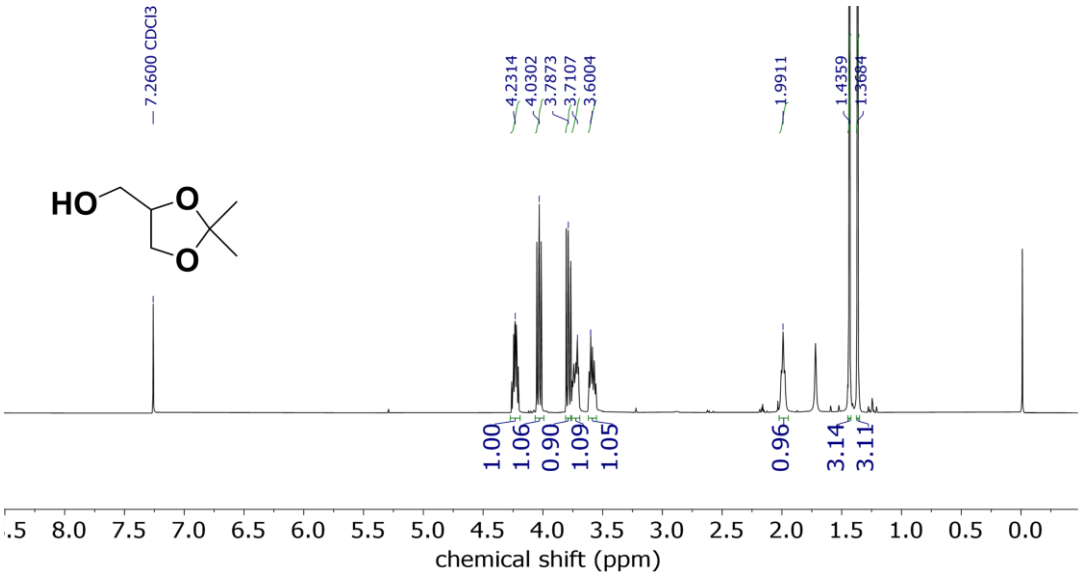

Figure S3.2: ^{1}HNMR of acetal protected glycrol in $CDCl_3$.

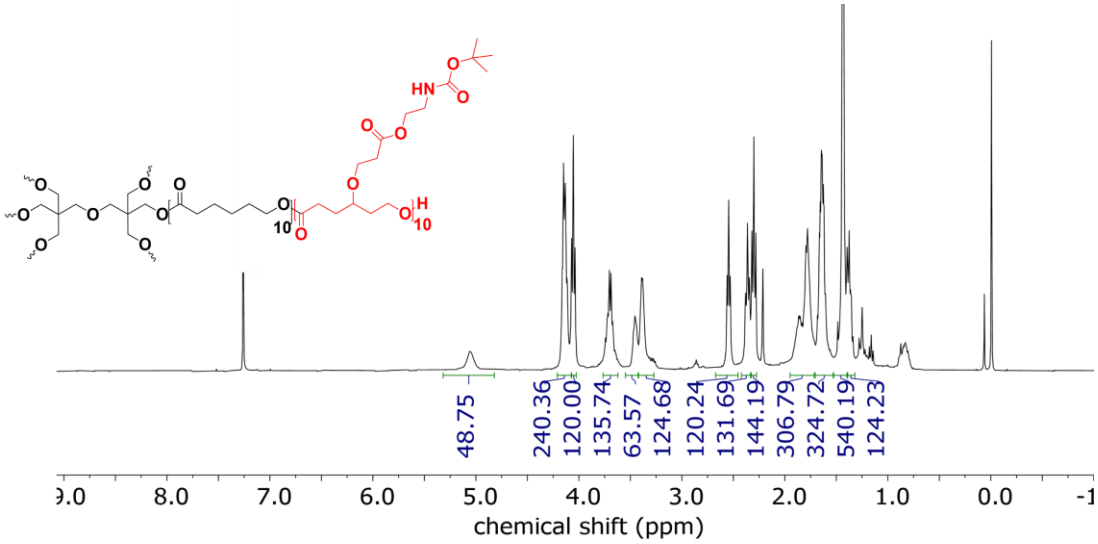

Figure S3.3: ^{1}HNMR of boc-protected cationic diblock copolyemr in $CDCl_3$.

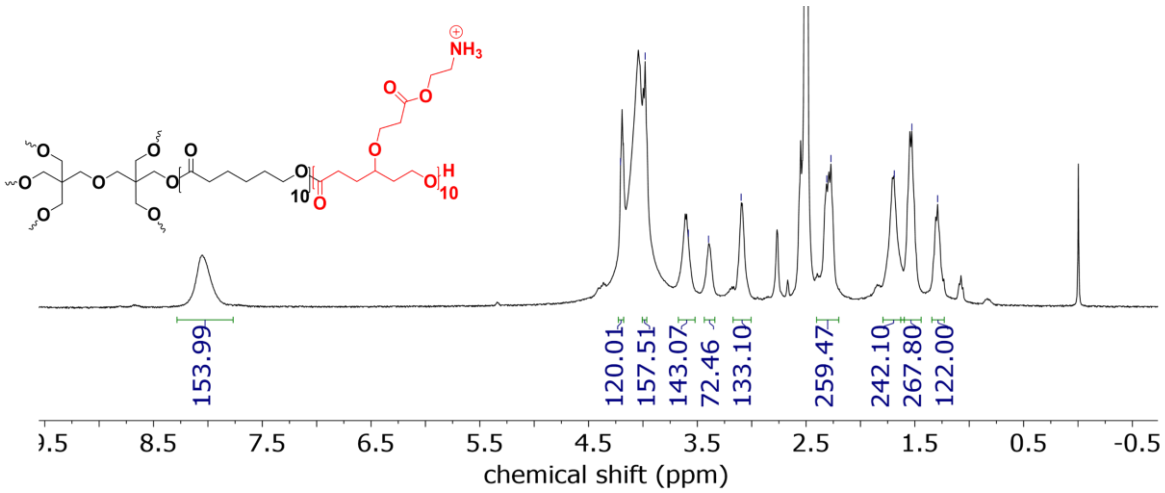

Figure S3.4: ^{1}HNMR of cationic diblock copolyemr in DMSO-d_6.

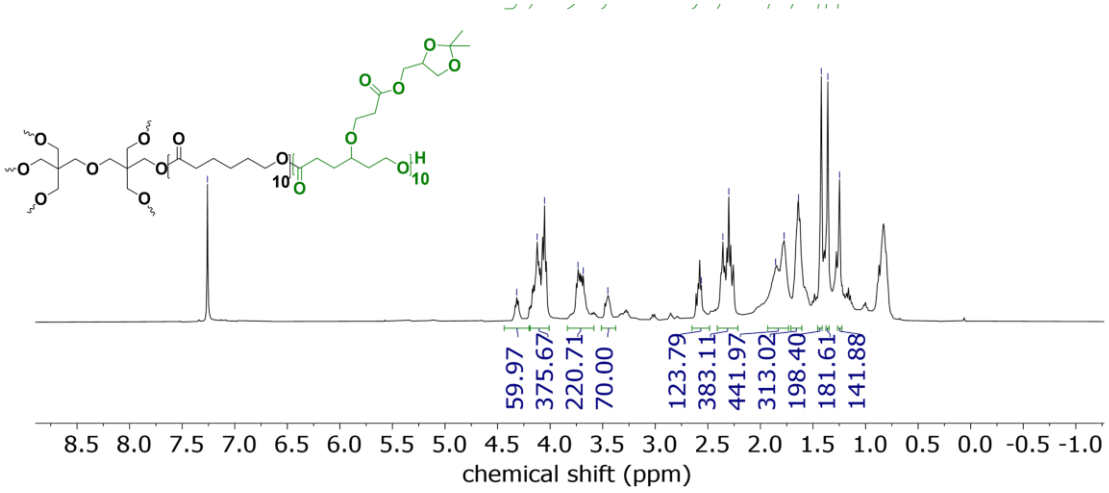

Figure S3.5: ^{1}HNMR of acetal-protected neutral diblock copolyemr in $CDCl_3$.

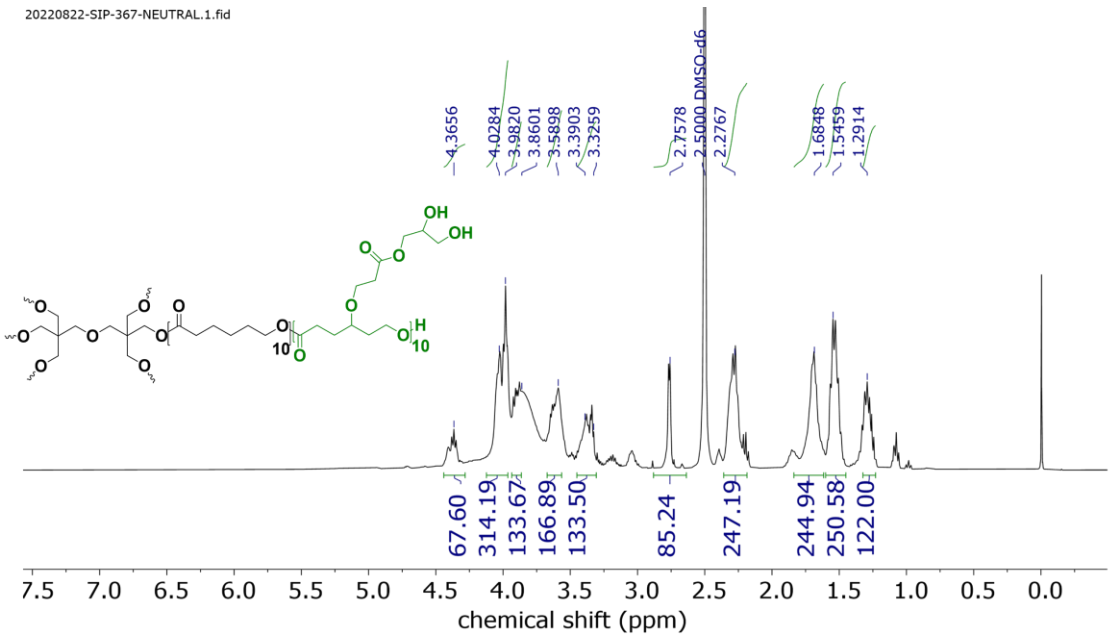

Figure S3.6: ^{1}HNMR of neutal diblock copolyemr in DMSO-d_6.

Chapter 4

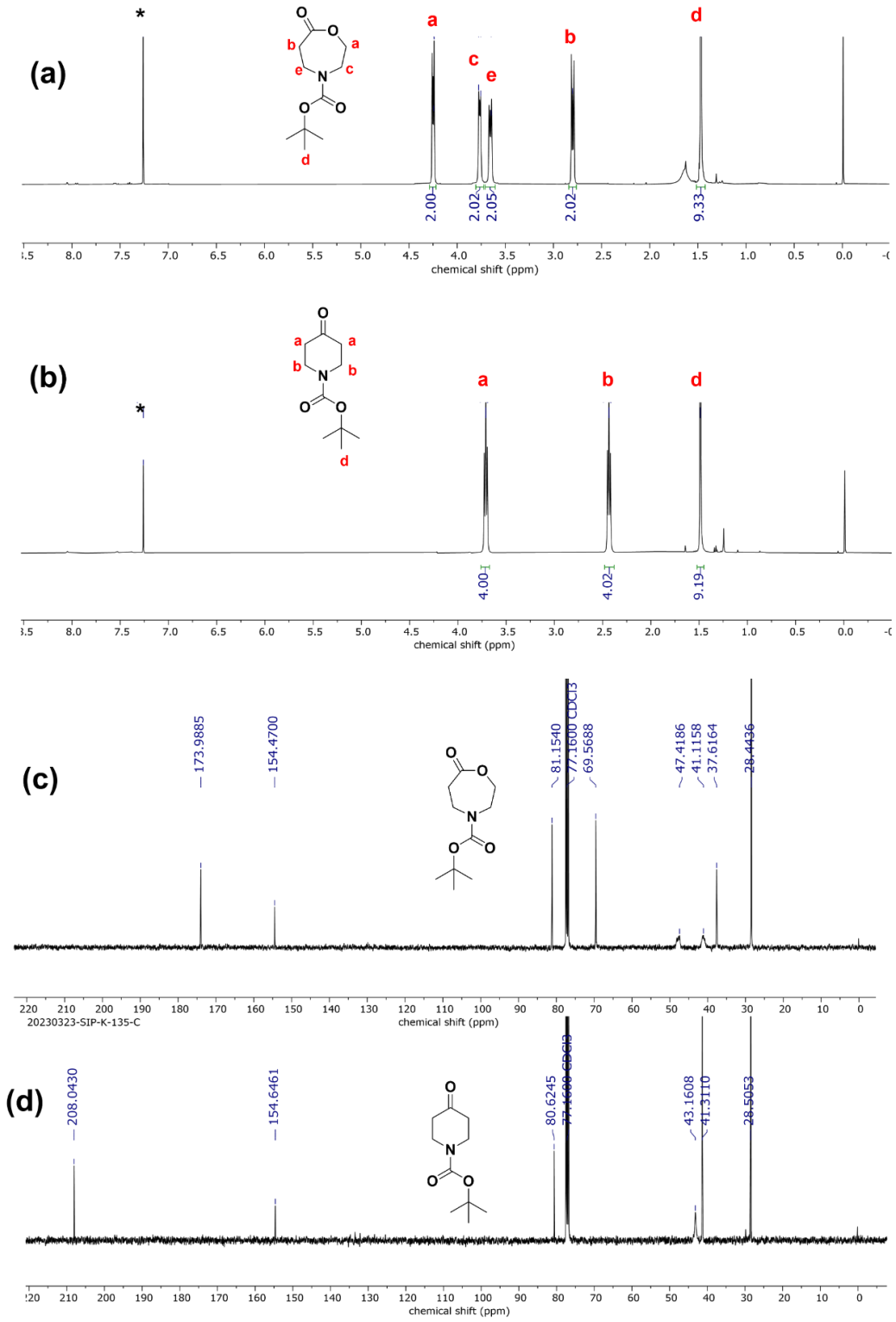

Figure S4.1: ^{1}HNMR of (a) Monomer **M1.** (b) Compound **1**. ^{13}CNMR of (c) monomer **M1**. (d) Compund **1** in $CDCl_3$.

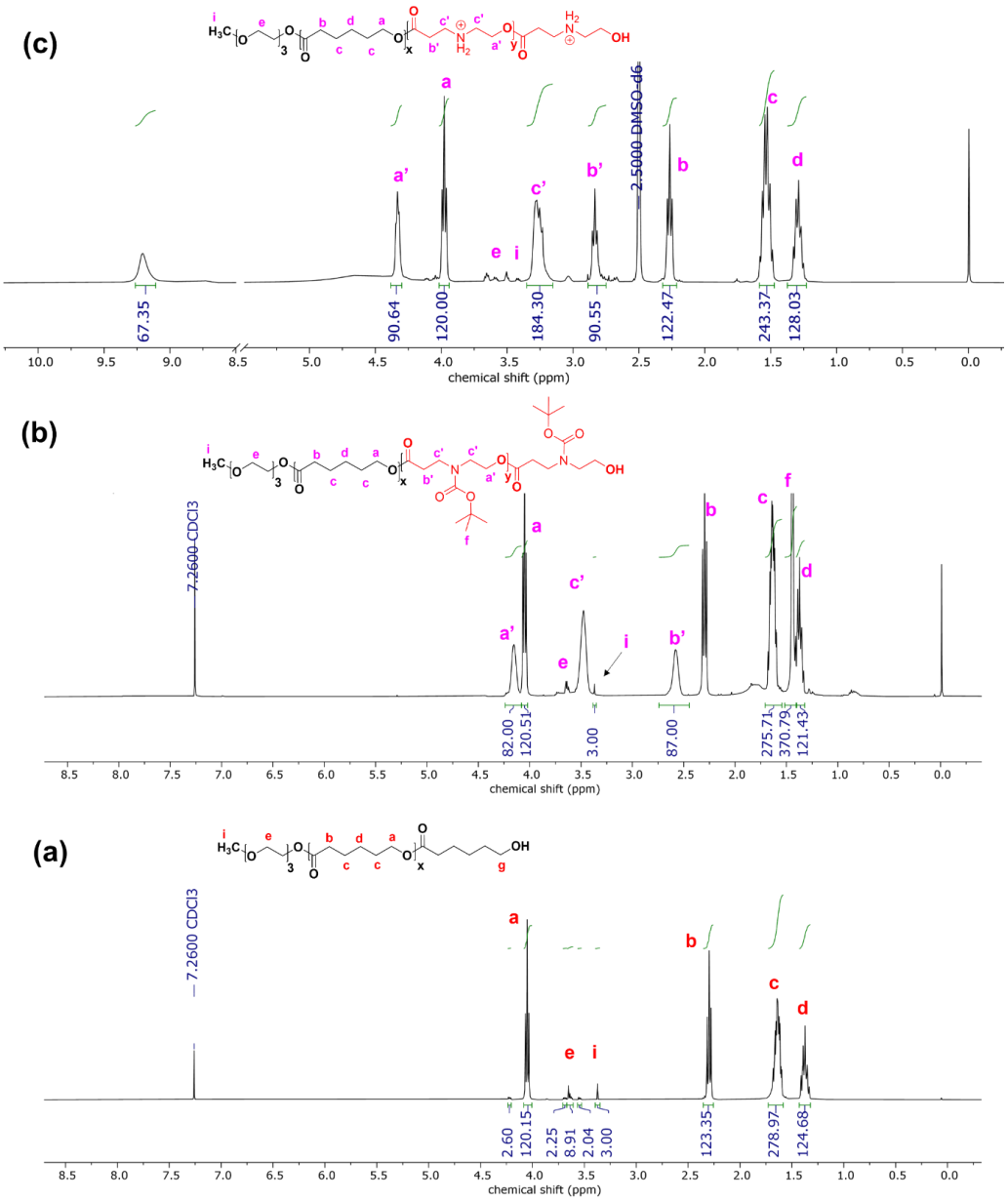

Figure S4.2: ^{1}HNMR stack plot of (a) PCL in $CDCl_3$. (b) PCL-*b*-PAE in $CDCl_3$. (c) Cationic-AB di-block polymer in DMSO-d_6 .

Note: Deprotection was confirmed by disapperance of t-Boc peak at 1.5ppm. Degree of polymerisation in PCL was determined by comparing intensities of C**H₃** protons in initiator (denoted by ***i***) to the protons ***a*** corresponding to -C**H₂**-O-C=O of polymer backbone and estimated as 60 for PCL. For PCL-*b*-PAE diblock copolymer, the degree of polymerisation was determined by comparing intensities of C**H₃** protons in initiator (denoted by ***i***) to the protons ***a'*** corresponding to -C**H₂**-O-C=O of newly formed PAE block and estimated as 44 for PAE.

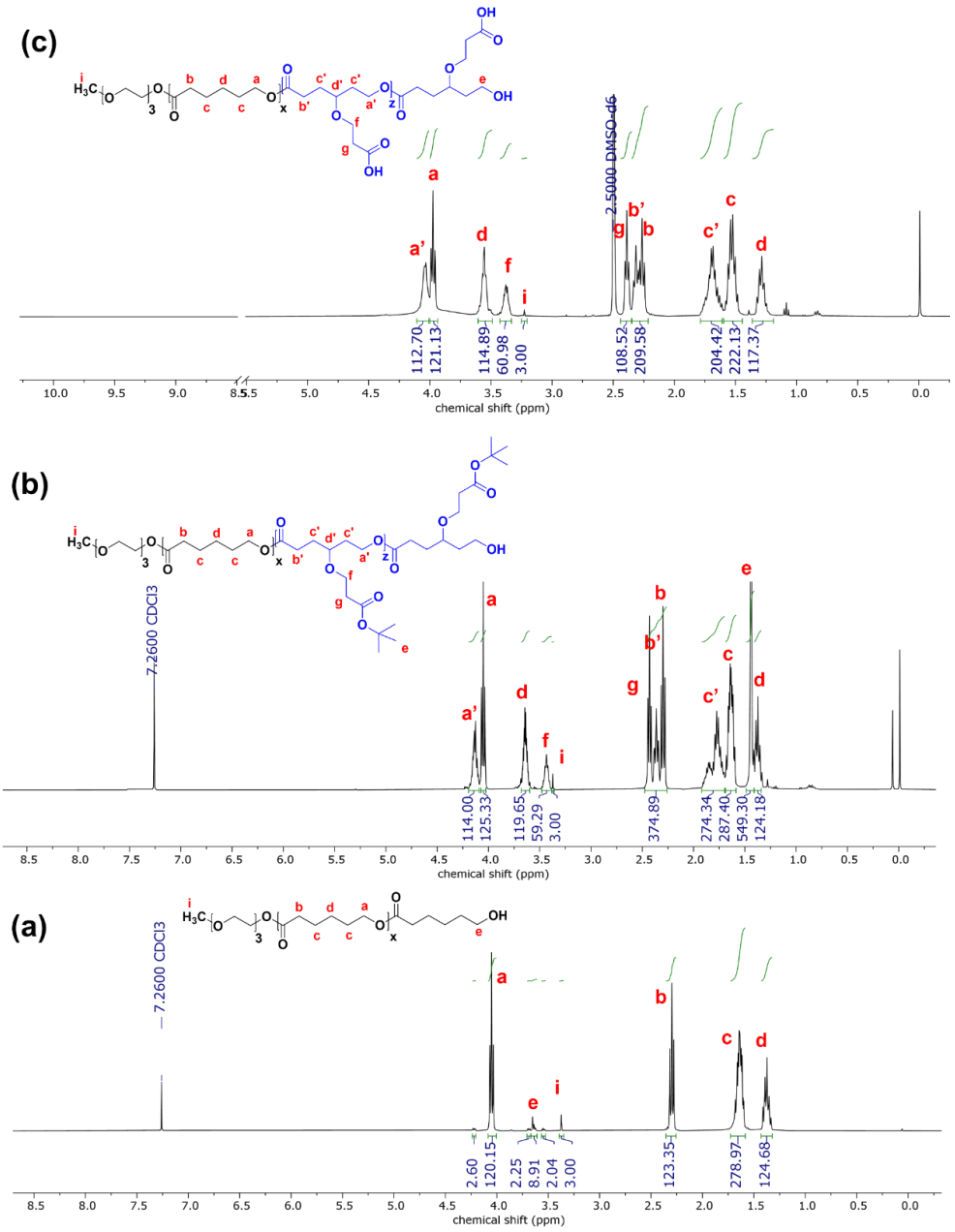

Figure S4.3: [1]HNMR stack plot of (a) PCL in $CDCl_3$ (b) PCL-b-tBuPCL diblock in $CDCl_3$. (c) Anionic-AC di-block polymer in DMSO-d_6.

Note: Deprotection was confirmed by disapperance of t-Butyl peak at 1.5ppm. Degree of polymerisation in PCL was determined by comparing intensities of C**H₃** protons in initiator (denoted by ***i***) to the protons ***a*** corresponding to -C**H₂**-C=O of polymer backbone and estimated as 60 for PCL. For PCL-b-tBuPCL diblock copolymer, the degree of polymerisation was determined by comparing intensities of C**H₃** protons in initiator (denoted by ***i***) to the protons ***a'*** corresponding to -C**H₂**-O-C=O of newly formed carboxylic substitued polycaprolactone block and estimated as 55 for tBuPCL block.

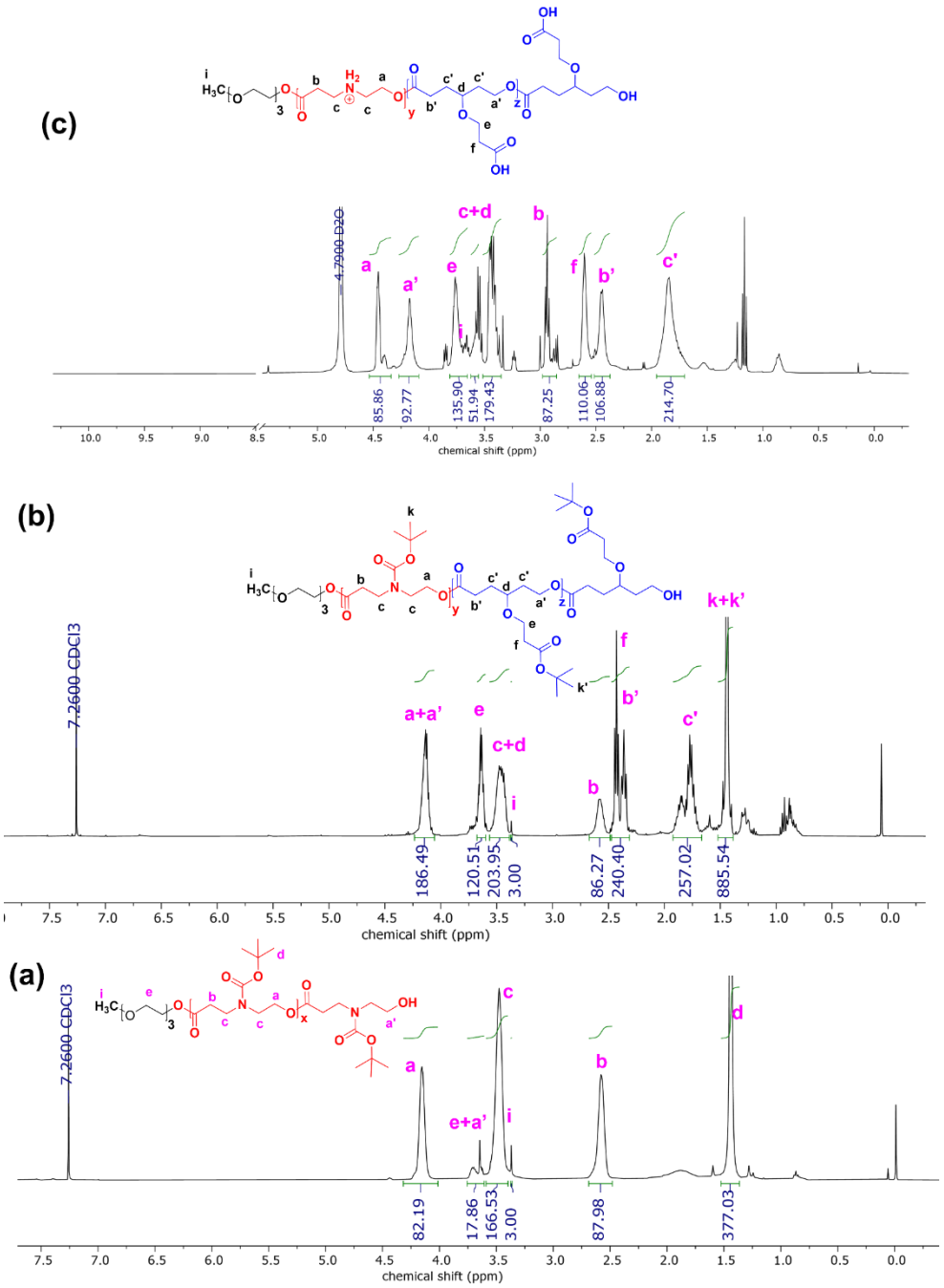

Figure S4.4: [1]HNMR stack plot of (a) PAE $CDCl_3$ in (b) PAE-*b*-tBuPCL in $CDCl_3$. (c) Zwitterionic-BC di-block polymer in D_2O .

Note: Degree of polymerisation in PAE was determined by comparing intensities of C**H**$_3$ protons in initiator (denoted by ***i***) to the protons ***a*** corresponding to -C**H**$_2$-O-C=O of PAE polymer backbone and estimated as 44 for PAE. Degree of polymerisation for tBuPCL block in di-block was determined by comparing intensities of initiator C**H**$_3$ protons (denoted by ***i***) to the C**H**$_2$-C=O of tBuPCL bakbone (denoted by ***b'***) and estimated to be 55 in tBuPCL block.

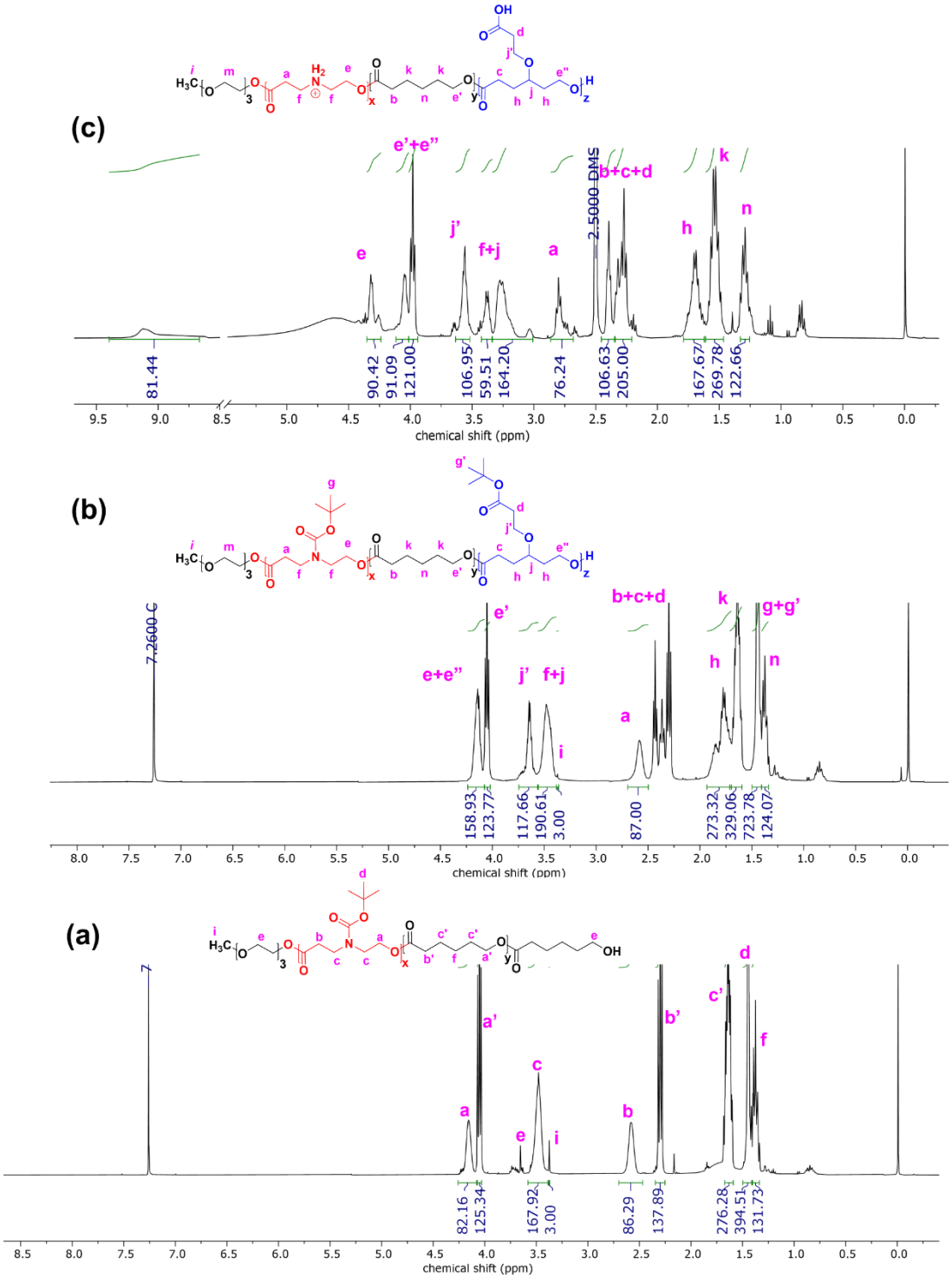

Figure S4.5: [1]HNMR stack plot of (a) PAE-*b*-PCL diblock polymer. (b) PAE-*b*-PCL-b-tBuPCL triblock polymer. (c) Zwitterionic BAC triblock polymer in DMSO-d_6 .

Note: Degree of polymerisation was estimated similarly to di-block polymer as mentioned earlier.

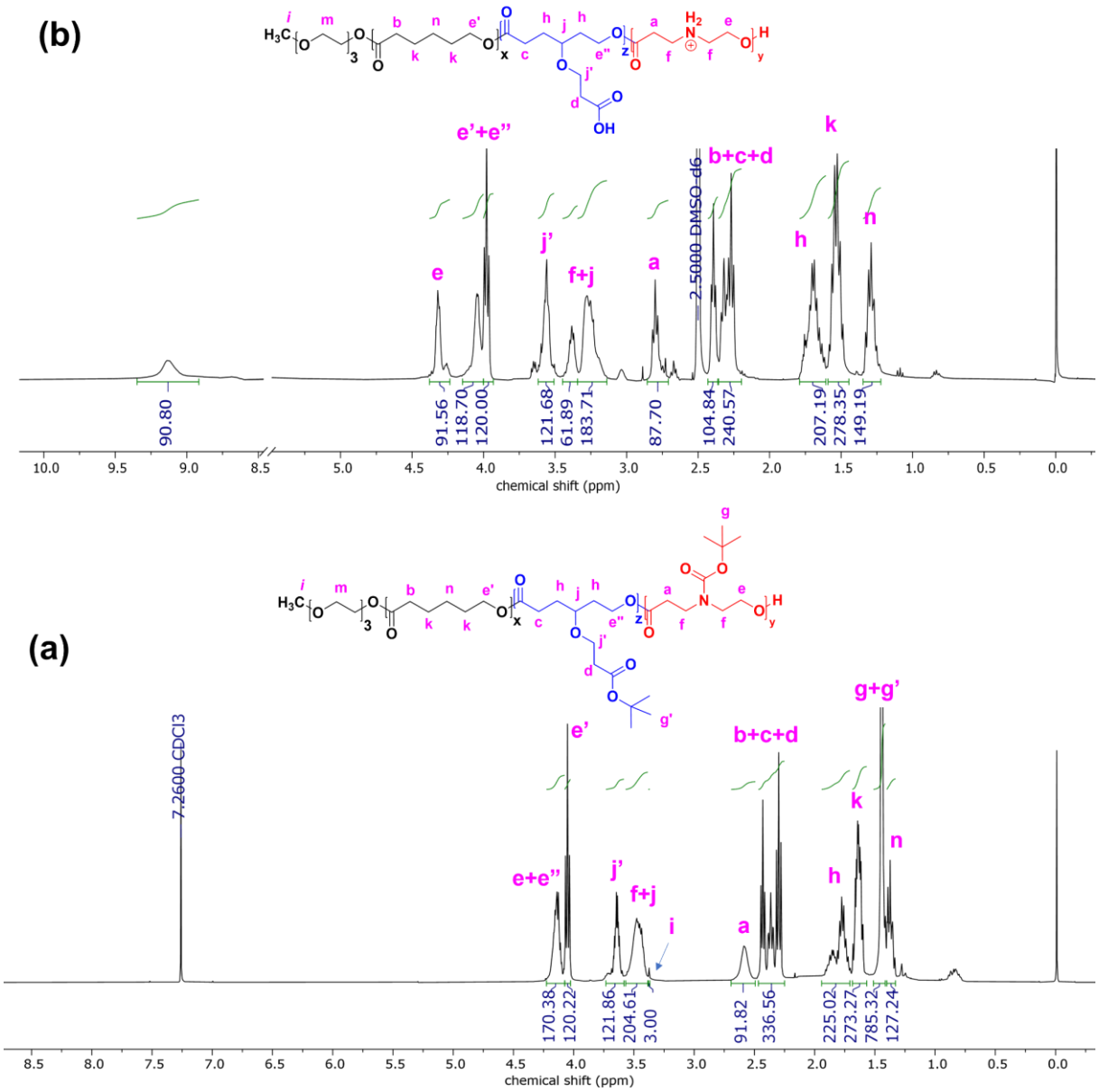

Figure S4.6: ^{1}HNMR stack plot of (a) PCL-b-tBuPCL-b-PAE triblock in $CDCl_3$ (b) Zwitterionic ACB triblock polymer in DMSO-d_6 .

Note: Degree of polymerisation was estimated by comapring intensities of C**H**$_3$ protons of initiator (denoted by i) to that of C**H**$_2$-O-C=O of PCL backobone (denoted by ***e'***), C**H**$_2$-C=O of PAE backbone (denoted by ***a***) and C**H**$_2$-C=O of tBuPCL backbone (denoted by ***c***). Estimated as 60 for PCL, 55 for tBuPCL and 44 for PAE blocks respectively.

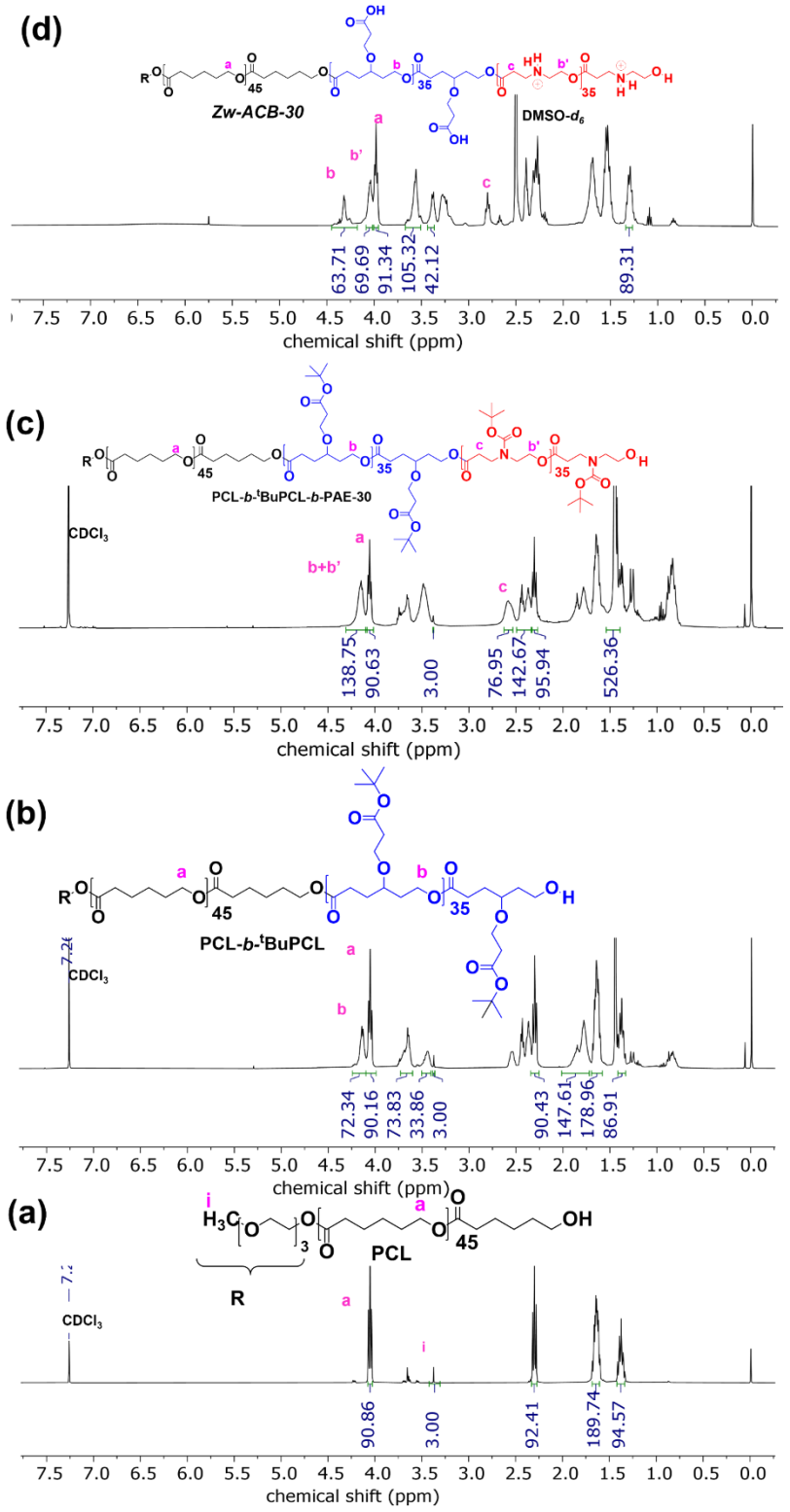

Figure S4.7: ^{1}HNMR stack plot of (a) PCL-45 $CDCl_3$ (b) PCL-b-tBuPCL in $CDCl_3$ (c) PCL-b-tBuPCL-b-PAE triblock in $CDCl_3$ (b) Zwitterionic ACB-30 triblock polymer in DMSO-d_6 .

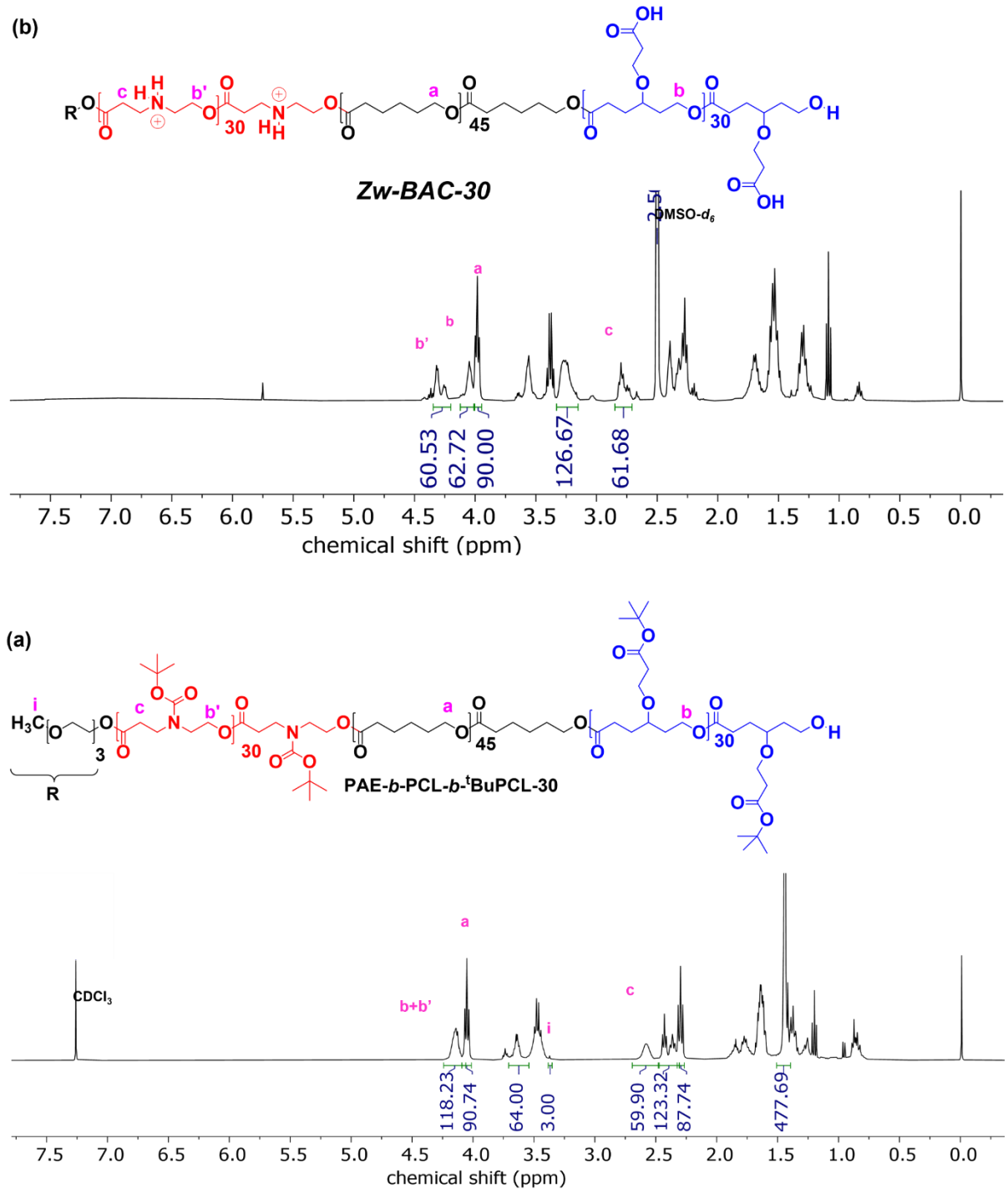

Figure S4.8: ^{1}HNMR stack plot of (a) PAE-b-PCL-b-tBuPCL triblock in $CDCl_3$ (b) Zwitterionic BAC-30 triblock polymer in DMSO-d_6 .

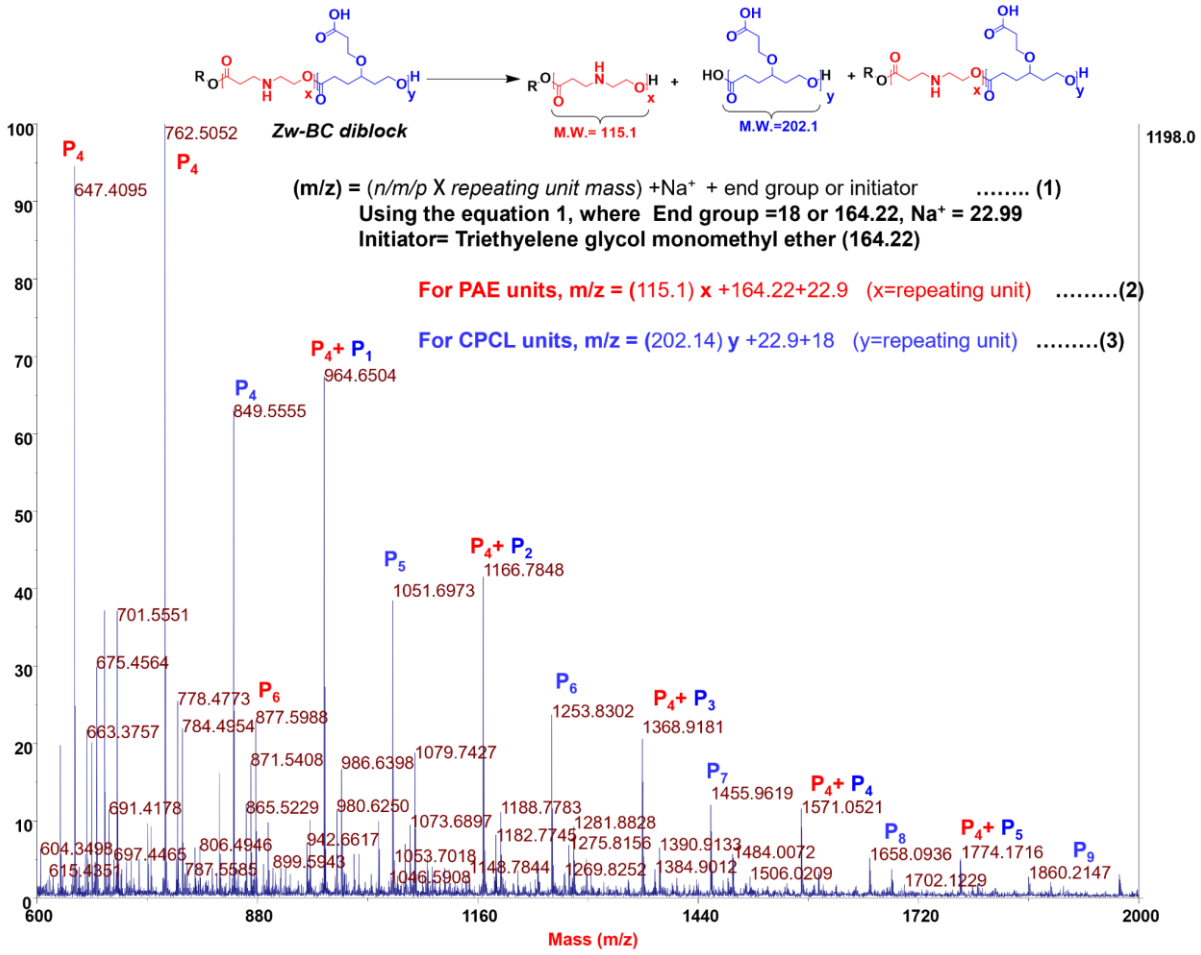

Figure S4.9: MALDI-TOF spectra of Zw-BC diblock after incubating with esterase enzyme in pH 7.4. at 37ºC for 24h. Peaks are assigned for degraded oligomers in spectra.

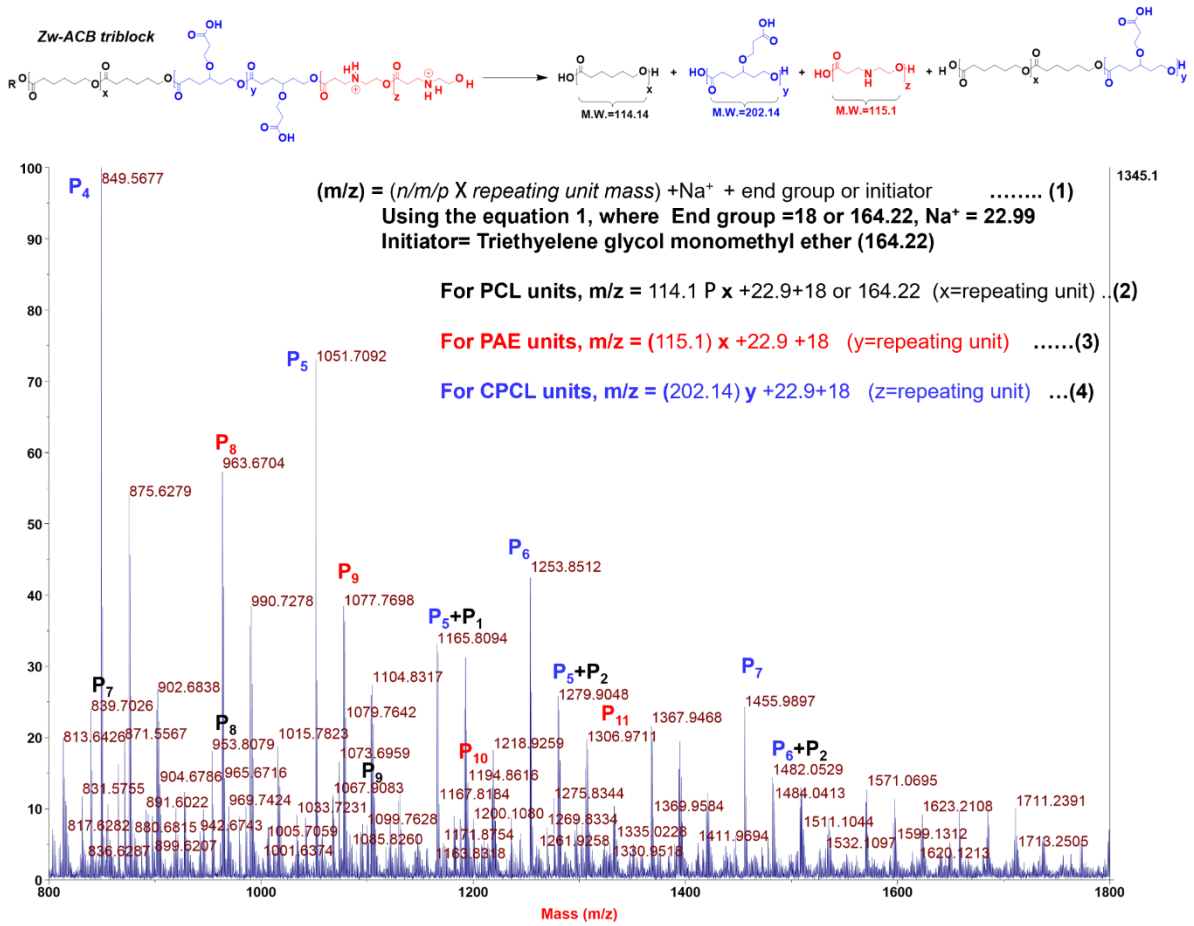

Figure S4.10: MALDI-TOF spectra of Zw-ACB triblock after incubating with esterase enzyme in pH 7.4. at 37ºC for 24h. Peaks are assigned for degraded oligomers in spectra.

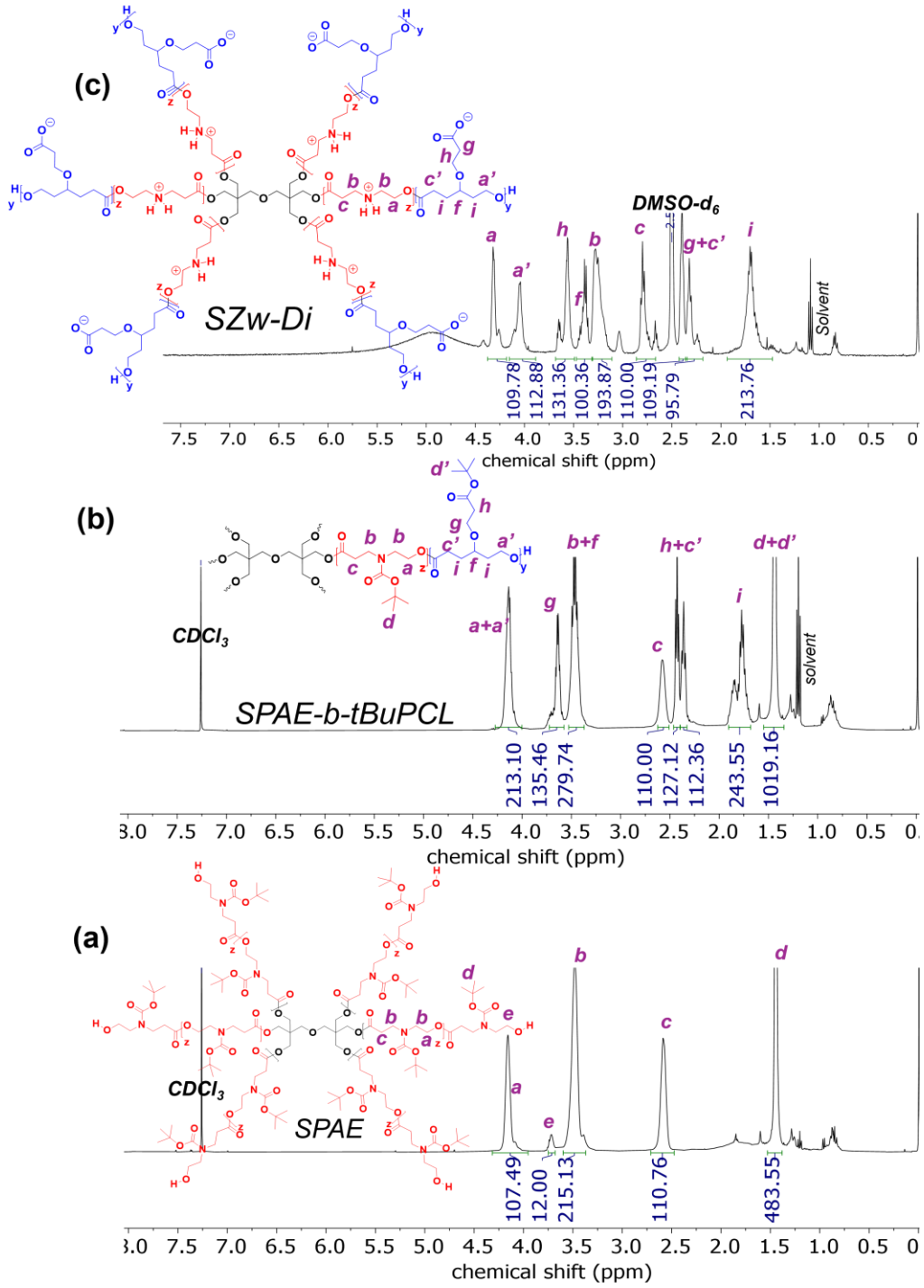

Figure S5.1: [1]HNMR plots of (a) SPAE in *CDCl₃*. (b) SPAE-*b*-*t*BuPCL in *CDCl₃*. (c) SZw-Di in *DMSO-d₆*. **Note:** Peaks are assigned alphabetically. The degree of polymerization (DP) for SPAE was estimated by comparing integration of end group protons (***e***) with the proton corresponding to -C**H**$_2$-O-CO- ester backbone ***(a).*** DP in SPAE-*b*-*t*BuPCL was estimated by comparing integration of proton ***c*** (PAE) to proton ***h*** *(tBuPCL)*.Deprotection was successfully confirmed by disappearance of ***d*** and ***d'*** protons (tButyl groups) in SZw-Di.

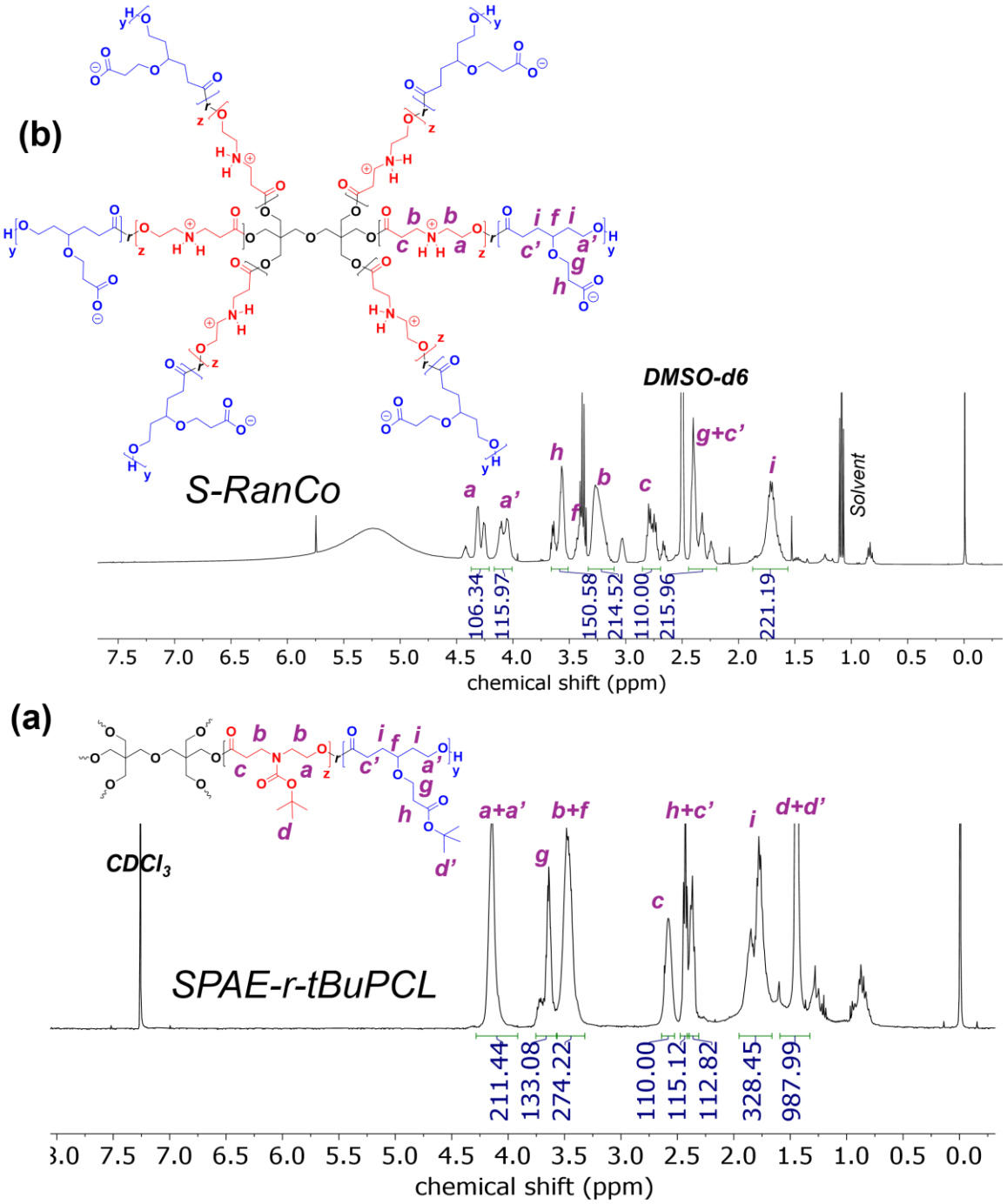

Figure S5.2: [1]HNMR plots of (a) SPAE-*r*-tBuPCL in *$CDCl_3$*. (b) S-RanCo in *DMSO-d_6*. **Note:** Peaks are assigned alphabetically. DP for SPAE-*r*-*t*BuPCL was estimated by comparing integration of proton ***c*** corresponding to CO-C**H**$_2$ in PAE units with protons ***g*+*h*** *(**g** protons are for 120 protons in tBuPCL and **h** protons are 12 end group protons in PAE respectively)*.Deprotection was successfully confirmed by disappearance of ***d*** and ***d'*** protons (tButyl groups) in S-RanCo.

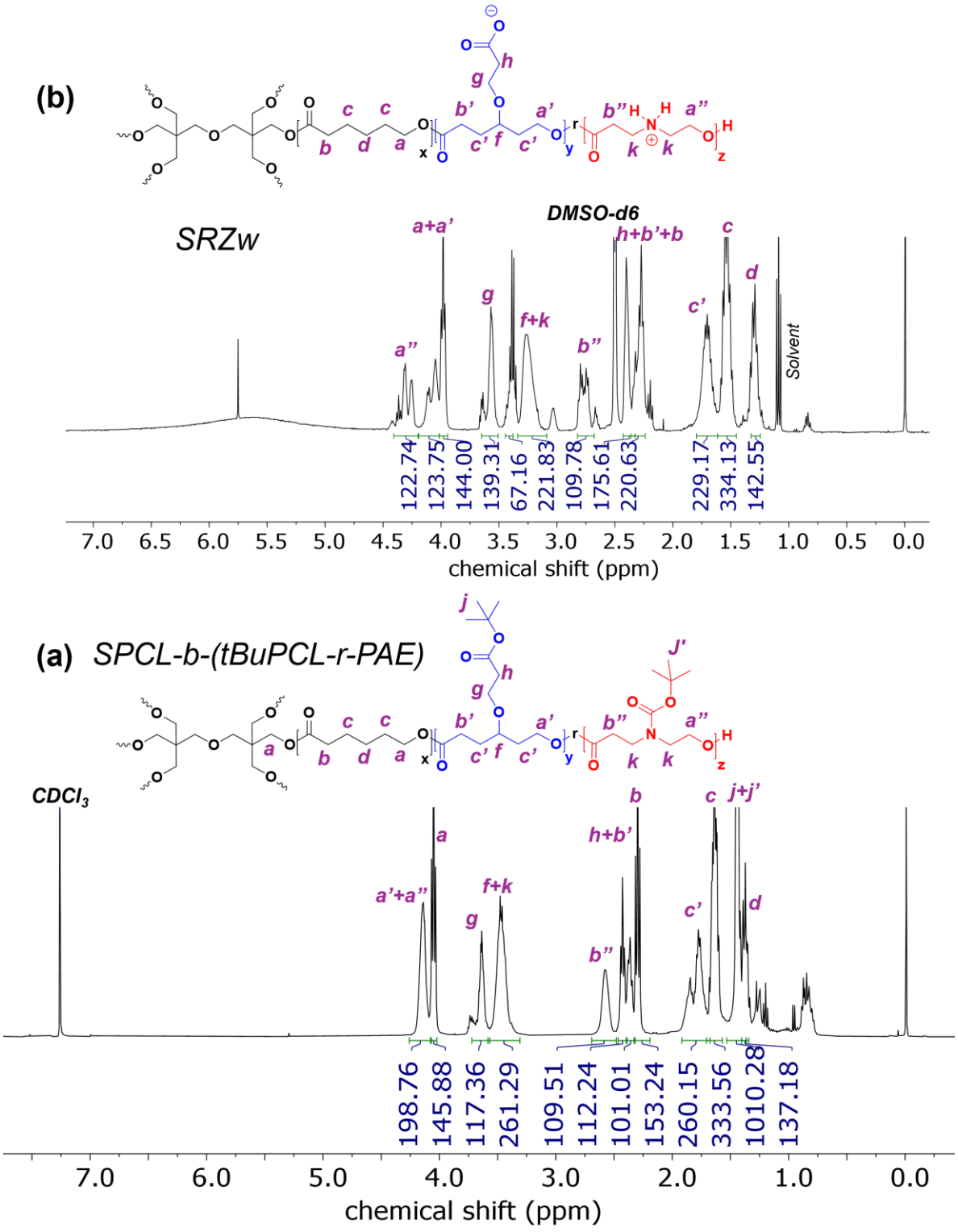

Figure S5.3: [1]HNMR plots of (a) SPCL-*b*-(tBuPCL-*r*-PAE) in *CDCl*$_3$. (c) SRZw in *DMSO-d*$_6$. **Note:** Peaks are assigned alphabetically. DP for SPCL-*b*-(tBuPCL-*r*-PAE) random copolymer was estimated by comparing integration of ***a*** protons corresponding to -C**H**$_2$-O-CO- of SPCL macroinitiator with protons ***b"*** of PAE and ***h+b'*** protons of *t*BuPCL. Deprotection was successfully confirmed by the disappearance of ***j*** and ***j'*** protons (tButyl groups) in SRZw.

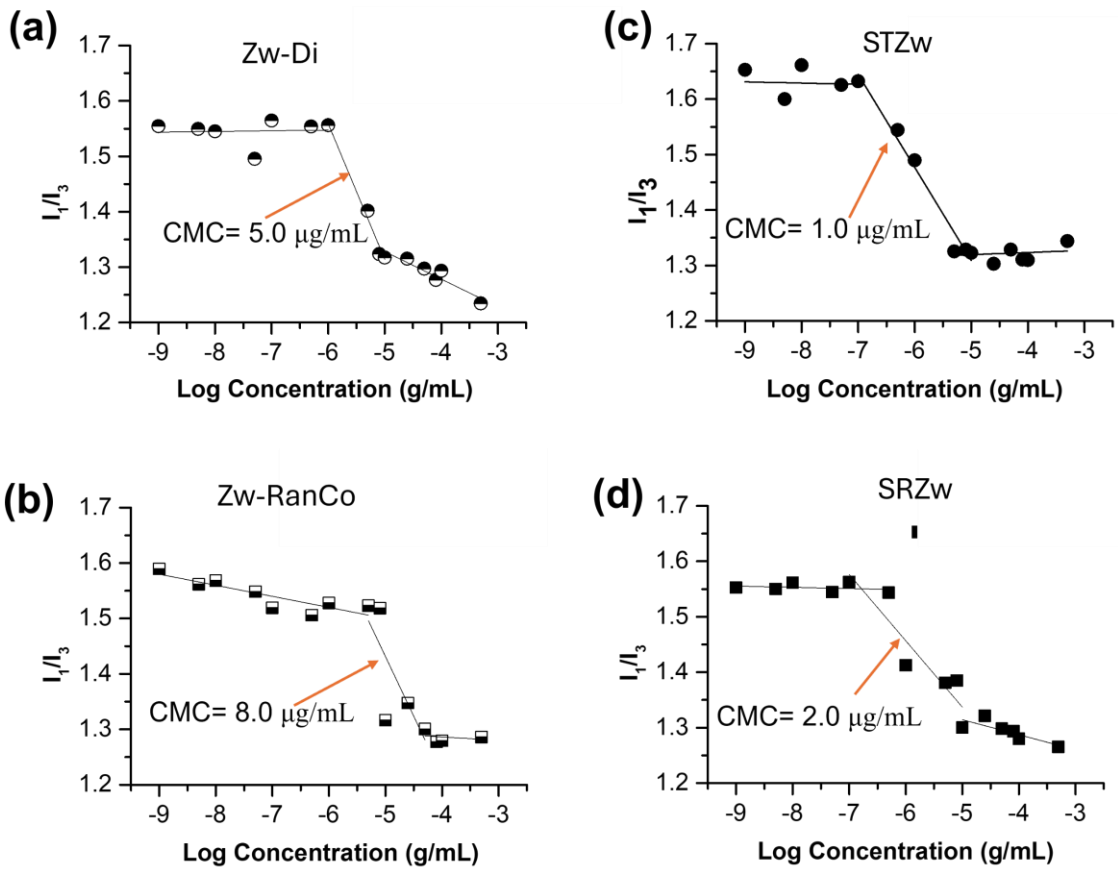

Figure S5.4: CMC plots of star zwitterionic polymers.

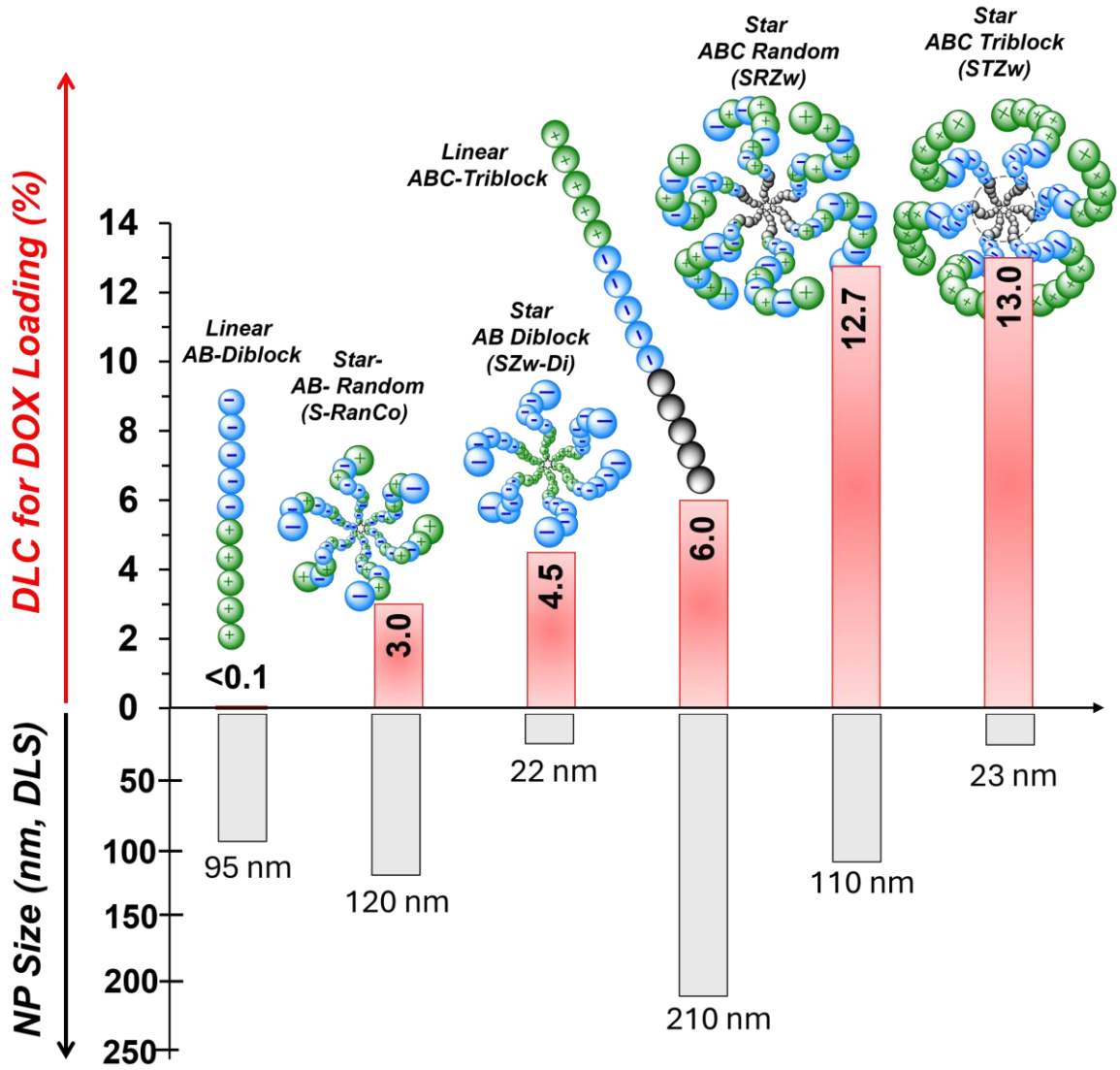

Figure S5.5: Comparative drug loading content and sizes of linear and star zwitterionic polymers.